Radio over Fiber (RoF) for the future home area networks

Joffray Guillory

UNIVERSITY OF PARIS-EST
DOCTORAL SCHOOL MSTIC
MATHEMATIQUES, SCIENCES ET TECHNOLOGIES DE
L'INFORMATION ET DE LA COMMUNICATION

P H D T H E S I S

to obtain the title of

Ph.D. of Science

of the University of Paris-Est
Specialty : Electronics, Optronics and Systems

Defended by

Joffray GUILLORY

Radio over Fiber for the future Home Area Networks

Thesis Advisor: Catherine ALGANI and Anna PIZZINAT

Prepared at Conservatoire National des Arts et Métiers (CNAM)
ESYCOM laboratory
and at France Télécom R&D - Orange Labs
RESA/ANA/ASHA Team

Defended on October 30, 2012.

Jury:

Reviewers:	Pr. Béatrice CABON	-	INPG - IMEP (France)
	Pr. Giovanni TARTARINI	-	University of Bologna (Italy)
Advisors:	Pr. Catherine ALGANI	-	CNAM - ESYCOM (France)
	Dr. Anna PIZZINAT	-	Engineer, France Télécom (France)
Examinators:	Dr. Éric TANGUY	-	University of Nantes - IETR (France)
	Dr. Stéphane FORMONT	-	Engineer, Thales (France)
Invited:	Dr. Benoît CHARBONNIER	-	Engineer, France Télécom (France)

Acknowledgments

First, I would like to thank ***Sylvain Meyer*** who has given me the opportunity to work on this topic and who has followed me during my first Ph.D. year. Thanks for all his advices and the work made together. Then, I wish to express my gratitude to ***Anna Pizzinat*** from France Télécom R&D - Orange Labs, my CIFRE (Convention Industrielle de Formation par la Recherche) advisor, who has followed me during my Ph.D. years. Her support was valuable, she has trusted me in all my initiatives and she has let me supervise two interns, Yacine Ait Yahia and Khalil Chikha. Thank you both too for all the work we have made together.

I also want to thank my university advisor, ***Catherine Algani*** from CNAM, who has read all my papers and my manuscript with all her attention. I have appreciated this invaluable help and the suggestions provided.

During these three last years, I had the honor of participating actively in the French collaborative project ORIGIN. I want to thank all its members for all the technical discussions we have exchanged. I think to Camilla Kärnfelt, Michel Ney, Daniel Bourreau, Adonis Bikiny, Gaëtan Guével, HongWu Li, Éric Tanguy, Guillaume Lirzin, Anne Chousseaud, Christophe Canepa, Grégory Gougeon. A special thanks to Anne-Laure Billabert for the exchanges we had about the RoF simulations she conducts, to Jean-Luc Polleux for its suggestion about analog characterizations, to Marc Brunet for all the electronic cards he has conceived for my work and for the ORIGIN project and to Yannick Paugam for the demonstration made together at JCOM 2012. A special thanks also to Carlos Viana and Marc Rosales for all the measurements we have made together, but also for their friendship. With all of you, I have learnt a lot. I hope we will have other opportunities to work together.

Additionally, I would like to thank my colleagues from Orange Labs for the support that I received. In particular, I think to the RESA/ANA/ASHA team: Luiz Anet Neto for all the discussions we had about OFDM, Jacky Etrillard and Benoît Charbonnier for the technical exchanges, Philippe Guignard and Francis Richard for our cooperation on the multiservice and multiformat topic, Naveena Genay my dear office colleague, Philippe Chanclou, Laurent Guillo, Bertrand Le Guyader, Bernard Landousies, Stéphane Gosselin, Fabienne Saliou, and all those I might forget. I also want to thank Noëlla Evanno, Daniel Lecoq, Olivier Bouffant, Abdelhak Graoui from the RESA/DEAN/OCI team, David Bernard from RESA/WASA/WIDE and Isabelle Siaud from RESA/WASA/CREM.

Lastly, I offer my gratitude to Béatrice Cabon, Giovanni Tartarini, Éric Tanguy, Stéphane Formont and Benoît Charbonnier for serving on my committee and for reading this thesis.

Abstract

Title: "Radio over Fiber for the future Home Area Networks".

The evolution of the Home Area Network (HAN) is lead by the proliferation of connected devices inside the home and the deployment of high broadband access network which now allows the delivery of services that can exceed 1Gbit/s. To ensure efficient in-house exchanges, the HAN has to move rapidly toward multi-Gigabit/s connections, in particular the wireless connectivity generally preferred by the customers. Current wireless systems have limited capacities, but new radio standards delivering data-rates up to 7Gbit/s are emerging. Nevertheless, as they address the unlicensed millimeter-wave band, from 57 to 66 GHz, their radio coverage is limited to a single room. Indeed, at such frequencies, the free-space losses are high and the waves do not cross the walls.

This thesis proposes to solve this problem by means of the Radio over Fiber (RoF) technology. This consists in capturing the 60GHz radio signals emitted in one room, transposing them on optical signals for transmission through optical fibers, and reemitting them in another room. Thus, several RoF transducers will be installed in the home and interconnected by a suitable optical infrastructure to create systems acting at the same time as repeaters and as distribution systems. From the viewpoint of the HAN market, such systems will be competitive only if they are low cost. As a consequence, this work focuses on direct modulation with direct detection (IM-DD) at Intermediate Frequency (IF). In other words, the 60GHz signal is down-converted at a lower frequency around 5GHz before the laser modulation and up-converted to 60GHz after the photodetection. Concerning the optical fiber, silica multimode fiber (MMF) is privileged as it allows the use of low cost and largely available optoelectronic devices working at 850nm.

The thesis proposes different RoF architectures, from point-to-point interconnecting two single rooms to multipoint-to-multipoint acting as logical buses over the building. After an analog characterization of the optoelectronic components, the RoF link and the domestic cable, these architectures are designed, built and characterized step by step using OFDM modulation according to existing wireless 60GHz standards. Real-time transmissions between commercial devices have also been performed to validate these architectures.

Moreover, advanced RoF infrastructures are proposed. First, the RoF systems can be easily improved if the access to their optical media is managed by the radio MAC layer. This approach is therefore studied showing its feasibility. Secondly, an optical system, seen by users as a premium product, has to support the legacy home services commonly used as well as the new ones that could emerge in the future. Thus, innovative multiservice and multiformat infrastructures conveying on a unique optical cable wired IP data, broadcast terrestrial or satellite television, the 60GHz wireless connectivity, and specific formats as HDMI signals are proposed and tested.

Keywords: Optical communications - Wireless communications - Radio over Fiber (RoF) - Home Area Network (HAN) - Millimeter-waves - Intensity Modulation with Direct Detection (IM-DD) - Multimode fiber (MMF).

Résumé

Titre : « Radio sur Fibre pour les futurs Réseaux Locaux Domestiques ».

L'évolution des Réseaux Locaux Domestiques (RLD) est influencée par l'augmentation irréfrénée du nombre de terminaux connectés dans nos domiciles et par le déploiement de réseaux d'accès optiques haut débit qui délivrent désormais des services dépassant le Gigabit/s. Pour continuer à échanger efficacement les données, les RLD doivent évoluer vers le multi-Gigabit/s, et plus particulièrement la très appréciée connectivité sans fil. Les systèmes radio actuels ont des capacités limitées, néanmoins de nouveaux standards dont le débit excède 7Gbit/s voient le jour. Mais comme ces derniers exploitent la bande millimétrique, entre 57 et 66 GHz, leur couverture radio est limitée à la taille d'une pièce. En effet, à de telles fréquences, les pertes en espace libre sont très élevées et les ondes ne traversent pas les murs.

Cette thèse propose de résoudre cette limitation au moyen de solutions Radio sur Fibre (RoF pour *Radio over Fiber*). Cette technique consiste à capturer les signaux radio émis dans une première pièce, puis à les transposer sur des signaux optiques pour les transmettre par fibre optique jusqu'à une seconde pièce où ils seront réémis. Plusieurs transducteurs RoF seront donc installés dans le domicile et interconnectés entre eux au moyen d'une infrastructure optique adaptée, créant ainsi des systèmes se comportant à la fois comme répéteurs and comme système de distribution. Pour le marché du RLD, de telles solutions sont compétitives seulement si elles sont bas coût. Par conséquent, ce travail se focalise sur la modulation directe avec détection directe (IM-DD) en Fréquence Intermédiaire (FI). En d'autres termes, le signal radio à 60GHz est translaté à une plus faible fréquence, autour de 5GHz, pour moduler directement un laser, puis il est restitué à 60GHz après la détection directe. Concernant la fibre optique, la multimode silice (MMF) est privilégiée puisqu'elle permet l'utilisation de composants optoélectroniques bas coût et largement disponibles.

Cette thèse propose différentes architectures RoF, du point-à-point reliant deux pièces au multipoint-à-multipoint agissant comme un bus logique à travers le bâtiment. Après une caractérisation analogique des composants optoélectroniques, du lien RoF et du câble domestique, ces architectures sont construites et caractérisées étape par étape sur la base d'une modulation OFDM conforme aux standards radio 60GHz. Des transmissions temps réel entre terminaux commerciaux sont également réalisées afin de valider ces architectures.

Pour finir, des infrastructures RoF avancées sont proposées. Premièrement, les systèmes RoF peuvent être améliorés si l'accès à leur couche optique est contrôlé par la couche MAC radio. Cette approche est donc étudiée, démontrant ainsi sa faisabilité. Deuxièmement, les systèmes optiques, perçus par les utilisateurs comme des produits premium, doivent supporter aussi bien les services de base du RLD que ceux qui vont émerger dans les années à venir. Ainsi, des infrastructures multiservice et multiformat innovantes transportant sur un unique câble optique des données IP, la télévision hertzienne et satellite, les signaux radio 60GHz et d'autres formats spécifiques tels que l'HDMI sont proposées puis testées.

Mots clés: Communications optiques - Communications sans fil - Radio sur Fibre (RoF) - Réseau Local Domestique (RLD) - Ondes millimétriques - Modulation directe avec Détection directe (IM-DD) - Fibre multimode (MMF).

Table of Contents

List of Figures

List of Tables

Nomenclature

3GPP	3rd Generation Partnership Project
a.u.	arbitrary unit
ABF-T	Association Beamforming Training
AC	Alternating Current
ACK	Acknowledgement
ACR	Attenuation to Crosstalk Ratio
ADC	Analog to Digital Converter
AFC	Automatic Frequency Control
AGC	Automatic Gain Control
AID	Association ID
ANSI	American National Standards Institute
AP	Access Point
APC	Angled Physical Contact
AT	Announcement Time
AV	Audio/Visual
AWG	Arrayed-Waveguide Grating
B&S	Broadcast and Select
Balun	Balanced - Unbalanced
BF	Beamforming
BI	Beacon Interval
BSS	Basic Service Set
BSSID	Basic Service Set Identification
BT	Beacon Time
CBP	Contention Based Period
CDF	Cumulative Distribution Function
CDOWN	Down-Counter
CDWM	Coarse Wavelength-Division Multiplexing
CES	Consumer Electronic Show
CIFRE	Convention Industrielle de Formation par la Recherche
CNAM	Conservatoire National des Arts et Métiers

CO	Central Office
CP	Control PHY
CPR	Chirp-to-Power Ratio
CS	Central Station
CSMA/CA	Carrier Sense Multiple Access/Collision Avoidance
CSR	Carrier to Signal Ratio
CYTOP	CYclic Transparent Optical Polymer
D	Destination station
DAA	Detect And Avoid
DAC	Digital to Analog Converter
DC	Direct Current
DFB	Distributed FeedBack laser
DFC	Distributed Coordination Function
DFT	Discrete Fourier Transform
DGCIS	Direction Générale de la Compétitivité, de l'Industrie et des Services
DIFS	DCF Interframe Space
DIY	Do It Yourself
DMD	Differential Mode Delay
DR	Dynamic Range
DRB	Dual-Rail Bipolar
DSB	Double SideBand
DSB-SC	Double-SideBand with Suppressed Carrier
DSO	Digital Storage Oscilloscope
DSP	Digital Signal Processing
DTT	Data Transfer Time
DVB-T	Digital Video Broadcasting-Terrestrial
E/O	Electro-Optic
EAM	Electro-Absorption Modulator
ECMA	European Computer Manufacturers Association
EDC	Electronic Dispersion Control
EDCA	Enhanced Distributed Channel Access
EIA	Electronic Industries Alliance
EIRP	Equivalent Isotropically Radiated Power
ELFEXT	Equal Level Far End Crosstalk
EMF	Electro-Magnetic Fields
EMI	Electromagnetic Interference
ENA	Electrical Network Analyzer

Er:Yb	Erbium Ytterbium
ESA	Electrical Spectrum Analyzer
ESYCOM	Électronique, SYstèmes de COmmunications et Microsystèmes
FC	Ferrule Connector
FCC	Federal Communication Commission
FD/AF	Full-Duplex / Amplify and Forward
FDM	Frequency-Division Multiplexing
FEC	Forward Error Correction
FEXT	Far End Crosstalk
FFT	Fast Fourier Transform
FP	Fabry-Pérot
FSAN	Full Service Access Network
FSR	Free Spectral Range
FST	Fast Session Transfer
FTTH	Fiber To The Home
FWQM	Full Width at Quarter Maximum
GaAs	Gallium Arsenide
GI	Graded Index
GI	Guard Interval
GMSK	Gaussian Minimum Shift Keying
GP	Grant Period
GS	Glass Substrate
GUI	Graphical User Interface
HAN	Home Area Network
HbbTV	Hybrid broadband broadcast television
HD	High Definition
HD/DF	Half-Duplex / Decode and Forward
HDMI	High Definition Multimedia Interface
HomePNA	Home Phoneline Networking Alliance
HPA	High Power Amplifier
HPT	Heterojunction bipolar Photo-Transistors
HRP	High Rate Physical
HSI	High Speed Interface
I/O	Input/Output
IBSS	Independent Basic Service Set
ID	Identity
IEC	International Electrotechnical Commision

IEEE	Institute of Electrical and Electronics Engineers
IETR	Institut d'Électronique et de Télécommunications de Rennes
IF	Intermediate Frequency
IFoF	Intermediate Frequency over Fiber
IIP3	Input Third-order Intercept Point
IM-DD	Intensity-Modulation with Direct-Dectection
IM3	Third-order Intermodulation
IMC	Impedance Matching Circuit
IMEP	Institut de Microélectronique, Electromagnétisme, Photonique
InGaAs	Indium Gallium Arsenide
INPG	Institut National Polytechnique de Grenoble
IP	Internet Protocol
IP3	Third-order Intercept Point
IPCP	Inter-Period Correlation Processing
ISI	Inter-Symbol Interferences
ISM	Industrial Scientific Medical
ISO	International Organization for Standardization
ITU-T	International Telecommunication Union's standardization
LAN	Local Area Network
LC	Lucent Connector
LCA	Levin-Campello Algorithm
LED	Light Emitting Diode
$LiNbO_3$	Lithium Niobate
LNA	Low Noise Amplifier
LO	Local Oscillator
LOS	Line Of Sight
LP	Linear Polarization
LRM	Long Reach Multimode
LRP	Low Rate Physical layer
LTE	Long Term Evolution
MAC	Medium Access Control
MCS	Modulation and Coding Scheme
MER	Modulation Error Ratio
MGWS	Multi-Gigabit/s Wireless Systems
MIMO	Multiple-Input Multiple-Output
ML-FPL	Mode-Locked Fabry-Pérot Laser
MLL	Mode-Locked Laser

MMF	Multimode Fiber
MMIC	Monolithic Microwave Integrated Circuit
MoCA	Multimedia over Coax. Alliance
MS	Multiformat Switch
MSTIC	Mathématiques, Sciences et Technologies de l'Information et de la Communication
MZM	Mach Zehnder Modulator
NAS	Network Attached Storage
Nd:YAG	Neodymium-doped Yttrium Aluminium Garnet
NEP	Noise Equivalent Power
NEXT	Near End Crosstalk
NF	Noise Figure
NICT	National Institute of Information and Communications Technology
NLOS	Non Line Of Sight
NRZ	Non Return to Zero
NRZI	Non Return to Zero Inverted
O/E	Opto-Electronic
OADM	Optical Add and Drop Multiplexer
OCS	Optical Carrier Suppression
OFDM	Orthogonal Frequency-Division Multiplexing
OIP3	Output Third-order Intercept Point
OLT	Optical Line Terminal
ONT	Optical Network Terminal
ONU	Optical Network Unit
ORIGIN	Optical-Radio Interface for Gigabit Indoor Networks
OSA	Optical Spectrum Analyzer
PAPR	Peak to Average Power Ratio
PBSS	Personal Basic Set Service
PC	Physical Contact
PCB	Printed Circuit Board
PCI	Peripheral Component Interconnect
PCIe	Peripheral Component Interconnect express
PCP	PBSS Control Point
PDF	Probability Density Function
PER	Packet Error Rate
PHY	Physical layer
PIN	P-type, Intrinsic, N-type
PLL	Phased-Locked Loop

PMMA	PolyMethyl MethAcrylate
PoE	Power over Ethernet
POF	Plastic Optical Fiber
PON	Passive Optical Network
PP	Polling Period
ppm	part per million
PRBS	Pseudo-Random Binary Sequence
PSD	Power Spectral Density
RA	Receiver Address
RF	Radio Frequency
RGB	Red Green Blue
RIN	Relative Intensity Noise
RLS	Relay Link Setup
RMS	Root Mean Square
RoF	Radio over Fiber
ROSA	Receiver Optical Sub-Assembly
RS	Relay Station
RSS	Responder Sector Sweep
RSUS	Relay Supportable Station
RUS	Relay Usable Stations
RXSS	Receive Sector Sweep
RZ	Return to Zero
S	Source station
SC	Single Carrier
SC	Square Connector
SER	Symbol Error Rate
SFP	Small Form Pluggable
SI	Step Index
SIFS	Short Interframe Space
SiGe	Silicon Germanium
SLS	Sector Level Sweep
SMF	Singlemode Fiber
SMSR	Side-Mode Suppression Ratio
SOA	Semiconductor Optical Amplifier
SP	Service Period
SP	Sub-Projects
SPL	Self-Pulsating Laser

SPR	Service Period Request
SS	Sector Sweep
SS-Feedback	Sector Sweep Feedback
SSB	Single SideBand
STA	Station
TA	Transmitter Address
TDLS	Tunneled Direct Link Setup
TDM	Time-Division Multiplexing
TDMA	Time Division Multiple Access
TEM	Transverse Electro-Magnetic
TFC	Time-Frequency Code
TGac	Task Group ac
TGad	Task Group ad
Ti:Al_2O_3	Titanium Sapphire
TIA	Telecommunications Industry Association
TIA	Transimpedance Amplifier
TOSA	Transmitter Optical Sub-Assembly
TTL	Transistor-Transistor Logic
U-NII	Unlicensed National Information Infrastructure
USB	Universal Serial Bus
UWB	Ultra-WideBand
VCSEL	Vertical Cavity Surface-Emitting Lasers
VHT	Very High Throughput
VNA	Vector Network Analyzer
VOD	Video on Demand
VoIP	Voice over IP
WDM	Wavelength-Division Multiplexing
WGA	Wireless Gigabit Alliance
Wi-Fi	Wireless Fidelity
WiGig	Wireless Gigabit Alliance
WiMAX	Worldwide Interoperability for Microwave Access
WLAN	Wireless Local Area Network

Introduction

Since the late 1990s, wireless technologies have been developed to replace the wires installed in the Home Area Networks (HAN). One of the most successful interfaces is the IEEE 802.11 standards also known as Wi-Fi. The current generation can achieve theoretically up to 600Mbit/s, but in the coming years higher data rates will be needed. Indeed, the ability to deliver high bit rate services through the optical access networks and the increasing needs in terms of device interconnection inside the home will boost the throughput requirements. And this tendency will keep growing as new usage models arrive continuously: thus, the instantaneous data rate in the HAN could reach 10Gbit/s. As a result, these last years, new wireless technologies appeared.

The current Wi-Fi technologies exploit the 2.4 or the 5 GHz unlicensed bands, but because these frequencies know a huge success, they tend to become very saturated. To preempt this and increase the connection speeds, the industrials are going towards the unlicensed millimeter-wave band, from 57 to 66 GHz. This band is widely available around the world, it is not yet massively used, it offers large channels of 2.16GHz bandwidth with high authorized emitted powers and it allows advanced integration into radio terminals thanks to miniaturization at such frequencies. Thus, wireless systems able to achieve data rate up to 7Gbit/s and dedicated to HAN are emerging or are under development. With this speed, users can really start to replace every domestic cable they use, even High Definition Multimedia Interface (HDMI) cables that convey uncompressed High Definition (HD) video signals.

Recently, in 2009, the IEEE 802.11ad group has been created dealing with 60GHz components for IEEE 802.11 family systems. It should lead the competition that occurs between industrials thanks to Wi-Fi certification. Additionally, the first Wi-Fi 60GHz chipsets are expected at the second half of 2013, and by 2016 they could account for more than 40% of the total Wi-Fi market [41].

However, these wireless systems have a coverage limited to a single room and to a small indoor open area due to the high propagation attenuation at 60GHz and to non-propagation of millimeter-waves across the walls. Therefore, the main challenge to be resolved by this thesis consists in finding solutions to extend the radio coverage to the entire HAN, and to interconnect wireless devices located in different rooms.

⋆ ⋆ ⋆

This thesis is divided into five chapters. In the first chapter, the HAN background is described. It is explained that multi-Gigabit/s data rates will be required in the future and that the current domestic standards are not ready. In this context, the optical fiber has an opportunity to introduce the HAN as its backbone, in particular against solutions based on existing home wiring or on wireless technologies. The optical fiber is a promising solution, but not for the final connectivity to the devices since it will be difficult for the customers to come back to wired terminals: this is not adapted to all the situations. Therefore, popular Multi-Gigabit/s Wireless Systems (MGWS) have to emerge.

After a brief state of the art of the current wireless standards exploiting the centimeter-wave bands, as well as a description of their radio modulation methods, Single Carrier (SC) and Orthogonal Frequency-Division Multiplexing (OFDM), an overview of the rich 60GHz ecosystem is drawn. Solutions to improve the radio coverage of the MGWS are presented. However, as these solutions are not completely satisfactory, a new way has to be explored.

In the second chapter, Radio over Fiber (RoF) architectures distributing 60GHz radio signals to several access points spread around the home and connected by a suitable optical infrastructure are

proposed. Several studies have already been carried out on RoF transmission techniques for 60GHz applications. Consequently, the state of art of the main methods proposed in the literature is described, then the solution the most adapted to the domestic constraints is identified. From the viewpoint of the HAN market, a RoF system can represent a competitive solution only if it is easy to deploy and if the RoF transducers are low cost and compact. As a result, this thesis is focused on direct modulation working at Intermediate Frequency (IF) with direct detection. In other terms, the millimeter-wave signal is down-converted at a lower frequency before modulating the optical source, then it is up-converted to 60GHz after the photodetection. This allows the use of low cost and largely available optoelectronic components designed for silica multimode fibers (MMF).

Besides, the optical infrastructure buried in the walls has to be transparent and able to adapt to the future wireless systems for several years since the lifetime of the radio standards is much shorter than the lifetime of a house. Therefore, the home network physical architecture has to be properly chosen. Different RoF architectures are proposed, from point-to-point to multipoint-to-multipoint, and analyzed in terms of transparency to the radio standards, throughputs they can support, power consumption, number of fibers they need and number of rooms they can cover. The technical impairments associated to each architecture are also taken into account, as multipath, echo, coupling, local oscillator, propagation delay and optical issues. Lastly, an inventory of possible solutions for each issue is proposed.

In chapters 3 and 4, the experimental work is organized as follows: after an analog characterization of the optoelectronic components, of the RoF link and of the domestic cable, the different RoF millimeter-wave wireless architectures are designed, implemented and tested using an OFDM modulation.

Chapter 3 is devoted to measurements and performance comparisons of different optoelectronic components that can be used in the RoF systems; principally, but not only, VCSELs and PIN photodiodes working at 850nm. Highly linear components are required since a direct modulation method with a direct detection will be used. To adopt the best components, accurate static (laser L-I curve, laser optical spectrum, photodiode I-V curve) and dynamic (S-parameters) characterizations are performed. The noises inherent to the RoF links are also measured, for small signal (Relative Intensity Noise, thermal noise and shot noise) and large signal (third-order intermodulation). It has to be underlined that different experimental methods have been proposed and experimented, particularly to determine the RIN and the non-linearity distortions, then compared to theoretical calculations.

In chapter 4, the proposed RoF architectures are realized and characterized using digital OFDM modulation according to existing wireless 60GHz standards. The performances of the RoF systems are quantified by means of three quality metrics: the Bit Error Rate (BER), the Signal to Noise Ratio (SNR) and the Error Vector Magnitude (EVM). The relationship among them is first deeply studied, then, the proposed RoF architectures are built and characterized step by step: from a direct radio link at IF taken as the baseline, a millimeter-wave free space propagation is added, then the different architectures are tested. All the results are analyzed, and as a final point, a real-time transmission between two commercial WirelessHD devices is performed to further validate all the architectures.

In chapter 5, advanced RoF infrastructures are proposed. First, a management of the optical media is presented in order to improve the quality of the RoF transmissions and minimize the Electro-Magnetic Fields (EMF) exposure. Between all the rooms of a home, i.e. all the RoF transducers, only the optoelectronic components that have to transmit or receive a radio signal are turned-on. An elegant solution proposed in this work consists in managing the access of the optical medium by reading information from the radio MAC layer in order to know the key parameters on ongoing communications. To have an efficient and implementation-friendly solution, the beamforming (BF) process introduced in the 60GHz radio standards is reused. The feasibility of this approach is theoretically studied on the basis of the IEEE 802.11ad radio MAC layer.

Lastly, the HAN is the convergence point of several worlds: computers, consumer electronics, television, etc... Consequently, the need for high capacity is not the only issue, another major challenge lies in the great heterogeneity of the signals to be delivered to the various home devices. Thus, advanced RoF infrastructures taking also into account a wireline connectivity like Ethernet, RF signals for broadcast terrestrial or satellite television and specific formats as HDMI signals are proposed. Thus, multiservice and multiformat architectures conveying on a unique optical cable all these services are

experimentally demonstrated.

It has to be noted that the work carried out in this thesis has allowed to fix the specifications and the design of integrated RoF transducers realized in the French collaborative project ORIGIN (Optical-Radio Interface for Gigabit Indoor Networks).

In the last section, the work is concluded and future tasks are discussed. To resume, this thesis investigates Radio over Fiber architectures for the future Home Area Networks taking into account the most advanced radio standards, low cost optoelectronic components made for multimode fiber, advanced management of the optical infrastructures, and multiservice and multiformat compatibility.

Chapter 1

Context of the thesis: state-of-the art of Multi-Gigabit/s wireless networks

1.1 The future Home Area Network

1.1.1 Evolutions lead by internal exchanges

The Home Area Network (HAN) is the part of the network located at home. Its main function consists in managing a large set of services, including the Internet, and distributing them to the different rooms of the house. This assignment becomes complex as today the number of connected devices inside the home increases, and each of them requires more and more of data rates. This tendency will keep growing in the next years since new services and new usages appear continuously. For instance, a High Definition (HD) film stored on a Network Attached Storage (NAS) can be read on a laptop, pictures can be sent from a computer to a television screen, or a game can be started on a gaming console to be finished on a smartphone. The revolution of the smart devices is occurring: more and more products have a network connection and simple things such as personal assistant (Karotz from Mindscape), weigh-scale (Body scale from Withings), toys (AR Drone from Parrot), etc... become a part of the domestic network [42]. That changes the way to conceive the HAN since consumers use a same network to connect all these products. The general trend goes towards the use of these devices everywhere at home with high data rate connectivity between them and with a domestic cloud based on a home mass storage server (a NAS or an advanced gateway). As a consequence, the amount of data exchanged in the HAN should drastically increase in a near future [43].

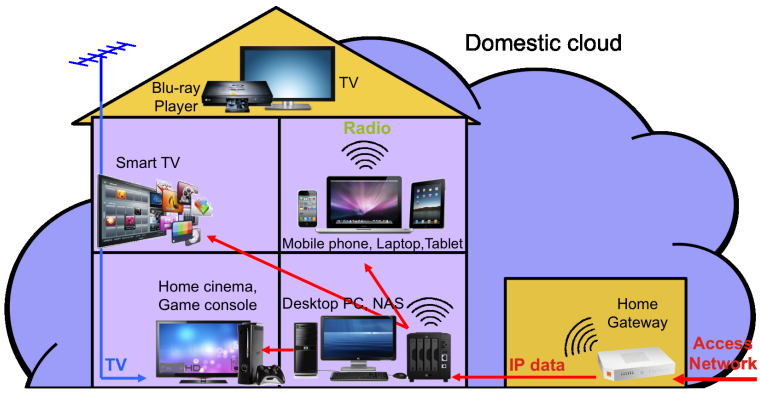

Figure 1.1: A typical connected house with multiple devices.

As proof of the amount of data exchanged, Universal Serial Bus (USB) 3.0 supports speed up to 5Gbit/s [44] and Thunderbolt supports speed up to 10Gbit/s [45]. So the data transmissions go towards multi-Gigabit/s flows to synchronize the mobile devices or connect a NAS to a computer. In a same time, these high speed devices use more and more networking. If all the current network cards are

compatible with 1Gbit/s Ethernet (1000Base-T) or with ∼300Mbit/s wireless connectivity (the IEEE 802.11 family), the market has to evolve toward multi-Gigabit/s network connectivities to substitute the usual cable and transport the future services.

One of the most demanding services is the exchange of uncompressed HD videos. In fact, a simple 16:9 picture in 1080p coded with 24 bits per pixel (i.e. RGB color coded over 8 bits) at 60Hz requires a data speed close to 3Gbit/s (equation 1.1). Figure 1.2 clearly shows the throughput that have to be supported to substitute the High Definition Multimedia Interface (HDMI) cables [1].

$$\begin{aligned} HD\ video\ data\ rates &= H_{pixels} \times V_{pixels} \times f_{refresh} \times D_{bits/pixel}. \\ &= (16/9 \times 1080) \times 1080 \times 60 \times 24 \\ &= 2.986\, Gbit/s. \end{aligned} \tag{1.1}$$

where,

- H_{pixels} is the number of vertical lines (horizontal resolution).
- V_{pixels} is the number of horizontal lines (vertical resolution).
- $f_{refresh}$ is the number of frames per second.
- $D_{bits/pixel}$ is the number of bits coding one pixel.

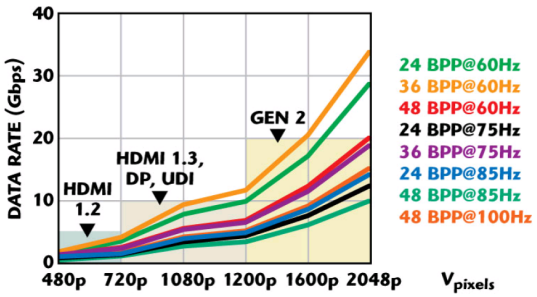

Figure 1.2: HDMI data rates, from [1].

Another example for the need of high data rates and for the diffusion of the connected devices to the whole home is the interactive (or smart) television. As foreseen by figure 1.3 and as explained in [46], its use will explode in the next five years, with already first overviews of the future such as, for instance, the Hybrid broadband broadcast television (HbbTV) initiative [47] that has been shown during the tennis tournament of Roland-Garros in 2011: real-time scores, match statistics, bios of all players, news, photos and a Twitter stream were broadcasted to the users through the Internet. It is expected that, in 2015, between 47% [2] and 67% [48] of all flat panel televisions shipped worldwide will have a network connectivity. This proportion of connected television is also growing thanks to additional devices that bring the Internet connectivity to the television such as the gaming consoles (Xbox, Wii or Playstation), the operators' set-top boxes, or the Apple TV and Google TV media players.

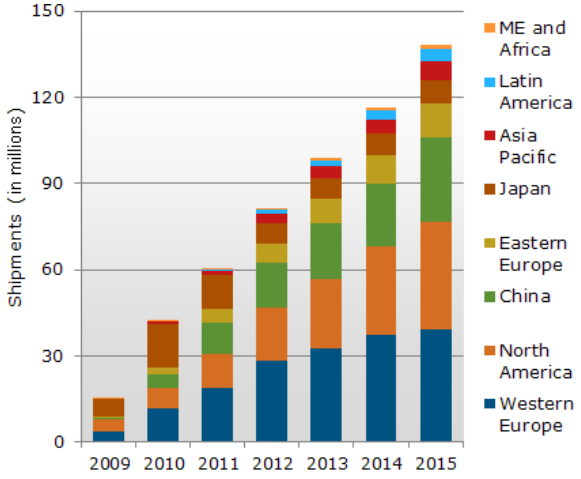

Figure 1.3: DisplaySearch connected television forecast, from [2].

To answer adequately to the consumers' aspirations regarding the home of the future, HANs require stable and high throughput, but also very low latency for interactive services such as online gaming, applications using client/server architectures [49], or telepresence.

1.1.2 Evolutions lead by high broadband access networks

The ultimate goal for a provider of telecommunications like Orange, is to satisfy the demand made by these new services, like remote backup, video conference, Video on Demand (VoD), Voice over IP (VoIP), data exchange in HD, ... Therefore, Fiber To The Home (FTTH) systems are currently deployed in the access network to answer effectively to the consumers' needs [50].

Two main optical access topologies can be deployed to interconnect the Central Office (CO) to the customers (figure 1.4), either point-to-point networks or Passive Optical Networks (PONs). In all the cases, these topologies consist in deploying a fiber from the provider's Optical Line Terminal (OLT) located in the CO and coordinating the transmissions to the customer's Optical Network Terminal (ONT). Sometimes, the ONT is also called Optical Network Units (ONU).

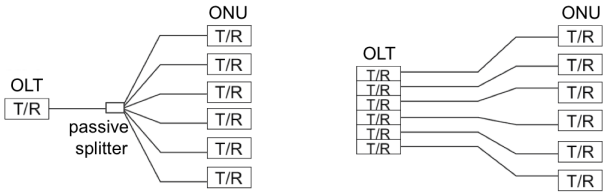

Figure 1.4: PON on the left and point-to-point network on the right.

In point-to-point networks, one fiber is used per user, with different wavelengths for upstream and downstream transmissions. On the contrary, in PONs, only one fiber is used between the CO and a passive splitter that splits and broadcasts a multiplex to all the users connected. As bandwidth is shared among users, data intended to, or coming from different users has to be multiplexed using a Time-Division Multiplexing (TDM), see figure 1.5. Other solutions are investigated for the future such as Wavelength-Division Multiplexing (WDM) or Frequency-Division Multiplexing (FDM)[1]. If a TDM or a FDM PON is deployed, the remote node is an optical splitter whereas if a WDM PON is deployed, the remote node is an Arrayed-Waveguide Grating (AWG) optical multiplexer (component combining and splitting optical signals of different wavelengths).

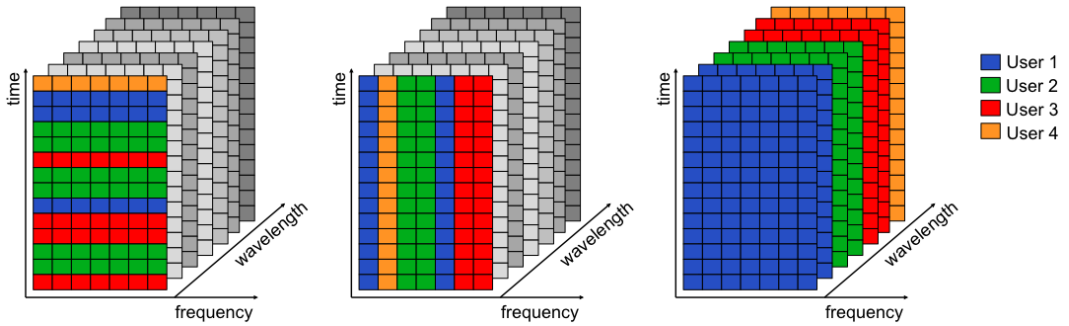

Figure 1.5: The different PON multiplex, TDM on the left, FDM in the middle, WDM on the right.

These high broadband optical systems, standardized by the Full Service Access Network / International Telecommunication Union's standardization (FSAN/ITU-T) and by the Institute of Electrical and Electronics Engineers (IEEE), are detailed in table 1.1. Theses PONs solutions are currently implemented by many operators through the world like in France where France Télécom - Orange deploys the GPON solution to deliver 100Mbit/s data rates per user in its commercial offers.

[1] Or variants such as Orthogonal Frequency-Division Multiplexing (OFDM).

Table 1.1: The different generations of PON Systems, from [36].

	Common names	Standards	Downstream	Upstream	Standardization
FSAN/ITU-T	APON	G.983.1/2	155Mbit/s	155Mbit/s	1995
	BPON	G.983.3-5	625Mbit/s	155Mbit/s	2000
	GPON	G.984.1-6	2.5Gbit/s	1.25Gbit/s	2001
	XGPON	NGA WP and NGA	10Gbit/s	10 or 2.5Gbit/s	2007
IEEE	1G-EPON	P802.3ah	1Gbit/s	1Gbit/s	2001
	10G-EPON	P802.3av	10Gbit/s	10 or 1Gbit/s	2007

FSAN/ITU-T is currently working towards the definition of a new generation PON driven by the enhancement of the delivered bandwidth. This next PON system, known as "Next Generation PON 2", will be based on four wavelengths working at 10Gbit/s (40Gbit/s aggregated) and operating under the same technical basis as the previous PON generations since each wavelength uses Time Division Multiplexing (TDM) / Time Division Multiple Access (TDMA) to manage the connectivity of N terminations to one optical port of the CO equipment.

To summarize, users will have soon high throughput at the input of their home. To avoid bottleneck in the HAN, the operators have also to ensure an efficient delivery of these data to the final user's devices. In other words, the HANs have to evolve rapidly.

1.1.3 Overview of the current HAN technologies

The need for high speed in-house exchanges increases due on the one hand to the interconnection of more and more devices at home and on the other hand to the deployment of high broadband systems in the access network. If today the Ethernet over copper pairs is the first response to the interconnection needs in the house, other solutions based on existing home wiring exist to convey the Internet Protocol (IP) signals.

- Two copper pairs with at least a category 5 specification to convey in full-duplex up to 100Mbit/s Ethernet (100Base-TX) over 100m.
- Four copper pairs with at least a category 5 specification to convey in full-duplex up to 1Gbit/s Ethernet (1000Base-T) over 100m.
- Powerline to convey IP data according to the ITU-T G.hn and IEEE Powerline standards and HomePlug (ratified IEEE's 1901 Broadband Powerline standard since 2010) solutions.
- Phoneline (cables at least category 3 compliant) to convey IP data according to the ITU-T G.hn standard and the HomePNA solutions (approved by the ITU-T as recommendations G.9951-4).
- Coaxial cable to convey IP data according to the ITU-T G.hn standard and the Multimedia over Coax. Alliance (MoCA), HomePNA and HomePlug solutions.

The market is fragmented among multiple technologies, but the recent ITU-T G.hn standard targets to unify this ecosystem with products supporting three wired options in one chip. The home solutions operating over several types of legacy home wires (G.hn, HomePNA, ...) are optimized for each medium: phone lines, coaxial cables and power lines. As a consequence, the data rates, provided in table 1.2, depend on the medium, and the practical delivered throughputs are generally less than the maximum speeds announced by the standards. For example, the HomePlug AV2 offers theoretically the Gigabit/s at the physical layer and 500Mbit/s at the MAC layer, in half-duplex. But the poor quality of the home existing wiring generally induces worse throughput, approximately 200Mbit/s for the power lines. In fact, these solutions are highly sensitive to the external noises such as the electrical interferences due to domestic devices. Globally, solutions based on existing home wiring are limited because they are conveyed on poor-quality cables subjected to Electromagnetic Interference (EMI) and because they have to coexist with xDSL on phone lines, with cable-modems and television services on coaxial cables, with amateur radio bands on power lines, etc... Finally, only category 5 copper pairs guarantee the bandwidth.

Table 1.2: Comparison between the main home wiring solutions. The indicated dates correspond to the standard realizations and the indicated throughputs are shared between the downlink and the uplink.

Solution	MoCA 2.0	HomePNA 3.1	HomePlug AV	HomePlug AV2	ITU-T G.hn
Date	June 2010	December 2006	August 2005	January 2012	October 2009
PHY rates	700 or 1400 Mbit/s	320Mbit/s	200Mbit/s	1Gbit/s	up to 1Gbit/s on coax
MAC rates	400 or 800 Mbit/s	200 or 140 Mbit/s	100Mbit/s	500Mbit/s	-
Notes	Two modes: Basic and Enhanced.	lower MAC throughput over phone lines.		Not again massively deployed.	Three wired options unified in one chip. Not yet deployed.

Another point has to be considered: the wireless connectivity is generally preferred for the final link to the device because the users find it more convenient and more flexible. After the 300Mbit/s data rate available today with the Wi-Fi (Wireless Fidelity) IEEE 802.11n, the trend is moving towards new standards that can achieve bit-rates up to 1Gbit/s in the centimeter-wave band, [3.1 - 10.6] GHz, and up to 7Gbit/s in the millimeter-wave band, [57 - 66] GHz. The associated technologies are described in part 1.3 in details as they represent one of the major topics of this manuscript. It has just to be noted that developing Multi-Gigabit/s Wireless Systems (MGWS) for the home is essential because it will be difficult for the customers to come back to wired terminals or to stay at low data rates.

Lastly, it has to be noted that the home is not only constituted of IP signals as it is the convergence point of several worlds: computers, consumer electronics, television, etc... Consequently, another major challenge lies in the great heterogeneity of signals to deliver to the various home devices: IP data for triple play services, Radio Frequency (RF) signals for broadcasted television (cable, terrestrial and satellite), specific formats as HDMI signals, etc... Today, all these signals are transmitted separately as they cannot be encapsulated in a unique format, and specific networks working on specific media are dedicated to each application. For example, Ethernet cables for IP data carry triple play services, coaxial cables for terrestrial or satellite television broadcasting convey RF signals, specific cables for HDMI links interconnect, for instance, a HD video player and a television set, ... Subsequently, it is proposed to transport all these home signals over optical fibers.

1.2 The opportunity/maturity of the optical transmission technologies

The introduction of optical fibers in the HAN addresses both the bit rate increase and the great heterogeneity of signals to deliver. This results from the performances of optical fibers: their very low attenuation, their very large frequency bandwidth, their high linearity and their perfect immunity to electrical interferences. Inside the home, it will be a natural extension of the access networks that will become all-optical with the deployment of the FTTH and an ideal media to provide a long life-span communication infrastructure, able to adapt to new digital and analogue standards for years.

Nevertheless, this new wire has to take up some constraints to be deployed inside the home: it has to tolerate a large number of tight radius bends (door and window corners), to convey signals over distances of up to 100m, to be low cost and simple to install. The latter two points are directly related since an easy installation will dispense with the intervention of a technician, and a customer or an electrician will be able to install the cable himself in a reduced time with a reduced cost.

Several kinds of optical fibers could be used to enable high-performance HANs: plastic optical fibers (POF), multimode silica fibers (MMF) and singlemode silica fibers (SMF).

1.2.1 SI POF

The Step Index (SI) Polymethyl Methacrylate (PMMA) POF is already massively deployed in several industries such as the automotive or the aerospace because it is a lightweight, EMI immune and low cost solution. Additionally, SI POF is gathering momentum in HAN market because of a good compromise between performances and implementation simplicity. Today, point-to-point POF links, working in the visible (typically 650nm), can be implemented to interconnect the customer's devices at 100Mbit/s

over 100m [51], up to 1Gbit/s over 50m if equalizers (pre- or post-equalization) compensate the small bandwidth of the SI POF [52], or up to 1Gbit/s over 75m if advanced signal modulations are adopted [53]. However, PMMA POF is limited to the transmission of digital signals, i.e. triple play services integrated over IP, and will not be able to support analog formats such as the terrestrial or satellite television due to limited bandwidth (100MHz for 100m [54]).

Nevertheless, the PMMA POF is considered as an interesting solution to be a flying lead between wall plugs and the users' devices. This POF can be easily cut to the wanted length using a small guillotine equipped with a simple razor blade. In addition, the optical injection is simple and the connector assembly is quick and easy because of the large core diameter of 980μm (the cladding diameter is 1mm). Therefore, its installation is performed in a couple of minutes by a technician unprofessional in optics and without the need of expensive equipments as shown in figure 1.6 where a Do It Yourself (DIY) kit is depicted.

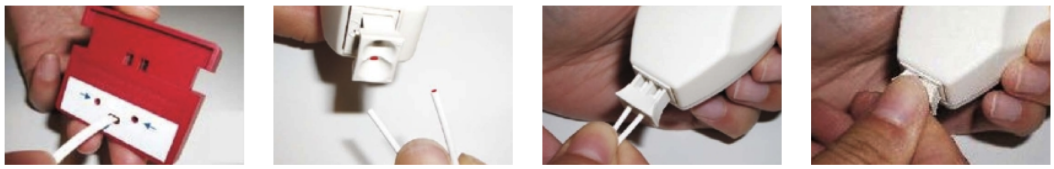

Figure 1.6: Firecomms point-to-point link at 100Mbit/s with its Do It Yourself kit, from [3].

This kit provides a 100Mbit/s Ethernet extension between two devices thanks to two POFs, one for the uplink and one for the downlink. This link has the advantage to be more discreet than a four copper pairs cable, a category 5 being typically 5mm thick whereas two POFs are about 2mm thick. Lastly, the optical sources used here are low cost Light Emitting Diodes (LEDs) in the visible that can be safely observed by a human eye and can so be used to check the integrity of the connections.

1.2.2 GI POF

The introduction of Graded Index (GI) Plastic Optical Fibre (POF), based on perfluorinated polymers commercially known as CYclic Transparent Optical Polymer (CYTOP), increases the POF bandwidth thanks to an optimized index profile. Experimentally, the GI POF can support a speed of 25Gbit/s over 100m [55] and enable the transmission of RF signals such as the terrestrial television broadcasting [56].

The GI POF, designed for a wavelength of 850nm, has a 120μm core diameter and 495μm cladding diameter [57]. Due to its small core size, the GI POF installation is complex compared to the PMMA and there is no convincing Do It Yourself kit.

If this fiber is certainly advantageous in terms of performances, the technology is finally not enough mature due to high manufacturing costs and low productivity: silica fibers as MMF or SMF will be preferred.

Table 1.3: Comparisons between the SI POF and GI POF solutions.

Fiber	SI POF	GI POF
Index profile	Step Index	Graded Index
Core diameter	980μm	120μm
Cladding diameter	1mm	495μm
Wavelength	typically 650nm (red)	850nm - 1310nm
Optical losses	>100dB/km at 650nm	<60dB/km at 850nm and 1310nm
Bend losses	2dB/km (1/4 circle, radius 12mm)	<0.06dB (1/4 circle, radius 25mm)
Bandwidth	100MHz for 100m	>300MHz.km

1.2.3 MMF

The multimode silica fibers (MMF) meet all the HAN requirements as they support all the kinds of signals, analog and digital, and high data rates. This fiber, with a graded index profile, a 50 or 62.5 μm core diameter and a 125μm cladding diameter, shows several unique properties as several transverse

modes propagate along the fiber. For example, due to the modal dispersion, the fiber bandwidth is limited and the signal gets distorted. As a result, the MMF has been classified from OM1 to OM4 (ISO/IEC standard 11801) depending on their fiber bandwidth as shown in table 1.4. These bandwidths are defined either under Over Filled Launch (OFL), i.e. when the fiber core is fully lighted and when all the fiber transverse modes are excited, or as a computed Effective Modal Bandwidth (EMBc), the minimum bandwidth that can be observed for any VCSEL.

Table 1.4: MMF bandwidth, from [37].

Fiber class	OM1	OM2	OM3	OM4
Wavelength	850nm			
OFL BW (MHz.km)	200	500	1500	3500
EMBc (MHz.km)	200	600	2000	4700
Wavelength	1310nm			
OFL BW (MHz.km)	500	500	500	500
EMBc (MHz.km)	600	1200	500	500

The current most deployed MMF, OM3, supports up to 10Gbit/s over short distances as shown in table 1.5. Several standards have been established depending of the wavelength and the Digital Signal Processing (DSP). For example, 10GBase-LRM (Long Reach Multimode) uses Electronic Dispersion Control (EDC) for equalization at the reception while 10GBase-LX4 uses Coarse Wavelength-Division Multiplexing (CWDM) to support 300m transmission distance over legacy MMF: four separate laser sources operating at 3.125Gbit/s are used at 1300nm.

Table 1.5: Standardized (blue) and typically supported (black) transmission distances dependent on existing standards, from [37].

Data rate	1Gbit/s		10Gbit/s	10Gbit/s	10Gbit/s
	1000Base-		10GBase-	10GBase-	10GBase-
	SX	LX	SR	LX4	LRM
Wavelength	850nm	1310nm	850nm	1300nm	1300nm
Transmission	serial		serial	CWDM	serial
OM1	275m	550m	33m	300m	220m
62.5μm	500m	1000m	65m	450m	220m
OM2	550m	550m	82m	300m	220m
50μm	750m	2000m	110m	900m	300m
OM3			300m	300m	220m
50μm	1100m	550m	300m	300m	220m
OM4					
50μm	1100m	550m	550m	300m	220m

In the last years, many studies have been carried out to improve their performances and nowadays it is easy to find high bandwidth MMF with reduced bend sensitivity like the ClearCurve fibers from Corning [58] or the MaxCap fibers from Draka [59]. These fibers present an optimized index profile showing very good bending performances thanks to an index depression between the core and the cladding as shown in figure 1.7. Thus, bending losses below 0.2dB at 850nm and below 0.5dB at 1300nm for two turns with a 7.5mm bend radius are announced. Having good bending performances is essential as the MMF are principally used today as backbone in building, campus, Local Area Networks (LAN) and data centers. Lastly, this fiber represents also an interesting solution for the home because it can be used with low cost optoelectronics components, either in the wavelength windows of 850nm or of 1310nm.

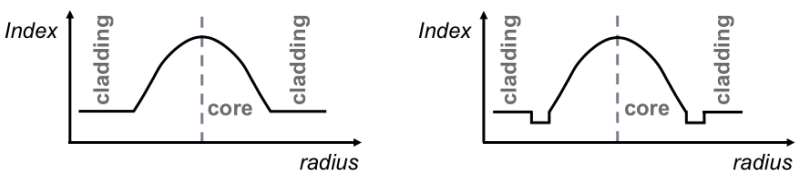

Figure 1.7: Difference between regular MMF on the left and bend-insensitive MMF on the right.

Recently, 40 and 100 Gbit/s multimode fiber systems have been defined (IEEE 802.3ba standard), and a new fiber class, OM4 (ISO/IEC standard, March 2011), has been specified for high-speed and extended-reach applications.

1.2.4 SMF

The silica singlemode fibers (SMF) are widely used in transport and access networks as they present a very low attenuation, a large wavelength window ([1200 - 1600] nm), and no practical limitation in terms of frequency bandwidth. Two types of SMF are generally used, the G.652.D or the bend-optimized G.657. This last one, defined at the beginning of 2006, is strongly attractive for FTTH.

Typical SMFs have a step index profile with a 9 μm core diameter and a 125μm cladding diameter. Therefore, even if the price per km of SMF is lower than the MMF thanks to a more massive market, the small core diameter and the small numerical aperture of the SMF reduce the coupling tolerances and increase the assembly costs due to the high precision required in the optical connectors. More difficult to handle by the users, SMF cannot be installed at home without the intervention of a specialist.

1.2.5 Summary

In the longer term, SMF is the only technology guaranteeing a high quality of cabling installed inside the walls for years and offering a perfect continuity with the optical access networks. Nevertheless, at mid-term, MMF would be preferred as it relaxes the alignment requirements with the end components, it is optimized for low cost optoelectronic components working at 850nm, and it has largely sufficient performances for the HAN. Indeed, MMF tolerates a large number of tight radius bends and conveys digital and analog signals over at least 100m.

To avoid choosing between SMF and MMF, deploying a Dual-Mode Fiber (DMF) capable of single- and multi-mode transmission [4] would have been a relevant option to answer both, the mid-term concern (a rational cost solution to penetrate the market) and the long-term concern (very high performances to be future proof), but this solution is not offered for sale. The principle of the DMF is depicted in figure 1.8: two different refractive index are combined to allow two kinds of propagation.

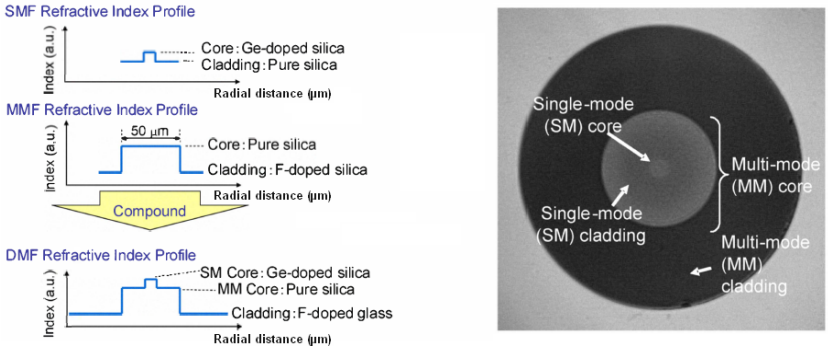

Figure 1.8: A basic DMF design on the left and a cross-section photograph on the right, from [4].

Finally, if it is recommended to install MMF as a home backbone because it is a future proof solution at mid-term, for the end connectivity up to the devices, “Do it Yourself” solutions that can be installed without any complexity are preferred, as the SI POF.

1.3 Towards Multi-Gigabit/s Wireless transmissions

1.3.1 Some theories and concepts on the radio systems

Through the world, people use increasingly their devices in a wireless way, in particular thanks to the popular Wi-Fi (Wireless Fidelity), the commercial name of the products based on the IEEE 802.11 standards. This solution has met the needs of its public: mobility, ease of use and flexibility. As a result, Wi-Fi is today widely available and is integrated everywhere: in computers, gaming consoles,

smartphones, tablets, printers, etc...

The IEEE 802.11 a/b/g/n standards exploit the 2.4 or the 5 GHz unlicensed band. As these frequencies know a great success, they begin to be very saturated, and in some public places like schools, coffees, or airports, they are already fully occupied. To preempt this, the latest 11n released amendment takes advantage of the two frequency bands optimizing the allocation of resources depending on the neighboring Wi-Fi systems. Thus, it can be protected against interferences.

Table 1.6: The two unlicensed frequency bands used by the Wi-Fi systems.

Band	Frequency band (GHz)	Band name
2.4	2.400-2.4835	Industrial Scientific Medical (ISM)
5	5.150-5.350 and 5.470-5.725	Unlicensed National Information Infrastructure (U-NII)

Figure 1.9 represents the channelization of the 2.4 and 5 GHz bands. In the 2.4GHz band, 13 channels can be exploited, but only 3 non-overlapping 20MHz bandwidth channels are available. In the 5GHz band, there are 23 non-overlapping 20MHz bandwidth channels. However, in each region of the world, local rules limit the number of allowed radio channels.

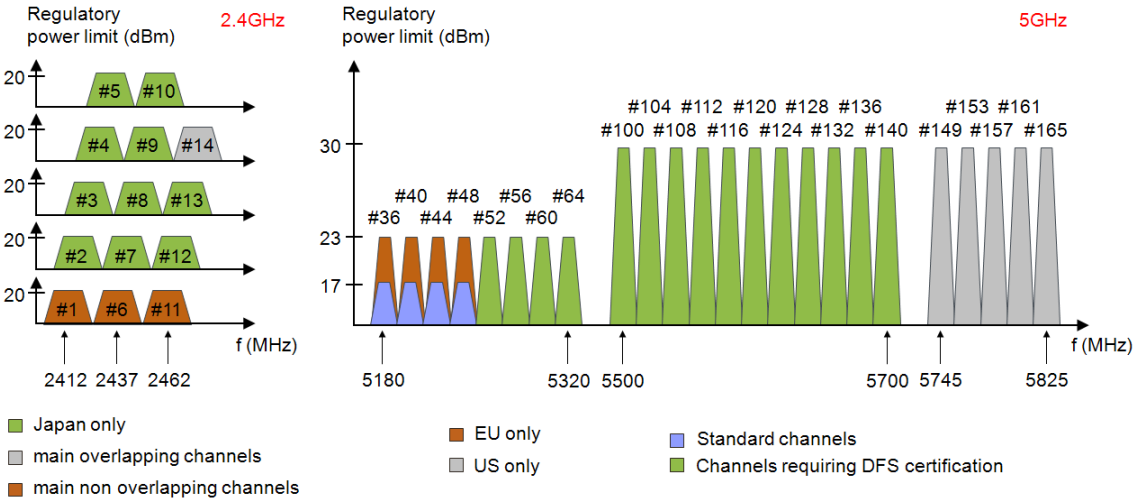

Figure 1.9: Channelization of the 2.4 and 5 GHz bands, adapted from [5].

The main challenge of the Wi-Fi systems is to follow the increase of the data rates. To answer to this issue the frequency dimension has been exploited in the IEEE 802.11n standard increasing the bandwidth from 20 to 40 MHz thanks to bondings between two adjacent channels. But, if the frequency dimension is a low cost and easy way to improve the single user throughput, it is a rare and precious resource to share between users.

Therefore, when the spectrum is limited, other resources are exploited. For instance, the latter 11n released has introduced the Multiple-Input Multiple-Output (MIMO) technology that takes advantage of the spatial dimension. In fact, the MIMO, characterized by information transmitted and received by multiple antennas, increases the signal robustness thanks to diversity techniques combined to smart chipsets exploiting the different independent channels used at the transmission and observed at the reception.

Futhermore, the wireless transmissions can be enhanced introducing time dimension improvements in order to reduce the ratio between the time during which data is transmitted and the time dedicated to management. To minimize the Medium Access Control (MAC) layer overhead, new aggregation techniques and efficient protocols are required.

Lastly, the spectral efficiency dimension, defined as the number of bits transmitted in a time/frequency slot, can also be exploited. As a reference, the IEEE 802.11n has theoretically a spectral efficiency up to 15bit/s/Hz (600Mbit/s over 40MHz), a value that depends in reality on the Modulation

and Coding Scheme (MCS) chosen. Concerning the modulation, currently two principal techniques are used in the high speed wireless systems, the Single Carrier (SC) and the Orthogonal Frequency-Division Multiplexing (OFDM). The latter will be described subsequently.

Finally, each evolution of the IEEE 802.11 standard has increased the data rates to meet the user demand (see table 1.7). If currently the IEEE 802.11n standard offers a theoretical throughput up to 600Mbit/s, a more realistic throughput in a typical home environment is included between 100 and 300 Mbit/s. As explained in section 1.1, these values will be insufficient for the future HANs.

Table 1.7: Theoretical data rates in 2 and 5 GHz bands.

Standard	PHY layer throughput	Frequency band used
IEEE 802.11 a	54Mbit/s	5GHz
IEEE 802.11 b	11Mbit/s	2.4GHz
IEEE 802.11 g	54Mbit/s	2.4GHz
IEEE 802.11 n	600Mbit/s	2.4 et 5 GHz

The IEEE 802.11 standards keep evolving in order to improve the user experience and to offer in a near future Very High Throughput (VHT). With this aim in mind, the IEEE VHT study group, formed in May 2007 [60], intends to provide Gigabit/s capacity. On the one hand, the Task Group ac (TGac) has been created in november 2008 to standardize a new release of the IEEE 802.11 family, the IEEE 802.11ac standard. This latter reuses the techniques seen in the 11n released, but with wider bandwidths (up to 160MHz), higher diagram constellations (up to 256-QAM), a larger number of antennas (up to 8), and introduces new concepts such as the multi-user MIMO. These evolutions will provide a maximum PHY layer throughput of 6.93Gbit/s in the 5GHz band, but 1.56Gbit/s might be a more practical and realistic maximum data rate for consumer devices [61].

In the same time, industrial groups have begun to exploit new radio bands offering wide bandwidth and promising high throughput, the Ultra-Wide Band (UWB) between 3.1 and 4.7 GHz, and the millimeter-wave band between 57 and 66 GHz. Thus, a rich ecosystem of standards, from normalized solutions to proprietary ones for specific markets such as HD video transmission, has emerged. The next sections will provide an overview of these future high data rates wireless solutions, including the VHT study group view.

Writing about wireless home solutions naturally induces to realize a picture of the Wireless Local Area Network (WLAN) systems having long ranges and so enabling a whole home coverage as it has been made previously with the IEEE 802.11 family, a technology able to cross the walls, and so to interconnect all the domestic devices. Paradoxically, in the next paragraphs we will present Wireless Personal Area Network (WPAN) systems limited to few meters ranges or to single room coverages. Generally, WPAN systems provide higher throughputs than WLAN ones, and if currently their use cases are limited to short point-to-point links, their scope of usages will be broadened with the next generation of products and with the solution proposed in the chapter 2.

Before detailing the new radio standards, it is necessary to define some vocabulary:

- The industrial consortiums (WirelessHD, WiGig ...) develop proprietary solutions and promote them in the standards organizations.
- The standards organizations (IEEE, ECMA, ...) define and publish radio systems, PHY and MAC layers.
- The trade associations (WiMedia Alliance, Wi-Fi Alliance) promote products from the market standards and certify interoperability between devices that meet the same label.

We also need to detail the two principal modulation techniques currently used in the high speed wireless systems, the Single Carrier (SC) and the Orthogonal Frequency-Division Multiplexing (OFDM).

Single Carrier (SC)

The SC modulation is generally used as the mandatory scheme of the 60GHz wireless standards due to its low-power consumption and its low-cost implementation with only one carrier as shown in figure 1.10.

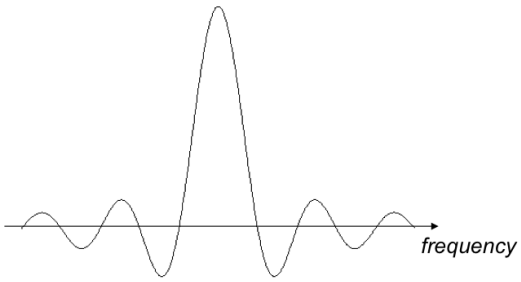

Figure 1.10: SC spectrum, from [6].

The data conveyed on this carrier are modulated using a Phase Shift Keying (PSK) modulation or a Quadrature Amplitude Modulation (QAM) according to constellation diagrams as the ones depicted in figure 1.11. In the case of QAM, the modulation scheme can be represented as an amplitude modulation of two waves with a 90° phase shift, one in phase (I) and the other in quadrature (Q). Thus, the symbols are considered as complex numbers.

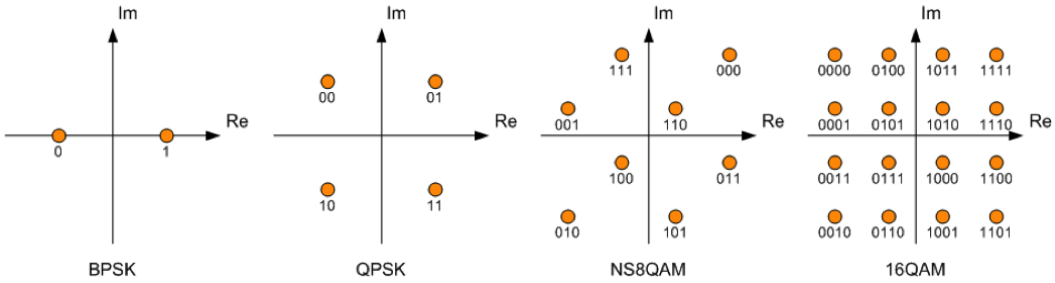

Figure 1.11: Some constellation mapping used in the wireless systems.

The 60GHz wireless systems have also adopted the Single Carrier Block Transmission (SCBT) technique [62], a derivate of the SC modulation where the symbols are coded by block as shown in figure 1.12.

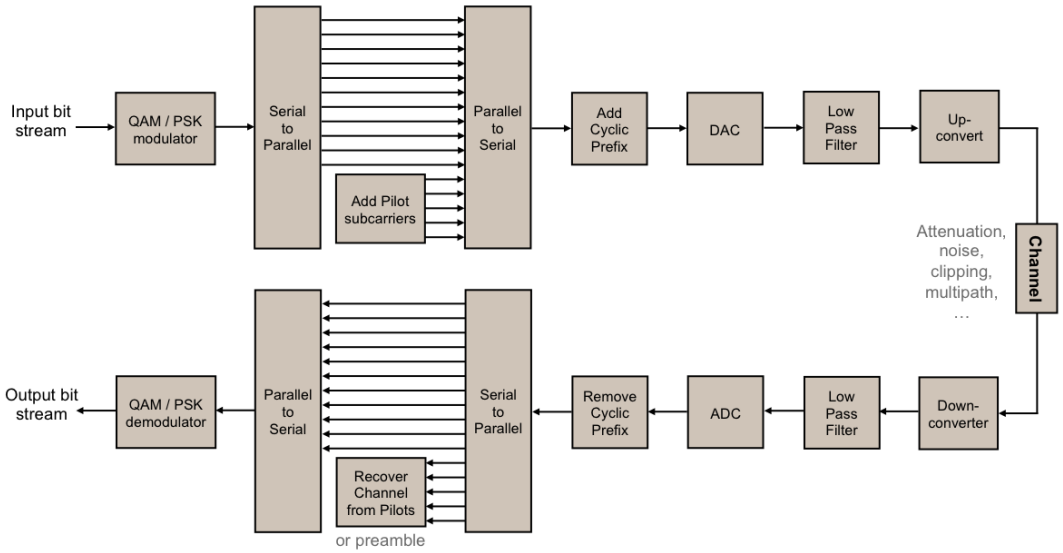

Figure 1.12: SCBT block diagram.

Compared to the SC modulation, the SCBT technique inserts a Cyclic Prefix (CP) or a Zero Pad Suffix (ZPS) in order to remove Inter-Block Interferences (IBI). A CP consists in copying the last samples of the current block and pasting them to the beginning of the block, while a ZPS consists in simply inserting zeros between adjacent blocks. The CP and the ZPS serve as guard times, but they are also a tool to

synchronize the signal in the time domain. In fact, if a CP is used, an autocorrelation will be realized to detect the repeatability and as a consequence the beginning of the block, while if a ZPS is used, the signal envelope will be calculated to detect the rising edges.

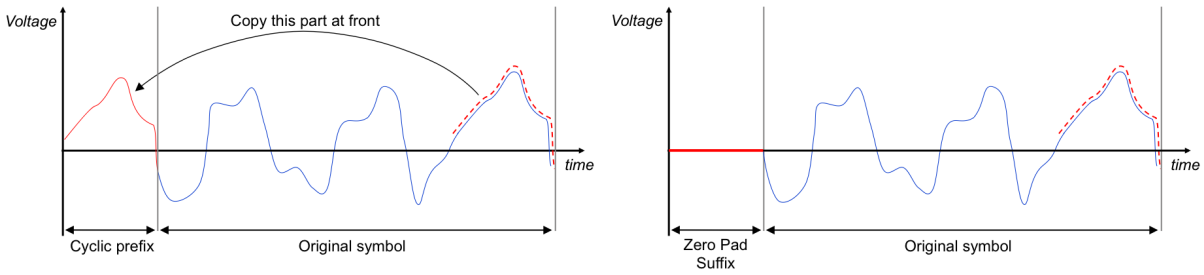

Figure 1.13: Cyclic Prefix (CP) and Zero Pad Suffix (ZPS).

The frequency error and the phase noise is tracked and compensated by a known pilot sequence added at the beginning of each SCBT block (figure 1.14). This sequence sent at the emitter is compared to the one received by the recipient to determine the channel response and compensate it.

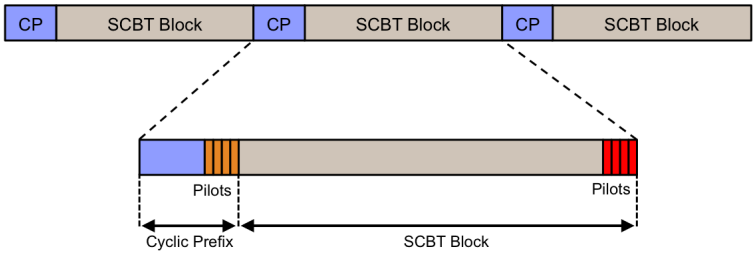

Figure 1.14: SCBT time diagram.

Advantages

- Low Peak-to-Average Power Ratio (PAPR).
- Low sensitivity to Carrier Frequency Offset (CFO).
- Low-power consumption and low-cost system implementation.

Disadvantages

- Capacity and power losses due to the guard interval.

Orthogonal Frequency-Division Multiplexing (OFDM)

With the increase of the data rates, the conventional modulation formats (NRZ, RZ, SC...) have reached their limits. Therefore, it has been necessary to find an advanced modulation format to communicate effectively at high speed whilst remaining robust to multipaths: the Orthogonal Frequency-Division Multiplexing (OFDM). The OFDM, originally implemented by the radio systems, is now a widely acclaimed modulation technique used in all the industrial sectors:

- in the broadcast video systems for coaxial cable (DVB-C) or terrestrial (DVB-T) and satellite (DVB-S) wireless transmissions.
- in the wireline access with ADSL, xDSL and most likely in the future PON systems. For instance, OFDM is considered as a promising solution for future broadband systems at 40 and 100Gbit/s [63] [64] [65].
- in the wireless access with WiMAX (IEEE 802.16e).
- in the cellular wireless systems, for example with the recent fourth generation standard (3GPP LTE).
- in the wireline home networks with Power Line Communication (PLC) based on the HomePNA standard or with the coaxial communication based on the MoCA solution.

– in the wireless home networks with WLAN and WPAN radio systems. The OFDM has been used for many years in the Wi-Fi systems (802.11 g/n).

Finally, it has to be noted that today the OFDM technique has also been implemented in the optic domain, using optical frequencies and optical processing instead of RF ones [66].

In OFDM, digital data are transmitted at high speed by spreading them over a large number of subcarriers, each of them being modulated at low data rates. The OFDM is a specific case of the FDM (Frequency Division Multiplexing) where the spectral spacing between adjacent subcarriers is minimized by using a base of orthogonal functions. So, even if the subcarriers overlap in the frequency domain, they can always be separated at the reception. An example of a base of orthogonal functions is given below:

$$g(t) \times cos\left(2\pi\left(f_0 + \frac{n}{T_{symbol}}\right)t\right) \tag{1.2}$$

where,

– $g(t)$ is the signal waveform.
– n is an integer: n = 0, 1, ..., N-1.
– N is the total number of subcarriers.
– T_{symbol} is the duration of a symbol.

The orthogonality saves spectral band compared to FDM techniques using different carriers in non-overlapping frequency bands. With regard to figure 1.15 where the spacing between frequencies is set at $1/T_{symbol}$, it is clear that the OFDM technique ensures bandwidth efficiency.

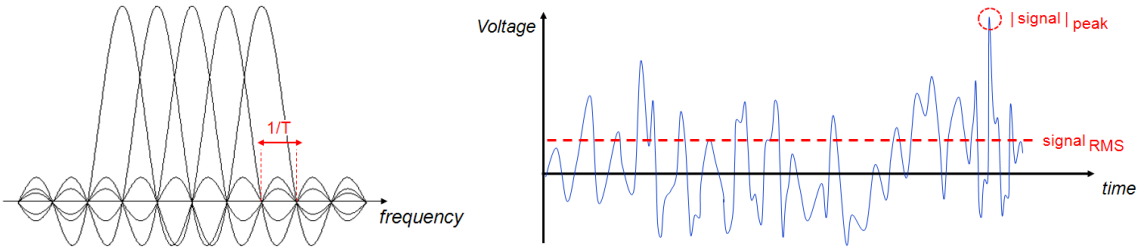

Figure 1.15: OFDM spectrum, from [6], and the corresponding signal in the time domain.

A simple way to project a signal on an orthogonal base consists in using a Discrete Fourier Transform (DFT). Thus, as described in figure 1.16, an inverse DFT is applied at the emission to obtain orthogonal subcarriers: in a first time, an input bit stream is converted into QAM or PSK modulated carriers, then these carriers are distributed in the frequency domain thanks to a Serial to Parallel block, afterwards an inverse DFT operation produces parallel samples in the time domain, and lastly a Parallel to Serial block transmits the created OFDM signal sample after sample. A reverse process is applied at the reception, except that a DFT is used to pass from the time-domain to the frequency-domain. To understand the necessity of the P/S and S/P blocks, the mathematical definitions of the DFT operations are recalled below:

$$iDFT:\ S(k) \rightarrow s(n) = \frac{1}{N}\sum_{k=0}^{N-1} S(k) \cdot e^{2i\pi n \frac{k}{N}} \tag{1.3}$$

$$DFT:\ s(n) \rightarrow S(k) = \sum_{n=0}^{N-1} s(n) \cdot e^{-2i\pi k \frac{n}{N}} \tag{1.4}$$

where,

– $s(n)$ is the sampled signal in the time-domain.
– $S(k)$ is the sampled signal in the frequency-domain.
– N is the total number of samples.

The spectrum of the OFDM signal is composed of subcarriers C_k positioned at the frequencies f_k spaced of $1/T_{symbol}$. Around these subcarriers the spectrum is broadened following a *sinc* function because of the spectrum of the time window T_{symbol}, the FT of a rectangular function being a *sinc* function. Finally, the bigger the number of subcarriers is, the stronger the complete signal spectrum tends towards a rectangular function.

In practice, to save processing time, Fast Fourier Transform (FFT) is preferred to build the base of orthogonal functions. The only constraint imposed by this choice is to use a number of samples equal to a power of two.

Each subcarrier carries complex numbers modulated in conventional schemes and forming constellation diagrams in which each point correspond to a group of bits typically Gray coded. Besides, some of these subcarriers, the pilot subcarriers, are modulated with a known sequence of datas in order to help to the channel recovery. This emitted sequence of pilot subcarriers, known by the transmitter and the receiver, is compared to the ones extracted at the reception side. Thus, the channel response can be estimated: the amplitude weight vector of each pilot subcarrier and the phase rotation on each OFDM symbol is calculated, and by interpolation, the attenuation coefficients and the phase shifts of all subcarriers between the pilot subcarriers is deducted. This channel equalizer corrects dynamically the OFDM signal at the output of the FFT in both frequency and time domains. As a consequence, it represents a perfect further solution to the use of a preamble to track the evolution of the channel transfer function.

Generally, a cyclic prefix is added to the OFDM symbols in the time-domain in order to increase the robustness of the signal against the channel spreading, to reduce the ISI and to facilitate the synchronization. The use of a CP is especially attractive in OFDM since FFT induces a periodic function: in equation 1.4, $S(k) = S(k + N/n)$. As a consequence, FFT can be realized using any sample as first sample: an error margin equal to the CP duration is allowed in the choice of the start of an OFDM symbol.

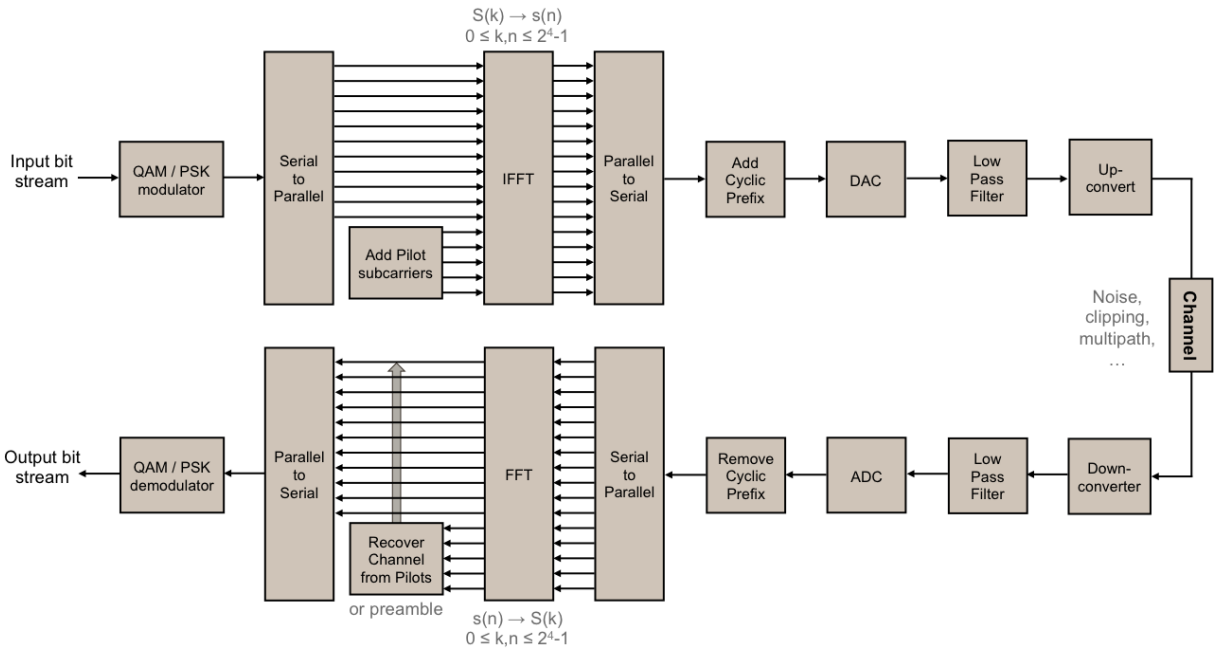

Figure 1.16: OFDM block diagram.

In the 60GHz wireless standards, all the subcarriers are modulated in the same way, excepted the pilot subcarriers. Nevertheless, in OFDM, an optional strategy consisting in encoding each subcarrier by a specific modulation scheme with a different data rate exists. With this adaptive subcarrier allocation (adaptive OFDM), the amplitude and the phase of each subcarrier are optimized according to the spectral response of the channel (in terms of noises, error rates, ...). For example, Levin-Campello Algorithm (LCA) can be chosen to maximize the capacity of a transmission, a Bit Error Rate (BER)

target being fixed under the constraint of a fixed RF power at the input of the system.

Advantages:

- High spectral efficiency: the bandwidth is optimally used thanks to the orthogonality property of the subcarriers. This provides high data rates using components with limited bandwidth.
- High flexibility in the bits allocation. Indeed, each subcarrier can be modulated independently of other subcarriers to offer the best data rate depending on the channel response.
- Reduced Inter-Symbol Interferences (ISI). When a symbol period is short compared to the delay spread (i.e. the interval for which a symbol remains inside the multipath channel), then ISI strongly impacts performances. However, as with OFDM technique, high speed data are transmitted in parallel over a large number of subcarriers, the duration of a symbol increases and so the probability to have ISI decreases.
- Robustness to the impulsive noise. Narrowband interferences affect only a small part of the subcarriers. With appropriate coding and interleaving techniques, an impulsive noise does not induce error in the data stream.
- Control of the software part. The modulation and coding scheme of OFDM is based on a well known and mastered algorithm, the FFT. There is no particular difficulty to implement it in the Digital Signal Processors (DSP).

Disadvantages:

- OFDM is sensitive to Carrier Frequency Offset (CFO) and phase noise. The orthogonality of subcarriers being the key element of the OFDM modulation, the local oscillator phase noise or the local oscillator frequency mismatch between the transmitter and the receiver, imply a loss of orthogonality between subcarriers and so deteriorations in the performances of the system. As the OFDM bandwidth is divided into thin sub-bands, tight synchronization is needed.
- OFDM systems are very sensitive to the imbalance between the I and Q channels. IQ imbalance causes mutual interference between pairs of symmetric subcarriers and implies a significant performance degradation of the overall system.
- High Peak-to-Average Power Ratio (PAPR). The main drawback of the OFDM technique is its large PAPR. If the OFDM subcarriers are added constructively during the inverse FFT process, large peaks will occur (figure 1.15) in the time domain and it will result in strong constraints on the modulation index of the optical source.
- High complexity of the electronics, especially to perform analog / digital conversions (ADC and DAC) at very high speeds, of the order of several GSa/s in the future radio systems.
- Energy needs. The electrical consumption of the digital components is a significant factor.

1.3.2 The centimeter-wave band - [3.1 - 10.6] GHz

Many variations of the future high throughput radio standards exist. All these systems, called Ultra-WideBand (UWB), are specified by the Federal Communication Commission (FCC) rules [67] as systems using a -10dB bandwidth higher than 20% of the central frequency, or using a -10dB bandwidth larger than 500MHz.

The microwave UWB, in the [3.1 - 10.6] GHz unlicensed band depicted in figure 1.17, is one of these systems. Concerning the regulation of this band, the FCC limits the power spectral density emission to -41.3 dBm/MHz, means -14dBm in a band of 528MHz. This low RF level is the main drawback of the microwave UWB standards as it induces short ranges limited to a single room or up to 10m.

$$P\ [dBm] = -41.3 + 10 \cdot log(528) = -14dBm \tag{1.5}$$

Additionally, the spectrum mask is not harmonized worldwide. Consequently, it is hard to design UWB chips. Indeed, only the UWB band group 6 is available worldwide, even if in Europe a Detect And Avoid (DAA) mechanism is required yet. For information, DAA is a technique based on the detection of a licensed signal and on the reduction of the radio power level in the band where a signal is detected to minimize and to prevent interferences.

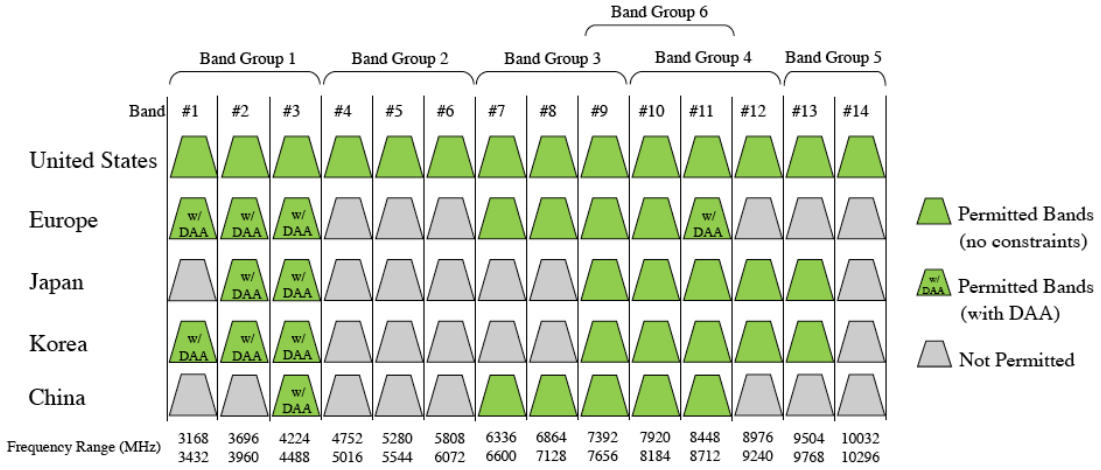

Figure 1.17: The centimeter-wave band from 3.1 to 10.6 GHz and the spectrum allocation, from [7].

Two main kinds of UWB technology exist: the UWB multiband OFDM and the UWB impulse radio. The UWB multiband OFDM consists in transmitting OFDM symbols successively over several radio bands in order to reduce Inter-Symbol Interferences (ISI) and exploit diversity. Nevertheless this technique is complex and costly. On the contrary, the UWB impulse radio, based on the transmission of very short pulses optimized to occupy the entire allowable frequency band and to reduce the electrical consumption of the radio front end, is more simple.

The pulse shapes typically used for the UWB communications are generally Gaussian, with short duration to occupy a large bandwidth of the order of a few GHz. However, as the use of Gaussian pulses induces a non-zero average amplitude, leading to peaks at low frequencies, pulse shapes designed from the first derivative of the Gaussian pulse (Gaussian monocycle) or its second derivative are preferred. An example is provided in figure 1.18, where the microwave band has been divided into two distinct frequency bands, [3.1 - 4.85] and [6.2 - 9.7] GHz. Thus, the U-NII band for Wi-Fi remains free of any UWB signals. It has to be noted that the pulses are closer to wavelets than Gaussian pulses as they are depicted in Intermediate Frequency (IF) [68] [8].

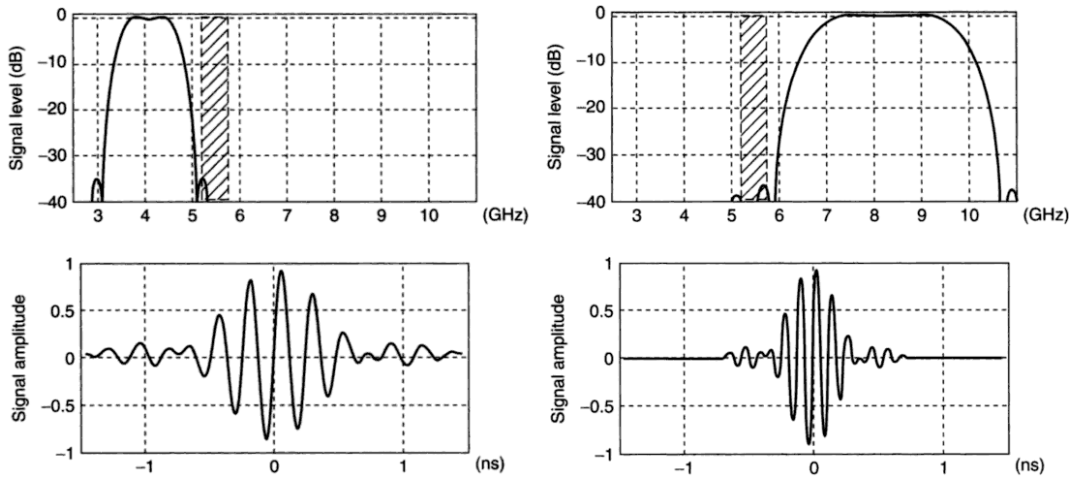

Figure 1.18: UWB wavelets, from [8]. Two different pulse shapes can be observed, in the frequency domain (above) and in the time domain (below): the first one, on the left, corresponds to the [3.1 - 4.85] GHz frequency band while the second one, on the right, corresponds to the [6.2 - 9.7] GHz frequency band.

About standardization, the IEEE 802.15.3a task group has been created in 2001, one year before the opening of the UWB spectrum mask by the FCC. It specified a new radio standard with data rate up to 1Gbit/s which were supposed to be the solution to the low data rates of the Wi-Fi systems, but within the task group a competition between different technical choices from the UWB Forum (supporting the impulse radio solution) and the Wimedia Alliance (supporting the multiband OFDM) has delayed the

standardization process and finally blocked it. As a consequence, in 2005, the Wimedia Alliance [69] has published its own specification under the ECMA-368 standard.

ECMA-368

The Wimedia PHY, or ECMA-368, operates in the [3.1 - 10.6] GHz band, a band divided into six band groups composed of three or two 528MHz bandwidth bands as shown in figure 1.17). In each band group, the OFDM symbols are transmitted using a hopping sequence called Time-Frequency Code (TFC) where successive OFDM symbols are emitted over different bands. An example of TFC is given in figure 1.19.

TFC number	Band ID					
1	1	2	3	1	2	3
2	1	3	2	1	3	2
3	1	1	2	2	3	3
4	1	1	3	3	2	2
5	1	1	1	1	1	1
6	2	2	2	2	2	2
7	3	3	3	3	3	3
8	1	2	1	2	1	2
9	1	3	1	3	1	3
10	2	3	2	3	2	3

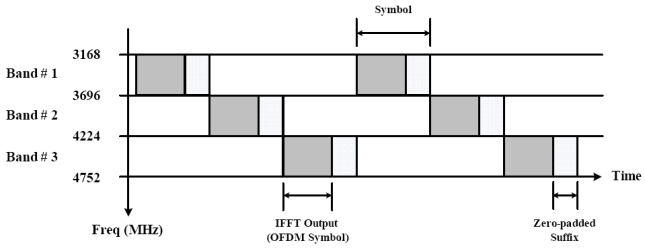

Figure 1.19: Hop sequence for TFC in the band group 1 on the left and an example with the TFC number 1 on the right.

To improve the transmission, ECMA 368 can employ two types of redundancy, either a Time-Domain Spreading (TDS) where same data is transmitted over two different OFDM symbols, or a Frequency-Domain Spreading (FDS) where data is transmitted over two carriers within a same OFDM symbol. Each of these redundancy schemes reduces the throughput, but improves the signal robustness.

Finally, the UWB is able to deliver data rates between 53.3 and 480Mbit/s over short distances. Even if new data rates up to 1Gbit/s have been announced, today no product is commercially available. However, small semiconductor companies, such as Alereon and Veebeam, keep developing UWB radio chipsets and sometimes new products are announced as recently at the Consumer Electronic Show (CES) 2012 with the Samsung Central Station wireless monitor. But, the latter seems support only compressed video. This technology is also used today for the Wireless-USB (W-USB) and the wireless audio systems [70]. W-USB is the wireless extension to the popular USB developed by the USB Implementers Forum (USB-IF). Besides, during the specification of the Bluetooth 3.0, the previous iteration of the short-range wireless technology, the Wimedia MB-OFDM UWB radio platform has been considered for high data-rate operation, but instead, a PHY solution close to the IEEE 802.11g was preferred [71].

Finally, the UWB has not convinced the market and today only a few products are available. The pros and cons of UWB, with respect to other home networking solutions, are:

Advantages:

- a low power consumption.
- an ability to accommodate to local regulatory by operating in different spectrums thanks to TFC adjustment.

Disadvantages:

- Constraints on the emitted power.
- the frequency-hopping nature of the UWB signals is complex and costly.
- the data-rate limitation to 480Mbit/s.
- the inter-system interference (U-NII band and implementation of DAA mechanisms).

Instead of the microwave UWB, the industrial has high hopes invested in future 60GHz solutions that clearly represent the future of the Multi-Gigabit/s Wireless Systems.

1.3.3 The millimeter-wave band - [57 - 66] GHz

The millimeter-wave systems offer several advantages compared to existing communication systems thanks to a large license-free band from 57 to 66 GHz. Although this bandwidth is comparable to the centimeter-wave one, 9GHz versus 7.5GHz, the millimeter-wave band is most attractive as it is widely available around the world and not yet massively used. This band, depicted in figure 1.20, has been divided in wider channels, 2.16GHz versus 528MHz, with less limited emitted powers as described in table 1.8. A last key factor is the miniaturization of the antennas at such frequencies: this allows advanced integration into radio terminals such as cellphones or laptops.

Channel Number	Low Freq. (GHz)	Center Freq. (GHz)	High Freq. (GHz)	Nyquist BW (MHz)	Roll-Off Factor
A1	57.240	58.320	59.400	1,728	0.25
A2	59.400	60.480	61.560	1,728	0.25
A3	61.560	62.640	63.720	1,728	0.25
A4	63.720	64.800	65.880	1,728	0.25

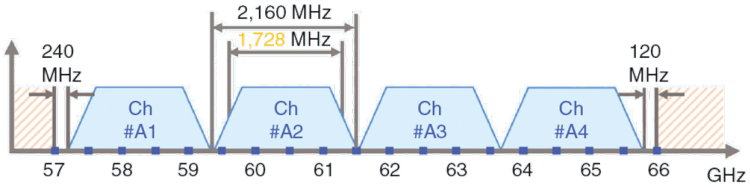

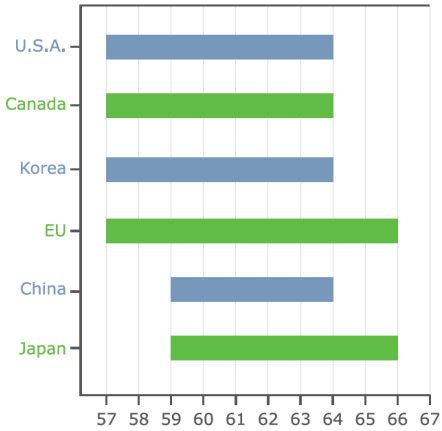

Figure 1.20: Channelization of the millimeter-wave band on the left and worldwide spectrum availability on the right, from [9].

Table 1.8: Worldwide power regulation in the millimeter-wave band [38] [33] [39].

Region	Unlicensed band	Max.Tx power	EIRP	Antenna gain
USA	57.05-64 GHz	27dBm	40dBm average / 43dBm peak	-
Canada	57.05-64 GHz	27dBm	40dBm average / 43dBm peak	-
South Korea	57.0-64.0 GHz	10dBm	27dBm	-
Europe	57.0-66.0 GHz	13dBm	57dBm peak	37dBi
Australia	59.4-62.9 GHz	10dBm	57dBm	-
Japan	59.0-66 GHz	10dBm	57dBm	47dBi max

As shown in table 1.8 and in figure 1.20, the available spectrum and the Equivalent Isotropically Radiated Power (EIRP) can vary depending of the regions of the world[2]. The EIRP is the power radiated in the direction of maximum antenna gain and it corresponds to the power applied to an isotropic antenna to obtained in this direction the same emitted power. As a result:

$$EIRP = Transmitter\ power\ output + Antenna\ gain \tag{1.6}$$

The large and unlicensed millimeter-wave band enable multi-Gigabit/s wireless exchanges and some usage models that can be associated solely with the 60GHz systems, for example the wireless display. In fact, the ability to transport uncompressed HD video is a major differentiating feature from the 2.4 and 5 GHz, or the UWB band which are not able to convey a throughput of 3Gbit/s with a packet loss rate of 10^{-8} and a maximum delay of 10ms as required for an uncompressed 1080p video [60]. The other applications proposed by the 60GHz band are the synchronization of mobile devices, the high speed upload and download of large files to/from a home server, the internet... More globally, the idea consists

[2]The regulatory agencies regulating the use of the millimeter-wave band are:

- the Federal Communications Commission (FCC) for United States of America (USA)
- the Conference Européenne des Postes et Télécommunications (CEPT) for Europe, i.e. the European Conference of Postal and Telecommunications Administrations.
- the Australian Communications and Media Authority (ACMA) for Australia
- the Millimeter Wave band Frequency Study Group (MWFSG) for South Korea

in substituting all the cables usually present between computers, tablets, mouses, keyboards, screens, hard disks, etc... All these usage models are summarized in figure 1.21.

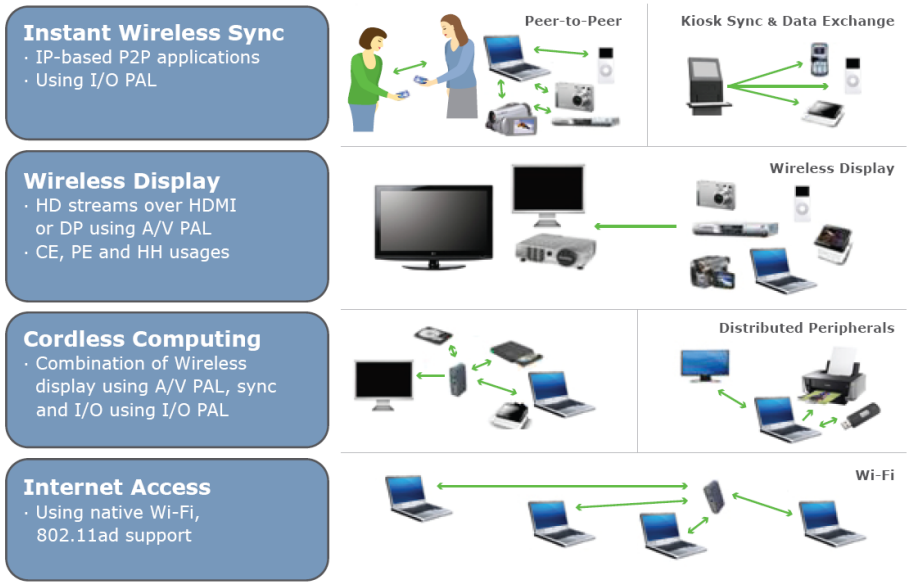

Figure 1.21: Usage models supported by the millimeter-wave band, from [9].

The 60GHz is considered very attractive by research laboratories, industry and standard groups. Consequently the millimeter-wave ecosystem has rapidly grown and is become quite complex. Two generations of 60GHz systems are trying to live together. The first one, dedicated to WPAN applications, has resulted in the achievement of the ECMA-387 [72] and IEEE 802.15.3c [73] standards, both largely influenced by the WirelessHD consortium [10]. The second generation, most recent, is for both WPAN and WLAN applications. The latter has led to the definition of the IEEE 802.11ad standard [33] resulting from the WiGig consortium [74]. The IEEE 802.11ad standard aims at guaranteeing the user experience of the IEEE 802.11 family and also at maintaining the networking possibilities, but by exceeding the Gigabit/s.

Finally the competition to impose one standard is rough and complex, but the IEEE 802.11.ad standard, supported by the WiGig consortium, would lead the race thanks to a Wi-Fi certification ensuring a good marketing name. Table 1.9 resumes these radio standards.

Table 1.9: Overview of the radio standards of the millimeter-wave band, [57 - 66] GHz, with year of publication, data rates and industrial products outlook.

WirelessHD	IEEE 802.15.3c	ECMA-387	IEEE 802.11ad
2008	2009	2008	2012
up to 7 138 Mbit/s	up to 5 670 Mbit/s	up to 25 400 Mbit/s	up to 6 757 Mbit/s
Niche market	Existing products "WirelessHD"	Future likely to be compromised	Certified Products "Wi-Fi Alliance" in 2012. Should become the standard for 60GHz WPAN

WirelessHD

The WirelessHD consortium, lead by the chipset manufacturer SiBEAM, is composed of major industrial players such as Broadcom, Intel, LG, Panasonic, Philips, NEC, Samsung, Sony and Toshiba. This consortium puts forward one of the most promising applications that allows the huge bandwidth of the millimeter-wave band: the uncompressed HD video streaming. Indeed, this lets remove compression and decompression stages that introduce latency and quality degradation.

The WirelessHD specification was first published in January 2008 during the CES (specification 1.0). It was the first generation of 60GHz products on the market (as the Gefen products [75]), but

it has reached only a niche market due to high prices and limited possibilities since it offers only to substitute HDMI cables. However, this proprietary solution has made efforts to evolve: since January 2010 (specification 1.1) the WirelessHD supports USB bridging and data networking based on IP. Unfortunately, no commercial product supporting these new features has seen the light of day.

The Wireless Video Area Network (WVAN) term is sometimes used for a WirelessHD network, the latter consisting in a coordinator and one or more stations as shown in figure 1.22 [76] [10].

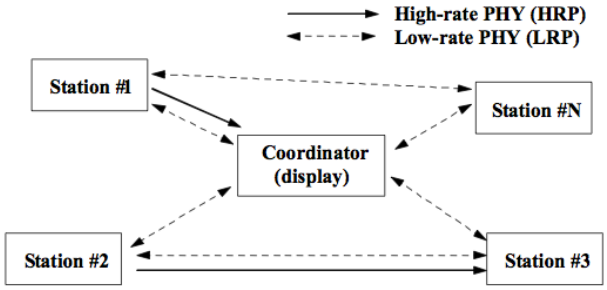

Figure 1.22: A Wireless Video Area Network (WVAN) based on WirelessHD, from [10].

Two PHY layers coexist in WirelessHD: a High Rate Physical layer (HRP) and a Low Rate Physical layer (LRP). The HRP layer is used to transfer data at speeds in excess of Gbit/s and to distances up to 10m thanks to the use of adaptive antennas. For these reasons, the HRP link is highly directional and can be used for unicast connections only. The LRP layer transports data at a rate lower than 40Mbit/s for the same distances up to 10m but using omni-directional antennas. Therefore, the LRP link can be used for unicast and broadcast connections. In addition, as all stations support the LRP layer, it is used for bidirectional links between stations (monitoring).

Table 1.10: General characteristics of the WirelessHD.

-	Data rates	Antenna technology	Use case
HRP	0.952 to 7.138 Gbit/s	directional link	High Definition video (multi-Gbit/s)
LRP	2.542 to 40.673 Mbit/s	omni-directional coverage	multi-Mbit/s bidirectional link

The specifications of the HRP and LRP OFDM layers are detailed in the table below.

Table 1.11: Specifications of the HRP and LRP OFDM PHY layers for WirelessHD solution.

Parameter	HRP value	LRP value
Occupied bandwidth	1.76 GHz	92 MHz
Sampling rate	2.538 GSa/s	317.25 MSa/s
Number of subcarriers	512	128
FFT period	201.73 ns	403.47 ns
Guard interval duration	25.22 ns	88.26 ns
OFDM symbol duration	226.95 ns	491.73 ns
Number of data subcarriers	336	30
Number of pilot subcarriers	16	4
Number of DC subcarriers	3	3
Number of null subcarriers	157	91
Number of reserved subcarriers	0	0
Modulation	QPSK, 16- or 64-QAM	BPSK

The HRP channels are located as defined in figure 1.20. Conversely, for one of these channels centered at f_c, three LRP channels are defined: they are centered at $f_c - 158.625\,\text{MHz}$, f_c or $f_c + 158.625\,\text{MHz}$, respectively. One example is provided in section 4.7, figure 4.81.

The WirelessHD consortium has been very active in the finalisation of the IEEE 802.15.3c standard. Consequently, the last generation of WirelessHD products complies with the 802.15.3c standard and is labeled "IEEE 802.15.3c compliant".

IEEE 802.15.3c

The IEEE 802.15.3c group has been formed in March 2005 under the leadership of the Japanese research center NICT (National Institute of Information and Communications Technology) in order to create a WPAN standard working at 60GHz. This is the first IEEE standard which operates in the millimeter-wave band and which has been designed for multi-Gigabit/s wireless transmission. This standard was published in september 2009, but currently no products can be found on the market, excepted WirelessHD products labeled "IEEE 802.15.3c compliant" [5].

Three PHY layers have been defined to meet different market segments, use cases and applications:

- Single Carrier (SC) mode based on SC modulations.
  PHY layer throughput: from 25.8 to 5280 Mbit/s.
  Modulation schemes: pi/2 BPSK, GMSK, QPSK, 8-QAM, 16-QAM, OOK and DRB.
- High Speed Interface (HSI) mode based on OFDM modulations (parameters shown in table 1.12).
  PHY layer throughput: from 32.1 to 5775 Mbit/s.
  Modulation schemes: QPSK, 16-QAM and 64-QAM.
- Audio/Visual (AV) mode based on OFDM modulations and on the WirelessHD specification.
  PHY layer throughput: from 952 to 3807 Mbit/s.
  Modulation schemes: BPSK for the LRP and QPSK and 16-QAM for the HRP.

The support of two types of modulation, SC and OFDM, offers different advantages. SC modulation, consuming low power and designed for low complexity, is the best choice for mobile devices running on battery. Its typical application will be the kiosk file downloading such as the synchronization of a smartphone with a computer, means point-to-point exchanges up to 1.5Gbit/s within 1m reach. On the contrary, OFDM modulation as the HSI mode described in the table 1.12 supports high speed and long-distance transmissions with multipaths. HSI mode, designed for low latency Non Line Of Sight (NLOS) bidirectional connectivity, is an important PHY layer for us as in the next chapters a major part of our tests will be conducted using this modulation scheme.

Lastly, the AV mode is composed of two PHY layers, a low throughput physical layer with omnidirectional coverage (LRP), and a high throughput physical layer with directional coverage to establish high speed exchanges (HRP). This AV mode corresponds to the WirelessHD specifications (table 1.11), excepted that the IEEE 802.15.3c specification of 2009 does not take into account the 64-QAM modulation.

ECMA-387

During the IEEE 802.15.3c development, the ECMA organization has developed a competing standard, the ECMA-387 that was published in December 2008 for an ISO approval in June 2009. The WiMedia Alliance was supposed to promote this standard, but as the trade association was in decline, ultimately it did not provide any support. No product has been launched on the market and now the standard is considered obsolete.

One important point of this standard is the possibility to support PHY rates up to 25Gbit/s thanks to channel bonding. This technology associates adjacent channels to obtain a larger bandwidth, up to 9GHz if the regional regulation allows for it, and consequently increases the throughput.

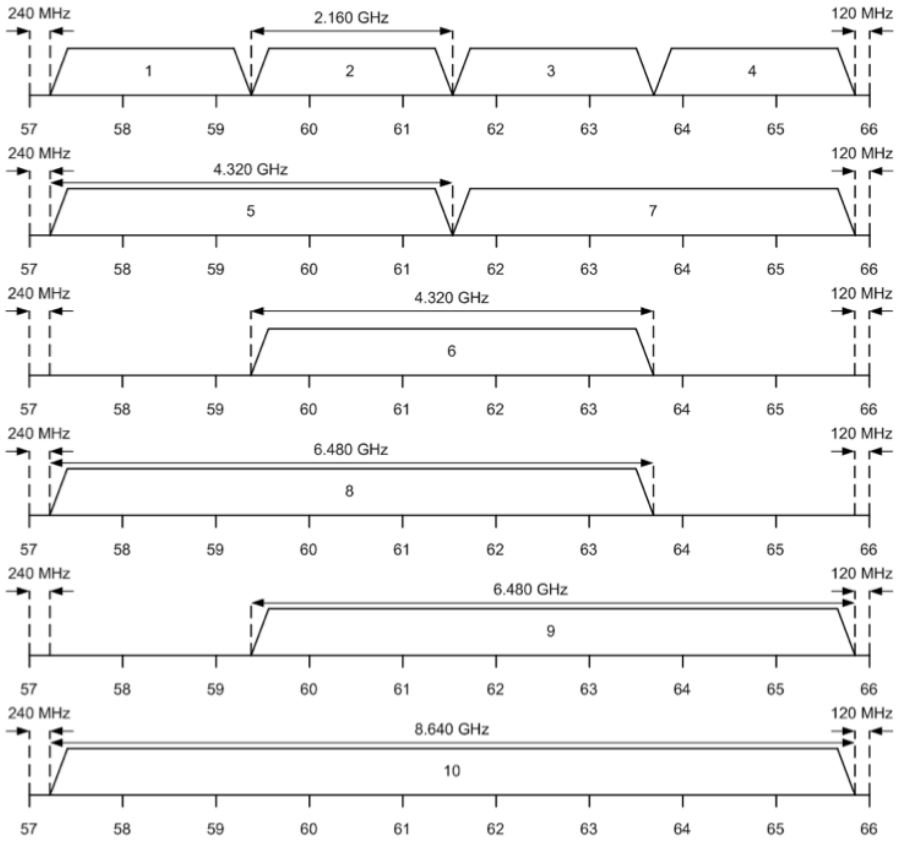

Figure 1.23: Channelization of 60GHz band with bonding.

The ECMA-387 standard is composed of three PHY layers to meet different market segments, use cases and applications:

- Type A based on SCBT and OFDM modulation with parameters shown in table 1.12.
  PHY layer throughput: from 397 to 6350 Mbit/s or up to 25.402Gbit/s with four bonded channels.
  Modulation schemes: BPSK, QPSK, NS 8-QAM and 16-QAM in SCBT, and QPSK and 16-QAM in OFDM.
- Type B based on SC modulation.
  PHY layer throughput: from 794 to 3175 Mbit/s or up to 12.701Gbit/s with four bonded channels.
  Modulation schemes: BPSK, QPSK.
- Type C based on SC modulation.
  PHY layer throughput: from 800 to 3200 Mbit/s.
  Modulation schemes: OOK and 4ASK.

Type A has been designed for WPAN applications and video streaming in Line Of Sight (LOS) and Non Line Of Sight (NLOS) environments, for a maximum range of 10m. Type B, the most economical mode, is able to convey video and data over short distances, typically less than 3m, but requiring LOS transmissions. Lastly, Type C, the simplest mode, supports only data point-to-point transmissions over 1m, without ensuring a quality of service.

Wireless Gigabit Alliance (WiGig or WGA)

The Wireless Gigabit Alliance (WiGig or WGA) was declared in May 2009 but this consortium had been formed for over two years. WiGig brings together influential industrial players as Intel, Broadcom, Atheros, Wilocity, and many others. The first WiGig specification was finalized in December 2009 (V1.0) and version 1.1 in 2011. This consortium has joined the IEEE 802.11ad task group.

IEEE 802.11ad

The IEEE 802.11ad standard, created in january 2009 and developed from the start as a new generation of Wi-Fi systems, deals with 60GHz components for the IEEE 802.11 family [5] [60]. If the competition to

impose one millimeter-wave standard is complex, the 11ad released, supported by the WiGig consortium, should lead the race since the 11ad products that will emerge on the market will be promoted by the Wi-Fi Alliance, thereby guaranteeing them opportunities. Indeed, it is expected that the IEEE 802.11ad chips will be installed in millions of devices, about 15 million units in 2015 according to In-Stat [77] or more than 40% of the total Wi-Fi market by 2016 according to the WiGig consortium [41]. These are the main reasons why the work carried out in this thesis has been focused on this standard (the study of the MAC layer in chapter 5) and why our HAN concept (described in chapter 2) has been presented to the Task Group ad (TGad) in January 2010 [78].

Some of the main contributors involved in the standardization process are Intel, Broadcom, Atheros, Marvell, Qualcomm, ST, Samsung, the Korean research centre ETRI and two operators, the Japanese NTT and the French France Télécom - Orange. The specification of the IEEE 802.11ad standard, based on the WiGig proposals, should be published in December 2012 (today only a pre-standard is available). As a consequence, IEEE 802.11ad products should be available in mass by 2013. Nevertheless, first products from Wilocity, based on the draft specifications, have been presented in January 2012 at CES [14]. Wilocity indicates that the key benefit of this technology is its speed [79]. For instance:

- Transferring 1000 photos between notebooks in 5 seconds (versus ∼1.5 minutes with 802.11n)
- Downloading a single 1080p movie to a tablet in 3 minutes (versus ∼1 hour with 802.11n)
- Uploading a 2-minute HD clip from a camcorder in 3 seconds (versus ∼1 minute with 802.11n)

In fact, as the other 60GHz wireless solutions, the data rate will be greater than 2Gbit/s in order to be more attractive than the current solutions such as the Wi-Fi at 2.4 and 5 GHz. At the same time, the IEEE 802.11ad standard maintains the Wi-Fi user experience and so the networking thanks to a backward compatibility with the previous 802.11 systems (same MAC architectures) and a new class of devices able to work in the 2.4, 5 and 60 GHz bands (more details in section 1.4.3).

This future Wi-Fi standard includes IP connectivity, but it also supports HDMI, DisplayPort, Universal Serial Bus (USB) and Peripheral Component Interconnect express (PCIe). It is therefore multiprotocol: IP, Audio-Visual (AV) and Input-Output (I/O) data can be used to communicate with various peripherals.

The IEEE 802.11ad standard is composed of four PHY layers to address different markets, use cases and applications:

- Control PHY (CP) based on SCBT modulation.
  PHY layer throughput: 27.5Mbit/s.
  Only one Modulation and Coding Scheme (MCS) for this mandatory PHY layer: DBPSK.
- Millimeter-wave OFDM PHY with parameters shown in table 1.12.
  PHY layer throughput: from 693.00 to 6756.75 Mbit/s.
  Modulation schemes: SQPSK (Spread QPSK), QPSK, 16-QAM, 64-QAM.
- Millimeter-wave SC PHY.
  PHY layer throughput: from 385 to 4620 Mbit/s.
  Modulation schemes: $\pi/2$ BPSK, $\pi/2$ QPSK, $\pi/2$ 16-QAM.
- Millimeter-wave Low Power SC PHY.
  PHY layer throughput: from 626 to 2502 Mbit/s.
  Modulation schemes: $\pi/2$ BPSK, $\pi/2$ QPSK.

As previously, SC modulation is designed for low power consumption and low complexity, but it presents nonetheless multiGigabit/s possibilities in LOS over short distances. As for OFDM, it is perfectly adapted to high speed rates in NLOS environment with a maximum range of 10m. Lastly, Control PHY is the most robustly coded mode as it is based on low throughput, code spreading, differential encoding and BPSK modulation. Thanks to this noise tolerance, Control PHY can be dedicate to the transmission of control channel messages.

Finally table 1.12 summarizes the specifications of different OFDM PHY layer: the IEEE 802.15.3c standard, HSI mode, the ECMA-387 standard, Type A, and the IEEE 802.11ad standard, OFDM PHY.

Table 1.12: OFDM PHY layer specification for the 60GHz standards.

Parameters	IEEE 802.15.3c HSI mode	ECMA-387 Type A	IEEE 802.11ad OFDM PHY
Occupied bandwidth	1.815 GHz	~1.904 GHz	1.815 GHz
Sampling rate	2.640 GSa/s	2.592 GSa/s	2.640 GSa/s
Number of subcarriers	512	512	512
FFT period	193.9 ns	197.53 ns	193.9 ns
Cyclic Prefix duration	24.24 ns	24.70 ns	48.5 ns
Cyclic Prefix length	64	64	128
OFDM symbol duration	218.18 ns	222.23 ns	242.4 ns
Number of data subcarriers	336	360	336
Number of pilots subcarriers	16	16	16
Number of DC subcarriers	3	3	3
Number of null subcarriers	141	133	0
Number of unused subcarriers	16	0	157
Modulation	QPSK 16-QAM, 64-QAM	QPSK 16-QAM	SQPSK, QPSK 16-QAM, 64-QAM

Some data in this table are linked. For instance, the occupied bandwidth, also called nominal used bandwidth, is the number of used subcarriers (data + pilots) multiplied by subcarrier spacing [27], with:

$$Subcarrier\ spacing = \frac{Sampling\ rate}{Number\ of\ subcarriers} \tag{1.7}$$

The occupied bandwidth is so lower than predicted by the sampling rate as no transmission occurs at the null subcarriers placed on both sides of the OFDM spectrum. These subcarriers provide a degree of freedom in the conception of OFDM signals and help to reduce the signal bandwidth playing the role of frequency guard bands. Likewise, the Direct Current (DC) subcarriers, corresponding to frequencies close to the center frequency of the transmitting station, are fixed to zero in order to simplify the design of the emitter and of the receiver. In fact, DC offset can be a problem for some components, particularly for the DAC and ADC [80]. A last important relationship of the table 1.12 is:

$$\begin{aligned} OFDM\ symbol\ duration &= Cyclic\ Prefix\ duration + FFT\ period \\ &= \frac{Cyclic\ Prefix\ length}{Sampling\ rate} + \frac{Number\ of\ subcarriers}{Sampling\ rate} \end{aligned} \tag{1.8}$$

1.4 Method to extend the radio coverage

1.4.1 Short radio ranges

The millimeter-wave band allows extremely fast transmissions, but it presents a major challenge since in radio communications the use of high frequencies is synonymous of reduced transmission distances. Indeed, the free-space path loss can be calculated as follows:

$$Free\text{-}space\ path\ loss\ [\text{dB}] = -10 \cdot \log\left(\frac{4\pi\, d}{\lambda}\right)^2, \text{ with } \lambda = \frac{c}{f}\,. \tag{1.9}$$

where,

- d is the propagation distance in free-space, [m].
- λ is the wavelength, [m].
- c is the velocity of light in the air, close to the speed in vacuum, $\sim 3\ 10^8 m/s$.
- f is the frequency of the radio wave, [Hz].

At 60GHz, equation 1.9 gives free-space losses equal to 68 and 88 dB for distances of respectively 1 and 10 m. The same calculations at 5GHz give losses of 46.4 and 66.4 dB, i.e. 21.6dB less.

To reduce the effects of the high channel attenuation at 60GHz and to allow the emergence of Multi-Gigabit Wireless Systems, the regulators have permitted high power level transmissions (table

1.8). However, even with that the wireless systems previously presented have a radio range limited to few meters, generally up to 10m. Additionally, millimeter-waves do not cross the walls, thereby the coverage is reduced to small indoor open areas or to single rooms.

Moreover, it is generally admitted that the oxygen molecules (O_2) induce additional attenuation at 60GHz [81]. Indeed, losses are greater at frequencies coinciding with the mechanical resonant frequencies of the gas molecules, and the first resonance of oxygen is located around 60GHz [82].

As the behavior of atmospheric oxygen is pressure dependent, we consider a typical case with a pressure at 1013mbar corresponding to the sea level. The example of figure 1.24 give us the attenuation for the 60GHz band. This result, based on a standard atmosphere, shows that up to 16dB/km can be observed, i.e. 0.16dB free-space losses for 10m propagation. Consequently, for the HAN, the atmospheric oxygen effects will be neglected.

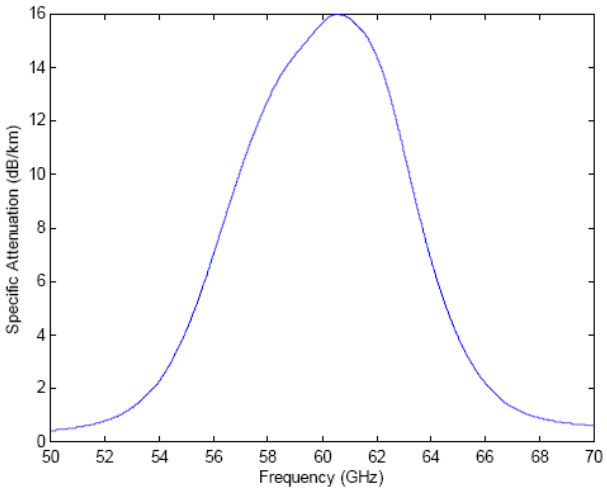

Figure 1.24: Attenuation due to the atmospheric oxygen as a function of the frequency, from [11].

On the contrary, the influence of obstacles such as furniture, walls or moving humans on the 60GHz channel has to be considered seriously as demonstrated in [12]. Among other things, the reference [12] shows the influence of a person on a radio signal at 67GHz thanks to the study of two cases: a living room scenario with a LOS transmission and a conference room scenario with NLOS transmission where a single reflection on a wall occurs. To characterize the impact of the human body, one person crosses the radio paths with different walking speeds and at different distances from the radio devices. Figure 1.25 shows the induced attenuation for each scenario. Two conclusions can be made: first, people attenuate the communication link by at least 15dB[3], and secondly, the influence of people on the radio wave propagation begins shortly before that someone cuts the radio beam due to diffraction around the person.

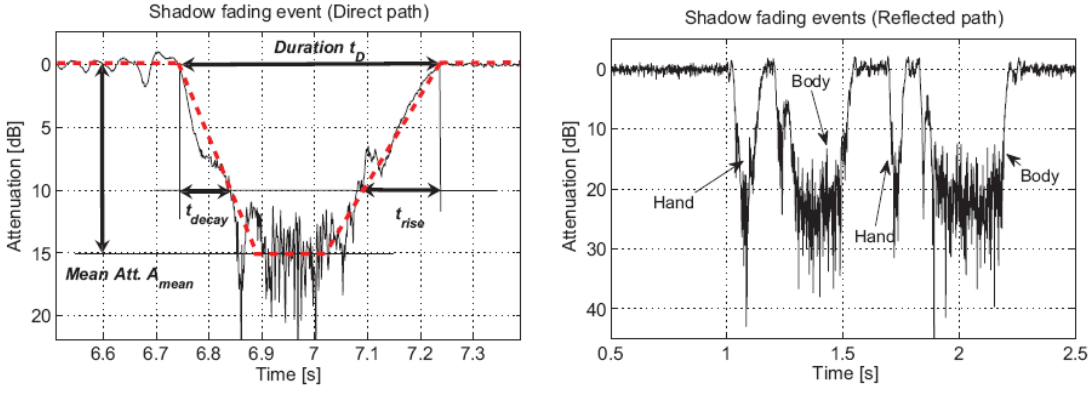

Figure 1.25: Human-induced shadowing events influenced by the human body and the swinging motion of the human hand at a frequency of 67 GHz. In dashed line the corresponding model, from [12].

[3]In this case, attenuation is mainly due to the H_2O absorption since a significant fraction of the human body is water

In the next sections, solutions to by-pass this coverage limitation are described.

1.4.2 The beamforming technology

Considering the high channel attenuation in the 60GHz band, it is advisable to use high gain antennas for transmission and reception. It is even more relevant to choose steerable directional antennas able to find automatically the best path between two stations according to the environment, the obstacles, etc... This is the beamforming (BF), a process used by a pair of stations to determine the best transmission and reception antenna patterns and so to achieve the necessary radio link budget for subsequent communication. After BF, the wireless stations communicate between them compensating the free-space path losses by concentrating radio power in a preferred direction, and improving the signal reception by rejecting interferences.

In practice, the BF is performed either by a set of directional antennas, as described in figure 1.27, or through the use of a phased-array antenna (or an adaptive array antenna) as shown in figure 1.28. It has to be noted that this technique is particularly well adapted to the 60GHz band as millimeter-wave antennas have small size. For example, a phased-array antenna composed of 40 elements ($10 \cdot log(40) = 16$dB gain) can be packed in $2.4cm \times 2.4cm$ thanks to millimeter wavelength (figure 1.26).

Figure 1.26: Murata WirelessHD receiver module, from [13]. Its dimensions are: 121.9×23.5×8.2 mm.

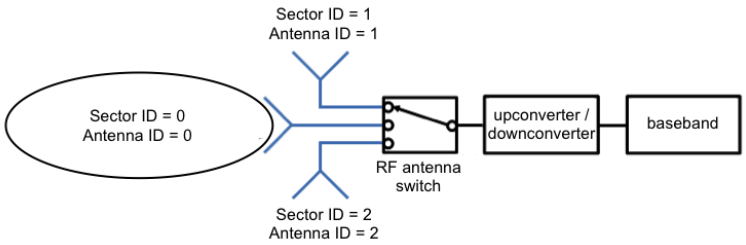

Figure 1.27: Multiple directionnal antennas.

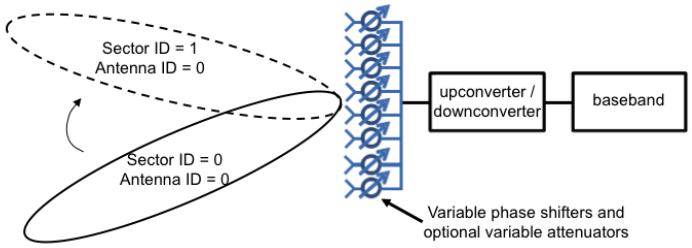

Figure 1.28: One smart antenna with multiple antenna elements (Phased-array antenna or adaptative array antenna).

The antennas specifications are manufacturer dependent, even if some limitations are imposed by the radio standards. For example, the IEEE 802.11ad standard defines a maximum number of elements for a set of directional antennas and a maximum number of sectors for a phased-array antenna. Indeed, in the radio MAC layer, the antennas, identified by antenna and sector IDs, are coded over 6 bits for the Sector ID fields and over 2 bits for the Antenna ID fields.

In the IEEE 802.11ad MAC layer, Antenna ID = [1:3] *and* Sector ID = [0:63].

The beamforming processes are described in the IEEE 802.15.3c standard under the name Directional CAP and in the IEEE 802.11ad standard under the name Beamforming. More details on Beamforming in IEEE 802.11ad will be given in chapter 5.

This is antenna-based beamforming and it does not have to be confused with the electronic beamforming used in the IEEE 802.11n chips (one of the MIMO techniques) and which takes advantage of signal processing techniques and multiple transmit paths to optimize the sent signal (almost always implemented using omni-directional antennas, excepted proprietary solutions such as the Ruckus Wireless one [83]).

1.4.3 The fast session transfer technology

The IEEE 802.11 family exploits three bands:

- the 2.4GHz band called Low Band
- the 5GHz band called High Band
- the 60GHz band called Ultra Band

The frequencies below 1GHz related to the television white spaces are here voluntary ignored as the corresponding transmission distances concern access use cases and not indoor ones. The systems operating at these frequencies are still under standardization in the IEEE 802.11af.

The 2.4 and 5 GHz radio bands provide a whole home coverage, but with limited throughputs. On the contrary, the 60GHz band offers multi-Gigabit/s data rates, but with a radio coverage reduced to a single room. The Fast Session Transfer (FST) allows the transition between the 60GHz band and the 2.4 and 5 GHz bands in order to have the best of the two worlds. The coverage can be temporarily increased to the detriment of the throughput, and vice versa. This multi-band operation, defined in the IEEE 802.11ad standard, offers a greatly improved user experience. Users with multi-band devices are able to access to the network, without interruption, with data rates at least as good as the current Wi-Fi products though enjoying the extra speed of the IEEE 802.11ad each time it is available. The most interesting in these multi-band devices, called sometimes tri-band devices [14] and at other times combo 60 GHz and 2.4 / 5 GHz devices [60], is that the users are unaware of which frequency is operating, the process is totally transparent.

Figure 1.29: Wilocity's chip for IEEE 802.11ad communications at 60GHz paired with a Qualcomm Atheros' chip for IEEE 802.11n networking, from [14].

1.4.4 Relay mode

Typically, each device transmits its own messages, but other paradigms exist as the relay operation. In relay operation, the point-to-point communications are replaced by cooperative schemes where distributed wireless devices collaborate together to transmit data between a transmitter and a receiver not necessarily directly visible. This concept was born at the end of the 60's, but it is has been implemented only recently in standards such as IEEE 802.11ad, IEEE 802.16 j/m (WiMAX), LTE-Advanced.

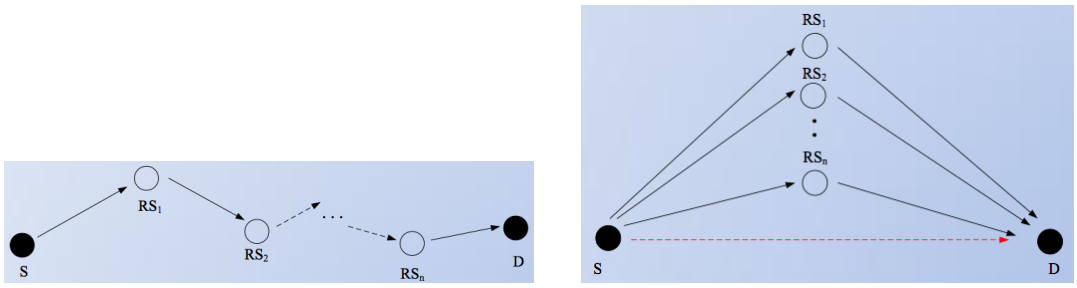

Figure 1.30: Multi-hop and MIMO relay systems, from [6].

The use of one or more intermediate cooperative devices, called Relay Stations (RS), in a transmission between a Source (S) and a Destination (D) station extends the radio coverage, enhances the signal robustness and improves the capacity. For devices located within a same radio coverage, the best relay path can be selected to minimize channel impairments, or parallel relay paths can be used simultaneously to bring diversity gain. In this latter case, devices share their antennas to form a virtual MIMO system, a convenient system in the low frequency bands where the size of antennas are important or in the frequency bands where the radiated power is limited. Lately, mesh networks can be built with stations being sometimes used as clients and at other times as nodes.

The relay stations can be classified in two groups. The first one corresponds to the transparent relaying techniques keeping the data and/or the waveform of the wireless signal intact. As only power scaling and/or phase rotation are allowed, this technique remains simple to be implemented and introduces no critical delay. The second relaying technique is called non-transparent or regenerative as it modifies the transmitted data and/or the waveform of the wireless signal. Thanks to regeneration, the noise acquired during one hop is not transmitted to the next hop and S-RS and RS-D links can be optimized separately.

Table 1.13: relaying techniques.

Transparent relaying techniques	Non-transparent relaying techniques
Amplify and Forward relaying (AF)	Decode and Forward (DF)
Linear Process and Forward	Estimate and Forward
Non Linear Process and Forward	Compress and Forward

As an example, a dual-hop AF relay system for OFDM signal with subcarriers permutations is proposed in [6]. Figure 1.31 represents this system requiring only a PHY layer. Indeed, the subcarriers permutations are realized depending on the SNRs received at the relay station and received by the final device, thus only channel estimations have to be realized.

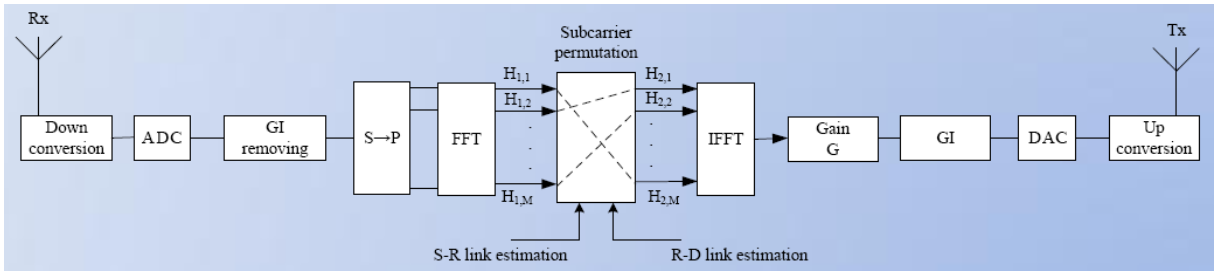

Figure 1.31: Block diagram of AF relay station (just uplink) with fixed gain and subcarrier permutation. This figure reuses the basic blocks of figure 1.16, for example the Guard Interval (GI) is a Cyclic Prefix or a Zero Pad Suffix.

Assuming that the ideal estimation of the S-RS and RS-D links is performed, different subcarrier permutations are allowed to minimize the BER of the system such as an allocation of the best SNRs of the S-RS link to the best SNRs of the RS-D link (Best to Best) or to the worst SNRs of the RS-D link (Best to Worst). In the given example, the Best to Best permutation scheme provides the more efficient results.

Another example of relay system for OFDM signal is proposed in [15] and [16]. It consist in high data-rate wireless repeaters composed of a first unit receiving the millimeter-wave signal and adapting it for a short range MIMO transmission through a wall, and of a second unit retransmitting in the air this signal coming from the wall. The principle of this system is described figure 1.32. In [16], the MIMO transmission is realized in Intermediate Frequency, at 5GHz, through a wall made of concrete blocks with a thickness of 120mm, corresponding to 13dB insertion losses. To measure experimentally the effectiveness of this short range MIMO link, the used IF signal is based on the IEEE 802.11n standard as MIMO systems are already developed in this standard. Finally, with a short range 4x4 MIMO transmission, 1.2Gbit/s has been achieved in 80MHz bandwidth.

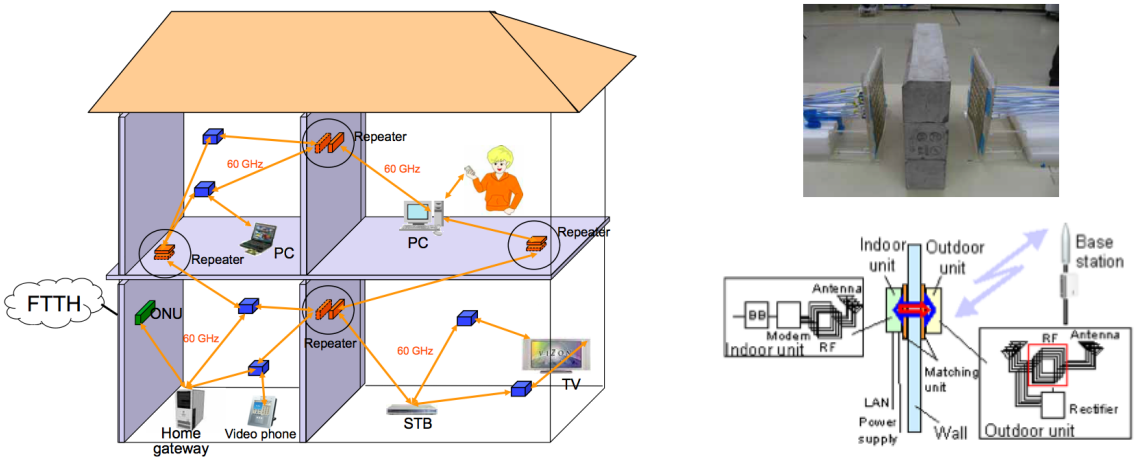

Figure 1.32: On the left, 60GHz wireless repeaters inside a Home Area Network [15]. Details are shown on the right with a picture of the MIMO antennas on the top [15] and a scheme of the repeater system on the bottom [16].

A last example is given in chapter 5 where MAC layer details on the relay mode of the IEEE 802.11ad standard are provided.

1.4.5 Several access points interconnected by Ethernet links

The range of the wireless systems can be extended by Access Points (AP) judiciously located in the home and interconnected thanks to Ethernet links. This solution is already massively adopted in LANs and campus to expand the coverage of Wi-Fi systems, and in these cases, the Ethernet backbone is based either on 100Mbit/s throughput to support the data rates of IEEE 802.11 a/b/g or on 1Gbit/s throughput to support the 11n release. To transport the signal conveyed by one millimeter-wave channel that can attain up to 7Gbit/s bit rate, it will be necessary to move towards 10Gbit/s solutions:

- either using the Ethernet 10GBase-T, also called IEEE 802.3an [84], which conveys 10Gbit/s in full duplex over four copper pairs of category 6 or 7 and on a maximum length of 100m.
- or using the Ethernet 10GBase-LRM which conveys 10Gbit/s in full duplex over silica MMF on a maximum length of 220m (see table 1.5).
- Technologies such as powerline or coaxial cable cannot be used because of their limited bandwidth.

It has to be noted that we can pass from the electrical solution to its optical counterpart easily, and vice-versa, using commercial media converters, for example Voltek products for 1Gbit/s throughput [85] or Alloy products for 10Gbit/s throughput [86].

With regard to the high-speed needs in the next 2-5 years, the optical solution seems the best choice. As a consequence, we obtain the HAN infrastructure depicted in figure 1.33.

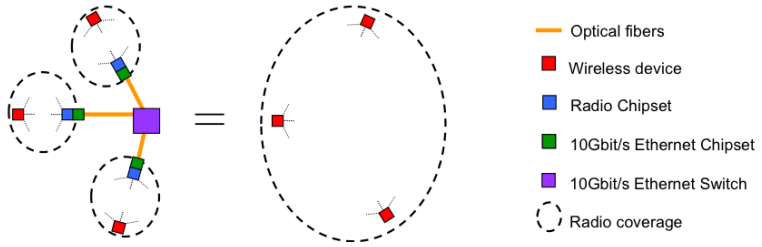

Figure 1.33: A HAN with several 60GHz APs interconnected by 10Gbit/s Ethernet links.

This solution based on different APs interconnected by 10Gbit/s optical Ethernet links presents several issues. First, with a 10Gbit/s backbone, the home infrastructure becomes insufficient as soon as channel bonding or more than one millimeter-wave channel is considered. Secondly, the introduction of a high speed Ethernet switch at the central node and of different chipsets inside each access point is a waste of energy due to multiple wireless / Ethernet conversions. Thirdly, these conversions introduce important latency in the system due to protocol adaptation. And lastly, the cost of such a system risks to be too high for home requirements. To sum up, this solution seems for the moment too complex and expensive to seduce massively the HAN market.

1.4.6 Summary

Solutions to improve the coverage limitation of the future wireless standards have been presented, but each of them presents some issues and is not completely satisfactory. The beamforming technology, which is implemented by default in the 60GHz standards, improves the coverage within the rooms and the open spaces increasing the signal gain and the interference rejection, but the signal still does not cross the walls. The Fast Session Transfer technology expands the radio range to the whole house but reduces the throughput to the speed of the 2.4 and 5 GHz Wi-Fi systems. The relay mode, an optional feature proposed by the future IEEE 802.11ad standard, could be an efficient solution, but only if a large number of devices supporting the relay mode are simultaneously used and if several repeaters are installed to pass through the walls. To finish, the use of several access points interconnected by Ethernet links offers a wide coverage and a high throughput, but it remains costly and needs a large number of access points consuming important quantities of energy. As a consequence, it is important to find a new way to improve the radio coverage inside the home.

From another point of view, having short ranges significantly reduces interferences between neighboring systems and makes the coexistence of a great variety of 60GHz systems possible in a single home, and even in a single room thanks to high directional antennas and spatial reuse techniques: two or more radio links can share the same frequency channel in the same space and at the same time as explained in [87].

1.5 ORIGIN project: Optical Radio Infrastructure for Gigabit/s Indoor Network

The work presented in this manuscript has been performed in the framework of the “ORIGIN” project (Optical Radio Infrastructure for Gigabit Indoor Networks), a collaborative project funded by DGCIS (Direction Générale de la Compétitivité, de l’Industrie et des Services, a unit of the French minister of the Economy, Industry and Employment). This project aims at proposing a new way to improve the very high bit rate radio coverage inside the home by means of the Radio over Fiber (RoF) technology.

ORIGIN has begun in January 2010 for a period of three years. It should lead to a pre-industrial prototype of a HAN using a Radio over Fiber infrastructure composed of RoF transducers, of a domestic cabling and of a central node. It is under the responsibility of Orange Labs / France Télécom and has three industrial partners - ACOME, Niji and SIRADEL - and three academic partners - Télécom Bretagne, ESYCOM (CNAM and ESIEE) and IREENA (become IETR in 2012).

Figure 1.34: The ORIGIN members.

The project outcomes are in chronological order:

- Analysis of the market and of the players
- Identification of service scenarios
- System specifications
- RoF transducers prototyping
- Performances measurement and validation
- Simulation of the complete system to write engineering rules
- Pre-industrial demonstration platform
- Business plan

The organization is divided into seven Sub-Projects (SP) as the following diagram:

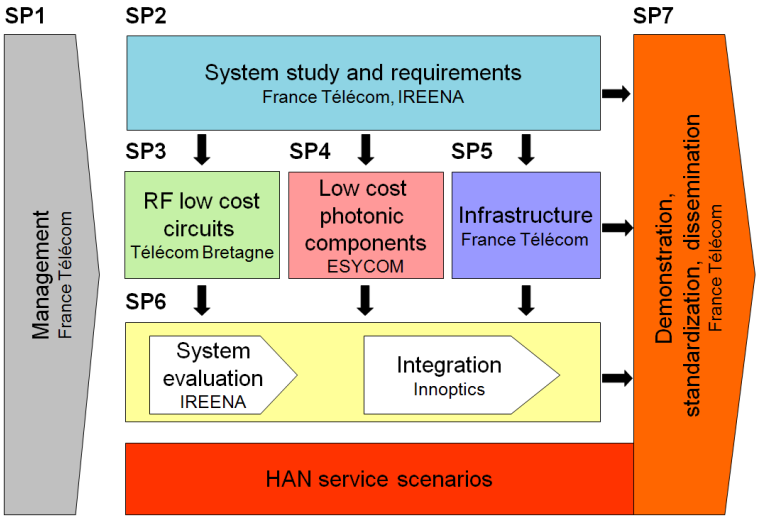

Figure 1.35: The ORIGIN structure and the partners in charge of each sub-project.

ORIGIN explores different optical architectures, starting with the simplest (point-to-point) but targeting a multipoint-to-multipoint architecture. An advantage of this target architecture is that our operator gateway is in line of sight to each terminal in the home, allowing us to provide operator services to these domestic devices. At the same time, each terminal is in visibility with one another, allowing them to exchange flows internally without loading the home gateway.

As a result, the Radio over Fiber technology and the state of art will be presented in chapter 2, the optoelectronic components that can compose the system will be studied in chapter 3, and the different RoF architectures that can be deployed inside the home will be characterized in chapter 4. These studies will determine the best specifications in order to optimize the transmission of a millimeter-wave radio signal inside the home. Afterwards, the last chapter will propose improvements for the HAN: infrastructure management to reduce the radiation and multiservice. In this last chapter, the ORIGIN results will also be presented.

Chapter 2

Radio over Fiber: a solution to expand the radio coverage of the millimeter-wave signals in the Home Area Network

2.1 Generalities and main application fields

2.1.1 Principle

To enlarge the coverage of the wireless millimeter-wave signals, hybrid systems combining fiber and radio technologies, called Radio over Fiber (RoF), are proposed. By definition, the RoF is focused on the optical transmission and it does not include necessarily a wireless one. Therefore, this thesis studies a specific case of RoF that associates the efficiency of the optical fibers for the distribution of radio signals to several wireless access points judiciously located in different rooms, with the main advantage of the wireless systems, the lack of wires and so the mobility. The paradigm offered by these systems is advantageous. Indeed, instead of distributing digital signals such as the Ethernet (IEEE 802.11ad) or the HDMI (WirelessHD) to communicate between each access point, a solution requiring conversions of signals (DAC and ADC) and protocols (buffering and latency, QoS issue, ...), the RoF systems distribute the radio signals in their native analogue format. In fact, the radio signals are only transposed onto an optical carrier by modulating the intensity light of a laser source, without changing the modulation format. However, this is possible only by the use of silica optical fibers that offer a wide bandwidth.

RoF transmissions can be used for multiple purposes such as the television distribution in the access network and inside the home or the transport of cellular signals between a base station and the remote antennas. In fact, this technology allows the transport of information over long distances with a low cost and high performances. In the HAN, the RoF technology aims at increasing the radio range seamlessly in order to cover the whole house: as shown in figure 2.1, different remote radio cells limited to the size of a single room (micro-cells) are connected together in order to have a single equivalent radio cell (macro-cell) in terms of radio.

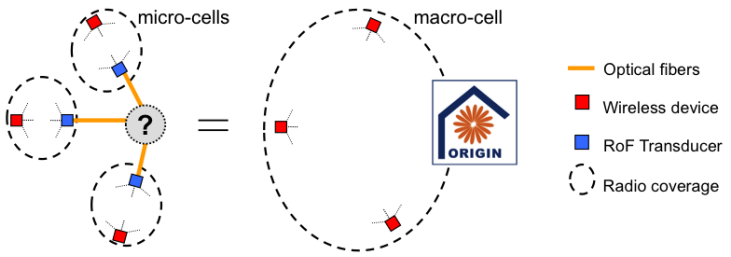

Figure 2.1: The paradigm offered by the Radio over Fiber (RoF) technology. The question mark is the RoF architecture interconnecting all the RoF transducers (section 2.3).

In the simplest case, a point-to-point link, two radio cells are unified placing at each end of a fiber a RoF transducer which transposes the radio signal into optical, and vice versa (E/O and O/E conversions at the interface between the wireless and wired medium). The components used for these transpositions are, respectively, a laser and a photodetector, as illustrated in figure 2.2.

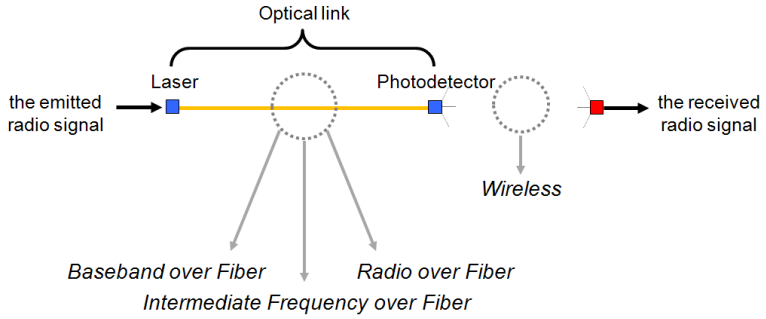

Figure 2.2: The RoF principle.

The RoF systems are usually classified into three main categories depending on the frequency range of the radio signal to carry: Baseband over Fiber, Intermediate Frequency over Fiber (IFoF) and Radio over Fiber (RoF).

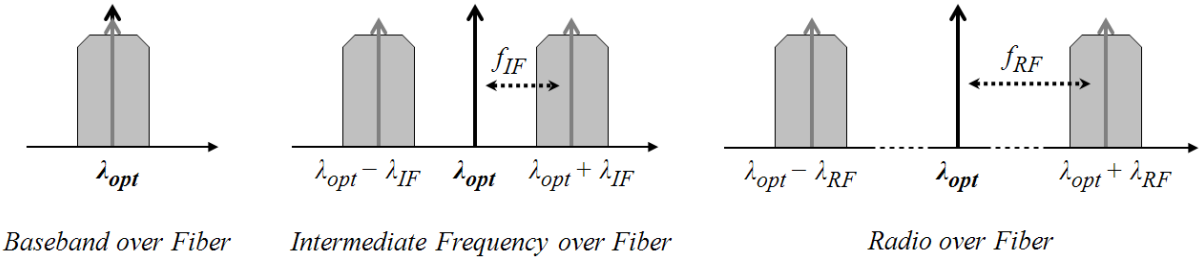

Figure 2.3: The different options that can be adopted to convey a radio signal.

Baseband over Fiber consists in transposing the radio signal in baseband before the optical transmission (center frequency is zero). However, the millimeter-wave radio signals can be modulated in OFDM: such a signal cannot be transposed in baseband, or only if a special type of multi-carrier modulation has been considered, with an Hermitian symmetry property between the subcarriers ($S(N-k) = S(k)^*$ for $k = 0$, ..., $N/2$ and with $S(k)$ the k^{th} subcarrier and N the total number of subcarriers [88]) to provide a modulated real-value signal. This alternative to conventional OFDM has not been adopted in the 60GHz radio standards, so Baseband over Fiber will not be considered subsequently. Digital baseband solutions (full radio demodulation or digital RoF [89]) are also not considered here as they not bring the remote antenna simplification that we want to obtain.

Intermediate Frequency over Fiber consists in transposing the radio signal at an Intermediate Frequency (IF) before the optical transmission. Thus, the required optoelectronic components bandwidths are reduced. This new center frequency can be included between the half of the value of the radio bandwidth (to avoid spectrum folding) and the original radio center frequency ($\sim$ 60GHz).

Lastly, Radio over Fiber consists in simply transposing the electrical radio signal onto an optical carrier for distribution over optical fiber, without changing the original radio center frequency at 60GHz. At the same time, the term “Radio over Fiber” is also used as a general term to refer to the three previous techniques.

The RoF systems allow substantial cost saving in the deployment of the future HANs since they greatly simplify the design of the wireless access points: no intelligence is required, only a physical layer. Indeed, in contrast to the example given in section 1.4.5 where radio access points are interconnected by Ethernet, the RoF transducers can be compact with a light weight, more reliable thanks to a lower complexity, and low power consuming too. Another great advantage due to the lack of a radio chipset in the transducers is the transparency to the radio layer protocols: the RoF links act as repeaters able to

carry indifferently any of the 60GHz wireless standards. In fact, only parameters of the physical layer of the radio signal are modified as the RF power (amplifier and attenuator) or the spectrum (filter, center frequency).

The home networks of tomorrow will be based on mixed architectures combining in a single system the advantages of the fiber optic (high-speed and low attenuation) and of the 60GHz wireless systems (high-speed and wireless). Thanks to the RoF, the mobility is get back, but not the health and hacking concerns: the radio waves remains well confined in the rooms where the RoF transducers have been installed and the users keep controlling the Electro-Magnetic Fields (EMF) exposure and sharing their data only inside their home.

Pros and cons of these systems are resumed as:

+ Radio coverage improvements.
+ Transparency of the system to radio layer protocols.
+ Simple remote antennas minimizing the risk of failure.
+ RoF transducers being compact and having light weight.
+ RoF transducers consuming low power.
+ Perspective of low cost.
+ Scalable and long-term optical infrastructure.
− Necessity to install new wires in houses.
− Additional noises and distortions on the signal due to the optical transmissions / conversions.

Different optical transmission techniques can be employed. The next section will describe the state of art of the main adopted methods, the ones described in figure 2.4.

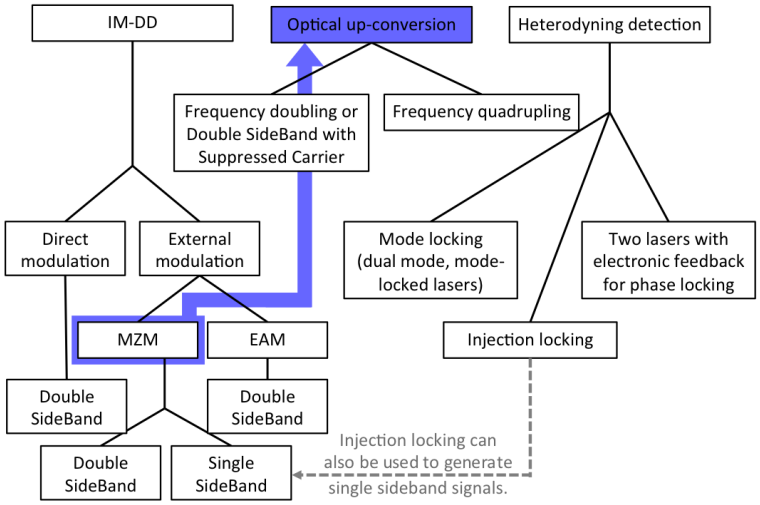

Figure 2.4: Classification of the main optical transmission / generation techniques of millimeter-waves.

2.2 The optical transmission / generation of millimeter-wave signals

2.2.1 Intensity Modulation - Direct Detection (IM-DD)

Direct modulation

The simplest technique for the transmission of a RF signal is the direct intensity modulation of a laser by driving its current. As it corresponds to an amplitude modulation, the optical spectrum presents two adjacent sidebands placed at both sides of the carrier frequency as depicted in figure 2.5. Consequently, the obtained output signal is called Double SideBand (DSB).

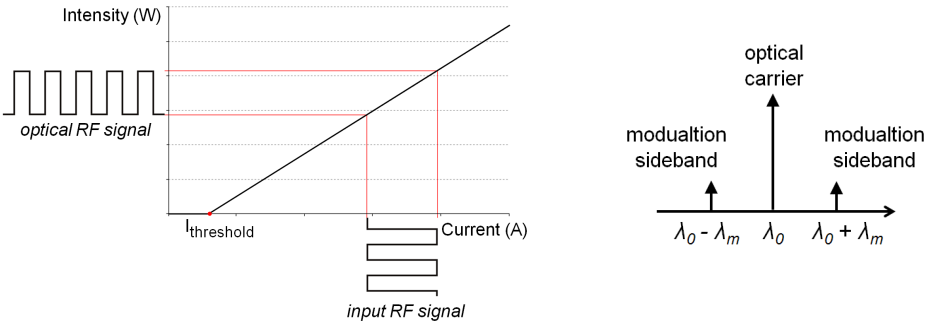

Figure 2.5: Direct modulation on the left and DSB signal on the right.

Even if this solution is low cost, it could become very expensive from the moment that high speed lasers are required. Therefore, the direct modulation is particularly well dedicated to IFoF systems. Additionally, IM-DD is limited by the fiber dispersion and the laser frequency chirp at very high frequency. To avoid the chirp, external modulations based on Mach Zehnder interferometers [90] [91] or on electro-absorption semiconductors are preferred.

Mach Zehnder Modulator (MZM for DSB or SSB transmission)

The Mach Zehnder Modulator (MZM) is a two-arms (or two-branches) interferometer: as depicted in figure 2.6, an incident optical wave is divided by a 50/50 splitter (Y_1) into two beams of equal intensity, which are guided in the two arms of the interferometer. On one arm, an applied electrical field introduces a phase shift on the optical signal exploiting the Pockels effect, an electro-optic effect appearing in some crystals such as the Lithium Niobate ($LiNbO_3$), the material most frequently used for this operation. Finally, at the output of the MZM, a second coupler (Y_2) allows the combination of the two mutually interfering waves. The optical output power equals to [17]:

$$P_{out} = \frac{P_{in}}{2}\left[1 + cos(\Delta\Phi(V))\right] \tag{2.1}$$

where P_{in} and P_{out} are the optical powers at the input and at the output of the MZM, respectively, and $\Delta\phi$ is the phase difference between the two interfering beams.

Equation 2.1 can be demonstrated calculating the signal at the output of the photodetector, which performs a quadratic detection. Indeed, the intensity is proportional to the square of the sum of the two optical fields within each arm of the MZM. This sum, represented by the electrical field E_0, is equal to:

$$\begin{aligned} E_0 &= \frac{A}{2}[cos(\omega_c t + \Delta\Phi(V)) + cos(\omega_c t)] \\ &= A\, cos\left(\omega_c t + \frac{\Delta\Phi(V)}{2}\right) cos\left(\frac{\Delta\Phi(V)}{2}\right) \end{aligned} \tag{2.2}$$

where A and ω_c are the amplitude and the angular frequency ($\omega_c = 2\pi f_c$) of the optical wave, respectively. As $cos(\omega_c t + \Delta\Phi(V)/2)$ falls outside the bandwidth of the photodetector, the output power is proportional to the square of $cos(\Delta\Phi(V)/2)$: equation 2.1 is thus obtained. Lastly, it has to be noted that an alternative MZM exists, the push-pull MZM where both arms are driven by a same RF signal, but with opposite phase. This one gives the same result at the output.

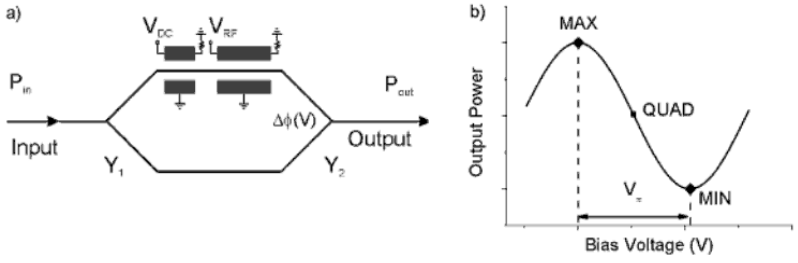

Figure 2.6: A single-drive MZM on the left and the corresponding power response on the right, from [17].

In figure 2.6, three singular operating points can be noted: the maximum point giving the full transmission, the quadrature point located in the middle of a linear area perfect to modulate the optical wave, and the minimum point giving the full extinction.

When the RF signal is transposed into the optical domain using a direct modulation or a MZM, two adjacent sidebands are observed in the frequency domain (figure 2.3) [90]. This double sideband (DSB) signal is affected by the chromatic dispersion which creates a phase difference between the two bands, a difference depending on the fiber length, the fiber dispersion parameter, the wavelength, and the modulation frequency. The worst case is a relative phase difference between the two bands of π at the photodetector involving destructive interferences. Nevertheless, some solutions exist:

- using dispersion compensating optical fibers.
- using an optical filter such as a Bragg grating filter to remove one sideband [92].
- using advanced modulations to generate a single sideband (SSB) signal.

To generate an optical signal in single sideband, a dual-drive MZM phase modulated on its two arms can be used [93].

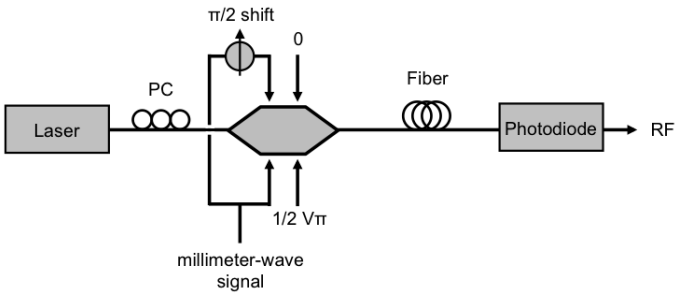

Figure 2.7: Modulation of a dual-drive MZM in order to obtain a SSB signal.

As depicted in figure 2.7, a laser emits a continuous optical wave with an amplitude A and an optical frequency f_c. This wave is then modulated by a RF signal of amplitude V_{AC} and frequency f_m using a dual-drive MZM operating at the quadrature point. Thanks to a $\pi/2$ phase shift between the two electrodes, instead of π, a SSB signal is observed at the output.

This output signal, represented by the electrical field E_0, can be written as the sum of two fields $A/2\ cos(\omega_c t + \Phi)$, with Φ the phase shift acquired on each arm:

$$E_0 = \frac{A}{2}[cos(\omega_c t + \beta\pi + \alpha\pi cos(\omega_m t)) + cos(\omega_c t + \alpha\pi sin(\omega_m t))] \tag{2.3}$$

where,

- $\alpha = (V_{AC}/2)/V_\pi$.
- $\beta = V_{DC}/V_\pi = 1/2$ (quadrature point).
- V_π is the modulation voltage required to change the phase by π in one arm, means to move from full transmission to full extinction.
- ω_c is the angular frequency of the optical wave, $\omega_c = 2\pi f_c$.
- ω_m is the angular frequency of the RF signal, $\omega_m = 2\pi f_m$.

Equation 2.3 can be developed as:

$$\begin{aligned} E_0 = \frac{A}{2}[&cos(\omega_c t + \beta\pi)cos(\alpha\pi cos(\omega_m t)) - sin(\omega_c t + \beta\pi)sin(\alpha\pi cos(\omega_m t)) \\ &+ cos(\omega_c t)cos(\alpha\pi sin(\omega_m t)) - sin(\omega_c t)sin(\alpha\pi sin(\omega_m t))] \end{aligned} \tag{2.4}$$

The decompositions of $cos(\alpha\pi sin(\omega_m t))$ and $sin(\alpha\pi sin(\omega_m t))$ in Fourier series can be written as Bessel functions of the first kind [94]:

$$\begin{cases} cos(\alpha\pi sin(\omega_m t)) = J_0(\alpha\pi) + 2[J_2(\alpha\pi)cos(2\omega_m t) + J_4(\alpha\pi)cos(4\omega_m t) + \cdots] \\ sin(\alpha\pi sin(\omega_m t)) = 2[J_1(\alpha\pi)sin(\omega_m t) + J_3(\alpha\pi)sin(3\omega_m t) + \cdots] \end{cases} \tag{2.5}$$

with $\alpha < 1/\pi$, i.e. a small RF signal amplitude, only the zero and first orders terms are significant:

$$\begin{cases} cos(\alpha\pi sin(\omega_m t)) \simeq J_0(\alpha\pi) \\ sin(\alpha\pi sin(\omega_m t)) \simeq 2J_1(\alpha\pi) sin(\omega_m t) \end{cases} \tag{2.6}$$

Equation 2.4 is now developed in Bessel functions of the first kind, and β is fixed to 1/2 (quadrature point):

$$\begin{aligned} E_0 &= \frac{A}{2}[cos(\omega_c t + \frac{\pi}{2}) cos(\alpha\pi sin(\omega_m t + \frac{\pi}{2})) - sin(\omega_c t + \frac{\pi}{2}) sin(\alpha\pi sin(\omega_m t + \frac{\pi}{2})) \\ &\quad + cos(\omega_c t) cos(\alpha\pi sin(\omega_m t)) - sin(\omega_c t) sin(\alpha\pi sin(\omega_m t))] \\ &= \frac{A}{2}[-sin(\omega_c t) J_0(\alpha\pi) - cos(\omega_c t) 2J_1(\alpha\pi) sin(\omega_m t + \frac{\pi}{2}) \\ &\quad + cos(\omega_c t) J_0(\alpha\pi) - sin(\omega_c t) 2J_1(\alpha\pi) sin(\omega_m t)] \\ &= \frac{A}{2}[J_0(\alpha\pi) cos(\omega_c t) - J_0(\alpha\pi) sin(\omega_c t) - 2J_1(\alpha\pi) cos((\omega_c - \omega_m)t)] \end{aligned} \tag{2.7}$$

The two first terms of the equation 2.7 correspond to the optical tone while the last term represents one adjacent sideband on the right. Therefore, the SSB signal observed at the output of the MZM has an amplitude equal to $A\,J_1(\alpha\pi)$. As shown in figure 2.8, the relationship among the amplitude of the modulating signal, α, and the amplitude of the output signal, $A\,J_1(\alpha\pi)$, can be approximated by a straight line passing through the origin and with a slope equal to $A\pi/2$.

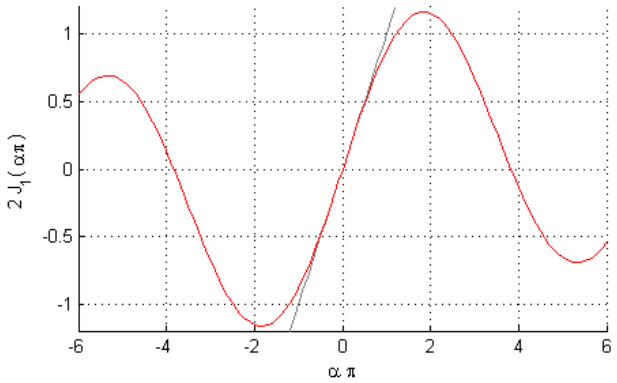

Figure 2.8: $2J_1(\alpha\pi)$ as a function of $\alpha\pi$.

As shown in [93] where this technique has been tested, the SSB modulation reduces significantly the dispersion effects. Lastly, it has to be noted that it is possible to go even further creating a tandem SSB signal [95] [96].

Electro-absorption modulator (EAM)

As the direct modulation technique presents a limited bandwidth, high speed external modulators can be preferred such as the MZM or the Electro-Absorption Modulator (EAM). The EAM represents a suitable and relevant solution for the millimeter-wave band as it is cost effective, compact and it offers high integration [97], especially with other semiconductor components such as SOAs or lasers since it is semiconductor-based. Nevertheless, it also presents some disadvantages as a high insertion loss, and generally it necessitates Impedance Matching Circuit (IMC) [98].

EAM exploits the absorption spectrum of semiconductors. Biasing a semiconductor crystal (with a voltage V) can change its absorption coefficient α (cm^{-1}) and thus modulate the propagating optical signal. The extinction ratio of an EAM, of active layer of length L (cm), is:

$$ER(V) = \frac{P_{out}(V)}{P_{in}} = e^{-\alpha(V)\times L} \tag{2.8}$$

The transfer function of a typical EAM is provided in [18] where the EAM is used to modulate simultaneously (electrical multiplex) a 2.5Gbit/s baseband signal, a sinusoidal microwave signal and a

155Mbit/s millimeter-wave signal centered at 59.6GHz. This clearly shows the large bandwidth of such components.

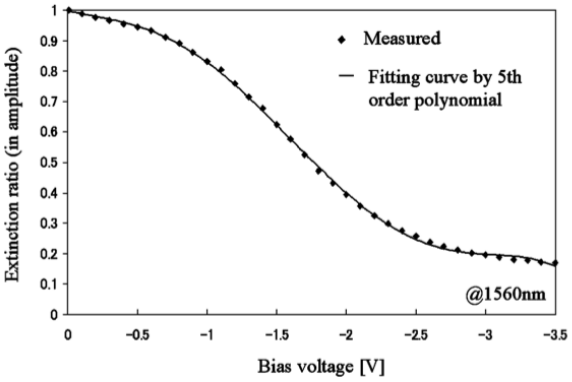

Figure 2.9: The measured extinction ratio of an EAM as a function of the bias voltage, from [18].

The electro-absorption structures can also be used as photodetectors, or as transceivers acting simultaneously as O/E and E/O converters. For example, this dual functionality contained in a single chip has been used in [97] as a photodiode at λ_1 for the data coming from a Central Station (CS), and also as a modulator for an unmodulated optical carrier at λ_2 coming from the same CS. This component removes the need of a laser at the remote site.

2.2.2 All optical up-conversion

This section introduces optical frequency up-conversion techniques based on advanced MZM and enabling to double [99], to quadruple [19] or to sextuple [95] a RF frequency, or to sum RF tones [95]. Only the frequency doubling and frequency quadrupling techniques will be presented as the other techniques are similar.

Frequency doubling

One solution for optical frequency doubling consists in creating a DSB signal and then suppressing the optical carrier. This goal can be achieved by modulating a dual-drive MZM biased at its minimum point as shown in the setup of figure 2.10. Compare to classic intensity modulations, the Optical Carrier Suppression (OCS) technique requires half RF carrier (relaxed modulation speed), occupies half optical bandwidth (great interest for WDM) and presents better performances (in terms of receiver sensitivity, propagation distance and power penalty) than DSB and SSB modulation according to [99].

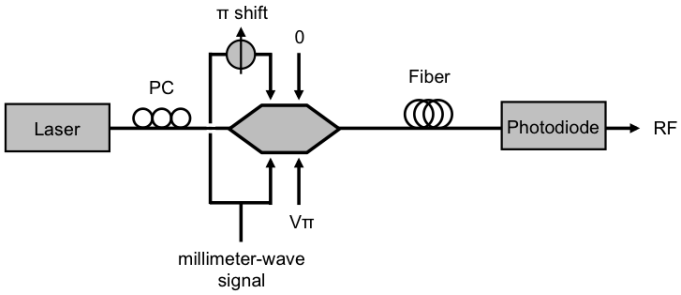

Figure 2.10: Optical carrier suppression technique.

To generate a DSB signal with suppressed carrier, a dual-drive MZM is biased at the minimum point and a π phase difference is applied between the two modulating signal. The output signal E_0 is:

$$E_0 = \frac{A}{2}\left[cos(\omega_c t + \beta\pi + \alpha\pi cos(\omega_m t)) + cos(\omega_c t + \alpha\pi cos(\omega_m t + \pi))\right] \tag{2.9}$$

where,

- $\alpha = (V_{AC}/2)/V_\pi$.
- $\beta = V_{DC}/V_\pi = 1$ (min point).

As a consequence:

$$E_0 = \frac{A}{2}\left[cos(\omega_c t - \alpha\pi cos(\omega_m t)) - cos(\omega_c t + \alpha\pi cos(\omega_m t))\right] \tag{2.10}$$

As shown in equation 2.10, only the optical tone is removed. The first term of the equation corresponds to the right side band and the second term to the left side band.

In [100], an alternative for frequency doubling is presented: a single-drive MZM creates a DSB signal, then an optical filter suppresses the optical carrier (DSB-SC). The setup is depicted in figure 2.11.

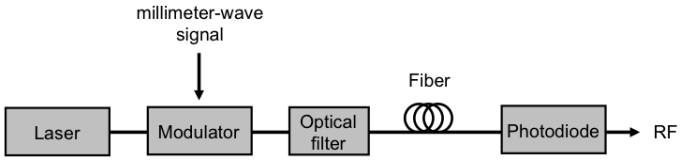

Figure 2.11: Double-sideband operation with suppressed carrier.

In [100], an optical carrier at 1550nm is modulated by a RF tone using a single-arm MZM, and is filtered in order to generate an oscillator at the double frequency after photodetection. Photodetected tones at 50 and 100 GHz are characterized: an optical carrier suppression of approximately 26dB were achieved and a phase noise levels of -69.8dB/Hz was measured at 10kHz from the carrier when the modulating oscillator had a phase noise level of -77.9dB/Hz. The main disadvantage of this doubling frequency technique is that the laser modulation speed is not enough relaxed. However, frequency quadrupling technique can be employed.

Frequency quadrupling

As depicted in figure 2.12, an integrated MZM (MZM-c), composed of two sub-MZMs (MZM-a and MZM-b) embedded in each of its arms, modulates an optical field coming from a laser source and defined as:

$$E_{in}(t) = Acos(\omega_c t) \tag{2.11}$$

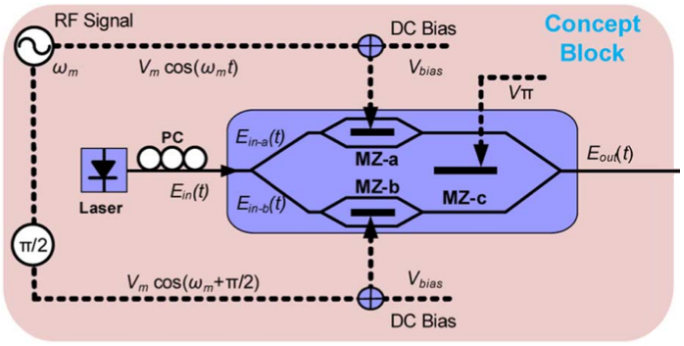

Figure 2.12: Optical up-conversion using a frequency multiplication technique, from [19].

MZM-c is biased at the minimum point (β=1) while MZM-a and MZM-b are biased at the maximum point (β=0). Therefore, the optical field at the output of MZM-c can be calculated reusing the equations 2.3 and 2.4:

$$E_0 = \frac{A}{2}\left[cos(\omega_c t)cos\left(\frac{\alpha\pi}{2}cos(\omega_m t)\right) + cos(\omega_c t)cos\left(\frac{\alpha\pi}{2}cos(\omega_m t + \pi/2) + \pi\right)\right] \tag{2.12}$$

with $\alpha = V_m/V_\pi$. After a development in Bessel functions of the first kind:

$$\begin{aligned} E_0 =& \frac{A}{2}[cos(\omega_c t)(J_0(\frac{\alpha\pi}{2}) + 2J_2(\frac{\alpha\pi}{2})cos(2\omega_m t + \frac{2\pi}{2}) + 2J_4(\frac{\alpha\pi}{2})cos(4\omega_m t + \frac{4\pi}{2}) \\ &+ 2J_6(\frac{\alpha\pi}{2})cos(6\omega_m t + \frac{6\pi}{2})) - cos(\omega_c t)(J_0(\frac{\alpha\pi}{2}) + 2J_2(\frac{\alpha\pi}{2})cos(2\omega_m t) \\ &+ 2J_4(\frac{\alpha\pi}{2})cos(4\omega_m t) + 2J_6(\frac{\alpha\pi}{2})cos(6\omega_m t))] \end{aligned} \tag{2.13}$$

Therefore:

$$\begin{aligned} E_0 =& \frac{A}{2}[cos(\omega_c t)(-2J_2(\frac{\alpha\pi}{2})cos(2\omega_m t) - 2J_6(\frac{\alpha\pi}{2})cos(6\omega_m t)) \\ &- cos(\omega_c t)(2J_2(\frac{\alpha\pi}{2})cos(2\omega_m t) + 2J_6(\frac{\alpha\pi}{2})cos(6\omega_m t))] \\ =& A[J_2(\frac{\alpha\pi}{2})cos(\omega_c t + 2\omega_m t) + J_2(\frac{\alpha\pi}{2})cos(\omega_c t - 2\omega_m t) \\ &+ J_6(\frac{\alpha\pi}{2})cos(\omega_c t + 6\omega_m t) + J_6(\frac{\alpha\pi}{2})cos(\omega_c t - 6\omega_m t)] \end{aligned} \tag{2.14}$$

The first two terms of equation 2.14 correspond to two sidebands centered at $\lambda_c - 2\lambda_{RF}$ and $\lambda_c + 2\lambda_{RF}$, respectively, while the last two terms correspond to two sidebands centered at $\lambda_c - 6\lambda_{RF}$ and $\lambda_c + 6\lambda_{RF}$. Theoretically, others terms exist at $\lambda_c \pm 10\lambda_{RF}$, $\lambda_c \pm 14\lambda_{RF}$, etc... but these high order terms have been neglected in equation 2.13 because they are insignificant for a modulation range between 0 and π. In fact, as shown in figure 2.13, only the terms of amplitude equal to $J_2(\alpha\pi/2)$ are kept. Finally, the photodetected signal is centered at $4\,\omega_m$ as the optical tone has been removed.

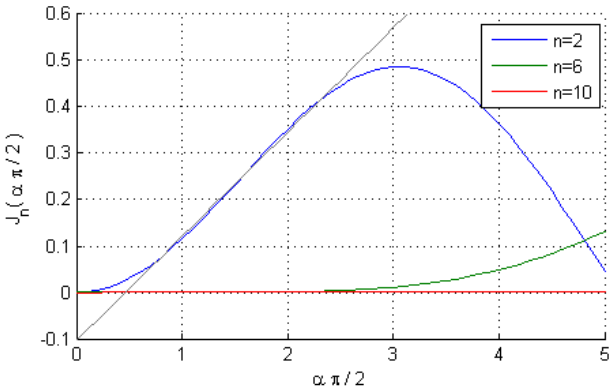

Figure 2.13: $J_n(\alpha\pi/2)$ as a function of $\alpha\pi/2$.

2.2.3 Optical coherent (heterodyne) detection methods to generate millimeter-waves

A large part of papers about RoF takes advantage of optical heterodyne detection methods to generate and transmit millimeter-wave signals. This technique consists in emitting two optical fields separated by the target RF frequency:

$$E_1 = E_{01}\cos(\omega_1 t) \text{ and } E_2 = E_{02}\cos(\omega_2 t) \tag{2.15}$$

where E_1 is the first optical field at the angular frequency ω_1 ($\lambda_1 = 2\pi c/\omega_1$) and E_2 is the second optical field at ω_2. The optical mixing of these two fields on a photodiode creates a millimeter-wave radio signal. Indeed, because of its quadratic detection, the photodetected current is proportional to the square of the sum of the optical fields:

$$i_{PD} = (E_1 + E_2)^2 = E_{01}^2\,\frac{1+\cos(2\omega_1 t)}{2} + 2E_{01}E_{02}\cos[(\omega_1 - \omega_2)t] + E_{02}^2\,\frac{1+\cos(2\omega_2 t)}{2} \tag{2.16}$$

As the first harmonic terms are too high to be detected by the photodiode, only the $E_{01}E_{02}cos((\omega_1 - \omega_2)t)$ term remains: it shows that the beat signal is controlled by the frequency spacing between the two

optical fields. For instance, at 1550nm, the required wavelength separation between the two optical fields has to be equals to 484.7pm to obtain a frequency spacing of 60.48GHz.

$$\Delta\nu = \frac{c}{\lambda^2}\,\Delta\lambda = \frac{299792458}{(1550\ 10^{-9})^2}\ 484.7\ 10^{-12} \simeq 60.48\ 10^{9}\ Hz \tag{2.17}$$

Consequently, for high frequency generation, optical heterodyning is a promising technique removing the need of millimeter-wave oscillators at the emission and relaxing the laser modulation speeds. However, the photodiode still requires high bandwidth since it has to detect the beat signal of the incoming optical waves.

The different approaches to generate the two optical fields necessary to the optical heterodyne detection method are briefly described below.

Dual-wavelengths system

A first method to emit two optical waves consists in using two separate lasers. Practically, one is modulated by a radio signal while the other, called local oscillator laser or reference laser [101], emits a continuous optical wave. Figure 2.14 presents the typical setup of such a system.

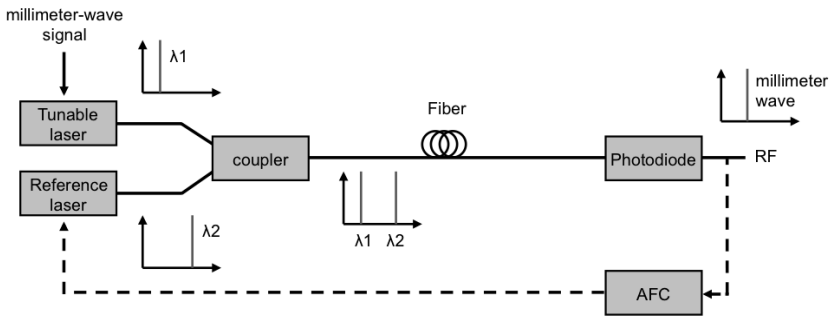

Figure 2.14: A two wavelengths system.

In the example given in [101], two DFB lasers emitting around 1.54μm are used to generate a millimeter-wave signal between 60 and 70 GHz. The directly modulated laser is fed by a Pseudo-Random Binary Sequence (PRBS) NRZ signal at 140Mbit/s while the reference laser is stabilized by an Automatic Frequency Control (AFC) loop in order to maintain a fixed center millimeter-wave frequency. After combining the two optical fields, the signal is transmitted over SMF up to 12km-length. The authors indicate that the millimeter-wave carrier has a large linewidth of approximately 4MHz due to important laser phase noises, which are transposed in the millimeter-wave domain and reduce the performances. Nevertheless, a BER below 10^{-9} is obtained in this example.

One of the main advantage of a two wavelengths system is its high flexibility: frequencies from some Megahertz up to the Terahertz can be generated choosing a suitable couple of wavelengths. For instance, in [100], a tunable reference laser source around 1.55μm generates millimeter-wave tones from 66 to 116 GHz.

However, the frequency spacing between the two optical sources has to be finely controlled to keep the radio signal stable, and generally an electronic feedback is required and the low cost lasers highly sensitive to temperature changes are proscribed. Anyway, if the two wavelengths systems do not provide acceptable signal purity due to uncorrelated laser phase noise terms, other heterodyne generation methods exist.

Injection locking

To obtain two wavelengths with correlated phase-noise terms, a mode locking can be realized injecting an external optical field inside the two laser cavities generating the wavelengths necessary to the optical heterodyne detection method. With injection, a laser such as a Fabry-Pérot can be locked at one mode: the characteristics of the semiconductor can be modified for single mode operation with a Side-Mode

Suppression Ratio (SMSR) higher than 50dB as shown in [102].

In an injection locking technique as the one depicted in figure 2.15, a master laser is modulated (directly or externally as below) by a sinusoidal signal creating therefore two sidebands, while two slave lasers, placed in parallel and fed by the master laser, are unmodulated. The slave lasers are injection locked to the lower and upper sidebands, respectively. Hence, with correlated phase noise terms at the output of the two injection-locked lasers, the phase noise will be cancelled using heterodyning detection.

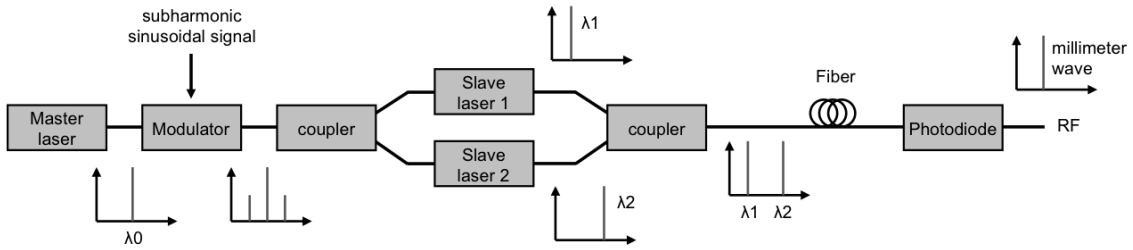

Figure 2.15: A two wavelengths system with optical injection locking technique, adapted from [20].

This technique has been demonstrated in [101] where a 62.5GHz signal has been generated locking the -10^{th} and +10^{th} sideband harmonics of a master laser directly modulated by an oscillator at 3.125GHz. Concerning the performances, the millimeter-wave tone presents a phase noise of -70 and -90 dB/Hz at offset frequencies of 1 and 100 kHz, respectively. Lastly, in [103], it is noticed that injecting external light into semiconductor lasers can also significantly increase the modulation bandwidth, reduce the Relative Intensity Noise (RIN) and decrease the Chirp-to-Power Ratio (CPR).

Since optical injection is mentioned, it has to be noted that a SSB signal generation technique can compete with the one using a MZM and cited page 41. Figure 2.16 describes this new SSB method where a strong optical injection locking with a positive frequency detuning is applied, i.e. the master laser frequency, f_{inj}, is higher than the slave cavity mode frequency, f_c.

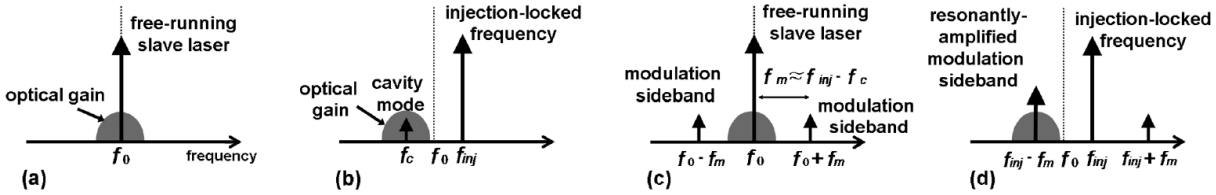

Figure 2.16: A free-running slave laser emission spectrum in (a), with an external light injection in (b), with a direct RF modulation in (c) and with both in (d), from [21].

On the one hand, as explained previously and as illustrated in figure 2.16 (c), a free-running slave laser directly modulated by a millimeter-wave signal generates two sidebands. On the other hand, this free-running slave laser, when it is not directly modulated but when it is under the optical injection of a first laser, as depicted in figure 2.16 (b), its cavity mode is shifted. In fact, the injected field enhances the stimulated emission inside the slave laser cavity. As a consequence, the carrier density is reduced, the index of refraction decreases and the cavity resonance is shifted towards a longer wavelength. In other terms, the injection-locked laser operates at a frequency different from its cavity resonance condition [104].

Now, figure 2.16 (d) presents the case in which the free-running slave laser is injection-locked by an optical carrier and modulated by a millimeter-wave signal in such a way that the frequency spacing between the cavity mode frequency, f_c, and the optical injection-locked frequency, f_{inj}, equals to the millimeter-wave frequency, f_m:

$$f_m = f_{inj} - f_c. \tag{2.18}$$

As a result, the lower sideband is resonantly amplified by the cavity mode while the upper sideband is unchanged. As shown in figure 2.16 (d), the free-running slave laser generates an asymmetric signal, i.e. a SSB signal.

Dual-mode lasers

Conventionnal distributed feedback (DFB) semiconductor lasers are designed to operate in single mode. Nevertheless, two optical modes can be produced in a same cavity working on the Bragg reflector design. Thus, a dual-mode laser is forced to operate in the degenerate modes on either side of the stop-band [105] [106]. These optical sources are simple to implement since they are integrated on a single chip that provides high power and high purity, characteristics that are transferred to the generated millimeter-wave signals.

In [22], an interesting example is provided: a dual-mode Self-Pulsating Laser (SPL) is used to obtain two wavelengths locked and so achieve phase-noise terms cancellation after heterodyning detection. This component depicted in figure 2.17 consists in two active DFB sections (250μm long) with different Bragg wavelengths (2.5nm difference) plus an integrated phase section (400μm long) which selects one DFB mode at the wavelength λ_1 and tunes it relative to the beating laser mode at λ_2. The corresponding optical spectrum shows two modes around 1.55μm (figure 2.17).

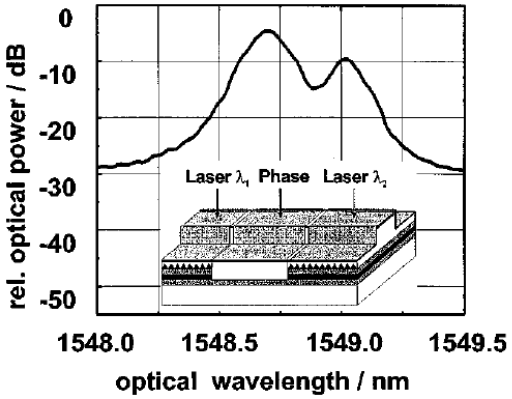

Figure 2.17: A dual-mode SPL composed of two DFB sections plus an integrated phase section and the corresponding optical spectrum, from [22].

The frequency spacing between these two optical tones is fixed to 40GHz thanks to a subharmonic sinusoidal signal at 10GHz modulating the two laser sections. This electrical modulation induces sidebands for each laser section, and when one of the sidebands from one section overlaps the second laser section, an injection-locking occurs. To summarize, each laser section is injection-locked by a sideband of the other section [107].

The dual-mode lasers represent good optical sources for the generation of millimeter-waves. Among other things, they provide frequency flexibility, even if this one is lower than in the case of two separate lasers systems: as noticed in [22], frequencies from 5 to 50 GHz can be obtained varying the lasers bias current settings (and so modifying the Bragg grating design), or from 40 to 60 GHz as shown in [105]. Good signal purity is also obtained and without electronic feedback: as noticed in [107], the millimeter-wave carrier has a low linewidth, less than 10Hz.

Mode-Locked Lasers (MLL)

Another easy-to-package solution to generate millimeter-wave signals consists in using Mode-Locked Lasers (MLL). Due to self-oscillation, a MLL emits extremely short pulses at a repetition frequency corresponding to the laser's Free Spectral Range (FSR). As shown in figure 2.18, a laser under mode-locked condition is characterized by a wide spectrum where a constant phase relationship is imposed among the different optical modes. As a result, after heterodyning detection a series of RF carriers equal to multiples of the FSR are produced: a bandwidth-limited photodetector filters the optical mixing and selects only the desired millimeter-wave frequency. In [108], it is shown that the recovered power at $f_c =$ FSR accounts for less than 10% of the over-all electrical beat power.

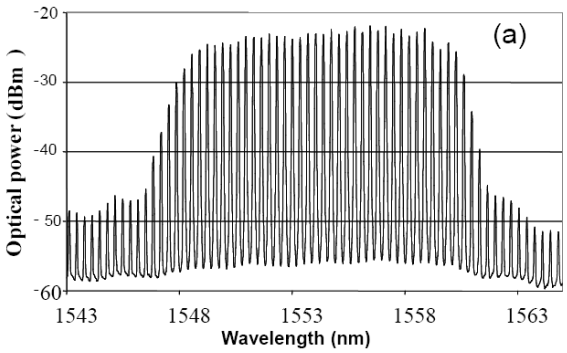

Figure 2.18: Optical spectrum of a MLL with equally spaced optical modes, from [23].

2.2.4 Comparison

The presented state of the art of the optical transmissions (and generations) of millimeter-waves is not exhaustive, but the most adopted solutions have been briefly presented.

The use of RoF in HAN imposes some particular constraints and specifications:

- cost,
- performance,
- and integration compactness.

To reduce the costs of the RoF systems, it is imperative to make the transducers as simple as possible. For instance, solutions based on complex modulation of MZM such as SSB generation or optical up-conversion have to be proscribed. High performances are not necessarily required in a home environment where the distances do not exceed 100m, the system has only to be reliable and affordable to all. As a consequence, well-tried solutions not requiring high bandwidth components are preferred. An optical up-conversion or a heterodyne detection at 60GHz is not recommended, these techniques relaxing only the laser modulation speed. The IM-DD techniques in Intermediate Frequency are more pertinent solutions, and in particular the direct modulation since it offers a high-level of integration. In fact, the RoF transducers have to be compact and discreet to be accepted by a large part of users. Implementing today a millimeter-wave to IF conversion before the optical transmission, and vice versa after the photodetector, makes sense. With the introduction of the new millimeter-wave radio systems, as the IEEE 802.11ad solutions of the popular Wi-Fi family, the industry makes lot of efforts to attack the mass market and cut prices. Mixers and oscillators at such frequencies are becoming low cost since these components form a part of the millimeter-wave front end of the future products.

The direct modulation in IF is a basic solution, nevertheless it remains competitive compared to other methods. Indeed, in [109], this technique has been compared to a mode-locked laser emission with a heterodyne detection. The transmitted signal is an OFDM signal with QPSK subcarriers working at 3.08Gbit/s according to IEEE 802.15.3c standard, HSI mode.

The IM-DD optical transmission is first realized at 4.5GHz using low-cost optoelectronic components at 850nm typically made for 10Gbit/s digital communication. At the reception the radio signal is up-converted into 60GHz by a local oscillator at 54.5GHz in order to be transmitted in free-space over 10m. The same OFDM signal at 4.5GHz is then transmitted by directly modulating a Mode-Locked Fabry-Pérot Laser (ML-FPL) at 1550nm whose self-pulsating frequency is 54.8GHz. At the reception, a heterodyne detection up-converts the radio signal into 60GHz thanks to a high speed photodiode presenting a 70GHz bandwidth. Finally, the performances are similar:

- IM-DD: EVM of 18.7% and CNR of 23dB for a 300m-length MMF (OM3).
- MLL with heterodyne detection: EVM of 19.0% and CNR of 21.5dB for a 50m-length SMF.

This confirms the choice of the simplest solution, the most efficient: the IF over Fiber that requires no expensive optoelectronic components.

2.3 The practical RoF architectures

In an optical HAN, the fiber infrastructure buried in the walls has to be transparent and able to adapt to the future radio systems for years since the lifetime of these radio standards is much shorter than the lifetime of a house. As a consequence, the home network physical architecture has to be properly chosen.

2.3.1 The point-to-point architecture

Two different options of point-to-point RoF link can be achieved. The first one with a single hop in the air is called “remote antenna” while the second one with two free-space propagations is called “optical tunnel”. The optical tunnel is helpful to set a direct link between two rooms, but the remote antenna can be preferred to deport, for instance, the radio cell of a home gateway, because with only one free-space hop, it provides better performances.

As described in figure 2.19, these point-to-point RoF links consist in transducers placed at each end of a fiber cable to transpose the incoming RF energy in the optical domain, and vice versa. Thus, symmetrical links are obtained. Concerning the optical transmission, either a space duplexing with two fibers is used, one for the uplink and one for the downlink, or a wavelength duplexing is adopted to carry the radio signal over one fiber (two wavelengths coupled on one single fiber). This last solution, easy to install for the end users, is more expensive since it requires additional components such as optical filters, optical splitters, optical circulators or Optical Add Drop Multiplexer (OADM).

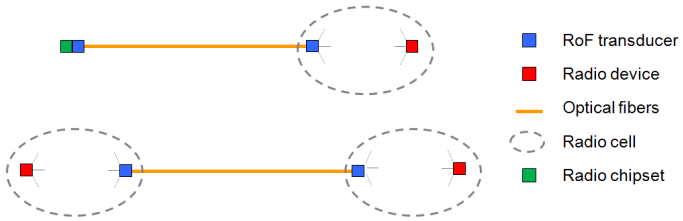

Figure 2.19: Two point-to-point RoF links: remote antenna (up) and optical tunnel (down).

As an example, figure 2.20 represents in detail a remote antenna link working at IF. In this case, the radio signal coming from a radio chipset is directly connected to a RoF transducer, without a first hop in free-space.

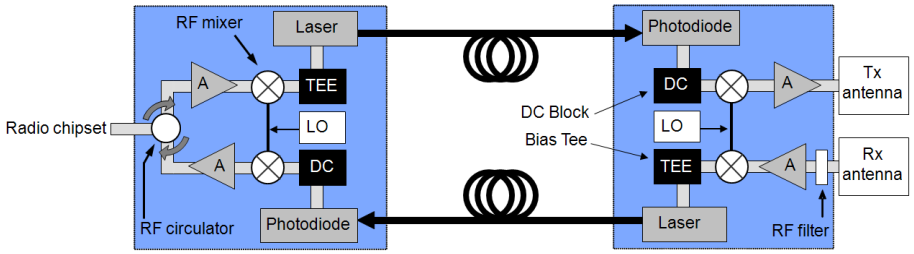

Figure 2.20: An IFoF remote antenna link.

The radio signal, in half duplex at the output of the radio chipset, is first separated into two ways by a RF circulator. Thus, the RoF link is full duplex with two distinct paths, one for the uplink and one for the downlink. It has to be noted that a RF switch controlled by the radio chipset could also have been implemented, but this option is more complex and less transparent.

Concerning the optical transmissions, an IM-DD solution is adopted: at the emission, the radio signal directly modulates the laser intensity, and at the reception, a direct photodetection recovers the signal. This is easy to implement, low cost, but limited by the bandwidth of the optoelectronic components. As a consequence, the IFoF option has been preferred, especially to use low cost optoelectronics components. The millimeter-wave signal is therefore electrically down-converted to a lower Intermediate Frequency (IF) thanks to a Local Oscillator (LO) before modulating the laser, and at the reception, an

up-conversion is achieved.

The main distortion in a RoF system is due to the laser non-linearity. Therefore, the power of the radio signal is optimized before the E/O conversion, generally thanks to an Automatic Gain Control (AGC) amplifier since the Dynamic Range (DR) of the lasers is limited. Amplifiers and attenuators can also be used before the free-space transmission to control the radiated power and respect the regional rules in terms of EIRP. Lastly, RF filters are introduced, especially after the receiving antenna to remove spurious signals and improve again the signals modulating the laser.

Other designs can be used such as the asymmetrical link depicted in figure 2.21. This architecture simplifies the remote antenna using a reflective component at the remote end to prevent the biasing of an optical source at this level. This component, generally called Reflective Electro-Optic Transceiver (REOT), simultaneously provides the photodetection of a RF signal carried down by a first wavelength λ_1 and the reflection and modulation of a second wavelength λ_2 used to carry back the signal. Thus, both wavelengths are generated at the central nodes by two laser diodes. Nevertheless, the asymmetrical aspect of this system can increase the costs.

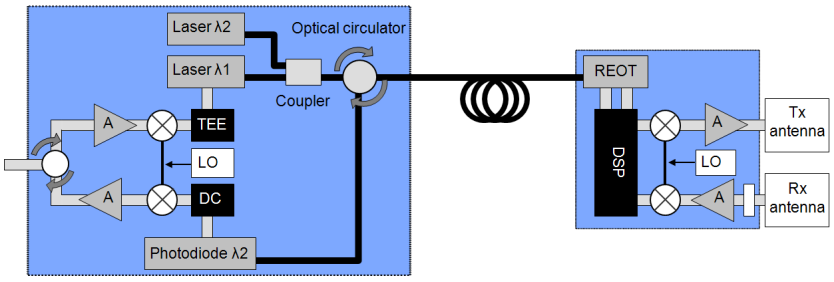

Figure 2.21: Remote antenna architecture using a remote reflective component. This design is more adapted to the remote antenna since it is an unsymmetrical architecture. DSP = Digital Signal Processing.

To boost the radio coverage to the whole home, i.e. to a multiroom environment, other architectures are investigated.

2.3.2 The active star architecture

The active star architecture depicted in figure 2.22 uses several remote antennas connected to a same switch containing all the technological complexity and network intelligence. This switch at the central node requires RoF interfaces to transpose the optical radio signals into electrical ones in baseband, and vice versa. Therefore, one radio chipset is needed per optical link: this is costly, not transparent to the radio standards, but allows the regeneration of the signal between two rooms, and so better performances.

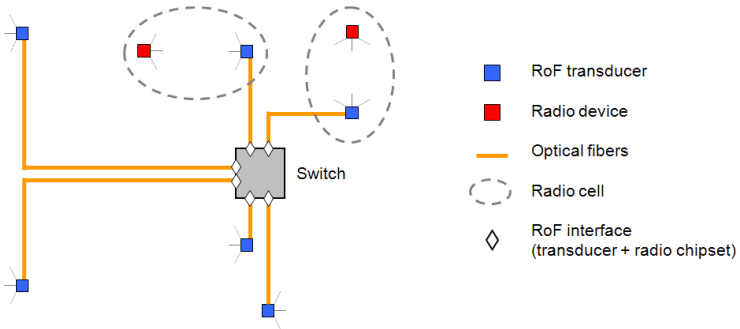

Figure 2.22: The active star architecture where independent optical point-to-point links interconnect the RoF transducers to the switch.

The active star architecture gives the best *Bandwidth* × *Range* / *Branch* product. However, with a significant number of branches, its cost becomes excessively high. Consequently, more cost-effective infrastructures using less active components thanks to shared optical media will be preferred.

2.3.3 The point-to-multipoint architecture

This architecture, close to a PON as shown in figure 2.23, splits the signal coming from the central node into different optical links thanks to a 1xN optical splitter. Naturally, a wavelength duplexing is preferred, like in the access network where two wavelengths are coupled on a same fiber. Otherwise, in the previous bi-fiber approach, two splitters have to be implemented: one to share the downstream optical power equally between all the branches and one to combine the upstream optical powers from the different branches.

In this architecture, only one point-to-point link can be active at a time. The capacity of the network is so reduced. Additionally, stations located in different rooms are completely hidden from each other. Thus, for contention-based radio protocols where several stations compete for the channel access, the throughput is severely degraded as studied in [110]. Lastly, since the full home flows pass through the switch, the radio chipset implemented at the central node has to be adapted, for example an Access Point (AP) based on the Infrastructure MAC architecture of the Wi-Fi systems (see chapter 5).

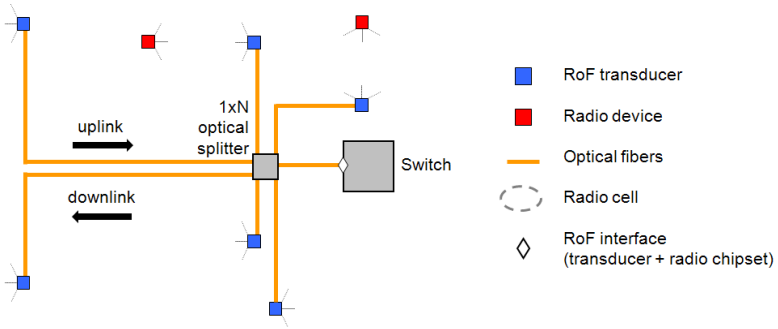

Figure 2.23: The point-to-multipoint architecture.

For all the reasons cited previously, the point-to-multipoint architecture is recommended only for broadcast use cases, like the delivery of the television service. Indeed, better architectures exist for direct exchanges between rooms.

2.3.4 The optical multipoint-to-multipoint architecture

The multipoint-to-multipoint architecture is based on a NxN optical splitter. As depicted in figure 2.24, each laser of each remote antenna is connected to an optical input of the splitter and each photodiode of each remote antenna is connected to an optical output of the splitter. When a RoF transducer transmits data to the fiber, the signal is divided to all the optical outputs of the NxN splitter, and thus, all the antennas receive the data. Thanks to this passive optical component, all the wireless devices are visible from one-another through the optical fibers, whatever the distance between them, as if they were face-to-face in a same room. Finally, this optical infrastructure can be seen as a multiple input / multiple output repeater, or as an optical logical bus.

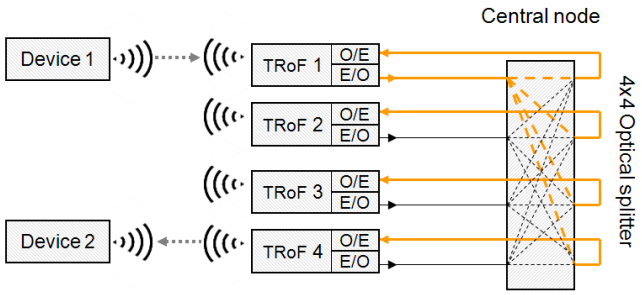

Figure 2.24: The optical multipoint-to-multipoint architecture with details about the mechanism of the optical splitter.

A key point of this transparent architecture is that the radio protocol alone is enough to control communications on the optical infrastructure. The radio access methods, such as Time Division Multiple Access (TDMA) or Carrier Sense Multiple Access with Collision Avoidance (CSMA/CA), are compatible with this architecture. For CSMA/CA, symbol collisions on the infrastructure are detected by the radio protocol implemented only in the user's devices. In fact, the RoF transceivers are made of purely physical layer components without any intelligence. Besides, as the optical links are not independent, the data rate is now shared between the different remote antennas, but because in a HAN the number of users is limited, this architecture seems the best compromise between cost and efficiency.

Lastly, it has to be underlined that one of the main challenges of this architecture, as the previous, is to support the high optical losses induced by the splitter, for instance 12dB for sixteen ports. So, even if this architecture is very interesting in terms of power consumption (null at the central node), it can be very demanding for the optoelectronic components.

2.3.5 The electrical multipoint-to-multipoint architecture

The electrical multipoint-to-multipoint architecture is based on a NxN RF splitter. As previously, the lasers of the RoF transducers are connected to the inputs of the splitter while the photodiodes are connected to its outputs, but, compared to its optical counterpart, opto-electronic (O/E) and electro-optic (E/O) conversions at the input and at the output of the RF splitter are added. This architecture acts again as a logical bus, broadcasting the signal coming from any transmitter to all the receivers connected to the infrastructure. And as previously, the radio protocol alone is able to control communications on these architectures and to manage possible collisions since the radio access methods are compatible with the bus topology.

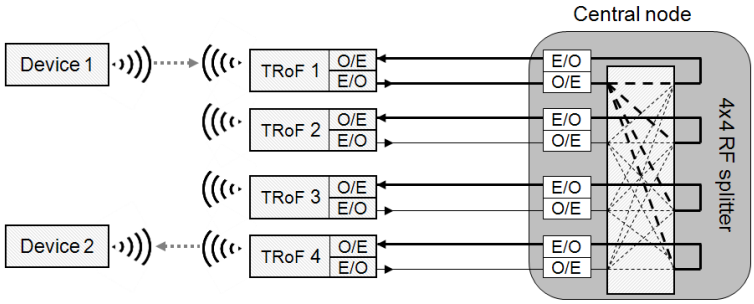

Figure 2.25: The electrical multipoint-to-multipoint architecture.

The advantage of the electrical version is the possibility to adjust the power level of the radio signals at the central node, but the new O/E and E/O conversions may add extra noises and increase the power consumption. Finally, it has to be noted that an electrical version of the point-to-multipoint architecture could also be imagined like proposed for the multipoint-to-multipoint architecture.

2.3.6 Comparison between the RoF architectures and discussion

Except for the optical tunnel, the RoF architectures present a central node with several point-to-point links spreading until RoF transducers located in different rooms. Therefore, an optical infrastructure can be first deployed inside the home, and later a complex RoF architecture can be installed choosing the correct central node (active switch, 1xN optical splitter, NxN optical splitter, ...). Concerning the point-to-point links between the central node and the RoF transducers, bi-fiber cables is advised in order to be compatible with the optical passive multipoint-to-multipoint architecture.

In order to choose the most adapted architecture, different parameters have to be investigated: the transparency to the radio standard, the total throughput, the power consumption (high if radio chipsets are integrated to the architecture), the number of fiber used between the central node and the transducers, the number of rooms that could be connected... All these points are summarized in table 2.1:

Table 2.1: Comparison of the HAN RoF architectures.

	Transparency	Throughput	Consumption	Fiber/link	number of rooms
optical tunnel	yes	optimal	medium	2 for symmetry	2
remote antenna	no	maximum	high	1 or 2	2
active star	no	maximum	high	1 or 2	limited by the cost
opt. pt-to-mpt	no	shared	high	1 preferred	limited by opt. losses
opt. mpt-to-mpt	yes	shared	low	2	limited by opt. losses
elect. mpt-to-mpt	yes	shared	medium	1 or 2	?

A high data rate is no more compatible with the transparency to the radio protocols. Indeed, the active star architecture, which allows high throughput thanks to independent point-to-point links and regeneration at the central node, is not able to convey a priori more than one standard due to the presence of radio chipsets at the central node. On the contrary, the multipoint-to-multipoint architecture is transparent to the radio standard as it uses a passive and transparent splitter, but the throughput is shared between different remote antennas. Lastly, the point-to-multipoint architecture has the two disadvantages: use of 1xN splitters and necessity to have a radio chipset at the central node.

Other technical issues peculiar to some architectures as the one described in section 2.4.7 can change such decisions. Consequently, the next section presents the technical challenges that have to be resolved in the Radio over Fiber systems. Concerning the architecture performances, experimental comparisons will be conducted in the chapter 4.

2.4 The technical challenges to be resolved in the Radio over Fiber systems

2.4.1 Multipaths

The multipaths, produced by the reflection of radio waves on the walls or on objects, create interferences, either between consecutive symbols (intersymbol interference - ISI), or within a same symbol (intrasymbol interference). At 60GHz, since the distances are very short and the free-space losses significant, the multipaths are low and the guard intervals protecting against ISI are short. However, the RoF architectures make achievable transmission distances between the wireless devices longer, and so the propagation delays through the optical fibers can create additional multipath interferences, especially for the shared architectures.

The multipath interferences induced by the RoF systems can be classified in three categories. The first one appears when two RoF transducers are located inside a same area, for instance to cover a large room. In fact, as shown in figure 2.26, two transducers connected by different sections of fibers lead to different propagation times and therefore to delayed interferences. These interferences occur either at the reception for any terminal within the reach of the two transducers (figure on the left), or at the emission when two transducers capture a same signal and repeat it in the RoF network until the final user device (figure on the right). Lastly, it has to be noted that the RoF network can also capture its own signal, create feedback loop, i.e. a coupling between two transducers, and increase again multipath interferences.

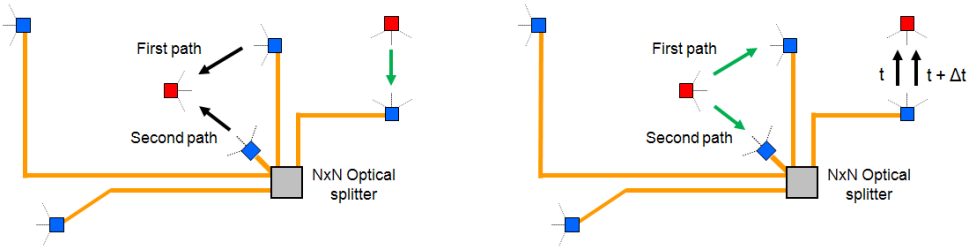

Figure 2.26: First case of multipath.

The second case of multipath interferences appears when two radio devices communicate directly between them inside a same room. As shown on the left in figure 2.27, the RoF network captures

the signals exchanged between two devices and reemits them with a time delay in the room creating interferences. This situation can be easily solved by the introduction of a simple rule: a RoF transducer has to be designed to operate in half-duplex, i.e. its photodiode is not turned on at the same time as its laser.

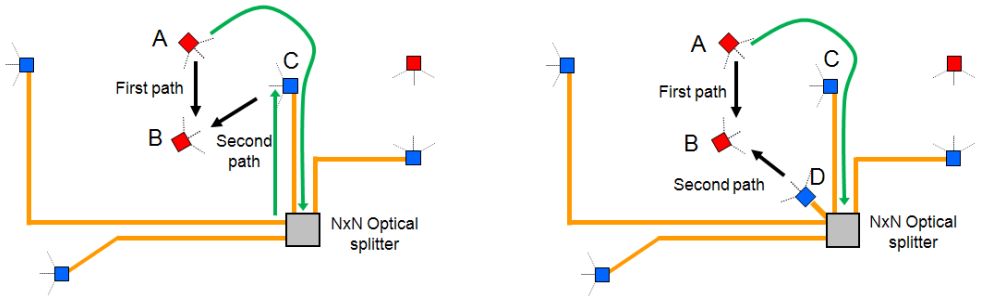

Figure 2.27: The second case of multipath on the left and the third case on the right. In the latter case, A sees C and B only while B sees A and D and possibly also C.

The third case corresponds to direct exchanges between two radio devices located in a large room where, in addition, two RoF transducers are present (figure 2.27, on the right). The signals transmitted by the device A are captured by B, but also by the RoF transducer C. The previous rule prevents delayed interferences from C, but a second path is created from D resending the signals captured by C. In fact, D is sufficiently far away from the equipment A to be not affected by the rule previously dictated and sufficiently close to B to communicate with it.

Finally, the two first cases of multipath interferences are only met when a shared architecture is implemented, for instance an optical multipoint-to-multipoint infrastructure. Indeed, when an active architecture is used, the switch at the central node can avoid the broadcast of data over different branches of the system. However, in the third case, the central node will have to detect that a direct communication occurs inside a same room, that it does not seem possible.

In general, a rigorous engineering during the RoF transducers implementation in the house resolves a large part of these issues, and the use of devices supporting the beamforming (high directional antennas) and the presence of guard intervals (cyclic prefix) resolves the rest of the interferences. The critical length between two paths corresponds to the guard interval between two OFDM symbols. They have been calculated as the duration of a guard interval multiplied by the speed of light and divided by the refractive index (which is equal to the unity in the air and to ∼1.4 in the fiber) and reported in table 2.2.

Table 2.2: Guard intervals between OFDM symbols and corresponding length.

OFDM standard	GI duration	free-space distance	fiber length
Wireless HD (HRP)	25.22ns	7.56m	5.4m
Wireless HD (LRP)	88.26ns	26.46m	18.90m
IEEE 802.15.3c (HSI mode)	24.24ns	7.27m	5.19m
ECMA-387 (type A)	24.70ns	7.40m	5.29m
IEEE 802.11ad	48.5ns	14.51m	10.36m

2.4.2 Echo

The radio devices operate in half-duplex, consequently when a device has finished to transmit, it switches in receive mode, and vice-versa. Nevertheless, it can receive its own frames when the echo delay becomes greater than the guard interval. For instance, for a radio transmission based on the IEEE 802.15.3c standard, HSI mode, the interframe space of 0.5μs corresponds to 150m of propagation on the air or 100m over the fiber: the guard interval is long enough to prevent any problem since it is expected that the fiber length in the home does not exceed 100m.

2.4.3 Coupling

Somes architectures, such as the optical tunnel or the multipoint-to-multipoint architecture, are "transparent" as they only transpose electrical signals in the optical domain, and vice-versa. They operate in full-duplex, even if the radio systems do not use this possibility. As illustrated in figure 2.28, this transparency can induce recoupling of the transmitted signal over the received signal.

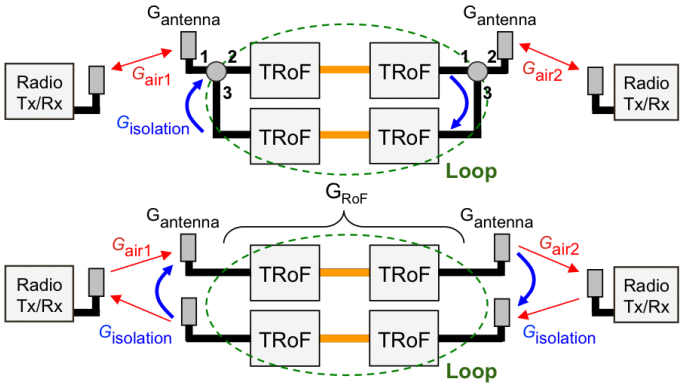

Figure 2.28: Optical tunnel with either a single antenna plus a RF circulator (top) or two separate antennas for receiving and transmitting (below).

If the radio signal emitted by the RoF network is in some way recoupled into the network (coupling between the Rx and Tx antennas or leakage through the circulators) and if the loop gain is positive, then a problem occurs: the radio wave power can become large and damage the optoelectronic components as well as create a strong perturbation to the radio environment. The system is stable only if:

$$G_{loop} = 2 \times (G_{RoF} + 2\,G_{antenna} + G_{isolation}) < 0 \tag{2.19}$$

where the RoF gain, which will be detailed in the next chapter, includes the gain of the RoF transducers plus the gain of the central node. Equation 2.19 has to be carefully considered when designing the RoF transducers, especially the antenna gains and the distance that separates them, the two parameters that fix the $G_{isolation}$ value.

2.4.4 Automatic Gain Control amplifier

The radio standards have anticipated the use of multiple networks inside a single environment. Consequently, distinct physical networks called Piconets (IEEE 802.15.3), Beacon Regions (ECMA-387) or Basic Service Sets (IEEE 802.11ad) can coexist in parallel, without interfere with each other, occupying a different channel of the millimeter-wave band.

Moreover, after the free-space propagation of a millimeter-wave signal with a fixed EIRP, the received power can vary by approximatively 30dB depending on the distance, see formula 1.9 for distances included between 30cm and 10m. To avoid any distortion from the optoelectronic components that can have a limited dynamic range, the RF power has to be optimized before the E/O conversion. Therefore, the RF power modulating the laser is maintained by an AGC amplifier in the middle of the dynamic range of the component.

When different networks (i.e. different channels) coexist, as shown in figure 2.29, the AGC amplifier, operating on the whole RF band, may lead to distortions for some coexisting networks. Indeed, if the different radio signals reaching the transducer have very different power levels, the AGC amplifier can be inefficient and the dynamic range of the laser can be exceeded. Even if the AGC amplifier is well-dimensioned, it is not possible to optimize the laser input power for each channel (except if the transducer deals with each channel separately). To avoid this, the system can simply operate on only one millimeter-wave channel, preferably the second channel (the mandatory one).

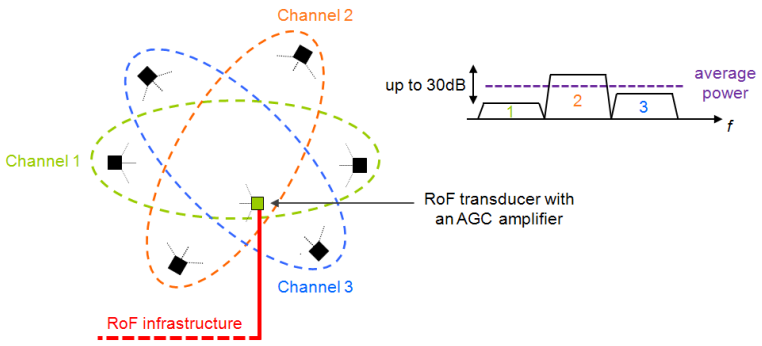

Figure 2.29: Example of three networks operating on three different channels. With very different power levels between these networks (30dB between the channels 1 and 2), the AGC amplifier is inefficient.

2.4.5 Local oscillators

Because one local oscillator is implemented per RoF transducer, the frequency difference between two transducers, Δ_{LO}, can exceed the center frequency tolerance defined by the radio standards. Figure 2.30 depicts a typical example for an optical tunnel working on the second channel of the millimeter-wave band.

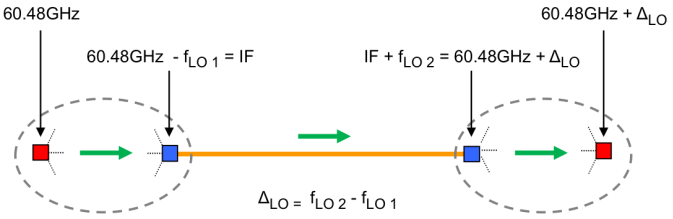

Figure 2.30: Oscillator frequency difference on a RoF optical tunnel.

In the IEEE 802.11ad standard, the transmitter center frequency tolerance shall be ±20ppm maximum for the 60GHz band. A part per million (ppm) corresponds to a ratio of 10^{-6}, so the required accuracy is ±1.2MHz for a central frequency set at 60GHz. Knowing that there are two local oscillators in a RoF link, the required accuracy will be twice as high, i.e. ±0.6MHz at 60GHz (considering the radio transmitter and receiver perfectly tuned).

To remove this issue, some infrastructures based on passive splitter such as the multipoint-to-multipoint architecture can easily distribute a local oscillator, for example multiplexing the frequency oscillator with the radio signal. Therefore, if a RoF transducer generates an oscillator frequency, all the other remote antennas receive the same oscillator frequency ($\Delta_{LO} = 0$). Consequently, point-to-multipoint and multipoint-to-multipoint architectures are well adapted to IFoF systems.

2.4.6 Propagation delay

A problem regularly mentioned in the literature [24] [110] is the additional propagation delays introduced by the optical fibers and that can exceed the timing boundary of the radio MAC layer. With distances up to 100m in the HAN, it becomes essential to study the impact of these delays and determine the maximum coverage distance that can be reached. With this in mind, a typical timing diagram based on the IEEE 802.11 standard and depicted in figure 2.31 has been studied.

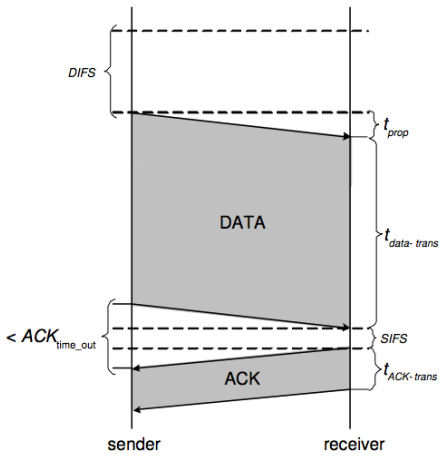

Figure 2.31: Timing diagram of a IEEE 802.11 transmission, from [24].

First, a station called "sender" senses the medium and, if the channel is idle during a DIFS (DCF Interframe Space) time, it transmits its data to a station called "receiver". The DCF, for Distributed Coordination Function, is the transmission method adopted and based on the Carrier Sense Multiple Access/Collision Avoidance (CSMA/CA), a mechanism for contention-based access where a collision is deducted if any acknowledgement (ACK) is received. After completing the data transmission, the sender waits for a ACK_{time_out} time the acknowledgment from the receiver. In a RoF system, due to the additional delay introduced by the optical fibers, the transmitted data reach the receiver after a propagation delay t_{prop}. After that, the receiver transmits an acknowledgement after a SIFS (Short Interframe Space) time. If the acknowledgement does not reach the sender before the ACK_{time_out} time, the sender has to resend the data packet until it receives an positive acknowledgement or it exceeds the maximum value of unanswered packet send.

The propagation delay can have significant impacts on the radio links and communication interruptions can occur if the intervals between frames become too large.

First, if a station waits for a DIFS time before transmitting, this is because the medium is implicitly reserved to allow other stations to send their acknowledgments during this interval. This DIFS time is defined as:

$$DIFS = SIFS + 2 \times Slot\_Time \tag{2.20}$$

where the $Slot\_Time$ is the time required by a station to detect transmissions from other stations while the SIFS interval is the time between the reception of the $DATA$ packet and the emission of the acknowledgement.

The time required by a station to emit its acknowledgement, from the "sender" station point of view, is the sum of t_{prop} (time taken to receive the $DATA$ packet) and of δ (processing time at the reception). Then, to receive the acknowledgement sent by the receiver, the sender has to wait t_{prop} again. Finally,

$$\delta + 2 \times t_{prop} < DIFS \tag{2.21}$$

The standard fixes δ to SIFS. As a result, the value of t_{prop} is limited by the value of $Slot\_Time$. For instance, in the IEEE 802.11b standard, $Slot\_Time$ is equal to 20μs, i.e. a propagation delay corresponding to 4km of silica optical fiber. In the WiGig / IEEE 802.11ad solution, $Slot\_Time$ is equal to 3μs, i.e. 600m of fiber.

In the HAN, where the distances typically do not exceed 100m, the propagation delay issues will not stop the communication. Nevertheless, the throughputs decrease when the delays increase because longer is the t_{prop} duration, more important is the probability that other stations start a radio emission and that one collision occurs [110].

2.4.7 Optical issues with shared architectures

The point-to-multipoint and multipoint-to-multipoint architectures, based on an optical splitter, are subject to some optical issues due to the use of multiple lasers simultaneously. First, the lasers that are turned-on without seeing a radio signal at their input are only noise for the photodiodes that receive data from another laser. Indeed, they copy the ambient noise by adding the E/O conversion noises (RIN). Then, they induce an excess of optical power at the reception: the shot noise increases and potentially an optical overload (saturation) of the photodiodes can happen. Lastly, optical heterodyning interferences, i.e. optical beating between the different lasers of the infrastructure, are detected at the output of the system. All these optical issues typical of shared optical architectures are resumed in figure 2.32.

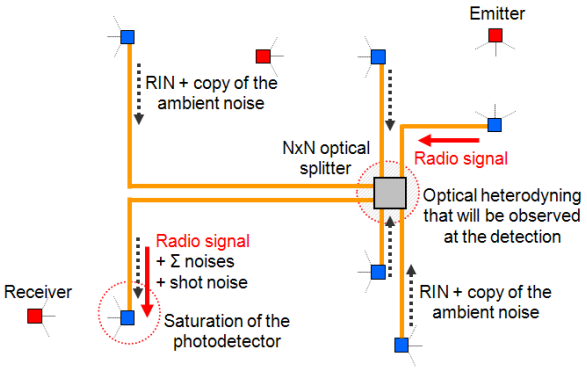

Figure 2.32: Optical issues with shared architectures.

In order to avoid such issues, the access to the media has to be controlled. For instance, a rule may be implemented to ensure that only one laser is turned-on at any time. More details on this topic will be given in chapter 5.

2.5 Summary and discussion

The solution depicted in figure 2.20 is retained as it remains easy to implement and low cost. In fact, the RoF transducers have to be built with basic blocks, and the simplest optical link that could be conceived consists in directly modulating the intensity of a laser by driving its current with a radio signal at IF, then using a direct photodetection for recovering it (IM-DD). The proposed design, based on a well-known technique, brings also reliability. However, the direct modulation has some disadvantages such as a limited dynamic power range at the input of the optical link. It is why in the next chapter optoelectronic components will be tested in order to make the good choices in terms of linearity.

About the fiber implementation inside the home, all the architectures previously presented can be deployed, the preference for one of them being just a question of usecases. For instance, an optical tunnel conveys perfectly a point-to-point WirelessHD flow between two rooms, and in this case, a multipoint-to-multipoint infrastructure will be over-dimensioned. On the other hand, the multipoint-to-multipoint architecture is perfect to enable multi-room transmissions based, for example, on the Wi-Fi IEEE 802.11ad. As a consequence, no RoF architecture has been selected yet. However, in chapter 4, comparisons will be performed to classify quantitatively their performances and decide, among other things, between the optical multipoint-to-multipoint architecture and its electrical counterpart. Lastly, the multiservice and multiformat architectures proposed in chapter 5 could also have an influence on the final choice.

Concerning the technical challenges to resolve for using these RoF architectures, some solutions have been proposed. They are summarized below:

- Multipath issues: introducing engineering rules such as one RoF transducer per room and RoF transducers operating in half-duplex.
- Echo issues: in principle no problem with the millimeter-wave radio standards as they use long enough interframe spaces.

- Coupling issues: paying attention to the RoF transducers design, especially the antenna gains and the distance that separate them.
- Automatic Gain Control amplifier issues: working on only one millimeter-wave channel, preferably the second channel (the mandatory one).
- Local oscillators issues: distributing an oscillator or working with precise and stable local oscillators.
- Propagation delay issues: limiting the fiber length. With distances up to 100m in the HAN, no problem will be a priori encountered.
- Optical issues with shared architectures: managing in real time the lasers even if the beating and the noises have to be characterized before to know their real impact (see chapter 4).

Chapter 3

Analog characterization of the optoelectronic components, the RoF link and the domestic cable

3.1 The optoelectronic components composing the RoF link

This chapter reports the measurements and the performance comparisons of different optoelectronic components that will be used in chapter 4 to transmit OFDM radio signals. High linear components are required since direct modulation with direct detection has been previously chosen. To adopt the best components, accurate static and dynamic characterizations are therefore performed.

In existing LANs, silica multimode fibers (MMF) have been widely adopted. Indeed, there are more than 30 millions of kilometers of legacy MMF already installed in campuses and building backbones world-wide [111]. Consequently, low cost optoelectronic components optimized for short reach transmissions over MMF are largely commercially available. These components, working at short wavelengths, typically 850nm and 1310nm, are therefore a perfect choice for home applications.

At the transmission side, Vertical Cavity Surface-Emitting Lasers (VCSEL) working at 850nm will be tested: a first one from Finisar packaged as a Transmitter Optical Sub-Assembly (TOSA) and designed for 10Gbit/s digital communications [112], and a second one from VI-Systems taking the form of a pigtailed laser and designed for 40Gbit/s digital communications [113].

VCSELs are efficient optoelectronic components with good linearity and high bandwidth. They are increasingly used for telecom applications as they offer many advantages compared to edge-emitting semiconductor lasers [114] [115]:

- A low manufacturing cost as these components can be directly tested on wafer, before the separation in discrete chips. There is no cleaving of the wafer to form the laser cavity, no additional facet coating.
- A perfectly controlled technology in the range of wavelengths covering the visible and near infrared, from 350nm to 980nm (in multimode). The excellent reliability at room temperature allows the use of uncooled lasers.
- A low threshold current with a high efficiency, and therefore a reduced energy consumption.
- A speed limit constantly pushed further. Today, VCSEL at 40Gbit/s are available [113].
- A possibility to create VCSEL array.

Nevertheless, VCSELs have:

- Low emitted optical power.
- Important Relative Intensity Noise (RIN).

At the reception, 850nm PIN photodiodes, also from Finisar and VI-Systems, will be used. The one from Finisar consists in a Receiver Optical Sub-Assembly (ROSA) module composed of a PIN photodiode on GaAs (Gallium Arsenide) cascaded with a transimpedance amplifier (TIA) whereas the VI-Systems component is a pigtailed module (50μm OM3) just composed of a GaAs PIN photodiode.

A solution at 1310nm will also be investigated for comparison: a Finisar Fabry-Pérot (FP) laser with a PIN photodiode on InGaAs (Indium Gallium Arsenide) cascaded with a TIA.

It has to be noted that some tests (S-parameters, IP3, P1dB) will require the use of an additional PIN photodiode at 850nm from New Focus, a photodetector offering a high bandwidth of 25GHz [116]. Likewise, singlemode components, a VCSEL from Raycan emitting at 1550nm [117] and a PIN photodiode from Nortel Networks [118], will be used to complete some measurements (L-I curve and RIN), even if they will not be used subsequently for RoF transmission.

All these components are commercially available. However, in the framework of the ORIGIN project, new optoelectronic components have been designed and realized: a VCSEL from U-L-M Photonics [119] and a Silicon Germanium (SiGe) Heterojunction bipolar Photo-Transistor (HPT) working at 850nm. The VCSEL promises a high efficiency while the HPT, a SiGe 80GHz technology transistor [120] [121] modified to detect the light injected into the Base (SiGe layer) and amplify it by the transistor's current gain, promises a highly linear behavior and a better integration of RF electronic technologies in a single chip. These components, tested during the third year of the project, will be compared in terms of performances to the commercial components[1].

Table 3.1: Summary of the lasers used[2].

Laser	Wavelength	Manifacturer	Reference	Optical connector
VCSEL	850nm	Finisar	HFE6192-761	LC/PC
VCSEL	850nm	VI-Systems	V40-850M	FC/APC
FP	1310nm	Finisar	FP-1310-10LRM-LCA	LC/PC
VCSEL	1550nm	Raycan	RC32xxx1-T	SC/APC
VCSEL	850nm	U-L-M Photonics	Glass Substrate (GS2)	LC/PC

Table 3.2: Summary of photodiodes used.

Photodiode	Wavelength	Manifacturer	Reference	Optical connector	TIA
GaAs PIN	850nm	Finisar	HFD6380-419	LC/PC	yes
GaAs PIN	850nm	VI-Systems	D30-850M	LC/PC	no
GaAs PIN	850nm	New Focus	Model 1481-S	FC/PC	no
InGaAs PIN	1310nm	Finisar	PIN-1310-10LR-LC	LC/PC	yes
InGaAs PIN	1550nm	Nortel Networks	PP-10G	FC/PC	yes

3.2 Static performances

3.2.1 The laser L-I curve

First, the emitted optical power of several lasers has been measured as a function of their bias current using an optical power meter. Thus, their L-I curve was plotted (figures 3.1, 3.2 and 3.3), and their electro-optic (E/O) conversion efficiency and their threshold current were calculated.

[1] The HPT has been briefly compared in terms of performances to commercial components in [122], but these results are finally not presented here as the study is not enough advanced.

[2] LC/PC stands for Lucent Connector / Physical Contact, FC/APC for Ferrule Connector / Angled Physical Contact, and SC for Square Connector.

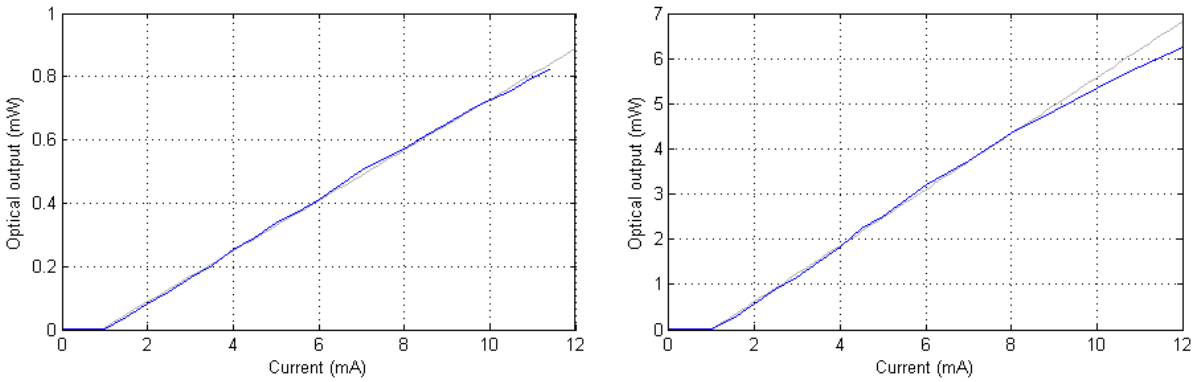

Figure 3.1: L-I curves of the Finisar VCSEL at 850nm on the left and of the VI-Systems VCSEL at 850nm on the right. In grey, the linear approximations are provided.

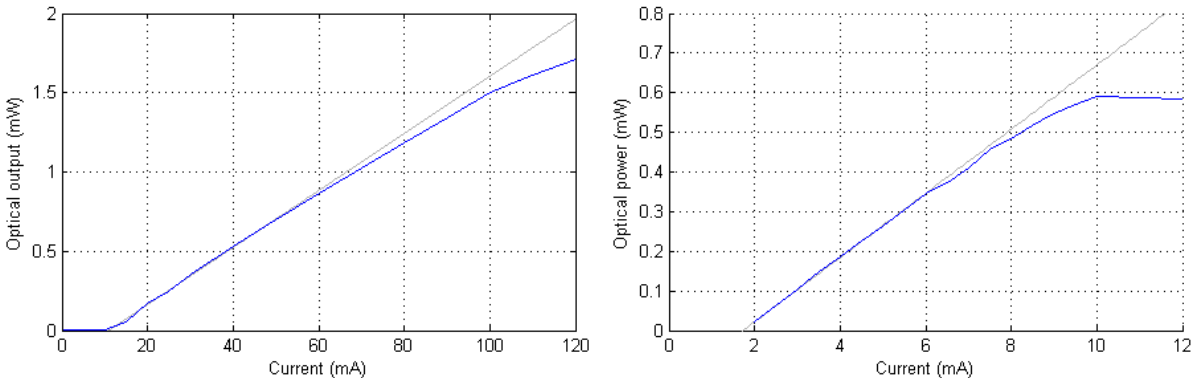

Figure 3.2: L-I curve of the Finisar FP at 1310nm on the left and of the Raycan VCSEL at 1550nm on the right.

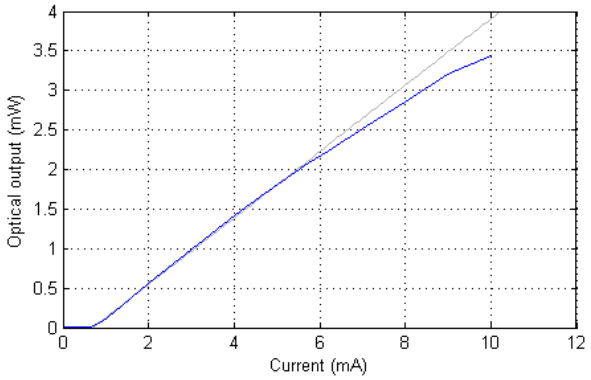

Figure 3.3: L-I curve of the U-L-M VCSEL at 850nm.

Table 3.3 summarizes the properties of each laser. It can be noted that the VI-Systems and U-L-M VCSELs are very attractive with their low threshold current and their high slope efficiency, at the opposite of the Finisar FP laser that has nevertheless a large linear range of 50mA to directly modulate the laser. Thus, the FP laser has a large dynamic optical power range of 1.25mW (∼1dBm), but this remains lower than the 5mW (∼7dBm) provided by the VI-Systems VCSEL.

Table 3.3: Summary of the L-I curves.

Optoelectronic components	Threshold current	Slope efficiency
Finisar MMF VCSEL at 850nm	0.9mA	0.08W/A
VI-Systems MMF VCSEL at 850nm	1mA	0.62W/A
Finisar MMF FP laser at 1310nm	11mA	0.018W/A
Raycan SMF VCSEL at 1550nm	1.7mA	0.081W/A
U-L-M MMF VCSEL at 850nm	0.7mA	0.42W/A

3.2.2 The laser output optical spectrum

VCSELs

Optical spectrum measurements have been realized for the Finisar, VI-Systems and U-L-M VCSELs connecting them directly to an Optical Spectrum Analyzer (OSA) with a spectral resolution of 0.01nm. Figures 3.4, 3.5 and 3.6 represent these measured optical spectra for different bias currents. For currents close to the threshold, the VCSELs are mainly singlemode with a wavelength near 851nm, 859nm and 854nm, respectively, whereas many higher longitudinal modes appear for higher current levels. For example, for the Finisar laser biased at 6mA, six modes can be observed with approximatively 0.35nm between two successive wavelength peaks.

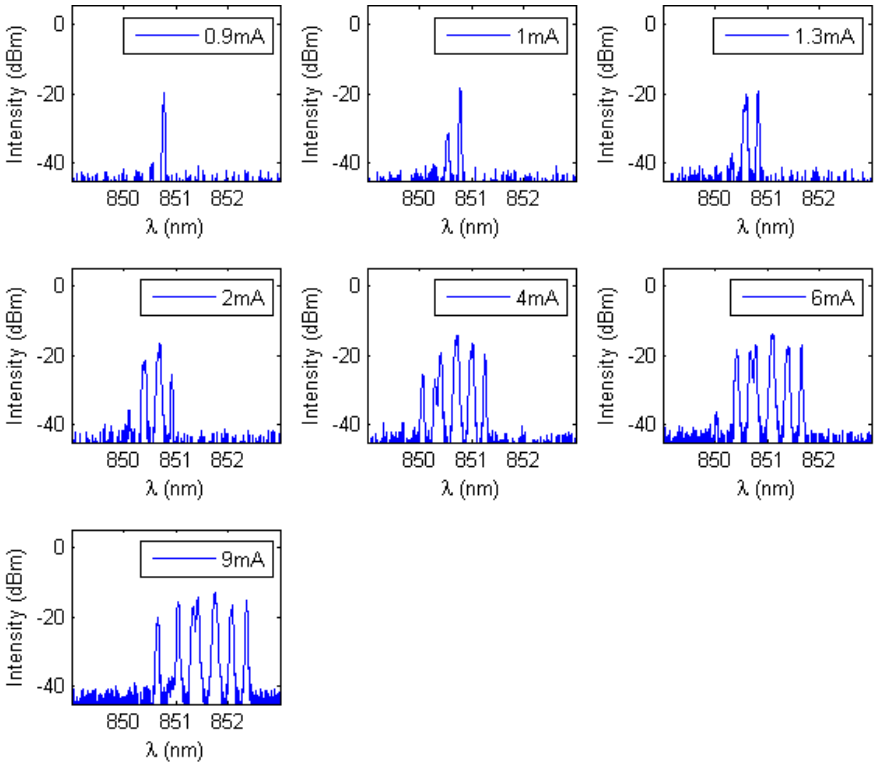

Figure 3.4: Optical spectrum of the Finisar laser for different bias currents.

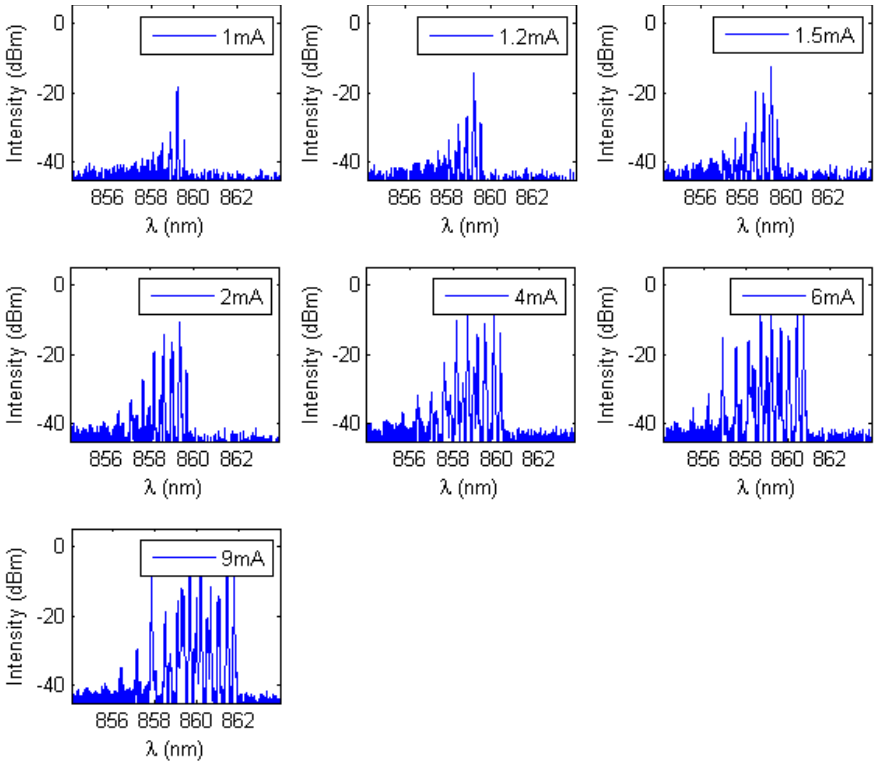

Figure 3.5: Optical spectrum of the VI-Systems laser for different bias currents.

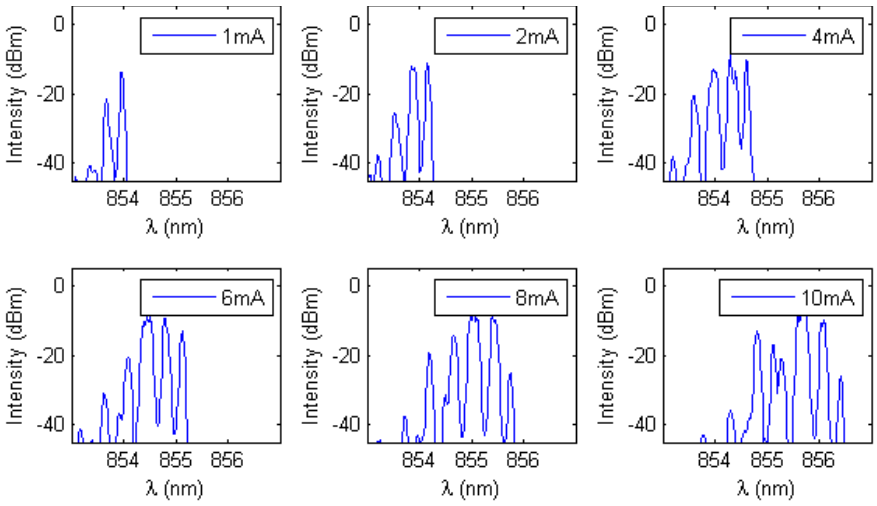

Figure 3.6: Optical spectrum of the U-L-M laser for different bias currents.

In the figures above, the noise floor of the OSA equals to -45dBm or less, that is enough to observe the multimode character of the VCSELs since a laser with a Side-Mode Suppression Ratio (SMSR) higher than 30dB is considered as singlemode.

The longitudinal behavior of the VCSELs could seem connected to the cavity resonator (Airy functions), but this is not the case. Indeed, the spectral interval does not match with the cavity length (or thickness as a VCSEL emits the beam perpendicularly to the active region) of such VCSELs, approximatively 100nm.

$$Cavity\ length = \frac{{\lambda_c}^2}{2n \times FSR} \neq \frac{(851\ 10^{-9})^2}{2 \times 3.5 \times 0.345\ 10^{-9}} \approx 300\mu m \tag{3.1}$$

where:

- λ_c is the central wavelength.
- FSR is the Free Spectral Range, i.e. the spacing between two successive emitted optical wavelengths.
- n is the refractive index of the medium, $\sim$3.5 for a semiconductor.

As a consequence, the apparition of higher longitudinal modes when the laser bias current increases cannot be explained with this approach. This phenomenon has been observed in [25] [123] [124] and the following explanation is given.

Each wavelength that can be observed in the optical spectra of figures 3.4, 3.5 and 3.6 corresponds to one of the transverse modes created in the laser cavity. Indeed, the multimode VCSELs usually have an active layer with a large diameter (about 15μm) that explains their transverse modes character. As shown in figure 3.7, each transverse mode has a spatial distribution of its Transverse Electro-Magnetic (TEM) fields that depends on the radial axis. Thus, the active layer can be divided into several zones, each of them representing an area where one of the fields is dominant in terms of intensity. Note that the literature usually describes this phenomenon using two mode models, LP01 and LP11 (LP stands for Linear Polarization), for didactic reasons.

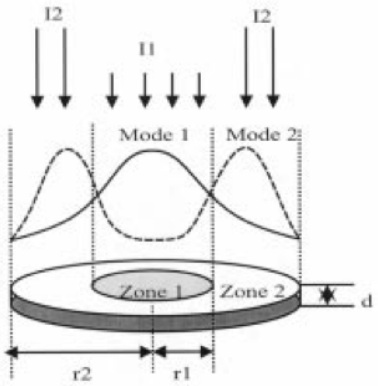

Figure 3.7: Distribution of the TEM fields in the active layer of a VCSEL, from [25].

In a VCSEL, the carrier density in the active zone is a function of the radial axis. It has to be recalled that the laser effect depends on the carrier concentration in the active layer and that the injection of carriers is controlled by the laser bias current. A minimal current density, $J_{threshold}$ in A/m^2, is so required to obtain the laser radiation.

As the TEM fields and the carrier density have a distribution depending on the radial axis, each transverse mode will not observe the same carrier density. So, when the bias current increases progressively, each mode does not appear at the same time: the fundamental mode, LP01, appears when the laser bias current exceeds its threshold value, the higher orders appearing successively with increasing current (figures 3.4, 3.5 and 3.6).

In addition, the carrier density variations along the radial axis generate variations of the refractive index in the medium. Since the emitted wavelength is related to the refractive index, each mode has its own wavelength, a wavelength that drifts when the bias current increases. This effect, called the chirp, is well known for lasers directly modulated as it results in a larger spectral width than the one observed in static measurements.

The measured chirps are represented in figures 3.8 and 3.9 where the different modes observed in the optical spectra above are plotted as a function of the wavelength. It has to be noted that the VI-Systems laser has a higher number of longitudinal modes, so a priori a stronger transverse mode character.

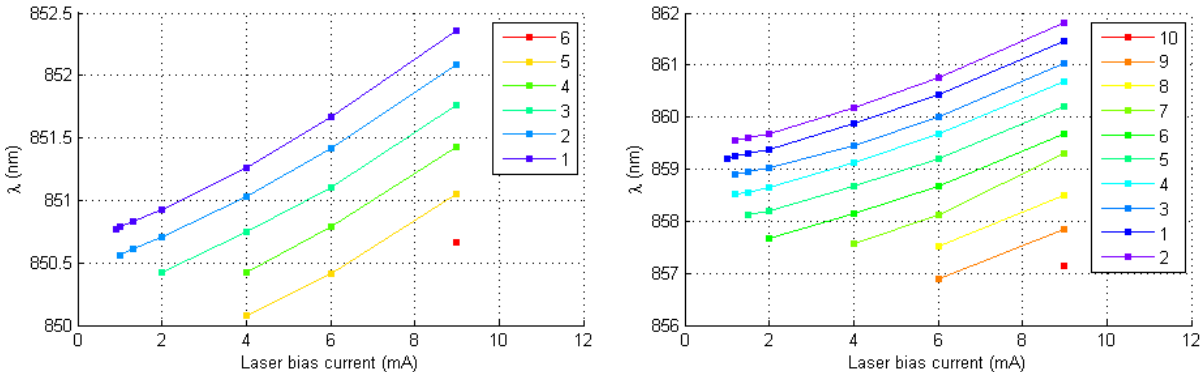

Figure 3.8: Evolution of the laser wavelengths (longitudinal modes) as a function of the bias current, or Chirp, for the Finisar laser on the left and for the VI-Systems laser on the right.

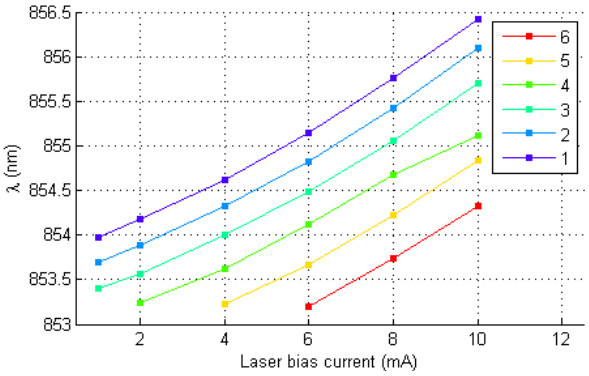

Figure 3.9: Chirp for the U-L-M laser.

When the laser bias current increases, the refractive index decreases due to the change of carrier concentration. Therefore, the wavelength λ of one mode increases since $\lambda = \lambda_0/n$, where λ_0 is the wavelength of the light in vacuum.

FP laser

Optical spectrum measurements with a resolution of 0.01nm have also been realized for the Finisar FP laser at 1310nm. A FP is a linear optical resonator consisting in two highly reflecting mirrors, as a consequence the laser is not purely monochromatic: as depicted in figure 3.10, a series of regularly spaced coherent spectral lines (the longitudinal modes) is observed with an amplitude profile determined by the gain curve of the active layer. Additionally, the chirp is observed with the wavelength that increases with the laser bias current.

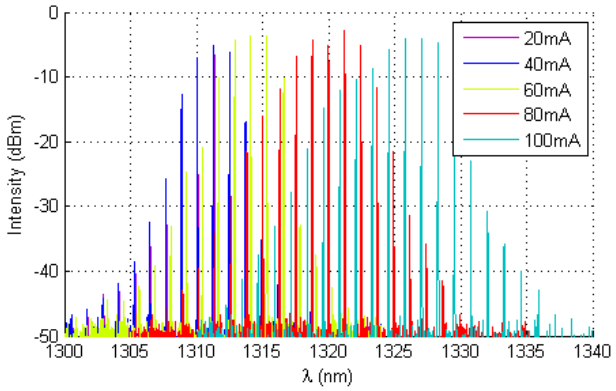

Figure 3.10: Optical spectrum of the Finisar FP laser at 1310nm for different bias currents.

Table 3.4 gives the wavelength corresponding to the longitudinal mode of highest intensity and the average observed FSR as a function of the laser bias current.

Table 3.4: FP laser optical spectrum characteristic.

Bias current (mA)	λ_{peak} (nm)	FSR (nm)
20	1311.3	1.2075
40	1311.3	1.2126
60	1314.1	1.2158
80	1321.2	1.2316
100	1327.0	1.2463

From the optical spectrum measured at a 20mA bias current, we can determine the cavity length, 203μm, a result consistent with the typical value of such a FP laser.

$$Cavity\ length = \frac{{\lambda_c}^2}{2n \times FSR} = \frac{(1311.3\ 10^{-9})^2}{2 \times 3.5 \times 1.2075\ 10^{-9}} \simeq 203\mu m \tag{3.2}$$

3.2.3 The I-V curves of the photodiode

The I-V curves of the photodiodes have not been measured, nevertheless the responsivity values provided by their datasheet have been reported in table 3.5.

Table 3.5: Photodiode responsivities.

Photodiode	Reference	Responsivity (A/W)	Transimpedance gain (Ω)
Finisar PIN at 850nm	HFD6380-419	0.5	2000
VI-Systems PIN at 850nm	D30-850M	0.4	-
New Focus PIN at 850nm	Model 1481-S	0.4	25
Finisar PIN at 1310nm	PIN-1310-10LR-LC	0.85	882.35
Nortel Networks PIN at 1550nm	PP-10G	0.88	500

The transimpedance gain is not always directly mentioned in the datasheets, nevertheless it can be calculated as the ratio between the conversion efficiency (V/W) and the photodiode responsivity (A/W). For instance, the New Focus photodiode has a conversion gain of 10V/W and a responsivity of 0.4A/W, which corresponds to a transimpedance gain of 25Ω. Lastly, this gain has to be divided by two if the photodiode output is differential (two RF outputs, *data* and $\overline{data}$) as we connect only one output, the second one being loaded by a 50Ω impedance.

3.3 Small-signal dynamic performances

3.3.1 Analytical calculation of the RoF link budget / RoF losses

The knowledge of the link budget is a fundamental point to optimize the radio transmissions and choose the most suitable amplification levels at the output of the RoF links. The link budget, in static, can be determined analytically for an optical link as the one represented in figure 3.11.

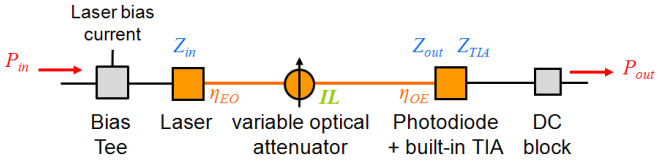

Figure 3.11: A typical RoF link with a photodiode including a transimpedance amplifier (TIA).

The RoF electrical gain is, in linear, the ratio between the electrical power at the output of the photodiode, P_{out}, and the electrical power at the input of the laser, P_{in}.

$$P_{in} = \frac{V_{in\,(AC)}^2}{Z_{in}} = \frac{Z_{in}^2 < I_{laser\,(AC)}^2 >}{Z_{in}} \tag{3.3}$$

$$P_{out} = \frac{V_{out\,(AC)}^2}{Z_{out}} = \frac{Z_{TIA}^2 < I_{PD\,(AC)}^2 >}{Z_{out}} \tag{3.4}$$

where,

- $V_{in\,(AC)}$ [V] is the average alternating voltage at the input of the laser, calculated with a Root Mean Square (RMS) definition.
- $V_{out\,(AC)}$ [V] is the average alternating voltage at the output of the photodetector.
- Z_{in} [Ω] is the impedance at the input of the laser.
- Z_{out} [Ω] is the impedance at the output of the photodiode.
- Z_{TIA} [Ω] is the transimpedance gain.
- $< I_{laser\,(AC)} >$ [A] is the average alternating current (AC) applied to the laser. In fact, the laser current is the sum of an alternating current, $I_{laser\,(AC)}$, and of a laser bias current, I_{Bias}.
- $< I_{PD\,(AC)} >$ [A] is the average alternating current provided by the photodetector.

If the laser is biased in the middle of its L-I curve and if the optical losses are fixed to IL, then the photodetected current is:

$$I_{PD\,(AC)} = P_{PD} \times \eta_{OE} = \frac{P_{laser}\ \eta_{OE}}{IL} = \frac{I_{laser\,(AC)} \eta_{EO}\ \eta_{OE}}{IL} \tag{3.5}$$

where,

- P_{laser} [W] is the dynamic optical power at the output of the laser.
- P_{PD} [W] is the dynamic optical power at the input of the photodiode.
- η_{EO} [W/A] is the slope efficiency of the laser.
- η_{OE} [A/W] is the photodiode responsivity.
- IL is the optical losses inserted in the optical link, in linear. It corresponds to the linear attenuation, the fiber bend losses and the optical connection losses.

Finally, the RoF electrical gain, G_{RoF}, is equal to:

$$G_{RoF\,lin} = \frac{P_{out}}{P_{in}} = \frac{Z_{in}}{Z_{out}} \times \left(\frac{Z_{TIA}\ \eta_{EO}\ \eta_{OE}}{Z_{in}\ IL} \right)^2 \tag{3.6}$$

This expression can also be expressed in decibel:

$$G_{RoF}\ [dB] = 20 \cdot log(\eta_{OE} \times \eta_{EO}) - 2 \times IL + 10 \cdot log\left(\frac{Z_{in}}{Z_{out}}\right) + 20 \cdot log\left(\frac{Z_{TIA}}{Z_{in}}\right) \tag{3.7}$$

where,

- IL [dB] is the insertion losses of the optical link, in logarithmic scale.

In the case of a photodiode without any TIA, the last term of equation 3.7 is removed and the ratio Z_{in}/Z_{out} is reversed.

3.3.2 S-parameters measurement

RoF links

S-parameters have been measured for the following RoF links using an Electrical Network Analyzer[3] (ENA):

[3]This network analyzer, an Agilent N5242A (10MHz - 26.5GHz), will be used for all the S-parameters measurements made in this thesis. This is a Vector Network Analyzer (VNA) measuring both amplitude and phase properties.

1. Finisar VCSEL at 850nm + Finisar GaAs PIN photodiode with the built-in TIA (S21 and S11).
2. VI-Systems VCSEL at 850nm + VI-Systems GaAs PIN photodiode (S21 and S11).
3. Finisar VCSEL at 850nm + New Focus GaAs PIN photodiode (S21).
4. VI-Systems VCSEL at 850nm + New Focus GaAs PIN photodiode (S21).
5. U-L-M VCSEL at 850nm + Finisar GaAs PIN photodiode with the built-in TIA (S21 and S11).
6. Finisar FP laser at 1310nm + Finisar InGaAs PIN photodiode with the built-in TIA (S21 and S11).

These links are composed of OM3 MMF, 1 or 2m-length fiber patch cords, and sometimes of additional optical losses in order to not saturate the receiver. Finally, the S11 and S21 parameters are represented below for frequencies up to 25GHz, for different laser bias currents, and for system input powers optimized to not saturate the RoF links.

1. First, the RoF link composed of the VCSEL at 850nm and of the GaAs PIN photodiode with the built-in TIA from Finisar is tested (figure 3.12). At 6.5mA bias current, a magnitude response of ∼-1.9dB is observed with a -3dB electrical bandwidth equal to 8.7GHz. In this frequency band, the laser input return loss is better than 6dB, i.e. $10^{-6/10} \simeq 0.25$ in linear. In other words, 25% of the input power is reflected and 75% of the power is transmitted. Consequently, 1.25dB electrical losses have to be considered at the laser input to take into account this mismatch.

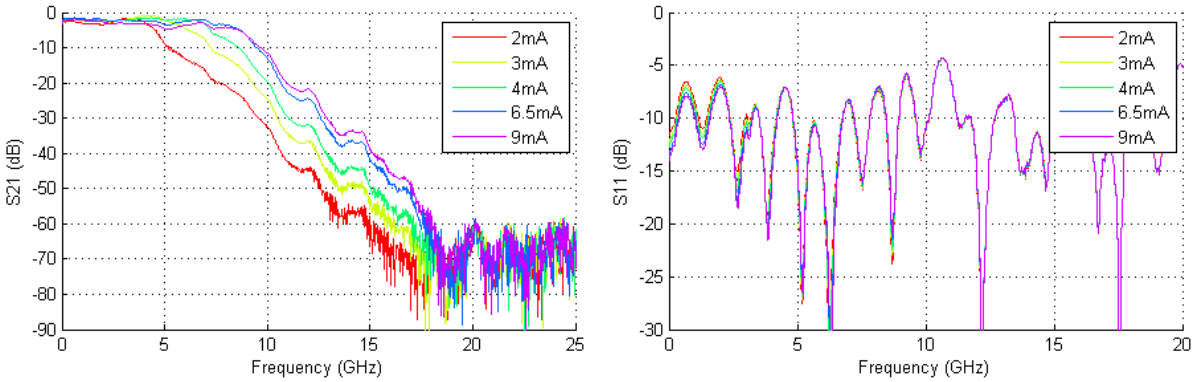

Figure 3.12: S21 parameter (on the left) and S11 parameter (on the right) of the Finisar RoF link at 850nm for different laser bias currents (Pin = -15dBm and IL = 0dB).

In order to have a static theoretical gain in agreement with the measures, 3.95dB additional electrical losses have to be added. These are probably introduced by the evaluation boards no differentially driven and by additional optical losses difficult to evaluate precisely (coupling between the optoelectronic components and the fiber).

$$\begin{aligned} G_{RoF} &= 20 \cdot log(\eta_{EO} \cdot \eta_{OE}) - 2 \times IL + 10 \cdot log(Z_{in}/Z_{out}) + 20 \cdot log(Z_{TIA}/Z_{in}) \\ &\quad - electrical\ losses \\ &= 20 \cdot log(0.08 \times 0.5) - 2 \times 0 + 10 \cdot log(60/50) + 20 \cdot log(2000/60) - 1.25 - 3.95 \\ &\simeq -1.91 dB. \end{aligned} \tag{3.8}$$

2. The same measurements have been performed for the second RoF link composed of the VCSEL at 850nm and of the GaAs PIN photodiode from VI-Systems.

At 6mA bias current, the laser input reflection coefficient is -6dB in the worst case, i.e. 1.25dB of additional electrical losses. However, in order to have a theoretical gain[4] in agreement with the experimental measurements, 2.3dB losses are added. The gain is thus equal to -28dB as shown in figure 3.13.

$$\begin{aligned} G_{RoF} &= 20 \cdot log(0.62 \times 0.4) - 2 \times 3.14 + 10 \cdot log(50/50) + 20 \cdot log(25/50) - 1.25 - 2.3 \\ &\simeq -28.0 dB. \end{aligned} \tag{3.9}$$

[4] Z_{out} and Z_{TIA} are not provided by the VI-Systems datasheet. As a consequence, typical values for a photodiode without TIA have been used, i.e. the ones from the New Focus photodiode ($Z_{out} = 50\Omega$ and $Z_{TIA} = 25\Omega$).

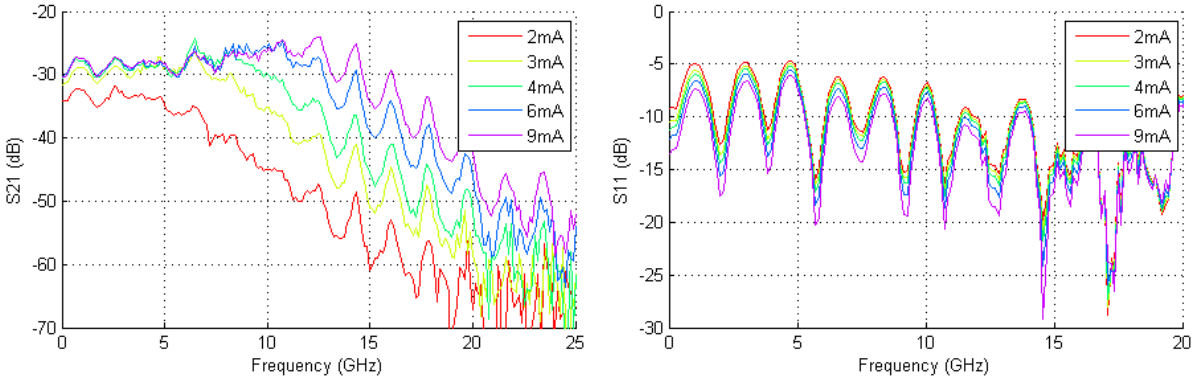

Figure 3.13: S21 parameter (on the left) and S11 parameter (on the right) of the VI-Systems RoF link at 850nm for different laser bias currents (Pin = 0dBm and IL = 3.14dB).

3 & 4. In order to determine precisely a laser bandwidth, measurements can be realized with high bandwidth photodiodes. The New Focus photodiode presents a bandwidth of 25GHz, largely higher than the Finisar laser at 850nm, but probably similar to the bandwidth of the VI-Systems laser designed for 40Gbit/s digital communication. Consequently, the S21 measurements in figure 3.14 show that the bandwidth of the Finisar laser is approximately 9GHz at 6.5mA. Concerning the use of the VI-Systems VCSEL, the S21 response is less bumpy than previously (figure 3.14, on the right, versus figure 3.13, on the left), probably due to a better photodiode matching, but the -3dB bandwidth remains the same, ∼16GHz.

At 6.5 and 6 mA bias currents, the RoF gains at low frequencies are -46 and -34 dB, respectively, while according to the analytical equations they should be:

$$\begin{aligned} G_{Finisar} &= 20 \cdot log(0.08 \times 0.4) - 2 \times 0 + 10 \cdot log(60/50) + 20 \cdot log(25/60) - 1.25 \\ &\simeq -38.0dB. \end{aligned} \tag{3.10}$$

$$\begin{aligned} G_{VI-Systems} &= 20 \cdot log(0.62 \times 0.4) - 2 \times 5 + 10 \cdot log(50/50) + 20 \cdot log(25/50) - 1.25 \\ &\simeq -29.4dB. \end{aligned} \tag{3.11}$$

The important differences observed between the analytical and experimental results can be explained by overestimated New Focus photodiode responsivity or transimpedance gain, or by significant coupling issues.

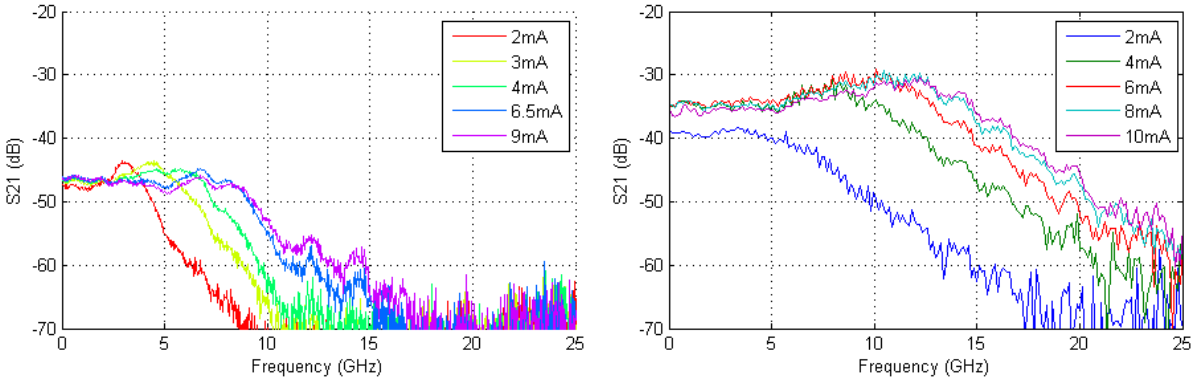

Figure 3.14: S21 parameter of RoF links at 850nm composed of the Finisar VCSEL with the New Focus photodiode (on the left) and of the VI-Systems VCSEL with the New Focus photodiode (on the right) for different laser bias currents. The laser input powers are fixed to -10 and 0 dBm, and the optical losses to 0 and 5 dB, respectively.

5. As reported in figure 3.15, the U-L-M VCSEL at 850nm has also been tested using as photodetector the Finisar GaAs PIN photodiode.

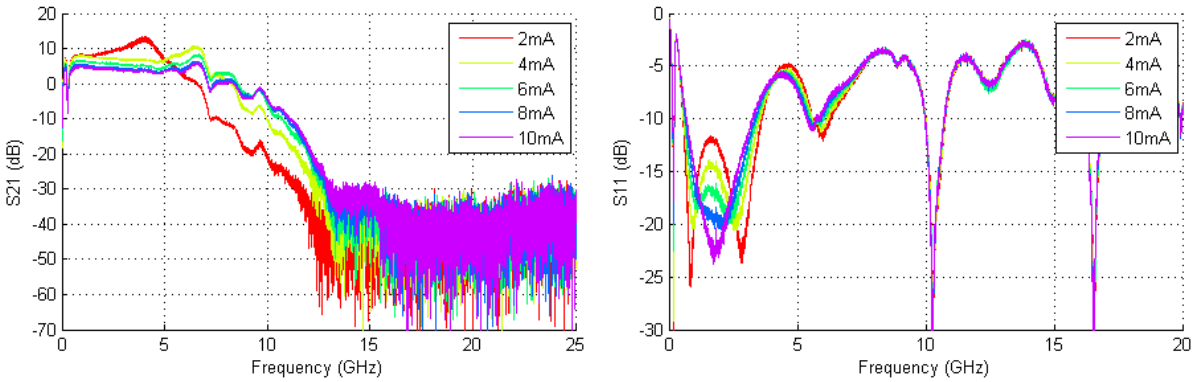

Figure 3.15: S21 parameter (on the left) and S11 parameter (on the right) of the U-L-M VCSEL at 850nm with the Finisar photodiode for different laser bias currents (Pin = -30dBm and IL = 5dB).

$$G_{RoF} = 20 \cdot log(0.7 \times 0.5) - 2 \times 5 + 10 \cdot log(50/50) + 20 \cdot log(2000/50)$$
$$\simeq 12.9dB. \tag{3.12}$$

6. Lastly, the RoF link composed of the FP laser at 1310nm and of the InGaAs PIN photodiode with the built-in TIA from Finisar has been tested. The S11 is higher than -3dB, more than 50% of the signal is so reflected. In the worst case, -2dB is observed, i.e. $10 \cdot log(1 - 10^{-2/10}) \simeq 4.3$dB additional losses to include.

$$G_{RoF} = 20 \cdot log(0.018 \times 0.85) - 2 \times 1.5 + 10 \cdot log(50/50) + 20 \cdot log(882.35/50) - 4.3$$
$$\simeq -18.7dB. \tag{3.13}$$

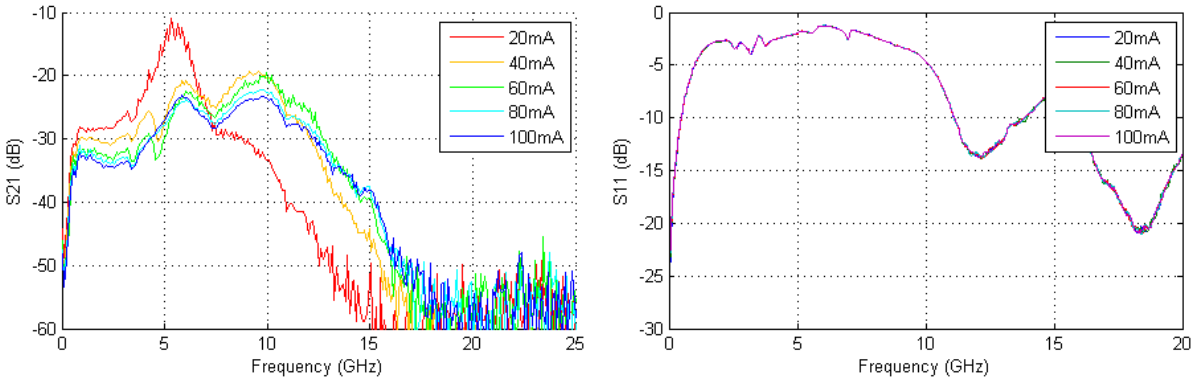

Figure 3.16: S21 parameter (on the left) and S11 parameter (on the right) of the Finisar RoF link at 1310nm for different laser bias currents (Pin = 5dBm and IL = 1.5dB).

Finally, the analytical gains provide only a coarse idea of the link performances, generally overestimated of some decibels. Therefore, the S21 measurements remain essential to determine precisely the link gains, but also the link bandwidths. Globally, the measured bandwidths are sufficient to convey at least one of the channels of the millimeter-wave band, i.e. 2.16GHz. To transmit the whole millimeter-wave band, a high laser bias current will be preferred to increase the RF bandwidth, even if in practice a compromise should be found to work in a linear modulation range, which requires a current in the middle of the L-I curve.

Among all the tested components, the Finisar components at 850nm provide a high gain and a flat response: they seem good choices for low cost RoF links. However, this needs to be confirmed by noise measurements.

Finisar GaAs PIN photodiode with the built-in TIA at 850nm

The response of the Finisar photodiode can be estimated from its slope efficiency, η_{OE}, but this method does not take into account the frequency behavior. However, since the New Focus photodiode has a

higher bandwidth than the Finisar one, 25GHz versus 10GHz according to their datasheet, the response of the Finisar photodiode can be determined from the difference of the S21 parameters of the RoF links represented in figure 3.17. In fact, these two links use the same laser, the Finisar VCSEL at 850nm.

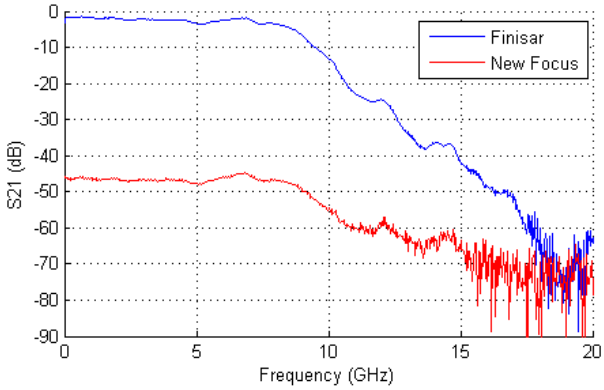

Figure 3.17: S21 of the RoF links composed of the Finisar VCSEL biased at 6.5mA and of either the Finisar photodiode, in blue, or the New Focus one, in red (from the figures 3.12 and 3.14).

Before subtracting the two S21 curves, it is necessary to normalize them relative to one another removing the response of the photodiodes and of the TIAs (equation 3.14). A corrective term has also been added to minimize the difference at DC. Lastly, it has to be noted that these equations have no physical sense, they are not consistent since η_{RX} is in A/W.

$$S21_{normalized} = S21_{measured} - 20 \cdot log\left(\eta_{RX}\right) - 20 \cdot log\left(\frac{Z_{TIA}}{Z_{in}}\right) + Correction. \tag{3.14}$$

$$S21_{normalized,\ Finisar} = S21_{measured} - 20 \cdot log(0.5) - 20 \cdot log\left(\frac{2000}{60}\right) + 0.$$

$$S21_{normalized,\ New\ Focus} = S21_{measured} - 20 \cdot log(0.4) - 20 \cdot log\left(\frac{25}{60}\right) + 4.75.$$

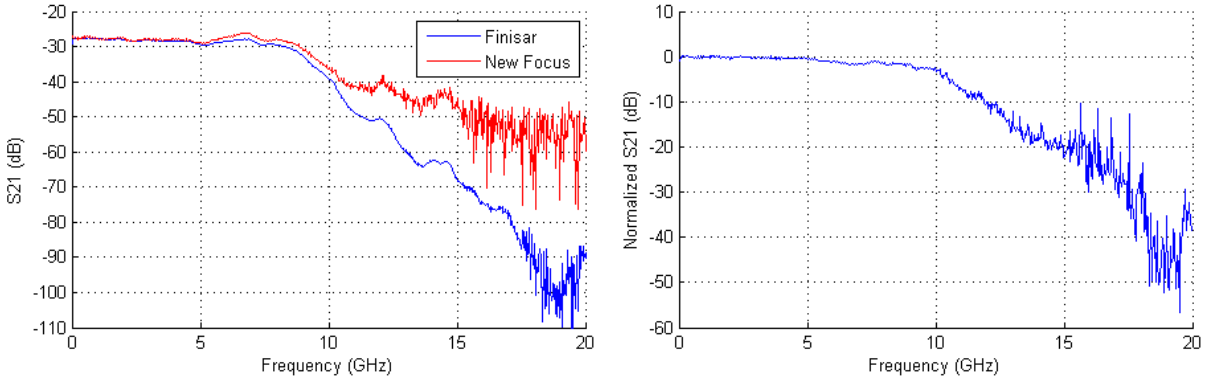

Figure 3.18: On the right, the frequency response of the Finisar photodiode calculated as the difference of the two curves on the left: the normalized S21 of RoF links built with the same Finisar laser biased at 6.5mA and either the Finisar photodiode at the reception, in blue, or the New Focus photodiode, in red.

As shown in figure 3.18, the frequency response of the Finisar photodiode is measured as a difference of S21 parameters: its -3dB bandwidth is 9.9GHz. In this section, the measurement has been made for a 6.5mA laser bias current, but the frequency response of the photodiode is obviously independent of this parameter. This has been verified. Lastly, it has to be noted that this kind of measure can be improved using a laser with a bandwidth largely higher than the photodiode to characterize.

3.4 The noises inherent to RoF links: very low level distorsions

3.4.1 Some theory

In a RoF system, the noise contributions have to be taken into account. Indeed, the optoelectronic components bring three kinds of noise [125]:

- The Relative Intensity Noise (RIN) coming from the laser.
- The shot noise coming from the photodetector.
- The thermal noise coming from the electronic stages, especially at the reception.

The Relative Intensity Noise (RIN) is defined as the Power Spectral Density of the optical fluctuations normalized to the average optical power emitted:

$$RIN\ [1/Hz] = \frac{< \delta P^2 >}{< P >^2} \tag{3.15}$$

where δP is of the optical power fluctuations and $< P >$ is the average optical power emitted.

The RIN power at the output of the photodiode is:

$$P_{RIN}\ [W/Hz] = \frac{P_{opt}^2 \times RIN \times Z_{TIA}^2 \times \eta_{OE}^2}{Z_{out}} \tag{3.16}$$

where:

- P_{opt} is the optical power received by the photodiode.
- RIN is the Relative Intensity Noise of the laser.
- Z_{TIA} is the transimpedance gain.
- η_{OE} is the photodiode responsivity.
- Z_{out} is the photodiode output impedance.

When the optical losses increase by 1dB, the RIN power decreases by 2dB. Therefore, if the RIN is the dominant noise of the system, the SNR will be independent of the optical losses since, according to equation 3.7, the radio signal strength will also decrease by 2dB for each optical dB added.

The shot noise is a consequence of the discretization of the energy carried by the photons. In fact, the optical source provides an optical beam composed of randomly emitted photons (principally spontaneous emission). These photons arrive on the photodiode in a totally chaotic order according to a Poisson distribution, and generate an electrical noise during the O/E conversion due to the random conversion of photons into photo-electrons. As a consequence, this noise called shot noise is proportional to the received optical power.

The shot noise power at the output of the photodiode is:

$$P_{shot\ noise}\ [W/Hz] = \frac{2q \times P_{opt} \times \eta_{OE} \times Z_{TIA}^2}{Z_{out}} \tag{3.17}$$

where $q = 1.6\ 10^{-19}$ C is the elementary charge of an electron.

When the optical losses increase by 1dB, the shot noise power is also reduced by 1dB. Therefore, if the shot noise is the dominant noise of the system, for a given RF power at the input of the laser, the SNR will decrease proportionally to the optical losses.

In a RoF link, the thermal noise comes from the electronic stages of the photodiode, principally from the transimpedance amplifier (TIA). It can be defined using the Noise Equivalent Power (NEP in $W/\sqrt{Hz}$), a measure of the thermal noise at the output of the photodector expressed as an equivalent optical power at the input of the photodiode. In other words, the NEP is a measure of the sensitivity of the receiver.

The thermal noise power at the output of the photodiode is:

$$P_{NEP}\ [W/Hz] = \frac{(Z_{TIA} \times \eta_{OE} \times NEP)^2}{Z_{out}} \tag{3.18}$$

The thermal noise is independent of the optical power received by the photodiode, P_{opt}. As a consequence, if the thermal noise is the dominant noise of a RoF link, for a given RF power at the input of the laser, the SNR will decrease by 2dB when the optical losses increase by 1dB, stronger than a case of dominant shot noise.

3.4.2 Relative Intensity Noise (RIN)

RIN measurement of the Finisar VCSEL: first method

To measure the laser RIN, the setup described in figure 3.19 is realized. Since the laser is not modulated, the Electrical Spectrum Analyzer (ESA) measures only the sum of each noise of the system. In order to isolate the RIN, the total received noise is recorded for different power lighting the photodetector thanks to a variable optical attenuator.

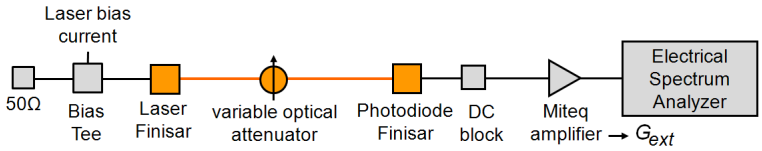

Figure 3.19: The experimental setup used to measure the RIN.

As the detected power due to the RIN could be lower than the noise floor of the spectrum analyzer, it is required to amplify it at the reception (by G_{ext}). Finally, the RIN power at the output of the photodiode is:

$$P_{RIN}\ [W/Hz] = \frac{P_{opt}^2 \times RIN \times Z_{TIA}^2 \times \eta_{OE}^2}{Z_{out}} \times G_{ext} \tag{3.19}$$

The other noises detected at the output of the systems are the shot noise and the thermal noise generated by the photodetector, by the RF amplifier and by the spectrum analyzer. Among all these contributions, only the RIN decreases proportionally to the square of the optical losses. As it can be seen on figure 3.20, based on a logarithmic scale, a 1:2 slope is observable[5]. Thus, for each frequency, the noise power is plotted as a function of the optical power at the input of the photodiode, and approximated by a second order polynomial. Then the laser RIN is extracted from the second order coefficient of the polynomial and from the knowledge of equation 3.19.

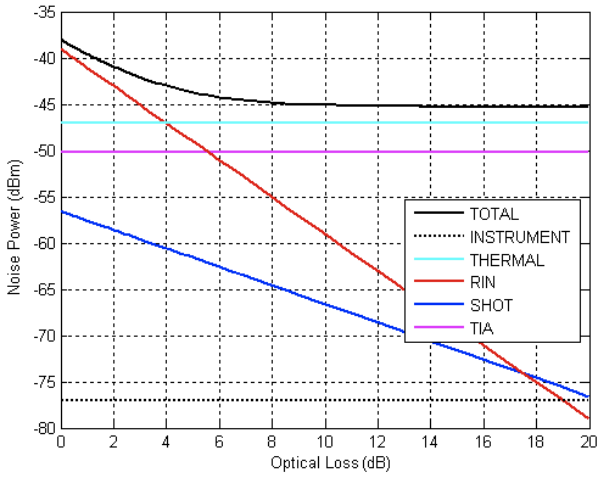

Figure 3.20: Evolution of the noise contributions (arbitrary noise values at an arbitrary frequency).

[5]This figure does not correspond to experimental measures, but to arbitrary noise values at an arbitrary frequency. It just provides the shapes of the different noise contributions.

This measure is effective as long as the RIN is predominant compared to the shot noise, which is generally true for low optical losses. Therefore, a large number of samples are captured for small values of optical losses. An example is given in figure 3.21 where a noise power measurement is performed for the Finisar laser at 4mA and a RF carrier at 5.98911GHz. At this measurement point the RIN is -124.5dB/Hz. It has to be noted that each measurement point is averaged by a factor 10 directly on the spectrum analyzer to improve the measurements precision.

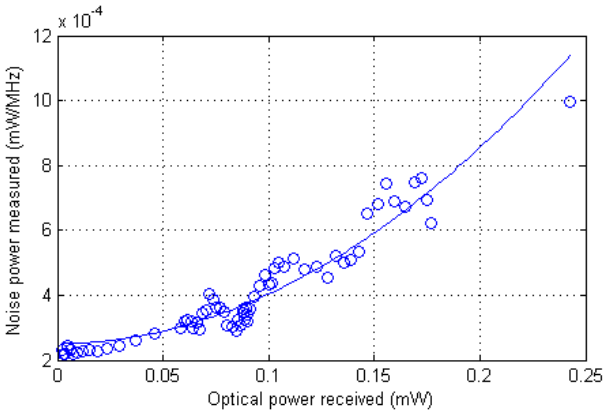

Figure 3.21: Measured noise power as a function of the optical power at the input of the photodiode. The circles represent the measurement points and the solid line the second order polynomial approximation.

Finally, the polynomial approximation in figure 3.21 is:

$$Measured\ noise\ power\ [mW/MHz] = POL(1)\ P_{opt}^2 + POL(2)\ P_{opt} + POL(3) \tag{3.20}$$

where:

- P_{opt} is expressed in units of mW.
- $POL(1)$ is expressed in units of $mW^{-1} \times MHz^{-1}$.
- $POL(2)$ is expressed in units of MHz^{-1}.
- $POL(3)$ is expressed in units of $mW \times MHz^{-1}$.

Only the RIN evolves as the square of the optical losses. As a consequence, the RIN power at the output of the photodiode (equation 3.19) is equal to:

$$P_{RIN} = POL(1)\ P_{opt}^2 \tag{3.21}$$

After the conversion of $POL(1)$ in $W^{-1} \times Hz^{-1}$, the RIN is:

$$RIN\ [W/Hz] = \frac{POL(1)\ Z_{out}}{Z_{TIA}^2\ \eta_{OE}^2\ G_{ext}} \tag{3.22}$$

where G_{ext} is the gain of the Miteq AFS4-00101000-20-10P-4 amplifier (appendix A.3.1, figure A.54).

The calculated RINs are represented in figure 3.22, in blue, as a function of the frequency and for different laser bias currents. In order to improve the results, the photodiode response represented in figure 3.18 has also been taken into account when these curves were plotted. Finally, when the laser bias current increases, it is verified that the RIN decreases, and that the peak of the RIN due to the relaxation oscillation frequency of the laser moves towards the high frequencies. However, the RIN value is not in agreement with the datasheet of the Finisar VCSEL, i.e. -130dB/Hz max at 6.5mA.

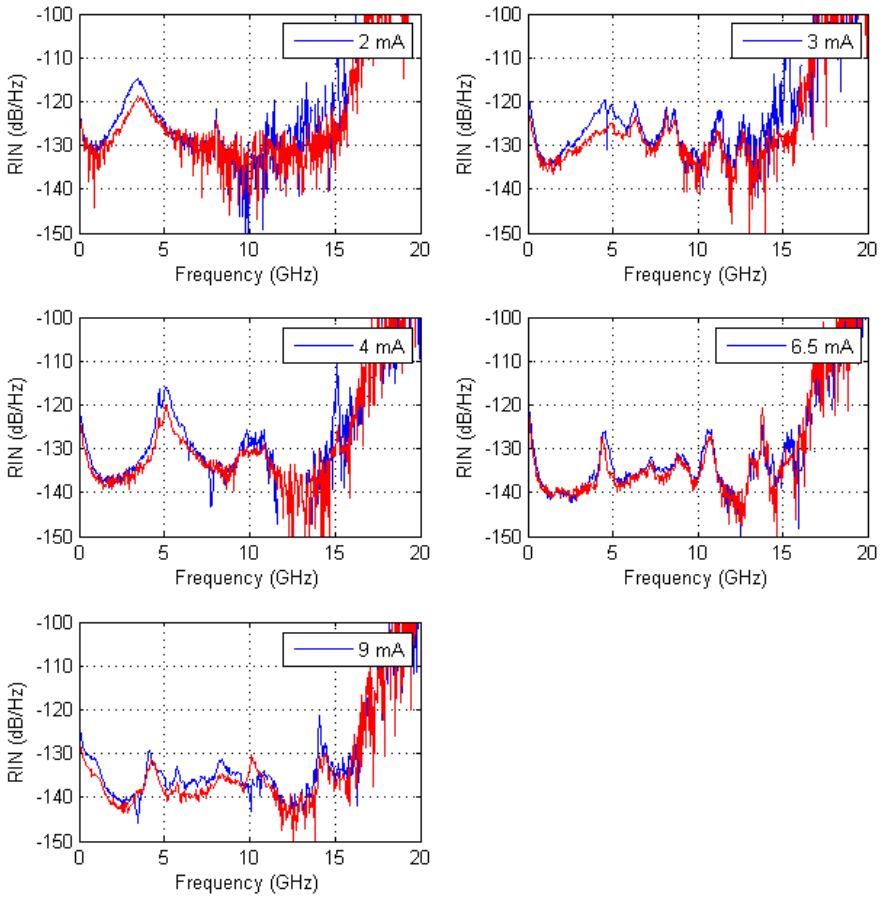

Figure 3.22: The measured RIN according to the method 1, in blue, and to the method 2 (next section), in red.

To validate the RIN measurement, it has also been verified that the contribution of the shot noise is in agreement with the expected value:

$$\begin{aligned} P_{shot\ noise}\ [W/Hz] &= 2q\ \frac{\eta_{OE}\ Z_{TIA}^2}{Z_{out}}\ P_{opt} \\ &= 2 \times 1.6\ 10^{-19}\ \frac{0.5 \times 2000^2}{50}\ P_{opt} \\ &= 1.28\ 10^{-14}\ P_{opt} \end{aligned} \tag{3.23}$$

For simplicity, the shot noise power at the output of the photodiode is normalized to the average optical power at the input of the photodiode. As a consequence, the expected value is $1.28\ 10^{-14}\ Hz^{-1}$.

This shot noise power is then calculated from the first order coefficient of equation 3.20. Indeed, only the shot noise evolves linearly as a function of the optical losses as shown in figure 3.20. Finally, with P_{opt} and $POL(2)$ converted in W and Hz^{-1}, respectively, the normalized shot noise power at the output of the photodiode equals to:

$$\frac{P_{shot\ noise}}{P_{opt}} = \frac{POL(2)}{G_{ext}} \tag{3.24}$$

The results are reported in figure 3.23. They are in agreement with the theory, at least up to 10GHz[6]. Beyond, the shot noise, as the RIN previously, is not valid since the system is outside its bandwidth.

[6]The results are not perfect as the *polyfit* function provided by Matlab to obtain a polynomial approximation from experimental measurements does not allow to fix coefficients. In fact, fixing $POL(3)$ at the value of the thermal noise, i.e. the minimal measured noise (when P_{opt} is null), could improve the results.

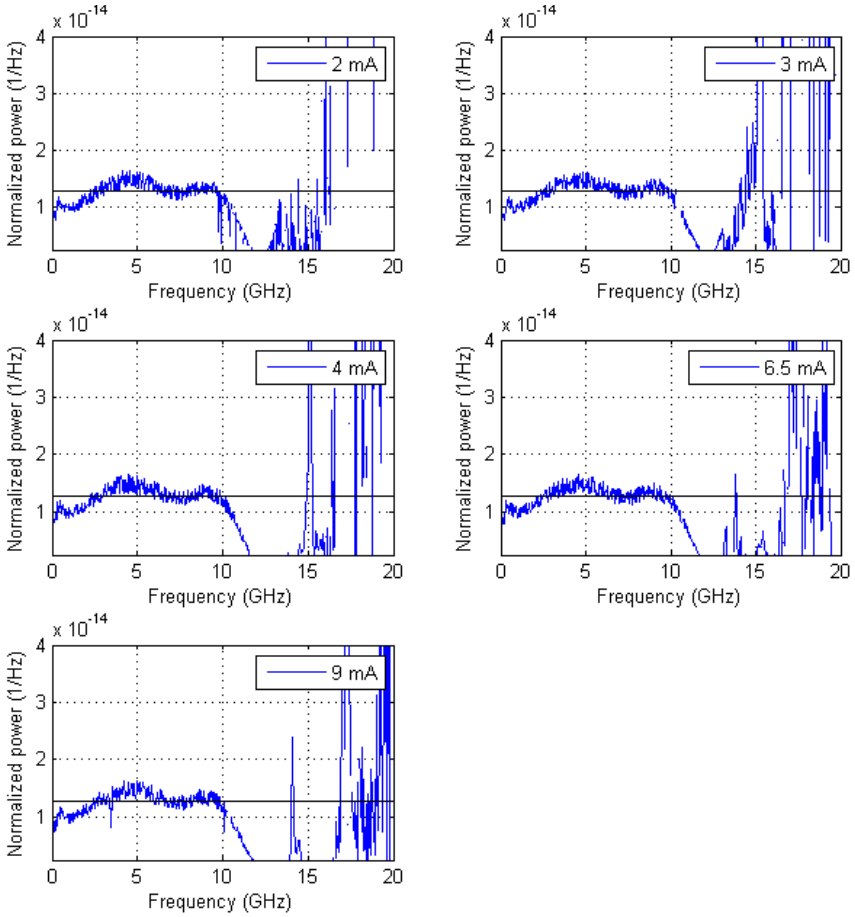

Figure 3.23: The measured shot noise coefficient in blue, and the theoretical value in black.

RIN measurement of the Finisar VCSEL: second method

A second method based on the same setup than the one in figure 3.19 has been evaluated to measure the RIN of the Finisar VCSEL. Two measurements are performed:

- a first one with the laser turned-on to measure the total noises contribution.
- a second one with the laser turned-off. In this case the noise power measured at the output of the system is composed only of the thermal noises of the photodetector, of the RF amplifier and of the spectrum analyzer.

Under the assumption that the shot noise is very small compared to the RIN, the RIN equals to:

$$RIN\ [dB/Hz] = 10 \cdot log\left(\frac{difference\ of\ the\ measured\ noise\ powers}{A\ I_{ph}^2\ Z_{out}}\right) \tag{3.25}$$

where:

- A is the reception gain, in linear: $A = 10^{(20 \cdot log(Z_{TIA}/Z_{out}) + G_{ext})/10}$.
- I_{ph} is the photodetected current.
- Z_{out} is the impedance of the photodiode.

The difference of the measured noise powers corresponds to the laser intensity noise amplified by the reception stage while the product $I_{ph}^2\ Z_{out}$ corresponds to the average electrical power detected by the photodiode. Consequently, equation 3.25 is, by definition, the RIN (equation 3.15). To improve the results, the photodiode response (figure 3.18) has also been taken into account.

The RIN curves obtained with this second method have been plotted in figure 3.22, in red. It can be observed that the curves of the two methods differ from only 1 or 2 dB, a difference probably due to the gain values. Finally, the good agreement between the red and the blue curves valid the two approaches tested.

RIN measurement of the Finisar VCSEL: third method

The previous measurement can be improved removing the condition that the shot noise has to be very small compared to the RIN. Instead of realizing a second measure with the laser under test turned-off, which consists in calculating only the thermal noise, a new measure is performed using an optical source with a negligible intensity noise on the spectral bandwidth where the RIN has to be known. Thus, at the reception, both the shot noise (for a same optical power received) and the thermal noise are measured. Typically, a solid-state laser with relaxation oscillation frequencies located at low frequencies, below 100MHz, is used. For example, in [126], a Erbium Ytterbium (Er:Yb) laser is used to characterize a laser at 1550nm whereas a Neodymium-doped Yttrium Aluminium Garnet (Nd:YAG) laser is used at 1μm. In our case a Titanium Sapphire (Ti:Al_2O_3) laser is a good choice as it can emit wavelengths in the range from 650nm to 1100nm. In [127], such a laser is used at 760nm: a relaxation oscillation frequency around 20MHz is observed.

Discussion on the measures

The first method has been compared with a commercial test bed in order to verify the laboratory RIN measurements presented in figure 3.22. Agilent provides an accurate RIN measurement system, the N4371A, operating at 1310 and 1550 nm for singlemode lasers. As a consequence, the RIN of a multimode laser at 850nm cannot be measured. Therefore, the laboratory-made setup proposed in this work and the Agilent setup have been compared using the singlemode VCSEL at 1550nm from RayCan (RC32xxx1-T).

In the Agilent RIN measurement system, the laser signal is converted to an electric signal by a PIN photodiode, amplified by a low noise amplifier and measured with a spectrum analyzer. To measure the RIN, the amplified laser intensity noise is isolated from the other noise sources: the shot noise which is calculated from the average photocurrent (measured by a multimeter) and the thermal noise which is obtained when laser signal is turned-off (measured during a calibration step). Finally, very low RIN value can be obtained, up to -160dB/Hz between 10MHz and 20GHz.

In the laboratory-made RIN setup, a Nortel Networks PP-10G PIN photodiode with a built-in TIA is used at the reception [118], and cascaded with an external Miteq JS41-00102000-27-10P LNA (appendix A.3.1). The photodiode main characteristics are responsivity of 0.88A/W, transimpedance gain of 500Ω, 11GHz bandwidth, and 50Ω output impedance.

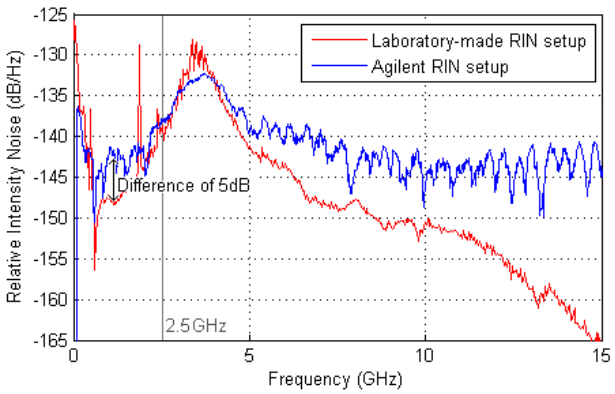

Figure 3.24: RIN of the RayCan VCSEL for a bias current of 6mA according to the laboratory-made setup, method 1, in red, and to the Agilent setup, in blue.

Compared to the previous measurements, the frequency response of the photodiode has not been considered. Nevertheless, the results are in good agreement taking into account that the laser is designed for 2.5Gbit/s applications: an incertitude of only 5dB/Hz is observed.

RIN measurement of other lasers

1. The RIN of the VI-Systems VCSEL has been measured using the first method. The reproducibility of the experimentation has been checked performing the measurements with two different photodiodes: either the Finisar photodiode with the built-in TIA, or the New Focus photodiode with external

amplifiers (a Miteq AFS4-00101000-20-10P-4 amplifier, a 10dB RF attenuator and a Miteq AFS44-00102000-30-10P-44 amplifier, i.e. a total external gain of 65dB as measured in appendix A.3.1).

The results presented in figure 3.25 show a general fair agreement, excepted at 9mA. Sometimes interferences appear on the RIN curves as at 6GHz where an important additional noise appears for a laser bias current equal to 2 or 6 mA. The source of these interferences has not been clearly identified but they may be attributed to different relaxation oscillation frequencies for the different transverse modes [25] [124]. In fact, the transverse modes have different spatial carrier consumptions: they do not share a single carrier reservoir. In [124], it is explained that the RIN exhibits several peaks when some transverse modes are filtered (spatial filtering), which can be due to the VCSEL-fiber and fiber-photodiode couplings.

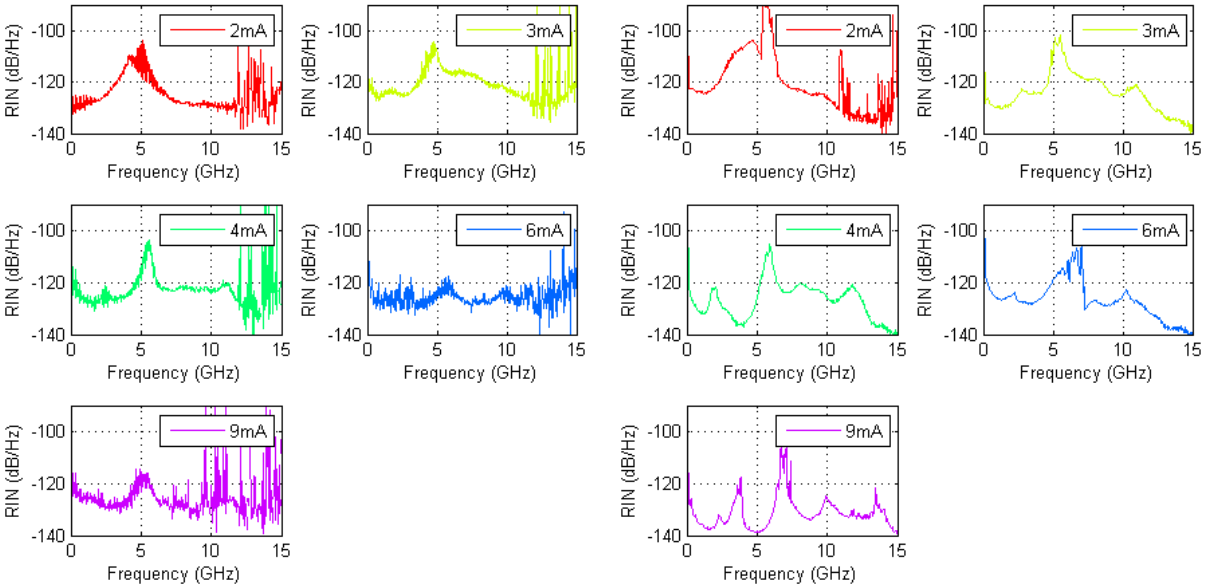

Figure 3.25: RIN of the VI-Systems VCSEL for different values of bias current measured by the Finisar photodiode on the left and measured by the New Focus photodiode on the right, method 1.

The VI-Systems photodiode can also be used at the reception. Concerning the RIN of the Finisar VCSEL, no good result has been obtained with this photodiode, probably due to a sensibility issue. In fact, this photodiode is designed to work with the VI-Systems VCSEL, a laser emitting a high optical power. Concerning the RIN of the VI-Systems VCSEL, no good result has been obtained as ripples appear on the curves. This time, the bad impedance matching of the photodiode limits the results. These two RIN measurements have been reported in appendix A.5.

2. The RIN of the U-L-M VCSEL has been measured using the Finisar GaAs PIN photodiode working at 850nm. The results, presented in figure 3.26, are excellent for a laser bias current of 6mA with a RIN of -140dB/Hz at 5GHz and a peak due to the relaxation oscillation frequency rejected at high frequencies, around 8GHz.

3. The RIN of the Finisar VCSEL at 1310nm has finally been measured using the Finisar InGaAs PIN photodiode followed by an external Miteq AFS3-00101200-22-10p-4 amplifier with 20dB gain at 5GHz (appendix A.3.1). At 45mA, the measured RIN (figure 3.27) is higher than the value reported in the datasheet, i.e. -130dB/Hz. Nevertheless, since the RIN decreases when the bias current increases, RIN values under -130dB/Hz are obtained from 70mA. The peak of the RIN due to the relaxation oscillation frequency of the laser is not very marked, and it does not seem to move to the high frequencies when the bias current increases.

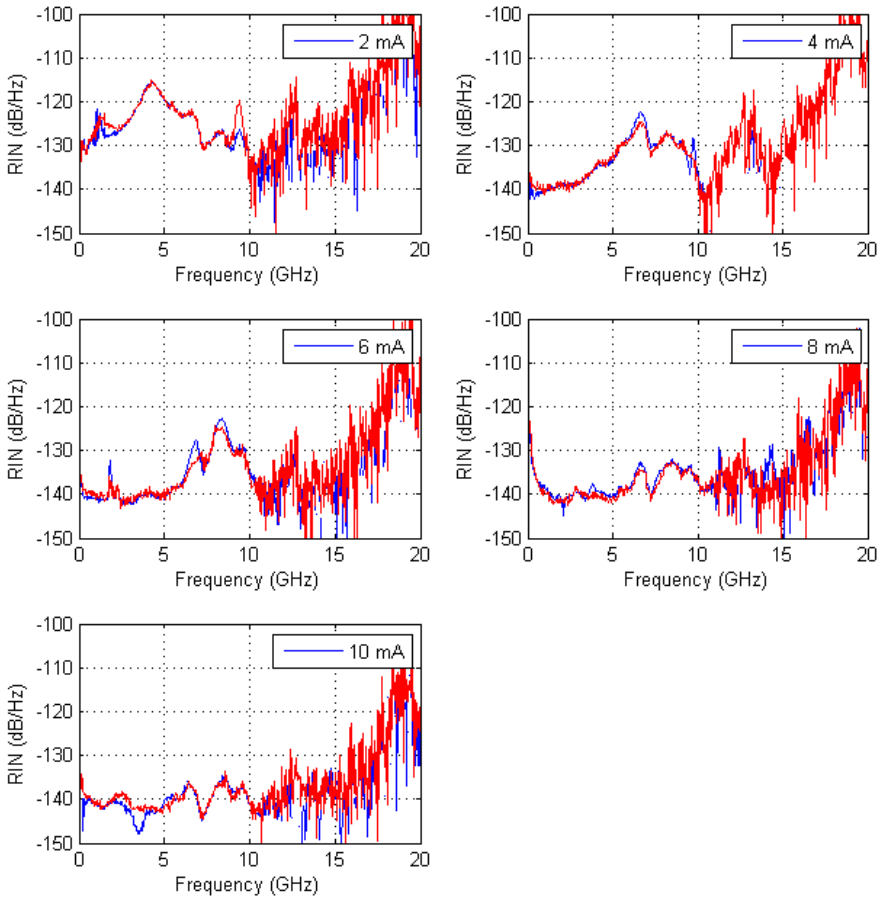

Figure 3.26: The RIN of the U-L-M Photonics VCSEL according to the method 1, in red, and to the method 2, in blue.

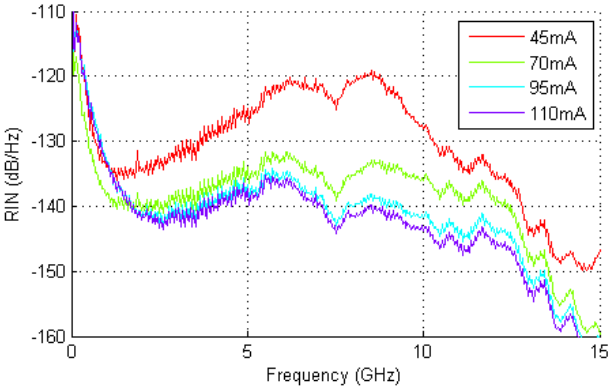

Figure 3.27: RIN of the Finisar FP laser at 1310nm according to the method 1 and for different laser bias current.

Lastly, table 3.6 summarizes the obtained results. The "Average RIN" value provided in this table is the average RIN observed by a radio signal of 2GHz bandwidth centered at 5GHz (as a reminder the millimeter-wave signal will be transposed at IF).

Table 3.6: RIN values for lasers biased in the middle of their L-I curve.

Laser	Wavelength	Bias current	Average RIN	Peak of RIN
VCSEL Finisar	850nm	6.5mA	-135dB/Hz	-125dB/Hz at 4.5GHz
VCSEL VI-Systems	850nm	6mA	-125dB/Hz	-120dB/Hz at 5.5GHz
VCSEL U-L-M	850nm	6mA	-140dB/Hz	-125dB/Hz at 8.3GHz
FP Finisar	1310nm	70mA	-135dB/Hz	-132dB/Hz at 6GHz
VCSEL Raycan	1550nm	6mA	-140dB/Hz	-130dB/Hz at 4GHz

3.4.3 Thermal noise at the receiver

The NEP has been measured for the Finisar GaAs PIN photodiode at 850nm and the Finisar InGaAs PIN photodiode at 1310nm. The thermal noise power is observed by connecting these photodiodes, supplied with a 3.3V bias voltage, to an electrical spectrum analyzer with a resolution bandwidth of 100kHz (RBW and VBW), but with no incident optical power. From this noise power measurement (figure 3.28, on the left), the NEP is calculated according to the equations below:

$$P_{NEP}\ [W/Hz] = \frac{Photodiode\ thermal\ noise_{\,lin} - Spectrum\ analyzer\ noise_{\,lin}}{RBW} \tag{3.26}$$

$$NEP\ [W/\sqrt{Hz}] = \frac{\sqrt{P_{NEP}\ Z_{out}}}{Z_{TIA}\ \eta_{OE}} \tag{3.27}$$

The NEP of the two photodiodes are represented in figure 3.28 on the right as a function of the frequency. These measurements are reliable as long as the spectrum analyzer noise can be neglected, that means up to 7GHz at 1310nm and up to 11GHz at 850nm. Finally, the Finisar photodiode at 1310nm is less noisy than the photodiode at 850nm, its NEP curve being $20pW/\sqrt{Hz}$ lower.

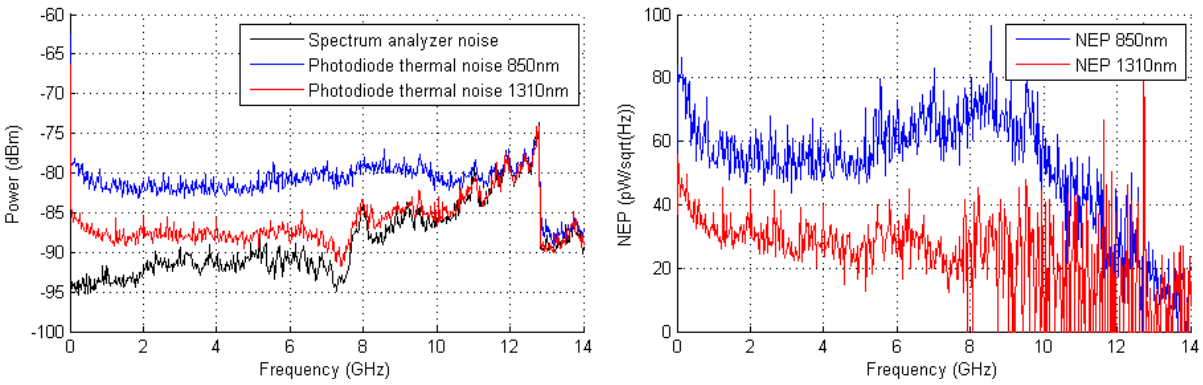

Figure 3.28: Noise power measured in a bandwidth of 100kHz on the left, and deduced NEP for the Finisar photodiodes at 850nm and 1310nm on the right.

The NEP of the VI-Systems and New Focus photodiodes has not been measured because their thermal noise cannot be differentiated from the spectrum analyzer noise. In fact, they do not include a TIA. Nevertheless, it is possible to estimate the minimum thermal noise power observable at the output of these photodiodes using the equation below:

$$P_{Thermal}\ [W/Hz] = 4k_BT \tag{3.28}$$

where,

- k_B is the Boltzmann's constant, $k_B = 1.38\ 10^{-23} J/K$
- T is the temperature, in Kelvin.

3.5 Large signal dynamic performances: non-linearities distorsions

3.5.1 IP3 measurements of the Radio over Fiber links

When two close frequencies, f_1 and f_2, are applied to a non-linear system, new frequencies called third-order intermodulation (IM3) products are created at $2f_1 - f_2$ and $2f_2 - f_1$. They are generally located in the bandwidth of the RF signal, especially for OFDM modulated signals, and are therefore difficult to remove by filtering[7].

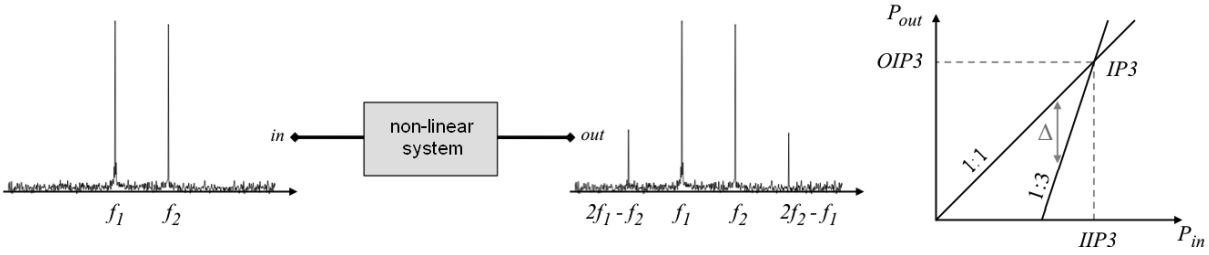

Figure 3.29: Definition of the third-order intermodulation products.

The RF powers at f_1 and f_2 at the output of a non-linear system increase linearly with the input power, while the third-order intermodulation products evolve with the cube of the input power. So, when the output power is plotted as a function of the input power, in logarithmic scale, a 1:1 slope is obtained for the linear response, and a 1:3 slope for the cubic one, as shown in figure 3.29.

The third-order Intercept Point (IP3) is defined as the power of one fundamental tone at the intersection between the linear and cubic responses regardless of possible compression. The IP3 can be calculated either at the input of the system (IIP3), or at the output of the system (OIP3). To determine the input IP3, the setup of figure 3.30 has been realized and automated with Labview to obtain accurate results.

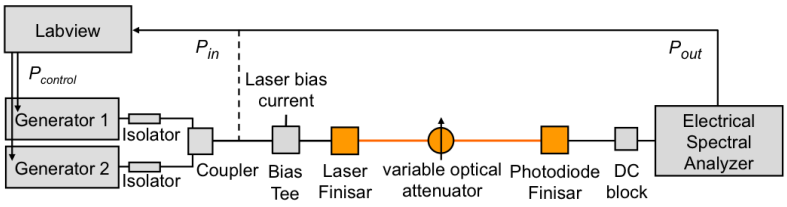

Figure 3.30: The experimental setup used to measure the IP3.

Two tones, f_1 and f_2, from two separated RF generators are combined thanks to a RF coupler. The difference between f_1 and f_2 is fixed to 10MHz, a typical spacing between OFDM subcarriers. Indeed, in the IEEE 802.15.3c OFDM standard, HSI mode, the subcarrier spacing is 5.0625MHz. Concerning the central frequency, $0.5 \times (f_1 + f_2)$, it is fixed to 3GHz or 5GHz as subsequently the RoF transmission will be realized in Intermediate Frequency, at 4.5GHz (see chapter 4).

An example of an IP3 measurement is given in figure 3.31 where the RoF link composed of the Finisar VCSEL at 850nm biased at 6.5mA and directly connected to the Finisar GaAs PIN photodiode, without optical loss, is tested. On the left, a first measure is performed in back-to-back, i.e. at the output of the coupler. The two emitted tones, f_1 and f_2, and the third-order tones, $2f_1 - f_2$ and $2f_2 - f_1$, are measured using a spectrum analyzer configured with a RBW and a VBW fixed to 3Hz. In addition, the measure is realized tone after tone with a 500Hz span, thus a very low noise level is observed, -135dBm[8]. The observed third-order tones, coming from the non-linearity of the spectrum analyzer, will be neglected subsequently as the corresponding input IP3 is very high, 21.6dBm. Indeed, with limited

[7] Only the dominant intermodulation products are considered in this study: IM3 are the most influent, IM5, IM7, and so on are therefore ignored. Concerning the harmonic products, i.e. even intermodulation products such as IM2, they are located out of the radio band.

[8] The noise figure of the spectrum analyzer is therefore: $-135 - 10 \cdot log(RBW \times 4K_BT) = -135 - 10 \cdot log(3 \times 4 \times 1.38\,10^{-23} \times (273 + 25)/10^{-3}) = 28.1dB$.

laser input powers and RoF losses, a sufficient back-off from the ESA IIP3 is always taken. On the right, a second measure is performed at the output of the RoF link. Compression appears for high input power, nevertheless the IP3 can be determined extending linearly the measurement points: the IP3 is obtained for an output power of -5.50dBm, i.e. -4.62dBm at the input of the system. The relationship between P_{in} and P_{out} is known as the figures below have the same x-axis. For example, in this RoF link, ∼1dB is lost.

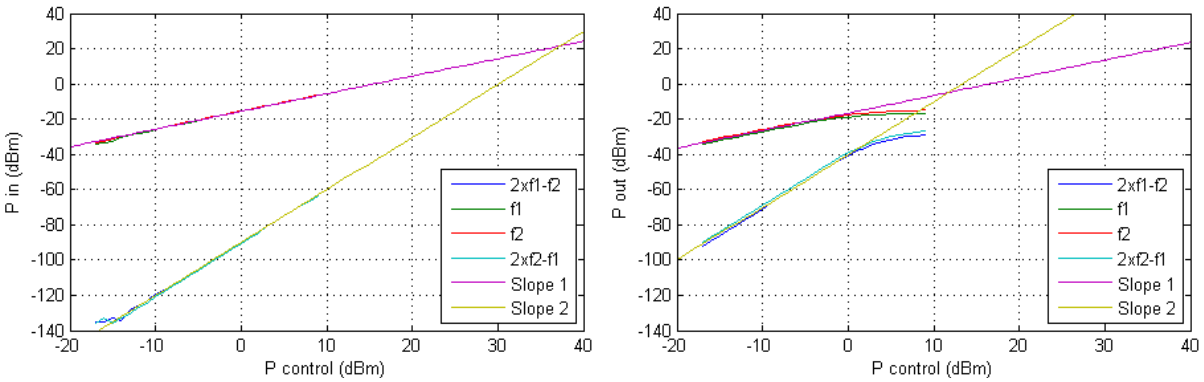

Figure 3.31: IP3 curves in back-to-back on the left and at the output of the system on the right.

In a RoF link, the optical insertion losses can influence the IP3. In fact, if the non-linearities mainly come from the photodiode, the difference between the linear and cubic responses, called Δ in figure 3.29, will decrease when the optical power received by the photodiode will increase (for a fixed laser input power). In theory, the slope followed by Δ is 1:2 (1:3 slope − 1:1 slope), but since the optical losses induce double electrical losses (equation 3.7), the slope factor is 4. On the contrary, if the non-linearities of the RoF link only come from the laser, Δ will be a constant since the laser non-linearities are independent of the optical losses.

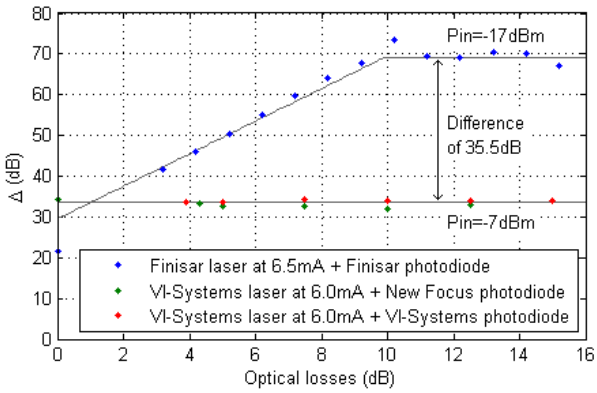

Figure 3.32: Δ as a function of the optical losses. The laser input power is fixed to -7dBm for the VI-Systems VCSEL and -17dBm for the Finisar VCSEL.

In figure 3.32, Δ is plotted as a function of the optical losses for three different RoF links. If the Finisar RoF link at 850nm shows non-linearities caused by the photodiode and its built-in TIA for optical losses below 10dB, the RoF links based on the VI-Systems laser have non-linearities only due to the optical source. This explains why the same results have been observed for RoF links based on the same laser, but having different photodiodes. As a consequence, in these particular cases only one IP3 measure is necessary to know the performances of the RoF links, a measure that can be made for an arbitrary optical loss value. Lastly, a difference of 35.5dB is observable between the Δ due to the Finisar VCSEL and the Δ due to the VI-Systems VCSEL: the input IP3 of the Finisar VCSEL is so $(this\ difference/2) + (Pin\,Finisar - Pin\,VI\text{-}Systems) = 7.75dB$ higher than the input IP3 of the VI-Systems VCSEL. In fact, Δ decreases of 2dB when the input power increases by 1dB, hence the factor 2.

Table 3.7: Measured IIP3 for different configurations at 850nm. The Finisar laser has been tested at 3GHz while the VI-Systems laser has been tested at 5GHz.

Laser	Finisar	Finisar	Finisar	Finisar	Finisar	Finisar	Finisar
Bias current (mA)	4	9	6.5	6.5	6.5	6.5	6.5
Optical losses (dB)	0	0	0	5	8	10	12.5
Photodiode	Finisar	Finisar	Finisar	Finisar	Finisar	Finisar	Finisar
Input IP3 (dBm)	-5.18	-3.38	-4.62	6.64	14.4	17.35	16.99
RoF losses (dB)	-2.97	-3.89	-1.00	-11.46	-19.37	-21.48	-28.21

Laser	Finisar	Finisar	Finisar	Finisar	Finisar	Finisar	Finisar
Bias current (mA)	2	3	4	6.5	9	6.5	6.5
Optical losses (dB)	12.5	12.5	12.5	12.5	12.5	0	5
Photodiode	Finisar	Finisar	Finisar	Finisar	Finisar	New Focus	New Focus
Input IP3 (dBm)	-8.05	4.63	9.39	15.83	21.29	16.88	16.1
RoF losses (dB)	-25.43	-26.35	-27.81	-29.51	-30.45	-39.77	-53.83

Laser	VI-Systems	VI-Systems	VI-Systems	VI-Systems	VI-Systems	VI-Systems
Bias current (mA)	4	6	9	4	6	9
Optical losses (dB)	5	5	5	5	5	5
Photodiode	New Focus	New Focus	New Focus	VI-Systems	VI-Systems	VI-Systems
Input IP3 (dBm)	6.69	9.08	12.95	6.21	9.71	14.94
RoF losses (dB)	-34.85	-34.53	-34.42	-31.24	-31.00	-30.96

Table 3.7 summarizes the IIP3 values obtained for different RoF links. First, assuming that for high optical losses, the non-linearities are only due to the lasers, the IIP3 of the Finisar laser biased at 6.5mA is 17dBm, whereas the IIP3 of the VI-Systems laser biased at 6mA is 9dBm. The Finisar VCSEL presents a higher IP3 than the VI-Systems VCSEL, by about 8dB as previously predicted. Then, more the laser bias current is high, more the RoF links will be linear. Indeed, for each RoF link tested, the IIP3 increases when the bias current is put away from the laser threshold. Lastly, it can be noted that the VI-Systems and the New Focus photodiodes are highly linear because they do not include a built-in TIA. Photodiode including a TIA are less efficient in terms of non-linearity, such as the PIN photodiode at 1310nm from Finisar (figure 3.33).

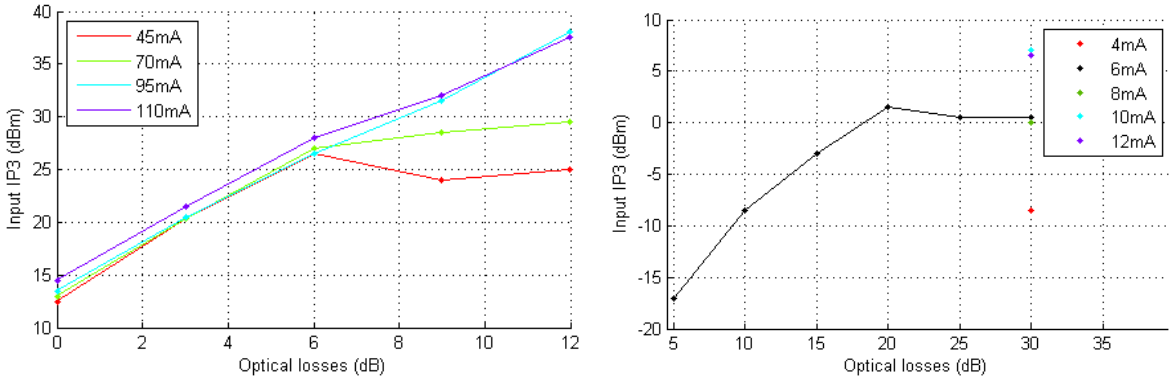

Figure 3.33: Input IP3 at 5GHz of a RoF link composed of the Finisar components working at 1310nm (on the left) and of the U-L-M VCSEL at 850nm with the Finisar photodiode (on the right) as a function of the optical losses for different laser bias currents.

3.5.2 IP3 measurements of the Finisar photodiode: first method

Some theory

The goal of this section is to determine the IP3 of a photodiode. Until now, just the non-linearities of the RoF links and of their lasers are known, however the IP3 of the photodiodes can be determined working on the definition of the third-order intercept point recalled in figure 3.34. To calculate this IP3, a reasoning based on electrical power is followed, even if the photodiode input power is optical.

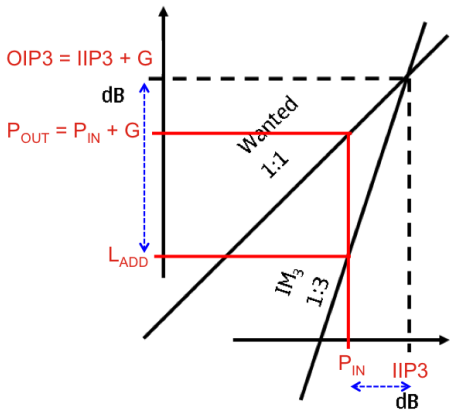

Figure 3.34: The different variables considering in the calculation of the third-order intercept point.

The power of the non-linearities at the output of a RF system, L_{out}, is related to the power of the non-linearities at its input, L_{in}. In order to establish the relationship between L_{in} and L_{out}, the system gain, G, the input third-order intercept point, $IIP3$, and the signal power at the input of the system, P_{in}, have to be known. In fact, from the figure 3.34, some equations can be set:

$$\begin{aligned} IIP3_{dBm} - P_{in\,dBm} &= \frac{1}{3}\left(OIP3_{dBm} - L_{ADD\,dBm}\right) \\ &= \frac{1}{3}\left(IIP3_{dBm} + G_{dB} - L_{ADD\,dBm}\right) \end{aligned} \tag{3.29}$$

where L_{ADD} is the non-linearities added by the RF system.

$$\begin{aligned} L_{ADD\,dBm} &= OIP3_{dBm} - 3\left(IIP3_{dBm} - P_{in\,dBm}\right) \\ &= IIP3_{dBm} + G_{dB} - 3\left(IIP3_{dBm} - P_{in\,dBm}\right) \\ &= 3\,P_{in\,dBm} - 2\,IIP3_{dBm} + G_{dB} \end{aligned} \tag{3.30}$$

The power of the non-linearities at the output of the RF system is equal to the sum of the non-linearities at its input, amplified by the system, and of the non-linearities added by the system:

$$\begin{aligned} L_{out\,dBm} &= 10 \cdot log(10^{L_{ADD\,dBm}/10} + 10^{(L_{in\,dBm}+G_{dB})/10}) \\ &= f(G_{dB}, IIP3_{dBm}, P_{in\,dBm}, L_{in\,dBm}) \end{aligned} \tag{3.31}$$

From these equations it is possible to calculate the photodiode IIP3 as shown in the next section.

Test of the first method

Previously, the input IP3 of the Finisar RoF link at 850nm has been determined measuring the power at the output of the system at $2f_1 - f_2$, f_1, f_2 and $2f_2 - f_1$ as a function of the RF input power. From these measurements, the input IP3 of the photodiode can be calculated.

First, the equivalent photodiode electrical input power is calculated from the laser input power on the basis of the link characteristics.

$$P_{in\ PD} = P_{in\ laser} + (G_{laser} - electrical\ losses) - 2\ Optical\ losses \tag{3.32}$$

where G_{laser} is the laser gain or the gain of a RoF link having an ideal photodiode ($\eta_{OE} = 1$A/W and $Z_{TIA} = Z_{out} = 50\Omega$). It equals to $20 \cdot log(\eta_{EO}) + 10 \cdot log(Z_{IN}/50) + 20 \cdot log(50/Z_{IN})$. As a reminder, the electrical losses at the laser input have been defined in section 3.3.2.

Secondly, the powers measured at the output of the system are adjusted in order to obtain the powers of the carriers at $2f_2 - f_1$ and $2f_1 - f_2$ without the non-linearities introduced by the laser and the optical link:

$$P_{out}(2f_2 - f_1) = 10 \cdot log(10^{P_{out}(2f_2-f_1)/10} - 10^{(L_{in\ PD}+G_{PD})/10}) \tag{3.33}$$

with:

$$\begin{aligned} L_{in\ PD} &= L_{ADD\ laser} - 2\ Optical\ losses \\ &= 3\,P_{in} - 2\,IIP3_{laser} + G_{laser} - 2\ Optical\ losses \\ &= 3\,(P_{out} - G_{RoF}) - 2\,IIP3_{laser} + G_{laser} - 2\ Optical\ losses \end{aligned} \tag{3.34}$$

where:

- $IIP3_{laser}$ equals to 17dBm at 3GHz.
- $L_{in\ laser}$ is neglected.

The IP3 curve for the Finisar RoF link at 850nm (figure 3.31) has been reported below substituting the input and output powers at $2f_1 - f_2$, f_1, f_2 and $2f_2 - f_1$ by the new values determined from the equations 3.32 and 3.33. The corresponding figure is represented in 3.35 for different optical losses.

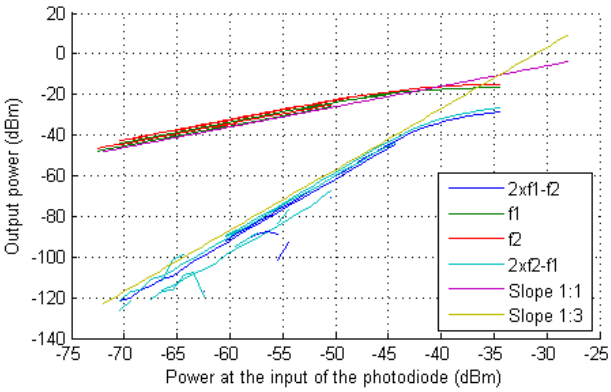

Figure 3.35: Power at the output of the photodiode at $2f_1 - f_2$, f_1, f_2 and $2f_2 - f_1$ as a function of the power at the input of the photodiode (electrical equivalent).

Finally, the IP3 obtained at the input of the photodiode is -34.5dBm. This value does not have a great physical meaning as it corresponds to an electrical power at the input of a photodiode. The advantage of this value only lies in Matlab simulations or in comparison between photodiodes. In this case, the photodiode is considered as a black box with a gain (G_{PD}), a P1dB, a NF and an IP3 value. The photodiode gain is the gain of a RoF link having an ideal laser ($\eta_{EO} = 1$W/A and $Z_{in} = 50\Omega$):

$$G_{PD} = 20 \cdot log(\eta_{OE}) - 10 \cdot log(Z_{out}/50) + 20 \cdot log(Z_{TIA}/50) = 26dB \tag{3.35}$$

Consequently, the output IP3 equals -8.5dBm: $OIP3 = IIP3 + G_{PD} = -34.5 + 26$ (in agreement with figure 3.35).

Lastly, from the knowledge of the IP3 of the Finisar VCSEL at 850nm and of the IP3 of the Finisar GaAs PIN photodiode, the IP3 of RoF link is plotted as a function of the optical losses in order to check the values of table 3.7. The input IP3 of the laser is set to 17dBm and the input IP3 of the photodiode to -34.5dBm. The signal power at the output of the system, P_{out}, and the power of the non-linearities, L_{out}, are calculated as follows:

- $P_{out} = P_{in} + G_{laser} + G_{PD} - electrical\ losses - 2\ Optical\ losses.$
- $L_{out\ laser} = f(G_{laser} - electrical\ losses, IIP3_{laser}, P_{in}, L_{in})$, with L_{in} fixed at -∞.
- $L_{out\ fiber} = L_{out\ laser} - 2\ Optical\ losses.$
- $L_{out\ PD} = f(G_{PD}, IIP3_{PD}, P_{in} + G_{laser} - electrical\ losses - 2\ Optical\ losses, L_{out\ fiber})$.

All these parameters are known. Now, to determine the IP3 of the RoF link, for each value of optical losses, the input power of the RoF link is increased until $L_{out\ PD}$ equals to P_{out}: at this point, P_{in} is equal to the IIP3. The operation is repeated for different optical losses to obtain the curve in figure 3.36: a good agreement can be observed.

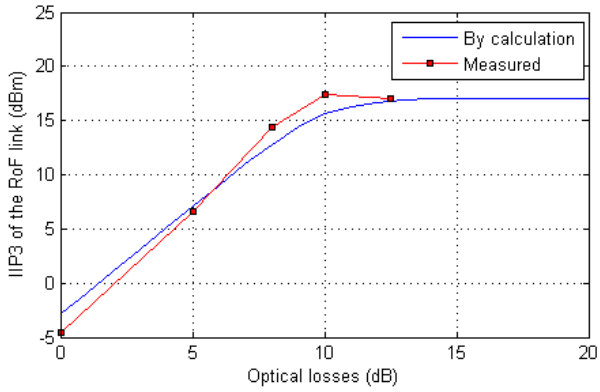

Figure 3.36: Comparison between the calculated and the measured IIP3s as a function of the optical losses.

3.5.3 IP3 measurements of the Finisar photodiode: second method

A second method has been investigated to measure the third-order intercept point of the photodiode only. The idea consists in sending two RF carriers at the input of the photodiode without additional third-order carriers. A highly linear laser can be used or, as described in figure 3.37, two RF carriers can be conveyed to the photodiode by two different lasers and combined using an optical coupler.

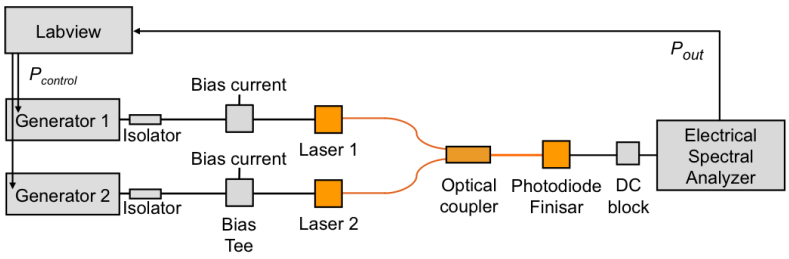

Figure 3.37: Measurement setup of the third-order interception point of the photodiode.

Figure 3.38 represents the RF powers at the output of the photodiode as a function of the control power. The OIP3 is equal to -9dBm, a value that differs by only 0.5dB from the one calculated with the first method. The validity of this second method is therefore verified.

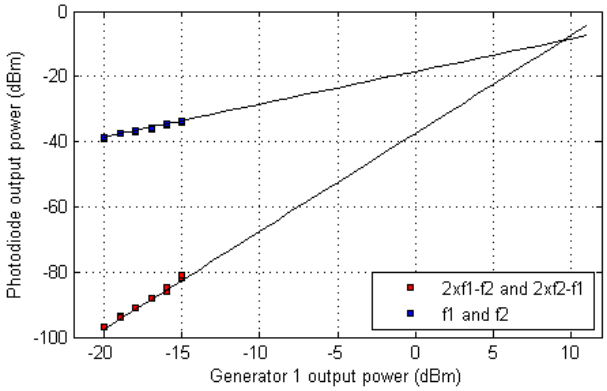

Figure 3.38: RF power at the output of the photodiode measured at $2f_1 - f_2$, f_1, f_2 and $2f_2 - f_1$ as a function of the control power.

3.5.4 1dB gain compression measurement (P1dB)

The 1dB compression point (P1dB) is the power level for which the gain G decreases by 1dB from its linear value, i.e. for small signals when no saturation occurs. The P1dB can be measured at the input

or at the output of RF and optoelectronic components:

$$output\ P1dB_{dBm} = input\ P1dB_{dBm} + G_{dB} - 1 \tag{3.36}$$

Globally, it has been preferred to not measure the P1dB in order to avoid the degradation of the components. Nevertheless, some values can be given, for instance the P1dB of the RoF link composed of the Finisar VCSEL at 850nm, biased at 6.5mA, and directly connected, without optical loss, to the Finisar GaAs PIN photodiode. In fact, in the IP3 curves of figure 3.31, the compression of the transmitted signal is clearly visible: the input P1dB equals to -15dBm. It has to be noted that this behavior disappears when the optical losses increase because the photodetector saturates before the laser, particularly the built-in TIA. Using the same method, an input P1dB around 5dBm has been measured for a RoF link composed of the VI-Systems VCSEL biased at 6mA, 5dB optical losses, and the VI-Systems PIN photodiode.

Other P1dB values have been observed when the S-parameters have been measured: the input P1dB is between 0 and 10 dBm for a RoF link composed of the VI-Systems VCSEL biased at 6mA, 5dB optical losses, and the New Focus photodiode, and between 5 and 10 dBm for a RoF link composed of the Finisar FP laser at 1310nm biased at 40mA, 1.5dB optical losses, and the Finisar photodiode.

The Finisar VCSEL at 850nm is not a very efficient solution with a low input P1dB, however its good S21 response compensates this in great part. Indeed, the E/O and O/E conversion efficiencies, as the noise levels (RIN, thermal noise, ...) count just as much.

3.5.5 Clipping

For high input levels, the RF and optoelectronic components saturate and their gain decreases: this is the compression. But generally, before that compression happens, clipping occurs, for instance when, in a optoelectronic system, the signal current that directly modulates the laser falls below the laser threshold current. An example is depicted in figure 3.39.

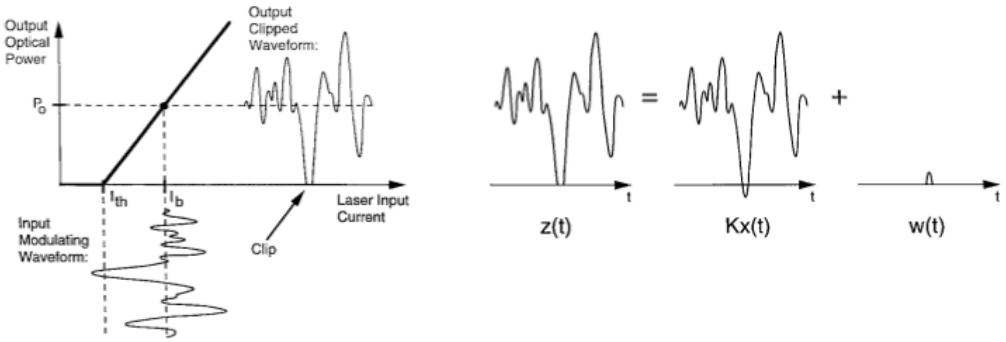

Figure 3.39: A laser clipping on the left and the clipped signal as the sum of two signals on the right, from [26].

This clipping induces signal distortions represented by an additive noise source consisting of a train of impulse functions. In a time-based model, the clipped signal can be written as the sum of two signals [128] [26] [129]:

$$z(t) = k \times x(t) + w(t) \tag{3.37}$$

where,

- k is an attenuation factor (the laser response).
- $x(t)$ is the modulating signal.
- $w(t)$ is an additive noise waveform representing the clipping events.

From now, it is considered that $x(t)$ is an OFDM signal. Therefore, according to the central limit theorem (appendix A.2 and chapter 4), $x(t)$ corresponds to a Gaussian random process with a flat power spectrum over the band of frequencies $[f_a, f_b]$, and according to [129], $w(t)$ has three main properties

based on asymptotic statistical properties originally due to Rice [130]. Firstly, $w(t)$ can be approximated by a Poisson pulse sequence occurring at an average rate of:

$$\lambda = \sqrt{\frac{f_b^3 - f_a^3}{3(f_b - f_a)}}\ e^{-1/(2\mu^2)}, \text{ with } \mu = \frac{x_{bias} - x_{th}}{variance(x(t))}. \tag{3.38}$$

Secondly, the probability density of the duration for each clipping event, i.e. the time interval between a down crossing and subsequent up crossing of the laser threshold current, follows a Rayleigh distribution. Thirdly, the shape of each pulse can be approximated by a second order polynomial (parabolic).

To summarize, when clipping occurs, the performances of the OFDM signals are degraded, but not significantly as this kind of signal is resistant to the impulse noises: narrowband interferences affect only a small part of the subcarriers and with appropriate coding and interleaving techniques, an impulsive noise does not induce errors in the data stream.

3.6 Time response of the optoelectronic components

This section presents time response measurements for the switching-on and -off of the optoelectronic components. The point-to-multipoint and multipoint-to-multipoint RoF architectures need to have only one laser turned-on at a time to avoid optical beating. Similarly, it is preferable to have only one photodiode turned-on at a time to minimize electromagnetic radiation in the home and avoid multipath. More details on these issues will be given in the chapter 5, but it can already be announced that time responses lower than 1μs are necessary for a good working of some advanced architectures.

A direct optical link is performed between a Finisar VCSEL and a New Focus photodiode interconnected by 4m-length MMF. The laser bias current is modulated at 2MHz (i.e. a time period of 0.5μs) when the photodiode is power supplied continuously. Thus, at the output of the optical link, an oscilloscope can observe the turning-on of the laser through the photodiode since no RF signal is conveyed and no DC block is placed at the output.

As shown in figure 3.40, on the left, a signal generator provides a first signal to supply the laser (in green) and a second one for synchronization (in blue). On the right, the photodetected signals at the output of the optical link are compared with the synchronization signal.

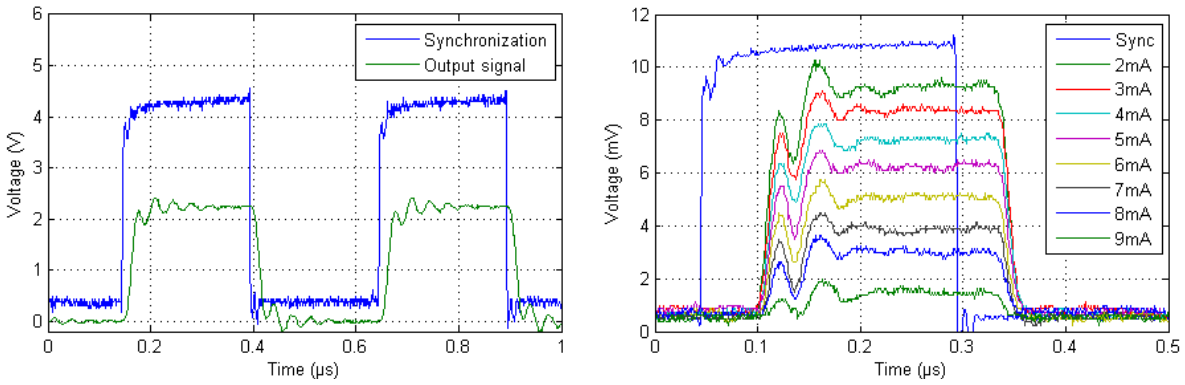

Figure 3.40: The output signal (the one modulating the laser) and the synchronization signal of the signal generator on the left, and the time response of the Finisar laser for different laser bias currents on the right. On the right, the synchronization signal has been adapted to the scale.

A 80ns delay is observed between the rise of the synchronization curve and the first peaks on the photodetected intensity curves. In order to estimate the laser time response it is necessary to subtract the delay between the signal supplying the laser and the synchronization signal (30ns) and the delay corresponding to the propagation time into the 4m-length MMF (20ns, $t = d/v = 4\ m\ /\ 2\ 10^8\ m.s^{-1}$). Consequently, the time response of the laser ignition is ~30ns. Lastly, it has to be noted that the laser bias current has no visible impact on the time response.

Then, about 70ns is required after the laser ignition to obtain a stabilized output optical power. The reason for this instability is probably not intrinsic to the laser, it is the result of the ripple observed on the signal supplying the laser as shown on the left in figure 3.40.

After that, the same procedure has been applied to measure the time response to turn-off the laser, a time equal to ∼10ns.

Similar measurements have also been realized to determine the time response of the Finisar photodiode with the built-in TIA using an optical link with a laser continuously supplied, and a photodiode bias voltage and a TIA power supply both modulated. The TIA needs to be turned-off as the extinction of the photodiode bias voltage is not enough to completely cut-off the signal transmission. However, this induces too important time response for our application, 20μs for the switching-on and 35μs for the switching-off. Finally, a switch placed on the RF line at the output of the photodiode will be preferred at the reception side, see section 5.2.3.

Tests have also been conducted to know the VI-Systems time response: 15μs has been measured for the laser ignition and 20μs for the laser extinction.

3.7 Characterization of the domestic cable: the optical fiber

3.7.1 Multimode fiber bandwidth

The MMF performances are not only determined by the characteristics of the fiber itself, but also by the interplay between the laser and the fiber, and even the photodetector. In fact, the fiber bandwidth will depend on the launching condition as the modal dispersion differs with the set of modes excited and propagated in the MMF. For example, different characteristics are obtained with an Over Filled Launch (OFL), injection with the fiber core fully lighted and all the fiber transverse modes excited, or a Restricted Mode Launch (RML), injection with only one fiber path lighted and an individual mode privileged. As a consequence, the results give in this part are only available with the components used, i.e. the VCSEL at 850nm and the GaAs PIN photodiode from Finisar. For such a laser biased at 7mA, in the middle of its L-I curve, the emission is considered as OFL (in principle, OFL corresponds to a LED emission).

The setup of figure 3.41 is realized in order to measure the S21 parameter of different MMFs. This parameter is calculated, with logarithmic units, as the difference between the S21 of an optical link composed of a 50cm-length MMF (reference) and the S21 of the tested fiber. Thus, only the optical fiber response is retained. It has to be noted that this measurement is electric, with optical losses counting double. Additionally, the system bandwidth is limited to 10GHz as Finisar components have been used (see section 3.3.2). Lastly, the laser input power is fixed to -15dBm to not saturate the photodetector.

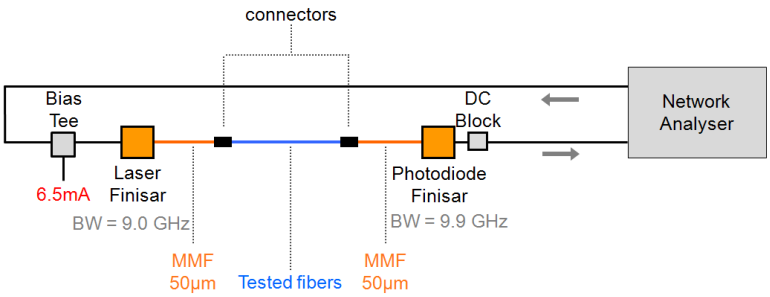

Figure 3.41: The experimental setup used to measure the S21 parameter of different MMFs.

The tested multimode fibers are:

- an OM2 MMF from Draka.
- a bend-insensitive OM3 MMF from Corning, called ClearCurve [58].
- a bend-insensitive OM3 MMF from Draka, called MaxCap [59].

The measured S21 parameters are represented in figures 3.42 and 3.43. The fiber bandwidths are not compatible with RoF transmissions at 5GHz for distances higher than 100m, but this is largely sufficient for a typical HAN. Besides, the OM3 MMF will be preferred.

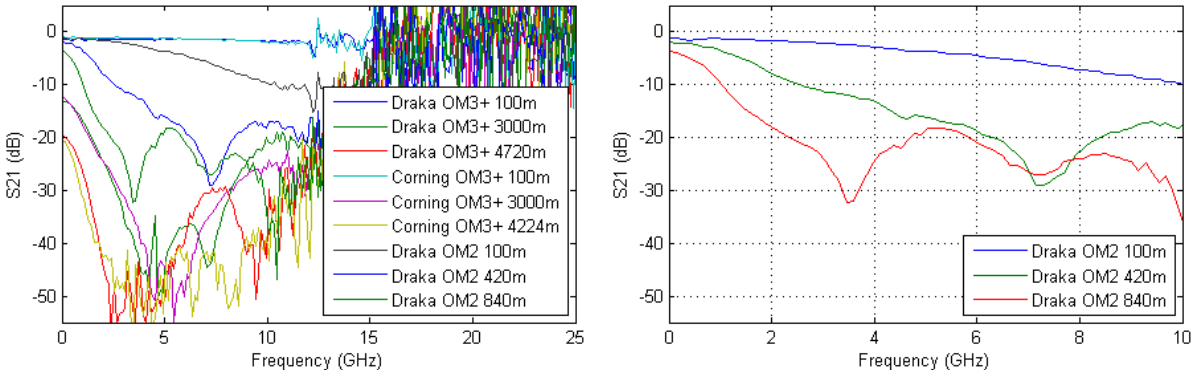

Figure 3.42: S21 parameters of different MMFs on the left, and zoom on the OM2 MMF from Draka on the right.

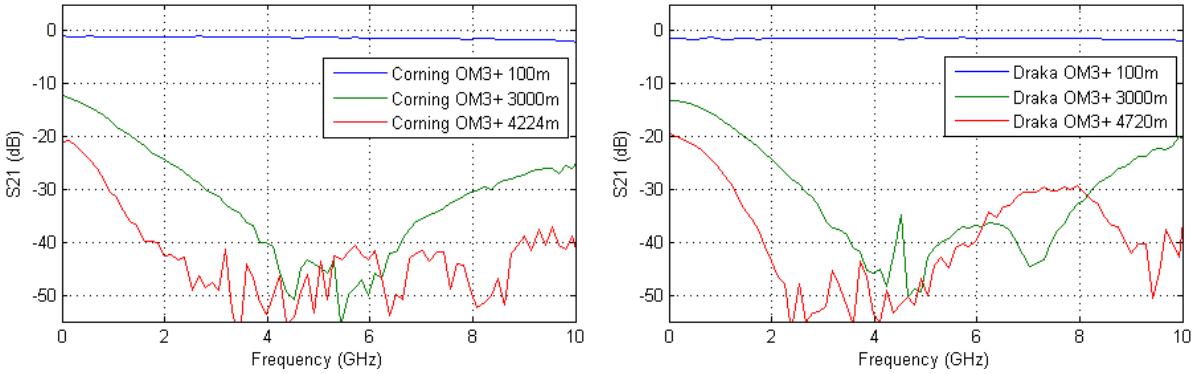

Figure 3.43: Zoom on the S21 parameters of the OM3+ MMFs from Corning on the left and from Draka on the right.

The S21 parameters decrease when the fiber length increases, and strong power degradations appear at certain frequencies. The frequencies of these penalties, which depend on the fiber length, are reported in table 3.8. They are due to the modal dispersion, the chromatic dispersion (a 50μm MMF typically exhibits a chromatic dispersion of ∼-100ps/nm/km at 850nm), but also to the chirp since the laser is directly modulated. In fact, when the laser intensity is modulated, the laser wavelength and the set of injected modes are also modulated.

Table 3.8: Frequencies corresponding to the maximum power degradations versus the fiber length.

fiber ▼ | *length* ▶	420m	840m	3000m	4224m	4720m
Draka OM2	7.2GHz	3.6 & 7.2GHz			
Draka OM3+			5.3GHz		3.4GHz
Corning OM3 +			4.9GHz	3.6 & 9.4GHz	

In literature, the OFL modal bandwidth is generally used to characterize the modal bandwidth of a MMF under a LED excitation whereas the Effective Modal Bandwidth (EMB) is used to characterize the modal bandwidth under a VCSEL excitation. Draka (which has been contacted) announces for 750m-length of its OM3+ fiber an OFL modal bandwidth equal to 8GHz and an EMBc (“c” stands for computed) equal to 6GHz. This last value corresponds to 4.5GHz.km, i.e. a very good fiber close to OM4 performances as shown in table 1.4. Nevertheless, this value is more optimistic than the bandwidth predicted in figure 3.43, ∼2.2GHz.km, because the EMBc is theoretical and it does not take into account the chromatic dispersion, and the Finisar VCSEL is highly polychromatic.

For information, the EMBc method combines the properties of the fiber, based on standardized Differential Mode Delay (DMD) measurements, and the properties of different light sources, based on more than 10 000 standards-compliant VCSELs (TIA-455-220A, Annex D). In fact, different EMB are calculated for a series of fiber/laser combinations, then only the minimum result is selected to guarantee a fiber performance for any VCSEL. For this reason, this method considering only the worst case is also called minimum EMBc.

The standardized DMD curves for the Draka MMF are represented in figure 3.44 for the two 750m-length fiber extremities with a singlemode pulse of ∼90ps Full Width at Quarter Maximum (FWQM).

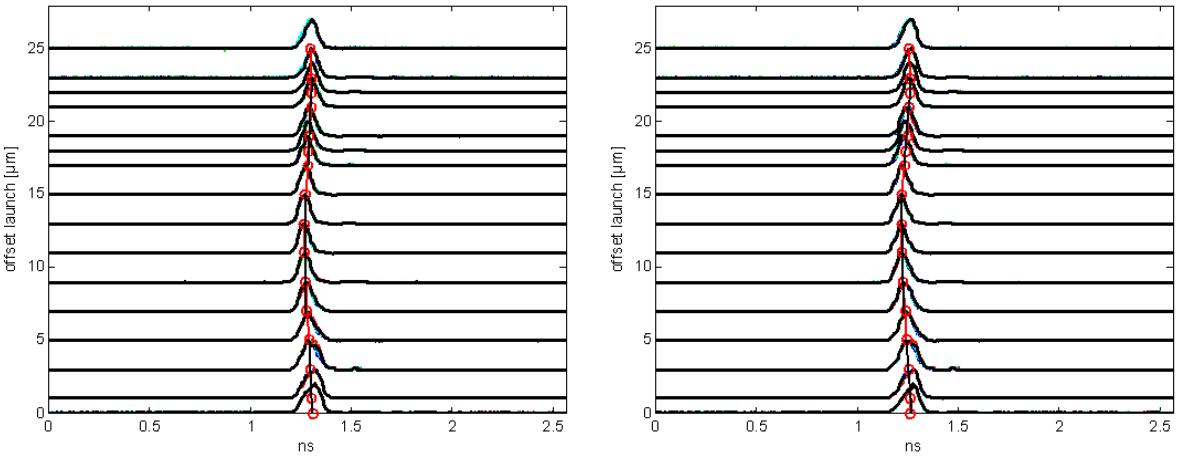

Figure 3.44: Measured DMD traces at 850nm.

The DMD is a fiber measurement (FOTP-220) consisting in measuring both modal time delay and mode coupling as a function of the radial position: a singlemode pulse (∼5μm spot size) scans the core of a 50/125μm MMF with increments of at most 2μm. Indeed, using Restricted Mode Launch (RML) condition it is possible to scan the core of a MMF and map the behavior of each transverse mode which has its own velocity.

3.7.2 Transmitting at 850nm wavelength over singlemode fibers

Currently, MMFs are largely used for LAN and short-distance applications, but the use of SMF for the home infrastructure would be preferred at long term. Indeed, SMF provides higher capacity and multiformat capabilities [131] thanks to CWDM components available on the market for the C window. A last argument for SMF is also the interest of a unique fiber for all the layers of the telecommunication networks, from the core to the home network. Conversely, VCSELs at 850nm are an attractive solution as they are inexpensive high-speed devices. Therefore, transmitting at 850nm wavelength over SMF presents the best of the two worlds: a low cost system adapted to the HAN and a way forward for the future.

As a result, in this part, the following SMFs have been tested with the Finisar components working at 850nm.

- a conventional G652 SMF (C-SMF).
- a ClearCurve from Corning.
- a BendBright-XS (BBXS) from Draka.
- a Finelight from Prysmian.

In a first time, the optical powers emitted by the laser and transmitted through different fibers are measured in order to determine the insertion losses due to the coupling between MMF and SMF. Table 3.9 resumes the obtained results.

Table 3.9: Optical insertion losses.

P_{in} (dBm)	Configuration			P_{out} (dBm)	IL (dB)
-2.91	2m-length MMF	-	-	-2.91	-
-2.91	2m-length MMF	0.75m-length SMF	2m-length MMF	-15.15	12.24
-2.91	2m-length MMF	0.75m-length SMF	-	-14.40	11.49
-2.91	2m-length MMF	1m-length SMF	2m-length MMF	-15.07	12.16
-2.91	2m-length MMF	1m-length SMF	-	-14.90	11.99
-2.91	2m-length MMF	215m-length SMF	2m-length MMF	-16.45	13.54
-2.91	2m-length MMF	1505m-length BBXS	2m-length MMF	-19.50	16.59
-2.91	2m-length MMF	4297m-length Finelight	2m-length MMF	-23.70	20.79

About 12dB optical losses have been measured when the signal from a MMF is injected into a SMF: during the MMF/SMF coupling some transverse modes have been lost as they cannot propagate in a SMF. As a consequence, with at least 24dB electrical losses, a RoF transmission is not conceivable on SMF, especially for multipoint-to-multipoint architectures.

Normally, in a SMF, only the LP_{01} fundamental mode exists. But, the 850nm wavelength emitted by the Finisar VCSEL is under the cut-off wavelength of a SMF, typically 1.2μm [132]. As a consequence, several modes propagate in the SMF, and so modal dispersion occurs. For example, according to [133], at 850nm the use of 1300nm-optimized 9/125μm SMF allows the propagation of two modes.

The S21 parameters of these different fibers are represented in figure 3.45. With a flat response up to 10GHz, the FineLight fiber from Prysmian should be eventually preferred for home applications.

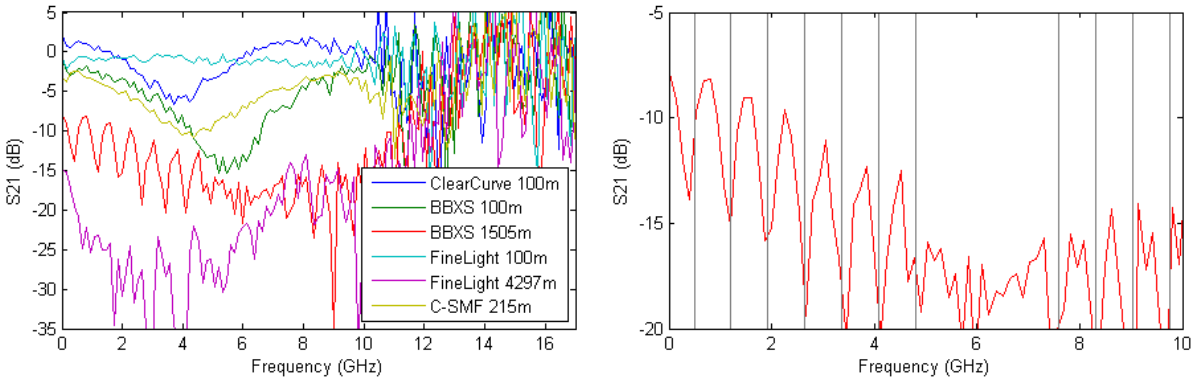

Figure 3.45: S21 parameters of different SMFs on the left, and a focus on the 1505m-length BendBright-XS fiber from Draka on the right.

Figure 3.45 shows, as previously, some degradations in the S21 parameters at certain frequencies. The frequencies corresponding to the maximum power degradations are 5.4GHz for the 100m-length BBXS, 4.4GHz for the 215m-length C-SMF and 4.0GHz for the 100m-length ClearCurve. Concerning the 1505m-length BBXS fiber, the frequencies are globally regularly located at $0.72\ k - 0.23$, k being an integer: 0.47GHz, 1.20GHz, 2.00GHz, 2.66GHz, 3.45GHz, 4.11GHz,... The same kind of curves can be found in [133].

3.7.3 Measurement on the couplers

The key element for a smooth functioning of an optical multipoint-to-multipoint architecture is the behavior of the optical splitter, that depends on the optical sources used and their transverse multimode character. Therefore, tests have been conducted using different lasers: the Finisar VCSEL at 850nm, the VI-Systems VCSEL at 850nm and the Finisar FP laser at 1310nm. In this part, 4x4 and 8x8 optical splitters are tested, with expected insertion losses of 6 and 9 dB, respectively.

$$Insertion\ losses = 10 \cdot log(splitter\ size), \tag{3.39}$$

where the splitter size is the number of optical branches at the input (or at the output) of the splitter.

Measurement on the couplers with the Finisar VCSEL at 850nm

The first tested splitter is a 4x4, designed for transmission at 850 and 1310 nm over MMF, with a 50μm core diameter, and a 125μm cladding diameter. The insertion losses of each port of this optical splitter excited by a Finisar VCSEL at 850nm are reported in table 3.10. As the VCSEL is biased at 6.5mA and so presents a strong transverse multimode character, the splitter is well balanced with optical losses varying from 5.84 to 6.77 dB. With a 6.33dB average value, the theory is confirmed.

Table 3.10: Insertion losses (dB) of a 4x4 splitter based on 50μm MMF and excited by a Finisar VCSEL at 850nm.

out ▼ | in ▶	1	2	3	4
1	5.98	6.47	5.91	6.68
2	5.84	6.35	6.38	6.57
3	6.49	6.20	6.36	6.77
4	6.74	6.02	6.14	6.40

Average: 6.33dB / min: 5.84dB / max: 6.77dB

Two other 4x4 multimode splitters have been tested, one based on a 62.5μm core diameter, and another based on a 105μm core diameter (table 3.11). These splitters are well balanced, nevertheless the theory did not predict the average insertion losses of the splitter based on 105μm MMF: 14.16dB have been measured for 6dB expected. This is probably due to the use of 62.5μm patch cords to interconnect the laser to the splitter and the splitter to the optical power meter. In fact, additional losses appear when the optical beam passes from a large core diameter to a smaller.

Table 3.11: Insertion losses (dB) of a 4x4 splitter based on 62.5μm (on the left) and 105μm (on the right) MMF and excited by a Finisar VCSEL at 850nm.

out ▼ | in ▶	1	2	3	4
1	4.63	6.71	5.71	7.50
2	5.73	7.29	5.10	5.23
3	6.24	6.87	5.58	5.18
4	6.44	4.94	6.41	6.16

Average: 5.98dB
min: 4.63dB / max: 7.50dB

out ▼ | in ▶	1	2	3	4
1	13.94	13.90	13.90	14.25
2	14.35	14.06	13.77	13.99
3	14.15	14.73	14.12	13.95
4	14.18	14.58	14.43	14.27

Average: 14.16dB
min: 13.77dB / max: 14.73dB

Lastly, tests have been realized over a 8x8 optical splitter designed for transmission at 1310 and 1550 nm over SMF. The insertion losses of this optical splitter are reported in table 3.12: the splitter is here unbalanced due to the 850nm wavelength.

Table 3.12: Insertion losses (dB) of a 8x8 splitter based on SMF and excited by a Finisar VCSEL at 850nm.

out ▼ | in ▶	1	2	3	4	5	6	7	8
1	30.07	41.25	30.94	25.42	33.82	19.87	15.40	6.29
2	16.98	26.55	19.80	12.22	45.85	35.24	30.20	20.13
3	16.17	26.03	39.95	28.72	20.37	7.71	29.08	20.30
4	5.51	15.49	28.78	18.13	29.79	18.21	40.05	30.97
5	27.75	17.79	7.80	18.20	31.11	39.85	16.46	26.86
6	37.98	27.96	18.26	28.73	24.05	32.11	5.88	16.27
7	26.41	16.27	30.13	40.85	8.20	18.01	18.66	28.91
8	15.33	5.41	20.65	30.77	20.38	30.05	28.84	38.95

Average: 24.07dB / min: 5.41dB / max: 45.85dB

Measurement on the couplers with the other VCSELs at 850nm

The 4x4 optical splitter based on 50μm MMF, the same as previously, has also been characterized using the VI-Systems and the U-L-M Photonics VCSELs at 850nm. Both lasers are biased at 6mA, thereby,

thanks to the large number of transverse modes emitted, the splitter is well balanced. In fact, similar results as the ones found with a Finisar VCSEL at 850nm have been obtained.

Table 3.13: Insertion losses (dB) of a 4x4 splitter based on 50μm MMF and excited by a VI-Systems laser (on the left) or by a U-L-M Photonics laser (on the right).

out ▼ | in ▶	1	2	3	4
1	6.91	7.47	6.27	6.66
2	6.34	6.79	7.05	7.40
3	7.01	6.84	6.95	7.05
4	7.49	6.86	6.80	6.67

Average: 6.91dB
min: 6.27dB / max: 7.49dB

out ▼ | in ▶	1	2	3	4
1	6.71	5.46	6.75	6.39
2	7.41	6.22	6.04	5.65
3	5.37	6.06	6.91	6.85
4	7.18	7.07	5.42	5.91

Average: 6.34dB
min: 5.37dB / max: 7.41dB

Measurement on the couplers with the Finisar FP laser at 1310nm

Concerning the Finisar FP laser at 1310nm, biased at 50mA, it has been tested with a 8x8 optical splitter designed for transmission at 850 and 1310 nm over 50μm core diameter MMF. This FP laser, according to its datasheet, is designed to meet the MMF launch conditions, nevertheless its transverse multimode character seems poor since the splitter is not well balanced as shown in table 3.14.

Table 3.14: Insertion losses (dB) of a 8x8 splitter based on 50μm MMF and excited by a Finisar FP at 1310nm.

out ▼ | in ▶	1	2	3	4	5	6	7	8
1	14.98	10.88	9.04	8.13	7.96	12.15	13.56	13.16
2	16.12	12.01	9.33	4.70	6.00	12.72	13.63	12.56
3	3.46	14.17	11.83	9.27	10.15	13.55	7.69	13.20
4	9.14	13.77	11.55	11.39	9.91	14.77	3.07	14.16
5	12.06	13.26	4.22	9.55	8.88	7.42	16.26	8.10
6	8.29	14.19	8.59	10.01	11.04	9.68	13.98	4.10
7	14.53	3.90	13.77	14.66	12.61	6.80	11.81	8.37
8	13.10	5.72	11.86	13.01	13.06	5.36	14.58	9.53

Average: 10.63dB / min: 3.07dB / max: 16.26dB

3.8 Characterization of the domestic cable: the copper pair

3.8.1 Bandwidth and Attenuation to Crosstalk Ratio measurements

The domestic cable will be a hybrid cable (as shown in chapter 5, section 5.2.2) consisting in two optical fibers for the RoF transmission, downlink and uplink, plus one quad copper cable for remote powering. Remote powering makes the RoF implementation easier since the transducers can be installed far from electrical wall plugs, typically high on the walls for a better radio coverage. Moreover, the RoF transducers cannot have an electrical transformer supplied with high voltages of one hundred of volts as compact products consuming low power with a low operating temperature are required. Smaller and more efficient transformers supplied in 48V are therefore preferred.

The copper cable has also to be able to convey RF tones at 10MHz in order to implement an optical access management (see chapter 5), or to convey 100Base-TX Ethernet if the user wants a wired connectivity quickly deployable. In fact, some users can prefer in a first time a wired solution, then switching later towards RoF solutions.

In this part, a copper link (5/10mm diameter) is so characterized in terms of S-parameters. Three parameters have been measured from 10MHz (limitation due to the network analyzer) to 500MHz: the attenuation, the Near End Crosstalk (NEXT) and the Far End Crosstalk (FEXT). At the far end of the cable, near the receiver, the transmitted signal is weak as the attenuation has reduced its level, so the crosstalk has a significant effect. Indeed, at the near end of the cable, near the emitter, the transmitted signal is strong and largely interferes signals received on other pairs (full-duplex transmission). Consequently, to carry a digital signal, the -3dB bandwidth is generally not measured, only the Attenuation to

Crosstalk Ratio (ACR) matters. This is similar to the SNR in the analog domain and it is used when a digital signal is conveyed in full-duplex on twisted pairs.

$$ACR = Attenuation - NEXT. \tag{3.40}$$

To measure these S-parameters, a 50m-length quad copper cable has been connected to baluns, with a 300MHz bandwidth and a 50:100 impedance ratio (Ω), to transform the RF unbalanced signal from the network analyzer into a balanced signal, and vice-versa. It has to be noted that if a pair is untwisted over more than ∼15mm, the crosstalk measurements will be incorrect as spurious peaks can appear on the NEXT, for example. Moreover, the use of RJ45 connectors has to be avoided to only measure the crosstalk of the cable. Consequently, all the wire has been soldered.

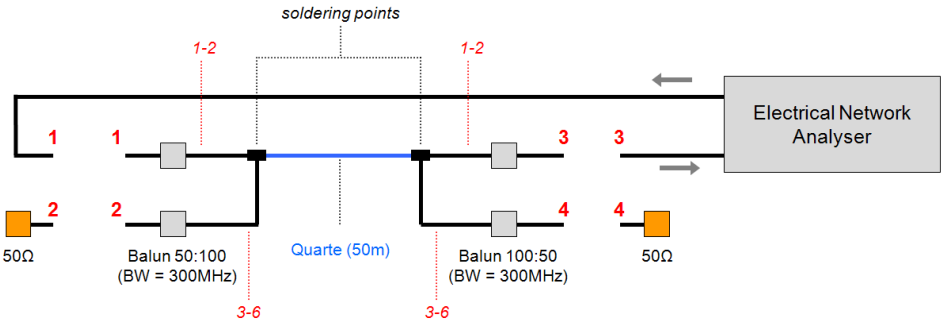

Figure 3.46: The experimental setup used to characterize the S-parameters of the quad copper cable.

Table 3.15: Connection to use in figure 3.46.

S paremeter	Connection
Attenuation	11 / 22 & 33 / 44
NEXT	11 / 23 & 32 / 44
FEXT	11 / 22 & 34 / 43

The three measured S-parameters are represented in figure 3.47. The -3dB bandwidth of the quad copper is, by extrapolating the curve between DC and 10MHz (where the attenuation equals to -4.7dB), close to 16MHz.

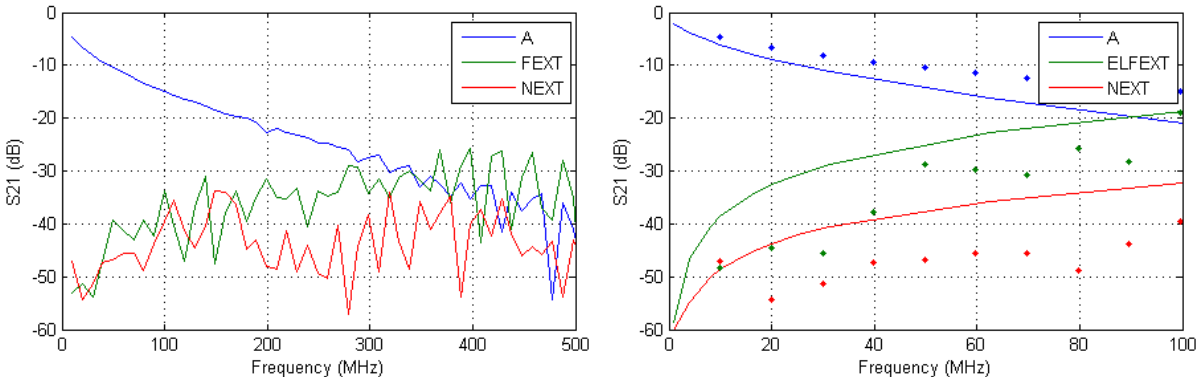

Figure 3.47: Measured S-parameters on the left and comparison between the measurements (dots) and the requirements for a category 5e cable (curves) on the right.

Concerning the ACR, it has to be greater than 12dB at 100MHz to carry a Fast Ethernet signal (Corel 120), which is verified as shown in figure 3.47. Other requirement can be found in the literature depending on the category of the cable. For example, the category 5, which allows speeds up to 100Mbit/s and so the use of 100BASE-TX, is described in the ANSI/TIA/EIA-568 standard[9]. The required Attenuation,

[9]ANSI = American National Standards Institute. TIA = Telecommunications Industry Association. EIA = Electronic Industries Alliance.

NEXT and Equal Level FEXT (ELFEXT is the crosstalk when the attenuation is subtracted from the FEXT) are provided in table 3.16 for a permanent link[10].

Table 3.16: Requirements for a category 5e cable and a permanent link configuration, from [40].

Frequency	Attenuation	ELFEXT	NEXT
1.0	2.1	58.6	60
4.0	3.9	46.6	54.8
8.0	5.5	40.6	50.0
10.0	6.2	38.6	48.5
16.0	7.9	34.5	45.2
20.0	8.9	32.6	43.7
25.0	10	30.7	42.1
31.25	11.2	28.7	40.5
62.5	16.2	22.7	35.7
100.0	21	18.6	32.3

3.9 Summary and discussion

This chapter was devoted to the characterizations of different optoelectronic components that will be used in RoF systems, principally VCSELs for their good compromise between efficiency and cost, and PIN photodiode for their simplicity and reliability. First, static (laser L-I curve, laser optical spectrum, photodiode I-V curve) and dynamic (S-parameters) characterizations have been performed.

The knowledge of the link gain is a fundamental point to optimize a radio transmission and choose the most adapted amplification level at the output of a RoF link. This gain should be preferably measured since the analytical calculation does not provide accurate results and does not provide bandwidth information. Among all the tested components, the Finisar components working at 850nm provide a high link gain and a flat response: they seem good choices for low cost and high performance RoF links.

The noises inherent to the RoF links have also been measured, for small (RIN, thermal noise and shot noise) and large (third-order intermodulation) signals. To determine the RIN, two different methods have been evaluated: one based on the fact that among all the noise contributions, only the RIN decreases with a slope proportional to the square of the optical losses, and another based on the subtraction of two noise measures, a first measure with the laser under test turned-on and a second one with this laser turned-off. These two methods have conducted to same results, which proves their accuracy. Even the comparison of these methods with a commercial test bed has validated these measures. Lastly, a third method has been presented, but not tested: this can be the topic of a future work.

Different experimental methods have also been tested to determine the IP3 parameter of differents optoelectronic components (laser and photodiode). For first method, the third order non-linearities of each RoF link have been measured, then the IP3 of the lasers has been decorrelated to the IP3 of the photodiodes using an analytical approach. Another method has consisted in plotting the IP3 parameter of the RoF links as a function of the optical losses: when the result is independent of the losses, the measured IP3 correspond to non-linearities of the laser. The IP3 parameter of the photodiodes is then measured injecting the two fundamental RF tones on two different lasers (thus, no IM3 coming from lasers), then combining them in the optical domain using an optical splitter. Again, similar results have been obtained with these different methods, which proves their accuracy. Finally, it has to be underlined that the RoF link at 1310nm (FP laser and PIN photodiode with a built-in TIA) has given interesting results in terms of linearity, especially in point-to-point configuration (zero optical loss).

In this chapter, the HAN cable has also been characterized. In fact, the structured cabling buried in the walls will be installed for at least 15 to 20 years. It must meet the HAN technical and economic requirements: efficiency with a simple, rapid and aesthetic installation. The chosen solution is a hybrid

[10]The permanent link consists in a permanently installed cabling, up to 90m, with one connection at each end. The permanent link excludes both the cable portion of the field test instrument cord and the connection to the field test instrument [134] [40]

cable consisting in two optical fibers for the RoF transmission (downlink and uplink) and one quad copper cable for remote powering. With regard to the measured fibers responses, a low bend sensitivity multimode fiber (OM3+ MMF) will be preferred, with transmission distances up to 100m, largely sufficient fiber-lengths for typical HANs. Besides, the copper cable presents good performances in terms of frequency response and crosstalk, and among other things it is able to convey a 100Mbit/s Ethernet signal.

Chapter 4

Experimental studies of the RoF millimeter-wave wireless architectures

4.1 Analysis of a laboratory generated OFDM signal

4.1.1 BER, SNR and EVM: definition and theoretical aspects

The Bit Error Rate, the Signal to Noise Ratio and the Error Vector Magnitude are three figures of merit to measure and quantify the performances of a transmission system. Moreover, their analysis can be helpful to understand the distortions on the signal.

The Bit Error Rate (BER) is the number of incorrect received bits over the total number of transmitted bits. If the BER is a precise figure of merit and offers a simple way to compare communication systems between them, it is not always simple to measure it as it requires to know simultaneously the received and the emitted bits. Also, BER is not adequate to understand the origins of the distortions on the received signal.

$$BER = \frac{erroneous\ bits}{total\ number\ of\ transmitted\ bits} \tag{4.1}$$

The Signal to Noise Ratio (SNR) defines the signal quality as the ratio of the received signal power to the received noise power. As it can be simply measured with an Electrical Spectrum Analyzer (ESA), the SNR is a popular parameter used to adjust a setup and optimize its performance.

$$SNR_{lin} = \frac{Signal\ power}{Noise\ power} \tag{4.2}$$

The Error Vector Magnitude (EVM) is a figure of merit for digital modulated signals, like Phased-Shift Keying (PSK) or Quadrature Amplitude Modulation (QAM), measuring in the complex plane the error between received symbols and ideal transmitted symbols. By definition, EVM is the ratio of the error vector power to the reference vector power as shown in figure 4.1.

$$EVM_{lin} = \sqrt{\frac{P_{error\ vector}}{P_{reference}}} \tag{4.3}$$

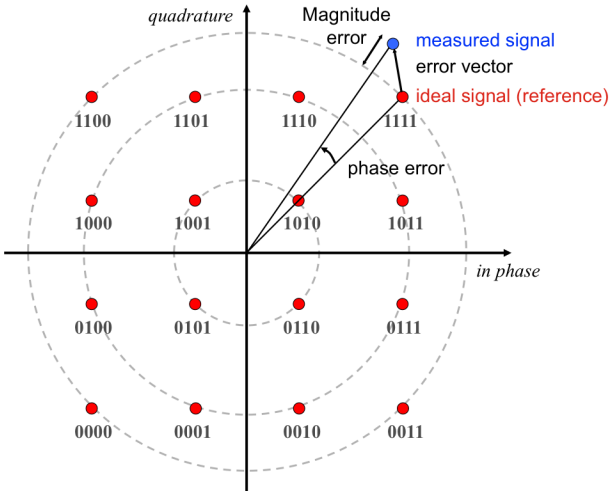

Figure 4.1: Constellation diagram for a 16-QAM modulation and EVM measurement.

EVM measurement requires complex mathematical operations to demodulate the received signal (as BER), but the observation of the constellation diagram is helpful to determine the cause of the distortion over the signal as described in [28].

Previously, the EVM and the SNR have been defined in linear units, but they can also be expressed in logarithmic units (dB) or as a percentage (%):

$$EVM_{dB} = 20 \cdot log(EVM_{lin}) \tag{4.4}$$
$$EVM_{\%} = 100 \cdot EVM_{lin} \tag{4.5}$$
$$SNR_{dB} = 10 \cdot log(SNR_{lin}) \tag{4.6}$$

The relationship among BER, SNR and EVM can be established [135] under the assumption of Additive White Gaussian Noise (AWGN) channel model (appendix A.1) and perfect recovery of the carrier frequency and phase. SNR is related to EVM by:

$$SNR_{lin} = \frac{1}{EVM_{lin}^2}; \tag{4.7}$$

BER is closely related to EVM and can be simply calculated for rectangular constellations in a binary Gray code representation. The bit error probability P_b, i.e. a BER measured on an infinite time interval, is equal to:

$$P_b = \frac{2\,(1-\frac{1}{L})}{log_2(L)}\, Q\left(\sqrt{\frac{3\ log_2(L)}{L^2-1} \times \frac{2}{EVM_{lin}^2 \times log_2(M)}}\right) \tag{4.8}$$

where M is the number of states, or the number of points forming the constellation diagram. It is an integer related to the complex modulation, the power of two of the number of bits per symbol. L is the number of levels in each dimension of the constellation diagram.

examples: $M = 2^1$ and $L = 2$ (BPSK) $M = 2^2$ and $L = 2$ (QPSK) $M = 2^4$ and $L = 4$ (16-QAM).

The function $x \to Q(x)$ is the complementary Gaussian error function defined as the probability that a random variable normally distributed is included in the interval $[x, +\infty[$.

$$Q(x) = \int_x^{\infty} \frac{1}{\sqrt{2\pi}} e^{-y^2/2} dy = \frac{1}{2}\ erfc(x/\sqrt{2}) \tag{4.9}$$

The complementary Gaussian error function is replaced by the error function by substituting the variable t: $t = y/\sqrt{2}$. Therefore, $dt = dy/\sqrt{2}$ and the integral of the *erfc* function varies between $x/\sqrt{2}$ and $+\infty$.

$$erf(x) = \frac{2}{\sqrt{\pi}} \int_0^x e^{-t^2} dt \qquad \text{and} \qquad erfc\,(x) = 1 - erf(x) = \frac{2}{\sqrt{\pi}} \int_x^{\infty} e^{-t^2} dt \tag{4.10}$$

The BER can be expressed in different ways, for example [136] provides a BER expression based on Modulation Error Ratio (MER), [137] provides the reasoning to obtain an equation such as 4.8, and [138] gives the expression of Symbol Error Rate (SER) for different constellation diagrams.

In the following, the EVM will be used as the main figure of merit. It is preferred to BER since it offers shorter computation time, and also preferred to SNR since it provides a better accuracy in the cases of non flat radio spectrum. Finally, it is always possible to link EVM to a SNR or a BER value using a channel model as it has been done above with an AWGN channel. This relationship among EVM, SNR and BER is plotted in figure 4.2 for different modulation schemes:

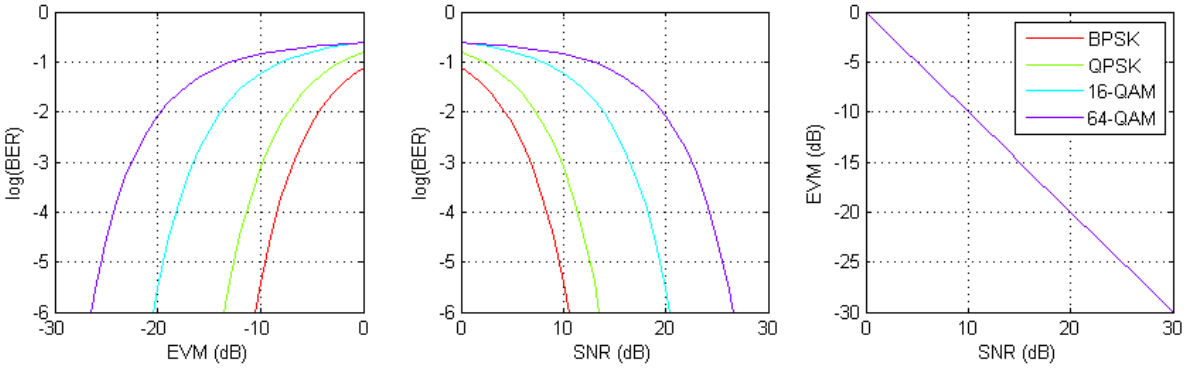

Figure 4.2: Relationship among EVM, SNR and BER for different modulation schemes.

4.1.2 Implementation of a direct electrical link at Intermediate Frequency, and characterization of the generated signal and the AWGN channel

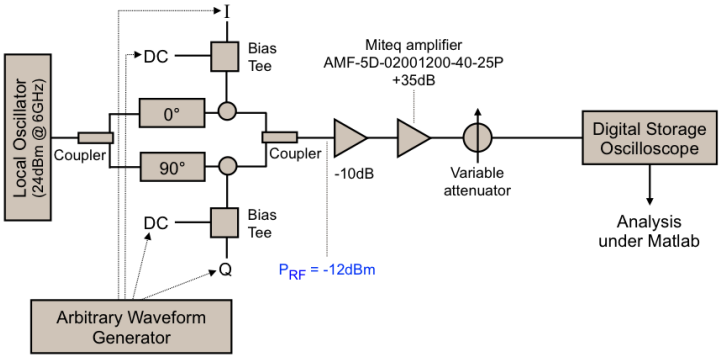

Figure 4.3: Experimental setup testing the OFDM signal in Intermediate Frequency, at 6GHz.

The experimental setup depicted in figure 4.3 has been built to characterize a radio transmission according to IEEE 802.15.3c standard, HSI mode. A pseudorandom OFDM signal, created in baseband under Matlab (see appendix A.7), feeds a dual outputs Arbitrary Waveform Generator (AWG) with 10 bits resolution, 10GSa/s sample rate, and 5GHz bandwidth. The generated In-phase (I) and Quadrature (Q) components are then transposed to Intermediate Frequency (IF), at 6GHz, by mixing them with a RF oscillator splitted in two paths with a 90° phase shift. Finally, these two components are combined by a RF coupler to create the IF-OFDM signal written in equation 4.11.

$$s(t) = I \times cos(2\pi f_0 t) + Q \times sin(2\pi f_0 t), \text{ with } f_0 = 6GHz. \tag{4.11}$$

At the output of the radio emitter, amplifier and attenuator stages control the IF signal power, then a real-time Digital Storage Oscilloscope (DSO), with 13GHz bandwidth and 40GSa/s speed, receives the signal transmitted through the system for analysis under Matlab and calculation of the BER, SNR and EVM.

Two modulation schemes are considered:

– QPSK modulation for a 3.08Gbit/s PHY rate.
– 16-QAM modulation for a 6.16Gbit/s PHY rate.

The PHY rate is the product of the number of bits per symbol, 2 in QPSK and 4 in 16-QAM, by the number of data subcarriers per OFDM symbol, 336 for IEEE 802.15.3c (mode HSI), and by the number of OFDM symbols per second, i.e. the inverse of the OFDM symbol duration, here 218.18ns.

The I and Q baseband signals observable at the analog outputs of the AWG are represented in figure 4.4. These signals have been captured by the digital oscilloscope and plotted under Matlab performing FFTs. The y-axes are consequently in dBr, not in dBm. However, the SNR (or Carrier to Noise Ratio, CNR, to be more accurate) can be estimated: it is equal to approximately 35dB. It has to be noted that the radio spectrum of the I component, on the left, is easily recognizable with its pilot subcarriers and the induced large (but widely acceptable) shoulder.

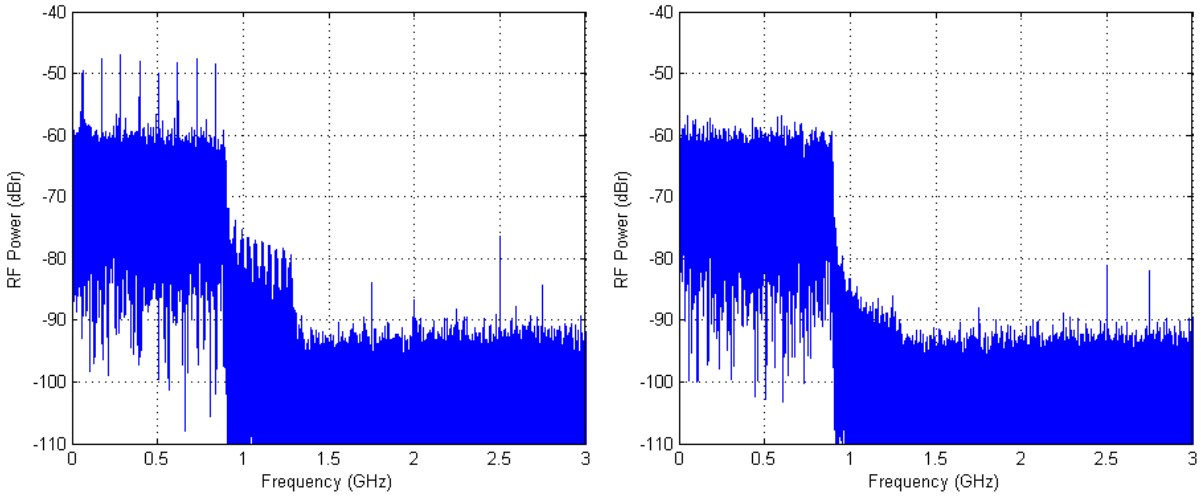

Figure 4.4: Spectrums at the output of the AWG, with the real part of the generated QPSK baseband signal on the left and the imaginary part on the right.

After translation to IF and combination by a RF coupler, the IF-OFDM signal centered at 6GHz with a 1.815GHz bandwidth is obtained. This signal is represented in the time domain in figure 4.5 for a 16-QAM modulation and Zero Pad Suffix (ZPS) as inter-symbol spacing, and in the frequency domain in figure 4.6 for QPSK and 16-QAM modulations. The SNR is about 30dB when the Carrier to Signal Ratio (CSR) varies between 15dB and 25dB. For a direct link the CSR parameter has not a high impact, but in a complex radio system composed of a large number of RF and optoelectronic components, it has to be minimized to avoid possible saturation. Therefore, the LO carrier level is adjusted adding DC components to the baseband signals as shown in figure 4.3. Nevertheless, the carrier has to remain above the other subcarriers to let the demodulation software determine the center frequency.

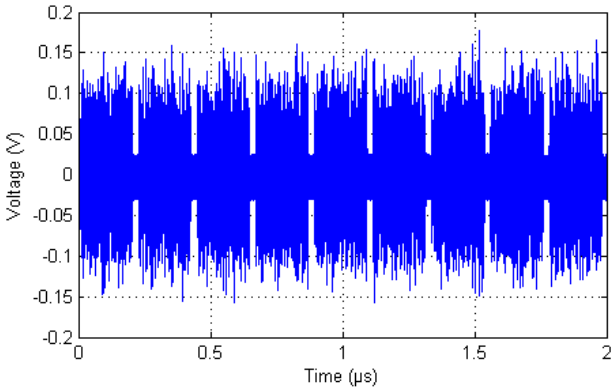

Figure 4.5: Generated OFDM signal in the time domain for a 16-QAM modulation.

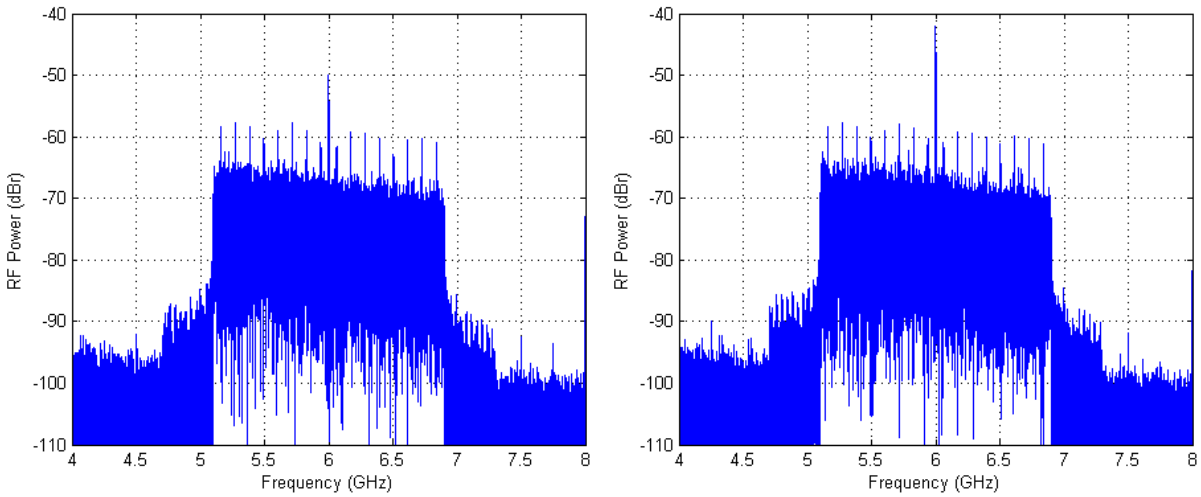

Figure 4.6: Spectrums of IF-OFDM signals: QPSK modulation on the left and 16-QAM modulation on the right.

According to the central limit theorem, any sum of random, independent and normally distributed variables converges, under certain conditions (see appendix A.2), toward a Gaussian random variable [139]. Consequently, the generated OFDM signal, which is simply the inverse DFT (the sum operator) of a PRBS sequence, is normally distributed. Indeed, a PRBS sequence can be considered independent[1] and normally distributed if the number of samples is high.

As shown in figure 4.7, the representation in time domain of OFDM signals follows, as predicted, Gaussian distributions, centered ($\mu = 0$) but not reduced ($\sigma = 1$). These histograms, represented in gray (or gray plus blue), have been plotted using Matlab and its function *hist*. To obtain perfect Gaussian distributions, like the ones in blue, i.e. not bumpy, it has been necessary to remove the guard intervals between the OFDM symbols. After that, each histogram has been approximated by a Gaussian function that has been added in red in figure 4.7, whose equation is:

$$y = k_1 \times \frac{1}{\sigma\sqrt{2\pi}} e^{-\frac{(x-\mu)^2}{2\,\sigma^2}} \tag{4.12}$$

where k_1 is a factor to scale the theoretical function to the experimental points, μ and σ are the average and the standard deviation of the voltage vector, respectively. Below, μ is null and σ has been calculated only from the OFDM symbols and equals to 0.0446 in QPSK and 0.0458 in 16-QAM.

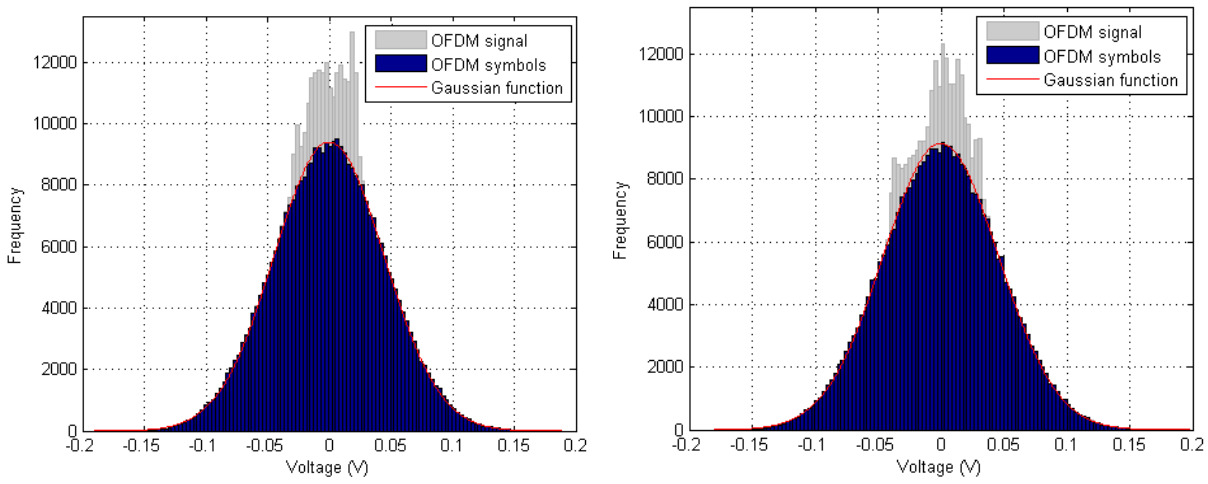

Figure 4.7: Histograms of the generated OFDM signals in time domain: QPSK modulation on the left and 16-QAM modulation on the right.

[1] In statistics, "independent" means that the occurrence of one result (here, having a 0 or a 1) makes it neither more nor less probable that the other occurs.

The Gaussian voltage distribution shows that the generated PRBS is long enough to be considered random. Yet, in the FFT, the pilot subcarriers set to 1 and the null subcarriers set to 0 are also taken into account: in a set of 512 subcarriers, 336 subcarriers are data, 16 are pilots and 160 are nulls. Only the half subcarriers is randomly generated, but it does not invalidate the central limit theorem because by definition the null subcarriers are equal to zero, and the pilot subcarriers are only a small proportion of the subcarriers.

The Gaussian voltage distribution can be seen as the cause of impairments. Indeed, the generated voltage includes important peak values which have to be transmitted without distortion or clipping to ensure a correct demodulation at the reception. Therefore, highly linear RF and optoelectronic components have to be used. The linearity of the components is characterized principally by IP3 and P1dB values, whereas the linearity requirements, dependent on the transmitted radio signal, are characterized by the average power and the Peak to Average Power Ratio (PAPR). With regard to equation 1.4, the PAPR can become very high as the subcarriers combining constructively induce very high voltage values [128].

From the capture of the OFDM signal in figure 4.5, the average power and the PAPR are calculated [140]:

$$Average\ power\ [dBm] = 10 \cdot log\left(\frac{mean(voltage^2)}{input\ impedance}\right) \tag{4.13}$$

$$PAPR\ [dB] = 10 \cdot log\left(\frac{power_{peak}}{power_{RMS}}\right) = 10 \cdot log\left(\frac{max(|voltage|^2)}{mean(voltage^2)}\right) \tag{4.14}$$

where *voltage* is a row vector corresponding to the time waveform captured by the digital oscilloscope.

Table 4.1 gives experimental values. The PAPR remains the same for QPSK and 16-QAM modulation schemes as it only depends on the number of subcarriers. As for the average power obtained from equation 4.13, it is in agreement with the values displayed by a RF power meter, give or take one decibel. This decibel difference can be explained by different time-integrations between the two measurement methods and by different insertion losses between the two instruments.

Table 4.1: Power Measurements.

Modulation scheme	QPSK	16-QAM
EVM (%)	4,87	4,85
IF power calculated under Matlab (dBm)	-14,44	-14,16
IF power measured using a power meter (dBm)	-13,28	-13,02
Peak voltage (mV)	190,1	197,1
Average voltage (mV and RMS)	42,4	43,8
PAPR (linear)	20,07	20,98
PAPR (dB)	13,04	13,06

One of the best way to characterize an OFDM signal consists in studying its constellation and measuring its EVM value. Practically, EVM is measured from the data subcarriers as the Euclidean distance between the received symbols and the closest ideal constellation points. Consequently, the equation provided by the IEEE 802.15.3c standard [27], the one also implemented in the demodulation program, is somehow different from the previous definition (equation 4.3) as it does not necessitate to know the transmitted symbols.

$$EVM_{lin} = \frac{1}{N_p}\left(\sum_{i=1}^{N_p}\sqrt{\frac{1}{P_{avg}\,N_s\,N_{dsc}}\sum_{j=1}^{N_s}\left(\sum_{k=1}^{N_{dsc}}\left((I_{ijk}-I^*_{ijk})^2+(Q_{ijk}-Q^*_{ijk})^2\right)\right)}\right) \tag{4.15}$$

where:

- N_p is the number of captured frames.
- N_s is the number of symbols per frame.
- N_{dsc} is the number of data subcarriers per OFDM symbol.
- P_{avg} is the average power of the constellation.
- (I^*_{ijk}, Q^*_{ijk}) is the complex coordinate of the jth measured symbol in the kth subcarrier of the ith frame.
- (I_{ijk}, Q_{ijk}) is the complex coordinate of the nearest constellation point for the jth measured symbol in the kth subcarrier of the ith frame.

Since in the proposed setup the emitted signal is a pseudo random sequence of OFDM symbols, without frame structure, equation 4.15 is reduced to its root term. From figure 4.8, representing the QPSK and 16-QAM constellation diagrams of the OFDM signals, EVM measurements have been realized: they are equal to 4.87% and 4.85%, respectively. These measures have been performed after phase and amplitude corrections, and using only the data subcarriers represented in blue. The red symbols, at the coordinates (0,0) and (1,0), correspond to the null and pilot subcarriers. As a general rule, the EVM at the output of the IF direct link, in figure 4.3, is always lower than 6% for a power at the input of the digital oscilloscope included between -32 and 12 dBm, i.e. a power range of 40dB. Table 4.2 reports some EVM measurements.

Table 4.2: EVM as a function of the IF power at the input of the oscilloscope.

Oscilloscope input power (dBm)	EVM (%)
9.4	5.5
-11.9	4.6
-14.4	4.9
-32.6	5.9
-54.0	20.0

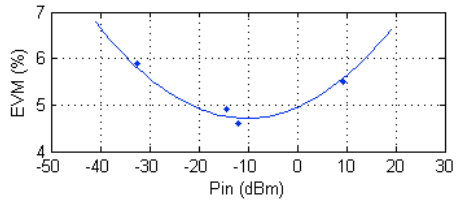

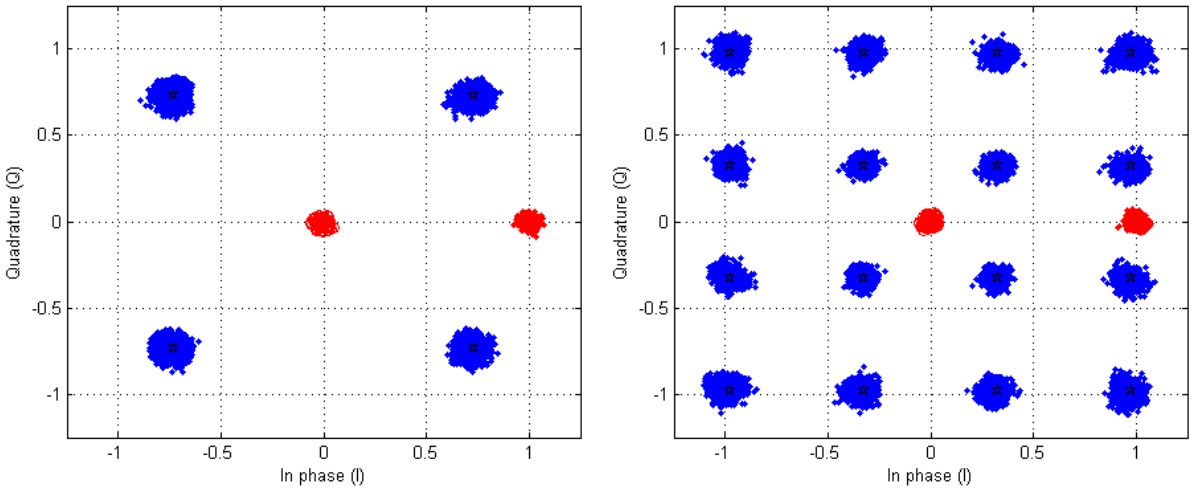

Figure 4.8: Constellation diagrams for the QPSK modulated signal on the left and the 16-QAM modulated signal on the right.

In order to check if the constellation diagrams in figure 4.8 correspond to an AWGN channel, the probability density function and the cumulative distribution function of the distance of the received complex symbols from the nearest constellation points have been plotted. They have to respect the Rayleigh law [140], which is simply the norm of a two-dimensional Gaussian vector with independent coordinates, centered and with the same variance.

The experimental Probability Density Function (PDF) and Cumulative Distribution Function (CDF) are represented in blue in figures 4.9 and 4.10 [2]: after having centered each complex symbol of the constellation diagrams in the origin, the number of experimental points included in a circle of radius R (distance from the origin) is counted. The theoretical functions are added in red.

The Rayleigh probability density function is:

$$y = k_2 \times \frac{x}{\sigma^2}\, e^{-\frac{x^2}{2\sigma^2}} \tag{4.16}$$

k_2 is a factor to scale the theoretical function to the experimental measurements, and σ is the average of the standard deviations of real and imaginary parts of the constellation points.

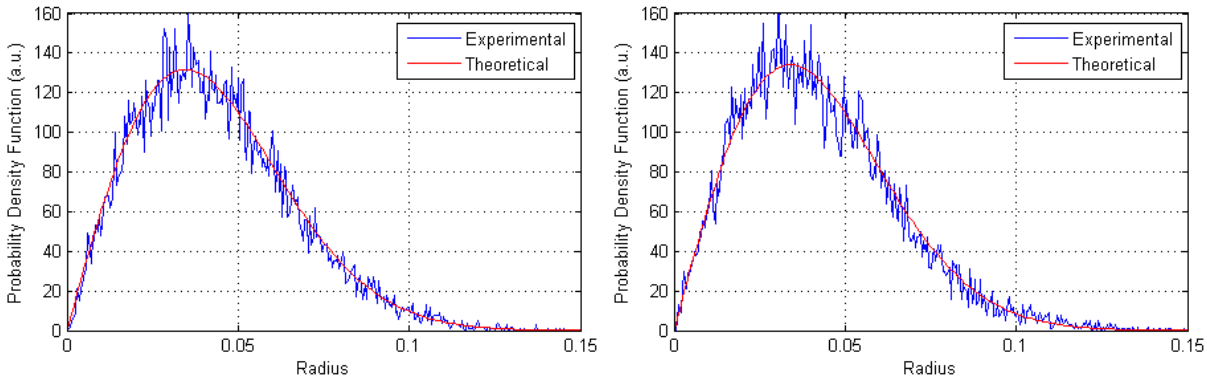

Figure 4.9: Probability density function for the QPSK modulated signal on the left and the 16-QAM modulated signal on the right of the distance of the received complex symbols from the nearest constellation points.

The Rayleigh cumulative distribution function is:

$$y = k_3 \times \left(1 - e^{-\frac{x^2}{2\sigma^2}}\right) \tag{4.17}$$

k_3 is the number of measurement points composing a constellation diagram, i.e. the number of data subcarriers per OFDM symbol multiplied by the number of captured OFDM symbols. In this case, $k = 336 \times 44 = 14784$.

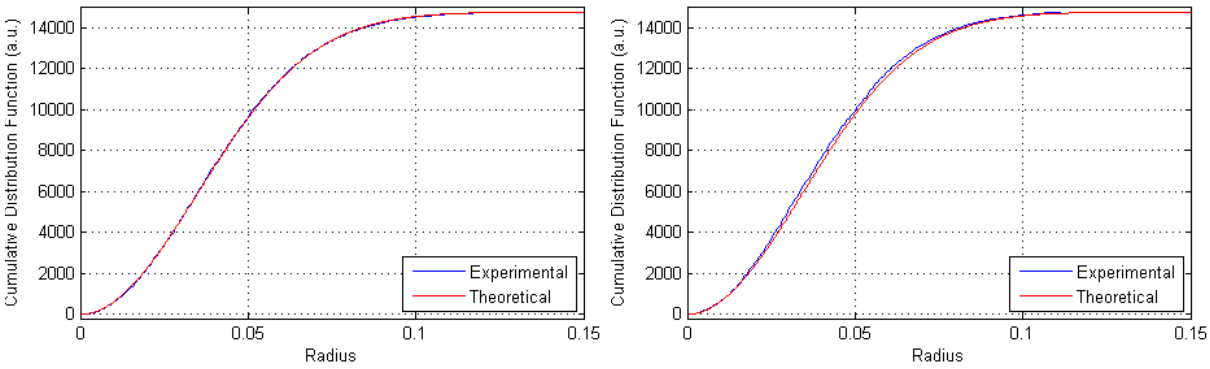

Figure 4.10: Cumulative distribution function for the QPSK modulated signal on the left and the 16-QAM modulated signal on the right of the distance of the received complex symbols from the nearest constellation points.

Finally, the transmission realized in the direct IF link depicted in figure 4.3 can be considered as an AWGN channel since both voltage vector and constellation diagram follow a Gaussian distribution. The following part consists in verifying the relationships among EVM, SNR and BER.

[2] Speaking of PDF and CDF is a little abusive as the curves are not normalized. Indeed, in figures 4.9 and 4.10, the shapes of the curves are correct but the numerical values does not vary between zero and one. The PDF and CDF terms are just use for simplicity, no dedicated word existing. Lastly, it has to be noted that the axis are expressed in arbitrary unit (a.u.).

4.1.3 Experimental validation of the relationships among EVM, SNR and BER

This part aims at verifying the relationship among EVM, SNR and BER. At first, the EVM has been calculated from figure 4.8 using only the data symbols as explained in equation 4.15. After that, the SNR has been determined from figure 4.6. As the radio spectrum is not flat at the reception, two SNRs have been measured, one for the low frequencies and another for the high frequencies, then these values have been averaged. Finally, the BER has been calculated comparing the binary sequence received by the oscilloscope with the one emitted by the AWG. In the constellation diagrams in figure 4.8, each complex symbol is affected to x bits according to a Gray bits allocation, x being equal to 2 in QPSK and 4 in 16-QAM. The Gray code has been chosen to verify equation 4.8 and to respect the IEEE 802.15.3c standard.

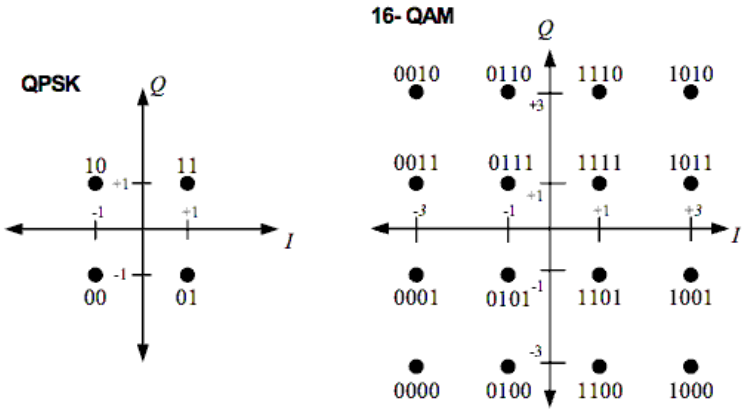

Figure 4.11: Bits allocation of the QPSK and 16-QAM symbols according to the IEEE 802.15.3c standard [27].

The BER calculation is quite complex since it is necessary to synchronize the binary sequence originally sent with the received signal, and it is above all long. In fact, to calculate accurately a BER of 10^{-8}, at least 1 billion of bits need to be compared one to one. Because one OFDM symbol contains 336 data subcarriers, and because the oscilloscope records 44 OFDM symbols in one capture, 1 billion of bits correspond to 33 820 captures in QPSK and 16 910 captures in 16-QAM. Therefore, in the following measurements, only the BER value higher than 10^{-5} are certain, i.e. about 340 captures in QPSK or a measure running during several hours.

Consequently, it is preferred to estimate the BER from the EVM instead of calculating it, but beforehand the accuracy of the estimation has to be checked. With this aim in mind, figures 4.12, 4.13 and 4.14 have been plotted, with points to represent the experimental values and lines to represent the theoretical curves.

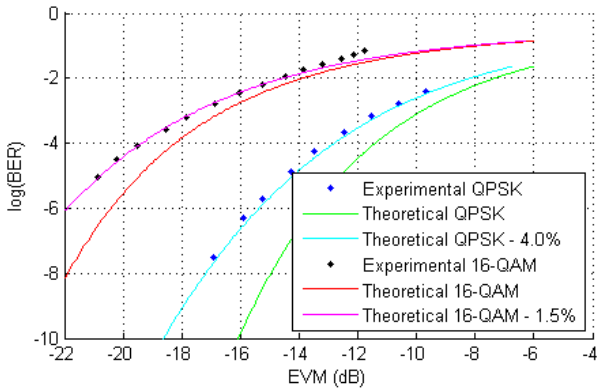

Figure 4.12: The BER versus the EVM.

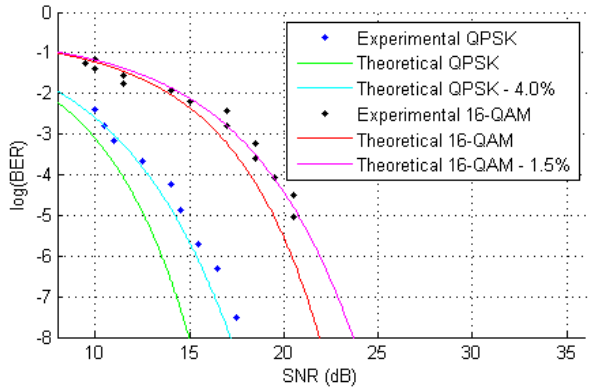

Figure 4.13: The BER versus the SNR.

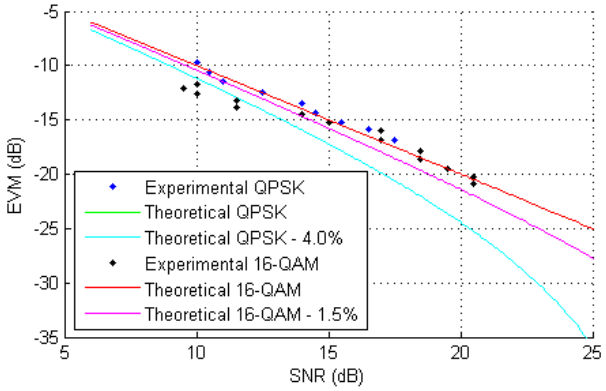

Figure 4.14: The EVM versus the SNR.

The relationship among EVM and SNR is validated, but a problem appears with the BER. In fact, it has been necessary to add 4% to the EVM values in QPSK and 1.5% in 16-QAM to match the theory to the experimentation (and the equivalent in terms of SNR). Among the two hypothesis that have to be confirmed to apply equation 4.8, only the Gaussian noise channel hypothesis has been checked. The perfect recovery of the signal is not guaranteed due to the lack of standards to demodulate it at the reception. It is therefore not possible to state that the EVM values reported above are as good as values that would be obtained by a commercial radio receiver. However, the next part will try to find the sources of error between the theoretical and experimental relationships among EVM and BER.

4.1.4 The three identified sources of error in the relationships among EVM, SNR and BER

The reasons that can be excluded

One source of error could be the clipping introduced by the RF amplifier present in the setup of figure 4.3. However, this amplifier does not induce voltage clipping as shown in figure 4.15. In fact, the input 1dB compression point (P1dB) is equal to -12.5dBm in the radio band: with a delivered power of -12dBm at the output of the RF coupler, plus a 10dB attenuator in front of the amplifier, an adequate power back-off of at least 9.5dB is guaranteed (see appendix A.3.2). Nevertheless, it has to be noted that the S21 parameter of the RF amplifier is not flat over the 2GHz bandwidth of the radio signal, which explains the shape of the spectrum in figure 4.6.

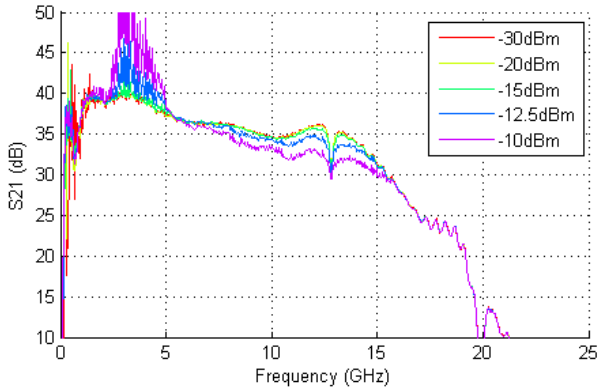

Figure 4.15: Measured S21 parameter for the Miteq AMF-5D-02001200-40-25P amplifier as a function of the RF input power. This amplifier has a Noise Figure (NF) of 4dB according to its datasheet.

Generating the I and Q components in baseband and translating them into IF with an external system is more appropriate because the AWG has a bandwidth limited to 5GHz. Regrettably, the external system used to translate the baseband signals to 6GHz is particularly difficult to build since it requires two local oscillators with a perfect 90° phase shift, a quadrature realized here manually with variable delay lines. If this quadrature is lost, a distorted constellation appears, where each constellation point is multiplied by a constellation of smaller amplitude and having undergone a rotation [137]. This loss of quadrature between the I and Q components, generally called IQ imbalance, has been mathematically intoduced in equation 4.18, then it has been illustrated in figure 4.16 where each parameter has been isolated.

$$s(t) = I \times cos(2\pi f_0 t) + G_Q \times Q \times sin(2\pi f_0 t + \Phi_Q) \tag{4.18}$$

where,

- G_Q is the amplitude imbalance.
- Φ_Q is the phase imbalance.

Finally, comparing figure 4.16 with the constellation diagrams obtained in figure 4.8, it can be written that the bad relationship among EVM and BER does not come from an IQ imbalance. Indeed, in figure 4.8, neither amplitude distortion nor phase distortion is observed. Lastly, it has to be noted that if the presence of such an impairment had been confirmed, it would have not been possible to verify it from figure 4.7 as this effect is equivalent to AWGN, consequently the voltage distribution remains Gaussian [141].

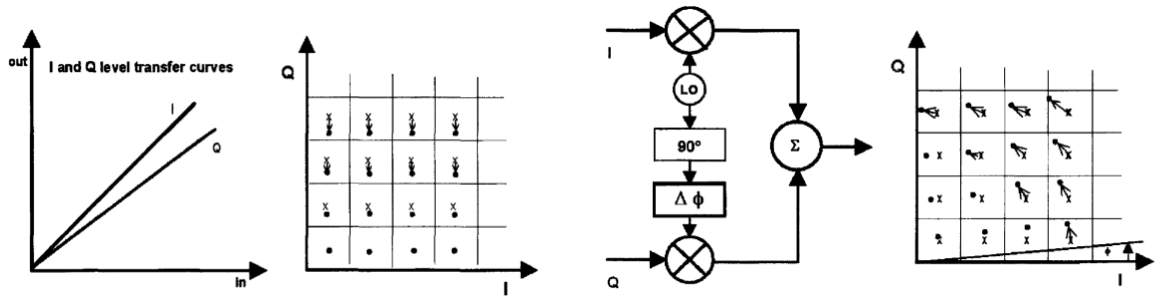

Figure 4.16: Effects of IQ imbalance on constellation diagrams [28]. On the left, the amplitude imbalance is represented by different I and Q level transfer curves, while on the right, the phase imbalance is represented by the add of a phase component to the sine wave oscillator. The effects on the constellation diagrams are shown directly next to the right of these figures.

First source, the spectrum response

A detailed analysis has revealed that the adopted methodology was perhaps inadequate. Let us recall that the experimental EVM has been measured from equation 4.15 according to the IEEE 802.15.3c standard. Then, this EVM has been reinjected into equation 4.8 to obtain the BER. In other words:

1. For an OFDM symbol, the EVM values were measured for each subcarrier,
2. then, these values were averaged according to equation 4.15,
3. and finally, the BER has been evaluated from equation 4.8.

However, it would be preferable to follow this second methodology:

1. the EVM values should have been measured for each subcarrier,
2. then, the BERs should have been evaluated from equation 4.8,
3. and finally, these BER values should have been averaged.

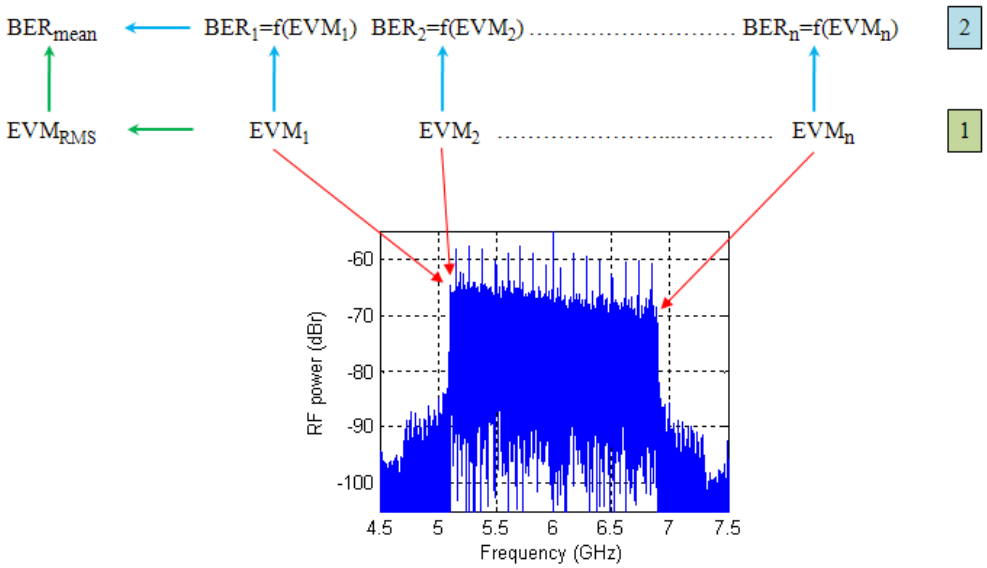

Figure 4.17: Two different ways to calculate the BER of a multicarrier modulated signal.

The first method is generally the one described and used in literature. In [142] and [143], the power levels of the different subcarriers remain stable over the radio spectrum since the used standards have low bandwidth, for instance the IEEE 802.11a has a 20MHz bandwidth. On the contrary, in the millimeter-wave band, the large 2.16GHz bandwidth of the channels induces power levels depending of the subcarrier position: the high frequencies are generally more attenuated, and in the worst case the radio spectrum is bumpy.

Simulations under Matlab coupled to spectrum captures can help to recover the correct BER. First, from the radio spectrum represented in figure 4.18, a mask taking into account the 6dB difference between the low and high frequencies is plotted. Then, using this mask, the SNRs, and therefore the EVMs, are determined for each subcarrier. From these values, the BER is calculated according to two approaches: in the first one, BER is calculated from the average EVM, and in the second one, BER is defined as the average of the BERs of each subcarrier. The two obtained BERs are represented in figure 4.18, in solid and dotted lines, respectively.

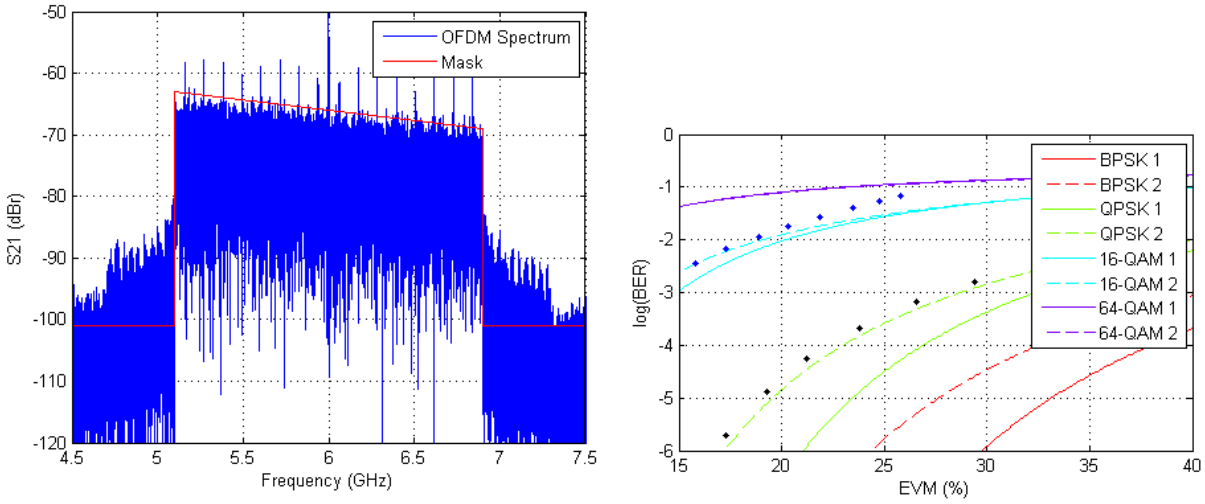

Figure 4.18: Radio spectrum with linear mask on the left and the EVM versus BER curves on the right.

The second method, in dotted lines, meets the experimental points, especially for the QPSK modulation. In the previous section the error was estimated to be 1.5% in 16-QAM and 4% in QPSK. Figure 4.19 represents this error, i.e. the difference between the dotted and solid lines, as a function of the average EVM. For EVM values between 15 and 30 %, the previous estimated error is retrieved: in QPSK the error is equal to approximatively 4% whereas in 16-QAM the error decreases from 1.5 to 0 %.

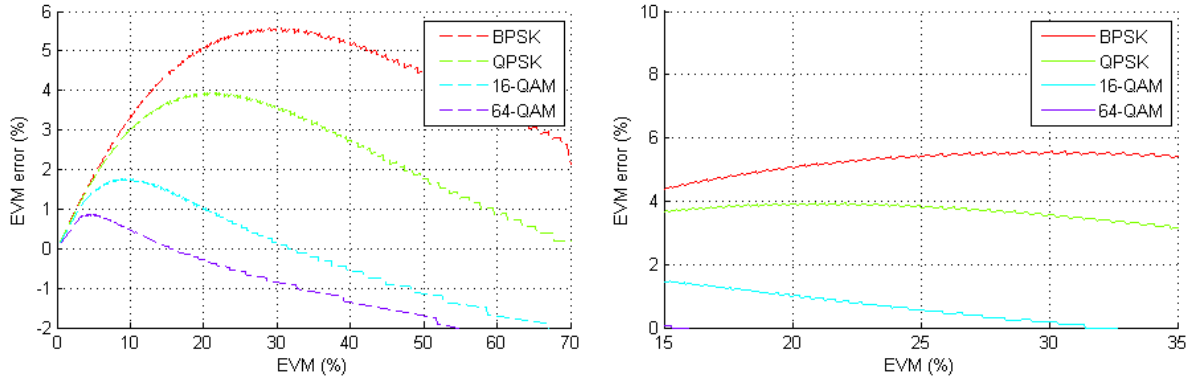

Figure 4.19: The EVM error, i.e. the EVM that should be added to equation 4.8 to obtain the right BER, as a function of the average EVM, and a zoom on the right.

The fitting method used to build the spectrum mask has a high impact on the BER results. In fact, if instead of approximating the radio spectrum by a linear curve, the exact SNRs of each subcarrier are considered, the new estimated BER can differ largely. An example is given in figure 4.20 where 336 values corresponding to the data subcarriers of the radio spectrum have been extracted to build the mask. The new estimated BER curves have been plotted, in cyan and magenta, for the QPSK and 16-QAM modulated signals, respectively. The curves describing the conventional relationship among EVM and BER are still present, in green and red. The new estimated BER clearly diverge from the classic curves, but also from experimental measures reported in orange and grey.

At the same time, additional measurements have been performed in order to validate the methodology explained in figure 4.17: the experimental EVM values of each subcarrier have been extracted and the BER has been calculated according to the two methods. These results are represented in black while the corresponding real BER is represented in blue. Finally, there is really a gap between the two BER calculations used, and if the spectrum mask helps to retrieve this difference, any of the two methods reach the expected BER.

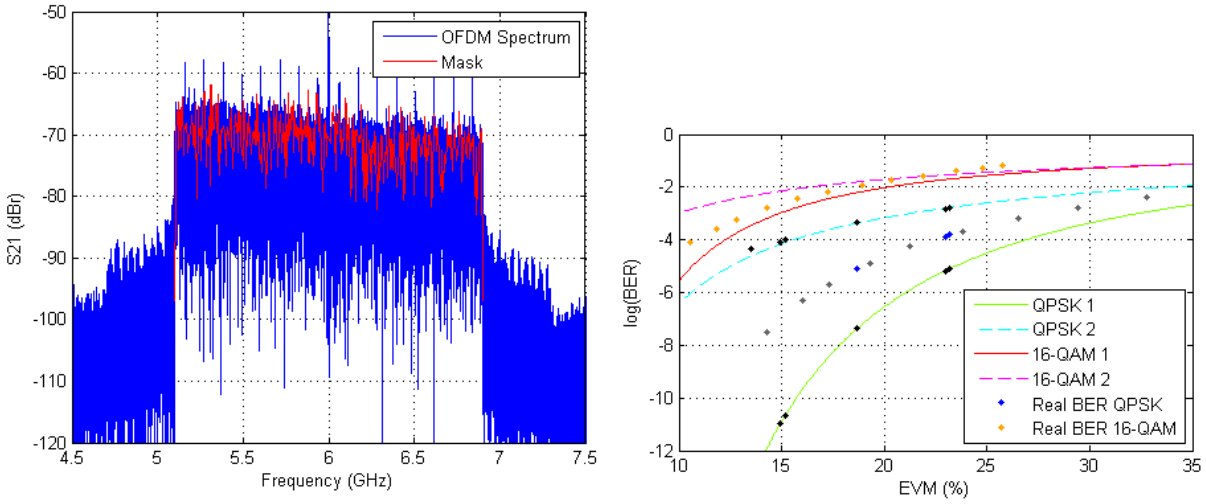

Figure 4.20: Radio spectrum with its mask built from the 336 data subcarriers on the left and the corresponding EVM versus BER curves on the right.

It has to be noted that even if the results of figure 4.18 are acceptable, a deviation appears in 16-QAM between the experimental and theoretical BER curves when the average EVM becomes higher than 20%. This error is explained in the next part.

Second source, the reference points used in the EVM measurement

The second source of error is connected to the reference points used to measure the EVM. For a correct EVM measurement, it is necessary to know which symbols are originally sent. Without this information, the algorithm in equation 4.15 does not calculate the EVM comparing the received symbols to the transmitted symbols, but estimates it comparing the received symbols to the nearest ideal symbols, i.e. those being geographically the closest. This method can induce too optimistic EVM values as shown in figure 4.21: the error between the expected (real) and the estimated (measured) EVMs increases with the real EVM value, but also with the size of the constellation diagram.

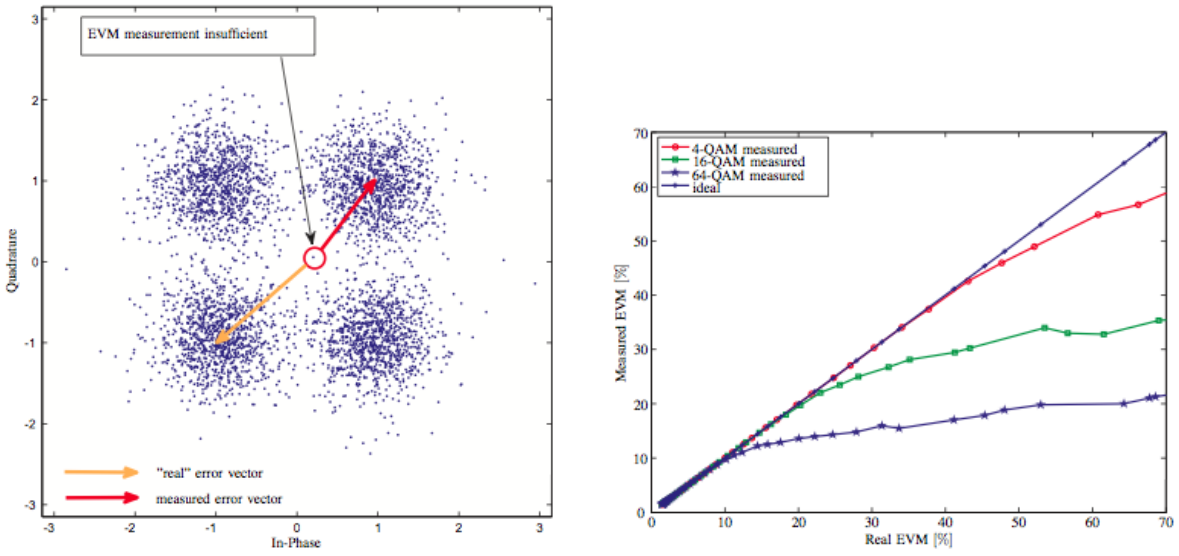

Figure 4.21: Demodulation issue for noisy symbols on the left and receiver measurement inaccuracies for different modulation schemes on the right, from [29].

Figure 4.21 has been remade using the previous experimental measurements (figure 4.12). To obtain the same curves than above, the measured EVMs have been corrected by 4 and 1.5 % for the QPSK and 16-QAM modulation schemes, respectively, and the real EVM has been calculated from the experimental BER. The result is presented in figure 4.22.

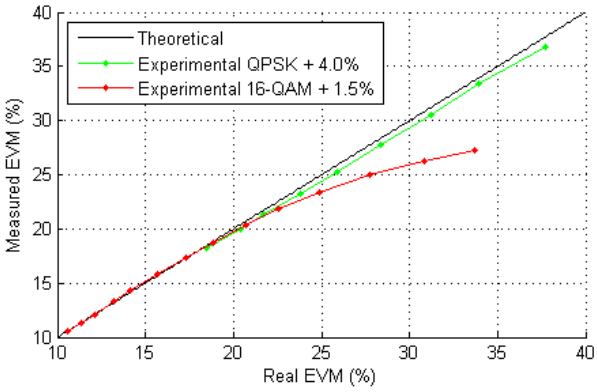

Figure 4.22: Relationship between expected and measured EVM for QPSK and 16-QAM modulation schemes.

Third source, the channel recovery

To apply the relationships between BER, SNR, and EVM, a perfect recovery of the carrier frequency and phase is required [135]. In the work presented in the previous section, the channel response was estimated from the sixteen pilot subcarriers of each OFDM symbol, a method that leads to imperfect frequency and phase estimations. One way to illustrate this point consists in verifying the probability density function of the OFDM signal in the time domain before and after the linear pilot-based channel recovery: an example is given in figure 4.23 for a QPSK signal with an EVM of 9.70%. After the channel recovery, the PDF is less well approximated by a Gaussian.

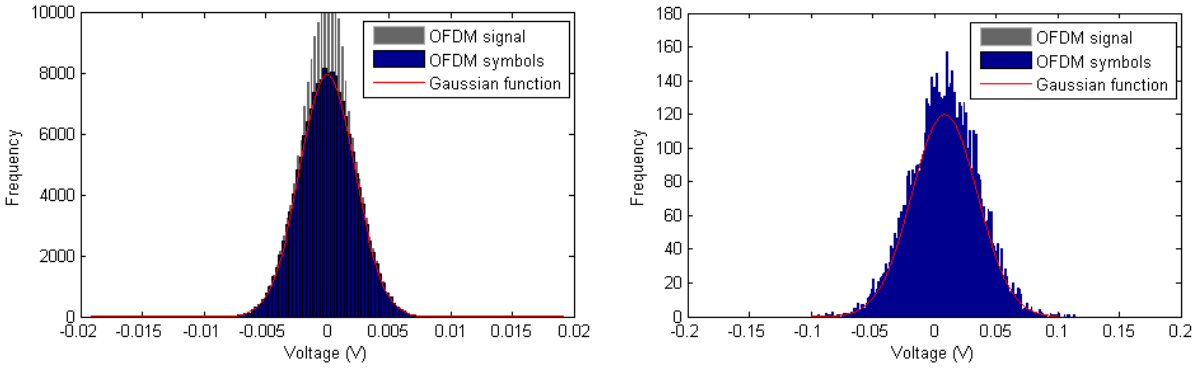

Figure 4.23: Voltage distribution as a Gaussian, on the left before and on the right after the pilot-based channel recovery.

The literature analyzes and simulates the impact of imperfect channel estimation on the BER, but a simple expression between BER and EVM is lacking. In order to verify if a better recovery of the carrier frequency and phase would be able to improve the relationship among EVM and BER, a preamble has been added to the OFDM signal using a design inspired by the IEEE 802.15.3c (A/V mode) and WirelessHD standards. In these standards, the HRP preamble is composed of eight OFDM symbols with the first four symbols presenting a double RF power than the remaining symbols. This additional power facilitates the preamble detection and simplifies the synchronization based on cross-correlation technique.

Therefore, in the 32 OFDM symbols sequence transmitted by the AWG, one symbol is amplified by 3dB and used as preamble (only one to limit the overhead, 3.13%). This method induces a higher PAPR, but this last one can be reduced fixing cleverly the binary sequence of the preamble [144] [145]. Here, without optimization, the new PAPR is equal to 14.4dB, i.e. a PAPR increase of less than 1.5dB.

Thanks to this preamble, a first channel estimation is realized. Tracking in the time domain is not possible because only one preamble symbol has been implemented. As a result, the pilot subcarriers still compensate the frequency offset error and prevent the OFDM signal from distortions due to fast variations of the channel.

Figure 4.24 provides the new trace for the QPSK modulated OFDM signal in the time domain and its new probability density function after the channel recovery. It has to be noted that the voltage distribution is closer to a normal distribution than the same signal without preamble (figure 4.23). The corresponding EVM is 11.33%, i.e. an increase of ∼1,5% probably due to the highest PAPR.

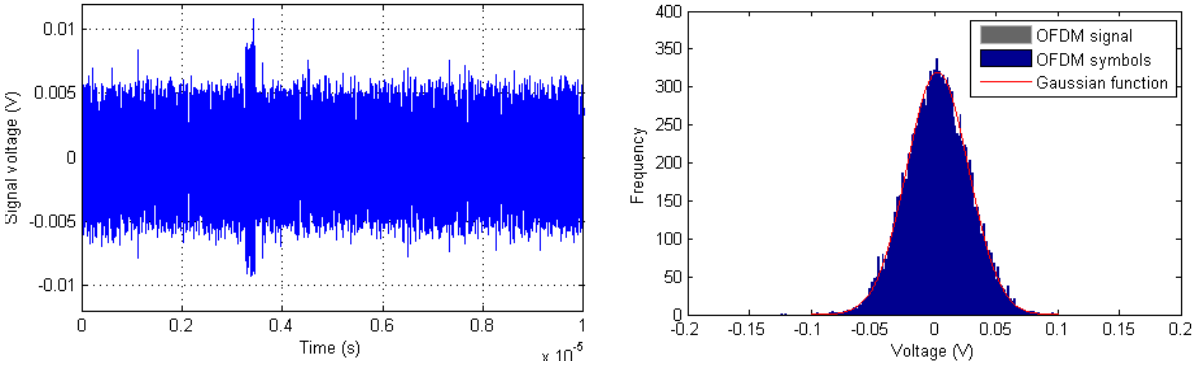

Figure 4.24: OFDM signal in time domain with one +3dB preamble symbol and voltage distribution on the right after preamble-based and pilot-based channel recovery.

Figure 4.25 represents the BER as a function of the average EVM. Two experimental BERs have been measured: the first one, in cyan, after a pilot-based channel equalization whereas the second one, in blue, after an additional preamble-based channel equalization. Theses two experimental curves can be directly compared as they use the same OFDM signal, modulated in QPSK, with a +3dB preamble OFDM symbol to keep the same PAPR, even if in one case we do not get advantage of it. Besides, estimated BER have also been plotted: the first one, in green, represents the theoretical BER from the average EVM whereas the second one, in red, represents the average of the theoretical BERs calculated from the EVMs of each subcarrier.

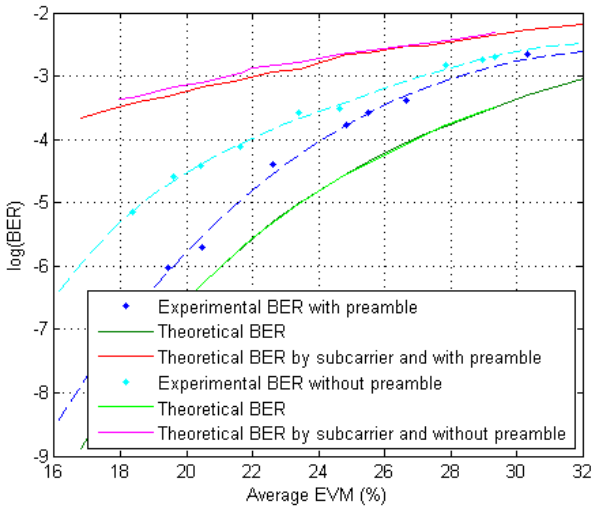

Figure 4.25: Theoretical and experimental BERs as a function of the average EVM for different channel recoveries, in QPSK.

As proven by figure 4.25, an imperfect channel knowledge leads to higher BERs and thanks to the implementation of a preamble, system performances are improved: for example, for an average EVM equal to 20%, the BER decreases of a factor 10. It has to be noted that the new curve, in blue, is closer to the first theoretical BER, the one calculated from the average EVM, than the rectified curve, the one taking in consideration the EVM of each subcarrier. This phenomena is hard to explain as, on the one hand, it seems natural to observe better BERs, but, on the other hand, it seems unusual to observe BERs going away from the rectify theoretical curve.

Summary

First, it has been checked that no clipping of RF amplifiers and no IQ imbalance occurred. Then, the equation used to determine the BER has been questioned. Two methodologies have been identified to calculate the theoretical BER, but no one conducts to the expected values. Subsequently, the first proposed method will continue to be used, the one given in the IEEE 802.15.3c standard and that calculates the BER from the average EVM.

After that, an error related to the algorithm of measure has been identified and validated. When the received symbols are compared to the nearest ideal symbols instead of the transmitted symbols, errors appear. However, these errors have only a small impact on the results and they no really improve the relationship between EVM and BER, in particularly for EVM lower than 23% in QPSK and 36% in 16-QAM.

Finally, it has been supposed that the channel recovery was imperfect, and a preamble has been added to improve it. Thus, experimental BERs closer to the theoretical values, the ones calculated from the average EVMs, have been obtained. The channel recovery seems imperfect: this is probably the main reason that can explain our bad results.

Subsequently, the two identified and validated sources of errors will not been corrected. In particular, the implementation of a preamble creates an overhead, increases the PAPR and brings complexity in the demodulation process.

4.2 Digital characterization of one free-space radio link at 60GHz

Until now, the laboratory-made radio signal has been characterized and its limits have been determined in terms of figures of merit. Even if the relationship among EVM, SNR and BER is not as expected, it remains a good way to compare different setups. Now, the RoF architectures described in chapter 2 will be built step by step in order to determine the impact of each element. In this section, the complex modulated radio signal will be translated at 60GHz, then it will be propagated in free-space up to 15m.

4.2.1 Characterization of the setup realizing a wire millimeter-wave radio link

The setup depicted in figure 4.26 is realized in order to characterize a free-space transmission at 60GHz. The conveyed radio signal is unchanged from section 4.1. Indeed, the previous setup, represented in grey, has been kept to generate and analyze the IF-OFDM signal centered at 6GHz. Between the emission and reception blocks, the OFDM signal is up-converted to 59.7GHz, in the frequency range corresponding to the second channel of the unlicensed millimeter-wave band (see section 1.3.3). This channel, the mandatory one, should be centered at 60.48GHz but the used millimeter-wave local oscillators cannot be tuned with precision: the first oscillator generates a single tone at 53.7GHz for the up-conversion while the second oscillator generates a tone at 52.6GHz for the down-conversion. Consequently, at the reception, the OFDM signal is centered at 7.1GHz instead of 6GHz.

$$6\ GHz + 53.7\ GHz\ (1^{st}\ LO) - 52.6\ GHz\ (2^{th}\ LO) = 7.1\ GHz \tag{4.19}$$

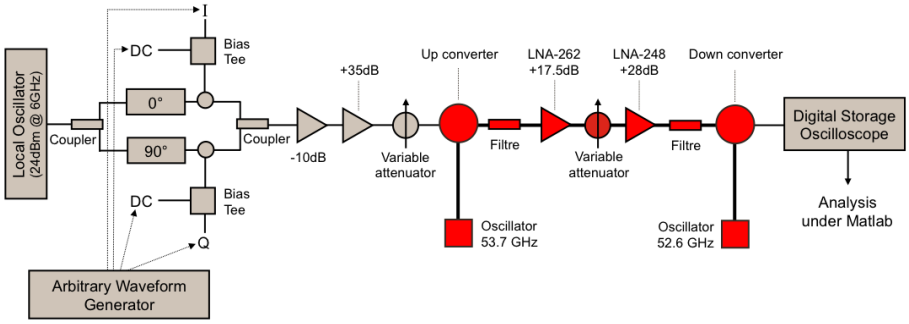

Figure 4.26: Experimental setup testing the millimeter-wave OFDM signal centered at 59.7GHz.

EVM measurements have been performed as a function of the IF power at the input of the up-converter and as a function of the millimeter-wave power at the input of down-converter. The characterizations of the variable millimeter-wave attenuator and of the Low Noise Amplifiers (LNA) working at 60GHz are provided in appendix A.4.

As shown in figure 4.27, the optimum IF power at the input of the first mixer is around -12dBm. For powers higher than -4dBm, the EVM curves overlap due to the first mixer saturation. For low powers, EVM increases with the millimeter-wave losses due to noises introduced by the down-converter.

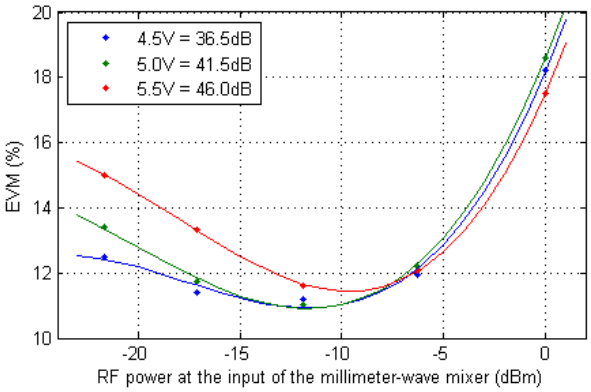

Figure 4.27: EVM as a function of the RF power at the input of the first mixer for three different voltage values applied to the millimeter-wave variable attenuator. 4.5, 5.0 and 5.5V applied to the variable attenuator correspond to 36.5, 41.5 et 46dB millimeter-wave losses, respectively. The OFDM signal is modulated in QPSK.

4.2.2 A single millimeter-wave free-space radio link

The setup depicted in figure 4.28, used as a baseline, transmits millimeter-waves in free-space. At the radio emitter, the power delivered to the first mixer is fixed to -12dBm, the best experimental value obtained previously. This signal, up-converted to 59.7GHz, is filtered as described in appendix A.4 (figure A.61), amplified by a High Power Amplifier (HPA) to obtain a power of 8.6dBm, then applied to a V-band 20dB gain horn antenna. The Equivalent Isotropically Radiated Power (EIRP) is therefore equal to 28.6dBm, a value very close to the typical EIRP of commercial devices, i.e. 27dBm (section 4.7), and in agreement with the maximum EIRP allowed in USA, i.e. 40dBm average (table 1.8). After a first hop in free-space, the signal is received by a second horn antenna with 20dB gain and boosted by a LNA. The radio signal is then down-converted in order to be captured by the digital storage oscilloscope.

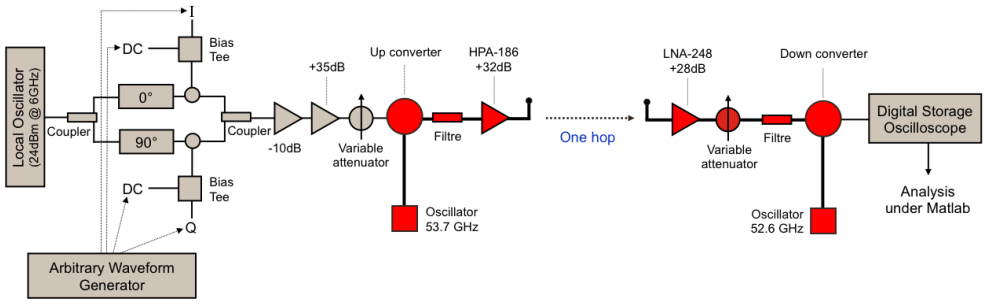

Figure 4.28: A single millimeter-wave free-space radio link.

Figure 4.29 represents the EVM at the reception as a function of the millimeter-wave attenuation placed just before the down-converter mixer, and for different free-space distances, from 1 to 15 m. Two modulations, QPSK and 16-QAM, have been considered.

No significant variation is noticed between the different tested distances, just a reception attenuation shift equivalent to the different free-space losses. Even for short distances, 1m for example, the first LNA at the reception side does not saturate and the millimeter-wave attenuator can adjust sufficiently the RF power to have a suitable power at the down-converter input. Finally,only a small evolution of

the minimal EVM value is observed when the distance increases: from 12% to 14% in QPSK and from 14% to 16% in 16-QAM.

The EVM depends only on the SNR. As a result, there should be no difference between QPSK and 16-QAM modulated signals. However, in figure 4.29, a difference of 2% is noticed, probably due to different alignments between the radio emitter and the radio receiver. In fact, the measurements were made several weeks apart.

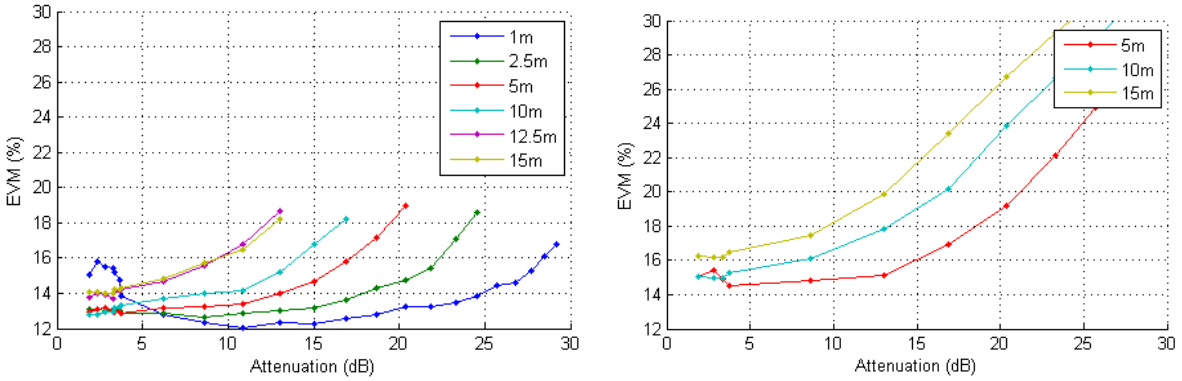

Figure 4.29: EVM for a single millimeter-wave radio link as a function of the attenuation at the reception, for a QPSK signal on the left and a 16-QAM signal on the right.

The millimeter-wave gain at the reception that gives the best EVM values for free-space propagation distance from 2.5 to 15 m is 25dB, plus 20dB antenna gain, i.e. a total gain of 45dB that does not compensate entirely the free-space propagation losses (that are 91.5dB for 15m).

Figure 4.30 resumes the previous results representing the EVM as a function of the power at the output of the millimeter-wave attenuator. Something new appears in these curves: the EVM could be enhanced a little more providing more power at the input of the down-converter mixer to reach the floor of the bell-shape curves, especially for distance higher than 10m.

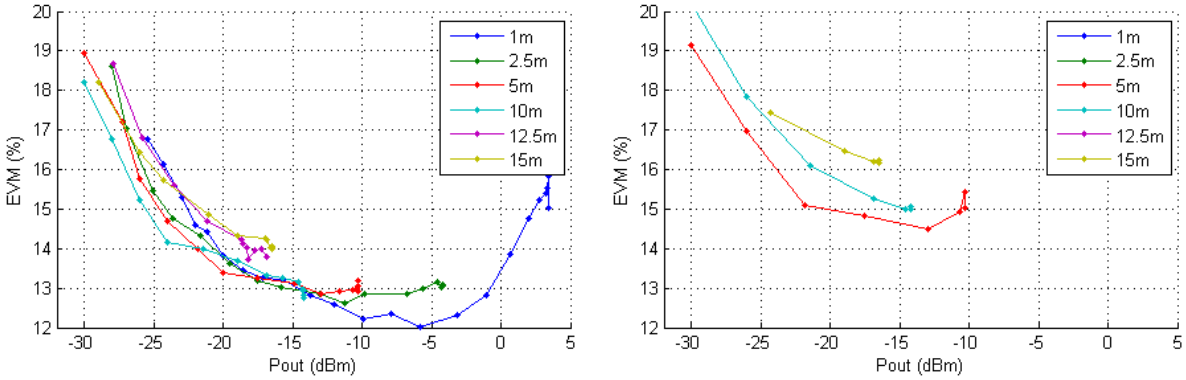

Figure 4.30: EVM for a single millimeter-wave radio link as a function of the power at the output of the millimeter-wave attenuator (input of the down-converter), for a QPSK signal on the left and a 16-QAM signal on the right.

For a QPSK modulation scheme, some additional measurements have been carried out to characterize the free-space propagation. First, the signal power has been measured at the reception as a function of the distance thanks to a millimeter-wave power meter placed just before the down-converter. The experimental results have been represented in figure 4.31 and compared to theoretical values:

$$\begin{aligned} P_{down\text{-}converter\ input} = {} & 27dBm\ (EIRP) + 20 \cdot log\left(\frac{3 \cdot 10^8}{4\,\pi\ 59.7 \cdot 10^9}\right) + 20dB\ (horn\ antenna) \\ & + 28dB\ (LNA\text{-}248) - 1.9dB\ (variable\ attenuator\ intrinsic\ losses) \\ & - f(voltage)\ (variable\ attenuator) \end{aligned} \tag{4.20}$$

The RF losses of the variable millimeter-wave attenuator, $f(voltage)$, is defined in figure A.59, in appendix A.4.

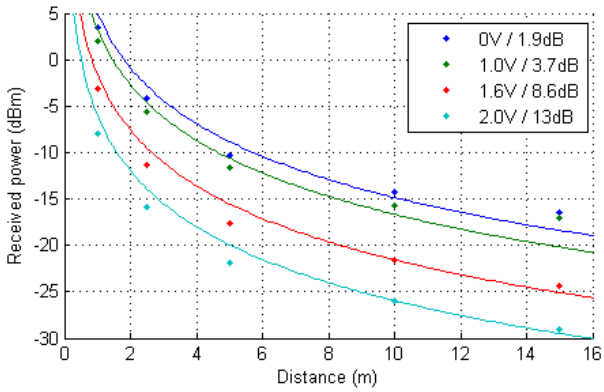

Figure 4.31: The received signal power, with experimental points and theoretical lines, as a function of the free-space distance and for different millimeter-wave attenuations.

As shown in figure 4.31, the measured signal powers fit well with the theoretical values: the maximal observed differences are 2dB for 5m distance, 1dB for 10m distance and 3.2dB for 15m distance.

Then, the received IF radio spectrum has been plotted, in figure 4.32, for a distance fixed to 5m and for an instantaneous EVM equal to 12.37%. Similar results are obtained for a 16-QAM modulation scheme.

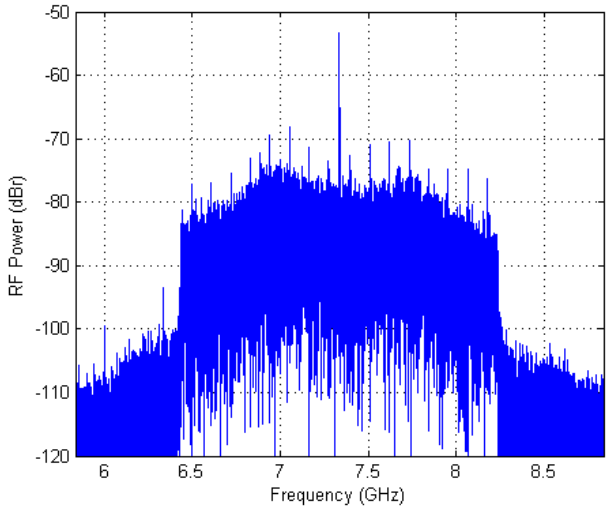

Figure 4.32: IF radio spectrum at the reception after a 5m-length hop.

As a reminder, the BER can be estimated from EVM only if the channel noise is Gaussian. As a consequence, figure 4.33 was plotted to check if the sum of the OFDM signal and the noises remains distributed normally and therefore if each one is an independent Gaussian variable. Figure 4.33, representing the voltage distribution of the received OFDM signal, has also to be compared to figure 4.7 representing the same measurement but for a direct radio link in IF. With an additional translation at 60GHz plus a propagation in free-space, the new voltage distribution remains well approximated by a Gaussian curve, even for high voltage levels where no clipping appears. However, the initial 13.04dB PAPR has been reduced to 11.68dB, i.e. a loss of 1.36dB. Either a very light clipping has occurred (which is a priori not the case as shown below) or the average power has increased, especially the noise power (which is a priori the case as shown below).

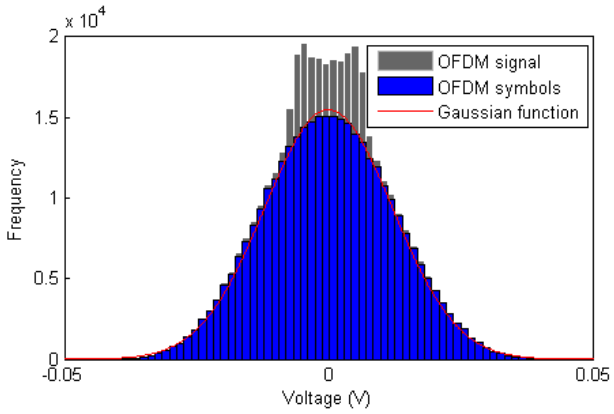

Figure 4.33: Voltage distribution for a QPSK modulated signal after a single millimeter-wave free-space radio link (5m).

The voltage distribution indicates if the channel response is properly Gaussian, while the distribution of the complex symbols in the constellation diagram indicates if the demodulation process of the OFDM signal under Matlab, based the channel equalization by pilot subcarriers, keeps the channel properties. As can be seen in figure 4.34, the BER can be calculated a priori without problem as the theoretical curves, in red, fit well the experimental distributions.

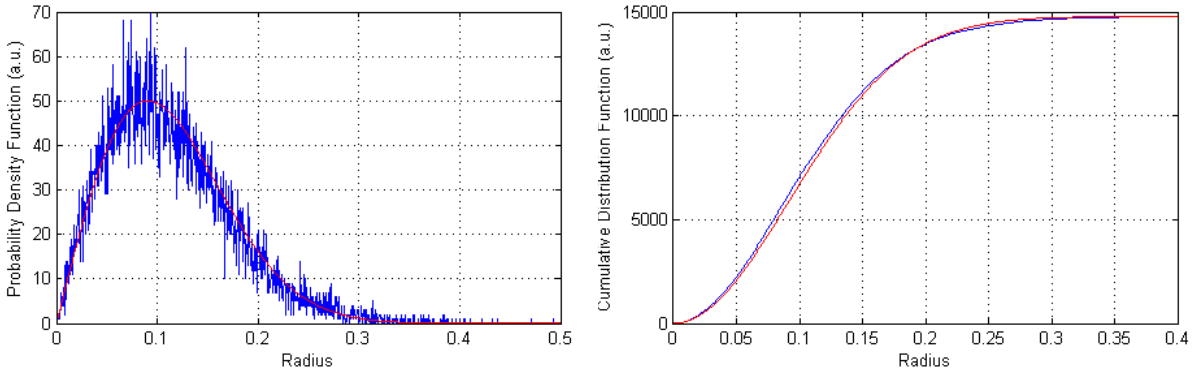

Figure 4.34: Probability density function on the left and cumulative distribution function on the right of the complex symbols in the constellation diagram of a QPSK modulated signal after a single millimeter-wave free-space radio link (5m).

Figure 4.35 represents the constellation diagram corresponding to this single 5m-length millimeter-wave free-space radio link. However, the OFDM signal is now modulated in 16-QAM.

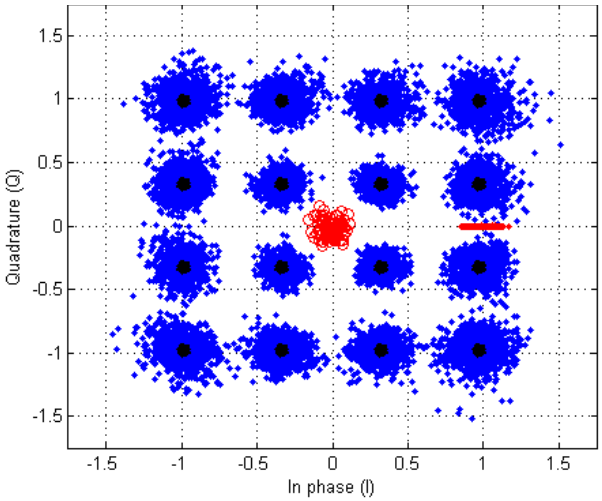

Figure 4.35: Constellation diagram of a 16-QAM modulated signal.

The BER has been calculated as a function of the EVM for different free-space distances and for a 16-QAM modulated signal, a modulation scheme that provides higher BERs, and therefore fastest measurements, than a QPSK one. The BER curves, shown in figure 4.36, have been plotted using the same measurement points as the ones in figures 4.30 and 4.29. In fact, these measures have been made in parallel.

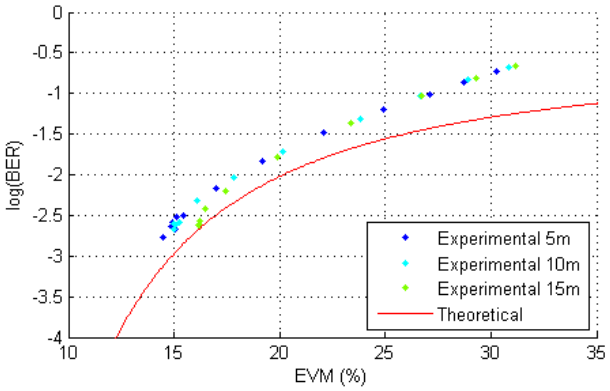

Figure 4.36: EVM versus BER after a first hop in free-space for a 16-QAM modulated signal.

Globally, whatever the free-space distance, 5, 10 or 15m, the BER curves remain the same. Only for EVMs lower than 18%, a little enhancement of the BER is observed for the 15m-length hop. In fact, when the distance increases, the antennas loose their alignment, the secondary paths are largely mitigated, and the high frequencies are greatly attenuated. All these effects significantly modify the radio spectrum, and so the BER curves.

A difference persists between the theoretical BER and the experimental values. For high EVM values, the error calculation is probably based on wrong reference symbols since the disconnect between the two curves escalates from 20% as already seen previously, in figure 4.22. For low EVM values, the theoretical BER is also better than the experimental one, a phenomenon that can be explained by the bumpy aspect of the radio spectrum.

4.2.3 The two identified sources of error in the relationships among EVM, SNR and BER

First source, the spectrum response

Additional measurements have been realized on the single millimeter-wave free-space radio link in order to check the experimental BER according to the two methods described page 112. Thus, the bumpy IF radio spectrum and its noise level have been captured after a 5m-length hop as shown in figure 4.37. To measure the noise spectrum, the AWG and the local oscillator at 6GHz have been switched-off while the other RF components were switched-on. With this method, the noise coming from non-linearities (IM3) is ignored, only the thermal noise of each component is considered.

The EVM values of each subcarrier have been recorded, then different EVM versus BER curves have been plotted in figure 4.38:

- the theoretical EVM versus BER curve (solid line in cyan).
- the theoretical BER calculated from the experimental average EVM (pink points).
- the theoretical BER calculated from the radio spectrum of figure 4.37 (dashed line in cyan).
- the theoretical BER calculated as the average of the BER values of each subcarrier (green points). These BER values are calculated from the experimental EVM values of each subcarrier.
- the experimental BER values (blue points).

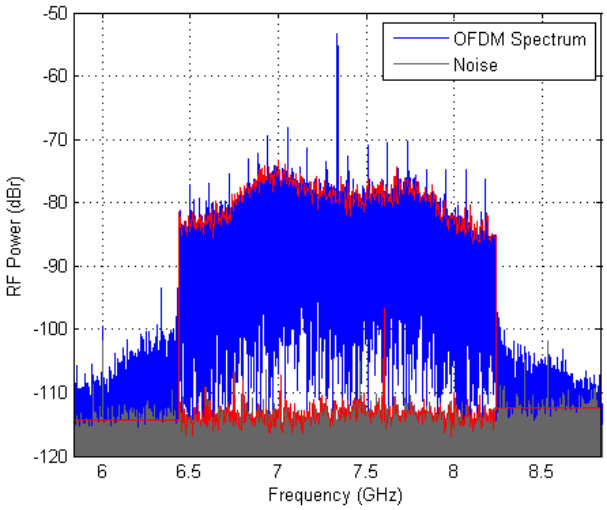

Figure 4.37: Radio spectrum and its noise level at the reception after a 5m-length hop for a 16-QAM modulated signal. The masks are represented in red.

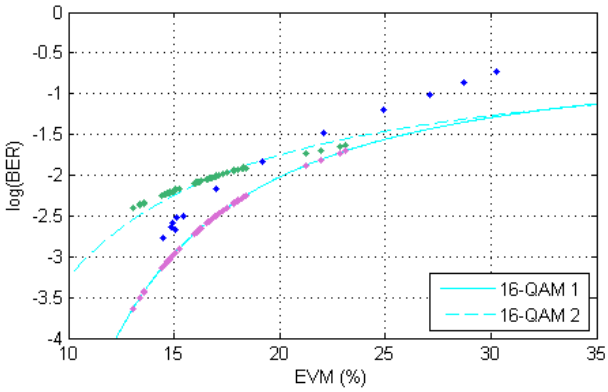

Figure 4.38: EVM versus BER after a 5m-length free-space hop and for a 16-QAM-modulated signal.

As previously, the experimental BER does not match with the theoretical values: when the radio spectrum is too bumpy it is difficult to draw a relashionship between EVM and BER. Therefore, since no reliable relationship can be established, subsequently only the experimental BER, the EVM or the radio spectrum will be measured.

Second source, the phase recovery

After some investigation, it has been detected that the millimeter-wave oscillator feeding the up-converter mixer, in the setup of figure 4.28, drifts in the frequency domain. Consequently, the phase of the pilot subcarriers follows a sine curve in the time domain as shown in figure 4.39. To remove this impairment, the Matlab demodulation algorithm has been modified to correct the phase over several consecutive OFDM symbols, but symbol by symbol. This Matlab code is described in appendix A.7.

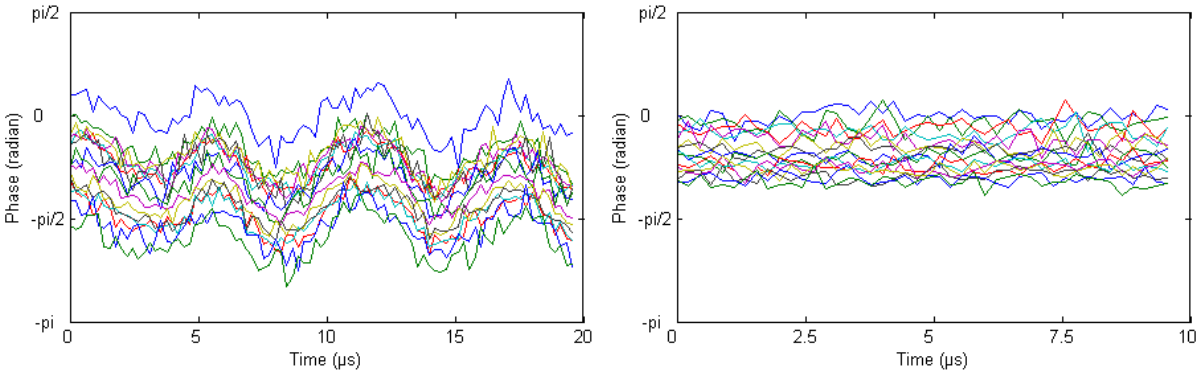

Figure 4.39: Evolution of the phase of the pilot subcarriers as a function of the time, before correction on the left, and after correction on the right. Each curve corresponds to a pilot subcarrier.

Figure 4.40 shows the impact of this frequency drift on the constellation diagram. If before code rectification, on the left, the symbols are hardly distinguishable, after correction, on the right, the problem is solved. Nevertheless, the constellation diagram becomes odd with pilot subcarriers, located at the coordinates (1,0), having a phase fixed to zero.

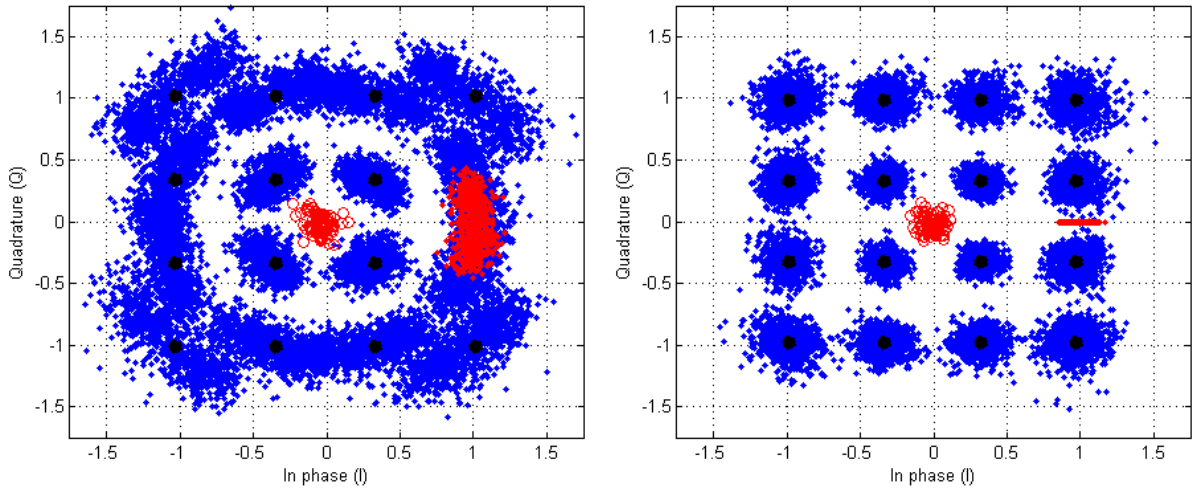

Figure 4.40: Constellation diagram before and after the demodulation code modification that compensates the frequency drift of the millimeter-wave oscillator.

In figure 4.35, the Matlab code rectification had already been applied as shown its pilot subcarriers. Subsequently, this code rectification will be applied to all measurements (when the millimeter-wave oscillator is used).

4.3 Digital characterization of the RoF links at an Intermediate Frequency of 5GHz

After having characterized the millimeter-wave radio emitter and radio receiver, and before studying the different optical architectures, RoF links working at IF are analyzed. Three main parameters are observed:

- the laser bias current.
- the laser input power.
- the optical losses (to simulate different architectures).

In this section, a QPSK modulated signal is transmitted modulating directly a laser and recovered using direct photodetection (IM-DD). Several RoF configurations are compared:

1. Finisar VCSEL at 850mn + Finisar GaAs PIN photodiode with the built in TIA.
2. VI-Systems VCSEL at 850mn + VI-Systems GaAs PIN photodiode.
3. Finisar FP laser at 1310mn + Finisar InGaAs PIN photodiode with the built in TIA.
4. U-L-M VCSEL at 850mn + Finisar GaAs PIN photodiode with the built in TIA.

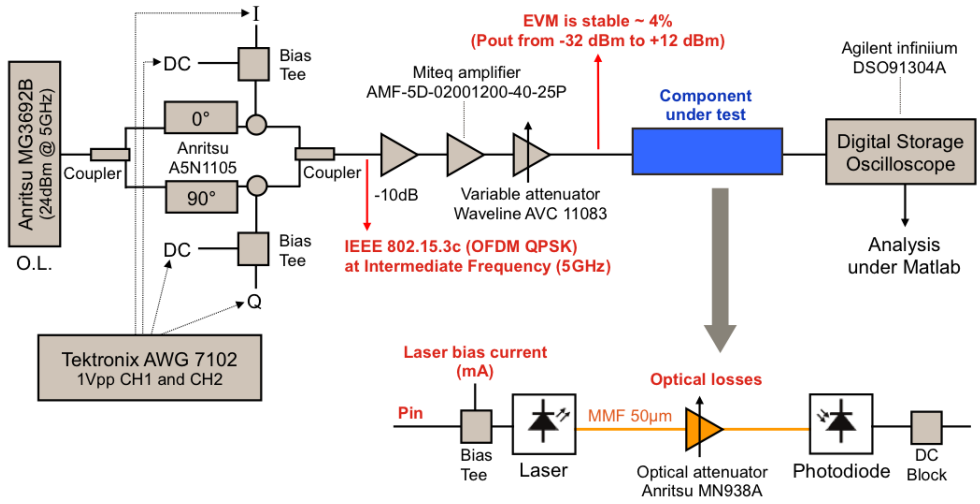

Figure 4.41: The experimental setup characterizing RoF links at an IF of 5GHz.

In the experimental setup depicted in figure 4.41, IF is fixed to 5GHz, a good choice to propagate the OFDM signal through a low cost optical link[3]. All the fibers are OM3 MMF patch cords of few centimeters length, thus, the total fiber length does not exceed 1m: the linear optical attenuation and the dispersion effects can so be neglected. Nevertheless, an optical attenuator with 2.9dB intrinsic losses is introduced to study the impact of the linear optical attenuation, of the insertion losses of the optical connectors, of the fiber bend losses, or of the presence of an optical splitter.

The RoF links have been characterized in terms of EVM only, the relationship between EVM and BER having been established in figure 4.12. Nevertheless, it has to be noted that this relationship is a priori correct only for small EVM values, i.e. at the optimized point when the optical noises can be neglected. In fact, from the example of the Finisar components working at 850nm, it can be written that the RIN (figure 3.22), the shot noise (figure 3.23) and the thermal noise (figure 3.28) are not perfect white noises (particularly the RIN).

4.3.1 Finisar VCSEL and PIN photodiode at 850nm

The VCSEL working at 850nm and the GaAs PIN photodiode with a built-in TIA from Finisar are studied. Figure 4.42 presents the measured EVM at the output of a point-to-point RoF link with no additional optical loss (i.e. without the attenuator of figure 4.41) as a function of the laser input power and for different laser bias currents.

[3]This frequency differs from the one of figure 4.3 where an IF at 6GHz was required to up-convert the OFDM signal in the second channel of the millimeter-wave band.

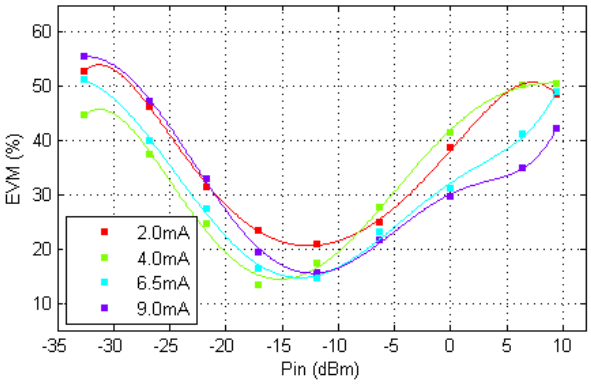

Figure 4.42: EVM at the output of the RoF link as a function of the laser input power and for different bias currents. The optical losses are null.

The minimal observed EVM, obtained for a laser bias current of 4mA and a laser input power of -17.1dBm, is 13.4%. Compared to the ∼4% of the direct link at IF, without RoF, the EVM has increased by 9%. The other points that can be deducted from the figure 4.42 are:

- At 2mA, the important deterioration of the EVM can be explained by a bias current close to the current threshold of the laser (0.9mA).
- Between 4 and 9 mA, for low laser input power, the EVM increases with the laser bias current since increasing the bias current also increases the emitted optical power, and therefore shot noise and saturation effects on the optical receiver.
- Between 4 and 9 mA, for high laser input power, the EVM decreases when the laser bias current increases since increasing the bias current decreases the RIN and improves the IP3 of the RoF link.
- The optimal laser input power is ∼-15dBm. This value corresponds to the input P1dB of the RoF link (see the section 3.5.4).
- Even if the increase of the laser bias current shifts the RIN peak toward the high frequencies, the impact on the OFDM signal is negligible in figure 4.42 as the signal has a large bandwidth. Indeed, between 4 and 9mA this peak does not really change, staying around 4.5GHz.

From figure 4.42, the laser input power leading to the minimum EVM is plotted as a function of the bias current. This optimum power, represented in red in figure 4.43, has also be determined performing a 6^{th}-degree polynomial approximation of the measurement points of figure 4.42. The values thus obtained are shown in blue in figure 4.43.

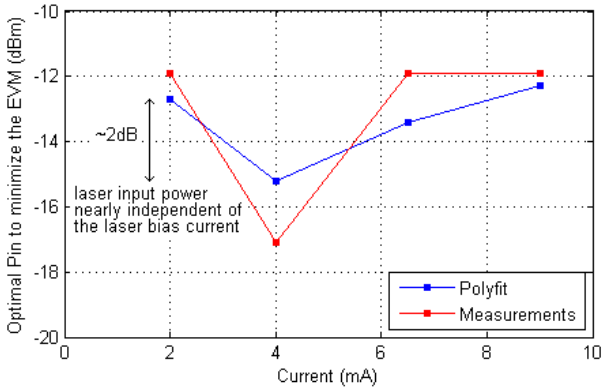

Figure 4.43: The laser input power leading to the minimum EVM as a function of the bias current, with in red the optimal power from the measurement points of figure 4.42, and in blue after a polynomial approximation of these points.

Even if the number of points in figure 4.43 is limited, it can still be written that the optimal laser input power is -14dBm (±1dBm) and that it is nearly independent of the laser bias current.

In a second time, optical losses are added in the link in order to simulate point-to-multipoint and multipoint-to-multipoint RoF architectures. The laser bias current is fixed to 6.5mA, in the middle of the L-I curve. Figure 4.44 shows the EVM at the output of the RoF link as a function of the laser input power for different optical losses.

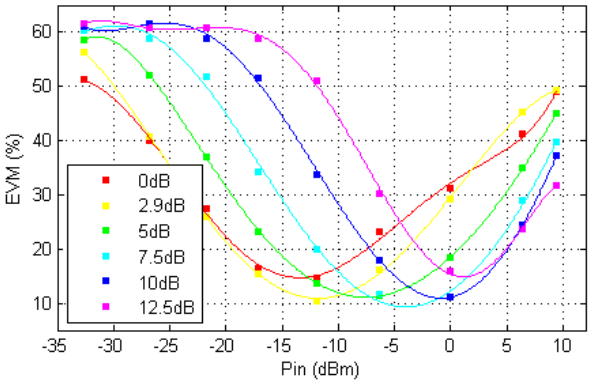

Figure 4.44: EVM at the output of the RoF link as a function of the laser input power for different optical losses. The laser bias current is fixed to 6.5mA.

In figure 4.44, the different EVM curves do not overlap. Before any analysis, some principles have to be recalled for a given laser input power (see sections 3.3.1 and 3.4.1):

- When the optical losses increase, the RIN decreases: for each dB added to the optical link, the detected RIN power decreases of 2dB. If the RIN is the dominant noise of the link, the SNR, and so the EVM, are constant regardless of the optical losses.
- When the optical losses increase, the shot noise decreases: for each dB added to the optical link, the shot noise power is reduced of 1dB. If the shot noise is the dominant noise, the SNR, and so the EVM, decrease when the optical losses increase.
- Lastly, if the thermal noise is the dominant noise of the link, the EVM decreases when the optical losses increase: the SNR evolves with a slope factor equal to -2, a more important evolution than a regime where the shot noise is dominant.

In figure 4.44, the shape of the curves remains globally the same, with a similar minimum EVM around 10%, excepted the RoF link without optical loss where the minimum EVM is higher due to non-linear effects in the photodiode and the built-in TIA (the laser input power is close to the P1dB of the link) and due to RIN at the emission. Beyond 12.5dB optical losses, the minimum EVM starts increasing due to laser saturation as an important RF laser input power is needed to compensate the optical losses and due to dominant thermal noise at the reception.

If the shape of the curves remains globally the same when the optical losses increase, the laser input power leading to the minimal EVM is shifted towards high RF powers. Thus, the optical losses are compensated. Besides, for low laser input powers, the dominant noise is the thermal noise as for a given input power, the EVM increases strongly with the optical attenuation. Nevertheless, in case of very low optical attenuation (0 and 2.9dB), the superposition of the EVM curves indicates that the predominant noise is rather the RIN. For high laser input power and increasing optical losses, the EVM curves tend to overlap. This is particularly true for optical losses higher than 7.5dB, when the photodetected signal becomes insufficient to induce non-linearities: consequently, these ones come from the laser that saturates. Before 7.5dB optical losses, the small difference between two curves for a given laser input power indicates that the dominant noise is the shot noise.

In figure 4.45, the laser input power leading to the minimum EVM is plotted as a function of the optical losses, with in red the optimal RF power from the measurement points of figure 4.44 and in blue after a 6^{th} degree polynomial approximation.

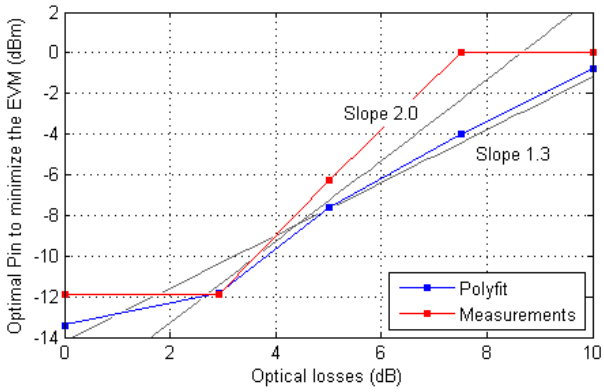

Figure 4.45: The laser input power leading to the minimum EVM as a function of the optical losses, with in red the optimal power from the measurement points of figure 4.44, and in blue after a polynomial approximation of these points.

The curves in figure 4.45 can be well fitted by a straight line with a slope of 1.3 (the first grey line), while a line with a slope of 2 (the second grey line) is expected since the electrical losses correspond to the double of the optical losses when they are expressed in logarithmic scale. The straight line fits quite well the central part of the experimental curve. However, at the beginning of the curve, the slope is lower because of predominant noises at low RF input level on one hand and the saturation of the built-in TIA at high RF input level on the other hand. In the final part of the curve, the laser non-linearity impacts the slope.

4.3.2 VI-Systems VCSEL and PIN photodiode at 850nm

This part consists in determining the degradation induced by a RoF link composed of optoelectronic components from VI-Systems, and comparing it to the previous Finisar link. It has to be noted that a Miteq AFS44-00102000-30-44-10p amplifier (G=41dB, see appendix A.3.1) has been added at the output of the link to measure the EVM in good conditions as the VI-Systems photodiode does not include a TIA.

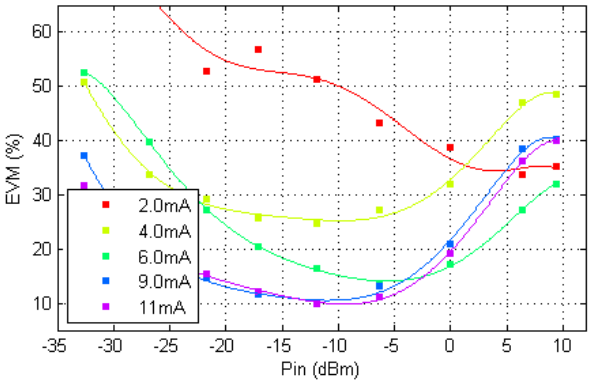

Figure 4.46: EVM at the output of the RoF link as a function of the laser input power and for different bias currents. The optical losses are fixed to 12dB.

Figure 4.46 presents the measured EVM at the output of the link as a function of the laser input power and for different laser bias currents. The introduced optical losses, 12dB, avoid the photodiode saturation taking a sufficient back-off from the maximum input optical power permitted by the photodiode: 2mW at 850nm for a laser peak power of 3mW according to its datasheet.

The minimum measured EVM of 9.90% has been obtained for a laser bias current of 11mA and a laser input power of -11.9dBm. A similar result had been observed with the Finisar optoelectronic components, but with 7.5dB optical losses (see figure 4.44). Otherwise, compared to the ∼4% of the direct link at IF, the EVM has increased by 6%. The other points revealed by figure 4.46 are:

- At 2mA, the important deterioration of the EVM is explained by a bias current close to the threshold current of the laser (1mA).
- Between 2 and 9 mA, for a given laser input power, the EVM is enhanced when the laser bias current increases: the RIN and the non-linearities are reduced.
- Even if the increase of the laser bias current shifts the RIN peak toward the high frequencies, the impact on the OFDM signal is negligible as the signal has a large bandwidth. Indeed, between 4 and 9 mA, this peak does not really change and it remains around 5.5GHz.
- The EVM curve at 9mA is very close to the one at 11mA. The optimal laser input power is observed, -14dBm.

For approximatively 12dB optical losses, i.e. a 16x16 splitter, an EVM of 10.5% is obtained with this RoF link composed of VI-Systems components, a bias current of 9mA and an input power of -11dBm, while an EVM of 14.9% had been observed with a link based on Finisar components, a bias current of 6.5mA and an input power of 1dBm. To understand why a better EVM is obtained with VI-Systems components, an analysis based on the analog characterizations of the chapter 3 is performed. In this analysis, the non-linearities are ignored because the input powers are low compared to the input IP3 of these links, approximatively 16dBm, and to the input P1dB.

First, the RF power at the input of the Finisar VCSEL is 12dB higher than the power at the input of the VI-Systems laser, but this advantage is annihilated by the laser gain responses. The latter have been evaluated considering equation 3.7 and ideal photodiodes with $\eta_{OE} = 1\text{A/W}$ and $Z_{TIA} = Z_{out} = 50\Omega$:

$$\begin{aligned} \textit{Finisar laser gain}&: \ 20 \cdot log(0.08) + 10 \cdot log(60/50) = -21.1dB \\ \textit{VI-Systems laser gain}&: \ 20 \cdot log(0.62) + 10 \cdot log(50/50) = -4.2dB \end{aligned}$$

As a result, more dynamic optical power is emitted by the VI-Systems laser, 4.9dB to be precise ($= 21.1 - 4.2 - 12$). This gain does not improve the RoF performances since it is balanced by a RIN higher by 7.5dB. In fact, the worst RIN value measured in the radio band, between 4 and 6 GHz, is equal to -118dB/Hz for the VI-Systems laser when -125.5dB/Hz has been measured for the Finisar VCSEL. As a consequence the optical SNRs at the output of the lasers are similar, with nonetheless a small advantage for the Finisar VCSEL. This affirmation has not been experimentally checked as it requires to have an OSA with an extremely high resolution.

After that, the optical power received by the VI-Systems photodiode is higher, -16dBm versus -5dBm. Consequently, the shot noise of the VI-Systems link has a more significant impact.

$$\begin{aligned} \textit{Finisar photodiode input power}&: \ 10 \cdot log((6.5mA - 0.9mA) \times 0.08mW/mA) - 12.5dB = -16dBm \\ \textit{VI-Systems photodiode input power}&: \ 10 \cdot log((9mA - 1mA) \times 0.62mW/mA) - 12dB = -5dBm \end{aligned}$$

The analysis of the RIN and shot noise goes against the EVM results, it is because they are negligible for a RoF link with 12dB optical losses. In this case, the dominant parameter is the thermal noise, and it is sizeable for the Finisar photodiode: a NEP of $70\text{pW}/\sqrt{Hz}$ has been measured in the radio band. Concerning the VI-Systems photodiode, the thermal noise depends partly on the LNA implemented at the output of the photodetector. This last one has a Noise Figure[4] of 3dB max according to its datasheet.

At the output of the RoF links, the thermal noises are estimated to:

$$\begin{aligned} P_{Thermal\ Finisar} &= (Z_{TIA} \times \eta_{OE} \times NEP)^2 / Z_{out} \\ &= (2000 \times 0.5 \times 70 \cdot 10^{-12})^2 / 50 \\ &\simeq 0.98 \cdot 10^{-16} W/Hz \end{aligned} \tag{4.21}$$

$$\begin{aligned} P_{Thermal\ VI\text{-}Systems} &= (4\, K_B\, T) \times 10^{G_{ext}/10} \times 10^{NF_{ext}/10} \\ &= (4 \times 1.38 \cdot 10^{-23} \times 293) \times 10^{41/10} \times 10^{3/10} \\ &\simeq 4.06 \cdot 10^{-16} W/Hz \end{aligned} \tag{4.22}$$

[4]NF, the ratio, in linear, of the input SNR to the output SNR

And the RF powers are equal to:

$$\begin{aligned} P_{RF\ Finisar} &= 1dBm\ (input\ power) - 21.1dB\ (laser\ gain) - 2 \times 12.5dB \\ &\quad (optical\ splitter) + 26.0dB\ (photodiode\ gain) \\ &= -19.8dBm \end{aligned} \tag{4.23}$$

$$\begin{aligned} P_{RF\ VI\text{-}Systems} &= -11dBm\ (input\ power) - 4.2dB\ (laser\ gain) - 2 \times 12dB \\ &\quad (optical\ splitter) - 8.0dB\ (photodiode\ gain) + 41dB\ (G_{ext}) \\ &= -6.2dBm \end{aligned} \tag{4.24}$$

Consequently, the RF power at the output of the Finisar RoF link is 13.6dB lower than the power at the output of the VI-Systems link, but at the same time the thermal noise is only 6.2dB lower. Therefore, a better SNR is observed at the output of the VI-Systems link and the limiting parameter is the thermal noise, the other noises being not able to explain the EVM results for 12dB optical losses.

Other optical losses values have been tested in order to simulate different sizes of point-to-multipoint and multipoint-to-multipoint architectures. The measured EVM values at the output of the RoF link are reported in figure 4.47 as a function of the laser input power and for two laser bias currents, 6 and 11 mA. As the system runs smoothly, it has been decided to reduce the optical losses up to 5dB.

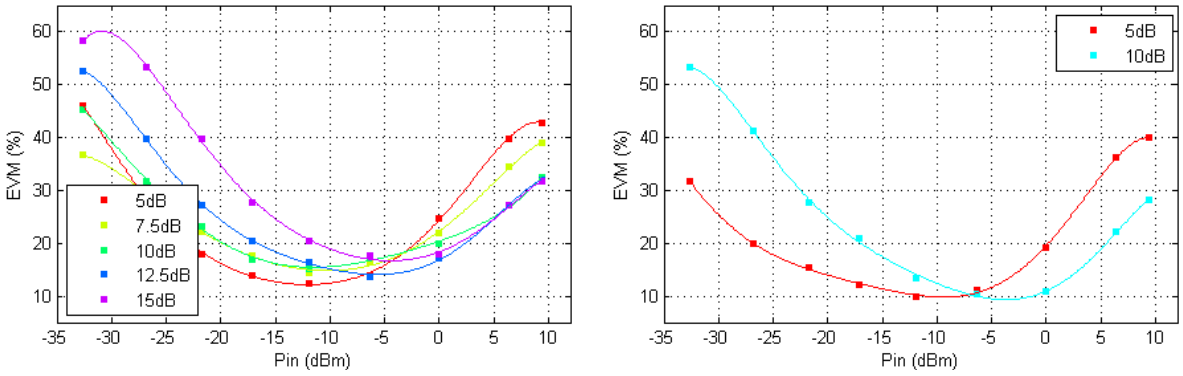

Figure 4.47: EVM at the output of the RoF link as a function of the laser input power for different optical losses. The laser bias current is fixed to 6mA on the left and to 11mA on the right.

In figure 4.47, when the optical losses increase, the laser input power leading to the minimal EVM is shifted towards high RF powers. As a result, at 6mA, when the optical losses increase, the minimum observed EVM is degraded due to laser saturation. In fact, for high input powers, the EVM curves tend to overlap: the non-linearities come from the laser, particularly beyond 10dB optical losses. On the contrary, for low laser input powers, the thermal noise is dominant as the EVM increases strongly with the optical losses. At 11mA, non-linearities observed for high laser input power come from the reception stage. In fact, the EVM decreases strongly with the optical losses and the minimum observed EVM is not degraded when the optical losses increase since the laser saturation observed at 6mA has been pushed away taking back-off from the threshold current. To be more accurate, clipping seems to occur at 6mA.

In order to prove that the minimum observed EVMs are degraded at 6mA due to laser clipping, the VI-Systems L-I curve has been studied. In figure 4.47, the EVM is optimal for a laser input power of -12dBm (RMS power). In this case, the peak power is equal to 1dBm as the PAPR of the OFDM signal is 13dB. Since $P = UI = RI^2$, the peak current of the signal modulating directly the laser is:

$$I_{peak} = \sqrt{\frac{10^{-3} \times 10^{P_{peak}/10}}{Z_{in}}} = \sqrt{\frac{10^{-3} \times 10^{1/10}}{50}} = 5mA. \tag{4.25}$$

This value is the limit current before clipping[5] as the bias current has been fixed to 6mA and the threshold current is equal to 1mA. Figure 4.48 expands the study to include the different optical losses. For example, for 10dB optical losses, the minimum observed EVM correspond to 5mA for a laser bias current of 6mA, and to 10mA for a laser bias current of 11mA: from the laser point-of-view, the optimal modulation depth is not obtained at 6mA, therefore the measured EVM is higher, 15.2% versus 10.4%. As shown on the left figure, clipping becomes acceptable only to compensate high optical losses (>10dB), when the thermal noise dominates.

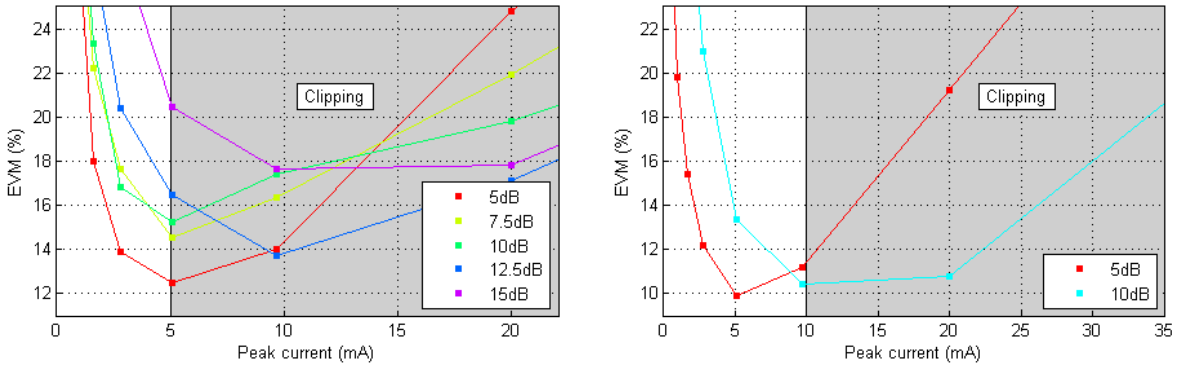

Figure 4.48: EVM as a function of the peak current modulating the laser for different optical losses. The grey color corresponds to areas where clipping occurs.

4.3.3 Finisar FP and PIN photodiode at 1310nm

Tests on the Finisar FP laser and the Finisar PIN photodiode working at 1310nm have been carried out using the setup described in figure 4.41, without external amplifier at the output of RoF link, even if the link gain is low. First, the EVM has been measured as a function of the laser input power for different laser bias currents and for optical losses fixed to 1.5dB.

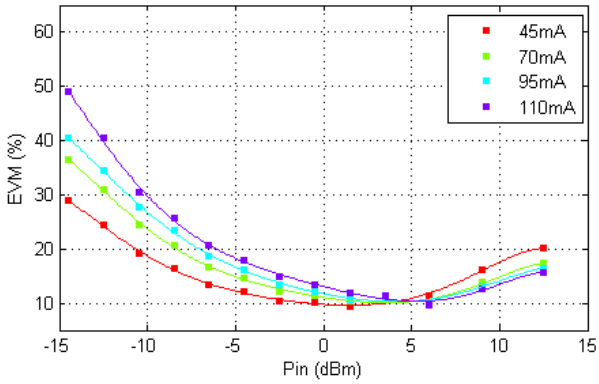

Figure 4.49: EVM at the output of the RoF link as a function the laser input power for different bias current. The optical losses are fixed to 1.5dB.

In figure 4.49, the minimal observed EVM, obtained for a bias current of 45mA and a laser input power of 2dBm, is equal to 9.3%. This is a great improvement compared to the point-to-point Finisar RoF link at 850nm where the best EVM was 13.4%. Other measurements have been realized at 45mA, but with different optical losses as shown in figure 4.50.

[5]Assuming that the peak current corresponds to negative value.

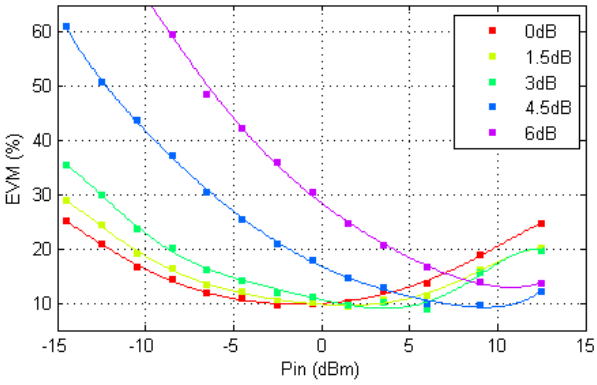

Figure 4.50: EVM at the output of the RoF link as a function the laser input power for different optical losses. The laser bias current is fixed to 45mA.

Figures 4.49 and 4.50 can be analyzed following the same reasonings as previously. The interesting point is the comparison of the point-to-point configuration with the previous results since the FP laser has not a good transverse multimode behavior to be used with an optical splitter (see section 3.7.3). Thus, the red curve of figure 4.50 is compared to the cyan curve of figure 4.42, i.e. a EVM of 9.3% is compared to an EVM of 14.6%. To understand what makes the difference, an analysis based on the analog characterizations of the chapter 3 has been performed.

First, the ratio between laser input power and RIN is studied. At 1310nm, the laser input power leading to the optimal EVM is higher, -1dBm versus -14dBm, but this performance is compensated by a lower laser gain response (evaluated in equivalent electric considering an ideal photodiode), -34.9dB versus -21.1dB. Thereby, the same dynamic optical power is emitted. Besides, the RIN is better at 850nm despite the presence of a peak at 4.5GHz due to the laser frequency relaxation oscillation: in the radio band, up to -125.5dB/Hz is observed at 850nm for a laser bias current of 6.5mA versus -122.5dB/Hz at 1310nm for a bias current of 45mA. As a result, the RIN cannot explain why better results are obtained at 1310nm.

Concerning the shot noise, the optical power received by the photodiode working at 1310nm is higher than the power received at 850nm: the power received at 850nm equals to (6.5mA-0.9mA)×0.08mW/mA=0.45mW and at 1310nm to (45mA-11mA)×0.018mW/mA=0.61mW.

As the RIN and the shot noise values are lower at 850nm, only the thermal noise can make a difference. In fact at 1310nm, the thermal noise, expressed as a NEP, is 20pW/$\sqrt{Hz}$ lower than at 850nm for a similar dynamic optical power received by the photodiode. However, in point-to-point configurations, the thermal noise is generally not the limiting parameter. So, to understand why better results have been obtained at 1310nm, the influence of non-linearities been have investigated.

Concerning the gain compression, the input P1dB equals to -15dBm at 850nm and to +5dBm at 1310nm. The necessary power back-off experimentally measured for the radio signal is 8dB when the PAPR of this OFDM signal is 13dB (see appendix A.3.2). As a consequence, the required back-off is clearly not respected at 850nm with a laser input power of -14dBm, even if this last one leads to the optimal EVM value. At 1310nm, the power back-off seems enough since no EVM improvement has been observed increasing the optical losses, on the contrary of the RoF link at 850nm where the built-in TIA limits the performances.

Concerning the non-linearities, the input IP3, measured with two tones separated of 10MHz (a typical space between OFDM subcarriers), is equal to -4.6dBm for a point-to-point RoF link at 850nm (tones centered at 3GHz) and to 12.5dBm at 1310nm (tones centered at 5GHz). The back-off is equal to 9.4dB at 850nm and to 13.5dB at 1310nm, i.e. a fundamental tones to intermodulation products ratio of 18.8 and 27 dB, respectively.

The point-to-point RoF link composed of the FP laser at 1310nm and of the InGaAs PIN photodiode with a built-in TIA is clearly more linear than the RoF link at 850nm. Consequently, better results are obtained at 1310nm.

4.3.4 U-L-M VCSEL and Finisar PIN photodiode at 850nm

At last, a RoF link working at 850nm and composed of the U-L-M VCSEL and of the Finisar photodiode has been tested. This is an important evaluation since the U-L-M VCSEL will be implemented in the RoF transducers developed in the ORIGIN project. Moreover, the study of the Finisar photodiode, for a second time (the first study is the configuration 1), but under the lighting of a different laser, is convenient to decorrelate some effects, or confirm previous conclusions.

Figure 4.51 presents the EVM measured at the output of the RoF link as a function of the laser bias current. The optical losses are fixed to 10dB because the optical power emitted by the U-L-M VCSEL goes up to 5.4dBm at 10mA (3.5mW) and induces a saturation of the Finisar photodiode. In fact, according to its datasheet, the maximum incident optical power accepted by the photodiode is 0dBm average (1mW) and 4dBm peak (2.5mW).

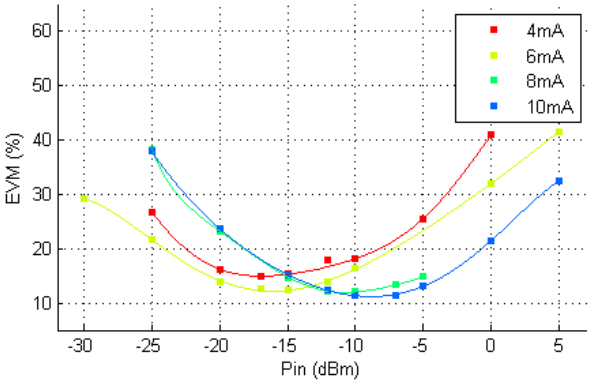

Figure 4.51: EVM at the output of the RoF link as a function the laser input power for different bias current. The optical losses are fixed to 10dB.

The minimal observed EVM is 11.2%. This measure has been obtained for a laser bias current of 10mA and a laser input power of -8.8dBm. Compared to the ∼4% EVM of the direct link at IF, the EVM has increased by 7.2%.

Previously, with the Finisar VCSEL, the optimal laser input power was nearly independent of the bias current. Here, it increases with the bias current, and in an important proportion between 6 and 8 mA, partly because the slope efficiency decreases strongly after 6mA as seen in section 3.2.1. In fact, the slope efficiency between 7 and 10mA is closer to 0.31W/A than to 0.42W/A, i.e. a S21 difference of:

$$\Delta\, S21 = 20 \cdot log(0.42) - 20 \cdot log(0.31) = 2.64dB. \tag{4.26}$$

However, even if the laser input power compensates the laser response evolution, the difference observed in figure 4.51 is not totally explained. In fact, the optimal laser input powers are -16dBm at 6mA and -11.5dBm at 8mA, which represents a difference of 4.5dB. About 1.9dB is not explained (4.5 − 2.6), as previously with the Finisar VCSEL (figure 4.43). Maybe that the increase of the shot noise with the bias current has also an impact.

In a second time, different optical losses are tested in order to simulate point-to-multipoint and multipoint-to-multipoint architectures. Figure 4.52 shows the measured EVM as a function of the optical losses and for a laser bias current fixed at 6mA, in the middle of the L-I curve.

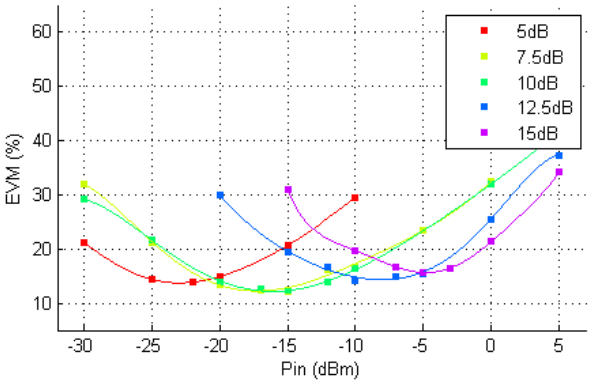

Figure 4.52: EVM at the output of the RoF link as a function the laser input power for different optical losses. The laser bias current is fixed to 6mA.

As previously, the shapes of the curves remain globally the same, only the laser input powers leading to the minimal EVMs are shifted towards high RF powers when the optical losses increase. Previously, when a Finisar laser was used in front of the Finisar photodiode, an optimal EVM was obtained for 7.5dB optical losses and -4dBm laser input power. Now, with the U-L-M laser in front of the Finisar photodiode, the optimal EVM is also obtained for 7.5dB optical losses, but with a -17dBm laser input power. These results correspond to similar dynamic optical powers at the input of the photodiode (expressed in equivalent electric):

$$P_{RF\ Finisar} = -4dBm + 20 \cdot log(0.08) + 10 \cdot log10(60/50) - 2 \times 7.5 = -40.15dBm \quad (4.27)$$

$$P_{RF\ U\text{-}L\text{-}M} = -17dBm + 20 \cdot log(0.42) + 10 \cdot log10(50/50) - 2 \times 7.5 = -39.54dBm \quad (4.28)$$

but to different optical power at the input of the photodiode:

$$P_{opt\ Finisar} = 10 \cdot log(0.08 \times (6.5 - 0.9)) - 7.5 = -10.99dBm \quad (4.29)$$

$$P_{opt\ U\text{-}L\text{-}M} = 10 \cdot log(0.42 \times (6.0 - 0.7)) - 7.5 = -4.02dBm \quad (4.30)$$

In this case, the optimal EVM (in relative) only depends of the RF power at the input of the photodiode, about -40dBm, and it is independent of the laser characteristics (since for 7.5dB optical losses the lasers are more linear than the photodiode as shown in figures 3.32 and 3.33) and of the optical power received by the photodiode. Nevertheless, for a given architecture, i.e. with fixed optical losses as above, the laser response plays an important role on the value of the EVM (in absolute). For example, the U-L-M VCSEL, that has a high slope efficiency, has to be modulated with low RF power, which leads to an important impact of the RIN on the SNR. In addition, this high slope efficiency leads to a high optical power and so to a strong shot noise at the reception. This remark is confirmed by figure 4.51 where the increase of the laser bias current, that decreases the slope efficiency, improves the EVM.

Lastly, multipoint-to-multipoint architectures working at 850nm and using a 16x16 splitter, i.e. approximatively 12dB optical losses, can be compared on the basis of optoelectronic components. For the RoF link composed of the U-L-M VCSEL and of the Finisar photodiode, an EVM of 14.3% is observed, while EVMs of 14.9% and 10.5% had been obtained for RoF link based on Finisar and VI-Systems components, respectively. The VI-Systems laser and photodiode provide better results as the VCSEL is not biased in the middle of its L-I curve, but at 11mA. At 6mA, VI-Systems components provide an EVM of 14.1%.

4.3.5 Optical issues in an optical multipoint-to-multipoint architecture

The setup of figure 4.53 highlights the optical issues that occur when an optical multipoint-to-multipoint RoF architecture is used. In this system, four Finisar VCSELs at 850nm are connected to a 4x4 optical splitter based on 50μm MMF, designed for transmission at 850 and 1310 nm, and having 6.33dB average insertion losses (table 3.10). The bias current of each VCSEL is adapted to target an optical output power of -3.25dBm, but only the first laser is modulated by a radio signal fixed to -3.8dBm, a value in agreement with figure 4.45. At the reception, a Finisar PIN photodiode detects the transmitted signals for analysis under Matlab and calculation of the link EVM.

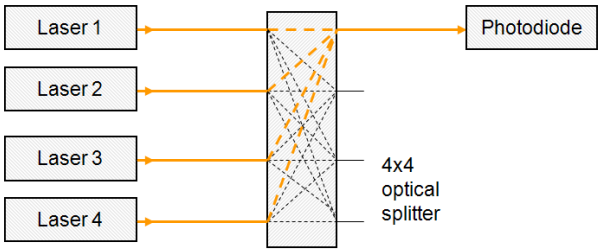

Laser	P_{RF}	I_{Bias}	$P_{opt,out}$
1	-3.8dBm	6.5mA	-3.25dBm
2	-	7.2mA	-3.22dBm
3	-	6.9mA	-3.22dBm
4	-	6.7mA	-3.26dBm

Figure 4.53: Experimental setup to highlight optical heterodyning interferences.

The four scenarios presented in figure 4.54 were tested. In the first case, only one laser is switched-on; the photodiode receives only the useful signal. In the second case, a second laser is turned-on adding RIN, enhancing shot noise, and generating optical heterodyning signals. The third and fourth cases correspond to the simultaneous operation of three and four lasers, respectively.

In figure 4.54, interferences appear on the radio spectrum from the moment that several lasers are turned-on simultaneously. These interferences, particularly intense at the lasers ignition, move along the spectrum over the time, and sometimes they overlap with the radio signal. Besides, as shown in the last spectrum of figure 4.54, where the first case with only one laser turned-on is compared to the fourth case with all lasers are turned-on, the global noise level increases due to the addition of each laser RIN and to the excess of shot noises as the received optical power increases.

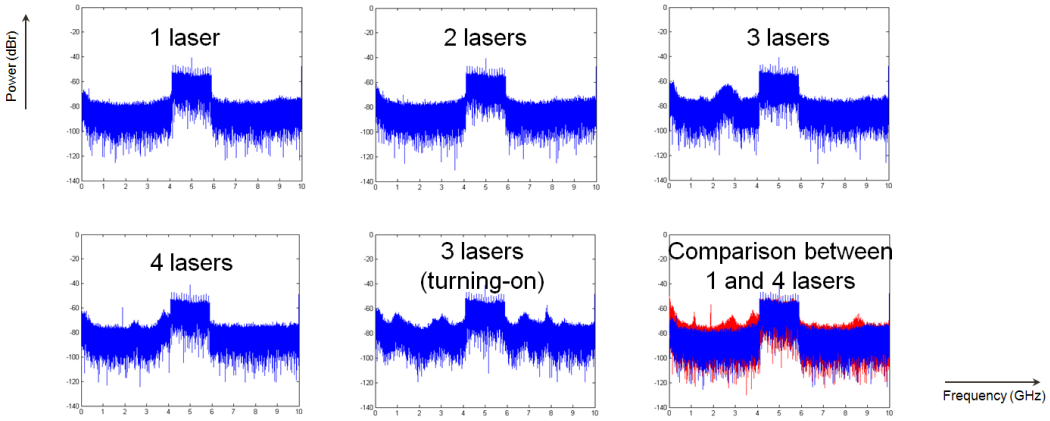

Figure 4.54: Shape of the radio spectrum with optical heterodyning interferences as a function a the number of active lasers.

At 850nm-wavelength, two laser having wavelengths separated by $\Delta\lambda = 0.012$nm generate an electrical signal at a 5GHz frequency. Indeed, from the formula $\nu = c/\lambda$, it can be written that $\Delta\nu = c \cdot \Delta\lambda/\lambda^2$ with λ the wavelength, ν the optical wave frequency and c the light velocity; therefore:

$$\Delta\lambda = \frac{\lambda^2 \cdot \Delta\nu}{c} = \frac{(850\ 10^{-9})^2 \cdot 5\ 10^9}{3\ 10^8} = 0.012nm \tag{4.31}$$

Additionally, the undesired generated microwave frequency is time-varying due to unstabilized lasers temperatures.

Lastly, table 4.3 shows the obtained EVM values at the output of the optical splitter over 20 measurements and for the four scenarios. The average EVM is calculated ignoring the extreme or unusual values highlighted by an asterisk. These errors can occur from a bad demodulation process under Matlab, but they seem particularly connected to lasers optical heterodyning that overlap the OFDM signal at the detection. Indeed, the number of erroneous values increases with the number of lasers operating simultaneously.

Moreover, the average EVM value increases of 3% between the scenarios 1 and 4 due to the addition of RINs and the excess of shot noise. Consequently, the previous results taking into account only optical losses were too optimistic.

Table 4.3: EVM measurements for a 4x4 optical multipoint-to-multipoint RoF architecture in IF.

Measure	1 laser	2 lasers	3 lasers	4 lasers
1	13.82	15.11	15.69	14.89
2	16.52	14.50	16.60	13.83
3	12.57	14.27	16.45	14.63
4	13.39	14.07	15.75	15.57
5	13.22	23.68 *	17.45	14.75
6	13.30	13.90	33.82 *	38.89 *
7	15.57	24.16 *	16.15	14.36
8	13.53	13.62	30.07 *	17.53
9	34.11 *	13.73	34.22 *	18.46
10	15.28	14.51	18.88	26.71 *
11	13.09	12.57	30.78 *	19.77
12	12.79	42.25 *	18.45	16.82
13	12.91	13.76	15.75	18.94
14	12.33	14.96	17.25	17.27
15	15.30	15.22	15.5	17.91
16	12.44	13.79	15.83	38.96 *
17	13.17	13.50	37.97 *	16.31
18	12.67	13.92	15.55	16.25
19	43.70 *	13.30	24.97 *	25.51 *
20	12.51	16.20	18.12	15.95
Average	13.58	14.17	16.68	16.45

4.3.6 Summary

Different RoF links working at IF have been analyzed. The results are summarized in table 4.4. As a general conclusion, it has been shown that the laser bias currents have to be fixed in the middle of their L-I curve, or slightly above preferably, and that the laser input powers have to be optimized depending on the optical losses. In fact, the RF power is increased to compensate the optical losses, the photodiodes being the components that generally saturate first, more precisely their built-in TIA. In fact, the power adaptation is less pronounced for a RoF link composed of VI-Systems components that not have a built-in TIA but an external LNA.

Table 4.4: Summary of the characterizations of the RoF links at an IF of 5GHz, for bias currents in the middle of the L-I curves (not necessarily the optimal value). Two configurations are considered, a point-to-point (0dB) and a multipoint-to-multipoint (12dB). Optical losses, bias currents, laser input powers, EVMs, and theoretical gains are provided.

Configuration	Finisar VCSEL at 850nm + GaAs PIN photodiode + TIA	VI-Systems VCSEL at 850nm + GaAs PIN photodiode + G_{ext}	Finisar FP laser at 1310nm + InGaAs PIN photodiode + TIA	U-L-M VCSEL at 850nm + Finisar GaAs PIN photodiode + TIA
Point-to-Point	0dB 6.5mA -13.4dBm 14.7%	0dB Photodiode Saturation	1.5dB 45mA +2dBm 9.3%	0dB Photodiode saturation
Gain / Output power	3.3dB / -10.1dBm	-	-11.4dB / -9.4dBm	-
Multipoint-to-Multipoint (16x16)	12.5dB 6.5mA +1.0dBm 14.9%	12dB 6mA -5.7dBm 14.1%	12dB Poor transverse multimode character	12.5dB 6mA -8dBm 14.3%
Gain / Output power	-21.7dB / -20.7dBm	4.9dB / -0.8dBm	-	-6.5dB / -14.5dBm
Optimal results	7.5dB 6.5mA -4.0dBm 9.3%	10dB 11mA -3.7 9.4%	3dB 45mA +3.6dBm 9.0%	10dB 10mA -8.8dBm 11.2%
Gain / Output power	-11.7dB / -15.7dBm	8.9dB / 5.2dBm	-17.4dB / -13.8dBm	-21.5dB / -30.3dBm

The optical losses are imposed by the chosen architecture, point-to-point or multipoint-to-multipoint, and in this latter case by the size of the optical splitter. For an optical multipoint-to-multipoint architecture, the Finisar VCSEL and PIN photodiode working at 850nm will be preferred because they allow building a RoF link without external amplifier and because they lead to a minimum EVM of

about 10% (4x4 or 8x8) or 15% (16x16). For a link without optical loss, the Finisar FP laser and PIN photodiode at 1310nm seem a good choice for the same raison than previously, and because these components are more linear than the Finisar ones at 850nm.

Figure 4.55 provides the tolerance of each parameter of the RoF link based on Finisar components working at 850nm. As an example, for a point-to-point link and an EVM target fixed to 16%, the RF power can be set to -15dBm and the bias current can vary between 3.8 and 7.3 mA, or the bias current can be set to 6mA and the RF power can vary between -17.2 and -11.3 dBm. Now, in a multipoint-to-multipoint architecture using a 4x4 optical splitter, i.e. 7dB optical losses (6dB plus 1dB additional loss for fiber bends), for a laser bias current set to 6.5mA and a EVM target fixed again to 16%, the RF power can vary between -9.8 and 1.2dBm. This dynamic range of 11dB shows again that the Finisar components at 850nm are more adapted to a multipoint-to-multipoint infrastructure (6dB dynamic range for a point-to-point link).

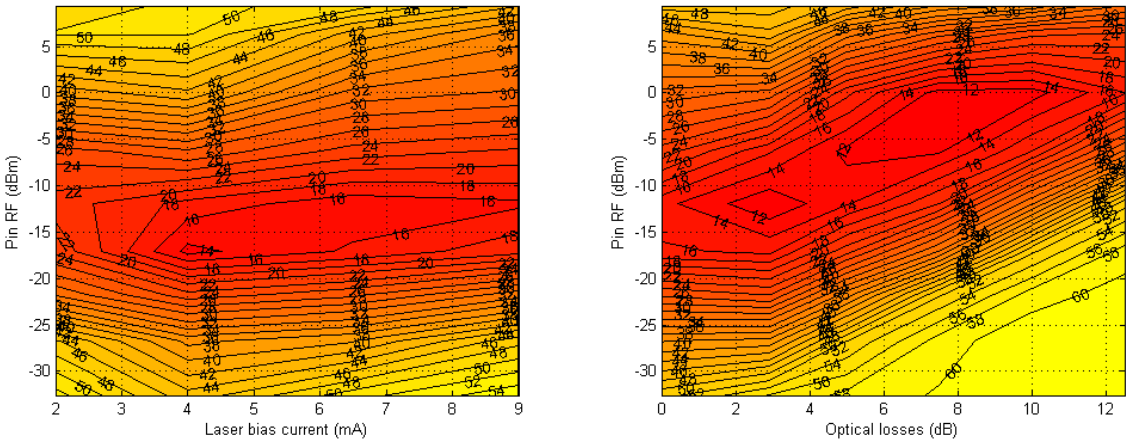

Figure 4.55: 2D map representing with different color the EVM (%) at the output of a RoF link composed of a VCSEL and of a PIN photodiode working at 850nm from Finisar. On the left, the optical losses are fixed to zero and, on the right, the laser bias current is fixed to 6.5mA.

For architectures using an optical splitter, optical issues occur, in particular optical heterodyning signals appear. These issues would question the EVM values measured in these last sections for the multipoint-to-multipoint architectures and taken into account only the optical losses. Actually, these results are still valid since solutions exist to turn-off unused lasers and emit a radio signal only where it is useful and when it is necessary. These solutions are presented in chapter 5.

In the next sections, different RoF architectures will be tested and compared using the Finisar VCSELs working at 850nm with the PIN photodiodes with a built-in TIA. In fact, these low cost components provide good performances. Besides, the tests could not be carried out with other components: for the optical multipoint-to-multipoint architecture, the Finisar components working at 1310nm do not have a very strong multimode transverse character to be used with multimode optical splitters, the VI-Systems components at 850nm are not sufficient in number to realize a complete setup, and the U-L-M photonics components have been received only recently. Nevertheless, for the electrical multipoint-to-multipoint architectures, some tests will also be realized using the Finisar components at 1310nm because they are efficient in point-to-point configuration, i.e. without optical loss, and they provide a good linearity.

4.4 Digital characterization of point-to-point and multipoint-to-multipoint optical RoF architectures

Optical RoF architectures including also propagations through the air are now considered. The point-to-point and multipoint-to-multipoint infrastructures can be studied together, a multipoint-to-multipoint architecture being a point-to-point link with additional optical losses corresponding to the presence of a NxN optical splitter. Consequently, in this section, point-to-point links with different optical losses will be characterized (in section 4.4.3). As seen previously, the RF power at the laser input has to

be optimized according to the optical losses. Therefore, an AGC amplifier will be set in front of each directly modulated laser to fix the input power, independently of the free-space losses, even if this amplifier increases a little the complexity and the cost. To simplify the RF chain and because the system does not know necessarily the optical losses there are in a HAN, a RoF link with a fixed laser input power will also be characterized (in section 4.4.2), always taking the linear attenuation, the fiber bend and the optical connection losses into account. Above all, an electrical repeater at 60GHz, without RoF link, is considered (in section 4.4.1) to have a reference value.

The tests will be mainly carried out using QPSK modulation, with only the downlink as the experimental setups are symmetric.

4.4.1 Electrical repeater at 60GHz

The setup in figure 4.56 represents an electrical repeater, with no RoF link. This setup allows to check if the electrical system tolerates the losses and the distortions corresponding to two air hops.

The upper part of figure 4.56 differs slightly from the setup of figure 4.28 as the different architectures have been characterized at different times, several months apart. At the radio transmitter, the power at the input of the horn antenna is again fixed to 8.6dBm, i.e. an EIRP of 28.6dBm. However, at the radio receiver, two LNAs are cascaded now, one before the millimeter-wave variable attenuator, and one after. Finally, for a radio link at 60GHz with a single hop, an EVM of 14% is obtained for free-space distances included between 5 and 10 m (comparable to 13% in section 4.2.2).

In the electrical repeater, after a first hop in free-space, the signal is picked up by a horn antenna, with 20dB gain, and boosted by a 28dB LNA plus a 32dB HPA. The received radio signal is then down-converted to IF at 4.5GHz and attenuated by 15dB in order to simulate the behavior of a RoF link. After that, the IF signal is up-converted to realize the second hop at 60GHz and to be captured by the radio receiver where the signal is sent on an oscilloscope and analyzed under Matlab. It has to be noted that the two millimeter-wave oscillators of the electrical repeater used for the down and up conversions, at 55.2GHz, are built using a 13.8GHz RF oscillator multiplied by four.

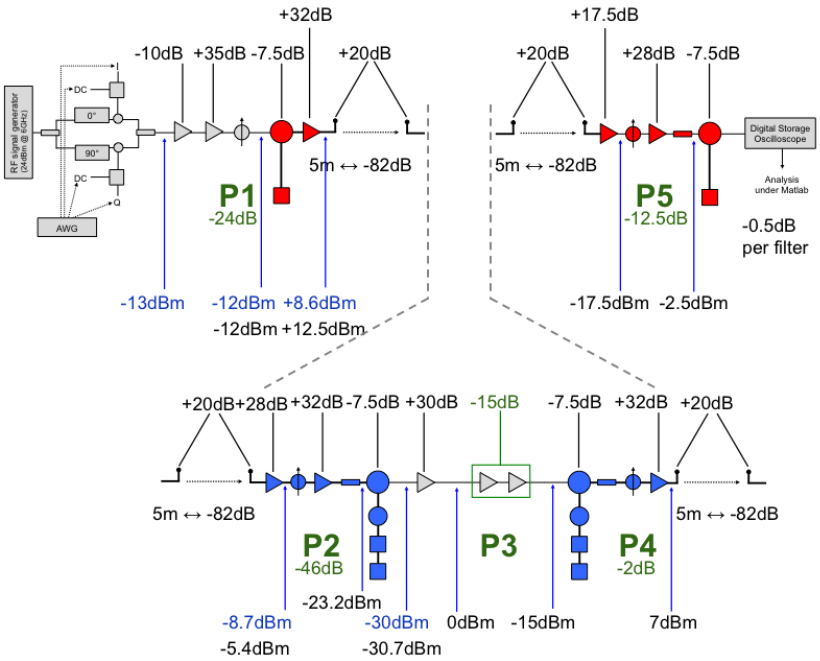

Figure 4.56: Experimental setup of the electrical repeater at 60GHz and its link budget. The points P1 to P5 indicate the different variable parameters. Above the figure are reported the RF gains, below in blue the measured power values, and below in black the theoretical power values.

Variable attenuators allow the optimization of the power applied not only to the input of each mixer (parameters P1, P2, P3, and P5), but also to the input of the horn antenna placed before the second air

hop (parameter P4). The adjustment of these parameters is not detailed here, only their optimal value is provided. More details can be found in ORIGIN deliverable 6.1 [146]. Lastly, the free-space distances are fixed to 5m for the two hops.

Figure 4.56 also provides the link budget. It can be noted that the EIRP for the second hop is 27dBm, a value that respects the regional rules. The gains indicated in the figure have been measured, except the ones of the antennas and mixers whose values have been extracted from their datasheet. Concerning the mixers, -7.5dB gain seems too optimistic with regard to the power measured in front of the horn antennas: for instance, 8.6dBm against 12.5dBm expected for the first mixer. Nevertheless, the down-converters and up-converters accept a large range of input powers, between -23 and 0 dBm (figure 4.30) and between -20 and -8 dBm (figure 4.57), respectively.

In fact, figure 4.57 represents the measured EVM as a function of the parameter P3: for a RF power fixed to 0dBm at the input of P3 and a RF attenuation between 8 and 20 dB, the EVM remains below 20%. Consequently, at the output of the IF link, it is not necessary to use an AGC amplifier as mixers operate over a wide dynamic. Nevertheless, some tests with an AGC amplifier will be performed in section 4.4.4 for confirmation.

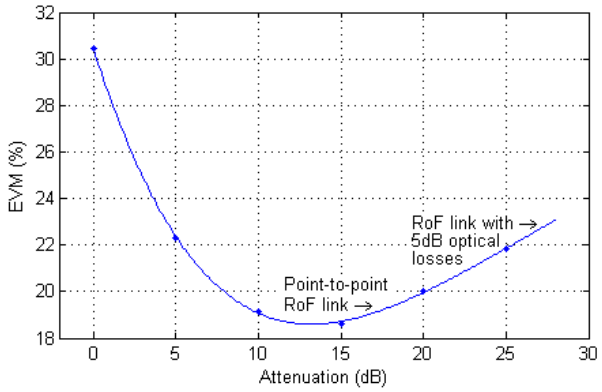

Figure 4.57: EVM as a function of P3 parameter, i.e. the RF attenuation applied to the input of the up-converter. The P3 input power is fixed to 0dBm.

The P3 parameter simulates the response of a RoF link. For example, the S21 parameter of a Finisar RoF link at 850nm, with a laser bias current of 6.5 mA, has been evaluated experimentally in 3.3.2. It has a flat response in the radio band and is equal to:

$$S21\ [dB] \simeq 2 \times optical\ losses - 3 \tag{4.32}$$

To optimize the IF power applied to the up converter, an attenuation of 15dB is necessary for P3, which corresponds approximately to a zero-optical loss RoF link. Indeed, with 0dBm before P3 (figure 4.56), an attenuation of 14dB is needed to obtain the optimum IF power at the laser input (figure 4.45). Moreover, 3dB RF losses are added for the S21 parameter (equation 4.32). So, to simulate a RoF link without optical loss, 17dB RF attenuation is required (14dB + 3dB). This point has been reported in figure 4.57.

Finally, as shown in figure 4.32, for the configuration of figure 4.56, the measured EVM is 18.5%. Thanks to the different optimization of the RF power along the link, the introduction of the electric repeater has increased the EVM by only 4.5%.

4.4.2 Point-to-point architecture (optical tunnel)

The point-to-point RoF link depicted in figure 4.58 is considered. It reuses the setup of figure 4.56 replacing P3 by an optical link with a 300m-length OM3 MMF and the optoelectronic components from Finisar: the VCSEL at 850nm and the PIN photodiode with a built-in TIA. To simplify the RoF transducers design, the laser input power is fixed to -10dBm, the optimal value to minimize EVM for 4dB optical losses according to figure 4.45.

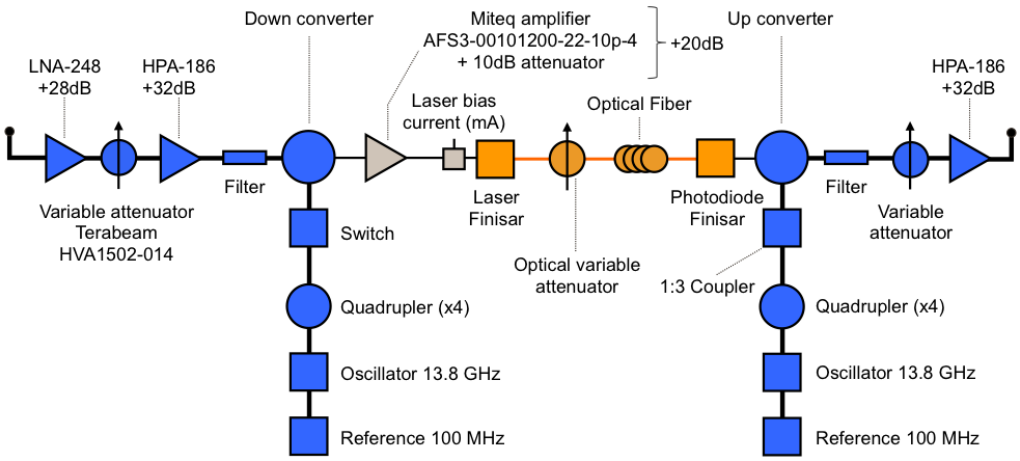

Figure 4.58: The RoF tunnel placed between the two hops in the air.

Table 4.5 provides the EVM as a function of the optical losses, from 2.2dB, the cumulative losses of the 300m-length MMF and of the intrinsic losses of the optical attenuator, to 6dB, the maximum considered value for a point-to-point link, a pretty much important value for an optical HAN, even considering the optical connections and the fiber bends. The measured EVM remains always below 25%, i.e. a theoretical BER better than $3.2 \cdot 10^{-5}$ in QPSK or an error-free transmission after coding implementation. Lastly, table 4.5 can be compared to figure 4.57: as expected, the EVM is slightly higher when a RoF link is introduced.

Table 4.5: EVM as a function of the total optical losses for 300m-length MMF and two 5m-length air hops.

Optical losses (dB)	EVM (%)
2.2	24.32
3.2	23.94
4.2	24.15
5.2	25.05

As a reminder, no AGC amplifier has been used here. As a consequence, in the worst case with 6dB optical losses the photodiode delivers an IF power of -22.7dBm at the up-converter: the EIRP is then 19.3dBm for the second hop and the received power after 5m free-space propagation is -62.7dBm. This last value respects the sensitivity of -65dBm of WirelessHD commercial devices, see section 4.7.

Figure 4.59 represents the received radio spectrum, for 3.2dB optical losses and 23.94% average EVM. The two LOs of the optical tunnel working at the same frequency, 55.2GHz, the center received frequency is:

$$6GHz + 53.7GHz\ (1^{st}\ LO) - 52.6GHz\ (4^{th}\ LO) = 7.1GHz \tag{4.33}$$

Because of the large bandwidth of the standard channel, the received spectrum is bumpy: a ripple of about 7dB is introduced by the cumulated frequency responses of the RF circuits along the system. Nevertheless, the 16 pilot subcarriers are clearly visible.

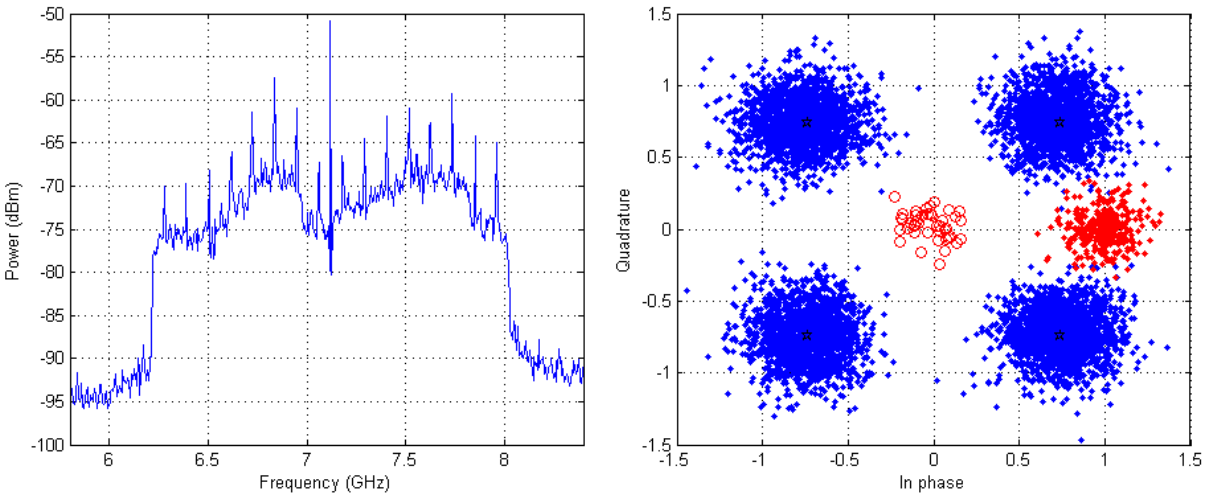

Figure 4.59: OFDM signal measured at the receiver on the left (using a spectrum analyzer), and the corresponding QPSK constellation diagram on the right. The instantaneous EVM value is 22.37%.

The signal has a bandwidth of 1.815GHz with an average level of -72dBm. As the bandwidth used on the spectrum analyzer is 30kHz (RBW and VBW), the signal power is:

$$P = -72 + 10 \cdot log\left(\frac{1.815\ 10^9}{30\ 10^3}\right) \simeq -24dBm. \tag{4.34}$$

This spectrum measurement was performed after the other measures, when the second amplifier and the variable attenuator of the reception stage have been removed (ORIGIN deliverable 6.1, [146]). So, this value of -24dBm is consistent with the figures 4.56 and 4.58. The average noise level of the spectrum analyzer is -96dBm, and the minimal carrier-to-noise ratio (CNR) is:

$$CNR_{min} = -75 - -90 = 15dB \tag{4.35}$$

A single RoF link with two different hop lengths has been also investigated. The configuration is the same as above, except that the P2 and P5 parameters presented in figure 4.56 are optimized according the first and the second air distances. The measurements show identical results for 5m+2m and 2m+5m configurations. No free-space link configuration leads to larger damages on the system.

Table 4.6: EVM as a function of the free-space length for optical losses fixed to 3.2dB.

Distance	EVM (%)
5m + 5m	25,47
5m + 2m	22,52
2m + 5m	22,47

For the worst wireless link, the EVM, close to 25.5%, corresponds to a BER of 4.25 10^{-5} in QPSK.

4.4.3 Optical multipoint-to-multipoint architecture

To extend the radio coverage to the whole home, multipoint-to-multipoint architectures have to be considered. Compared to a point-to-point link, a multipoint-to-multipoint system operates with higher optical losses, up to 12dB for a 16x16 optical splitter. Thereby, the setup has to be optimized in order to enhance its performances. Firstly, the setup of figure 4.58 has been simplified, some high attenuation values allowing to remove some amplifiers like the second millimeter-wave HPA (HPA-186, G=32dB) after the first hop in free-space. Secondly, the measures have been automated using Matlab to find within 0.5dB the optimal laser input power for each optical losses value. The experimental setup is depicted in figure 4.60, and the millimeter-wave radio transmitter and receiver, not represented in the figure, are those of figure 4.28.

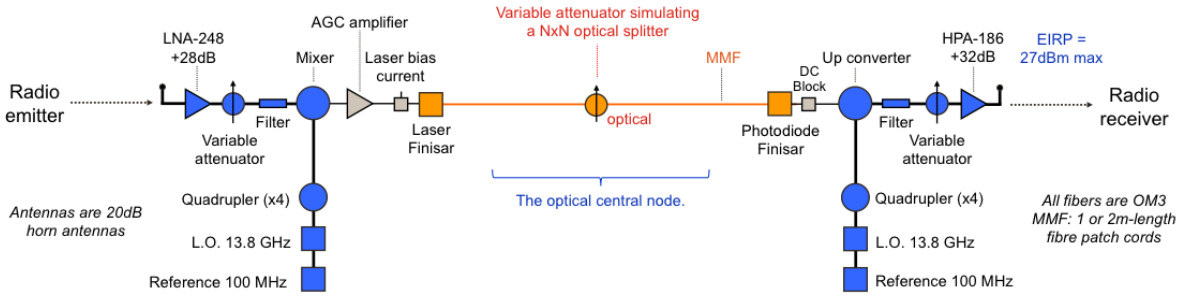

Figure 4.60: The experimental optical multipoint-to-multipoint architecture, with the E/O part of the RoF transducer on the left, the variable optical splitter in the middle simulating a NxN splitters, and the O/E part of the RoF transducer on the right.

In the RoF link of figure 4.60, the optical attenuator substitutes the presence of the NxN splitter. As the gain at the output of the RoF link is not adjusted, the EIRP is maximal for a point-to-point link, i.e. 27dBm, then the EIRP decreases with the optical losses. This point will be discussed in detail in the next section.

First of all, a 4x4 optical splitter with 7dB optical losses is simulated to extract some statistical measurements from a QPSK modulated OFDM signal. The setup, with two 5m-length hops in the air, is adjusted in order to obtain an optimal configuration and an EVM equal to 22.75%.

In the initial back-to-back configuration of table 4.1 the PAPR was equal to 13dB, but now it has decreased to reach 11.15dB: either the noise power has increased, or clipping has occurred; or both. This is confirmed by the voltage distribution of the OFDM signal that deviates from the Gaussian distribution, but does not converge toward the distribution of a third-order IM as shown in figure 4.61. Nonetheless, the channel is not a perfect AWGN channel. Figure 4.62 also confirms this point.

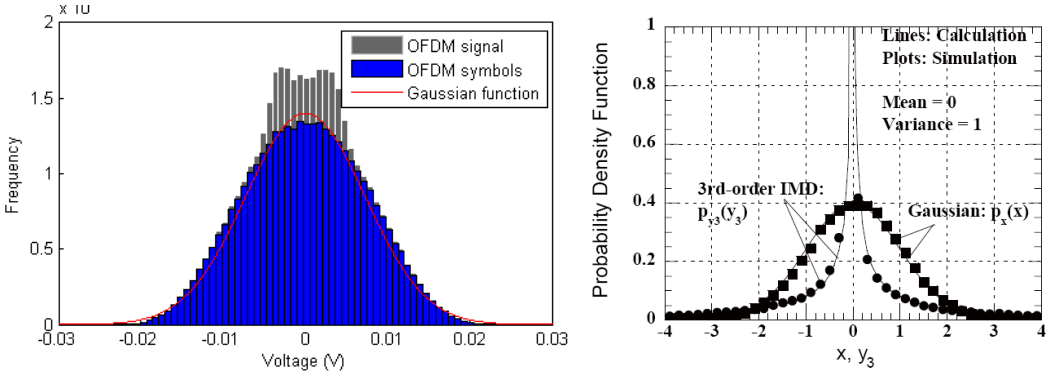

Figure 4.61: Voltage distribution of the OFDM signal and Gaussian fitting on the left, and theoretical curves for gaussian and third-order IM on the right, from [30].

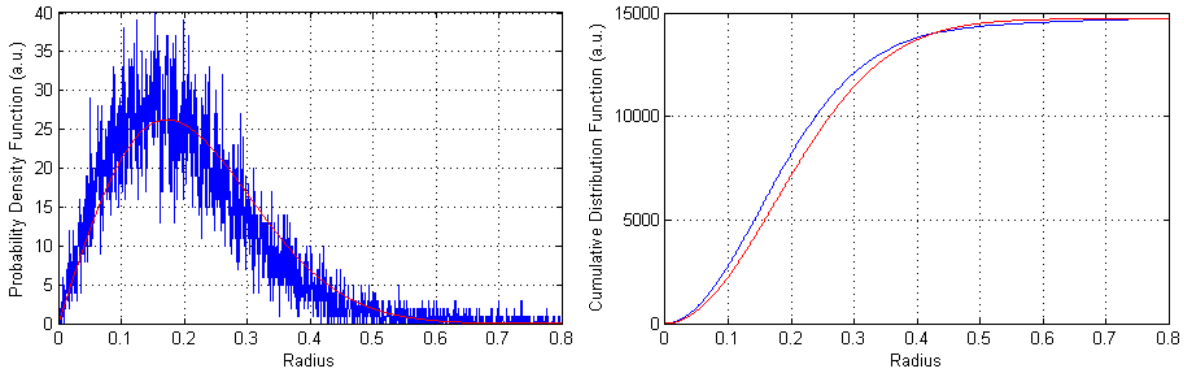

Figure 4.62: Probability density and cumulative distribution functions of the points of the constellation diagram and Rayleigh fitting.

Figure 4.63 represents the EVM as a function of the optical losses for different free-space distances. The curves have similar shapes, with only light differences probably due to antenna alignments. For a given free-space distance, the best EVM is stable and included between 20 and 22%. Compared to the free-space radio link at 60GHz, the EVM has increased by 6% to 8%. However, the measured EVM is particularly bad for a first 5m-length hop and a second 10m-length hop. This measure has been performed again optimizing the antennas alignments, but the same result has been obtained: a second 10m-length hop seems to be the system limit, even if an EVM of 25% remains a good value corresponding to a BER of $3.2 \cdot 10^{-5}$.

For zero optical loss, i.e. a point-to-point RoF link, the EVM is high because the PIN photodiode with the built-in TIA saturates and the RIN and the shot noise are significant at the reception. Between 4 and 9dB optical losses, the measured EVM is optimal as predicted in section 4.3. After 10dB the EVM increases due to dominant thermal noise and laser saturation as an important RF laser input power is needed to compensate the optical losses. The bad EIRP at the output of the second link also explains these bad results after 10dB.

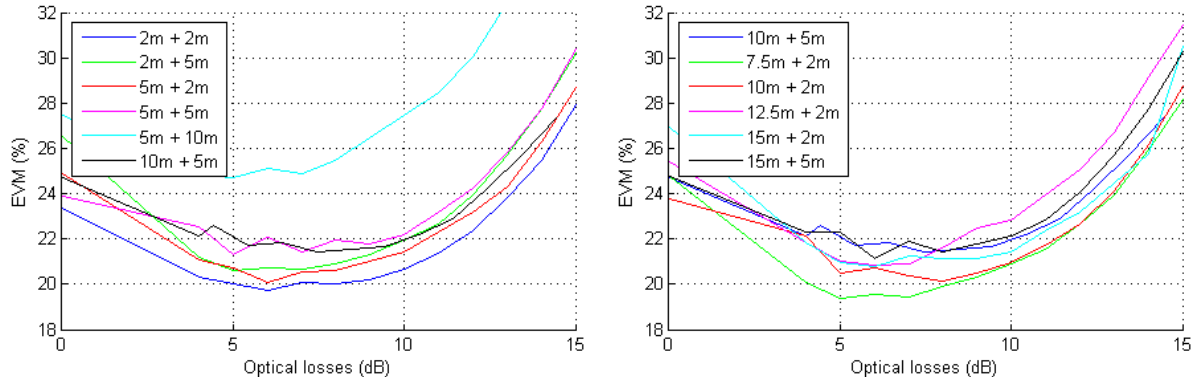

Figure 4.63: EVM for a QPSK modulated signal as a function of the optical losses for different free-space distances. Theoretically, the EVM is identical for 16-QAM modulated signals.

In this automated setup, for each measure, the laser input power leading to the minimum EVM has been noted and reported in figure 4.64 as a function of the optical losses and of the free-space distances. Finally, the higher the optical losses are, the higher the RF laser input power must be. The curves can be well fitted by a straight line of slope of 1.3. This coefficient is, as expected, the same that the one found in figure 4.45: consequently, it has been already justified.

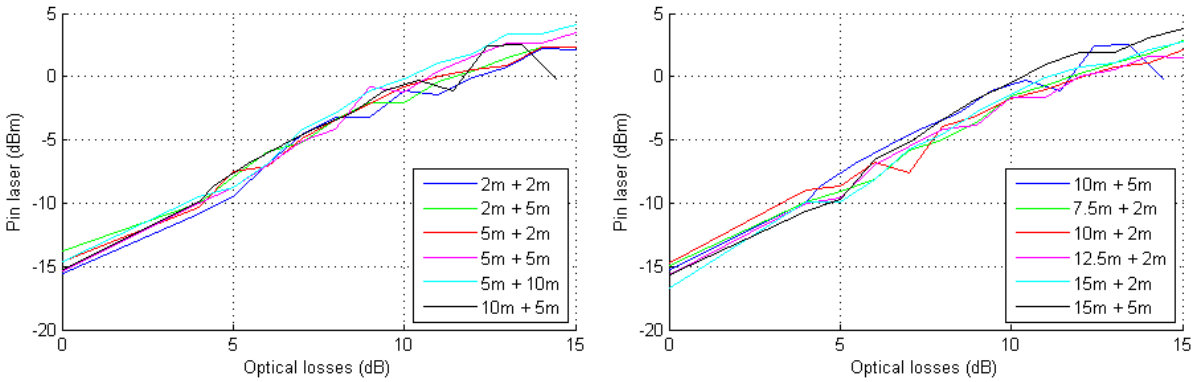

Figure 4.64: Optimal laser input power leading to the minimal EVM as a function of the optical losses and for different free-space lengths.

Finally, figure 4.65 represents the experimental BER as a function of the average EVM for QPSK and 16-QAM modulated signals. The theoretical BER curves for an AWGN channel have also been added. Even if the multipoint-to-multipoint RoF architecture is not a perfect Gaussian noise channel, the differences between the experimental and theoretical BER seem more linked to the use of bad reference points in the EVM calculation (section 4.1.4) and to a bad channel recovery under Matlab (section 4.1.4). In fact, the measured error remains the same than the one observed for a back to back link.

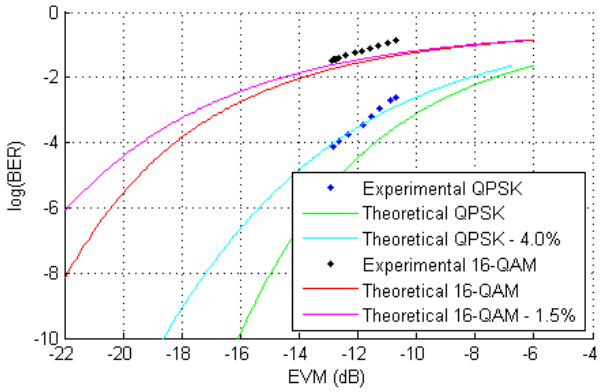

Figure 4.65: EVM versus BER for an optical multipoint-to-multipoint architecture with a 5m-length first hop plus 2m-length second hop.

4.4.4 Performances with an Automatic Gain Control amplifier at the output of the RoF link

Until now the RF power at output of the RoF link was not adjusted. Consequently, when the optical losses increased, the RoF output power decreased. A double penalty was applied to the radio signal as it was degraded firstly by the RoF link losses and secondly by the limited radiated power for the second hop in free-space. Therefore, in this section, new architectures with an AGC amplifier at the output of the RoF link are proposed[6]. As shown in figure 4.66, two solutions will be compared, one with the AGC amplifier inserted in the centimeter-wave part, at IF, and one with the AGC amplifier inserted in the millimeter-wave part, after the up-conversion stage.

[6]Speaking of "AGC amplifier" is a kind of misnomer (an abusive word) as in the experimental setups realized in this section, the AGC amplifiers consist in amplifiers followed by variable attenuators. This term is use for the sake of simplicity.

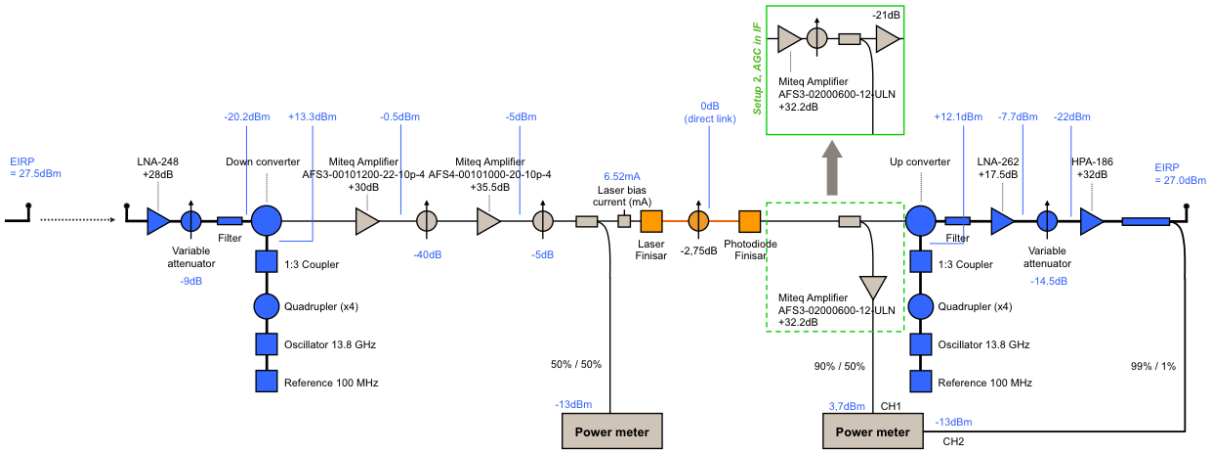

Figure 4.66: Experimental setups of the RoF architectures with an AGC amplifier at the output of the optical link, either in millimetric part or in centimetric part. The link budget is also provided for a RoF link without optical attenuator as described in blue and for a millimeter-wave AGC amplifier.

In figure 4.66, a link budget has also been calculated for a RoF link without optical loss, with a millimeter-wave AGC amplifier, and with two 5m-length hops. The EIRPs of the first and second hop in free-space equal to 27.5dBm and 27dBm, respectively, so the gain of the optical tunnel, 81.5dB, compensates completely the free-space propagation of the the first hop. Concerning the detail of the gain values, they are not always precisely determined. In fact, some values can be debated as the power level just before the down-converter: it has been measured at -20.2dBm for a -16dBm theoretical value:

$$\begin{aligned} P &= 27.5dBm\ (EIRP_1) - 82dB\ (5m\text{-}length\ hop) + 20dB\ (horn\ antenna) \\ &\quad + 28dB\ (LNA\text{-}248) - 9dB\ (variable\ RF\ attenuator) - 0.5dB\ (filter) \\ &= -16dBm \end{aligned} \tag{4.36}$$

Not represented in figure 4.66, -12.2dBm has been measured just before the millimeter-wave attenuator at the radio receiver (figure 4.28) when -6.5dBm was expected:

$$\begin{aligned} P &= 27dBm\ (EIRP_2) - 82dB\ (5m\text{-}length\ hop) + 20dB\ (horn\ antenna) + 28dB\ (LNA\text{-}248) \\ &= -6.5dBm. \end{aligned} \tag{4.37}$$

In these two previous comparisons between theoretical and experimental measures, differences of 4.2 and 5.7 dB have been observed. Probably the free-space losses are too optimistic regarding the figure 4.31 and the antenna alignment.

Optical losses are then added. To optimize EVM, the laser input power is adjusted manually according to figure 4.45 where $P_{in\ laser} \simeq -12.5dBm + optical\ losses$. Table 4.7 provides the corresponding RoF link budget measures.

Table 4.7: The RoF link budget.

$P_{in\ laser}$ (dBm)	-13.00	-9.93	-7.61	-4.43	-2.57	-0.06	2.30	4.97
Optical losses (dB)	0	2.75	5	7.5	10	12.5	15	17.5
$P_{out\ photodiode}$ (dBm)	-18.5	-20.4	-22.2	-24	-26.6	-28.4	-31	-32.9
$S21_{RoF}$ (dB)	-5.50	-10.47	-14.59	-19.57	-24.03	-28.34	-33.30	-37.87
$2 \times$ optical losses $+ 3$ (dB)	3	8.5	13	18	23	28	33	38

If theoretically the RoF S21 parameter equals twice optical losses plus the optoelectronic components response ($\simeq$-3dB), in practice a small difference is observed. Indeed, for high optical losses the S21 parameter is in agreement with the theory, but for low optical losses, the photodiode with its built-in TIA saturates. In fact, the input P1dB for a link without optical loss is -15dBm (section 3.5.4). Besides, the output power evolves linearly, with a slope of 0.8dB. Consequently the output EIRP evolves also linearly as shown in figure 4.67 in which the cumulated gain observed between the photodiode output power and the EIRP is equal to 45.5dB.

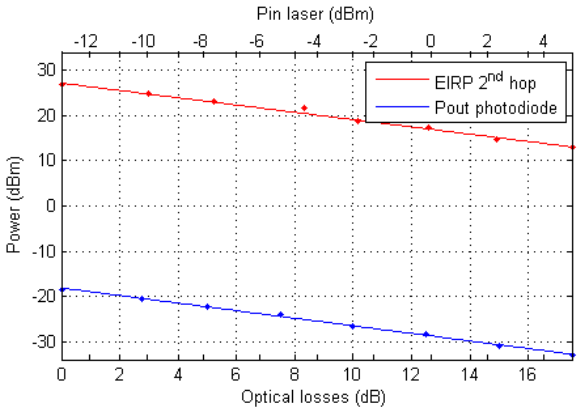

Figure 4.67: RF power at the photodiode output and the EIRP of the second air hop for a RoF architecture without AGC amplifier implemented at the output of the optical link as a function of the optical losses.

Now, in order to keep an EIRP value of 27dBm on the second hop, a variable attenuator at the output of the RoF link is tuned according to the optical losses, either the one in the millimeter-wave part of figure 4.66, or the one located in the centimeter-wave part and described in the green square of the same figure. A third configuration without AGC amplifier has also been tested, the corresponding setup being the one described in section 4.4.3. The performances of these three multipoint-to-multipoint architectures are summarized in figure 4.68. It has to be noted that for all measurement points the EIRP is checked precisely using a powermeter.

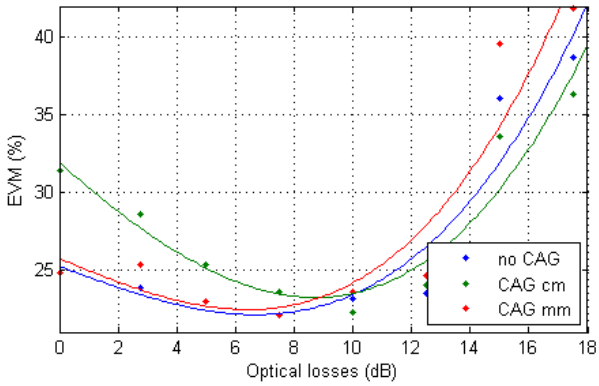

Figure 4.68: EVM at the output of multipoint-to-multipoint RoF links as a function of the optical losses for different AGC configurations.

As shown in figure 4.68, the implementation of an AGC amplifier provides only little improvements, the AGC working at IF given even worse results due to the new components inserted. In fact, the RF amplifier located at the output of the photodiode saturates: without optical loss, 13,7dBm is obtained at the output of the amplifier when the output P1dB equals 10dBm (from datasheet). Anyway, what matters is the enhancement of the architecture for high optical losses, beyond 10dB, when the EVM becomes higher than 25%, i.e. a BER higher than $3.2 \cdot 10^{-5}$. And in this case, a sufficient power back-off from the P1dB is met. As a consequence, the EVM gain in figure 4.68 does not justify the establishment of an AGC amplifier. After 10dB optical losses, the SNR is already significantly degraded at the output of the photodiode, and it is not possible to improve it by an amplifier. Finally, in the next sections, no AGC amplifier will be used at the output of the RoF links.

4.4.5 Highlighting the optical issues

The behavior of the multipoint-to-multipoint RoF architecture has also been characterized in real conditions using a 4x4 optical splitter instead of an optical attenuator. As the used VCSELs present a large number of transverse modes, the MMF splitter is well balanced, with 6.3dB (±0.5dB) insertion losses.

The setup depicted in figure 4.69 has been characterized in terms of EVM using the millimeter-wave radio emitter and receiver of figure 4.28 and two 5m-length hops in the air. Only the main (first) laser is modulated by an input QPSK radio signal. The laser bias current is fixed to 6.5mA whereas the bias currents of the three other VCSELs are adapted to target the same optical output power of -3.25dBm. In the EVM measurements, four scenarios were tested. In the first case, only one laser is switched-on, the photodiode receiving only the useful signal. In the second case, a second laser is turned-on adding RIN, increasing the shot noise, and generating optical heterodyning signals. The third and fourth cases correspond to the simultaneous operation of three and four lasers respectively.

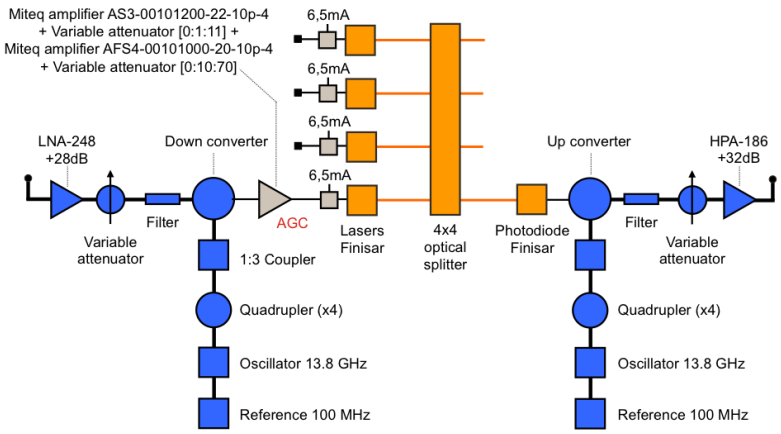

Figure 4.69: Experimental setup of a multipoint-to-multipoint RoF architecture with a 4x4 optical splitter and four lasers active simultaneously.

Table 4.8 shows the obtained EVMs at the output of the architecture over 22 measurements and for the four scenarios. The average EVM is calculated ignoring the extreme or unusual values highlighted by an asterisk. These errors can occur from a bad demodulation process under Matlab, but they seem particularly connected to laser optical beatings (as previously in section 4.3.5). Indeed, the number of erroneous values increases with the number of lasers operating simultaneously because interferences arising from optical beatings occur and overlap with the received OFDM signal.

Table 4.8: EVM measurements for a multipoint-to-multipoint RoF architecture with a 4x4 optical splitter.

measure	1 laser	2 lasers	3 lasers	4 lasers
1	21.63	25.85	28.57	26.28
2	21.84	23.62	34.86 *	25.61
3	21.77	23.05	28.87	25.02
4	21.57	26.35	28.92	32.26 *
5	21.36	23.76	28.32	27.05
6	21.79	24.21	28.58	26.14
7	33.58 *	47.18 *	32.13 *	33.39 *
8	21.46	29.23 *	32.49 *	23.99
9	21.93	25.79	28.46	24.97
10	22.04	26.81	27.92	27.67
11	21.94	26.21	27.74	27.38
12	41.71 *	26.59	41.05 *	27.96
13	21.63	25.80	27.66	36.80 *
14	21.85	25.95	27.45	27.34
15	23.56	27.19	27.98	27.77
16	22.21	26.81	30.38 *	27.61
17	22.91	26.22	44.63 *	40.58 *
18	21.65	31.72 *	27.80	27.67
19	21.24	27.56	27.98	34.11 *
20	21.70	26.75	24.92	27.67
21	21.70	27.36	24.90	28.60
22	21.84	23.87	28.25	25.25
Average	21.88	25.78	27.77	26.71

The average EVM increases with the number of laser used simultaneously, for example +5% is observed between the scenarios 1 and 4. As already explained, the simultaneous operation of multiple lasers induces the addition of each laser RIN and an excess of shot noises as the received optical power increases. However, it has to be noted that the EVM value found in section 4.4.3, when the splitter is simulated by optical losses, is recovered as long as only one laser is turned-on.

If the optical multipoint-to-multipoint RoF architecture seems advantageous due to a unique and passive component, it induces optical beating at the detection between the different active lasers, which create interferences over the radio signal. In the next section, an electrical version of the multipoint-to-multipoint RoF architecture is proposed to avoid these additional distortions, then it is compared to its optical counterpart in terms of performances.

4.5 Digital characterization of electrical multipoint-to-multipoint RoF architecture

4.5.1 Finisar VCSEL and PIN photodiode at 850nm

In the optical architecture, the central node is simply composed of a NxN optical splitter. In the electrical architecture, this setup is more complex with a photodiode for the O/E conversion, then two 1xN RF splitters (as no NxN RF splitter is commercially available) and at last a laser for the E/O conversion. Thus, in this electrical central node, the OFDM signal remains in IF and the same optoelectronic components than those used on the RoF transducer sides are used: the VCSELs working at 850nm and the GaAs PIN photodiodes with a built-in TIA from Finisar. The tested electrical multipoint-to-multipoint architecture is represented in figure 4.70. As previously, in front of each laser, RF amplifiers cascaded by variable attenuators adjust the RF power to minimize the EVM and variable optical attenuators in the point-to-point RoF links simulate the linear attenuation and the bend losses, and in the same time improve in part the EVM as the built-in TIA of the PIN photodiode saturates at low optical losses. The optical losses are fixed to 3.6dB and 5.3dB for the first and the second RoF links, respectively. The tests have been conducted with a QPSK modulated signal and two 5m-length hops in the air.

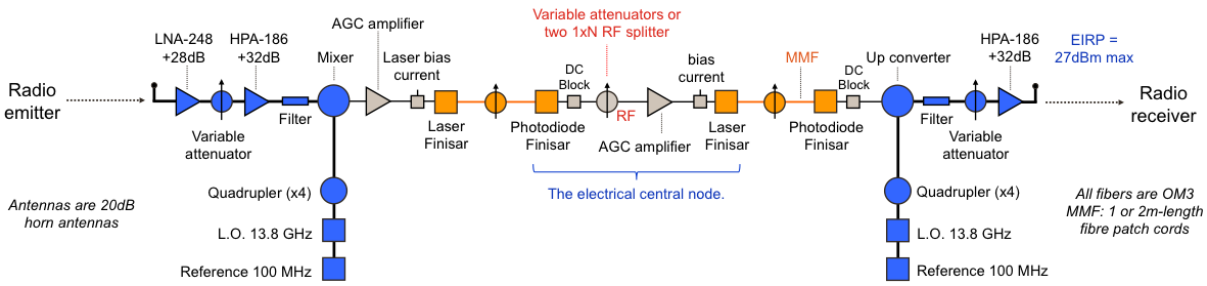

Figure 4.70: Experimental electrical multipoint-to-multipoint architecture, with the Rx part of the RoF transducer on the left, the electrical central node in the middle with two 1xN RF splitters or a variable RF attenuator to simulate them, and the Tx part of the RoF transducer on the right.

In figure 4.70, an AGC amplifier, composed of a RF amplifier followed by a variable attenuator, is located at the output of the two 1xN RF splitters. With regard to the Friis' formula (equation 4.38), the choice of this location seems irrelevant since minimizing the total noise factor involves to position the amplifiers before the attenuators.

$$F = F_1 + \frac{F_2 - 1}{G_1} + \frac{F_3 - 1}{G_1 G_2} + \frac{F_4 - 1}{G_1 G_2 G_3} + ... + \frac{F_n - 1}{G_1 G_2 G_3 ... G_{n-1}} \tag{4.38}$$

where

- F is the total noise factor of a RF chain composed of n elements.
- F_k is the noise factor, in linear, for the k^{th} device.
- G_k is the power gain, in linear, of the k^{th} device.

Nevertheless, in a well designed setup, only the noise factor of the first element is significant, here the first millimeter-wave LNA at the output of the horn antenna. On the contrary, at the central node, i.e.

in the middle of the transmission chain, the noise factor terms are neglected. This latter point has been confirmed by experimental results: EVM is exactly the same for an AGC amplifier before or after the two 1xN splitters. Finally, it has be chosen to place this AGC amplifier after the two 1xN splitters to create a symmetry with the centimeter-wave part of the RoF transducers and so to simplify the design of the central node. However, an amplifier taking place between the two 1xN splitter should also be a judicious solution as the amplifier stage will be merged into a unique point for all RoF links and the cost will be reduced.

Concerning the EVM measurements, firstly, a variable RF attenuator is used to simulate the different sizes of the two 1xN RF splitters. Results are reported in blue in figure 4.71; previous results concerning the optical architecture are also added in the same figure, in red, in order to draw a parallel between these two different technical solutions.

With attenuators simulating the splitters, a straight line is obtained for the electrical architecture, with constant EVMs around 28% as an AGC amplifier is used after the RF attenuator to optimize laser input power. As a reminder, in the optical architecture a bell-shaped curve has been measured with minimum EVMs around 22% for optical losses varying between 5 and 9dB. Thus, the two curves of figure 4.71 meet for 14dB losses, corresponding theoretically to a 16x16 optical splitter plus 2dB additional losses for fiber bends, or two 1x4 electrical splitters plus 1dB additional loss. Before 14dB losses, the optical architecture is more advantageous than its electrical counterpart thanks to an EVM lower than 28%. For reference, an EVM of 32.5% corresponds to a BER of 10^{-3} in QPSK (equation 4.8).

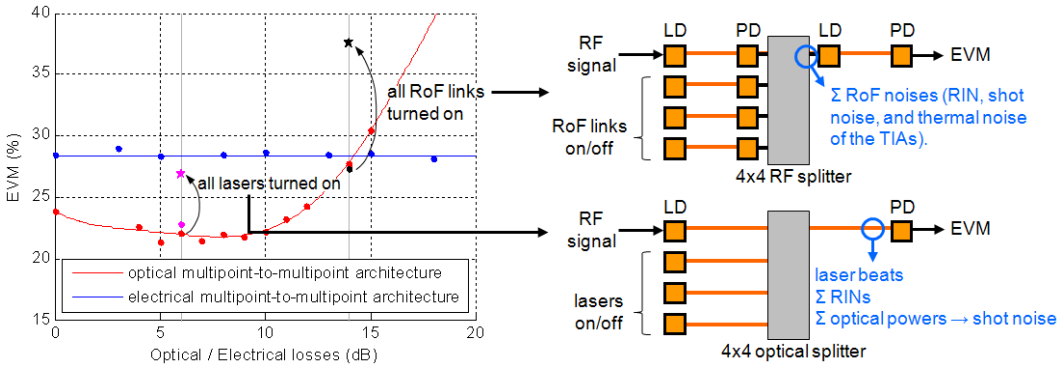

Figure 4.71: Comparison between optical and electrical architectures, with splitters simulated by attenuators (red and blue) and two 5m-length hops in the air. The performances with real splitters have also been added to the plot (magenta and black) with only the main (first) laser modulated by a QPSK radio signal.

The voltage distribution of the QPSK modulated signal received at the output of the electrical multipoint-to-multipoint architecture is represented in figure 4.72. It has to be noted that it differs largely from a normal distribution, consequently, the relationship among BER, EVM and SNR will be difficult to establish.

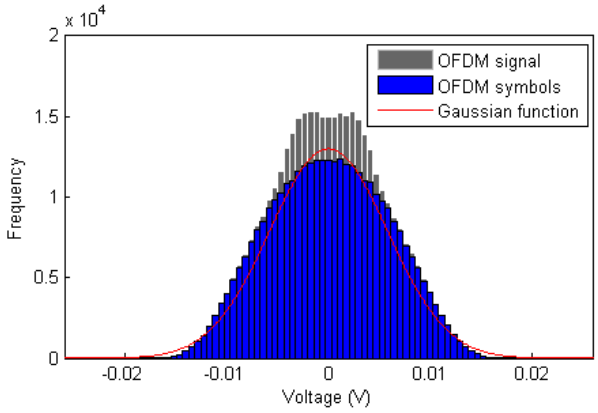

Figure 4.72: Voltage distribution of the OFDM signal and Gaussian fitting (5m+5m and 6dB RF losses).

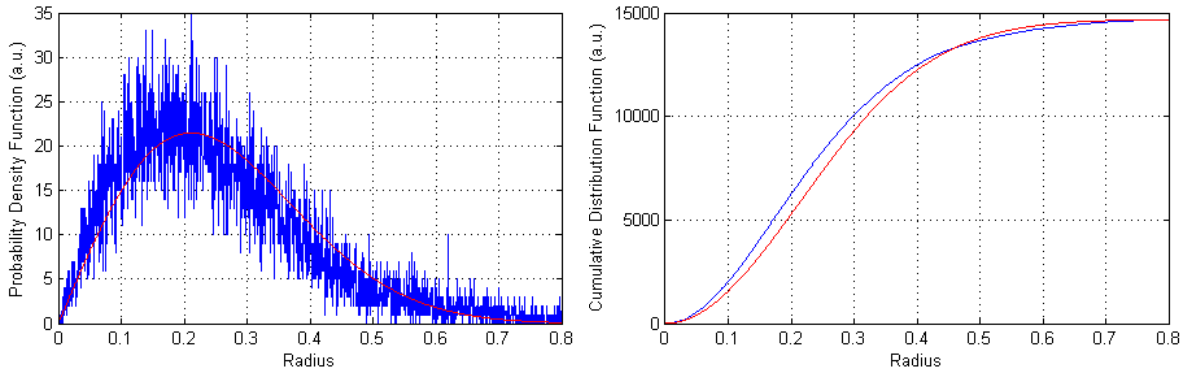

Figure 4.73: Probability density and cumulative distribution functions of the experimental constellation diagram points and Rayleigh fitting (5m+5m and 6dB RF losses).

Figure 4.74 represents the experimental BER as a function of the average EVM for a QPSK modulated signal. The theoretical BER curves of an AWGN channel are also added, but as predicted, the experimental results present strong differences with the theory. This difference seems more pronounced than previously, in part because the measured EVMs are important and that bad reference points are used in the EVM calculation, see part 4.1.4.

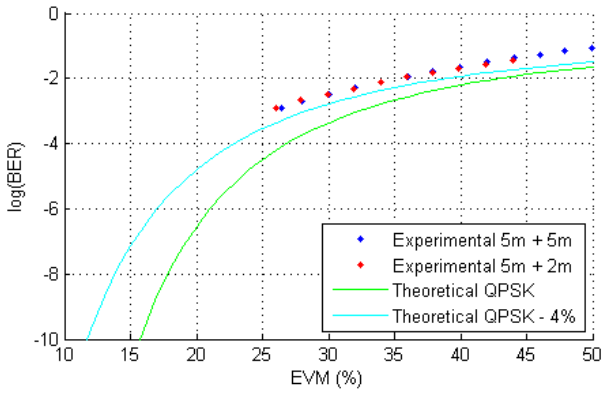

Figure 4.74: EVM versus BER for an electrical multipoint-to-multipoint architecture with a 5m+2m and a 5m+5m configurations.

Additional measures have been performed over different air propagation distances and reported in table 4.9. Firstly, the EVM increases with the distance, and secondly, an effect of symmetry is observed: the EVM value is the same for the 2m+5m and 5m+2m configurations. There is not a hop in free-space that penalizes the system more than another.

Table 4.9: EVM over an electrical multipoint-to-multipoint RoF architecture simulated with 6dB RF losses, i.e. two 1x2 RF splitters. As shown in figure 4.71, results will be the same for other architecture sizes.

free-space distance	2m+2m	2m+5m	5m+2m	5m+5m
EVM	26.01%	27.34%	27.18%	28.05%

Tests have also been conducted using two 1x4 splitters instead of attenuators for the two 5m-length hops. As shown in table 4.10, the two 1x4 splitters used correspond to 14.0dB (±1dB) electrical losses. The previous EVM value is recovered as long as only one laser is turned-on, but when the setup is completed with other RoF links, the resulting average EVM increases to 37.6%. This result has been reported in figure 4.71, in black, and details are given in tables 4.11 and 4.12 for different optical configurations. Among other things, if only the photodiodes of each point-to-point RoF links are turned-on, the EVM value equals to 30.4% meaning that the impact of the thermal noises is low: RIN and shot noise are the main reasons for these deteriorated results.

Table 4.10: Behavior of the two cascaded 1x4 RF splitters. The insertion losses are included between 13.0 and 15.1dB, with an average of 13.8dB when theoretical losses are equal to 12dB.

	1	2	3	4
1	-13,6	-13,8	-14,1	-13
2	-13,7	-13,4	-13,5	-15,1
3	-13,4	-13,1	-14,4	-14
4	-14,8	-13,4	-13,1	-14,7

EVM measurements are provided in tables 4.11 and 4.12 for different optical configurations, i.e. different optical losses and different optoelectronic components turned-on/off. As the number of additional optical attenuators being on hand is limited, the optical losses inserted in the additional RoF links of the table 4.12 are obtained by 1x2 optical splitters. The additional optical losses values are then 4.12, 3.51 and 3.87dB, respectively. Concerning the reported EVMs, only an average value is given as the measurements are stable over a long time. Each laser has a 6.5mA bias currents and each photodiode a 3.3V bias voltage. On the three additional RoF links, numbered #2, #3 and #4, -3, -3.69 and -3.99dBm optical powers are respectively emitted.

Table 4.11: EVM on the electrical multipoint-to-multipoint RoF architecture, with no optical loss on the additional RoF links.

RoF link 1	RoF link 2	RoF link 3	RoF link 4	EVM
on	off	off	off	27.33%
on	on	off	off	32.06%
on	off	on	off	34.95%
on	off	off	on	31.15%
on	on	on	off	36.56%
on	on	on	on	37.57%

Table 4.12: EVM on the electrical multipoint-to-multipoint RoF architecture, with ∼3dB optical losses on the additional RoF links.

RoF link 1	RoF link 2	RoF link 3	RoF link 4	EVM
on	off	off	off	28.60%
on	on	on	on	35.97%

Between tables 4.11 and 4.12, the performances are improved by ∼1.5% as the SNR at the output of the architecture is higher. Indeed, the noises coming from the additional RoF links decrease by a factor $2 \times optical\ losses$ for the RIN and by a factor $1 \times optical\ losses$ for the shot noise (formulas 3.16 and 3.17).

Lastly, figure 4.75 shows the effect of the additional RoF links on the received radio spectrum. The two architectures, optical and electrical, are represented to draw a parallel. In the optical architecture, the corresponding EVM values are 22% for one laser turned-on and 26% for all lasers turned-on. In the electrical architecture, the EVM values are 28% and 36%, respectively. These radio spectrums show clearly that the SNR values are correlated to the EVM values.

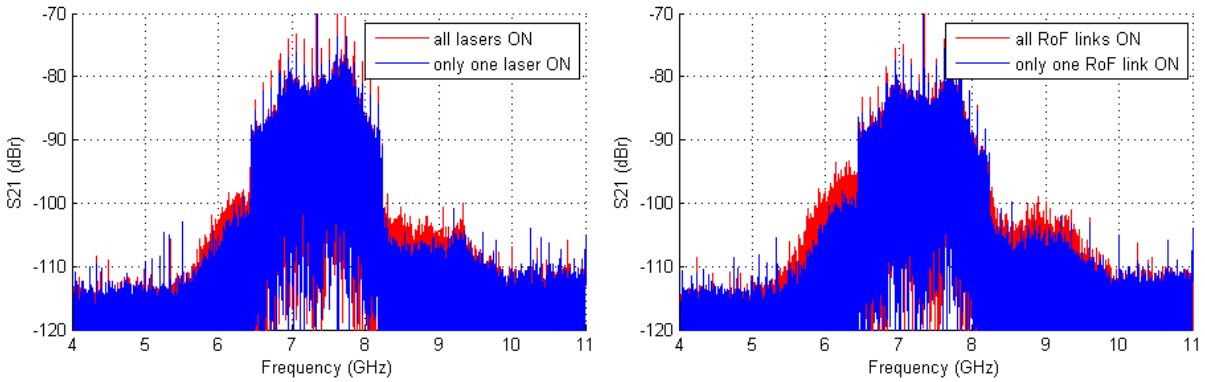

Figure 4.75: The received radio spectrum for the optical multipoint-to-multipoint architecture on the right and its electrical counterpart on the left.

4.5.2 Finisar FP and PIN photodiode at 1310nm

A comparison between optical and electrical multipoint-to-multipoint architectures has been realized in terms of EVM. The electrical solution presents the advantage to be laser beats independent, but it induces higher EVM values. Consequently, an optical link based on more linear components, the FP laser working at 1310nm and the PIN photodiode with a built-in TIA from Finisar, is proposed in order to improve the performances. The tests have been conducted only on the electrical multipoint-to-multipoint architectures as the FP laser at 1310nm induces bad uniformity of the optical splitter.

As the used optoelectronic components provide good performances in point-to-point configuration, no optical losses are inserted in the RoF links. The laser input powers are fixed to -1dBm for the first link and -0.9dBm for the second, the optimal values to minimize the EVM, see figure 4.50. It has to be noted that the components of the first RoF link are the ones digitally characterized in section 4.3 and analog characterized in chapter 3. However, it is difficult to generalize the behavior of one FP laser to the others, for example the L-I curve repetability strongly depend on the laser chip. Therefore, for a fixed laser bias current, different optical powers can be obtained. In our case, it has been preferred to fix the emitted optical power to -2.20dBm, that corresponds to 40mA and 70mA for the first and the second FP laser, respectively. For the three additional RoF links, emitting also -2.20dBm optical power, their laser bias current is fixed to 53, 44 and 43mA, respectively. All the photodiodes have a 3.3V bias voltage.

The experimental setup and the configuration remain the same than previously: a QPSK modulated signal, two 1x4 splitters and two 5m-length hops. EVM measurements are provided in table 4.13 for different optical configurations. This table has to be compared to table 4.11 giving the same measurements, but for Finisar VCSELs and PIN photodiodes with a built-in TIA at 850nm. Concerning the reported EVMs, only an average value is given as the measurements are stable over a large time.

Table 4.13: EVM on the electrical multipoint-to-multipoint RoF architecture composed of the FP laser and PIN photodiode from Finisar.

RoF link 1	RoF link 2	RoF link 3	RoF link 4	EVM
on	off	off	off	24.12 %
on	on	off	off	24.65 %
on	off	on	off	25.63 %
on	off	off	on	23.95 %
on	on	on	off	26.35 %
on	on	on	on	26.46 %

With only the main laser turned-on, an EVM of 24.12% is obtained. Compared to the multipoint-to-multipoint infrastructure based on the optoelectronic components at 850nm, an impairment of 3% is observed. Nevertheless, it is always higher than the optical solution, by 2%. When the setup is completed with other RoF links, the resulting average EVM increases to 26.5%, the same results as the optical multipoint-to-multipoint architecture at 850nm, but with stable measurements as no laser beats

occur. Lastly, if only the photodiodes of each point-to-point RoF links are turned-on, the EVM value equals to 24.80% meaning that the impact of the thermal noises is low: RIN and shot noise are the main reasons for these deteriorated results.

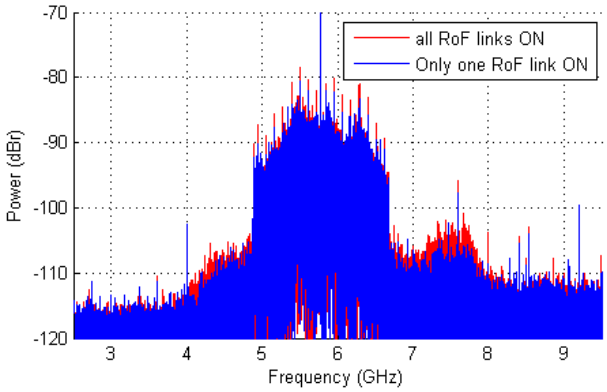

Figure 4.76: The received radio spectrum for the electrical multipoint-to-multipoint architecture composed of the FP laser and PIN photodiode from Finisar.

Finally, figure 4.76 shows the effect of the additional RoF links on the received radio spectrum. The corresponding instantaneous EVMs are 23.87% for one laser turned-on and 26.24% for all the lasers turned-on. As shown in the radio spectrums, an increase of 2.37% of the EVM impacts weakly the SNR.

4.6 Digital characterization of optical point-to-multipoint RoF architecture

The point-to-multipoint RoF architecture is a kind of multipoint-to-multipoint RoF architecture where all the transmissions are sent or received by a central radio device directly connected to the optical infrastructure. Thus, a 1xN splitter is used instead of a NxN one. This kind of infrastructure will be proposed in chapter 5 to directly connect an Access Point (AP) to a RoF infrastructure, without hop in the air, and to manage the optoelectronic components. Therefore, EVM performances will be determined on the assumption that only one laser is turned-on simultaneously. Assuming this point, optical splitter is preferred as it offers better performances up to 14dB of losses as shown in figure 4.71, i.e. a 16x16 optical splitter plus 2dB additional losses for fiber bends and connectors.

With only one hop in the air, the system is not symmetric anymore. Thus, two different experimental setups have been realized, one for the uplink and one for the downlink.

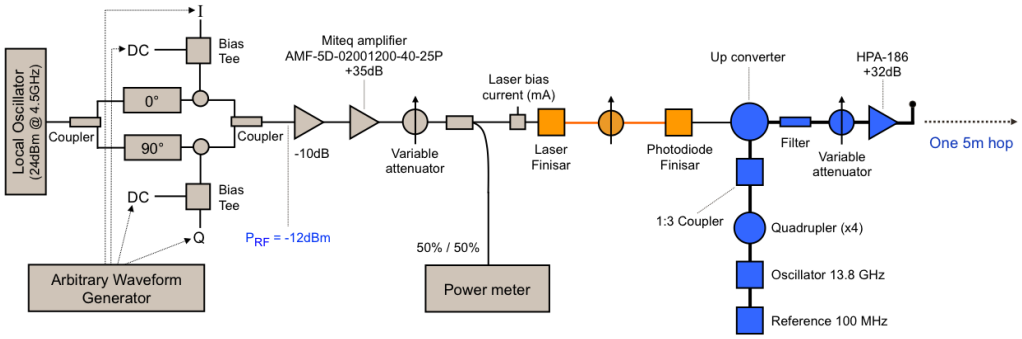

Figure 4.77: Experimental setup of the downlink of an optical point-to-multipoint RoF architecture.

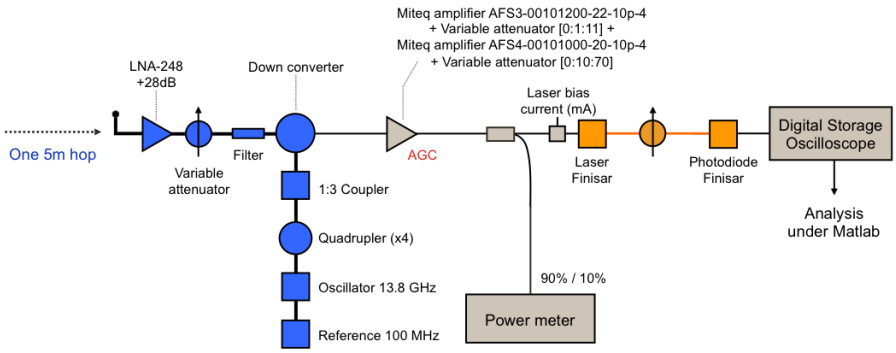

Figure 4.78: Experimental setup of the uplink of an optical point-to-multipoint RoF architecture.

The radio emitter and receiver, located at 5m from the RoF transducer, are those of figure 4.28. In the RoF link a variable optical attenuator is used since it well simulates the behavior of a 1xN optical splitter as long as only one laser is turned-on simultaneously. As previously, the laser input power is optimized as a function of the optical losses, but no AGC amplifier is implemented at the output of the RoF link. In this way, the radiated power at the output of the system decreases with the optical losses, and when no optical loss is inserted, the maximal EIRP of 27dBm is obtained.

EVM results are reported on figure 4.79. The system provides the same performances on the two transmission paths. There is no free-space link configuration leading to larger damages on the system. On the downlink as on the uplink, the minimal EVM of 18% is obtained for optical losses between 4 and 8 dB. Lastly, for 15dB optical losses, the EVM is near the BER limit, i.e. 32.5% for a BER of 10^{-3} in QPSK (see equation 4.8).

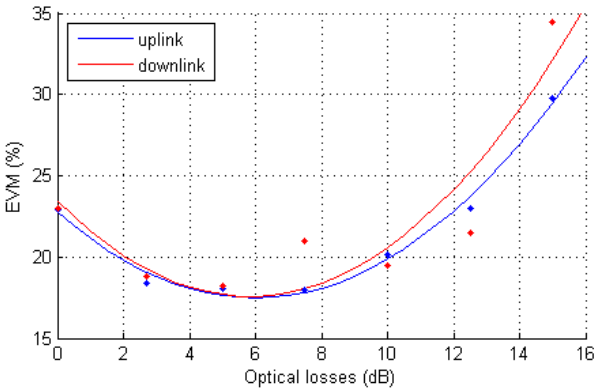

Figure 4.79: EVM point-to-multipoint.

4.7 RoF transmissions between two commercial WirelessHD devices

4.7.1 WirelessHD devices from Gefen

Finally a real-time transmission between two commercial WirelessHD devices working at ~3Gbit/s has been realized to validate the feasibility of the different RoF architectures. An uncompressed 1080i video from a Blu-ray player is displayed on a HD screen using the setup presented in figure 4.80 and where two paths are present, one for the downlink and one for the uplink. Thanks to full duplex RoF architectures, two wireless devices located in two rooms far away from each other can communicate as if they were in line of sight.

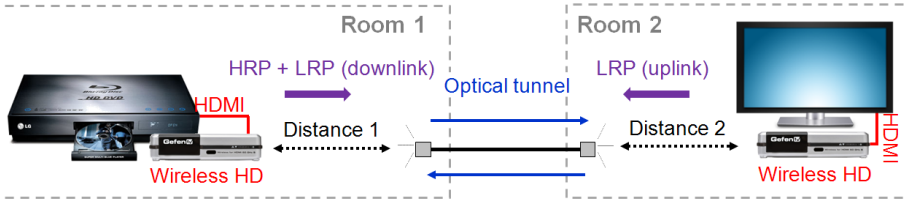

Figure 4.80: Real-time transmission between two commercial WirelessHD devices from Gefen.

The main properties of the WirelessHD devices from Gefen are a transmitted power of 27dBm (EIRP) and a receiver sensitivity of -65dBm[7]. The emitted radio signals, centered in the second channel of the millimeter-wave band, as the signals of the previous experiments, are represented in the frequency domain in figure 4.81.

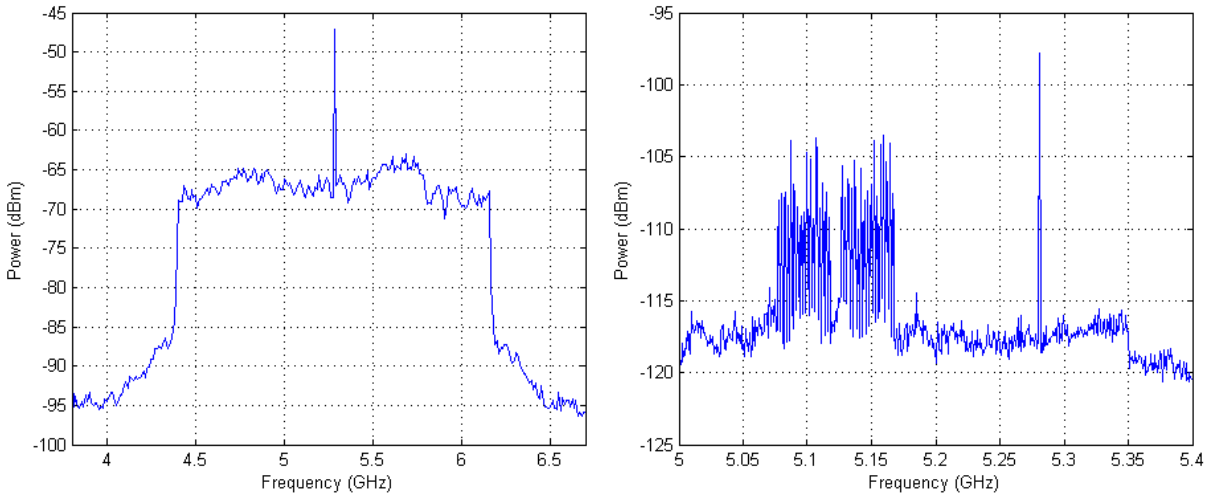

Figure 4.81: The WirelessHD radio spectrum emitted by the Gefen products. The signals have been captured at an IF of 5.28GHz, on a spectrum analyzer with RBW=VBW=30kHz for the downlink on the left, and with RBW=VBW=100Hz for the uplink on the right.

The downlink channel, at high data rate for video transmission, is called High Rate Physical layer (HRP), whereas the uplink channel, at a low data rate for monitoring, is called Low Rate Physical layer (LRP). LRP signal is also present over the downlink for monitoring, but only sporadically. Both are OFDM signals, but with different physical characteristics. For more details, see the chapter 1. Just note that the HRP signal, based on the IEEE 802.15.3c A/V mode, is similar to the IEEE 802.15.3c HSI mode. If in principle a date rate of 1.5Gbit/s is required to convey an uncompressed 1080i video (equation 1.1), we have no precise idea of the data rates transported and of the Modulation Coding Schemes (MCS) used by the Gefen products. Consequently, it has been tried to demodulate the WirelessHD signals to have more information. A capture of this signal is represented in figure 4.82.

[7]These devices have an EIRP fixed to 27dBm probably to be sold in South Korea (table 1.8).

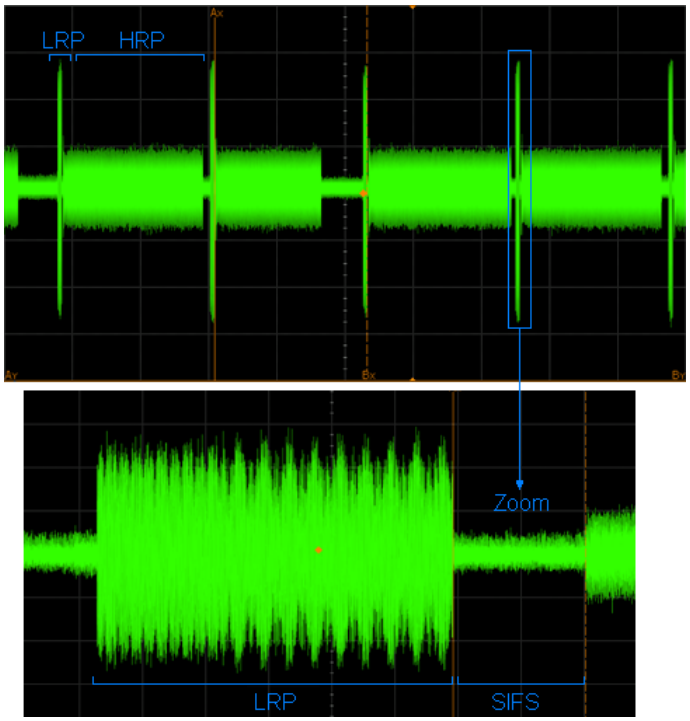

Figure 4.82: WirelessHD signals captured at the output of the RoF links after air hops, the downlink and the uplink being merged thanks to a 1x2 RF splitter.

In figure 4.82, several frames can be observed, but inside one, the OFDM symbols cannot be discriminated as no interval between symbols is present: CP are implemented instead of ZPS. Consequently, to synchronize the OFDM signal, the procedure described in figure 4.83 is followed.

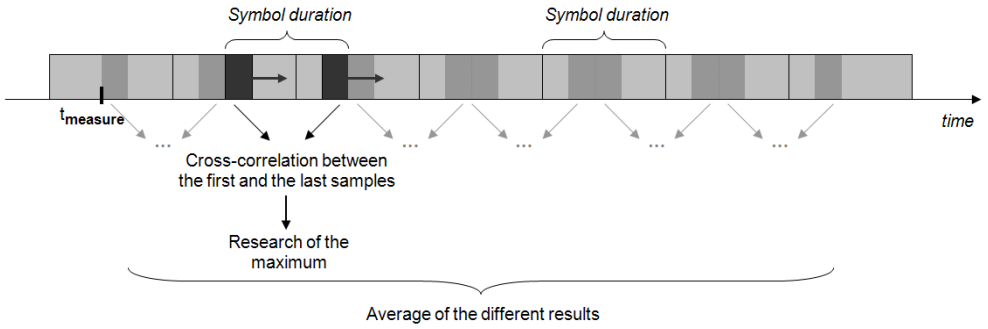

Figure 4.83: Cross-correlation technique between OFDM symbols and CPs.

The time waveform captured by the digital oscilloscope is divided under Matlab in different OFDM symbols of length "symbol duration" (see table 1.11). The zero-time of the first symbol is chosen arbitrary. Then, in each symbol, the cross-correlation of the 64 first samples[8] (CP size) and the 64 last samples (end of the symbol) is performed. Figure 4.84 represents the average cross-correlation over the HRP OFDM symbols as a function of the start time chosen for these OFDM symbols. As predicted by the theory, a triangle with a base being twice the guard interval is found, i.e. 50.44ns or 128 samples. When the similarity between first and last samples is maximal, a peak is obtain: the OFDM signal begins at 96.9ns.

[8] At the sampling rate of the OFDM signal. In fact, the sampling rate of the oscilloscope is different, 40GSa/s.

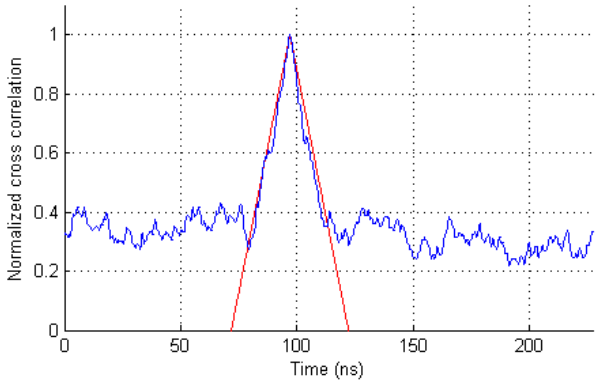

Figure 4.84: Cross-correlation of the HRP signal over a symbol duration, $T_{FFT} + T_{GI} \simeq 226.95ns$.

After synchronization of the OFDM symbols, the signal is demodulated. In the HRP signal, the pilot subcarriers, modulated in BPSK, are located in the spectrum according to equation 4.39: the position of the pilot subcarriers changes for each OFDM symbol.

$$\begin{aligned}
&\text{for } sym \text{ included between 0 and } N_{symbol} - 1 \\
&\{k = -177 + mod(3 \times sym\,, 22) : 22 : 177 \\
&\ k \neq (-1, 0, 1)\}, \\
&\text{where } sym \text{ is the symbol number,} \\
&\text{and } k \text{ is the index of the pilot subcarriers.}
\end{aligned} \tag{4.39}$$

Retrieving their location is quite hard, in fact the symbol number, *sym*, is unknown since capturing an entire frame is difficult due to limited equipment's memory and computing time. Additionally, the BPSK modulation rule is also unknown. If all the symbol numbers are tested to find the best amplitude correction, the ignorance of the BPSK modulation rule leads to bad phase correction as shown in the constellation diagram of figure 4.85.

Nevertheless, even if the demodulation suffers from phase issue, figure 4.85 let guess that the OFDM signal is modulated in QPSK. Considering the different WirelessHD MCS and the fact that an uncompressed 1080i video necessitates at least 1.5Gbit/s, the MCS used is probably a QPSK modulated signal with a 2/3 coding rate [10], i.e. a data rate of 1.904Gbit/s (2.856 Gbit/s PHY rate).

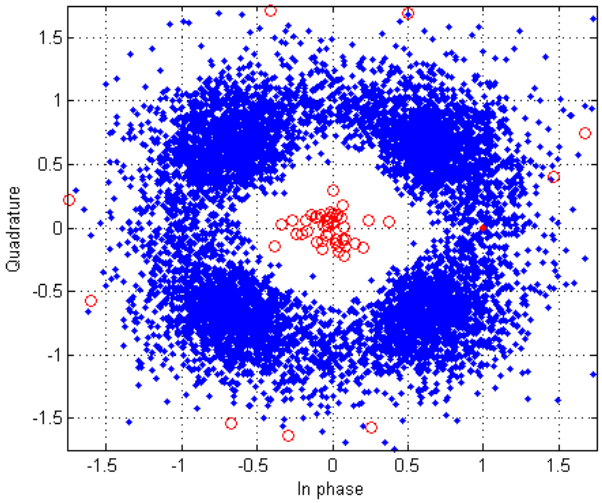

Figure 4.85: The HRP constellation diagram.

A similar work has been realized to demodulate the LRP signal. This time, the CP is composed of 28 samples, and the four pilot subcarriers, again modulated in BPSK, are located at fixed position.

The obtained constellation diagram, on the left in figure 4.86, shows a phase issue. In fact, the signal is close to an 8-PSK scheme when the standard announces BPSK modulation scheme. Thus, the phase is corrected taking the phase of the signal raised to the power 4: the obtained constellation diagram is represented on the right in figure 4.86.

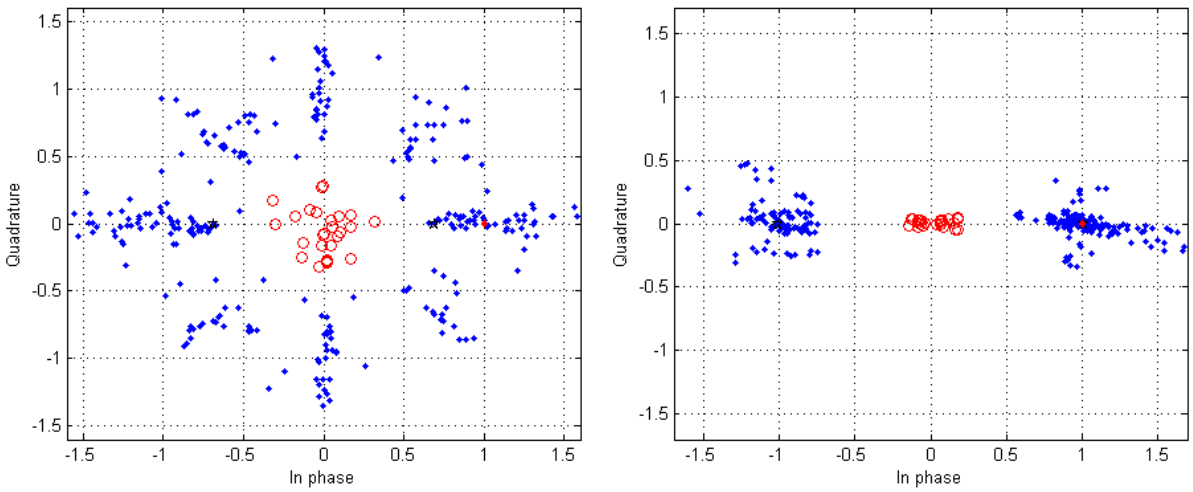

Figure 4.86: The LRP constellation diagram, with an EVM of 22.08% on the right.

To summarize, the setup used to check the feasibility of the different RoF architectures, in figure 4.80, has to convey two kinds of signal emitted by the Gefen WirelessHD products:

- a HRP one, with OFDM signal modulated in QPSK, with a coding rate of 2/3.
  The PHY rate equal 2.856 Gbit/s and the data rate 1.904 Gbit/s.
- a LRP one, with OFDM signal modulated in BPSK, with a maximum PHY rate of 40.673 Mbit/s.

4.7.2 Results for the different RoF architectures

Different RoF architectures have been tested, from the point-to-point to the multipoint-to-multipoint ones. In figure 4.87, one example corresponding to a point-to-point RoF architecture is provided. RoF is implemented only on the downlink as the system is symmetric, the uplink using a coaxial cable for convenience. In fact, if the system conveys successfully the HRP signal at 2.859Gbit/s PHY rates on the downlink, it will have no problem on the uplink operating at a lower data rate. Nevertheless some tests have also been performed with RoF implemented on both the uplink and the downlink, but not for all architectures.

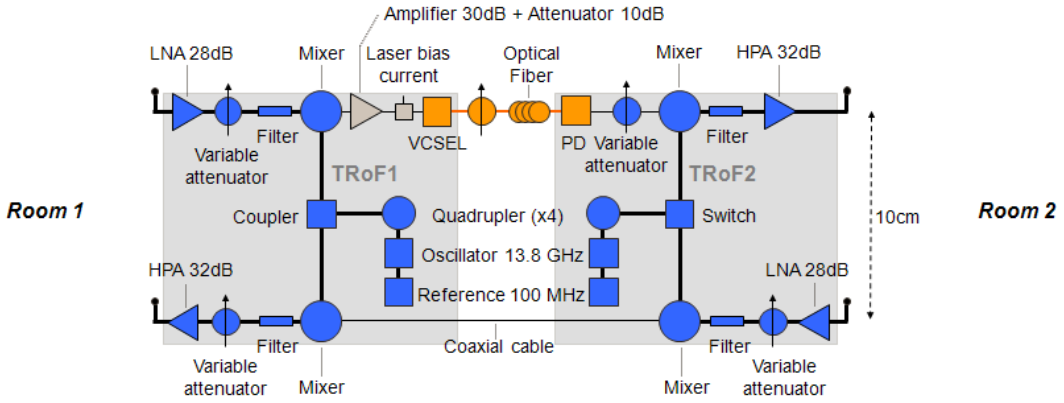

Figure 4.87: A full duplex point-to-point RoF architecture to test the commercial WirelessHD products from Gefen, with an optical downlink and a coaxial uplink.

Even if radio systems operate in half-duplex, a RoF transparent tunnel transmits and receives simultaneously. As a consequence, the adjacent Tx and Rx directional antennas have been separated by

a distance of 10cm to avoid coupling issues. Otherwise, strong perturbations to the radio environment can happen as explained in section 2.4.3.

In the example of figure 4.87, the free-space lengths are fixed to 5m plus 5m. The bi-directional transmission was successful over both a 50m-length OM2 MMF and a 100m-length OM2 MMF, but the system has not been able to operate with a 300m-length OM3 fiber probably due to restriction inside the radio MAC layer as detailed in section 2.4.6. Indeed, experimentally a limit of 106m-length fiber has been found: the propagation time cannot exceed $\simeq 0.5\mu$s. Deeper investigations described in table 4.14 have shown that this delay corresponds to the sum of propagation time over the downlink plus the propagation time over the uplink. Therefore, the system can operate with a 50m-length fiber over the downlink plus a 50m-length fiber over the uplink, which corresponds to the typical distances required for a HAN.

Table 4.14: Checkout that the system works as a function of the fiber length used on the downlink and on the uplink. For some distances, the SIFS has been measured on an oscilloscope.

Uplink	Downlink	Cumulated	works ?	SIFS
2.5m	-	2.5m	yes	2.13μs
-	2.5m	2.5m	yes	2.12μs
102.5m	-	102.5m	yes	2.64μs
-	102.5m	102.5m	yes	-
52.5m	52.5m	105m	yes	2.67μs
52.5m	54.5m	106.5m	no	-
108.5m	-	108.5m	no	2.68μs

This delay of 0.5μs seems linked to the time to change LRP transmission to HRP reception. In fact, the SIFS shall be less than 2.4μs according to WirelessHD [147]. In table 4.14, the SIFS for a 2.5m-length fiber was equal to 2.13μs while the SIFS for a 105m-length fiber was equal to 2.67μs (+0.54μs). Finally, the WirelessHD commercial products from Gefen accept a larger SIFS than recommended by the standard.

Now, the OM2 fiber length is fixed to 100m. To verify the robustness of the point-to-point link of the figure 4.87, a RF attenuator is added at the output of the photodiode. The RF attenuation can vary from 0 to 27 dB, beyond the connection stops.

Another major point for the success of a WirelessHD transmission is the accuracy of the Local Oscillator (LO). In [147], it is specified that the center frequency accuracy of the LRP and HRP PHY shall be less than ±20ppm (or μHz/Hz), and that the frequency of a station shall be less than ±1.5ppm of the frequency of the coordinator, which correspond to ±1209.60kHz and ±90.72kHz at 60.48GHz, respectively. This last value is essential for correct operation of the RoF architectures. As a consequence, it has been measured for the commercial devices from Gefen changing the value of one LO of the optical tunnel. For this purpose, a RF signal generator is used. The transmission is interrupted when the 13.8GHz oscillator is outside the window [13.8GHz−38kHz ; 13.8GHz+42kHz], which corresponds to an accuracy of ±160kHz at 60.48GHz, a value again largely better than the required one.

Other architectures than point-to-point RoF link have been tested:

- a multipoint-to-multipoint optical architecture based on Finisar components at 850nm and optical losses up to 17.5dB.
- a multipoint-to-multipoint electrical architecture based on two Finisar RoF links at 850nm and RF losses up to 14dB.
- a multipoint-to-multipoint optical architecture based on Finisar components at 850nm and on a 4x4 optical splitter.
- a multipoint-to-multipoint electrical architecture based on Finisar RoF links at 850nm and a 4x4 RF splitter.

The video signal has been transmitted successfully through all these architectures and no image degradation / interruption has been observed on the screen: they run smoothly, even when the corresponding EVM is unstable. The radio signal resists to optical disturbances. Since the interferences created by the optical heterodyning have low bandwidth compared to 2.16GHz bandwidth of the OFDM signal, an error

correction code associated with advanced interleaving techniques can provide adequate resistance to the signal. Cache memory of the radio signal at the receiver and requests for retransmission of lost frames could also explain the strength of the radio link.

4.8 Summary and discussion

One point has not been underlined very much until now, but each setup has been automated using Matlab in order to accelerate the measurements. The AWG, the variable RF and optical attenuators, the power meters and the Digital Storage Oscilloscope have been driven by GPIB, Ethernet, USB and RS232 links. This enables long periods of measurement without operator intervention. The only issue induced by this approach is the presence of 1x2 RF splitters, and so 3dB RF losses, in front of each laser to extract a part of the laser input power and check it.

If a final architecture should be chosen, a multipoint-to-multipoint architecture will be selected as it enables multiroom transmissions. However, several points have to be considered to optimize the performances link:

- The optimal laser input power strongly depends on the optical losses, which can vary due to linear attenuation or fiber bend losses, or due to users that want to change the splitter to have a larger number of ports.
- As a consequence, an AGC amplifier is required in front of each RoF link to fix the input power, independently of the free-space losses.
- On the contrary, it has been seen that an AGC amplifier at the output of the RoF link does not offer important improvements.
- Tests on WirelessHD devices have shown that a 10cm distance between the adjacent Tx and Rx directional antennas is sufficient to avoid coupling issues.
- No particular issues have been noted concerning the local oscillators, their accuracy is enough.
- Tests on WirelessHD devices have also shown that a 50m distance between two RoF transducers, i.e. 100m uplink plus downlink, is the maximum permitted propagation distance. That corresponds to a delay of 0.5μs in optical fibers with a refractive index of 1.4.

Table 4.15 resumes some EVM measurements performed in this chapter. For comparison, all the configurations are based on a QPSK modulated signal and on the same optoelectronic components, the VCSEL at 850nm and the PIN photodiode with the built-in TIA from Finisar. The laser bias current is fixed to 6.5mA. Concerning the multipoint-to-multipoint architectures, 4x4 splitter size and two 5m-length air hops are considered. When a splitter is used instead of RF or optical losses, that means that several RoF links are active, creating additional noises.

Table 4.15: Summary of some EVM measurements realized in this chapter.

Configuration	EVM
Direct link at Intermediate Frequency, at 6GHz	<6%
free-space radio link at 60GHz (from 5 to 10m)	13%
RoF link at Intermediate Frequency, at 5GHz, with 7dB optical losses	10%
Electrical repeater at 60GHz	19%
Optical point-to-point architecture with fixed laser input power	<25%
Optical multipoint-to-multipoint architecture with 7dB optical losses	22%
Optical multipoint-to-multipoint architecture with 4x4 splitter (7dB)	27%
Electrical multipoint-to-multipoint architecture with 14dB RF losses	28%
Electrical multipoint-to-multipoint architecture with 4x4 splitter (14dB)	37%

In this chapter, a comparison between the optical and the electrical multipoint-to-multipoint architectures has also been realized in terms of EVM. The electrical solution has the advantage to be laser beats independent and transverse multimode character independent, but it induces more important EVM values, at least for the transmission at 850nm (VCSEL and PIN photodiode from Finisar). Experimentations based on more linear components working at 1310nm (FP laser and PIN photodiode from Finisar) have nevertheless shown that the electrical solution can be a pertinent choice with an

EVM of 26% for a 4x4 architecture.

All the setups have been characterized with the same figure of merit to be compared. Indeed, as seen previously, the relationship between SNR, EVM and BER can be debated. Yet, perhaps the SNR is a better figure of merit to measure the distorsions acquired by a signal during its propagation, and thus quantify its performance, even for bumpy spectrums: in [31], the relationship between SNR and MAC throughput is provided for different MCS of the IEEE 802.15.3c standard, HSI and AV modes.

Figure 4.88 represents the MAC throughput as a function of the SNR. To plot these curves, the authors have used the channel model 1.3 developed in the TG3c. This model [148] is based on a residential environment, a typical home with multiple rooms and furnished with furniture, TV sets lounges, etc... Additionally, the scenario is Line-Of-Sight (LOS) and the antenna beamwidths are 30° for the transmitter and 15° for the receiver. According to the Matlab channel model from TG3c [149], we have:

$$G_{antenna} = 10 \cdot log\left(\frac{1.6162}{sin(10\pi/180/2)}\right)^2 - 3.01 \cdot \left(\frac{2 \times abs(fai)}{hpbw}\right)^2 \tag{4.40}$$

where,

- $abs(fai) < 1.3 \times hpbw$.
- fai is the angle of arrival in deg. Here, this angle equals $\sim 0°$.
- $hpbw$ is the half-power angle in deg.

Consequently, a 30° antenna beamwidth corresponds to a gain of 15.91dB in LOS while a 15° antenna beamwidth corresponds to a gain of 21.86dB.

Figure 4.88 shows the HSI and AV modes throughput considering the MAC layer overhead. The MAC efficiency with block acknowledgment (Blk-ACK) and 1KB payload, the best parameters, varies from 72% to 96% (as shown in [31], figure 12). For information, the Blk-ACK answers to several frames aggregating the different acknowledgment in a single frame.

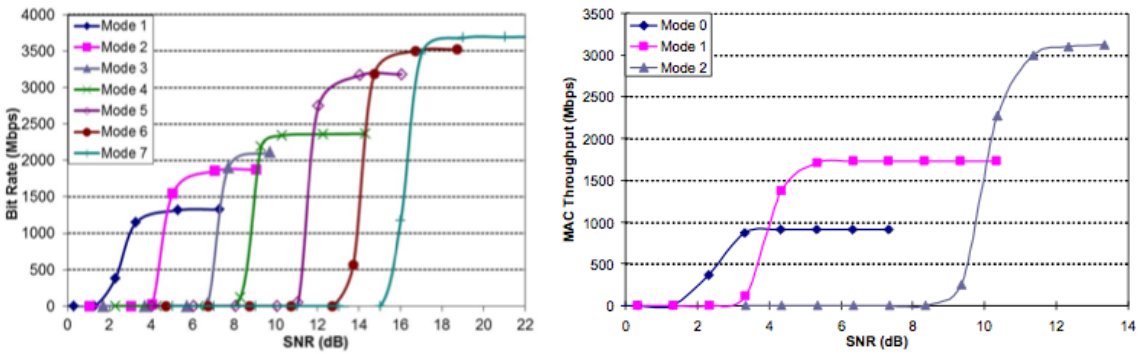

Figure 4.88: MAC throughput as a function of the SNR for different MCS, from [31]. In the HSI mode, on the left, the modes 1, 2 and 3 are QPSK, the modes 4, 5 and 6 are 16-QAM and the mode 7 is 64-QAM. Concerning the A/V mode, on the right, the modes 0 and 1 are QPSK while the mode 2 is 16-QAM.

As shown in figure 4.75, the SNR of the optical and electrical multipoint-to-multipoint RoF architectures are approximatively 10dB and 5dB in the worst case, respectively. This corresponds to 2Gbit/s approximatively and this is in agreement with the data rates conveyed by the WirelessHD signals, 1.904Gbit/s.

In this chapter, the measurements have been established thanks to a signal based on the IEEE 802.15.3c standard, but similar results would have been obtained with other millimeter-wave OFDM standards, like the IEEE 802.11ad standard, the future Wi-Fi. It's precisely this standard that is used in [32] to establish a relationship among Packet Error Rate (PER), BER, SNR, PHY and MAC throughputs, free-space distance... These results have been defined simulating a 60GHz channel built from measurements and ray-tracing.

Two examples based on the IEEE 802.11ad standard are given in figure 4.89. The first one, on the left, shows that the Forward Error Correction (FEC) is able to operate up to a BER of about $5 \cdot 10^{-3}$ for a QPSK modulated signal coding with a rate of 1/2. Nevertheless, to reach a throughput higher than 90% of the peak data rate, a BER of 10^{-5} is required. Assuming the theoretical relationship among BER and EVM (equation 4.8), BERs of $5 \cdot 10^{-3}$ and 10^{-5} correspond to EVMs of 38.5% and 23.5% in QPSK, respectively. All the configurations presented in table 4.15 are therefore supported by this MCS. However, assuming the experimental relationship established in figure 4.12, a BER of $5 \cdot 10^{-3}$ corresponds to an EVM of 34.5% while a BER of 10^{-5} corresponds to 19.5%. As a consequence, the electrical multipoint-to-multipoint architecture with a 4x4 splitter (14dB, and all the RoF links active) seems not able to convey a IEEE 802.11ad signal modulated in QPSK with FEC rate of 1/2.

The second example given in figure 4.89, on the right, shows the MAC throughput as a function of the SNR, a more reliable figure of merit independent of the demodulation process. With regard to the figure 4.75, which shows a SNR of approximatively 10dB for the optical multipoint-to-multipoint RoF architecture, and according to the figure 4.89, a data rate of 3.5Gbit/s can be reached (16-QAM and FEC rate of 5/8). Concerning the electrical multipoint-to-multipoint architecture, it seems able to convey a data rate of about 2Gbit/s in QPSK, which is this time in agreement with the previous exchanges realized in WirelessHD.

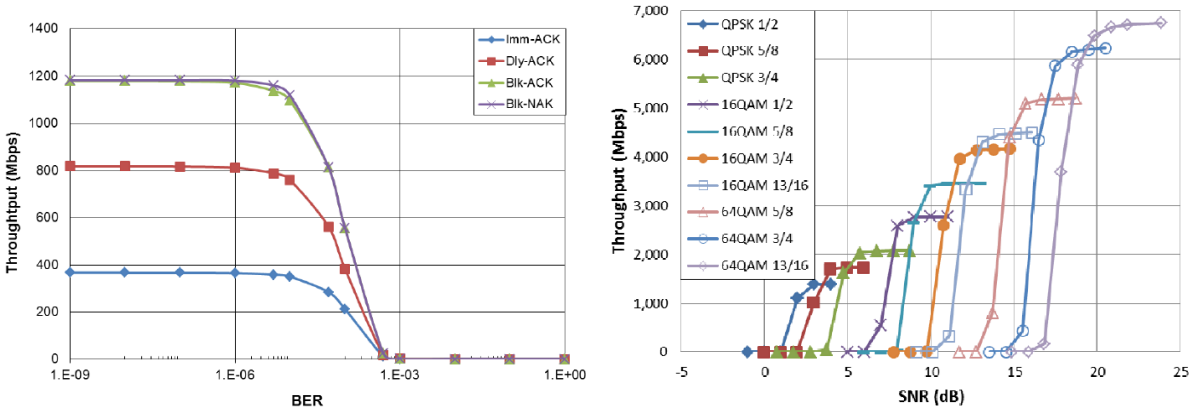

Figure 4.89: MAC throughput as a function of the BER for a QPSK 1/2 MCS on the left, and as a function of the SNR for different MCS on the right, from [32].

Chapter 5

Towards more complex Radio over Fiber infrastructures

5.1 An optical access management using the radio MAC layer

5.1.1 Purpose

The feasibility of the RoF architectures has been demonstrated in the previous chapters, however, some issues have also been put in evidence. The most impacting impairments concern the multipoint-to-multipoint architectures acting as logical bus, and particularly the optical one with these multiple lasers used simultaneously that induce an excess of noises (shot noise and RIN) and the presence of optical heterodyning interferences.

These issues can be overcome by controlling the access to the optical media. In other terms, the optical functions of the RoF transducers have to be activated only when and where they are needed to never have two lasers emitting or two photodetectors receiving at the same time. Thus, a laser will be turned-on only to transmit a radio signal through the optical network and a photodetector will be turned-on only to emit this optical signal on the air.

Furthermore, a continuous optical access management improves the Global Spectral Efficiency ($bit/s/Hz/m^2$) as the radio waves are confined only in the rooms where a networking capacity is required. Thus, minimizing the Electro-Magnetic Fields (EMF) exposure reduces the health concern, but also the hacking concern thanks to data always close to the end user. Last but not least, limiting the number of optoelectronic components turned-on simultaneously decreases the power consumption and makes the RoF system greener.

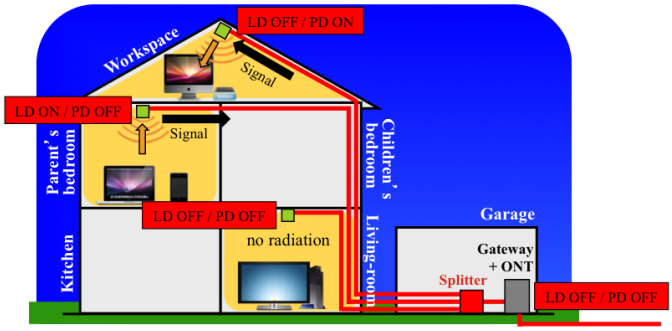

Figure 5.1: Example of optical access management. The electromagnetic power is radiated only in the room where there is a user in receive mode, here the workspace.

Limitation in the management using the radio PHY layer

In this section, a radio PHY layer approach able to resolve the different RoF issues listed in chapter 2 is investigated. One solution, already discussed previously, consists in running each RoF transducer in half

duplex. Applying this rule, and limiting the number of transducers in a room to one, can solve some architecture issues like multipath, echo and coupling.

To make each RoF transducer half duplex, the laser has to be turned-on only if it is driven by a useful signal; otherwise, the photodiode is turned-on. As a result, the RoF transducers analyze the signal delivered by their receiving antenna, for example performing a RF power detection after the AGC amplifier or measuring the control voltage of this amplifier. This method seems attractive as it is simple, low cost, transparent to the center frequency, and insensible to the modulation scheme, but in reality, it is very sensitive to interferences (such as spurious signals emitted in the same band) as explained in [150]. As a consequence, a more sophisticated technique is proposed in [150] to detect only the useful radio signal: an Inter-Period Correlation Processing (IPCP). From the knowledge of the period of OFDM symbols, it is possible to determine if a radio signal is relevant or not. Indeed, the IPCP can differentiate the radio signal to be distributed in the RoF infrastructure, for example an IEEE 802.11ad emission, from another signal that could be present in the home, for instance a point-to-point exchange in WirelessHD inside a room. For this, as presented in figure 5.2, an intercorrelation product between the incoming signal and the same signal delayed by one symbol period (Tr) is performed. To improve the reliability, three IPCPs can be realized in parallel between signals of different delays and averaged. A RF filter can also be added at the input of the system to remove spurious signals located outside the radio band of interest.

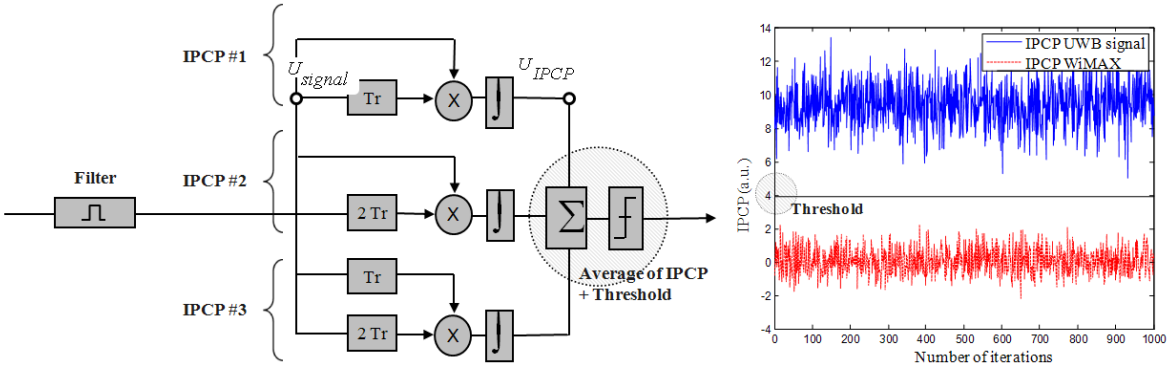

Figure 5.2: IPCP setup designed for an UWB signal (ECMA-368) on the left and the simulation results on the right for a UWB signal (above) and a spurious WiMAX signal (below).

This technique, always transparent to the frequency, allows to be selective to the radio standard. Indeed, the value Tr is different for each radio PHY layer. Therefore, if two separate standards coexist in a house, only one will be conveyed on the RoF infrastructure. Nevertheless, IPCP is costly and it induces long computing time.

In [150], this technique has been numerically evaluated under Matlab working in the centimeter-wave band, between 3.1 and 4.7 GHz, with the ECMA-368 standard (figure 5.2). The spurious signals are OFDM signals with different symbol periods, a WiMAX signal and a sine curve. The variable parameters of this calculation are the duration of the observation (integration time), the number of the first sample of the observation, the SNR of the useful signal (assuming Additive White Gaussian Noise) and the power difference between the useful signal and the spurious signals. For a reliable calculation in every instance, it has been chosen to realize three IPCPs in parallel with an integration time of 20 OFDM symbols. Figure 5.2 shows an example of an IPCP detection over 1000 iterations (random signal regenerated 1000 times) and with a SNR of 7dB. Here, the first sample starts with the OFDM symbols.

Figure 5.2 shows that it is possible to discern an ECMA signal from a spurious signal, but in fact it is only true with a long time of calculation: 20 symbols of 312.5ns and two delays of 312.5ns. The operation time is so equal to 6.875μs. The latency between the arrival of the radio signal and the decision to turn-on the laser is too long according to the ECMA-368 standard (this depends on the packet/frame synchronization sequence of a standard preamble).

As a consequence, as explained in [150], the radio PHY layer management is not the right solution. This will be especially true at 60GHz where the different standards have too similar OFDM symbol

periods. Additionally, when two RoF transducers are located in the a same room, inevitably two lasers will be turned-on simultaneously, and optical heterodyning interferences will be created. Lastly, the management of the photodiodes is impossible with this PHY layer approach.

Radio MAC layer management based on the beamforming technique

Another solution to manage the access of the optical medium consists in reading information from the radio MAC layer to know the key parameters on ongoing communications, like the source and destination stations. Additionally, to have an efficient and implementation-friendly solution, the beamforming (BF) process introduced in the 60GHz radio standards can be re-used.

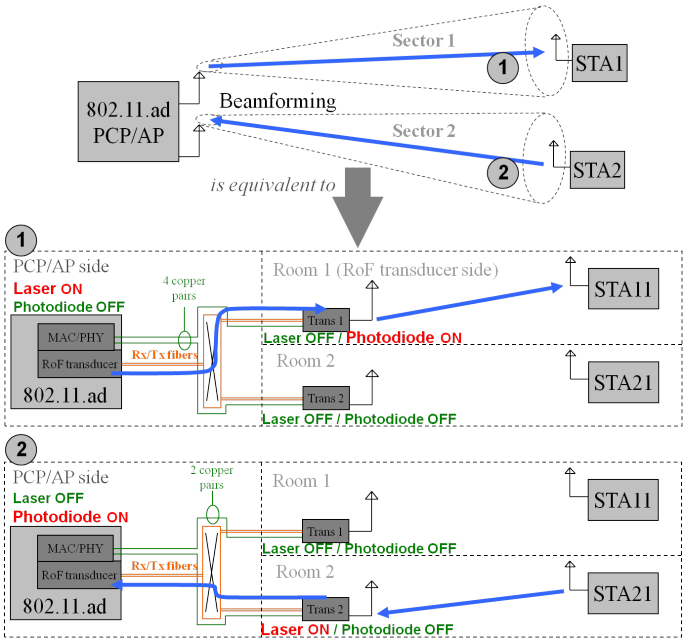

Figure 5.3: Adaptation of the BF process for a Personal basic service set Control Point / Access Point (PCP/AP) with a Phased Array Antenna to the RoF technology. The RoF infrastructure is an optical multipoint-to-multipoint architecture (NxN) while the copper infrastructure is an active star with N-1 point-to-point links. STA = Station.

The beamforming is a process used by a pair of millimeter-wave stations to determine the best transmission and reception antenna patterns, and consequently to achieve the necessary radio link budget for subsequent communications. Thanks to the BF, two stations communicate with narrow beams identified by sector and antenna identifiers (IDs) coded over 6 ([0:63]) and 2 bits ([0:3]), respectively according to the IEEE 802.11ad standard. This capacity of changing the antenna pattern towards different directions is reused to manage the optoelectronic components of a multipoint-to-multipoint RoF architecture, a sector or an antenna corresponding to a RoF transducer positioned in a room of the house as shown in figure 5.3. The optical network becomes a simple extension of the radio system, fully controlled by it, without proper intelligence.

One of the radio devices, directly connected to the optical infrastructure, e.g. an Access Point (AP) included into a Home Gateway, demodulates the radio signal, recovers useful BF data from the radio MAC layer in order to manage the optical access, and sends instructions to the different RoF transducers thanks to a simple monitoring signal. This solution leads to a very low cost system as only one dedicated radio chipset is necessary, all the other transducers remaining very simple. And this dedicated radio chipset already exists on the market since it is a simple millimeter-wave station compatible with BF and using phased array antennas [14] [151]. No new MAC layer is needed for the RoF, an adaptation of the digital core communicating between the common memory address bus of the radio MAC chipset and the phased array antennas will be sufficient [152].

As for the monitoring signal, it has to be modulated and demodulated in a cost effective way. It can be an electrical analog signal marked by the presence or the absence of RF carriers, for instance at

10MHz, and distributed thanks to two copper pairs (per RoF transducer), one pair to manage the laser, and one pair to control the photodetector. These copper pairs, included in the domestic cable with the optical fibers, can also be used to remotely power supply the RoF transducer according to the Power over Ethernet (PoE) PHY specification [153] [154]. It has to be noted that the monitoring signal cannot pass through the optical shared architecture because it must be intended to a specific transducer. Only the superposition of an active star copper infrastructure made of several point-to-point links with an optical multipoint-to-multipoint architecture makes sense. As shown in figure 5.3, this implies that the central radio chipset is collocated with the NxN optical splitter for an easier implementation in the home.

In the example of figure 5.3, when the central station emits a radio signal in the sector 1 using BF (first instant), the equivalent in the RoF infrastructure is: the laser of the RoF transducer directly connected to the radio chipset and the photodiode of the RoF transducer numbered 1 and located in the room 1 are turned-on. To turn-on the remote antenna, a RF tone is simply sent on the dedicated copper pair. Similarly, at the second instant, when the PCP/AP receives a radio signal from the sector 2, the photodiode of the RoF transducer directly connected to the radio chipset is turned-on and the laser of the RoF transducer numbered 2 and located in the room 2 is turned-on.

As shown in the previous chapter, even if a RoF transducer in a room has no BF and no phased array antenna, 2.856Gbit/s PHY rate and 1.904Gbit/s data rate can be achieved between two WirelessHD devices through a point-to-point RoF link with 50m-length multimode fiber and two 5m-hops in the air using 20dB gain horn antennas. Therefore, the link is sufficiently robust thanks to the BF process only included in the users' devices.

In the next part, an analysis of the radio MAC layer is proposed. This study, based on the IEEE 802.11ad standard [33] that will probably lead the market in the future, is helpful to understand the sequence of ignition and extinction of the optoelectronic components. It has to be noted that a less detailed study of the IEEE 802.15.3c standard has also be conducted during this thesis: [155] and [156].

5.1.2 The IEEE 802.11.ad MAC architectures

To enable the management of the optical functions from the radio MAC layer, the configuration of the network has to be known at any time, i.e. which antenna pattern is used, which antenna is transmitting, which antenna is receiving, etc... Before detailing deeply the radio MAC layer, it has to be recalled that three types of MAC architectures are defined in the IEEE 802.11ad standard.

Independent Basic Service Set MAC architecture

The Independent Basic Service Set (IBSS) is the most basic MAC architecture. It consists in only two stations in line of sight: as this use-case does not match with a multi-room approach, it will not be studied here.

Infrastructure MAC architecture (Basic Service Set)

The Infrastructure architecture is currently the most popular commercial use of the IEEE 802.11 standards since it provides Internet connectivity and Ethernet bridging. The IEEE 802.11ad standard shares similar MAC layer with IEEE 802.11 standards to provide interoperability with the Wi-Fi devices, therefore it also supports the Infrastructure architecture.

In this architecture, all the frames are sent or received by an Access Point (AP) giving access to any wireless station associated with this AP. Two stations cannot communicate directly with one another if one of them is not the AP, excepted the optional Tunneled Direct Link Setup (TDLS) mode that will not be considered here.

Ad-hoc MAC architecture (Personal Basic Set Service)

The Ad-hoc architecture, a new one introduced with the IEEE 802.11ad standard, allows each station to communicate directly with one another to form a network called Personal Basic Set Service (PBSS). In this network, coordinated by the PBSS Control Point (PCP), the Internet connectivity and the Ethernet bridging are not provided.

5.1.3 The IEEE 802.11ad MAC layer

The data necessary to the management of the optical layer will be recovered from the radio MAC layer of the PCP/AP[1], the central station that coordinates the MAC architectures. The PCP/AP shares the transmission channel in a Time Division Multiple Access (TDMA) structure named Beacon Interval (BI). Figure 5.4 shows this structuring element of the IEEE 802.11ad communications: it is composed of several sub-intervals, each of them having a different access rule, as detailed in the next subsections.

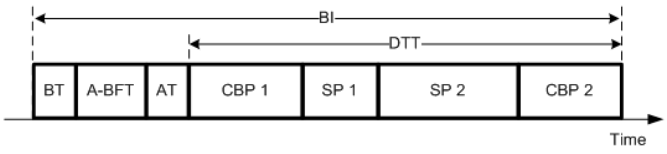

Figure 5.4: Beacon Interval (BI) structure, from [33]. BT = Beacon Time, ABF-T = Association Beamforming Training, AT = Announcement Time, DTT = Data Transfer Time, CBP = Contention Based Period, SP = Service Period.

The Beacon Time (BT)

The first slot of the BI is the Beacon Time (BT), an access period during which one or more beacons are transmitted to the entire network in order to provide a great part of the schedule of the BI. For this purpose, the PCP/AP transmits multiple beacons in a quasi-omni mode, i.e. the PCP/AP transmits a first beacon in the direction 1, a second beacon in direction 2, and so on. In practice, a pseudo-random sequence of directions is chosen to obtain after several BTs a quasi-omni-directional coverage.

Concerning the RoF aspects, on the PCP/AP side, the laser is turned-on to transmit the beacons to the RoF transducers through the optical infrastructure, and, on the RoF transducers side, the photodiodes are turned-on in a round-robin mode according to the beamforming technique. The selection of the photodiode to turn-on is made from the sector and antenna identifiers (Sector ID and Antenna ID fields) included in the Sector Sweep (SS) field of each beacon. Tables 5.1, 5.2 and 5.3 describe the content of a beacon and show where are located the Sector ID and Antenna ID fields.

Table 5.1: Beacon frame. FCS = Frame Check Sequence, RA = Receiver Address.

	Frame Control	Duration	RA	Body	FCS
Octets:	2	2	6	Variable	4

The Duration fields indicate the time until the end of the BT.

Table 5.2: Body field. BSSID = Basic Service Set Identification.

Order	Information
1	Sector Sweep
2	Timestamp
3	Beacon interval
4	Beacon Interval Control
5	mmWave Capability
6	PCP/AP Clustering Control
7	Robust Security Network
8	Multiple BSSID

The Sector Sweep (SS) field, described in table 5.3, contains the Antenna ID and Sector ID fields that determine the turning-on of the photodiodes.

[1]Generic name given to the central station, either an AP in the case of the infrastructure MAC architecture, or a PCP in the case of a Ad-hoc MAC architecture.

Table 5.3: Sector Sweep (SS) field.

	Direction	CDOWN	Sector ID	Antenna ID	RXSS Length
Bits:	1	9	6	2	6

As explained above, one of the roles of the BT consists in providing the schedule of the different access periods composing the BI. This is essential to predict early the management of the optoelectronic components.

The Beacon Interval Control field contains among other things an A-BFT Length field that indicates the size of the A-BFT period (defined as a number of Sector Sweep intervals). If this field is set to 0, the A-BFT will simply not occur. The Beacon Interval Control field also contains an AT Present field indicating the presence, or not, of an AT period in the current BI. Indeed, the AT and the A-BFT are optional. Lastly, the Extended Schedule element, described in table 5.4, details the DTT period with the different allocations for the SP and CBP, stored in ascending order of appearance in the BI.

Table 5.4: Extended Schedule element. CDOWN = Down-Counter, RXSS = Receive Sector Sweep.

	Element ID	Length	Allocation 1	Allocation 2	...	Allocation n
Octets:	1	1	15	15	...	15

Association Beamforming Training (A-BFT)

The second slot of the BI is the Association Beamforming Training (A-BFT). This optional period, presented in figure 5.5, is composed of Responder Sector Sweep (RSS) and Sector Sweep Feedback (SS-Feedback) frames. They aim at continuing the BF initiated during the BT, and thus at determining the best antenna patterns for transmission and reception. This phase is called Sector Level Sweep (SLS).

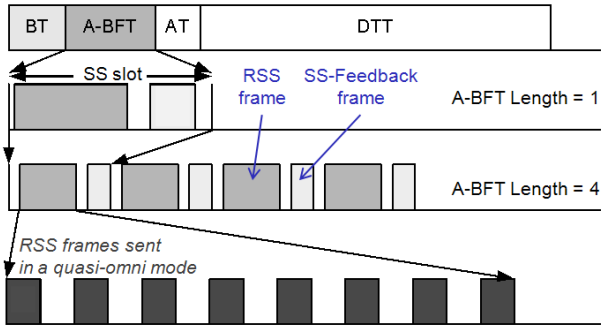

Figure 5.5: A-BFT period

First, a non PCP/AP station initiates the transmission during a SS slot among the many possibilities offered. This emission follows a random backoff procedure since all stations that have previously received a beacon from the PCP/AP can contribute to the channel access. Finally, RSS frames are sent to the PCP/AP as a response to the previous beacons in order to indicate the best antenna pattern used by the PCP/AP during the BT (identified thanks to the Sector and Antenna IDs). During the RSS frames exchanges, the PCP/AP is in reception mode using an omni-directional antenna pattern, whereas the non PCP/AP emitting stations are in a quasi-omni mode.

Therefore, during this period the photodiode on the PCP/AP side and all the lasers on the RoF transducers side are turned-on; the other components being turned-off. There is no other option as the PCP/AP uses an omni-directional antenna pattern. Obviously, the reception of the RSS frames will be degraded as optical beating, multipath interferences and coupling issues can occur, but as this period is contention-based, these impairments will be considered by the MAC layer as collisions and the damaged frames will be retransmitted.

Table 5.5: The Sector Sweep frame (SS and RSS).

	Frame Control	Duration	RA	TA	SS	SS-Feedback	FCS
Octets:	2	2	6	6	3	3	4

Table 5.6: SS-Feedback field.

	Sector select	Antenna select	SNR Report	Poll required	Reserved
Bits:	6	2	8	1	7

As shown in tables 5.5 and 5.6, the RSS frames received by the PCP/AP can link Sector ID and Antenna ID fields - the Sector select and Antenna select fields included in the SS-Feedback field - to the MAC addresses of the stations - the Receiver Address (RA) and Transmitter Address (TA) fields. Here, the address of the PCP/AP is indicated by the RA fields while the addresses of the non PCP/AP stations are pointed by the TA fields. Subsequently, the MAC addresses will be sufficient to manage the optical access. Indeed, to send data to a station RA, the PCP/AP, with the MAC address TA, will just use the Sector and Antenna IDs previously selected during the SLS phase.

After the RSS frames, the PCP/AP responds with an SS-Feedback frame, providing information on the best RSS frame received. The SS-Feedback frame contains RA and TA fields, hence the laser corresponding to the TA field, the PCP/AP, and the photodiode corresponding to RA field, one of the RoF transducers, are turned-on, the correspondence between the MAC addresses and the antenna patterns having just been made.

Finally, figure 5.6 sums-up the BF process and the corresponding actions on the optoelectronic components during the SLS phase. It has to be noted that a RoF transducer can be associated to several MAC addresses if several radio devices are used in a same room.

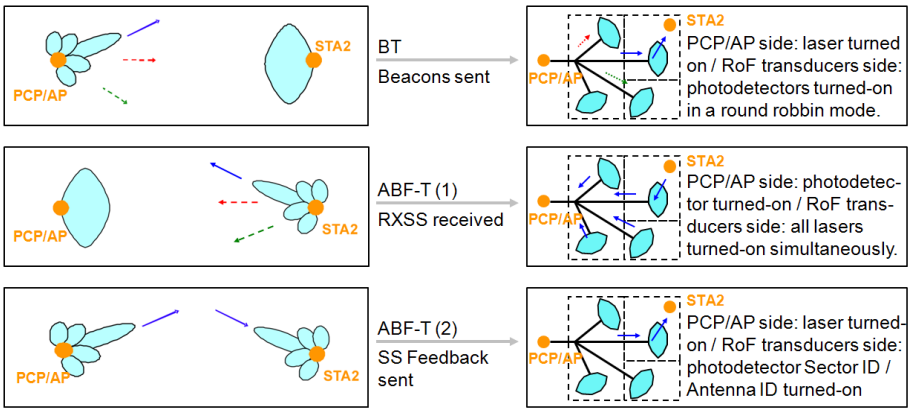

Figure 5.6: Beamforming process with radio approach on the left and with RoF approach on the right.

Announcement Time (AT)

The Announcement Time (AT) is an optional period for management frames providing access opportunities to the stations. As a reminder, the presence of an AT in a BI is indicated in the beacons by the AT Present field.

During the AT, request and response frames are exchanged between the PCP/AP and one or more non PCP/AP stations (figure 5.7). The PCP/AP can easily manage the optical access because it initiates all the transmissions and a station does not transmit during the AT except in response to a unicast frame from the PCP/AP. This response is always intended to the PCP/AP.

Concerning the RoF infrastructure, first, only the laser corresponding to the PCP/AP and the photodiode corresponding to the recipient RoF transducer are turned-on. When the PCP/AP has finished its transmission, it turns-off its laser to turn-on the one of its last recipient (and conversely for the photodiodes). To realize these operations, the TA and RA fields contained in each frame are used.

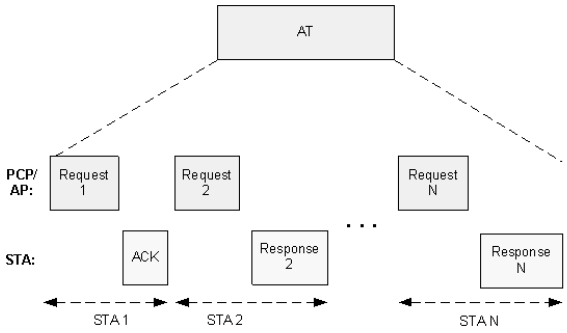

Figure 5.7: The AT period.

Data Transfer Time (DTT)

Lastly, the Data Transfer Time (DTT) takes place. It is a period for data frames transmissions, either in a Contention Based Period (CBP) managed by an Enhanced Distributed Channel Access (EDCA, close to CSMA/CA) mechanism, or in a Service Period (SP), a contention-free TDMA period.

The PCP/AP has provided the schedule of the DTT through BT and/or AT frames. Consequently, the start time, the duration, the channel access used (CBP or SP), the source and destination stations, etc... of each period of the DTT are already known. These informations are contained in the Allocation fields of the Extended Schedule element (table 5.7). For instance, the source and destination stations are pointed out by two fields, source and destination Association IDs (AIDs), theses fields being linked to the MAC addresses during the association procedure (not described here, but in [157]), themselves being associated to the Sector and Antenna IDs as seen previously. Another important parameter is the Allocation Control field presented in table 5.8 and its SPType field. SPType is set to 0 to indicate that the allocation is made for a SP and set to 1 to indicate that the allocation is made for a CBP.

Table 5.7: Allocation fields.

	Allocation Control	BF Control	Source AID	Destination AID	Allocation Start	Allocation Block Duration	Allocation Block Period	Number of Blocks
Octets	2	2	1	1	4	2	2	1

Table 5.8: Allocation Control field.

	SPType	TID	Pseudo-static	Truncatable	Extendable	PCP Active	Reserved
Bits:	B0	B1-B4	B5	B6	B7	B8	B9-B15

Concerning RoF aspects, the CBP is incompatible with the exact knowledge of which laser to use for emission and which photodiode to use for reception. Indeed, as all stations may compete for the channel access, the decision to emit can come from any station. Consequently, the PCP/AP uses an omni-directional antenna pattern in reception mode, like during the first part of an ABF-T period (figure 5.6). In this contention based period, all the lasers and all the photodiodes will be turned-on simultaneously. The symbol collisions, like the optical heterodyning interferences, will be detected by the radio protocol and the damaged radio signals will be retransmitted. It has to be reminded that the optical heterodyning interferences degrade the radio signal only sporadically as shown in chapter 4 (table 4.8): the transmission will work, but with a less good QoS.

On the contrary, the SP is still compatible with the management of the optical access. Indeed, during this contention-free period, a channel time is granted to a pair of stations. As the SPs are planed in the Schedule Extended Element, the management of the optoelectronic components is simple. An example is given below.

It has to be noted that dynamic allocations of SP can be employed. Indeed, a channel time reserved for a SP or a CBP can be reallocated thanks to Polling Period (PP) and Grant Period (GP) phases. These frames have been studied in [157]: they correspond to exchanges between non

PCP/AP stations and the PCP/AP and are manageable thanks to the RA and TA fields. Finally, the PCP/AP will send one or more Grant frames (one per destination station) to notify the new source and new destination stations of the dynamically allocated SPs, with the new agenda (SPInfo field).

If a SP can be dynamically allocated, it can also be extended and truncated dynamically after receiving a mmWaveCF-End and a Service Period Request (SPR) frames, respectively. These frames will be detected thanks to the Frame Control field (as shown in tables 5.5 and 5.1). Note that the possibility to extend and truncate a SP is indicated in the Allocation Control field.

Example of management of a Service Period (SP)

An example presents in the following the mechanism of the RoF management during SPs. In figure 5.8, the frames are exchanged between an AP and non AP stations as the network is based on an Infrastructure MAC architecture. The first SP is initiated by the AP in direction of a first station (STA1) whereas the second SP is initiated by a second station (STA2) in direction of the AP. In these exchanges, the source station is known thanks to the Source AID field contained in the Extended Schedule Element of a BT frame or in the SP Info field of a Grant frame, and the recipient station thanks to the Destination AID field.

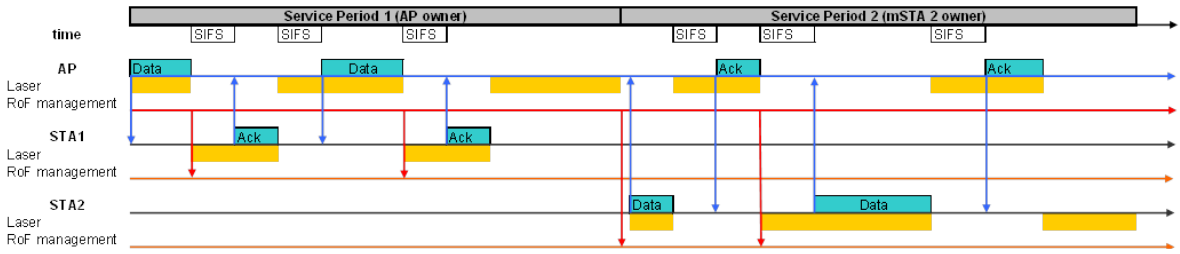

Figure 5.8: SP exchanges in an Infrastructure MAC architecture with the RoF monitoring signal. Only the laser ignition sequence is described, the mechanism for the photodiode being similar.

In the case where the AP initiates the exchange, first, the laser on the AP side and the photodiode on the RoF transducer side corresponding to the recipient station are turned-on. When the AP is in receiving mode the photodiode on the AP side and the laser on the RoF transducer side corresponding to the MAC address of the last frame transmitted by the AP are turned-on. The independence of the laser emissions is therefore proven: two lasers never emit in the same time slot.

Finally, it can be noted that the Short Inter-Frame Spaces (SIFS) allow a margin of error on the turning-on time of the optoelectronic components. Indeed, the SIFS is largely greater than the activation time of the lasers and the photodiodes (1μs versus a couple of nanoseconds, see section 3.6).

In the particular case of an Ad-hoc MAC architecture, exchanges can take place between two non PCP stations. If the PCP knows the two stations carrying out the exchange, and which of them initiates the exchange (Source AID), it does not know the moments when the transmitter / receiver roles are reversed. The prediction of these moments is not easy. One solution consists in using the optional relay mode [34] with the PCP playing the role of relay station.

The relay mode

The relay mode improves the reliability of a radio link between two stations, a source and a destination, by proposing a new indirect link via a relay station. The relay mode, an optional feature of the IEEE 802.11ad standard, is only compatible with the SPs: it has been studied to manage the optoelectronic components during this period for an Ad-hoc MAC architecture, when two non-PCP stations exchange together.

As depicted in figure 5.9, the source and destination stations are called Relay Usable Stations (RUS) and the relay station is called Relay Supportable Station (RSUS). In order to have a station operating as a RUS or as a RSUS, it is necessary that the station is already associated to the BSS and that it is directly visible by the PCP/AP.

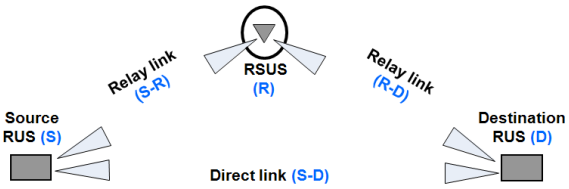

Figure 5.9: Principle of the relay mode.

The relay mode supports two scenarios: link switching and link cooperation. In the case of link switching, if the direct link between the source and destination stations is disrupted, the source station redirects its transmission via the relay station. The direct link can be resumed as soon as it is recovered. On the contrary, in the case of link cooperation, the relay station is actively involved in the direct communication between the source and destination stations since it is repeated at the same time by the relay station, which improves the signal quality.

Consequently, for a RoF system, the appropriate scenario is the link switching. As shown in figure 5.10, the RoF infrastructure is the only link until the relay station, i.e. until the PCP/AP directly connected to the optical architecture. Moreover, the direct link between two non PCP/AP stations is generally impossible since these stations are in separate rooms.

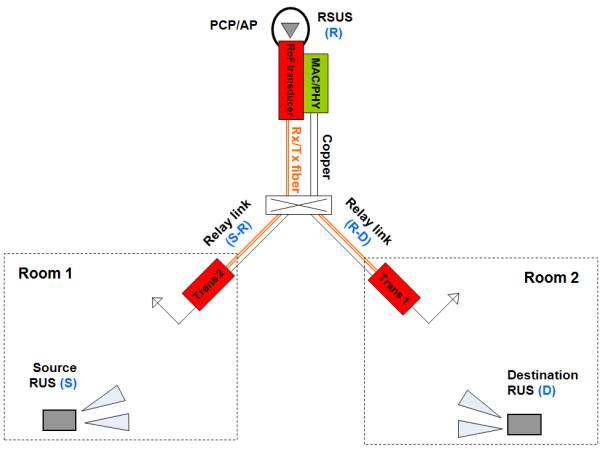

Figure 5.10: Implementation of the relay mode in a domestic RoF infrastructure.

The lack of direct links does not incriminate the initialization of the relay mode as explained below.

The Common Relay Setup

The Common relay setup procedure initializes the relay mode exchanges, in the case of link switching as in the case of link cooperation. The operations of this procedure are performed in the following order:

- Relay capabilities and RSUS discovery procedures.
- RSUS selection procedure.
- Relay Link Setup (RLS) procedure.

The Relay capabilities and RSUS discovery procedures

A source station that wants to operate in relay mode with a destination station has first to determine the capabilities of this destination station, i.e. if it is capable of relaying frames via itself and of using frame-relaying through a relay station, if it prefers to become RSUS rather than RUS, if it is capable of full duplex or half duplex, if it is capable of supporting link cooperating, etc... Therefore, in order to know its capabilities, the source station transmits to the PCP/AP a Relay Search Request frame, as described in figure 5.11.

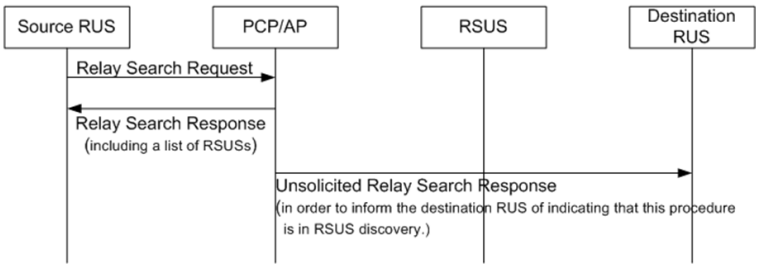

Figure 5.11: Relay capabilities and RSUS discovery procedures.

The PCP/AP answers to the source station by a Relay Search Response frame that provides the list of possible relay stations (RSUS). In the case of a RoF infrastructure, the PCP/AP has to be included in this list, it can even be judicious to restrict this list to the PCP/AP only to force the RoF infrastructure to become the repeater. Thus, the RSUS and the PCP/AP will become a single and unique station.

After the transmission of the Relay Search Response frame, the PCP/AP also notifies the destination station of the capabilities of the source station and of the list of the possible RSUS stations. Thus, the destination station is aware of the current procedure.

These exchanges take place during SPs. In the case of the Ad-hoc MAC architecture, the management of the optoelectronic components is not a problem since one of the two stations is always the PCP: the management will be the same as the one described previously, in figure 5.8.

The RSUS selection procedure

After that, the PCP/AP reserves SPs through Extended Schedule elements (transmitted during the BT) for exchanges between the RSUS stations (the PCP/AP for the RoF infrastructure) and the RUS stations that have been announced in the Relay Search Response frames previously transmitted:

- SPs where the source station is the Source RUS and the destination station is the RSUS.
- SPs where the source station is the RSUS and the destination station is the Destination RUS.

As shown in figure 5.12, direct radio exchanges occur between the RUS stations for the beamforming processing, the Multi-Relays Channel Measurement Request and Multi-Relays Channel Measurement Report frames. These direct exchanges, assessing the quality of the direct link from SNR measurements, can be realized activating all the lasers simultaneously. Thus, the direct link will have poor performances, and according to the link switching scenario, the transmission will be forced in relay mode.

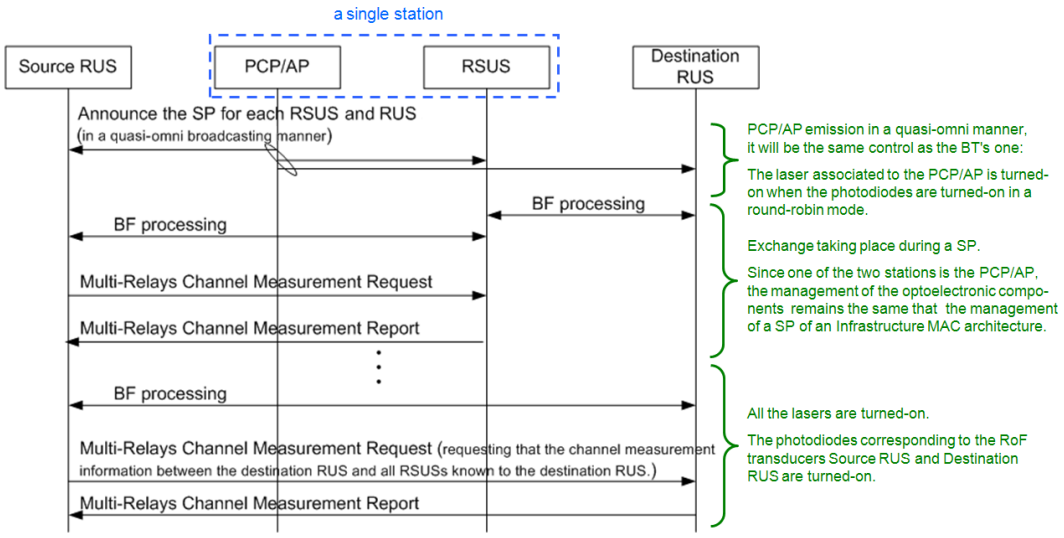

Figure 5.12: RSUS selection procedure.

The Relay Link Setup (RLS) procedure

After the selection of the RSUS, the Source RUS initiates a RLS procedure to finish the Common Relay Setup. This consists in providing to each station the Capability Information fields and the AID fields of the relay network, confirming the contribution of the Destination RUS, and validating that the Common Relay Setup was successfully complete.

These exchanges keep taking place during SPs and, as shown in figure 5.13, they are executed between a non PCP/AP station and the PCP/AP. As a result, the management of optoelectronic components is performed without any problem.

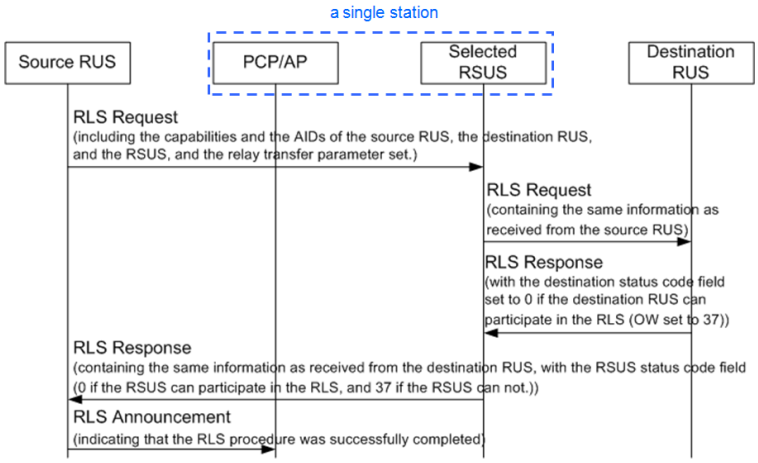

Figure 5.13: Relay Link Setup (RLS) procedure.

Transmitting data

As a reminder, the relay mode takes place during SPs. The RSUS (the PCP/AP) checks the value of the Source AID and Destination AID fields contained in each SP allocation, and if the AID fields match with Source RUS and Destination RUS values that have successfully completed the RLS procedure, then the RSUS operates as a relay station.

In a normal mode, when a SP begins, a Source RUS uses the direct link to initiate the transmission. Considering an Ad-hoc MAC architecture where by default all lasers are turned-on, the Source RUS will probably not receive acknowledgement frames back due to optical issues. Consequently, the strategy will change to use a relay link scenario (to force this strategy, the frames can even be voluntarily blocked turning-off the optoelectronic components), and after that the optoelectronic components could be managed.

In the IEEE 802.11ad standard, they are several operation modes: Full-Duplex / Amplify and Forward (FD/AF) and Half-Duplex / Decode and Forward (HD/DF).

Half-Duplex / Decode and Forward

The RoF system runs smoothly with a HD/DF relay as all communications pass through the relay station, the PCP/AP. However, as shown in figure 5.14, the throughput is halved in this two steps system: in a first step, a frame sent from a source station is captured by the relay station, and then in a second step, it is sent by the relay station to the final recipient. For more information, the management of the optical access is detailed in [157] with an example.

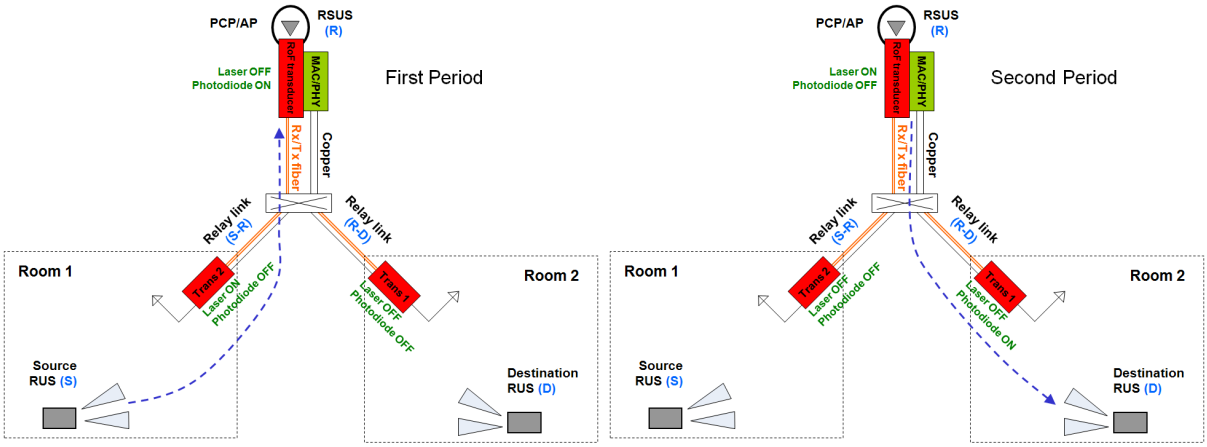

Figure 5.14: Illustration of a Half-Duplex / Decode and Forward relay mode with a S→R exchange on the left, then a R→D exchange on the right.

Full-Duplex / Amplify and Forward

FD/AF is the most interesting mode as the throughput is not divided by two. At the beginning of a SP, the relay station (RSUS) selects a first antenna pattern able to receive flows from the Source RUS and a second antenna pattern able to transmit these flows to the Destination RUS. Figure 5.15 depicts this mechanism.

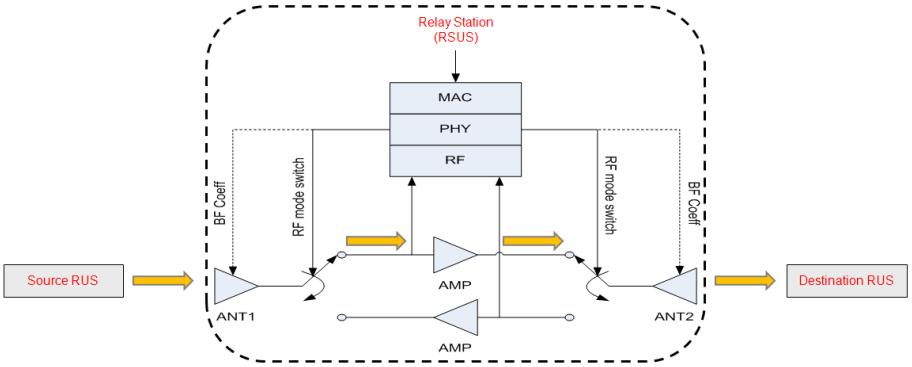

Figure 5.15: Mechanism of the Full-Duplex / Amplify and Forward relay mode, adapted from [34].

For each frame received, the RSUS shall follow the rules of the exchange sequence described in the standard. This includes the switching state (RX/TX) dictated by type of frame and the acknowledgment policy (ACK).

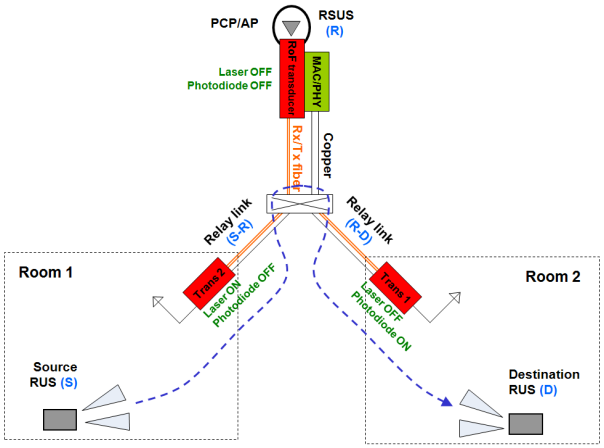

Figure 5.16: Illustration of the Full-Duplex / Amplify and Forward relay mode with a S→R→D exchange.

Figure 5.16 is based on figure 5.15, with the following analogy:

ANT1 and ANT 2 ↔ RoF transducer 1 and RoF transducer 2
Central RF circuit and switches ↔ Transparent optical splitter
Switch in position 1 ↔ laser RoF transducer 1 ON and photodiode RoF transducer 2 ON
Switch in position 2 ↔ photodiode RoF transducer 1 ON and laser RoF transducer 2 ON

Summary

The RoF technology enables multi-room transmissions for the 60GHz radio standards that have coverage limited to single room. In this context, an optical multipoint-to-multipoint architecture based on totally transparent optical components seems a good compromise between cost, effectiveness, and performance, but only if it is completed by a management of the optical access in order to remove the RoF issues and improve the Global Spectrum Efficiency.

It has been shown that the optical access can be managed reusing BF and cooperating with the IEEE 802.11ad radio MAC layer since the antenna patterns can be linked to MAC fields: Antenna ID, Sector ID, MAC addresses and Association IDs. The management of the optical access will run smoothly, particularly with the Infrastructure MAC architecture. It is precisely the architecture to promote because it constitutes currently the most popular use of the IEEE 802.11 standards and it meets the telecommunication operator requirements such as the Internet connectivity and the establishment of an Ethernet bridge. Besides that, the Ad-hoc MAC architecture is conditioned by the support of the optional relay mode. Table 5.9 resumes the conclusions for each access period.

Table 5.9: Summary.

Access Period		Implementation	RoF management
Beacon Time (BT)		Mandatory	Feasible.
Association Beamforming Training (ABF-T)		Mandatory	Feasible excepted during the RSS frames exchanges. ABF-T is a contention-based period where the optical beatings will be considered as collisions, and the frames retransmitted.
Announcement Time (AT)		Mandatory	Feasible.
Data Transfert Time (DTT)	Contention Based Period (CBP)	Mandatory	Contention-based period where the collisions are taken into account. No RoF management, but the RoF system works anyway with lower QoS.
	Service Period (SP)	Optional	Feasible for the Infrastructure MAC architecture, and for the Ad-hoc architecture if the Relay mode is supported.

Concerning the exchanges of data (DTT), two modes have been implemented in the IEEE 802.11ad standard:

- one not ensuring the QoS (CBP) and where the RoF management is not possible.
- one ensuring the QoS (SP) and where the RoF management is possible.

Finally, with the RoF management, these two access periods keep their properties.

The next step, when the IEEE 802.11ad chipsets will be available, is the implementation of this optical management in order to validate this concept and to evaluate its performances.

5.2 The ORIGIN project, a first step in the implementation of the optical access management

5.2.1 Purpose

The implementation of an optical access management as depicted in figure 5.3 is not possible today due to the fact that the IEEE 802.11ad radio chipsets are not yet available. However, such a solution has been partially realized by a proof of concept in which the central node has been reconceptualized. In fact, to overcome the lack of adapted radio chipset, a Graphic User Interface (GUI) is now proposed to control the optical multipoint-to-multipoint RoF architecture and select

one point-to-point link among the $N!\,/\,(2\,(N\text{-}2)!)$ links that can be established (N being the splitter size).

An example is presented in figure 5.17 for RoF transmissions based on WirelessHD devices from Gefen, products thought for point-to-point exchanges. The users can choose two rooms of their house to, for instance, broadcast a HD movie from their living-room to their kitchen during the dinner; and later, they can switch the radio link toward their bedroom to finish watching the movie. The benefits for the users are the reduction of the radiated emitted power (radio-waves not emitted in the baby's room) and a feeling to have the control of their home network. From a technical point-of-view, in this 4x4 optical architecture only two lasers are turned-on simultaneously. This does not remove completely heterodyning detections and additional noises but the interferences are greatly reduced as shown in table 4.3.

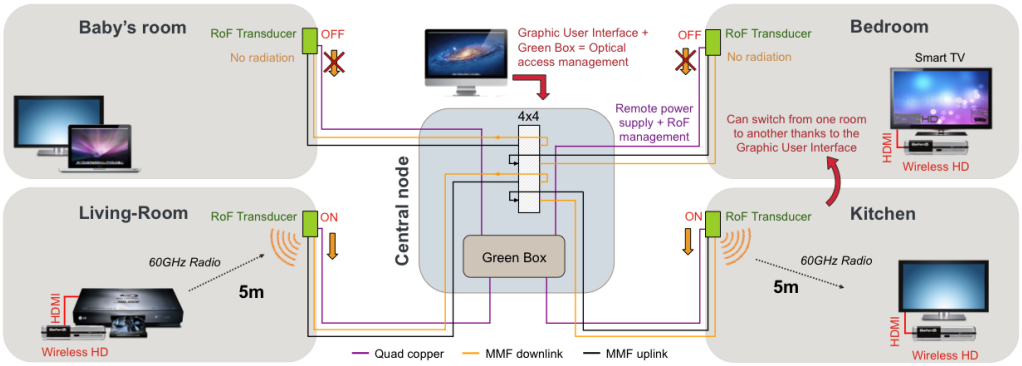

Figure 5.17: Optical access management on an optical multipoint-to-multipoint architecture (4x4) thanks to a Graphic User Interface (GUI).

The GUI replaces the IEEE 802.11ad radio MAC layer and the BF process, while a "Green Box" plays the role of interface between the GUI and the RoF transducers: it receives information from the users, then creates the required electrical monitoring signals to activate the wanted lasers and photodiodes.

In the following sections, details will be given on the realization of this proof of concept and on each element that constitutes it, i.e. the HAN infrastructure, the RoF transducers and the "Green Box", the key part to manage the optical access. All these elements have been developed in the ORIGIN project (section 1.5). It has to be underlined that such realizations are based on the results of this thesis.

5.2.2 The domestic cable and the HAN infrastructure

The cabling engineering developed in the ORIGIN project targets the market of new and/or highly renovated buildings. It is a structured cabling installed for 15 to 20 years that must meet the HAN technical and economic requirements. Hence all the infrastructure materials (cable, connection solutions and extremity boxes) are studied and developed to have a simple, rapid and aesthetic installation. The study made previously in section 5.1.1 leads us to develop a hybrid cable (figure 5.18). It consists of an optical cable with two 900μm modules including a low bend sensitivity multimode fiber (OM3+ MMF) for the RoF transmission and of a quad copper cable for the remote powering and the optical access management. The copper cable is compatible with Power over Ethernet (PoE) and 100Mbit/s Ethernet standard as it has been shown in chapter 3.

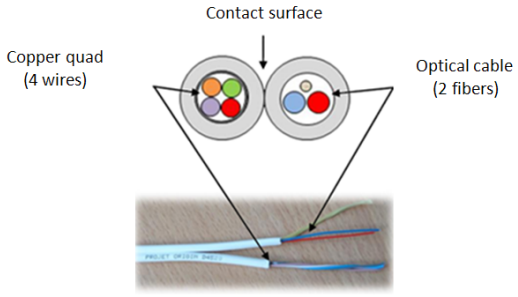

Figure 5.18: The ORIGIN hybrid cable with dimensions of 2×3.4mm, from ACOME.

For the cable connection, field mountable solutions are attractive since they use easy tools and need only a little training for the end user. For our application, the connection is based on mechanical splicing. The implementation of this solution is done in two steps (figure 5.19). First, the infrastructure is deployed with the installation of the hybrid cable and of wall plugs. In each room, a hybrid wall plug is thus available, with an access to a RJ45 port for a Fast Ethernet connection. Then, in a second time, the ORIGIN solution is deployed with the installation of RoF transducers high on the walls for a better radio coverage. The connection between a RoF transducer and a wall plug is done with a hybrid patch cord that is put in a sheath embedded in the wall.

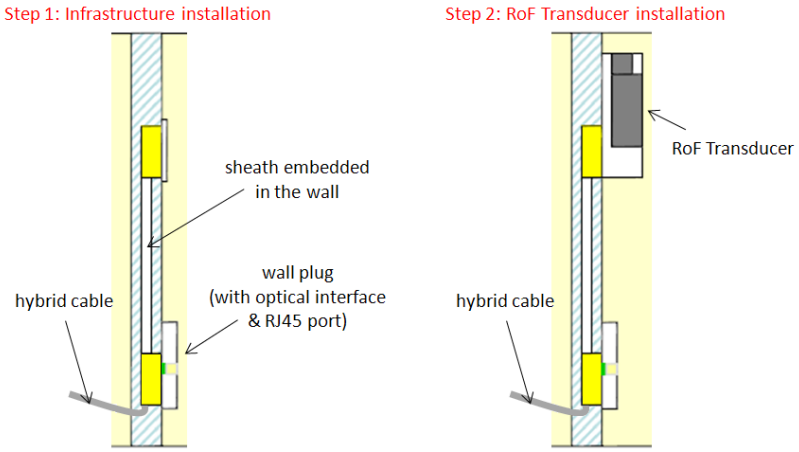

Figure 5.19: The ORIGIN installation, from Orange Labs.

5.2.3 The RoF transducers

Technical choices

Figure 5.20 shows the realized RoF transducers and figure 5.21 the corresponding block diagram. After the antenna reception, millimeter-wave signals are down-converted to a lower Intermediate Frequency (IF) in order to directly modulate the laser intensity (IM-DD). Then, after optical propagation, the IF signal is up-converted to millimeter-waves for emission in free-space. This solution enables the use of low cost optoelectronic and RF components. As shown in figure 5.21, the Local Oscillator (LO) is located at each end point.

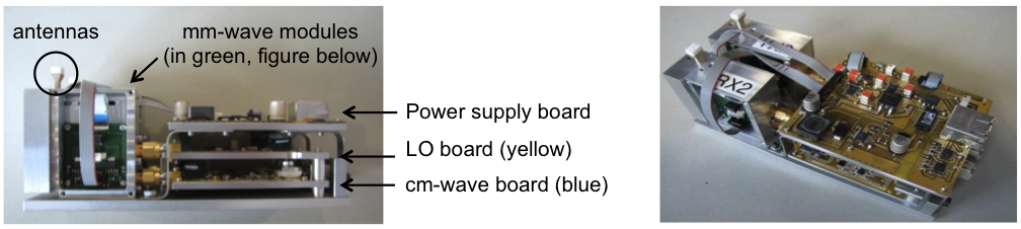

Figure 5.20: Photograph of a RoF transducer. Dimensions = 150×70×65 mm.

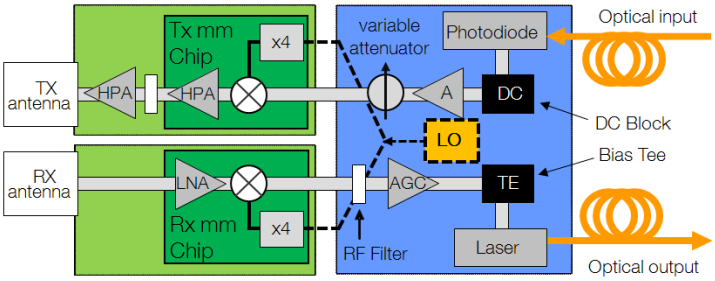

Figure 5.21: RoF transducer block diagram.

These choices are based on concepts (chapter 2) and experiments (chapter 4) made in this thesis. This is why the RoF transducers developed in the ORIGIN project have the same design than the one proposed in this manuscript. Now, each part of the RoF transducers will be presented briefly, but it has to be understood that this work emerges of three years between partners that have worked hard on the integration of the system.

The antennas

Horn antennas are fabricated using foam with permittivity close to the air one. After machining, the foam is covered with silver paint to metalize the antenna walls (figure 5.22). This concept has performances nearly as good as commercial available metal horn antennas (about 0.1dB additional losses), while the cost is only about one tenth of the metal one.

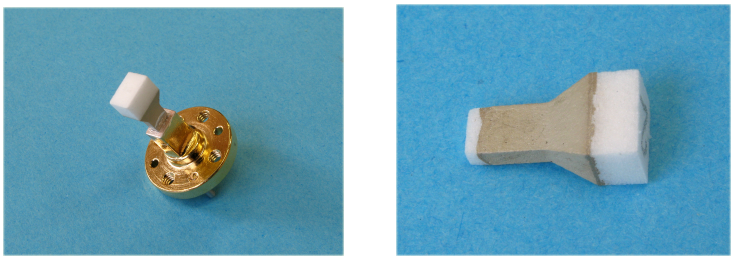

Figure 5.22: The horn antenna, from Télécom Bretagne.

The antenna gain is 10dB with aperture angles of 43° for the E-plane and 57° for the H-plane (figure 5.23). Nevertheless, as manufacturing antennas is simple and low cost, different gain values have been realized. Subsequently, tests will be conducted with 12dB horn antennas.

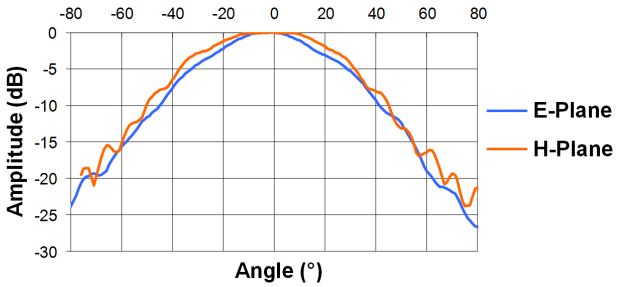

Figure 5.23: Measured radiation patterns.

The millimeter-wave modules

The system contains two millimeter-wave modules, a transmission one (TXmm) and a reception one (RXmm).

The TXmm module converts the IF input signal at 5GHz to 60GHz (figure 5.21) by means of a TX chip containing a multiplier, a mixer and a High Power Amplifier (HPA). After this Monolithic Microwave Integrated Circuit (MMIC), a microstrip high-pass filter suppresses the quite strong LO signal that remains on the RF output, and another HPA improves the output power of the TXmm module before the waveguide port where the antenna is positioned. The conversion gain of the TXmm module is about 3dB which is rather low: some improvements have to be made for the next generation of this module.

The RXmm module converts the 60GHz signal to 5GHz by means of a RX chip containing a multiplier, a mixer and a Low Noise Amplifier (LNA). The conversion gain of the RXmm module is ∼9dB and the Noise Figure (NF) is ∼10dB, values that should be improved subsequently.

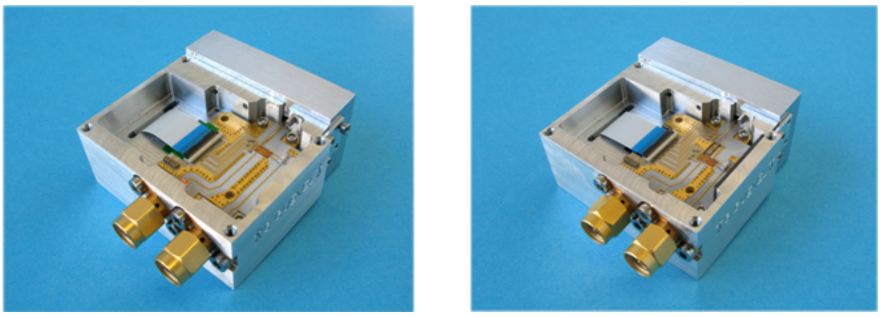

Figure 5.24: RXmm (left) and TXmm (right) modules, from Télécom Bretagne.

The RF cards, fabricated on Rogers RO4003 substrate, are assembled on a metal carrier and confined each in an individual metal package where a power supply card is also installed.

The LO board

The LO board creates the reference oscillator used in the millimeter-wave modules for the frequency conversions. This LO frequency, 13.82GHz, meets the radio standards with ±0.5ppm stability when, for example, ±1.5ppm is required by the WirelessHD.

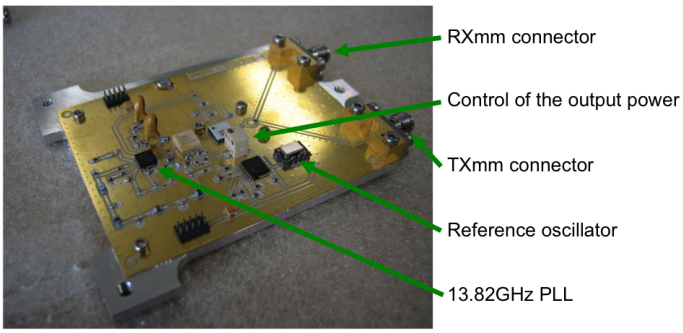

Figure 5.25: The LO board, from IETR. PLL = Phased-Locked Loop.

Finally, the RoF link transmits the radio signal, initially centered in the second channel of the unlicensed millimeter-wave band, at an IF of:

$$IF = 60.48\,GHz - 4 \times 13.82\,GHz = 5.20\,GHz. \tag{5.1}$$

The centimeter-wave board

The centimeter-wave board is placed between the millimeter-wave modules and the optoelectronic components. As shown in figure 5.26, the laser input power is optimized thanks to an Automatic Gain Control (AGC) amplifier that keeps the radio signal in the middle of the dynamic range of the optical source. This AGC amplifier has an adjustable set point and 30dB dynamic range. At the output of the photodiode, a variable attenuator adjusts the chain gain.

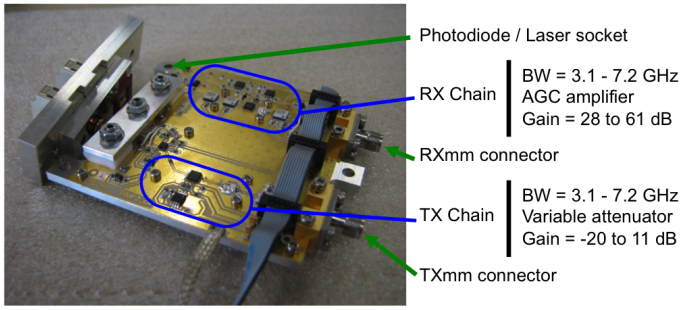

Figure 5.26: The centimeter-wave board, from IETR. The provided gains are measured values.

Moreover, switches have been placed on the centimeter-wave board to manage the optoelectronic components:

- At the reception, one switch controls the RF line at the output of the photodiode, and one switch controls the photodiode bias voltage (not the TIA power supply, Vcc, as explained in section 3.6).
- At the emission, one switch controls the RF line at the input of the laser, and one switch controls the laser bias current.

All these switches receive their Transistor-Transistor Logic (TTL) control signal from the power supply board (dashed line in figure 5.27).

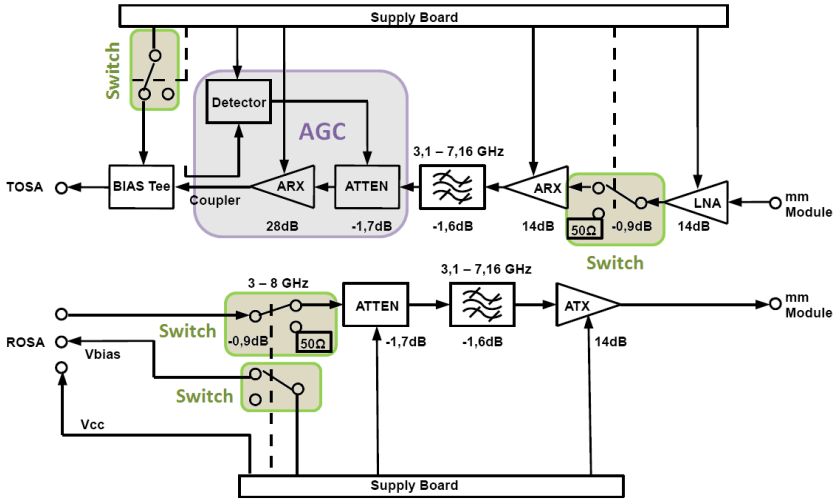

Figure 5.27: The centimeter-wave board block diagram.

The optoelectronic components

Low cost optoelectronic components working at 850nm have been implemented (figure 5.28). The TOSA was realized using packaging technology developed by ORIGIN partners. An 8μm aperture VCSEL from ULM photonics designed for 10Gbit/s digital application has been mounted on a Glass substrate (thickness 500μm) and integrated on a flex Printed Circuit Board (PCB) using a 50Ω access line. The optical interface was conceived using a LC/PC receptacle base and a ball lens to enhance the optical coupling with a 62.5μm MMF. The ROSA, from Finisar, is composed of a GaAs PIN photodiode and of a built-in transimpedance amplifier (TIA) designed for 10Gbit/s digital application (0.4A/W responsivity and 2kΩ transimpedance gain).

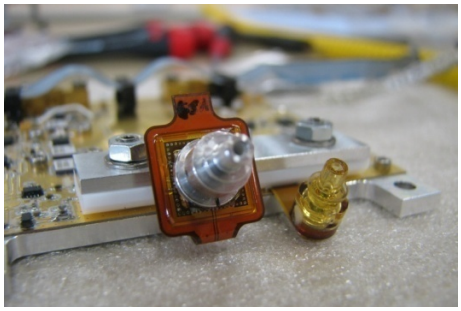

Figure 5.28: TOSA on the left and ROSA on the right.

These TOSA and ROSA are those on which characterizations have been performed in chapter 3. In particular, it has to be noted that the laser bias current has been fixed at 8mA. Lastly, in the future version of the RoF transducers, the ROSA will be replaced by the HPT briefly presented in [122].

The power supply board

This board generates the different voltages and currents required by the RoF transducers from the 48V input voltage (PoE) and controls the RF levels at the laser input (AGC amplifier set point) and at the photodiode output (variable attenuator).

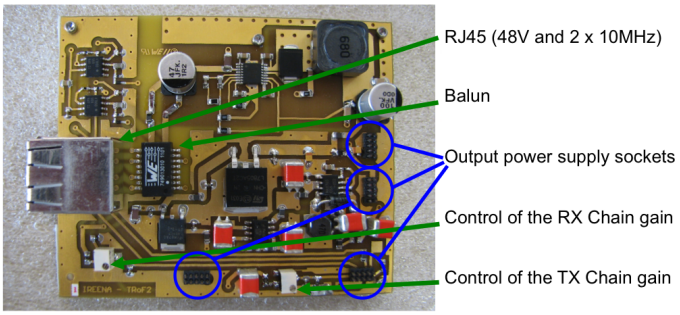

Figure 5.29: Power supply card, from IETR.

This board also includes the switching interface enabling the management of the optical infrastructure. To manage the optical layer, two monitoring signals are sent to each RoF transducer through the quad copper, one on the first pair for the laser control and one on the second pair for the photodiode control. Thus, the signals are very simple, just marked by the presence (turn-on) or the absence (turn-off) of a RF carrier at 10MHz. As depicted in figure 5.30, at the output of each copper pair, after a balun (Balanced - Unbalanced) separating the 48V from the monitoring signal, a half-wave rectifier followed by an operational amplifier converts the incoming RF tone to a constant voltage able to control the switches implemented on the centimeter-wave board (figure 5.27).

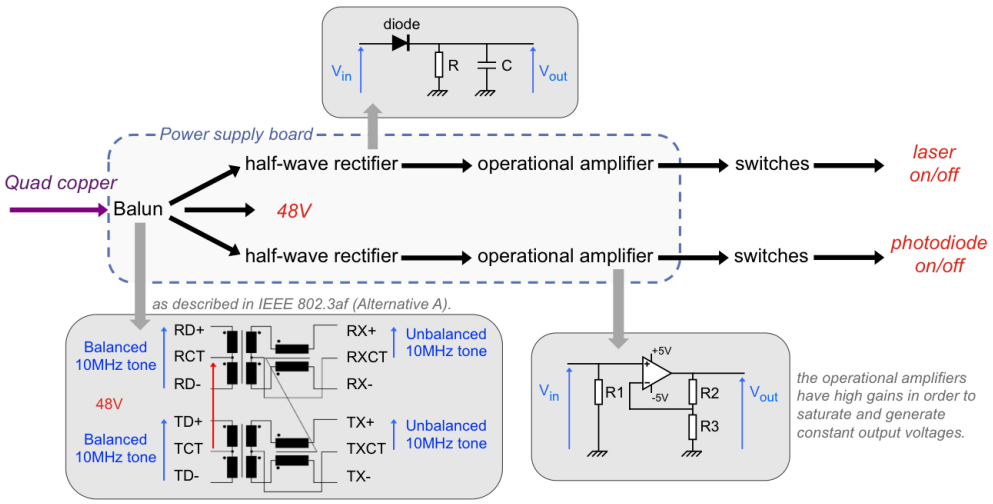

Figure 5.30: The switching interface block diagram.

5.2.4 The "Green Box"

The Green Box role consists in managing the optical layer, i.e. generating the required 10MHz tones. Thus, the unused lasers could be turned-off to remove the optical heterodyning detections and the unused photodiodes could be turned-off to reduce the Electro-Magnetic Field (EMF) radiations. This second function has given the name to the "Green Box".

As shown in figure 5.31, a 10MHz oscillator is shared between eight outputs, each of them being controlled by a RF switch. An output is then activated when it receives the expected command signal from a microcontroller (mbed from NXP [158]) controlled in turn by the Graphical User Interface (GUI) under Matlab. Today, Matlab communicates with the microcontroller through a serial interface over USB, but an Ethernet interface is currently being developed. Besides, the Green Box has been conceived for migration to an automated solution based on the BF process.

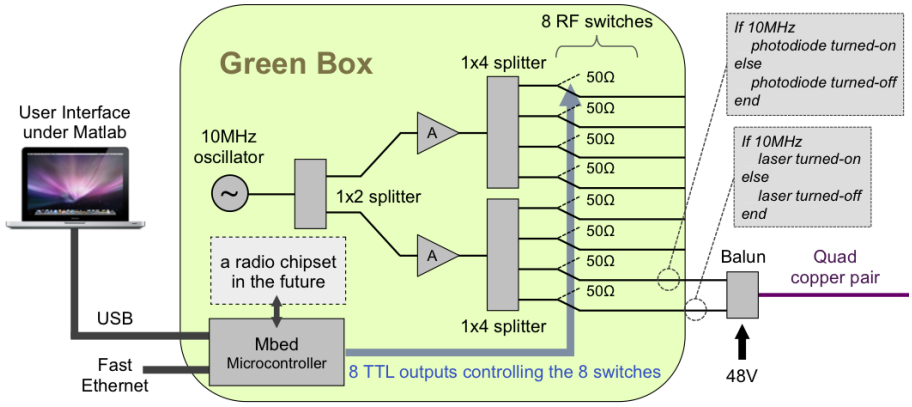

Figure 5.31: Green Box block diagram.

As shown in figure 5.31, the baluns remain external to the Green Box. Below, a photograph of the realized Green Box and a screen capture of GUI is provided.

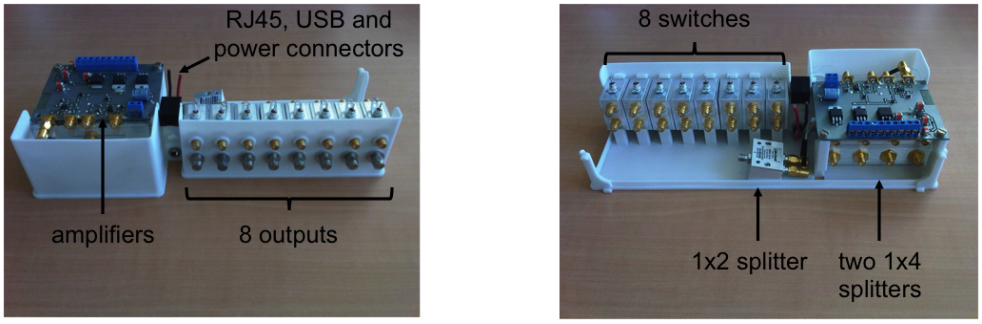

Figure 5.32: Photograph of the Green Box, from Orange Labs.

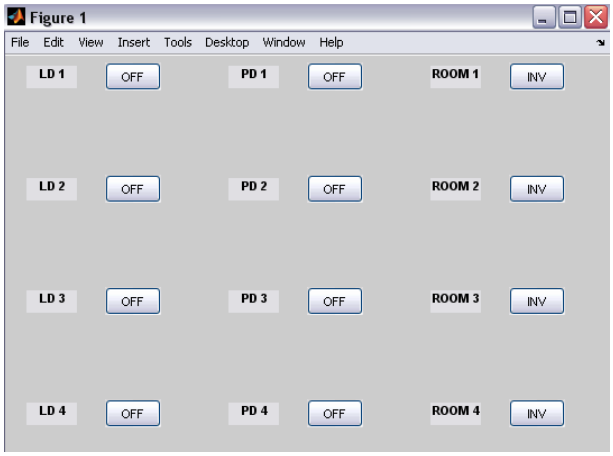

Figure 5.33: Graphical User Interface (GUI) under Matlab, from Orange Labs.

5.2.5 Results

The RoF transducers developed in the framework of the ORIGIN project have been tested with the laboratory-made radio emitter and receiver described in chapter 4.

First, a point-to-point optical link with 10dB optical losses and ~20m-length ORIGIN cable has been tested. These losses simulate an optical multipoint-to-multipoint architecture based on a 8x8 splitter (9dB theoretical optical losses) and managed by a GUI (no optical heterodyning detection). The experimental setup, represented in figure 5.34, used at the reception a 12dB gain horn antenna conceived by the

ORIGIN project, but at the emission, the 23dB gain horn antenna is a commercial product. Lastly, two RF attenuators, represented in grey, have been inserted in the setup to not saturate the laser at the emission (-20dB) and the TXmm module at the reception (-10dB). In practice, these attenuators are not useful (their presence is an experimentation mistake), the adjustable set point of the AGC amplifier before the laser and the variable attenuator at the output of the photodiode being enough to fix correct chain gains.

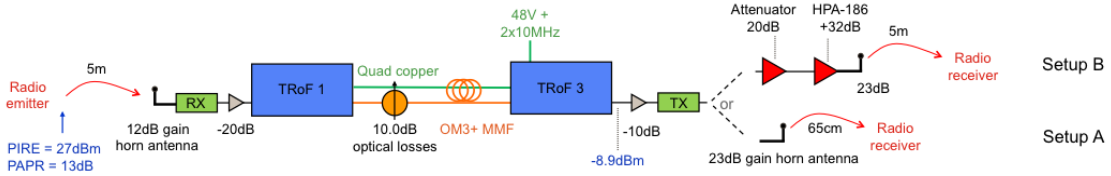

Figure 5.34: Optical multipoint-to-multipoint architecture.

In figure 5.34, setup A, the EIRP of the second hop is low, only 13.3dBm with a 23dB gain horn antenna. To obtain an acceptable result, the low emitted power is compensated by a short second hop in free-space: 65cm, i.e. 64.3dB free-space losses or a gain of 17.7dB compared to a 5m-length hop. Finally, the average EVM measured after optimization of the antenna alignment is 21.90%.

In order to achieve two 5m-length hops in free-space, an external amplifier has been added at the output of the second link (setup B). Thus, a new EIRP of 22.5dBm was measured[2]. At the reception, an average EVM of 24.47% is obtained. The signal is perfectly transmitted, with a received PAPR of 12.2dB showing that no clipping or compression has occurred (initial PAPR of 13dB), yet the performances are a little poorer. Indeed, in chapter 4, figure 4.63, an EVM of 22% had been obtained. This difference probably comes from a first RX antenna of lower gain, 12dB versus 20dB, and from a first millimeter-wave block of higher NF, 10dB versus <6dB[3].

In a second time, the electrical multipoint-to-multipoint architecture has been tested with two 1x4 RF splitters. In this case, the optical access management has also a significant benefit on the performances as shown in section 4.5. In order to not develop specific RF cards for the central node, the centimeter-wave boards of the RoF transducers are reused at the input and at the output of the RF splitters. However, due to the high gains of these cards, 30dB RF losses have been added between the two splitters. Thus, the average EVM is 28.94%.

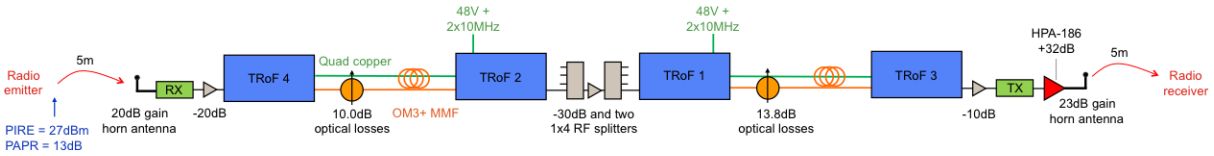

Figure 5.35: Electrical multipoint-to-multipoint architecture.

Tests have also been conducted over a long period (15h) to confirm the stability of the system. As shown in figure 5.36, from 5:45 p.m. to 8:45 a.m., just a few disruptions were observed in the beginning of the measurement when people cross the antenna-to-antenna paths. During the night, when nobody is present, the system runs smoothly. Nevertheless, the average EVM is slightly higher than the previous measurement as the setup has been placed along a wall, without proper alignment, to avoid obstruction of the corridor where the system were installed. Moreover, no overheating problems were noted.

[2]There is no coherence between the EIRPs of two setups of figure 5.34 as the gain of the TXmm module has been modified in the meantime playing with the grid voltages of its chips. It has to be noted that an EIRP of 28.5dBm can be obtained for setup B, but thermal issues can occur.

[3]The lasers are also different, one comes from U-L-M Photonics while the second comes from Finisar. However, this is not impacting as explained in chapter 4 (Friis' formula).

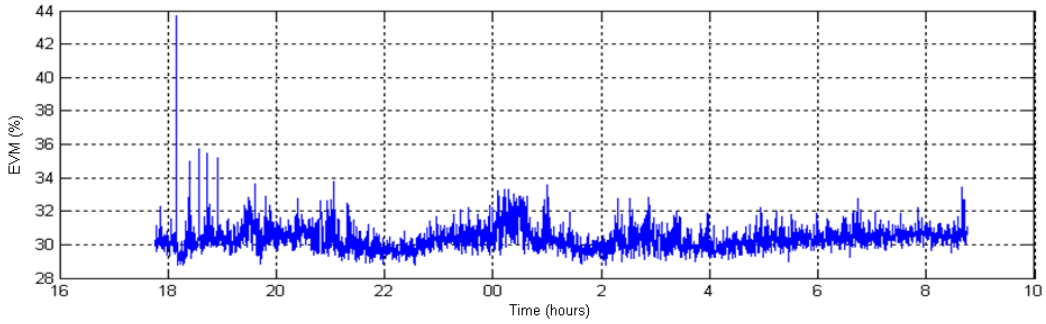

Figure 5.36: EVM for the electrical multipoint-to-multipoint architecture as a function of the time.

These two architectures, the optical and the electrical, have finally been tested with the commercial WirelessHD devices from Gefen. Some observations can be noted:

- The two architectures have run smoothly: the video signal has been transmitted successfully without image degradation.
- The effect of the two AGC amplifiers is clearly visible on the framed signal. Between the radio transmissions, the interframes are amplified by 30dB, which is seen as an important noise on the oscilloscope and on the electrical spectrum analyzer. However this does not disrupt the transmission.
- The frequency difference between the different local oscillators does not disrupt the transmission.

5.2.6 Power consumption

One important challenge for the future HAN is the decrease of their power consumption. Therefore, the consumption of the optical multipoint-to-multipoint architecture and of the electrical one have been compared to a coaxial tunnel composed of available commercial devices replacing each RoF transducer by a Gefen module plus a HDMI to SDI converter (figure 5.37). However, the coaxial tunnel is only able to transmit from a room 1 to a room 2, not the reverse path. For a bidirectional transmission the number of components has to be doubled.

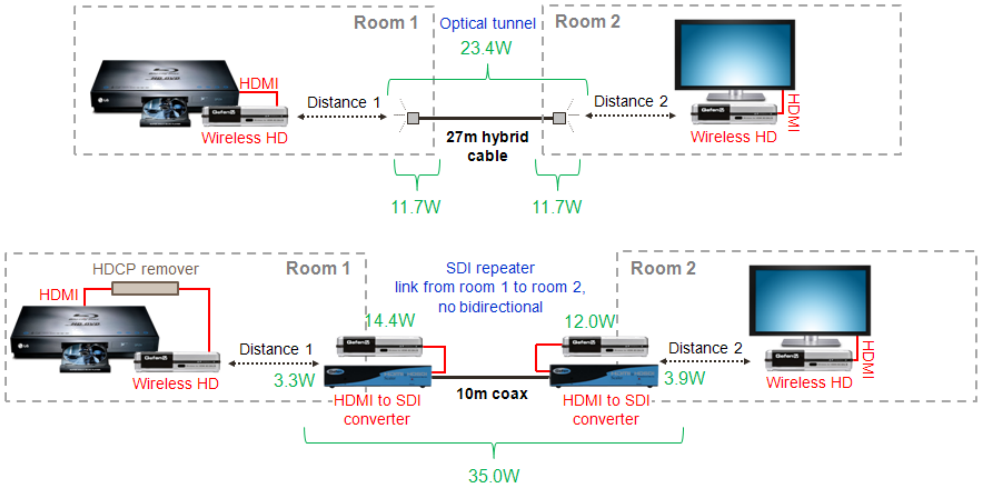

Figure 5.37: WirelessHD through the optical and coaxial tunnels and power consumption results.

Table 5.10 summarizes the energy consumption for each architecture under 220V. Concerning the RoF architectures, the tests have been conducted with the transducers remotely power supplied by the quad copper under 48V: in the table below, a transformer 220/48 volt with an efficiency of 85% has therefore been considered.

Table 5.10: Power consumption for each architecture under 220V.

Architecture	Power consumption
Bidirectional coaxial tunnel	$2 \times 35.0\text{W} = 70.0\text{W}$
Optical tunnel	23.4W
Optical multipoint-to-multipoint architecture (4x4)	46.8W
Electrical multipoint-to-multipoint architecture (4x4)	66.2W

The optical tunnel consumes 46.6W less than the bidirectional coaxial tunnel, thus being more energy efficient. Besides, it has to be noted that active 1x4 SDI splitters broadcasting one SDI flow towards four coaxial outputs are commercially available. This enables point-to-multipoint coaxial architecture, and power consuming only 3.6W. Doubling the number of equipments creates an architecture comparable to the electrical multipoint-to-multipoint RoF architecture. However, this solution is not energy efficient.

More details on the power consumption of the RoF transducers are provided in table 5.11.

Table 5.11: Details on the power consumption of the RoF transducers.

Element	Power consumption (W)
RoF transducer	$48\text{V} \times 207\text{mA} = 9.936\text{W}$
Centimeter-wave part (power, LO, cm boards)	$48\text{V} \times 138\text{mA} = 6.624\text{W}$
Millimeter-wave part (TX and RX modules)	$9.936\text{W} - 6.624\text{W} = 3.312\text{W}$
Power supply board only	$48\text{V} \times 21\text{mA} = 1.008\text{W}$

From this last table, the calculation determining the power consumption of an electrical multipoint-to-multipoint architecture based on two 1x4 RF splitters is simple:

$$4 \times 9.936\text{W} + 4 \times 6.624\text{W} = 39.744\text{W} + 26.496\text{W} = 66.240\text{W} \tag{5.2}$$

5.3 Multiservice and multiformat architectures

5.3.1 The purpose and the background

Section 1.1 has largely described the background of the Home Area Networks (HAN). If it has been shown that the increase of the data rate is the main challenge in a near future, it is not the only issue since a great heterogeneity of signals has to be delivered to various home devices: IP data for triple play services, Radio Frequency (RF) signals for terrestrial or satellite broadcast television, specific formats as High Definition Multimedia Interface (HDMI) signals to interconnect, for example, a High Definition (HD) player and a television set, ... and of course the radio. Today, all these signals are transmitted separately, as they cannot be encapsulated in a unique format, and specific networks working on specific media are dedicated to each application. Users have to deploy various networks within their home, such as copper cables for IP data, coaxial cables for broadcast television, specific cables for HDMI links... The wireless end-connectivity being the dominant trend, it might be thought that encapsulating all formats within a high-speed radio signal would be the ultimate solution, as proposed by the WirelessHD to transport HDMI signals. However, some users will keep using wired links for QoS reasons, electromagnetic radiation, or compatibility, their terminals not integrating the latest radio standards. Keeping two separate media, one wired and another wireless is therefore essential: the user must have the final choice.

The multiplicity of signals in the HAN is a reality, but also a problem: a solution to distribute all these signals on a single infrastructure has to be found. It was previously shown that the optical fiber is the best way to distribute the radio signals to the whole home and extend the wireless end-connectivity. It would be dangerous for a product based on optics, and so being regarded as a premium product, to not take into consideration all the HAN services. As a consequence, this section is focused on optical architectures conveying multiservice.

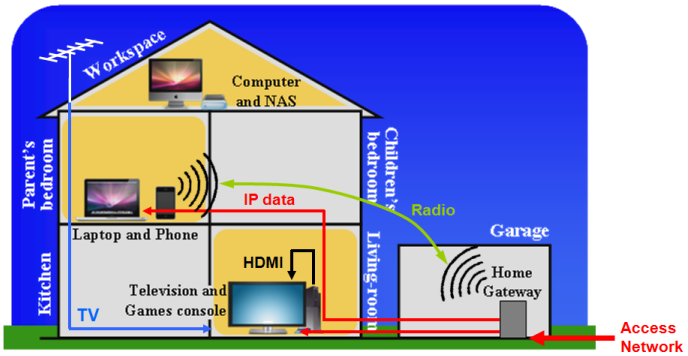

Figure 5.38: A home with multiservice and multiformat signals not unified.

Two main optical multiservice and multiformat infracstructures can be deployed depending of the RoF multipoint-to-multipoint architecture chosen:

- an active star architecture centered on a multiformat switch for the electrical RoF solution.
- a CWDM Broadcast and Select (B&S) architecture centered on a NxN optical splitter for the optical RoF solution.

These two architectures use the same approach than the previous RoF infrastructures, i.e. two optical fibers, one for the uplink and one for the downlink.

Multiformat active star architecture

The multiformat active star architecture is depicted in figure 5.39. The different domestic signals, including Ethernet, terrestrial and satellite broadcast television, and radio converge towards a Multiformat Switch (MS). This device integrates an Ethernet switch to manage the IP exchanges between the home devices, but also with the access network. The MS is also able to process the analog signals coming from the television antenna or from the satellite dish. In fact, they are duplicated before being sent to the different MS ports. The radio signals, coming from or going to the RoF transducers, share a radio bus inside the MS, like in the electrical multipoint-to-multipoint RoF architecture. A connection between the radio bus and the Ethernet switch can be imagined to enable the exchanges between wired and wireless applications. In this case a radio chipset is required. Finally, all these signals are multiplexed at each port of the MS and conveyed on optical multiformat links towards remote plugs (also called extenders) located in different rooms. These signals are then demultiplexed and delivered to the end user using the adapted interface. A similar process is applied for the uplink, except that no uplink is required for the broadcast television service.

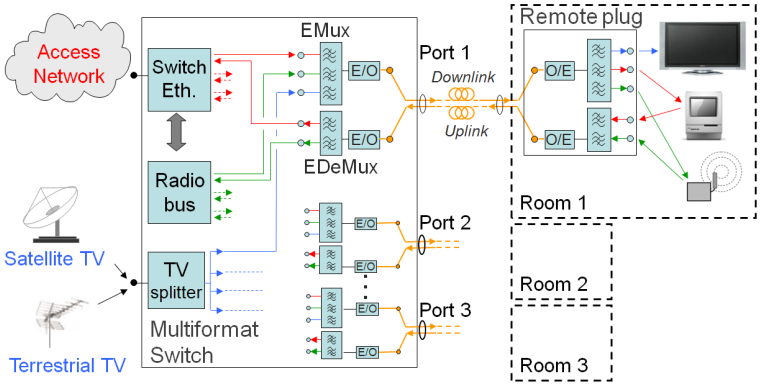

Figure 5.39: The multiformat active star architecture.

The main signals to be propagated on the multiformat links are depicted in figure 5.40. They include mainly Ethernet for IP data, terrestrial and satellite broadcast television and cm- or mm-wave radio signals. As far as IP data are carried by Fast Ethernet, the multiplexing of the different signals may be achieved in the electrical domain, as there is no risk of spectrum overlapping.

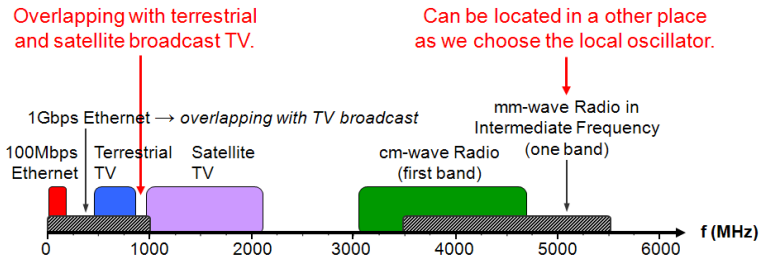

Figure 5.40: The electrical multiplex.

This solution has been first validated by an experimental setup based on graded index plastic fibers optimized at 850nm [56], then on OM2 silica MMF. The tested electrical multiplex was composed of Fast Ethernet, of digital terrestrial television (DVB-T standard) and of the first band of the Ultra Wide Band (UWB) radio signal (from 3.1 to 4.7 GHz). As previously, for low cost concern, direct modulation and direct photodetection have been used with the VCSELs and the GaAs PIN photodiodes with built-in TIA from Finisar.

In a near future, 1Gbit/s Ethernet will be needed to meet the requirements of the home applications. As shown in figure 5.40, the electrical spectrum of the Gigabit Ethernet overlap the terrestrial and satellite broadcast television: a simple electrical multiplex is no longer possible. In this case, a frequency transposition could be used, but finding the right location in the spectrum of the transposed signal is difficult, especially because Ethernet is a baseband signal. The most efficient solution consists in introducing an hybrid optical/electrical multiplexing as depicted in figure 5.41. The Ethernet signal is then carried by a separate wavelength, making easier the evolution later towards 10Gbit/s, while the other signals remain electrically multiplexed.

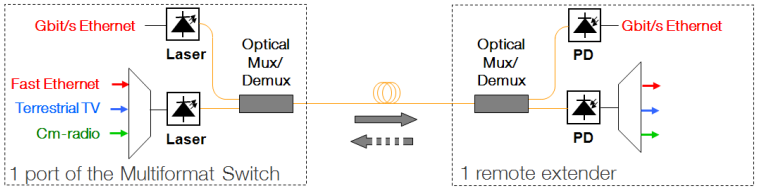

Figure 5.41: An hybrid optical and electrical multiplexing.

This possibility has been demonstrated in [159]. For the optical multiplex, wavelengths have been chosen in the CWDM grid to allow the insertion of Optical Add and Drop Multiplexers (OADMs) with a minimum impact on the optical budget. The transmitters used the FP laser at 1310nm presented in the chapter 3 for the electrical multiplex and a Small Form-factor Pluggable (SFP) module at 1290nm for the Gigabit Ethernet in baseband format. Even if one Gigabit Ethernet link was implemented on a separate wavelength, a Fast Ethernet channel was kept in the electrical multiplex since the lower part of the spectrum was free. Terrestrial digital television and UWB radio signals completed the electrical multiplex.

Lastly, a third setup based on the multiformat active star architecture has been tested with this time wavelengths chosen in different windows to reduce the cost. The 850nm VCSEL from Finisar was used for the electrical multiplex, while a bidirectional monofiber SFP module was dedicated to the baseband Gigabit Ethernet, using two wavelengths, at 1.3 and 1.5 μm, for a full-duplex transmission on a unique fiber. Thanks to different wavelength sensitivity, the photodiodes discriminate the services without any additional optical filters. Therefore, optical couplers were used instead of OADMs, but only on the downlink. Thus, the radio uplink, with a more complex electrical multiplex as it includes television broadcast services, has a favored optical budget.

Table 5.12: Configuration of the different setups tested.

	Setup 1	Setup 2	Setup 3
	Graded Index PoF	MMF with OADMs	MMF with optical splitters
electrical mux	850nm	1310 nm	850 nm
Gigabit Ethernet	not implemented	1290nm	1310nm downlink & 1550nm uplink

Broadcast and Select (B&S) architecture

The CWDM B&S architecture is based on a NxN optical splitter, like the optical multipoint-to-multipoint RoF architecture: in each room optical outlets are connected to this splitter through a dual-fibre cable with one fibre per transmission direction. Adding services by means of an electrical multiplex is not sustainable due to the low optical budget. Indeed, the electrical multiplexing requires to limit the RF power per service at the input of the laser to not saturate it, while the high optical losses require on the contrary to have an enough SNR at the reception.

Therefore, the different applications are implemented using CWDM technology to separate incompatible formats. At the reception side, an optical filter extracts only the wavelength corresponding to the wanted application. Different types of optical filters may be used, but OADMs are preferred as they select one wavelength by leaving the other ones being available at the output of the module (figure 5.42). It is then possible to cascade such add and drop filters on one optical outlet to provide connections to several services at the same point. An important advantage of this architecture lies in its great flexibility, as it is possible to emulate simultaneously various topologies like point-to-point, point-to-multipoint and multipoint-to-multipoint, by simply choosing the adapted combinations of transmitted or selected wavelengths.

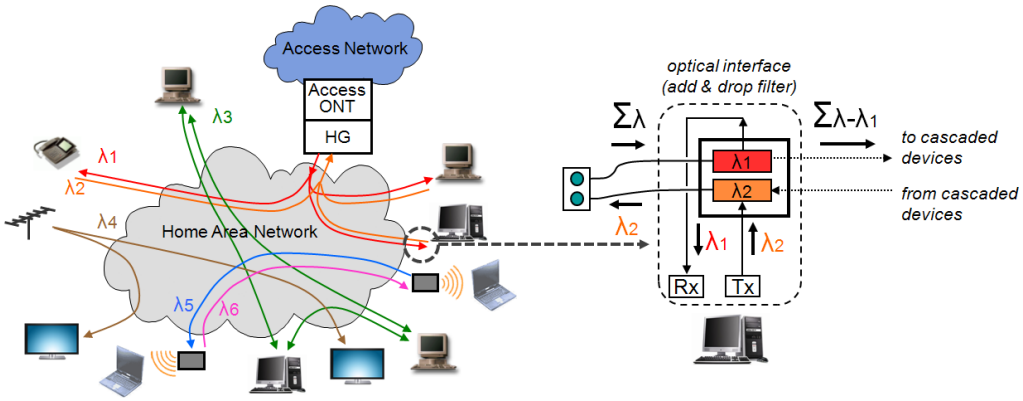

Figure 5.42: Example of different topologies simultaneously implemented on a CWDM B&S architecture, and focus on an optical outlet with Optical Add & Drop filters.

Compared to the multiformat active star, one important difference lies in the way that data exchanges at IP level are achieved. These exchanges usually are based on point-to-point links (switched Ethernet), which is not fitted to a CWDM approach on an NxN passive optical plant as it results in a waste of the wavelength resource, each bidirectional point-to-point link requiring two wavelengths. It is then necessary to implement protocols designed for shared medium applications.

The simplest protocol for shared medium is the CSMA/CD protocol. It was widely used in the LAN domain on coaxial Ethernet busses but its implementation slew down due to the emergence of products based on switched Ethernet in order to decrease the collision rate and increase the throughput. As the passive star is the best solution to realize an optical bus (in terms of logical topology), the CSMA/CD protocol gains interest again. Its main advantage is that, on a physical point of view, only one wavelength is shared between all the connected devices. Its main drawback is a poor QoS (Quality of Service) as this protocol was first designed for best effort exchanges, without real time requirements. However, its efficiency could benefit on one hand from the reduced number of devices in the home, and on the other hand from the short distances network.

On the contrary of the RoF, no optical beating occurs between CSMA/CD Ethernet sources as their lasers are turned-off when no Ethernet signal is emitted. In fact, the physical signal emitted is Non-Return-to-Zero (NRZ) coded with a zero level below the laser threshold current. By contrast, the solutions based on existing home wiring and designed for bus topology such as the HomePlug AV or the MoCA, both using advanced modulations, recreate the same optical issues as the ones occurring with the radio signals. Yet, they could be good solutions, even if their data rates lower than 1Gbit/s are not convincing.

Another more efficient protocol for shared medium has been developed for Passive Optical access Networks (PONs). Based on a multiplex in the time domain (Time Division Multiplexing downstream, Time Division Multiple Access upstream), this protocol could be applied to the CWDM B&S architecture, after being simplified to match the HAN requirements, with an adapted compromise between cost and performances. Only two wavelengths are then required, and the PON mechanisms guarantee a perfect QoS, also with coexisting real time and best effort traffic.

In the past, a CWDM B&S architecture based on SMF and on a 16x16 splitter has been demonstrated by an experimental setup [160] where six services ran simultaneously: a PON, a CSMA/CD LAN, a Gigabit Ethernet point-to-point link, a Fast Ethernet point-to-point link, the terrestrial broadcast television and an UWB radio signal transmission. The corresponding optical spectrum for this configuration is shown in figure 5.43. It has to be noted that several OADMs were cascaded at some optical outlets, demonstrating the compatibility of this architecture with the optical budget of the related applications.

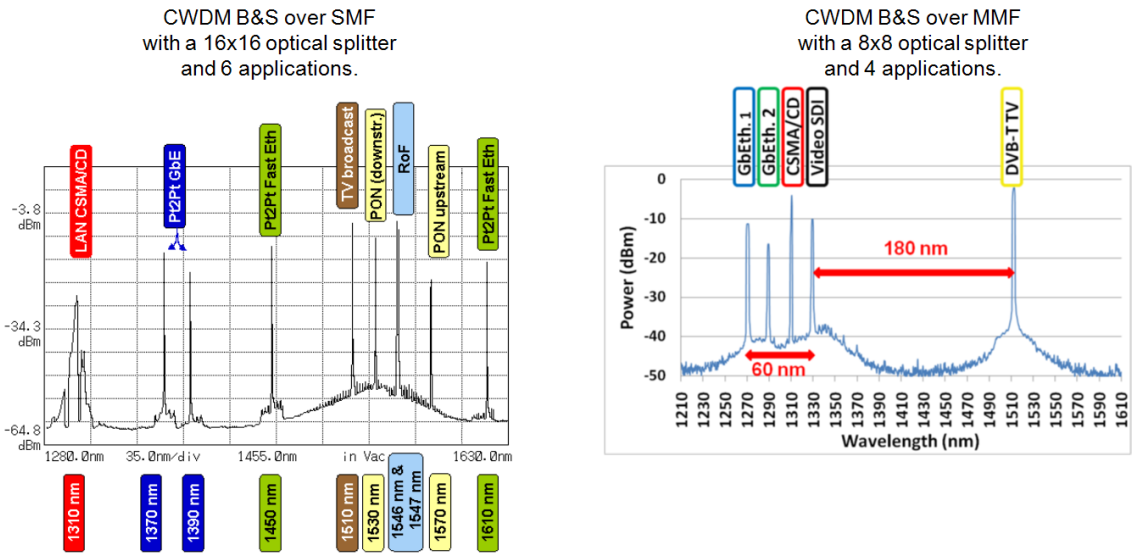

Figure 5.43: Observed optical spectrum on a singlemode (on the left) and a multimode (on the right) CWDM B&S setup.

A CWDM B&S architecture based on MMF and on a 8x8 splitter has also been realized and tested during this thesis [161] [162] with four applications running simultaneously: a CSMA/CD LAN, a Gigabit Ethernet point-to-point link, terrestrial broadcast television and digital video point-to-point link at 1.4Gbit/s (figure 5.43). For each application, OADM designed for MMF were used to select the dedicated wavelengths. The main difficulties raised by the lack of available optical transmitters dedicated to CWDM applications on MMF. Sources designed for SMF were then used, based on DFB (Distributed FeedBack) lasers, which exhibit a very narrow spectral width and a high coherency level. Perfectly tailored to SMF applications, these transmitters excite a very limited number of modes in the fiber, which strongly impacts the behavior of the multimode splitter and the uniformity of the power at its outputs. The optical budget is therefore seriously affected for some combinations of input and output ports of the splitter, leading in some cases to service interruption. The problem has been studied in details in [163] where simulations have been carried out to get a better understanding of the behavior of the multimode splitter according to the different source parameters.

5.3.2 Integration of the 60GHz radio link as a new service

In previous sections, MMF has been chosen to distribute the radio signal at 850nm. Consequently, opting for the CWDM B&S architecture to add new services is challenging as CWDM requires optical elements, such as optical filters, that are not commercially available for this type of fiber and in this optical window. Actually, WDM technology is mainly used in core and metropolitan networks, where only SMF components are used and where the constraints in terms of cost are not the same as in the home network.

Consequently, the multiformat active star architecture, the one corresponding to the electrical multipoint-to-multipoint RoF architecture, is preferred in a first time for multiservice and multiformat. This solution has the advantage to be laser beats independent and transverse multimode character independent. Then, the optoelectronic components used for the RoF service allow a large electrical multiplex as their bandwidth is up to 10GHz.

A proof of concept based on the electrical multipoint-to-multipoint architecture

A multiformat active star architecture distributing the Gigabit Ethernet, the digital terrestrial television and the second channel of the millimeter-wave radio band has been realized. The experimental setup is represented in figure 5.44.

The system is based on a hybrid optical/electrical multiplexing. The electrical multiplex, composed of the terrestrial television and of one channel of the millimeter-wave band down-converted into IF, is conveyed at 850nm using direct modulation with direct photodetection method with the VCSEL and the PIN photodiode from Finisar. The wavelengths for the Ethernet signal and the electrical multiplex were chosen in different windows to maintain system low cost. Thus, photodiodes discriminate them thanks to different wavelength sensitivities; neither optical filters nor OADM are necessary. Bidirectional monofiber SFP modules are used for the Gigabit Ethernet with two wavelengths for a full-duplex transmission on a unique fiber at 1.3 and 1.5 μm. Only the optical downlink includes two optical splitters (50:50 splitting ratio).

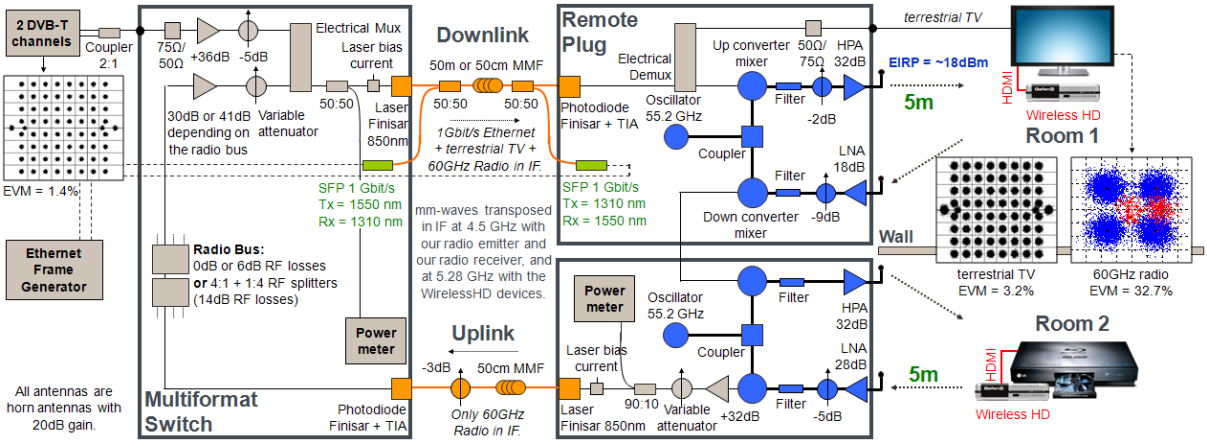

Figure 5.44: Experimental setup.

For the electrical multiplex, the laser input powers have been optimized. In the optical uplink, only composed of the radio signal, 3dB optical losses have been inserted to not saturate the photodetector. The laser input power is -9.5dBm. In the optical downlink, the two optical splitters and the 50m-length OM2 MMF induce 9dB optical losses. The optimal laser input power is -3.06dBm, with -13.77dBm for the terrestrial television and -3.45dBm for the radio signal.

The MS includes RF losses between the two RoF links to simulate a radio bus, 0 or 6 dB corresponding to RF splitters with respectively 1 (or point-to-point link) and 4 ports (theoretical value for a 4x4 splitter). After the radio bus, an amplifier followed by a variable attenuator simulates an Automatic Gain Control (AGC) amplifier that regains the right power level at the input of the second laser.

Concerning the performances, the full-duplex 1Gbit/s Ethernet signal, generated and analyzed by an Ethernet frame generator, has been achieved without error.

The television signals, composed of two Digital Video Broadcasting-Terrestrial (DVB-T) channels centered at 482 and 546 MHz, are generated by Peripheral Component Interconnect (PCI) cards according to the French standard and are tested with a television set or with a television analyzer. At the input of the MS, the television power equals -42.7dBm per channel: these levels are recovered at the output of the system, ±1dB. Table 5.13 resumes the other results for the channel centered at 482MHz. The constellation diagrams provided by the television analyzer have been represented in figure 5.44, at the input and at the output of the system, with 50m-length MMF and all the services transported simultaneously. With a television set, no reception degradation has been observed, as predicted by the pre-Viterbi BER and Carrier to Noise Ratio (CNR), which are under the limit value defined by the DVB-T standard.

Table 5.13: Terrestrial television results.

Configuration	50cm-length MMF				50m	Direct link	Limit values
Eth./Radio present?	no / yes	yes / yes	no / no	yes / no	yes / yes	-	-
EVM mean/peak (%)	2.9 / 11.8	3.0 / 13.0	2.8 / 10.7	2.8 / 11.2	3.2 / 14.2	1.4 / 8.1	4.4 / 22.0
CNR_{min} (dB)	28.2	27.6	29.4	28.5	27.1	31.6	24
pre-Viterbi BER	$9.0 \cdot 10^{-7}$	$3.8 \cdot 10^{-6}$	$3.5 \cdot 10^{-7}$	$4.8 \cdot 10^{-7}$	$2.1 \cdot 10^{-5}$	$>10^{-8}$	10^{-2}

The 60GHz radio signal is generated either by the WirelessHD commercial device in order to transmit a 1080i uncompressed HD video in real time or by the laboratory made radio emitter (chapter 4) in order to measure the link EVM. As a reminder, the laboratory made radio signal is center at 59.7GHz and emits with a 28.6dBm EIRP.

For radio transmission through the active star multiformat architecture, with all the services multiplexed, 50m-length MMF, two 5m-length hops in the air and a radio bus simulated by 0 and 6 dB RF losses, the setup provides an average EVM of 31.3% and 33.4%, respectively. Even if the EVM values are large, this is sufficient for a real time transmission between two commercial WirelessHD devices. Lastly, removing the television service of the electrical multiplex improves the EVM by 2%, and changing the fiber length from 50m to 0.5m improves also the EVM by 2%. For the real time transmission between the two commercial WirelessHD devices, no degradation has been observed on the television set, even with the two 1x4 RF splitter representing 14dB RF losses.

Finally, the 1Gbit/s Ethernet, the terrestrial broadcast television and the 60GHz radio signal can be delivered simultaneously on a unique MMF infrastructure based on the electrical multipoint-to-multipoint architecture.

A WDM-FDM approach to make the optical multipoint-to-multipoint architecture multiservice and multiformat compatible

To finish, an original approach has been tested to make the optical multipoint-to-multipoint architecture multiservice and multiformat compatible: at the emission, WDM technology achieves the separation between the home services while, at the reception, FDM technology recovers them. As a consequence, each signal has to be located in a different electrical spectral band and the photodetector have to be sensitive on a large optical spectral band.

This concept is presented in figure 5.45 for three services: a Fast Ethernet signal conveyed at 780nm, the terrestrial broadcast television at 825nm, and a 60GHz wireless connectivity transposed in IF and transmitted at 850nm. At the central node, the NxN optical splitter plays the role of optical multiplexer combining the different wavelengths, and at the reception, a unique GaAs PIN photodiode detects all the services (figure 5.46), then an electrical demultiplexer discriminates them.

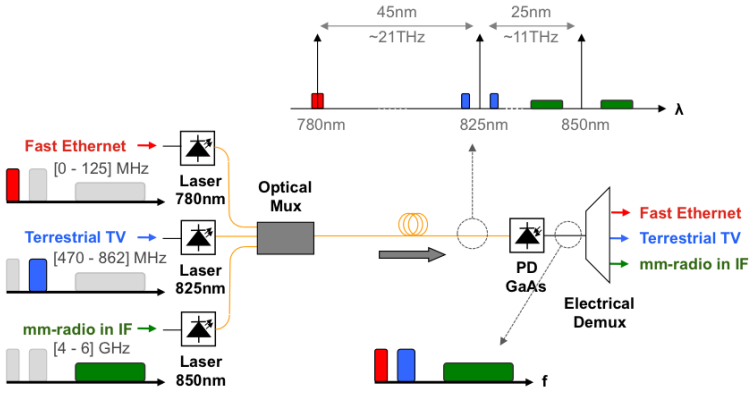

Figure 5.45: The WDM-FDM approach.

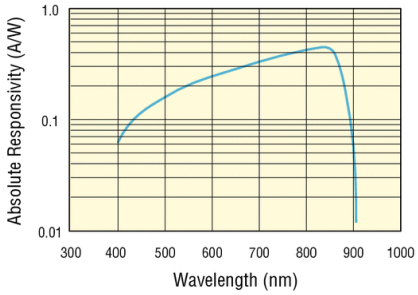

Figure 5.46: The GaAs spectral responsivity, from [35].

This approach has several advantages. First, as a wavelength is dedicated to the radio connectivity, the laser of each RoF transducer can be managed without impacting other services. Secondly, no optical heterodyning interferences occur as the resulting beatings are pushed away towards frequencies higher than the Terahertz, which are filtered by the photodetector. Thirdly, adding new services remains flexible. In fact, they can be injected from any room of the home. Fourthly, at the reception, no optical filter is required if the signals do not overlap in the frequency domain. Lastly, the use of different optical sources for each service reduces the RF power constraints at the input of the lasers.

In order to understand how such an infrastructure can be used at home, a typical usecase is presented in figure 5.47. A key point of the implementation of this solution lies in the fact that the optical multiplexing never takes place in a room, but always at the central node using the optical splitter. Indeed, the different services are injected from different wall plugs since the Ethernet and terrestrial broadcast television connectors are positioned close to the floor or at the level of a furniture element, while the RoF transducers are installed high on the walls for a better radio coverage. Additionally, the television is a broadcast service with only one injection point generally positioned close to the roof where the television antenna is installed and where no Ethernet signal is required.

Concerning the domestic services presented in figure 5.47, the Fast Ethernet uses a bus topology and a NRZI (NRZ Inverted) signal with a zero level below the laser threshold current to remove the optical beatings (i.e. 100Base-FX or SX), the terrestrial broadcast television is a set of OFDM channels emitted from only one laser, and the radio connectivity is a 60GHz OFDM signal transposed in IF and emitted from the different RoF transducers. To avoid optical heterodyning detections for this last service, the optical access is managed by a “Green Box” activating only the required laser and photodiode. Thus, as proposed previously, a hybrid cable is used with MMF for the distribution of the home services and with copper pairs for the power (all the remote plugs) and the RoF management (only the RoF transducers). The RoF access is managed either by a PCP/AP directly connected to the Green Box (IP transmission based on the IEEE 802.11ad standard, section 5.1.1) or, as proposed below, by a computer connected to the Green Box in Ethernet and activating the wanted point-to-point wireless HDMI link (section 5.2.4).

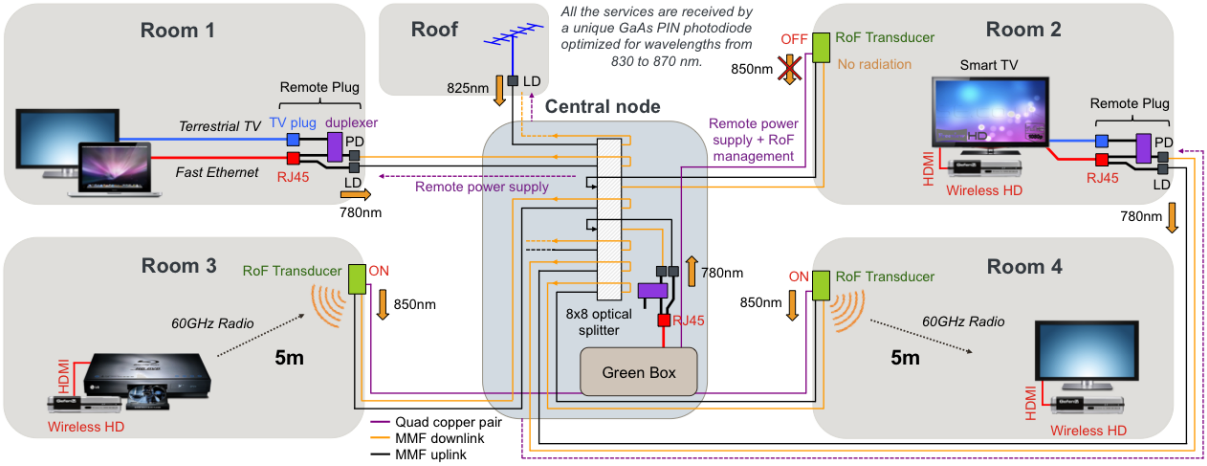

Figure 5.47: Example of a multiservice and multiformat HAN based on a multipoint-to-multipoint architecture with a WDM-FDM approach.

The experimental setup is depicted in figure 5.48. It is based on the example presented in figure 5.47, but in a simplified manner. Indeed, the optical splitter size is 4x4. However the three services have been implemented: the Ethernet (one link only), the terrestrial broadcast television, and the millimeter-wave radio connectivity (a full duplex link).

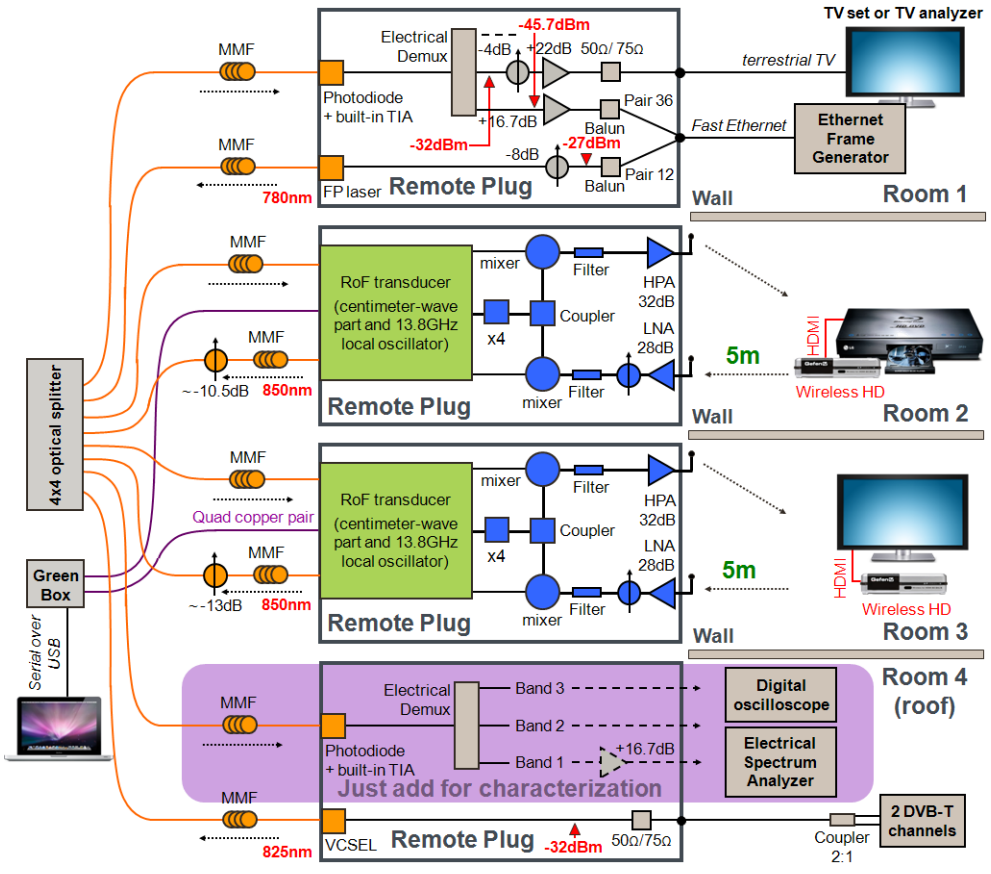

Figure 5.48: Experimental setup.

At the emission, a FP laser at 780nm, and two VCSELs, one at 825nm and one at 850nm, have been used (table 5.14). For this WDM multiplex, a VCSEL at 910nm has also been tested, but the Finisar GaAs PIN photodiode used at the reception does not detect properly this wavelength. Yet, having a third VCSEL would be a great advantage because the FP laser at 780nm has a poor transverse mode character inducing unequal optical powers at the outputs of the splitter. In fact, the insertion losses vary from 4.90 to 8.08 dB for an average value of 6.61dB. As a consequence, this optical source conveys the Ethernet signal, a digital signal a priori more robust.

Table 5.14: Lasers used for the WDM multiplex.

laser	FP laser at 780nm	VCSEL at 825nm	VCSEL at 850nm	VCSEL at 910nm
Manufacturer	unknown[4]	Finisar	U-L-M Photonics	Finisar
Slope efficiency (W/A)	0.043	0.083	0.420	0.085
Threshold current (mA)	2.4	1.5	0.7	1.9
Bias current used (mA)	10.83	2.04	7.70	-
Service	Fast Ethernet	Broadcast television	Radio signal	none

Normally, the radio signal at IF is not extracted at the same point as the Ethernet and the terrestrial broadcast television, but for the experience, the three services have been extracted from a unique photodiode using a triplexer:

- Band 1, from DC to 350MHz.
- Band 2, from 380MHz to 2.16GHz.
- Band 3, from 3 to 8 GHz.

Thus, from the multiplex of figure 5.49, the different services can be recovered as shown in figure 5.50. In these spectra, some spurious signals appear around 380MHz and at 2.41GHz (Wi-Fi transmission). In France, the [360.0 - 399.9] MHz radio band is shared between the air traffic control and the national police communication system, Acropol [164]. Probably that a civil aviation radio communication has been captured, the experience taking place close to an airport.

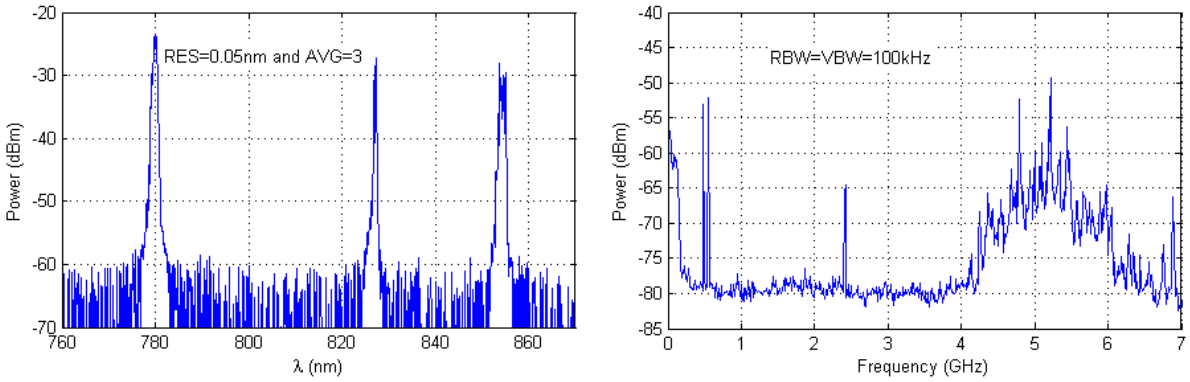

Figure 5.49: Multiplex of the home services in the optical (on the left) and electrical (on the right) domains.

[4]This laser comes from an Appointech SFP that has been disassembled.

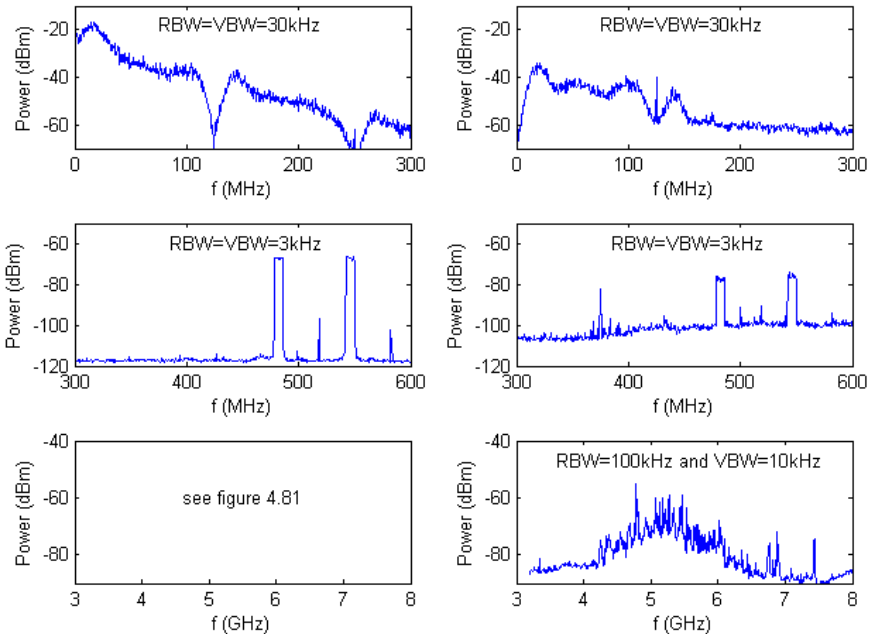

Figure 5.50: Electrical spectrum of each service at the input (on the left) and at the output (on the right) of the system.

For this proof of concept, a 100Base-TX Ethernet signal has been used. This is not a judicious choice since this is a three levels signal requiring a better SNR and inducing optical beatings (when no emission, the signal remains at the intermediate level), but no electrical source was available for two levels Ethernet signal. The corresponding eye diagram has been observed on a digital oscilloscope (1GHz bandwidth and 4GSa/s) and it has been synchronized using an edge trigger function (slope rising), not an external clock as usual. This brings additional distortions in the eye diagram, consequently the interpretation of figure 5.51 has to be considered carefully. Finally, between the input and the output of the system, when all the services are conveyed simultaneously, the signal-to-noise at the sampling point has been reduced by a factor four (6dB) and the opening of the eye, the time which the waveform can be successfully sampled (decision point), has decreased from 8 to 5 ns, approximatively. At the output of the triplexer, the Ethernet signal strength is:

$$-27dBm - 8dB\ (RF\ attenuator) - 5dB\ (point\text{-}to\text{-}point\ optical\ link) - 12dB\ (optical\ splitter)$$
$$-1.7dB\ (triplexer\ insertion\ losses) = -45.7dBm \tag{5.3}$$

The generated Ethernet signal has been received by an Ethernet frame generator with a success rate of 99.76% (tested over 51 minutes).

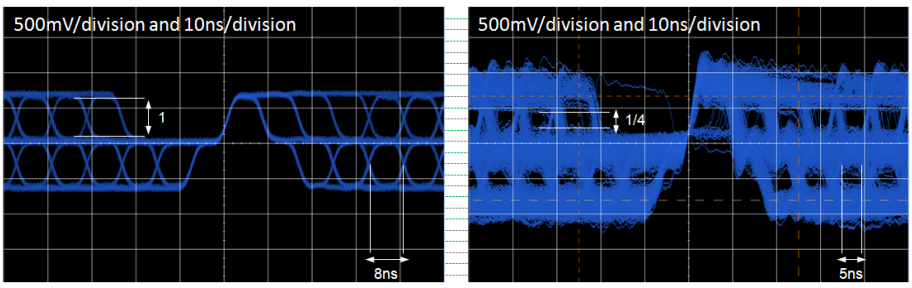

Figure 5.51: The Ethernet eye diagram at the input (on the left) and at the output of the system when all the services are conveyed simultaneously (on the right).

The television signal, composed of two DVB-T channels centered at 482 and 546 MHz, is generated by PCI cards according to the French standard and is tested with a television set. As shown in figure 5.50, the television power equals -32dBm per channel at the input of the system (-67dBm + $10 \cdot log$(8MHz/3kHz))

and -42dBm at the output of the triplexer:

$$-32dBm + 5dB\ (point\text{-}to\text{-}point\ optical\ link) - 12dB\ (optical\ splitter)$$
$$-3dB\ (triplexer\ insertion\ losses) = -42dBm \tag{5.4}$$

Table 5.15 resumes the other results for the channel centered at 546MHz after an amplification of 18dB (4dB attenuator followed by a Mini-Circuits amplifier, Gali 39+), and the corresponding constellation diagrams provided by the television analyzer are represented in figure 5.52. Lastly, with a television set, no reception degradation has been observed on the HD screen, even if the EVM peaks are higher than the limit value defined by the DVB-T standard. In fact, the final quality criterion remains the BER.

Table 5.15: Terrestrial television results (WDM-FDM).

Configuration	Through the setup		Direct link	Limit values
Eth./Radio present?	no / yes	yes / yes	-	-
EVM mean/peak (%)	3.69 / 39.76	3.92 / 43.76	1.4 / 8.1	4.4 / 22.0
CNR_{min} (dB)	26.8	26.5	31.6[5]	24
pre-Viterbi BER	$1.0 \cdot 10^{-4}$	$1.7 \cdot 10^{-4}$	$<10^{-8}$	10^{-2}

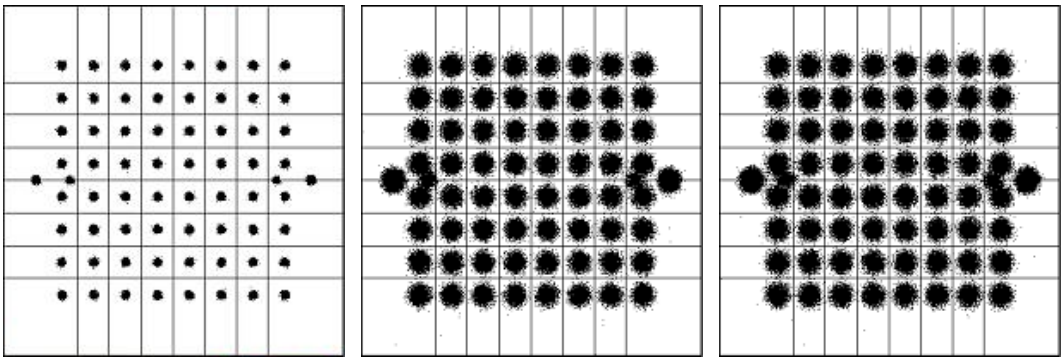

Figure 5.52: DVB-T constellation diagrams according to the French standard. On the left, the constellation at the input of the system, in the middle, the constellation at the output of the system when the television is multiplexed with the radio signal, on the right, when it is multiplexed with the Ethernet and radio signals.

Concerning the RoF link, the implemented transducers differ from the ones used in chapter 4. In fact, the centimeter-wave part and the local oscillator at 13.8GHz are the ones developed in the ORIGIN project (see section 5.2.3). For information, the centimeter-wave board includes an AGC amplifier to keep the radio signal in the middle of the dynamic range of the U-L-M VCSEL, and a variable attenuator to adjust the chain gain after the Finisar photodiode. Besides, each RoF transducer is fed by a Green Box providing the power under 48V and sending 10MHz carriers to activate the optoelectronic components. Because the U-L-M lasers emit high optical power, additional optical attenuators have been inserted in the optical links.

As a reminder, the WirelessHD transmission consists in framed signals. Consequently, at the reception, the observed spectrum is the sum of HRP signals, LRP signals, and of interframes amplified by the AGC amplifier by 30dB and seen as an important noise in the electrical spectrum. Moreover, as the half duplex transmission of the point-to-point WirelessHD link is not managed, two lasers are always turned-on and optical heterodyning detections occur. However, with only two lasers the impact remains limited as shown in figure 4.54. Experimentally, the measure of the EVM has not been performed but the WirelessHD signals have been conveyed successfully.

This proof of concept of the WDM-FDM approach has been tested at the end of my thesis. This experimentation is not totally complete as the setup has not been tested with different fiber lengths (only with short patch cords) and with optical splitters having a larger number of ports. Some points can be improved: using a Ethernet signal with two electrical levels, optimizing the laser and photodiode input

[5] As shown in the input television spectrum, in figure 5.50, the CNR is higher than 31.6dBm. This last value corresponds probably to the best value that can provide the television analyzer.

levels (RF power) of each service according to the others, recovering the correct system output levels for each service, implementing a VCSEL instead of the FP laser, and measuring the EVM for the 60GHz radio transmission.

5.3.3 Summary and perspectives

Before to conclude, it can be noted that a third way can be investigated to support multiservice and multiformat inside the home: the use of a hybrid domestic cable (two optical fibers and two copper pairs). Indeed, the copper pairs can be used to transport some services such as switched Ethernet signals since the copper topology consists in point-to-point links centralized at the central node. However, to avoid overlapping between the Ethernet and the RoF management signals, the monitoring RF tones have to be well located in the spectrum.

Finally, two multiservice and multifomat architectures have been proposed. Both integrate the millimeter-wave radio connectivity, either using an electrical multipoint-to-multipoint infrastructure or an optical one, and both support the Ethernet for IP data and RF signals for terrestrial broadcast television. Thus, a large set of services can be transported on a unique infrastructure and users can receive them from all their domestic outlets.

These two solutions have been experimentally demonstrated with success. Concerning the active star, the possibility to transport different signals in a hybrid optical/electrical multiplex maintains a reasonable cost while opening the way to far higher speeds for the future such as Ethernet at 10Gbit/s. Concerning the passive star based on a transparent NxN optical splitter, the WDM technology seems a pertinent solution, but the lack of optical filter for wavelengths around 850nm makes complex its implementation. The proposed solution consists in selecting one service at the reception working in the electrical domain: WDM and FDM technologies are thus combined. However, it limits the Ethernet speed to 100Mbit/s. Investigations have to be conducted to go further towards Ethernet at 1Gbit/s.

Due to these technical challenges that have still to be resolved, the active star remains the short term solution. However, the passive star is the architecture to promote because it offers greatest transparency, flexibility and upgradability. The capacity of such a network would be enormous, with the possibility to emulate at the same time several logical topologies, and the add of a new service is particularly simple with this architecture as it requires only the insertion of a new wavelength.

Conclusion

As shown in the first chapter, the evolution of the Home Area Network (HAN) is lead by two main trends, the proliferation of connected devices in the home and the deployment of high broadband access networks, especially the Fiber To The Home (FTTH) which allows the delivery of services that can exceed 1Gbit/s. As a consequence, to ensure efficient in-house exchanges, and keep guaranteeing a high Quality of Experience (QoE), the HAN has to evolve rapidly towards multi-Gigabit/s connections. At the same time, the users generally prefer the wireless connectivity for the final link to the device: Very High Throughput (VHT) wireless solutions are now needed.

To upgrade the HAN, the unlicensed millimeter-wave band, operating between 57 and 66 GHz, will be a foremost choice as it has unique characteristics that make it significantly attractive in comparison with the traditional Wi-Fi 2.4 or 5 GHz bands. In fact, advanced modulations associated with a wide channel bandwidth of 2.16GHz enable wireless transmissions up to 7Gbit/s. The two principal competing wireless standards for 60GHz applications are the WirelessHD, already available and transmitting High Definition (HD) uncompressed video, and the IEEE 802.11ad standard that will add IP, PCIe and USB capabilities. The IEEE 802.11ad will certainly have the most long-term success thanks to a Wi-Fi Alliance certification and new tri-band devices able to seamlessly integrate into existing 2.4 and 5 GHz Wi-Fi networks. It is expected that these chips will be available in 2013 and that they will be installed in millions of devices, about 15 million units in 2015 according to In-Stat [77]. Indeed, the semiconductor industry is now able to provide affordable 60GHz chips.

However, the signals resulting from these radio standards have short ranges due to high channel attenuation in the 60GHz band and due to millimeter-waves not crossing the walls. The wireless network capacity is so limited to a single room and to small indoor open areas. Solutions exist to improve the radio coverage, but none of them is completely satisfactory. Indeed, the Fast Session Transfer expands the radio range to the whole house but reduces the throughput to the speed of the 2.4 and 5 GHz Wi-Fi systems. The beamforming technology implemented in the 60GHz standards, improves the coverage within the rooms increasing the signal gain and the interference rejection, but the signal still does not cross the walls. The relay mode, an optional radio feature, is an efficient solution only if a large number of devices supporting it are simultaneously used and if several repeaters are installed to pass through the walls. Finally, the use of several access points interconnected by Ethernet links offers a wide coverage and a high throughput, but it remains costly and with high energy consumption. As a consequence, a new way to improve the radio coverage inside the home has to be found.

⋆ ⋆ ⋆

In chapter 2, Radio over Fiber (RoF) infrastructures acting at the same time as radio repeaters between the rooms of a home and as distribution systems have been proposed to solve this issue. In practice, several RoF transducers spread around the home and interconnected by optical fibers convert incoming electrical radio signals to optical ones, then distribute them optically through the home. At the reception, the RoF transducers bring back the radio signals in the electrical domain to reemit them in free-space. This approach is advantageous since, instead of distributing digital signals such as Ethernet (IEEE 802.11ad) or HDMI (WirelessHD), thus requiring conversions of signals and of protocols, the RoF technology distributes the signals in their native analog format. In addition to the radio coverage improvement, the pros and cons of RoF systems are:

+ Transparency of the system to radio layer protocols.
+ Simple remote antennas minimizing the risk of failure.
+ RoF transducers being compact and having light weight.

+ RoF transducers consuming low power.
+ Perspective of low cost.
+ Scalable and long-term optical infrastructure.
− Necessity to install new wires in houses.
− Additional noises and distortions due to the optical transmissions / conversions.

This solution might seem a very long term one, but today, it is already relevant to install optical fibers as a home backbone, for the future RoF systems and also for people who prefer to have wired connectivities. In fact, the optical fiber addresses both the bit rate increase and the great heterogeneity of signals to deliver (the radio signals included). Moreover, it is a mature solution and a future proof medium offering low attenuation, large RF bandwidth, high linearity and perfect immunity to electrical interferences.

Several studies have already been carried out on different optical transmission techniques for RoF applications at 60GHz, with a very long term view as they are based for instance on high speed Mach Zehnder Modulators (MZM), on optical frequency up-conversion or on optical heterodyne detection methods for millimeter-wave signals generation. In all these cases, high bandwidth photodetectors are required. In fact, as shown in the state of art of the main methods proposed in the literature (chapter 2), transmitting 60GHz radio signals can be a complex challenge.

From the viewpoint of the HAN market, a RoF system can represent a competitive solution only if it is easy to deploy and if the RoF transducers are low cost and compact. The RoF transducers have to be built with basic blocks. The simplest optical link that could be designed directly modulates the intensity of a laser by driving its current with a radio signal at Intermediate Frequency (IF), then uses a direct photodetection for recovering it (IM-DD technique). Implementing a local oscillator and the associated mixer to transpose millimeter-wave into IF before the optical transmission, and vice versa after the photodetection, does not constitute a challenge anymore. Indeed, with the introduction of the new millimeter-wave radio systems, the industry makes lot of efforts to attack the mass market and cut prices. Therefore, these components are becoming low cost since they are sub-circuits of the millimeter-wave front-ends of the future products. On the basis of these considerations, the IM-DD technique at IF has been adopted to conceive the RoF systems dedicated to the future HAN. The chosen IF is around 5GHz.

Concerning the optical fiber infrastructure, an hybrid cable has been chosen for installation within the walls: two silica low bend sensitivity multimode fibers (OM3+ MMF) for the RoF transmission, one fiber for the downlink and another for the uplink, plus one quad copper cable compatible with Power over Ethernet (PoE) for the remote powering and optical access management. The MMF, already widely adopted in LANs, allows the use of low cost and largely available optoelectronic devices and represents at the same time a good compromise for HAN deployment constraints.

In an optical HAN, the fiber infrastructure buried in the walls has to be transparent and able to adapt to the future radio systems for several years since the lifetime of these radio standards will be much shorter than the lifetime of a house. As a consequence, the home network physical architecture has to be properly chosen. This thesis has proposed different RoF architectures, from point-to-point to multipoint-to-multipoint, and has analyzed them in details considering these advantages and impairments.

The multipoint-to-multipoint architectures are preferred as they enable multi-room transmissions. Based on a NxN splitter, the lasers of each RoF transducer are connected to the inputs of the splitter and the photodiodes to the outputs. Thus, all the wireless devices are visible from one another as if they were face-to-face in a same room. These architectures act as logical buses. Two ways exist to design multipoint-to-multipoint architectures depending on the splitter: an optical or an electrical. The electrical architecture requires additional opto-electronic (O/E) and electro-optic (E/O) conversions at the input and at the output of the RF splitter, respectively, which increase the link noise. Therefore, the optical solution can seem advantageous due to a unique and passive component that consumes zero electrical power, but it induces optical beating at the detection between the different active lasers, which creates interferences over the radio signal. This point has been experimentally highlighted later in chapter 4. Finally, the electrical architecture is laser beats free, transverse multimode character free, and provides

stable results. However its performances are low. To improve this, low noise and linear components have to be adopted.

⋆ ⋆ ⋆

Chapter 3 has been devoted to the characterizations of the optoelectronic components used in the RoF systems, principally VCSELs at 850nm at the emission for their good compromise between efficiency and cost, and GaAs PIN photodiodes at the reception for their simplicity and reliability. A FP laser at 1310nm and an InGaAs photodiode have also been tested for comparison.

Static (laser L-I curve, laser optical spectrum, photodiode I-V curve) and dynamic (S-parameters) characterizations have been performed, and the noises inherent to the RoF links, for small signal (Relative Intensity Noise, thermal noise and shot noise) and large signal (third-order intermodulation), have been measured. Concerning these measurements, two points have to be underlined: firstly, the S21 parameters calculated analytically provide link gains generally overestimated of some decibels, experimental measurements are therefore still inevitable; secondly, the different experimental methods investigated to determine the RIN or the third order non-linearity distortions have all conducted to same accurate results. Concerning the results, it has been shown that the limiting parameters for RoF links using VCSELs and photodiode with built-in TIA are generally the RIN and the non-linearities of the reception stage. To be low cost, using optoelectronic components made for 10Gbit/s digital communication is judicious, but the performances are limited, especially for point-to-point configurations with low optical losses. In this case, the FP laser and its PIN photodiode at 1310nm from Finisar are prefered.

⋆ ⋆ ⋆

Chapter 4 has drawn a parallel between these analog characterizations, and digital results based on the transmission of an OFDM signal according to existing wireless 60GHz standards. OFDM has been chosen because this modulation offers the maximum capacity in hard environments such as Non Line Of Sight (NLOS) exchanges, and because it is demanding due to high sensitivity to IQ imbalance and Carrier Frequency Offset (CFO), and due to high Peak-to-Average Power Ratio (PAPR), thus implying strong constraints on the modulation index of the optical sources. As a consequence, if the system is validated for OFDM, it will be also validated for other radio modulation like SC.

EVM, SNR and BER have been taken as metrics to quantify the performances. The relationship among them has been plotted experimentally for a direct wired link at IF between the laboratory-made radio emitter and receiver. The obtained relationship between EVM and SNR matched well with the theory, but concerning the BER curves, it has been necessary to add 4% to the EVM parameter in the theoretical equations for QPSK, and 1.5% for 16-QAM, to obtain the expected experimental BER. Investigations have shown that the channel recovery was imperfect. Nevertheless, EVM has been kept as figure of merit to compare the different RoF architectures.

After that, the different proposed RoF architectures have been built and characterized step by step. A direct wired link at IF between the radio emitter and the radio receiver has been first characterized as the baseline. A reference EVM between 4 and 6 % has thus been measured. Then, RoF links have been introduced: the measured EVM has increased from 4% to 9% in the better case and can increase up to 15% in the worst cases depending on the optoelectronic components and on the optical losses. For instance, with a VCSEL at 850nm biased at 6.5mA and a GaAs PIN photodiode with a built-in TIA from Finisar, and 7dB optical losses, the EVM equals to 9.5%. As shown in the deep analysis performed in section 4.3 and that establishes the connection with chapter 3, the differences observed between the RoF links depend strongly on the linearities of the optoelectronic components, but also on the thermal noises when the optical losses become high (>10dB). The two key parameters for high performances are therefore high linearity to transmit OFDM signals, and high efficiency laser to support optical multipoint-to-multipoint architectures with a large number of ports.

Finally, IM-DD at IF is efficient, even with low cost optoelectronic components designed for digital applications. In comparison, a millimeter-wave free-space propagation provides an EVM between 12 and 14 % for distances from 1m to 15m, and the combination of the Finisar RoF link at 850nm, at IF with 6dB optical losses, with two millimeter-wave free-space propagations, which corresponds to an optical

multipoint-to-multipoint RoF architecture based on a 4x4 splitter, provides an EVM of 22% (figure 4.63):

$$22\% \text{ (}\textit{optical multipoint-to-multipoint architecture, 4x4 splitter}\text{)}$$
$$< 12\% \text{ (}1^{st} \textit{ hop}\text{)} + 10\% \text{ (}\textit{RoF link at IF with 6dB optical losses}\text{)} + 12\% \text{ (}2^{nd} \textit{ hop}\text{)}$$

However, in real conditions, the simultaneous operation of multiple lasers (at the input of the splitter) induces the addition of each laser RIN and an excess of shot noise as the received optical power increases. The average EVM increases, but it becomes also unstable due to heterodyning detection, which creates interferences over the radio signal. In this case, the electrical multipoint-to-multipoint architecture can be preferred, but only if it is used with linear and low noise components to obtain good results: since this architecture corresponds to two cascaded optical links, the FP laser and its PIN photodiode at 1310nm are well adapted. The results are resumed below for two 5-length hops in the air:

⇒ VCSEL at 850nm and GaAs PIN photodiode with a built-in TIA (Finisar)
- Optical multipoint-to-multipoint architecture with 7dB optical losses: 22%
- Optical multipoint-to-multipoint architecture with 4x4 splitter (7dB): 27% (unstable)
- Electrical multipoint-to-multipoint architecture with 14dB RF losses: 28%
- Electrical multipoint-to-multipoint architecture with two 1x4 splitters (14dB): 37% (stable)

⇒ FP laser at 1310nm and InGaAs PIN photodiode with a built-in TIA (Finisar)
- Electrical multipoint-to-multipoint architecture with two 1x4 splitters (14dB): 27% (stable)

As a final point, all the architectures have been validated performing a real-time transmission between two commercial WirelessHD devices at 2.856Gbit/s PHY rate and 1.904Gbit/s MAC rate. Thus, an uncompressed 1080i video from a Blu-ray player has been displayed on a HD screen using full duplex RoF links. All the architectures have run smoothly and no interruption of the video signal displayed on the screen has been observed.

⋆ ⋆ ⋆

In chapter 5, advanced RoF infrastructures have been proposed. The optical multipoint-to-multipoint architecture based on totally transparent optical components is a good compromise between cost, effectiveness, and performance, but only if it is completed by a management of the optical access in order to remove the optical heterodyning detections (multiple lasers turned-on simultaneously) and to reduce the Electro-Magnetic Field (EMF) radiations (multiple photodiodes turned-on simultaneously). It has been proposed to activate the optical functions of the RoF transducers only when and where they are needed to never have two lasers emitting or two photodetectors receiving at the same time.

An elegant solution consists in managing the access of the optical medium by reading information of the radio MAC layer to know the key parameters on ongoing communications, like the source and destination stations. To have an efficient and implementation-friendly solution, the beamforming (BF) process introduced in the 60GHz radio standards can be reused: instead of adjusting the direction of the signal energy in one room, the radio emission is switched between the different rooms of the home where RoF transducers have been installed. A theoretical study of the IEEE 802.11ad radio MAC layer has therefore been realized to prove the feasibility of this approach. It has been shown that the management of the optical access is possible, particularly with the Infrastructure MAC architecture. It is precisely the architecture to promote because it is the most popular use of the IEEE 802.11 standards and because it meets the telecommunication operator requirements such as the Internet connectivity.

Lastly, it has been reminded that the HAN is the convergence point of several worlds: computers, consumer electronics, television, etc... Consequently, the need for high capacity is not the only HAN issue, another major challenge lies in the great heterogeneity of the signals to be delivered to the various home devices. And for an optical system, seen as a premium product by the users, it will be risky to offer only one service. Thus, advanced RoF infrastructures taking into account a large variety of home services have to emerge. The two RoF multipoint-to-multipoint architectures are flexible and can easily support multiple services: the radio signal at IF has been multiplexed with an Ethernet signal for IP data and with DVB-T signals for broadcast terrestrial television. Different technical choices have been made to convey all these services on a unique optical cable as shown in the table below.

Table: Two multiservice and multiformat architectures integrating the 60GHz wireless connectivity.

Electrical multipoint-to-multipoint RoF architecture
WDM system, with FDM at 850nm
Full duplex Gigabit Ethernet on dedicated wavelengths (1310nm and 1550nm) Terrestrial broadcast television and 60GHz radio signal at an IF of 5GHz electrically multiplexed on a same wavelength (850nm)

Optical multipoint-to-multipoint RoF architecture
WDM at the emission / FDM at the reception
Fast Ethernet Bus (780nm) Terrestrial broadcast television (825nm) 60GHz radio signal at an IF of 5GHz (850nm)

Finally, this thesis has shown that the optical multipoint-to-multipoint RoF architecture has lot of advantages since it is based on a passive and transparent optical component not consuming electrical power. Moreover, good performances are obtained with EVM around 22%. However, this result can be observed only if an optical access management is implemented, a solution partially validated by a experimental proof of concept (the "Green Box"). Besides, multiservice is supported by this architecture thanks to WDM or WDM-FDM techniques, but for WDM, optical filters have to be commercially available, and for WDM-FDM, the Ethernet service is today limited to 100Mbit/s. As a consequence, this architecture is seen today as a long term solution for the HAN since certain technical barriers persist.

At mid-term the electrical multipoint-to-multipoint RoF architecture is more realistic. The performances are stable, even if slightly elevated. And the architecture supports several services, in particular Ethernet at 1Gbit/s or higher. Such a system is ready for industrialization, then market launch.

⋆ ⋆ ⋆

Suggestions for future works are now presented, in 9 points.

1. RoF infrastructures supporting simultaneously several millimeter-wave bands have to be imagined. It is a challenge to create such a system at a low cost as bandwidth and power constraints will be imposed to the optoelectronic components. A simple solution will consist in a system supporting only one band, but switching from one to another. In this case, the frequency of the local oscillator can be adjusted by the radio MAC layer. In fact, MAC fields provide information on the currently used channel and on the channel switch [157].

2. The design of the RoF transducers can be further simplified, maybe distributing the 13.8GHz local oscillator (LO before quadrupling) through the optical infrastructure. In this case a solution can be the use of WDM to distribute continuously a RF carrier on the optical infrastructure based on the NxN splitter, and FDM can be implemented at the reception to maintain low cost.

3. To go further in terms of performances, innovative highly linear and potentially low cost photodetectors have to be introduced. Heterojunction bipolar Photo-Transistors (HPT) currently developed by ORIGIN partners have to be characterized and compared to commercial devices to check if their promises, highly linear behavior and high photoresponsivity thanks to transistor gain, are kept.

4. More advanced optical transmission / generation techniques of millimeter-waves can be experimentally tested to quantify possible improvements, in particular when two point-to-point optical links are cascaded like in the electrical multipoint-to-multipoint architecture.

5. The laboratory-made radio emitter and receiver should be improved to provide performances close to commercial devices. The channel recovery should be improved to reduce the measured EVMs and to provide the adequate relationship between EVM, BER and SNR.

6. Real-time transmissions between commercial WirelessHD devices have been conducted. Tests have to be conducted with IEEE 802.11ad chips as soon as they will be commercially available.

7. The management of the optical access from the beamforming process introduced in the IEEE 802.11ad standard has been studied theoretically. Now, a proof of concept has to be realized. Its achievement will depend on the availability of millimeter-wave chipsets on the market, more particularly of development board. In parallel, actions can be conducted in standardization to integrate RoF aspects in the radio protocols.

8. The WDM-FDM approach allowing multiservice and multiformat on the optical multipoint-to-multipoint architecture has to be completed: tests on different fiber lengths, with different optical splitter sizes, implementation of two-levels Ethernet signals, optimization of the power levels, ...

9. Broadcast satellite television and specific formats as HDMI signals have to be added to the multiservice and multiformat architectures.

Appendix

A.1 Additive White Gaussian Noise (AWGN) channel model

As a reminder, an AWGN channel is modeled by a random signal, $x(t)$ (the voltage as a function of time), whose probability density function $p(x)$ follows a Gaussian (or normal) distribution:

$$p(x) = \frac{1}{\sqrt{2\pi}\sigma}\ e^{-\frac{1}{2}\left(\frac{x-\mu}{\sigma}\right)^2} \tag{A.5}$$

where μ et σ are the mean and the standard deviation of $x(t)$, respectively.

Generally, the cumulative distribution function is preferred to verify that a channel follow a Gaussian distribution. The cumulative distribution function of the real-valued random variable $x(t)$ is the function F_x, which associates $p(x <= a)$ to any real a.

$$F_x(a) = P(x <= a) \tag{A.6}$$

Therefore, the cumulative distribution function of a Gaussian is:

$$F_x(a) = \frac{1}{2}\left(1 + erf\left(\frac{a-\mu}{\sigma\sqrt{2}}\right)\right) \tag{A.7}$$

A.2 The central limit theorem.

The representation of an OFDM signal in the time domain checks the central limit theorem. This theorem states the convergence under certain conditions of a sequence of independent random variables to the normal distribution. In [139], this central limit theorem is defined as follows:

Soit $X_1, X_2, ..., X_n$ une suite de n variables aléatoires indépendantes de même loi (quelconque) ayant une moyenne μ et une variance finie σ^2. On définit la somme $S_n = X_1, X_2, ..., X_n$ et on établit le ratio :

$$\frac{S_n - n \cdot \mu}{\sigma \cdot \sqrt{n}}$$

où $n \cdot \mu$ et $\sigma \cdot \sqrt{n}$ représentent la moyenne et l'écart type de S_n, respectivement.
Le théorème central limite établit que la distribution de ce ratio tend vers la distribution normale lorsque n tend vers l'infini. Rigoureusement, cela signifie que :

$$P\left(\frac{S_n - n \cdot \mu}{\sigma \cdot \sqrt{n}} \leq x\right) \underset{n \to \infty}{\to} \Phi(x)$$

où $\Phi(x)$ est la fonction de répartition de la loi normale centrée réduite, exprimée par :

$$\Phi(x) = \int_{-\infty}^{x} \frac{1}{\sqrt{2\pi}} e^{-\frac{x^2}{2}} dx, \ -\infty < x < \infty$$

This result says that any sum of random, independent and identically distributed variables tends toward a random Gaussian variable.

A.3 The centimeter-wave components

A.3.1 S21 parameter of centimeter-wave components

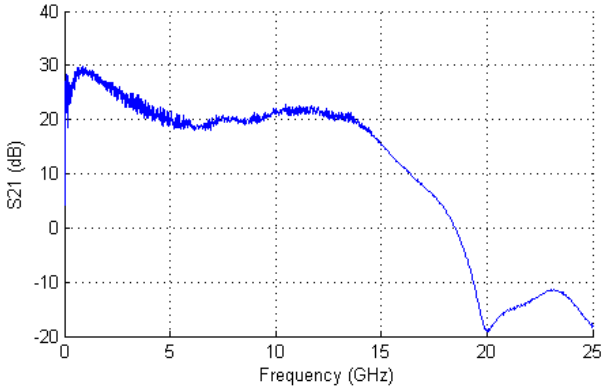

Figure A.53: S21 of the Miteq AFS3-00101200-22-10p-4 amplifier. According to its datasheet, NF = 2.2dB and OP1dB = 10dB.

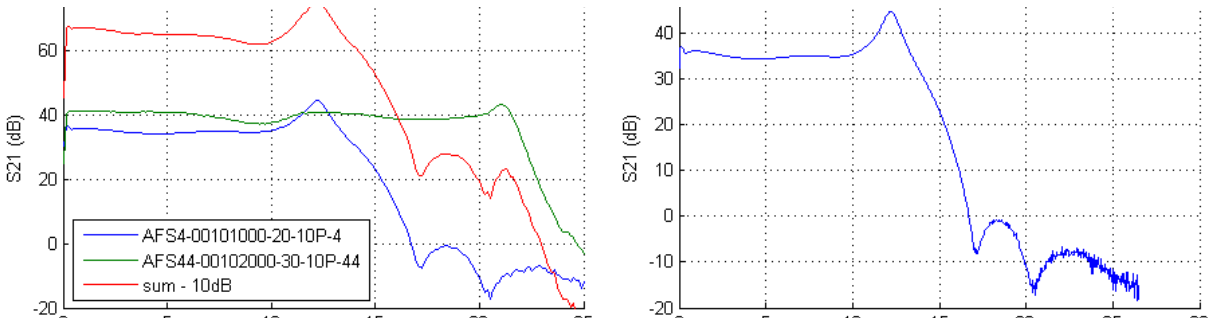

Figure A.54: On the left, S21 of the Miteq AFS4-00101000-20-10P-4 and AFS44-00102000-30-10P-44 amplifiers. With an additional 10dB RF attenuator between the two amplifiers, the total gain is equal to 65dB. On the right, S21 of the Miteq AFS4-00101000-20-10P-4 amplifier only. According to their datasheet, NF = 2dB and OP1dB = 10dB for the AFS4-00101000-20-10P-4 amplifier and NF = 3dB and OP1dB = 10dB for the AFS44-00102000-30-10P-44 amplifier.

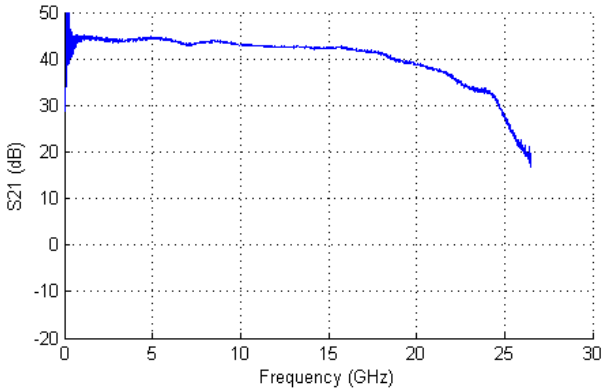

Figure A.55: S21 of the Miteq JS41-00102000-27-10P amplifier.

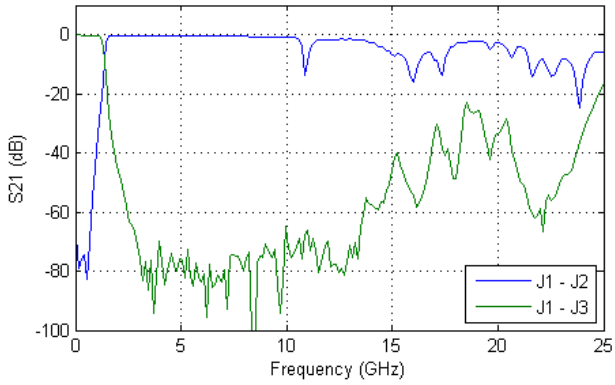

Figure A.56: Duplexer used in the laser time response measurement.

A.3.2 Power back-off

In order to determine the minimum power back-off to take at the input of the radio components, an OFDM signal modulated in QPSK and based on the IEEE 802.15.3c standard, HSI mode, is transmitted through a RF amplifier. The back-off measurement consists in varying the power at the input of the amplifier and looking for when the gain is compressed and when the EVM increases.

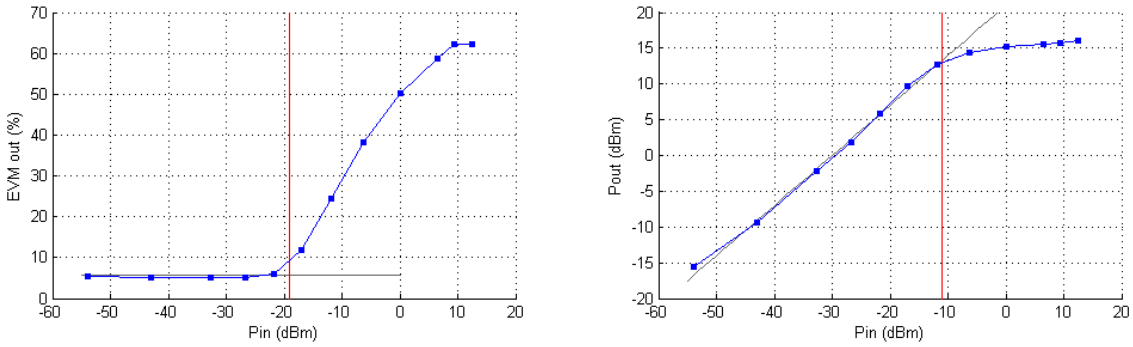

Figure A.57: Characterization of a QPSK modulated signal based on the IEEE 802.15.3c standard and having a PAPR of 13dB. The amplifier used is a Miteq AMF-5D-02001200-40-25P.

An input P1dB of -11dBm is measured. Besides, the EVM starts increasing from -19dBm at the input of the amplifier. Therefore, the power back-off is therefore equal to $(-11) - (-19) = 8dB$. It has to be noted that the PAPR of the used OFDM signal was 13dB, i.e. 5dB higher.

The P1dB provided in the other parts of this thesis have been measured using an electrical network analyzer, i.e. using a sinusoidal signal having a PAPR of 3dB. From this P1dB value, the required power back-off for an OFDM signal is lower. However, in this thesis, only the most demanding power back-off value has been considered: 8dB.

A.4 The millimeter-wave components

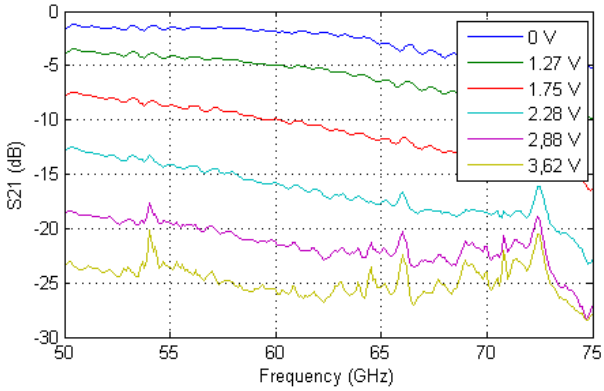

Figure A.58: Characterization of the Terabeam HVA1502-014 millimeter-wave attenuator: attenuation as a function of the frequency for different control voltage.

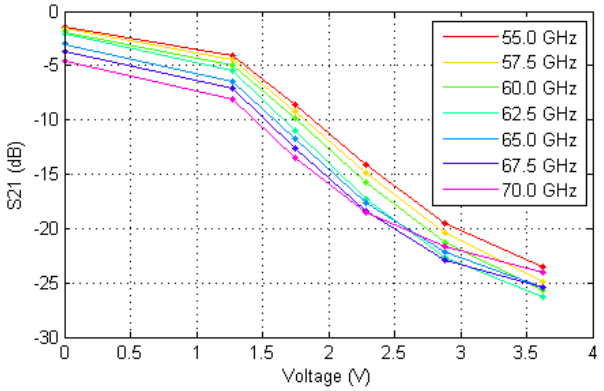

Figure A.59: Characterization of the Terabeam HVA1502-014 millimeter-wave attenuator: attenuation as a function of the control voltage for different frequency carriers.

According to the figure A.59, the millimeter-wave variable attenuator evolves linearly with the control voltage , excepted for the intrinsic losses equal to ∼2dB (0V - 1V). Finally, $Attenuation \simeq 9.6 \times Voltage - 6.6$. It has to be noted that the last attenuation value (3.62V) is arguable since its response is below the power-meter sensitivity.

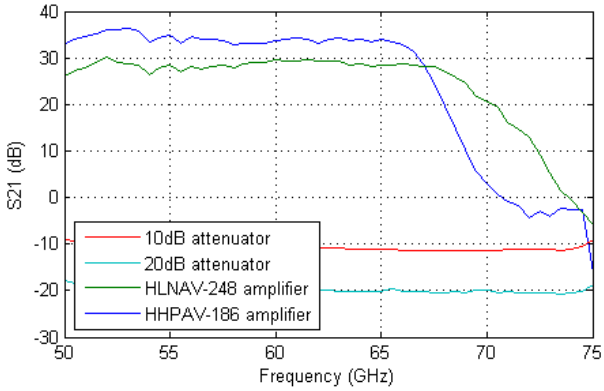

Figure A.60: S21 of two LNAs, the Terabeam HLNAV-248 and the Terabeam HLNAV-186, and of two millimeter-wave attenuators, 10 and 20 dB.

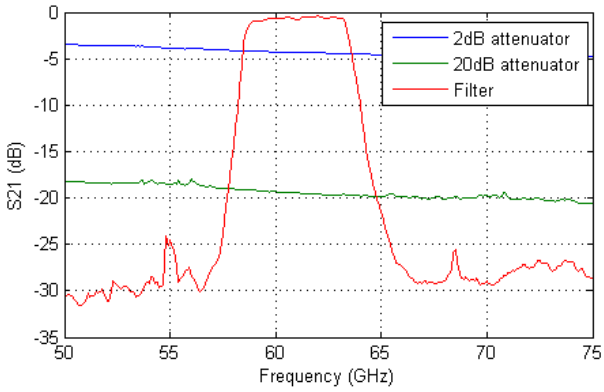

Figure A.61: S21 of a band-pass filter, from 58.5 to 63.5 GHz, compatible with the second channel of the millimeter-wave band, and of two millimeter-wave attenuators, 2 and 20 dB.

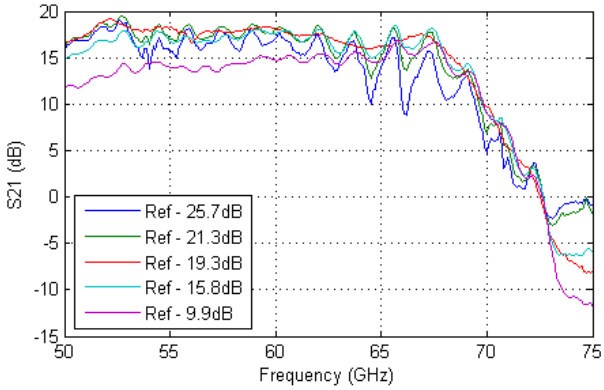

Figure A.62: S21 of the Terabeam HLNAV-262 amplifier for different input power (Ref $\simeq$ 8dBm). The input P1dB is therefore included between -2 and -8dBm.

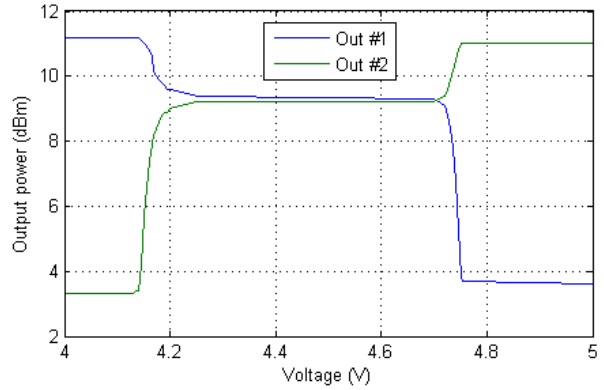

Figure A.63: Behavior of the millimeter-wave switch for an input frequency of 55.2GHz.

A.5 RIN measurements at 850nm using the VI-Systems photodiode.

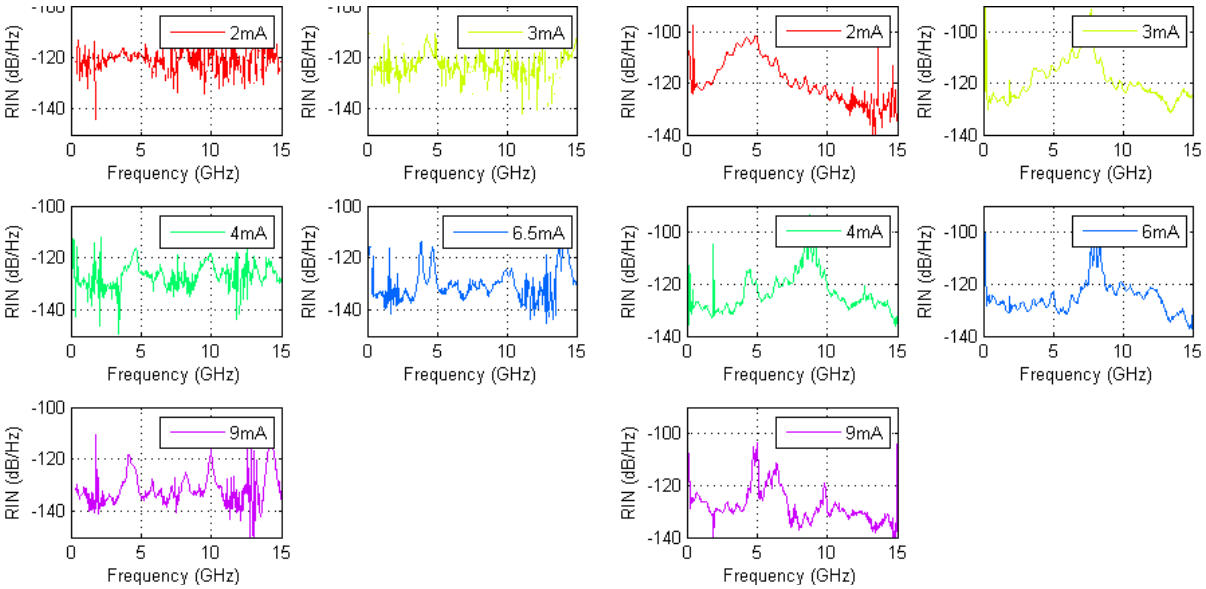

Figure A.64: RIN of the Finisar VCSEL at 850nm (on the left) and of the VI-Systems VCSEL at 850nm (on the right).

A.6 Additional digital characterization of RoF links at Intermediate Frequency, at 5GHz

A.6.1 VI-Systems VCSEL and Finisar PIN photodiode at 850nm

A hybrid RoF link is evaluated: the VI-Systems laser at 850nm with the Finisar GaAs PIN photodiode. If this link has no practical interest, the use of a laser with a bandwidth much greater than the bandwidth of the photodiode, it enables the comparison between the RoF links tested previously. Indeed, having only one optoelectronic component that differs is convenient to decorrelate some effects. The figures of this part will be the same measurements as the ones in chapter 4.

In figure A.65, for laser bias currents greater than 4mA, the optimal RF input power is about -12dBm. As previously (VI-Systems and Finisar RoF links), this value is independent of the laser bias current. Lastly, higher the bias current is, the lower the EVM is.

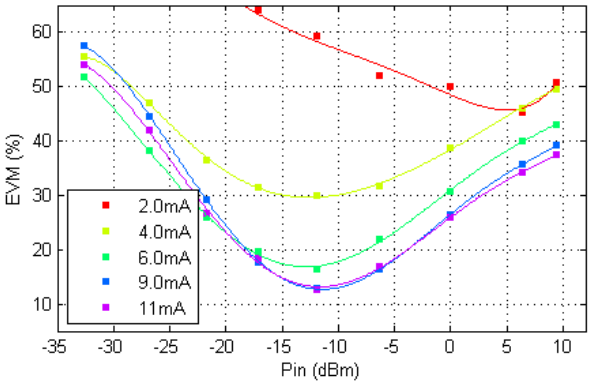

Figure A.65: EVM at the output of the RoF link as a function of the laser input power and for different bias currents. The optical losses are fixed to 12.5dB.

In figure A.66, the optimal RF power increases with the optical losses, a behavior already seen previously, every time a Finisar photodiode is used. In fact, the input power try to partially compensate the optical losses, but without saturate the reception stage. Finally, in the EVM versus optical losses curves, the different optimal RF powers do not provide the same EVM: there is an optimal value between high optical losses (photodetected signal power insufficient and so important impact of the thermal noise) and low optical losses (risk of saturation of the photodiode, especially the built-in TIA, so low laser input power and important impact of the RIN).

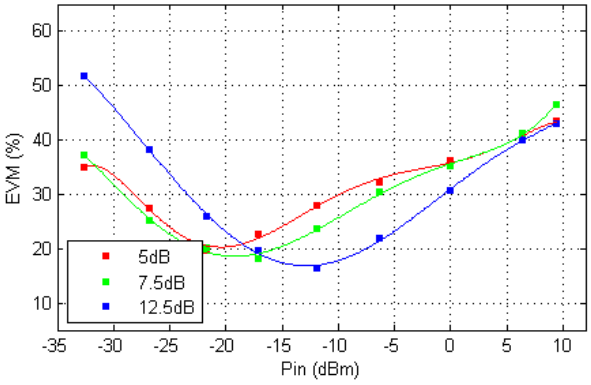

Figure A.66: EVM at the output of the RoF link as a function the laser input power for different optical losses. The laser bias current is fixed to 6mA.

A.7 The Matlab code

A.7.1 Modulation

Le programme Matlab *MainTX_IQ.m* a pour but de créer des signaux OFDM qui seront finalement chargés dans un AWG (Arbitrary Waveform Generator). L'AWG utilisé possède deux sorties, l'une sera utilisée pour le signal en phase (I pour *In phase*) et la seconde pour le signal en quadrature (Q pour *Quadrature*). Le création du signal OFDM, $Icos(2\pi f_0 t) + Qsin(2\pi f_0 t)$, sera finalisée de manière «*hardware*». Soit le programme principal *MainTX_IQ.m* :

```
% MainRX

clear all

%-------------------------------------------------
%------------------ Modulation -------------------
%-------------------------------------------------

% Default directory and filename
directory = 'C:';
filename_param = 'OFDM_Param_IN.mat';
filename_IN = 'OFDM_File_IN.mat';
filename_OUT = 'OFDM_File_OUT.mat';
filename_Results = 'OFDM_File_Results.mat';    % not yet implemented

% parameters
ParameterSet_802p15p3c
ComputeAdditionnalOFDMParameters_802p15p3c

% Main TX Sequence
BuildConstellation

% Generate the frequency domain signal
Freq_Signal = [];
NOT = 0;
MOD_SHIFT = [];
for ichan = 1:ND
    DataSequence
    PSKSequence
    % Store that channel along with the others:
    Freq_Signal = [Freq_Signal;psks];
end
MOD_SEQUE = Freq_Signal;

AddZerosAndPilots_802p15p3c
SymbolIFFT
AddGuardTime
SerializeTimeSignal
SetTimeScaleAndFrequencyTX
Resample4AWG
CW = 0;
InvSincOutputFilter
ComputeCharacteristics

% Store baseband copy for latter synchronization with xcorr
% OFDM Signal is currently I + i*Q
OFDM_Signal=Time_Signal;

% Save the signal:
filename = [directory,'\',filename_IN];
disp(['Saving to ',filename]);
Rec_Length = n_fft;
Sampl_Rate = FS_AWG;
save(filename,'Rec_Length','Sampl_Rate','OFDM_Signal'); % IMPORTANT
```

```
55
56 % write the parameter file:
57 filename = [directory,'\',filename_param];
58 disp(['Saving to ',filename]);
59 action=['save ''',filename,''' CW ND NFFT NZPS FS FS_AWG seed MOD_TYPE
60                  MOD_SHIFT Ns RF_Pow_Target CR_Target']; % IMPORTANT
61 eval(action);
62
63 Load_into_AWG7102
```

À présent, nous allons expliciter ce programme et les sous-programmes qui le composent.

Commençons directement par les lignes 17 et 18, avec les programmes *ParameterSet_802p15p3c* et *ComputeAdditionnalOFDMParameters_802p15p3c* qui fournissent les paramètres du signal OFDM que nous cherchons à créer : il s'agit de toutes les variables essentielles. Elles sont regroupées dans le tableau A.16 :

Table A.16: Variables définies par *ParameterSet_802p15p3c* et *ComputeAdditionnalOFDMParameters_802p15p3c*.

NFFT	Taille de l'IFFT/FFT du signal OFDM
NZ	Nombres de sous-porteuses nulles
NG	Nombres de sous-porteuses de gardes
NP	Nombres de sous-porteuses pilotes
NU	Nombres de sous-porteuses utilisateurs
ND	Nombres de sous-porteuses de données
NZPS	Taille du suffixe (*zero padded suffix*)
FS	Fréquence d'échantillonnage du signal OFDM [Hz]
CW	Fréquence centrale du signal OFDM; 0: bande de base
NS	Nombre de symboles OFDM à créer
MOD_TYPE	1: BPSK, 2: QPSK, 3: 8-QAM, etc...
Ts = (NFFT+NZPS)/FS	Période d'un symbole OFDM [s]
dt = 1/FS	Période d'échantillonnage du signal OFDM [s]

L'emplacement des sous-porteuses nulles, des sous-porteuses de gardes, des sous-porteuses pilotes, des sous-porteuses utilisateurs et sous-porteuses de données est également fourni, respectivement par les vecteurs *Idx_Zro*,*Idx_Grd*, *Idx_Plt*, *Idx_Usr* et *Idx_Dta*.

Nous connaissons alors toutes les variables essentielles. Dans un second temps, le programme *Build-Constellation* crée une constellation *Const* de référence liée à la modulation du signal OFDM. Cette constellation est conçue à partir du paramètre *MOD_TYPE*. Dans le cas d'une modulation QPSK, *Const* vaut :

$$Const = \frac{1}{2}\begin{pmatrix} 1 & 1 \\ 1 & 1 \end{pmatrix} \tag{A.8}$$

Ensuite, ligne 27 à 32 du programme principal, une boucle crée l'ensemble des sous-porteuses de données pour l'ensemble des *Ns* symboles, chacune portant une donnée aléatoire. À chaque passage de boucle, une sous-porteuse parmi les *ND* que contient un symbole est conçue, ainsi que ses *Ns* valeurs, une valeur différente par symbole. Au final, une matrice *Freq_Signal* représentant les sous-porteuses de donnée a été constituée, matrice où chaque ligne représente un symbole, et où chaque colonne représente une sous-porteuse. Soit une matrice *Ns* lignes par *ND* colonnes.

$$Freq\_Signal = \underbrace{\left.\begin{pmatrix} a_{1,1} & a_{1,2} & \cdots & a_{1,n} \\ a_{2,1} & a_{2,2} & \cdots & a_{2,n} \\ \vdots & \vdots & \ddots & \vdots \\ a_{m,1} & a_{m,2} & \cdots & a_{m,n} \end{pmatrix}\right\} Ns}_{ND} \tag{A.9}$$

Revenons sur cette boucle, et plus particulièrement sur deux programmes : *DataSequence* et *PSKSequence*.

Le programme *DataSequence* renvoie une matrice colonne nommée *sequence* d'une longueur égale à *Ns* (nombre de symboles). Chaque élément de cette matrice est une valeur aléatoire comprise entre 0 et $x-1$, x étant le nombre d'éléments composant la constellation *Const*. Par exemple, en modulation QPSK, la matrice *sequence* sera une suite de nombres aléatoires compris entre 0 et 3, chacun de ces nombres pouvant par la suite être associé à un point de la constellation du signal OFDM.

Le programme *PSKSequence* permet justement d'associer cette suite de nombres aléatoires à un point de la constellation. Ainsi une matrice ligne *psks* est créée. *psks* fournit la valeur complexe du signal. Par exemple, voici le principe de création du vecteur *psks* dans le cas d'une modulation QPSK, avec *iseq* le numéro du symbole.

$$\begin{array}{l} sequence(iseq) = 0 \rightarrow psks(iseq) = -1 + i \\ sequence(iseq) = 2 \rightarrow psks(iseq) = +1 + i \\ sequence(iseq) = 1 \rightarrow psks(iseq) = -1 - i \\ sequence(iseq) = 3 \rightarrow psks(iseq) = +1 - i \end{array} \tag{A.10}$$

Une fois les sous-porteuses de données créées, nous pouvons commencer à réaliser le signal OFDM : soit la matrice *ofdms* de *NFFT* lignes et *Ns* colonnes. Nous ajoutons alors aux sous-porteuses de données, les sous-porteuses nulles, c'est-à-dire celles qui sont inutilisées, les sous-porteuses pilotes et les sous-porteuses de gardes. La valeur des sous-porteuses pilotes est connue et égale à l'unité. Ainsi, à partir de ces sous-porteuses nous pourrons mesurer une version sous-échantillonnée de la réponse en fréquence du canal. À la réception, nous interpolerons cette réponse afin d'équilibrer l'ensemble du signal et récupérer des données les plus conformes possibles au valeurs émises. Soit le programme *AddZerosAndPilots_802p15p3c* (ligne 35) :

```
1  % allocate symbol memory
2  ofdms=zeros(NFFT,Ns);
3
4  % Insert data subcarriers
5  ofdms(IdxShft+Idx_Dta,:)=Freq_Signal;
6
7  % Set pilots subcarriers to 1
8  ofdms(IdxShft+Idx_Plt,:)=1;
9
10 % Zeros, guard and user data sub carriers are just left to zero...
```

Une transformée de Fourier inverse (IFFT) est ensuite exécutée sur ces sous-porteuses par le programme *SymbolIFFT* (ligne 36). Un signal temporel est ainsi généré.

Un intervalle de garde est placé après chaque symbole transmis : il s'agit des zéros de bourrage, ZPS en anglais pour *Zero-Padded Suffix*. Ces derniers réduisent les interférences entre symboles, interférences dues par exemple aux multi-trajets. Soit le programme *AddGuardTime* (ligne 37) :

```
1  % introduction of zero padded suffix (length = NZPS)
2  Npre = round(NZPS/2);
3  Nsuf = NZPS-Npre;
4  Prefix = zeros(Npre,Ns);
5  Suffix = zeros(Nsuf,Ns);
6  ofdms = [Prefix;ofdms;Suffix];
```

Notons qu'ici l'intervalle de garde est construit de manière symétrique (50% de zéro avant le signal et 50% après).

Le programme *SerializeTimeSignal* (ligne 38) crée la variable *ofdm_mod_seq* qui prend la valeur *ofdms(:)'*. La matrice ofdms *NZPS+NFFT* lignes par *Ns* colonnes, devient alors un vecteur de longueur *NZPS+NFFT*×*Ns*.

Le signal temporel généré précédemment est échantilloné à la fréquence $dt = 1/FS$. Le programme *SetTimeScaleAndFrequencyTX* (ligne 39) définie alors les axes temporel et fréquentiel respectant l'échantillonage du signal OFDM :

```
1  n_fft = length(ofdm_mod_seq);
2  t = [0:(n_fft-1)]*dt;
3  fmax    = 1/dt;
```

```
4  df = 1/(n_fft*dt);
5  f = [(-fmax/2):df:(fmax/2-df)];
```

Par la suite le signal est rééchantillonné par le programme *Resample4AWG* (ligne 40) afin de s'adapter à la fréquence de fonctionnement de l'AWG. La variable *ofdm_mod_seq* devient après rééchantillonage *Time_Signal*.

```
1  % Redefine the time scale
2  NZ0 = ceil(n_fft*FS_AWG/FS);
3  dt=1/FS_AWG;
4  t = [0:(NZ0-1)]*dt;
5
6  % Resample OFDM signal onto AWG window
7  Time_Signal = interpft(ofdm_mod_seq,2*NZ0);
8  Time_Signal = interpft(Time_Signal,length(t));
9
10 % Redefine the frequency scale
11 n_fft = length(Time_Signal);
12 fmax = 1/dt;
13 df = 1/(n_fft*dt);
14 f = [(-fmax/2):df:(fmax/2-df)];
```

À la ligne 41 du programme principal, *CW=0* nous rappel que le signal OFDM, *Time_Signal*, est en bande de base et vaut $I + iQ$.

Au final, le signal OFDM est chargé dans l'AWG grâce au programme *Load_into_AWG7102* (ligne 63). La partie réel du signal, *2*real(OFDM_Signal(1:n_fft))*, est chargée dans l'une des deux sorties de l'AWG, la partie imaginaire, *2*imag(OFDM_Signal(1:n_fft))*, est chargée dans la sortie restante de l'AWG. Pour rappel, *n_fft* correspond à la longueur du signal OFDM créé.

A.7.2 Demodulation

Le programme Matlab *MainRX.m* a pour but de démoduler des signaux OFDM récupérés par un oscilloscope numérique, puis de déterminer la valeur d'EVM associée à leur constellation. Soit le programme principal *MainRX.m* :

```
1  % MainRX
2
3  clear all
4
5  %-----------------------------------------
6  %---------------- Démodulation ----------
7  %-----------------------------------------
8
9  % Synthetic signal or inline
10 directory = 'C:';
11 filename_param = 'OFDM_Param_IN.mat';
12 filename_IN = 'OFDM_File_IN.mat';
13 filename_OUT = 'OFDM_File_OUT.mat';
14 filename_Results = 'OFDM_File_Results.mat';
15
16 %
17 verbose=true;
18
19 % Set to -1 if the Spectrum is NOT reversed
20 DIRN = -1;
21
22 ParameterSet_802p15p3c
23
24 N_Capture=0;
25 do_it = 1;
26 EVM_Record = Inf;
27
28 while (do_it) % si la case "continue" est cochée
```

```
29
30      tic  % counter start
31
32      % VERBOSE START
33
34      h_evm = [];
35      h_stop = [];
36
37      if verbose
38      figure(1);
39      fig1_child = get(gcf,'Children');
40      h_evm  = findobj(fig1_child,'Style','checkbox','String','EVM');
41      h_stop = findobj(fig1_child,'Style','checkbox','String','Continue');
42      h_rec = findobj(fig1_child,'Style','checkbox','String','Record');
43
44      if isempty(h_evm)
45      POS = get(gcf,'Position');
46      h_evm  = uicontrol('Style','Checkbox','String','EVM','Position'...
47                ,[POS(3)/4-25,POS(4)-15,50,15]);
48      set(h_evm,'Units','Normalized');
49      end
50
51      if isempty(h_stop)
52      h_stop = uicontrol('Style','Checkbox','String','Continue',...
53                'Position',[3*POS(3)/4-25,POS(4)-15,100,15],'Value',0);
54      set(h_stop,'Units','Normalized');
55      end
56
57      if isempty(h_rec)
58      h_rec = uicontrol('Style','Checkbox','String','Record','Position',...
59              [2*POS(3)/4-25,POS(4)-15,100,15],'Value',0);
60      set(h_rec,'Units','Normalized');
61      end
62
63      do_it = (get(h_stop,'Value')==get(h_stop,'Max'));
64      end
65
66      % VERBOSE STOP
67
68      N_Capture=N_Capture+1;
69      disp('-----------------------------------');
70      disp(sprintf('N_Capture = %d',N_Capture));
71
72      Load_from_DSO91
73
74      ComputeAdditionnalOFDMParameters_802p15p3c
75      BuildConstellationRX
76      SetTimeScaleAndFrequencyRX
77      PrepareXCorrInputPattern
78
79      if verbose;figure(1);subplot(4,2,1);PlotOFDMSignal; end
80
81      TimeSyncXCorrEnvDet_802p15p3c
82      FindLOFrequency_802p15p3c
83
84      do_evm = 0;
85
86      if (~isempty(h_evm))
87      do_evm = (get(h_evm,'Value')==get(h_evm,'Max'));
88      end
89
90      if (~do_evm) % début de la boucle de mesure d'EVM (si case cochée)
91
92      if verbose;figure(1);subplot(4,2,4);PlotSpectrumComputeSNR;
93      drawnow;
```

```
94      end
95      figure(2); PlotSpectrumComputeSNR;grid on;drawnow;
96      else
97
98      DeltaF  = 0;
99      DeltaFS = -35000;
100     DeltaFPrev=Inf;
101
102     STORED_SIGNAL=OFDM_Signal; %enregistre le signal, car dans chaque
103     %boucle le modifira. La restitution s'effectuera en début de chaque boucle
104
105     N_loop = 0;
106     N_loop_max = 10;
107
108     while (N_loop < N_loop_max) %les différentes boucles
109
110     N_loop=N_loop+1;
111     disp('-----------------------------------');
112     disp(sprintf('N_Loop = %d',N_loop));
113
114     OFDM_Signal = STORED_SIGNAL;
115     LO_FRQ = LO_FRQ + DeltaF; %correction sur la fréquence centrale
116     FS = FS + DeltaFS; %correction sur la fréquence d'échantillonnage
117
118     FilterSignalBand_802p15p3c
119     if verbose;figure(1);subplot(4,2,4);PlotSpectrumComputeSNR;end
120
121     DownConversion
122     InterpolatewithSyncTimeBase;
123
124     if verbose;figure(1);subplot(4,2,5);PlotTimeBaseBand;end
125
126     IsolateSymbols
127     SymbolFFT
128
129     if verbose;figure(1);subplot(4,2,6);PlotOFDMSymb;end
130
131     RemoveZeros_802p15p3c
132     RecenterSymbol_802p15p3c
133     ExtractPilotsandEqualize_802p15p3c
134
135     %Enregistre les valeurs actuelles de correction avant modification
136     DeltaFS_Prev = DeltaFS;
137     DeltaF_Prev = DeltaF;
138
139     FindFrequencyOffsetandCompensate
140
141     if verbose;figure(1);subplot(4,2,7);PlotOFDMSymbAfterEqualize; end
142     if verbose;figure(1);subplot(4,2,8);PlotConstellation;end
143
144     %Boucles conditionnelles réalisant la mesure d'EVM :
145
146     if ((abs(DeltaF)<50 & abs(DeltaFS)<50) | (abs(DeltaF+DeltaF_Prev)<1 ...
147         & abs(DeltaFS+DeltaFS_Prev)<1))
148     FitConstellation
149     ComputeEVMandBER
150     break
151     end
152
153     if (N_loop == N_loop_max)
154     FitConstellation
155     ComputeEVMandBER
156     break
157     end
158
```

```
159       end
160
161       % structure des résultats
162       Res.EVM(N_Capture,1)=EVM_MEAS_BAND;
163       Res.N_loop(N_Capture,1)=N_loop;
164       Res.SNR=SNR;
165       Res.POW=POW_MEAS_BAND;
166
167       dispdlg(sprintf('Cap#%d EVM = %2.2f %%',N_Capture,EVM_MEAS_BAND));
168
169       do_rec = 0;
170
171       if (~isempty(h_rec))
172       do_rec = (get(h_rec,'Value')==get(h_rec,'Max'));
173       end
174
175       if (do_rec & EVM_MEAS_BAND<EVM_Record)
176       EVM_Record = EVM_MEAS_BAND;
177       disp(['Recording signal with EVM of ',num2str(EVM_Record),'%']);
178       SaveSignal2Disk;
179       end
180
181       if (~do_rec)
182       EVM_Record = Inf;
183       end
184
185       end % fin de la boucle de mesure d'EVM
186
187       toc % counter stop
188
189 end % si la case "continue" est décochée
```

À présent, nous allons expliciter ce programme et les sous-programmes qui le composent.

Commençons directement par la ligne 22, avec le programme *ParameterSet_802p15p3c* qui fournit les paramètres du signal OFDM que nous cherchons à démoduler : il s'agit de toutes les variables essentielles. Elles sont regroupées dans le tableau A.17 :

Table A.17: Variables définies par *ParameterSet_802p15p3c*.

NFFT	Taille de l'IFFT/FFT du signal OFDM
ND	Nombres de sous-porteuses de données
NZPS	Taille du suffixe (*zero padded suffix*)
FS	Fréquence d'échantillonnage du signal OFDM [Hz]
MOD_TYPE	1: BPSK, 2: QPSK, 3: 8-QAM, etc...
Ts = (NFFT+NZPS)/FS	Période d'un symbole OFDM [s]
dt = 1/FS	Période d'échantillonnage du signal OFDM [s]

L'emplacement des sous-porteuses nulles, des sous-porteuses de gardes, des sous-porteuses pilotes, et des sous-porteuses utilisateurs est également fourni.

Les lignes 32 à 66 construisent l'interface graphique du programme Matlab.

Ensuite, le programme *Load_from_DSO91* (ligne 72) capture le signal OFDM affiché sur l'oscilloscope et le charge dans la variable *OFDM_Signal*. Notons que ce signal est échantillonné avec une période dT différente de la période d'échantillonnage initiale du signal OFDM, dt. Ce programme définit la variable dT, mais également le nombre de symbole valide capturé, Ns.

Le programme *ComputeAdditionnalOFDMParameters_802p15p3c* (ligne 74) précise quelques constantes supplémentaires, comme le nombre de sous-porteuses nulles , de gardes, pilotes, et utilisateurs, soit respectivement NZ, NG, NP, NU.

Le programme *BuildConstellationRX* (ligne 75) construit une constellation de référence à partir de la variable *MOD_TYPE* définie précédemment. Cette constellation est une matrice colonne se nommant *psks*. Celle-ci permettra après la démodulation du signal OFDM de déterminer l'EVM. Il s'agit ici de la constellation idéale à atteindre. Pour exemple, nous représentons ci-dessous la matrice *psks* dans le cas d'un codage QPSK,

$$psks = \frac{1}{2}\begin{pmatrix} \sqrt{-1+i} \\ \sqrt{1+i} \\ \sqrt{-1-i} \\ \sqrt{1-i} \end{pmatrix} \tag{A.11}$$

Le programme *SetTimeScaleAndFrequencyRX* (ligne 76) spécifie l'axe des temps T et des fréquences F du signal capturé par l'oscilloscope, mais également les valeurs de dT, *Twidth*, et dF. Soit le tableau A.18.

Table A.18: Variables définies par *SetTimeScaleAndFrequencyRX*.

Twidth	Durée du signal OFDM (temps de capture) [s]
dT	Période d'échantillonnage du signal OFDM [s]
T = [0:(Rec_Length-1)] * dT	Axe des temps [s]
dF	Pas de fréquence [Hz]
F	Axe des fréquences [s]

Le programme *PrepareXCorrInputPattern* (ligne 77) récupère le signal OFDM qui a été chargé dans l'AWG. En effet, ce signal fut enregistré au préalable dans un fichier texte, fichier que nous retrouvons grâce aux lignes 10 à 12 du programme principal. Ce signal servira de référence afin de déterminer le début du premier symbole OFDM du signal venant de l'oscilloscope. Mais dans un premier temps, certains paramètres du signal chargé dans l'AWG sont rappelés : *dT_IN*, *Twidth_IN*, *T_IN*, *dF_IN*, et *F_IN*. Ensuite le signal provenant du fichier texte est recalé avec le signal récupéré depuis l'oscilloscope, entre autres il est rééchantillonné afin d'avoir le même axe des temps : *T*. Au final, nous ne garderons que l'enveloppe de ce signal, et nous le nommons *OFDM_Signal_INBBx2_Envelop*.

Le programme *TimeSyncXCorrEnvDet_802p15p3c* (ligne 81) réutilise le signal précédemment créé afin de déterminer l'instant *T00*, instant de référence indiquant le début du premier symbole OFDM. Cet instant correspond au maximum du produit d'intercorrélation entre les deux signaux, celui chargé dans l'AWG et celui récupéré depuis l'oscilloscope.

```
1  OFDM_Signal_Envelop = abs(OFDM_Signal);
2
3  % Intercorrelation des deux enveloppes:
4  XCorrTime=abs(xcorr(OFDM_Signal_INBBx2_Envelop,OFDM_Signal_Envelop));
5
6  % Recherche d'un pic pour définir l'instant zéro (only positive delays)
7  [MxCorrTime,IndMxCorrTime]=max(XCorrTime);
8  N = max(length(OFDM_Signal_INBBx2_Envelop),length(OFDM_Signal_Envelop));
9  inddec=IndMxCorrTime-N;
10 T00=inddec*dT;
```

Le programme *FindLOFrequency_802p15p3c* (ligne 82) recherche la fréquence centrale du canal OFDM utilisé. Pour déterminer cette fréquence le signal OFDM est représenté dans le domaine fréquentiel, soit l'opération suivante : $fftshift(fft(OFDM\_Signal))$. Il suffit alors de rechercher l'indice m donnant la valeur maximale du signal. La fréquence correspondant à ce maximum, *F(m)*, est alors affinée.

Pour cela nous subdivisons l'axe des temps en plusieurs blocs, *sub_T*. *sub_F* est son équivalent dans le domaine fréquentiel. m est l'indice de l'axe *sub_F* correspondant à la fréquence centrale de la bande OFDM (*LO_FRQ*), ou celle s'en approchant le plus. Nous traçons alors l'évolution de la phase de *sub_F(m)* en fonction du temps. Nous supposons alors que cette évolution est linéaire et nous corrigeons la fréquence *LO_FRQ* par l'ajout du coefficient de cette pente.

```
1  % Calcul du spectre
2  Spectre_OUT = fftshift(fft(OFDM_Signal));
3
4  % First approximation: the LO is the max peak in the signal
5  [M,m] = max(abs(Spectre_OUT));
```

```
LO_FRQ = abs(F(m));

% Study the phase variation of the LO vs. time to fine tune it:
sub_Rec_Length = 2^floor(log2(Rec_Length/2));
sub_Twidth = (sub_Rec_Length*dT);
sub_T = [0:(sub_Rec_Length-1)] * dT;
sub_dF = 1/sub_Twidth;
sub_F = [ceil(-sub_Rec_Length/2):(floor(sub_Rec_Length/2)-1)] * sub_dF;

% find the LO index in the new frequency scale:
m = find(abs(sub_F-LO_FRQ)==min(abs(sub_F-LO_FRQ)));

% Compute LO phase vs time:
LO_Phase = [];
LO_Times = [];
indexes = [1:sub_Rec_Length];
while max(indexes)<Rec_Length
    Spectre_TMP = fftshift(fft(OFDM_Signal(indexes)));
    LO_Phase = [LO_Phase,angle(Spectre_TMP(m))];
    LO_Times = [LO_Times,T(indexes(1))];
    indexes = indexes+round(Rec_Length/100);
end
POL = polyfit(LO_Times,unwrap(LO_Phase-2*pi*sub_F(m)*LO_Times),1);

LO_FRQ = sub_F(m) + POL(1)/2/pi;
```

À partir de la ligne 108, nous commençons une boucle *while*. Chaque boucle effectue une série d'opérations visant à démoduler le signal OFDM. Si entre chaque boucle le signal OFDM reste inchangé, en effet nous repartons toujours du signal stocké dans la variable *STORED_SIGNAL* (ligne 102), les variables *Fs* et *LO_FRQ* sont quant à elles modifiées. Celles-ci sont corrigées au sein de la boucle grâce aux informations de phases portées par les sous-porteuse pilotes. La boucle s'arrête lorsque les valeurs de *DeltaFs* et *DeltaF* sont trop petites ou qu'elles n'évoluent pas suffisamment, ou bien lorsque nous avons atteint le nombre maximal de tour. *DeltaFs* est la différence entre l'ancienne valeur de *Fs* et la valeur actuelle de *Fs* (après correction). *DeltaF* est l'équivalent de *DeltaFs* pour la variable *LO_FRQ*. Initialement, *DeltaF* est nulle et *DeltaFS* vaut -35000 (ligne 98 à 100).

Le programme *FilterSignalBand_802p15p3c* (ligne 118) filtre le signal capturé afin de ne garder que le spectre utile. Cette opération consiste à la multiplication du signal dans le domaine fréquentiel par une fonction porte comprise entre *LO_FRQ - (FS/2+FS/16+eps)* et *LO_FRQ + (FS/2+FS/16+eps)*.

Après être revenu dans le domaine temporel, le programme *DownConversion* (ligne 121) passe le signal OFDM en bande de base : il est alors multiplié par la fréquence centrale *LO_FRQ*.

```
OFDM_Signal = OFDM_Signal.*exp(i.*2*pi*LO_FRQ*T)
```

Toujours dans le programme *DownConversion*, après le passage en bande de base, nous effectuons une opération de filtrage supplémentaire, en passe bas, afin de ne garder que le signal utile (c'est-à-dire en bande de base). Il s'agit de la multiplication dans le domaine frequentiel du signal par une fonction porte comprise entre *-(FS/2+FS/16+eps)* et *FS/2+FS/16+eps*.

Pour rappel nous travaillons toujours avec un signal dont l'échantillonnage correspond à celui de l'oscilloscope et non à l'échantillonnage initial du signal OFDM. La fonction *InterpolatewithSyncTimeBase* corrige ce point (ligne 122). Nous rappelons d'abord la définition de certains paramètres : *dt*, *SymPeriod*, *T0*, *Ns* et *t*. Ensuite, l'opération de rééchantillonnage sous Matlab se résume à ce simple calcul :

```
% axe des temps pour la démodulation OFDM
t=T0+[0:dt:(Ns.*SymPeriod)-dt];

% Interpolation du signal sur l'axe t
OFDM_Signal_RX = interp1(T,OFDM_Signal,t);
```

Notons que le signal OFDM a été rogné afin de débuter à l'instant *T00* (défini préalablement par *TimeSyncXCorrEnvDet_802p15p3c*, ligne 81), et afin de finir sur un nombre entier de symboles. Maintenant que le signal est échantillonné à sa valeur initiale, nous allons pouvoir extraire les différentes

sous-porteuses. C'est ce que permet la fonction *IsolateSymbols*. Dans un premier temps, la matrice du signal OFDM est redessinée (dans le domaine temporel) à partir de la fonction Matlab *reshape* de telle sorte que chaque ligne corresponde à un symbole OFDM différent. Une colonne correspondra ainsi à une sous-porteuse dans le domaine fréquentiel. Nous avons alors une matrice de *Ns* lignes et de *NFFT + NZPS* colonnes. Le programme *IsolateSymbols* permet également la suppression du suffixe (*zero padded suffix*).

$$OFDM\_Signal\_RX = \underbrace{\left.\begin{pmatrix} a_{1,1} & a_{1,2} & \cdots & a_{1,n} \\ a_{2,1} & a_{2,2} & \cdots & a_{2,n} \\ \vdots & \vdots & \ddots & \vdots \\ a_{m,1} & a_{m,2} & \cdots & a_{m,n} \end{pmatrix}\right\} Ns}_{NFFT+NZPS} \tag{A.12}$$

```
% Separate the OFDM symbols
OFDM_Signal_RX = reshape(OFDM_Signal_RX,NFFT+NZPS,Ns)';

% zero padded suffix removal
n2 = round(NZPS/2);
OFDM_Signal_RX_CP = OFDM_Signal_RX(:,n2+[1:NFFT]);
```

Ensuite le programme *SymbolFFT* (ligne 127) ramène simplement le signal OFDM dans le domaine fréquentiel (simple fft).

Le programme *RemoveZeros_802p15p3c* (ligne 131) ne garde que les éléments de la matrice *OFDM_Signal_Rx_CP* correspondant aux sous-porteuses pilotes, nulles, et données et ceci à partir de la connaissance de leurs emplacements (*Cf.* le programme *ParameterSet_802p15p3c*). Les sous-porteuses de gardes placées sur le vecteur [-256:-186 ; 186:256] sont supprimées.

Le programme *RecenterSymbol_802p15p3c* recadre les symboles de la constellation : le signal est multiplié par l'exponentiel de *-i*angle(mean(OFDM_Signal_Rx_CP))*, où *angle* est une fonction Matlab fournissant l'angle polaire du signal qu'il reçoit, compris en $-\pi$ et π.

Ensuite le programme *ExtractPilotsandEqualize_802p15p3c* (ligne 133) égalise le niveau de chaque sous-porteuse. En effet, au cours d'une capture l'amplitude et la phase de chaque sous-porteuse varient. Dans le but d'harmoniser le niveau des sous-porteuses nous mesurons la valeur moyenne de chaque sous-porteuse pilote sur l'ensemble des symboles. Nous obtenons alors un vecteur *Magnis* donnant l'amplitude moyenne de chaque sous-porteuse pilote. Nous faisons de même pour la phase. Pour rappel, le fonction *mean* de Matlab calcule la moyenne sur les colonnes d'une matrice. Soit :

```
Magnis = mean(abs(OFDM_Signal_RX_CP(:,id_pilots)));
Phases = angle(OFDM_Signal_RX_CP(:,id_pilots));
Phases = Phases-mean(Phases(1,:));
Phases = unwrap(mean(Phases));
```

Nous corrigeons alors l'amplitude et la phase de toutes les sous-porteuse du spectre, et uniquement à partir des données issues des sous-porteuses pilotes. En effet toute sous-porteuse pilote a par définition une phase nulle et une amplitude égale à l'unité. Nous affectons alors une nouvelle phase et une nouvelle amplitude à l'ensemble du spectre en supposant que le déphasage et l'amplitude varie linéairement en fonction de la position des sous-porteuses,

```
Equal = interp1(id_pilots,Magnis,[1:(NP+ND+NZ)],'linear','extrap') .*...
        exp(i*interp1(id_pilots,Phases,[1:(NP+ND+NZ)],'linear','extrap'));

OFDM_Signal_RX_CP = OFDM_Signal_RX_CP./(ones(Ns,1)*Equal);
```

Le programme *FindFrequencyOffsetAndCompensate* (ligne 139) cherche à corriger la valeur de la fréquence d'échantillonnage, *Fs*, et celle de la fréquence centrale de la bande OFDM, *LO_FRQ*.

Pour chaque sous-porteuse pilote, nous regardons en fonction du temps l'évolution de sa phase (il y a autant de points que nous avons de symboles capturés). Nous supposons alors que cette évolution est linéaire et nous l'approximons par une droite, le polynôme *POL* de degré égal à l'unité. Ainsi un vecteur *DeltaFS* est défini, fournissant une information de phase pour chaque sous-porteuse pilote. Si

toutes les valeurs de *DeltaFS* ne sont pas égales, c'est parce que la fréquence d'échantillonnage *Fs* n'est pas exacte. La correction à effectuer sur *Fs* est proportionnelle à l'évolution de *DeltaFS*, c'est-à-dire au coefficient de la pente de l'approximation linéaire. Ainsi Fs correspond à l'écart de phase moyen entre deux sous-porteuses pilotes. Pour résumer, il est normal d'avoir une évolution de la phase en fonction du temps pour une sous-porteuse pilote, mais il n'est pas normal d'avoir des évolutions différentes entre chaque sous-porteuse pilote : ces différences sont uniquement dues à un mauvais choix dans la valeur de FS.

La fréquence centrale du canal OFDM doit également être corrigée. La correction apportée sera *DeltaF*, valeur moyenne du dernier polynôme (car *Idx_Plt* vaut [-166:22:-12, 12:22:166], nous avons une symétrie par rapport au centre du spectre, le zéro du polynôme).

```
Phases = angle(OFDM_Signal_RX_CP(:,id_pilots));
Phases = Phases-mean(Phases(1,:));
Times  = [0:(size(Phases,1)-1)]*(NFFT+NZPS)/FS;
DeltaFS = [];

for i_pilot = 1:length(Idx_Plt)
    POL = polyfit(Times,Phases(:,i_pilot)',1);
    DeltaFS(i_pilot) = POL(1);
end

POL = polyfit(Idx_Plt,DeltaFS,1);
DeltaFS = (sign(DIRN)*NFFT) * POL(1)/2/pi;
DeltaF  = POL(2)/2/pi;
```

La boucle s'arrête lorsque les valeurs de *DeltaFs* et *DeltaF* sont trop petites ou qu'elles n'évoluent pas suffisamment, ou bien lorsque nous avons atteint le nombre maximal de tour. À ce moment, où nous cassons la boucle *while*, deux opérations sont effectuées : *FitConstellation* et *ComputeEVMandBER*.

Le programme *FitConstellation* superpose la constellation de référence *psks* sur la constellation du signal OFDM que nous voulons démoduler. C'est l'étape préalable au calcul de l'EVM. La constellation *psks* est donc modifiée en phase et en amplitude afin de correspondre le plus fidèlement à la constellation de notre signal OFDM. Dans ce but, les sous-porteuses pilotes sont extraites, puis leur angle moyen et leur amplitude moyenne sont calculés.

```
OFDM_Signal_RX_CP_PILO = OFDM_Signal_RX_CP(:,id_pilots);

Ampli0 = mean(abs(OFDM_Signal_RX_CP_PILO(:)));
Angle0 = mean(angle(OFDM_Signal_RX_CP_PILO(:)));

Consts = [{OFDM_Signal_RX_CP_DATA(:)},{psks}];

% Fit received constallation with ideal constallation by fminsearch
[x,M1] = fminsearch(@(X) Err_Const_OFDM_60GHz_plot(X,Consts,verbose),[Ampli0,Angle0]);
```

Ensuite la fonction Matlab *fminsearch* minimise la fonction *Err_Const_OFDM_60GHz_plot* en faisant varier le vecteur X autour de la valeur initiale *[Ampli0, Angle0]*. Le vecteur X est donc un vecteur ligne dont la première colonne est une amplitude et la seconde une phase. La fonction *Err_Const_OFDM_60GHz_plot* retourne la valeur de M1 qui servira par la suite à calculer l'EVM ($EVM = fonction(M1, M0)$). La troisième ligne de cette fonction (ci-dessous) montre la modification de la constellation de référence afin de minimiser l'erreur sur l'EVM. *Err* est la somme des distances séparant chaque point de la constellation du signal chargé depuis l'oscilloscope aux points de la constellation de référence. Ce calcul repose uniquement sur les sous-porteuses de données. La présence de l'opérateur *min* sert à ne garder que la distance minimale entre deux points, car pour une sous-porteuse de donnée (donc un point) nous avons une constellation *psks* (quatre points). Notons enfin que chaque distance est élevée au carré avant d'effectuer l'opération de somme, le résultat du calcul est donc proportionnel à la puissance de l'erreur.

```
function Err = Err_Const_OFDM_60GHz_plot(X,Consts,verbose)

Consts{2} = Consts{2}*X(1)*exp(i*X(2));

Err = sum(min(abs(Consts{1}(:)*ones(size(Consts{2}(:)'))) - ...
      ones(size(Consts{1}(:)))*conj(Consts{2}(:))').^2,[],2));
```

Pour rappel, le programme *FitConstellation* retourne le vecteur [x,M1], M1 le résultat optimale (minimale) de *fminsearch*, résultat trouvé en x.

Le programme *ComputeEVMandBER* renvoie la valeur de l'EVM. L'EVM vaut alors *100 * sqrt(M1/M0)*, ou *M0* est la valeur moyenne de la norme au carré des sous-porteuses de données sur l'ensemble des symboles, multipliée par le nombre de symboles. *M0* est ainsi proportionnel à la puissance du signal. La formule que nous utilisons pour la mesure d'EVM est la suivante :

$$EVM[\%] = 100 \times \sqrt{\frac{P_{error}}{P_{signal}}} \tag{A.13}$$

Soit le programme *ComputeEVMandBER* :

```
1 M0 = Nsymb * mean(abs(OFDM_Signal_RX_CP_DATA(:)).^2);
2 EVM_MEAS_BAND = 100*sqrt(M1/M0);
```

Personal scientific publications and patent

Papers published in journals with peer reviews

- J. Guillory, S. Meyer, I. Siaud, A.M. Ulmer-Moll, B. Charbonnier, A. Pizzinat and C. Algani, "Radio-over-Fiber architectures, Future Multigigabit Wireless Systems in the Home Area Network", *IEEE Vehicular Technology Magazine (VTM)*, vol. 5, no. 3, pp. 30-38. September 2010.

- J. Guillory, E. Tanguy, A. Pizzinat, B. Charbonnier, S. Meyer, C. Algani and H.W. Li, "A 60 GHz wireless Home Area Network with Radio over Fiber repeaters", *IEEE Journal Lightwave Technology (JLT)*, vol. 29, no. 16, pp. 2482-2488. August 2011.

International conferences with proceedings

9 publications as main author (presented in oral session) and 6 as co-author (3 presented in oral session and 3 presented in poster session).

- J. Guillory, P. Guignard, A. Pizzinat, O. Bouffant and B. Charbonnier, "Multiservice & Multiformat home network based on a low cost optical infrastructure", *European Conference on Optical Communication (ECOC)*. September 2009 - Vienna, Austria.

- J. Guillory, S. Meyer, I. Siaud, A.M. Ulmer-Moll, B. Charbonnier, A. Pizzinat and C. Algani, "RoF architectures for Multi-Gigabit Wireless Systems in the Home Area Network", 24^{th} Wireless World Research Forum (WWRF) - Working Group 5. April 2010 - Penang, Malaysia.
  Best paper award of the Wireless World Research Forum, Working Group 5.

- J. Guillory, Ph. Guignard, F. Richard, L. Guillo and A. Pizzinat, "Multiservice Home Network based on Hybrid Electrical & Optical Multiplexing on a Low Cost Infrastructure", *Optical Society of America (OSA) Optics & Photonics Congress (OPC) - Access Networks and In-house Communications (ANIC)*. June 2010 - Karlsruhe, Germany.

- F. Richard, Ph. Guignard, J. Guillory, L. Guillo, A. Pizzinat and A.M.J. Koonen, "CWDM Broadcast and Select Home Network based on Multimode Fibre and a Passive Star Architecture", *Optical Society of America (OSA) Optics & Photonics Congress (OPC) - Access Networks and In-house Communications (ANIC)*. June 2010 - Karlsruhe, Germany.

- F. Richard, Ph. Guignard, A. Pizzinat, L. Guillo, J. Guillory, B. Charbonnier, A.M.J. Koonen, E. Ortego Martinez, E. Tanguy and H.W. Li, "Optical Home Network based on an NxN Multimode Fiber Architecture and CWDM Technology", *Optical Fiber Communication (OFC) conference and exposition.* March 2011 - Los Angeles, USA.

- J. Guillory, E. Tanguy, A. Pizzinat, B. Charbonnier, S. Meyer, H.W. Li and C. Algani, "Radio over Fiber tunnel for 60 GHz wireless Home Network", *Optical Fiber Communication (OFC) conference and exposition.* March 2011 - Los Angeles, USA.

- J. Guillory, F. Richard, Ph. Guignard, A. Pizzinat, S. Meyer, B. Charbonnier, L. Guillo, E. Tanguy, H.W. Li and C. Algani, "Towards a Multiservice & Multiformat Optical Home Area Network", *14th ITG Conference on Electronic Media Technology.* March 2011 - Dortmund, Germany.

- C. Kärnfelt, M. Ney, D. Bourreau, A. Bikiny, G. Guével, Y. Paugam, F. Gallée, J. Guillory, A. Pizzinat, B. Charbonnier, S. Meyer, O. Bouffant, G. Delas, H.W. Li, E. Tanguy, M. Brunet, G. Lirzin, A. Chousseaud, C. Algani, A-L. Billabert, J-L Polleux, C. Canepa, G. Gougeon and V. Gouin, "ORIGIN - a 60 GHz Radio-over-Fiber Home Area Network project", *International Symposium on Green Radio over Fibre and All Optical technologies for Wireless Access Networks (GROWAN).* June 2011 - Brest, France.

- J. Guillory, A. Pizzinat, B. Charbonnier and C. Algani, "60GHz Intermediate Frequency over Fiber using a passive Multipoint-to-Multipoint architecture", *16th European Conference on Networks and Optical Communications (NOC).* July 2011 - Newcastle upon Tyne, United Kingdom.
  IEEE best paper award of the 16th European Conference on Networks and Optical Communications.

- J. Guillory, A. Pizzinat, Ph. Guignard, F. Richard, B. Charbonnier, Ph. Chanclou and C. Algani, "Simultaneous implementation of Gigabit Ethernet, RF TV, and radio mm-wave in a multiformat Home Area Network", *European Conference on Optical Communication (ECOC).* September 2011 - Geneva, Switzerland.

- P. Chanclou, F. Bourgart, B. Landousies, S. Gosselin, B. Charbonnier, N. Genay, A. Pizzinat, F. Saliou, B. Le Guyader, B. Capelle, Q.T. Le, F. Raharimanitra, A. Gharba, L. Anet Neto, J. Guillory, Q. Deniel and S. Deniel, "Technical options for NGPON2 beyond 10G PON", *European Conference on Optical Communication (ECOC).* September 2011 - Geneva, Switzerland.
  Invited Paper.

- J. Guillory, A. Pizzinat, B. Charbonnier and C. Algani, "Radio over Fiber architectures for 60GHz Wireless Systems in the Home Area Network", *14th International Symposium on Wireless Personal Multimedia Communications (WPMC).* October 2011 - Brest, France.
  Invited Paper.

- J. Guillory, Y. Ait Yahia, A. Pizzinat, B. Charbonnier, C. Algani, M.D. Rosales and J.L. Polleux, "Comparison Between Two 60GHz Multipoint RoF Architectures for the Home Area Network", *17th European Conference on Networks and Optical Communications (NOC).* June 2012 - Vilanova i la Geltru, Spain.

- L. Anet Neto, D. Erasme, N. Genay, J. Guillory, B. Charbonnier, P. Chanclou, T.-A. Truong and C. Aupetit-Berthelemot, "Experimental Investigation of Dispersion-induced Distortions in IMDD OFDM PON Transmissions", *European Conference on Optical Communication (ECOC).* September 2012 - Amsterdam, Netherlands.

- Ph. Guignard, J. Guillory, Ph. Chanclou, A. Pizzinat, O. Bouffant, N. Evanno, J. Etrillard, B. Charbonnier, S. Gosselin, L. Guillo and F. Richard , "Multiformat Home Networks using Silica Fibres", *European Conference on Optical Communication (ECOC).* September 2012 - Amsterdam, Netherlands.

Other communications

- J. Guillory, S. Meyer, B. Charbonnier, S. Roblot and T. Derham, "Radio over Fiber for an optimal 60 GHz Home Area Network", *IEEE Contribution 11-10-0011-00-00ad: conference call to present the RoF to the IEEE 802.11 Task Group 'ad' (TGad).* 7$^{\text{th}}$ January 2010.
  https://mentor.ieee.org/802.11/dcn/10/11-10-0011-01-00ad-radio-over-fiber-for-an-optimal-60-ghz-home-area-network.ppt

National conferences with proceedings

- J. Guillory, A. Pizzinat, P. Guignard, O. Bouffant, L. Guillo, F. Richard, et B. Charbonnier and P. Chanclou, "Réseau local domestique multiformat sur une infrastructure optique bas coût", *28ème Journées Nationales Optique Guidée (JNOG)*. July 2009 - Lille, France.

- F. Richard, Ph. Guignard, A. Pizzinat, L. Guillo, J. Guillory, B. Charbonnier, E. Tanguy and H.W. Li, "Architecture transparente en fibre multimode et technologie CWDM pour un Réseau Local Domestique multiformat", *29ème Journées Nationales Optique Guidée (JNOG)*. October 2010 - Besançon, France.

- J. Guillory, E. Tanguy, A. Pizzinat, B. Charbonnier, S. Meyer, H. W. Li, C. Algani, O. Bouffant, G. Delas, A. Chousseaud, M. Brunet, G. Lirzin, J-L. Polleux, A. Bikini, M. Ney, D. Bourreau, C. Kärnfelt, C. Canepa, G. Gougeon and V. Gouin, "Radio sur Fibre pour un Réseau Local Domestique millimétrique", *17ème Journées Nationales Micro-ondes (JNM)*. May 2011 - Brest, France.

- J. Guillory, E. Tanguy, A. Pizzinat, B. Charbonnier, S. Meyer, H. W. Li, C. Algani, O. Bouffant, G. Delas, A. Chousseaud, M. Brunet, G. Lirzin, J-L. Polleux, A. Bikini, M. Ney, D. Bourreau, C. Kärnfelt, C. Canepa, G. Gougeon and V. Gouin, "Radio sur Fibre pour un Réseau Local Domestique millimétrique", *Journée du Club Optique et Micro-ondes (JCOM)*. June 2011 - Rennes, France.

- J. Guillory, A. Pizzinat, P. Guignard and C. Algani, "Réseau Local Domestique Multiservice à Très Haut Débit", *Journée du Club Optique et Micro-ondes (JCOM)*. June 2012 - Lille, France.

Patent

- Inventors: S. Meyer et J. Guillory.
  Title of Patent: Procédé de traitement d'une demande de transmission d'un signal radio dans un système RoF.
  Application number (numéro de demande): 1052356.
  Submission number (numéro de soumission): 1000075601.
  Date of Patent: March 30, 2010.

Bibliography

[1] J. Laskar, S. Pinel, D. Dawn, S. Sarkar, B. Perumana and P. Sen. The Next Wireless Wave is a Millimeter Wave. *Microwave Journal*, vol. 50, no. 8, p. 22, August 2007.

[2] DisplaySearch. Connected TV Shipments to Exceed 138 Million Units in 2015, consulted in January 2012. http://www.displaysearch.com/cps/rde/xchg/displaysearch/hs.xsl/110705_connected_tv_shipments_to_exceed_138_million_units_in_2015.asp.

[3] Lawrence Thorne. Consumer-Friendly Plastic Optical Fiber Home Network Distribution, consulted in December 2011. http://www.iptvmagazine.com/2009_01/IPTVMagazine_2009_01_Optical_Home_Networking.html.

[4] H. Tanobe, M. Kobayashi, Y. Shibata, O. Moriwaki, R. Nagase, Y. Sakai. Dual-Mode Fibre (DMF) capable of single- and multi-mode transmission. *33th European Conference on Optical Communication (ECOC)*, Berlin, Germany, September 2007.

[5] L. Cariou, Ph. Christin, M.H. Hamon, S. Roblot, I. Siaud and M. Bellec. Future WiFi systems for Home Networks. *Internal White Paper, Orange Labs*, June 2010.

[6] M. Pejanovic-Djurisic. OFDM Relay Technologies for the New Generation Wireless Communication Systems. *14th International Symposium on Wireless Personal Multimedia Communications (WPMC)*, Brest, France, October 2011.

[7] Glenn Fleishman. Cutting the cord: the state of wireless HD video links, consulted in December 2011. http://arstechnica.com/gadgets/news/2009/02/cutting-the-cord-the-state-of-wireless-hd-video-links.ars.

[8] K. Siwiak and D. McKeown. *Ultra-wideband radio technology.* John Wiley & Sons, 2004.

[9] WiGig Alliance. Defining the Future of Multi-Gigabit Wireless Communications. *WiGig White Paper*, July 2010.

[10] WirelessHD Specification Overview, Specification Version 1.0a. August 2009.

[11] Adelia C. Valdez. *Analysis of atmospheric effects due to atmospheric oxygen on a wideband digital signal in the 60GHz band.* PhD thesis, Faculty of the Virginia Polytechnic Institute and State University (Virginia Tech), 2001.

[12] M. Jacob, C. Mbianke and T. Kürner. A Dynamic 60 GHz Radio Channel Model for System Level Simulations with MAC Protocols for IEEE 802.11ad. *IEEE 14th International Symposium on Consumer Electronics (ISCE)*, Braunschweig, Germany, June 2010.

[13] EEWeb, Electrical Engineering Community. WirelessHD Module from Murata, consulted in July 2012.
http://www.eeweb.com/news/wirelesshd-module-from-murata.

[14] Stephen Shankland. Wilocity: 60GHz wireless revolution begins at CES, consulted in November 2011. http://news.cnet.com/8301-30685_3-57326718-264/wilocity-60ghz-wireless-revolution-begins-at-ces/.

[15] K. Nishikawa. Ultra High-Speed Radio Communication Systems and Their Applications - Current Status and Challenges. *Omega Open Event*, Rennes, France, February 2010.

[16] Tomohiro Seki, Ken Hiraga, Kentaro Nishimori, Kenjiro Nishikawa, and Kazuhiro Uehara. High Speed Parallel Data Transmission and Power Transmission Technology for Wireless Repeater System. *5th European Conference on Antennas and Propagation (EUCAP)*, Rome, Italy, April 2011.

[17] Ignacio González Insua. *Optical generation of mm-wave signals for use in broadband radio over fiber systems.* Jörg Vogt Verlag, 2010.

[18] Kensuke Ikeda, Toshiaki Kuri and Ken-ichi Kitayama. Simultaneous Three-Band Modulation and Fiber-Optic Transmission of 2.5-Gb/s Baseband, Microwave-, and 60-GHz-Band Signals on a Single Wavelength. *Journal of Lightwave Technology*, vol. 21, no. 12, pp. 3194–3202, December 2003.

[19] Chun-Ting Lin, Po-Tsung Shih, Jyehong Chen, Wen-Qiang Xue, Peng-Chun Peng and Sien Chi. Optical millimeter-wave signal generation using frequency quadrupling technique and no optical filtering. *IEEE Photonics Technology Letters*, vol. 20, no. 12, pp. 1027–1029, June 2008.

[20] Markus Junker. *Investigation of Millimetre Wave Generation by stimulated Brillouin scattering for Radio Over Fibre Applications.* PhD thesis, School of Electronic & Communications Engineering, Dublin Institute of Technology, 2008.

[21] Hyuk-Kee Sung, Erwin K. Lau and Ming C. Wu. Optical Single Sideband Modulation Using Strong Optical Injection-Locked Semiconductor Lasers. *IEEE Photonics Technology Letters*, vol. 19, no. 13, pp. 1005–1007, July 2007.

[22] G. Grosskopf, D. Rohde, R. Eggemann, S. Bauer, C. Bornholdt, M. Möhrle and B. Sartorius. Optical Millimeter-Wave Generation and Wireless Data Transmission Using a Dual-Mode Laser. *IEEE Photonics Technology Letters*, vol. 12, no. 12, pp. 1692–1694, December 2000.

[23] M. Costa e Silva, A. Lagrost, L. Bramerie, M. Gay, P. Besnard and M. Joindot. Conversion sous-harmonique de fréquence d'horloge d'un signal très haut débit. *Journée du Club Optique et Micro-ondes (JCOM)*, Rennes, France, June 2011.

[24] B.L. Dang and I. Niemegeers. Analysis of IEEE 802.11 in Radio over Fiber Home Networks. *IEEE Conference on Local Computer Networks, 30th Anniversary*, Sydney, Australia, May 2005.

[25] L.G. Zei, S. Ebers, J.R. Kropp and K. Petermann. Noise Performance of Multimode VCSELs. *Journal of Lightwave Technology*, vol. 19, no. 6, pp. 884–892, June 2001.

[26] S. Lai and J. Conradi. Theoretical and Experimental Analysis of Clipping-Induced Impulsive Noise in AM-VSB Subcarrier Multiplexed Lightwave Systems. *Journal of Lightwave Technology*, vol. 15, no. 1, pp. 20–30, January 1997.

[27] IEEE Computer Society. IEEE Std 802.15.3c - Part 15.3: Wireless Medium Access Control (MAC) and Physical Layer (PHY) Specifications for High Rate Wireless Personal Area Networks (WPANs). Amendment 2: Millimiter-wave-based Alternative Physical Layer Extension. October 2009.

[28] Ulrich L. Rohde and David P. Newkirk. *RF/microwave circuit design for wireless applications.* John Wiley & Sons, 2004.

[29] B. Dusza, K. Daniel and C. Wietfeld. Error Vector Magnitude Measurement Accuracy and Impact on Spectrum Flatness Behavior for OFDM-based WiMAX and LTE Systems. *5th International Conference on Wireless Communications, Networking and Mobile Computing (WiCom)*, Beijing, China, September 2009.

[30] Y. Suzuki, S. Narahashi and T. Nojima. Bit Error Probability in the Presence of Third-Order Intermodulation Distortion Component from Power Amplifier of Different Mobile Systems. *IEEE Communications Letters*, vol. 15, no. 10, pp. 1041–1043, October 2011.

[31] Xiaoyi Zhu, Angela Doufexi and Taskin Kocak. On the Performance of IEEE 802.15.3c millimeter-wave WPANs: PHY and MAC. *6th Conference on Wireless Advanced (WiAD)*, London, UK, June 2010.

[32] X. Zhu, A. Doufexi and T. Kocak. Throughput and Coverage Performance for IEEE 802.11ad Millimeter-Wave WPANs. *IEEE 73rd Vehicular Technology Conference (VTC Spring)*, Budapest, Hungary, July 2011.

[33] IEEE 802.11ad pre-Standard. IEEE P802.11 Wireless LANs, PHY/MAC Complete Proposal Specification. *IEEE 802.11-10/0433r0*, May 2010. http://www.ieee802.org/11/.

[34] K. Chang (ETRI). Relay Operation in IEEE 802.11ad. *Proposal for IEEE 802.11ad - 10/0494r0*, May 2010.

[35] Newport website. Biased Photoreceivers, consulted in June 2012. http://www.newport.com/Biased-Photodetectors-818-BB-Series/139627/1033/info.aspx.

[36] Marek Hajduczenia and Henrique J.A. da Silva. Next Generation PON Systems - Current Status. *International Conference on Transparent Optical Networks (ICTON)*, Azores, Portugal, July 2009.

[37] R.E. Freund, C.A. Bunge, N.N. Ledentsov, D. Molin and C. Caspar. High-Speed Transmission in Multimode Fibers. *Journal of Lightwave Technology*, vol. 28, no. 4, pp. 569–586, February 2010.

[38] Su Khiong Yong and Chia-Chin Chong. An Overview of Multigigabit Wireless through Millimeter Wave Technology: Potentials and Technical Challenges. *EURASIP Journal on Wireless Communications and Networking*, vol. 2007, article ID 78907, pp. 1–10, 2007.

[39] F. Brunet, S. Roblot, I. Siaud, E. Conil, M.F. Wong and M. Bellec. Impact and Acceptance of 60 GHz systems. *Internal White Paper, Orange Labs*, November 2010.

[40] Standard TIA-EIA-568-B.1. Commercial Building Telecommunications Cabling Standard. Part 1: General Requirements. May 2001.

[41] Press release by WiGig. WiGig Taipei Summit Grand Debut - reveals the blueprint and market opportunities, consulted in June 2012. http://www.digitimes.com/supply_chain_window/story.asp?datepublish=2012/06/14&pages=PR&seq=203.

[42] Marketing Vision & Home LoB. Digital Home 2020. *Internal Special Report, Orange Labs*, April 2011.

[43] R. Gaudino, D. Cárdenas, M. Bellec, B. Charbonnier, N. Evanno, P. Guignard, S. Meyer, A. Pizzinat, I. Mollers and D. Jager. Perspective in Next-Generation Home Networks: Toward Optical Solutions? *IEEE Communications Magazine*, vol. 48, no. 2, pp. 39–47, February 2010.

[44] Intel's official website. USB (Universal Serial Bus), consulted in December 2011. http://www.intel.com/content/www/us/en/io/universal-serial-bus/universal-serial-bus.html?wapkw=usb.

[45] Intel's official website. Thunderbolt Technology, consulted in December 2011. http://www.intel.com/content/www/us/en/io/thunderbolt/thunderbolt-technology-developer.html.

[46] Bob Fox, Corinne Fresko and Fabien Lanne. The long-promised age of interactive TV finally dawns. *IBM White Paper*, September 2011.

[47] HbbTV's official website, consulted in January 2012. http://hbbtv.org/.

[48] Strategy Analytics. Connected Devices will account for 70 percent of Consumer Electronic Device Market Value in 2011, consulted in January 2012. http://www.strategyanalytics.com/default.aspx?mod=pressreleaseviewer&a0=5096.

[49] OnLive's website, consulted in January 2012. http://www.onlive.com/.

[50] Ph. Chanclou, F. Bourgart, B. Landousies, S. Gosselin, B. Charbonnier, N. Genay, A. Pizzinat, F. Saliou, B. Capelle, Q. Trung Le, F. Raharimanitra, A. Gharba, L. Anet Neto, J. Guillory, Q. Deniel and B. Le Guyader. Technical options for NGPON2 beyond 10G PON. *European Conference and Exposition on Optical Communications (ECOC)*, Geneva, Switzerland, September 2011.

[51] Orange's website, consulted in January 2012. http://abonnez-vous.orange.fr/residentiel/equipements/kit-fibre-optique.aspx.

[52] Mohamed Atef, Robert Swoboda and Horst Zimmermann. 1.25Gbit/s over 50m Step-Index Plastic Optical Fiber Using a Fully Integrated Optical Receiver With an Integrated Equalizer. *Journal of Lightwave Technology*, vol. 30, no. 1, pp. 118–122, January 2012.

[53] A. Antonino, S. Straullu, S. Abrate, A. Nespola, P. Savio, D. Zeolla, J.R. Molina, R. Gaudino, S. Loquai and J. Vinogradov. Real-time Gigabit Ethernet bidirectional transmission over a single SI-POF up to 75 meters. *Optical Fiber Communication Conference and Exposition (OFC)*, Los Angeles, CA, USA, March 2011.

[54] The Industrial Fiber Optics (IFO) website, specialized in the distribution of fiber optic products, Consulted in January 2012. http://i-fiberoptics.com/pof_selection_eska_mega.php.

[55] C.P. Caputo, P.J. Decker and S.E. Ralph. VCSEL-based 100m 25Gb/s Plastic Optical Fiber Links. *Optical Fiber Communication Conference and Exposition (OFC)*, Los Angeles, CA, USA, March 2011.

[56] J. Guillory, P. Guignard, A. Pizzinat, O. Bouffant and B. Charbonnier. Multiservice & multiformat home network based on a low cost optical infrastructure. *35th European Conference on Optical Communication (ECOC)*, Vienna Austria, September 2009.

[57] Whitney R. White, Lee L. Blyler, Jr. Miri Park. Manufacture of perfluorinated plastic optical fibers, consulted in December 2011. http://findarticles.com/p/articles/mi_m0NVN/is_26_24/ai_n13807420/?tag=content;col1.

[58] Corning's official website. ClearCurve OM3/OM4 multimode fiber, consulted in June 2010. http://www.corning.com/clearcurve/multimode/index.aspx.

[59] Draka's official website. Bend-Insensitive OM2, OM2+, OM3 and OM4 MaxCap Multimode Optical Fibers, consulted in January 2012. http://communications.draka.com/sites/eu/pages/bend-insensitive-MaxCap-multimode-optical-fibers.aspx.

[60] E. Perahia, C. Cordeiro, M. Park and L. Lily Yang. IEEE 802.11ad: Defining the Next Generation Multi-Gbps Wi-Fi. *7th IEEE Consumer Communications and Networking Conference (CCNC)*, Las Vegas, USA, January 2010.

[61] Agilent Technologies. Testing New-generation Wireless LAN. *Application Note*, October 2011.

[62] D. Birru, R. Chen, C.-T. Chou, S.-S. Eom, B. Gaffney, J.-K. Kim, Y.-S. Kim, K.-P. Kim, Y.-C. Ko, J. Laskar, W.-Y. Lee, M. Mc Laughlin, S. Pinel, A. Seyedi and H. Zhai. SCBT based 60GHz PHY Proposal. *IEEE 802.15-0681-02-003c*, July 2007.

[63] L. Anet Neto, A. Gharba, P. Chanclou, N. Genay, B. Charbonnier, M. Ouzzif, C. Aupetit-Berthelemot and J. Le Masson. High Bit Rate Burst Mode Optical OFDM for Next Generation Passive Optical Networks. *36th European Conference on Optical Communication (ECOC)*, Torino, Italy, September 2010.

[64] L. Anet Neto, P. Chanclou; B. Charbonnier; N. Genay; F. Saliou; R. Xia; M. Ouzzif; C. Aupetit-Berthelemot; J. Le Masson, E. Grard and V. Rodrigues. Up to 40Gb/s Optically Amplified AMOOFDM for Next Generation PON Networks. *Optical Fiber Communication Conference and Exposition (OFC)*, Los Angeles, CA, USA, March 2011.

[65] L. Anet Neto, G. Beninca de Farias, N. Genay, S. Menezo, B. Charbonnier, P. Chanclou and C. Aupetit-Berthelemot. On the Limitations of IM/DD WDM FDMA-OFDM PON with Single Photodiode for Upstream Transmission. *Optical Fiber Communication Conference and Exposition (OFC)*, Los Angeles, CA, USA, March 2012.

[66] D. Hillerkuss, R. Schmogrow, T. Schellinger, M. Jordan, M. Winter, G. Huber, T. Vallaitis, R. Bonk, P. Kleinow, F. Frey, M. Roeger, S. Koenig, A. Ludwig, A. Marculescu, J. Li, M. Hoh, M. Dreschmann, J. Meyer, S. Ben Ezra, N. Narkiss, B. Nebendahl, F. Parmigiani, P. Petropoulos, B. Resan, A. Oehler, K. Weingarten, T. Ellermeyer, J. Lutz, M. Moeller, M. Huebner, J. Becker, C. Koos, W. Freude and J. Leuthold. 26 Tbit.s^{-1} line-rate super-channel transmission utilizing all-optical fast Fourier transform processing. *Nature Photonics*, vol. 5, no. 6, pp. 364–371, June 2011.

[67] Federal Communications Commission (FCC). First Report and Order in The Matter of Revision of Part 15 of the Commission's Rules Regarding Ultrawideband Transmission Systems. *E.T-Docket 98-153, FCC 02-48*, April 2002.

[68] Emeric Guéguen. *Étude et optimisation des techniques UWB haut débit multibandes OFDM*. PhD thesis, INSA of Rennes, Electronic Specialty, October 2009.

[69] Wimedia's official website. wimedia.org, consulted in December 2011. www.wimedia.org.

[70] Wisair's website. wisair.com, consulted in December 2011. www.wisair.com.

[71] A. Bit, M. Orehek and W. Zia. Comparative Analysis of Bluetooth 3.0 with UWB and Certified Wireless-USB Protocols. *IEEE International Conference on Ultra-WideBand (ICUWB)*, Nanjing, China, September 2010.

[72] ECMA-387 Standard. High Rate 60GHz PHY, MAC and HDMI PAL. *1st Edition*, December 2008.

[73] IEEE 802.15.3c Standard. Wireless Medium Access Control (MAC) and Physical Layer (PHY), Specifications for High Rate Wireless Personal Area Network (WPANs). *Version 1.0a*, October 2009.

[74] Wireless Gigabit Alliance (WiGig). WiGig MAC and PHY Specification. *Version 1.0, final specification*, April 2010.

[75] Gefen's official website. Uncompressed HD extensions using 60 GHz wireless, consulted in February 2012. http://www.gefen.com/kvm/dproduct.jsp?prod_id=8255.

[76] D. Pepe and D. Zito. 60-GHz Transceivers for Wireless HD Uncompressed Video Communication in Nano-era CMOS Technology. *15th IEEE Mediterranean Electrotechnical Conference*, Valletta, Malta, April 2010.

[77] In-Stat website. WiGig/802.11ad-Enabled PC device Shipments to Approach 15 million in 2015, consulted in July 2012. http://www.instat.com/newmk.asp?ID=3361&SourceID=00000352000000000000.

[78] J. Guillory, S. Meyer, B. Charbonnier, T. Derham and S. Roblot. Radio over Fiber for an optimal 60 GHz Home Area Network. *IEEE 11-10-0011-01-00ad Conference Call*, January 2010. Available on: https://mentor.ieee.org/802.11/dcn/10/11-10-0011-01-00ad-radio-over-fiber-for-an-optimal-60-ghz-home-area-network.ppt.

[79] Marketwire website. Wilocity puts WiGig in action at CES 2012, consulted in July 2012. http://www.marketwire.com/press-release/wilocity-puts-wigig-in-action-at-ces-2012-1604813.htm.

[80] Loutfi Nuaymi. *WiMAX: Technology For Broadband Wireless Access*. John Wiley & Sons, 2007.

[81] Federal Communications Commission (FCC). Millimeter Wave Propagation: Spectrum Management Implications. *Bulletin Number 70*, July 1997.

[82] André Vander Vorst et Danielle Vanhoenacker-Janvier. *Bases de l'ingénierie micro-onde*. De Boeck Supérieur, 1996.

[83] Ruckus Wireless' website. The Not So Definitive Guide to Beamforming (December 26, 2010), Consulted in February 2012. http://www.theruckusroom.net/2010/12/beamforming-in-all-its-glory.html.

[84] IEEE's website. IEEE P802.3an (10GBase-T) Task Force, Consulted in February 2012. http://grouper.ieee.org/groups/802/3/an/public/index.html.

[85] Volktek's website, Consulted in February 2012. http://www.volktek.com.tw/eng/products_pd.php?stable=e_subhom_g2_w&sfiled=sdid&pno=1&stable1=e_prod_g_w&sfiled1=did&pno1=1&stable16=e_prod_g3_w&sfiled16=sdid&pno16=2&selid1=0&selid2=0.

[86] Alloy's website, Consulted in February 2012. http://www.alloy.com.au/10GbE_Mangd_Conv.htm.

[87] C. Cordeiro, S. Shankar, G. Basson, L. Chu, J. Yee, Y. Liu, Y. Seok, M. Park, S. Trainin, J. Trachewsky, C.C. Wang, C. Hansen. Spatial Reuse and Interference Mitigation in 60GHz. *IEEE 802.11-09/0782r0*, July 2009.

[88] Lunds Universitet's website, Elektro- och informationsteknik. OFDM and DMT: System Model, consulted in September 2012. http://www.eit.lth.se/fileadmin/eit/courses/eit140/ofdm_system.pdf.

[89] S.R. Abdollahi, H.S. Al-Raweshidy, S. Mehdi Fakhraie and R. Nilavalan. Digital Radio over Fibre for Future Broadband Wireless Access Network Solution. *6^{th} International Conference on Wireless and Mobile Communications (ICWMC)*, Valencia, Spain, September 2010.

[90] Anthony Ng'oma, Po-Tsung Shih, Jacob George, Frank Annunziata, Michael Sauer, Chun-Ting Lin, Wen-Jr Jiang, Jyehong Chen and Sien Chi. 21 Gbps OFDM wireless signal transmission at 60 GHz using a simple IMDD Radio-over-Fiber System. *Optical Fiber Communication Conference and Exposition (OFC)*, San Diego, CA, March 2010.

[91] Anthony Ng'oma, Michael Sauer, Frank Annunziata, Wen-Jr Jiang, Po-Tsung Shih, Chun-Ting Lin, Jyehong Chen and Sien Chi. 14 Gbps 60 GHz RoF link employing a simple system architecture and OFDM modulation. *IEEE International Topical Meeting on Microwave Photonics (MWP)*, Valencia, Spain, October 2009.

[92] J. Park, W.V. Sorin and K.Y. Lau. Elimination of the fibre chromatic dispersion penalty on 1550nm millimetre-wave optical transmission. *Electronics Letters*, vol. 33, no. 6, pp. 512–513, March 1997.

[93] G.H. Smith, D. Novak and Z. Ahmed. Technique for optical SSB generation to overcome dispersion penalties in fibre-radio systems. *Electronics Letters*, vol. 33, no. 1, pp. 74–75, January 1997.

[94] Brian C. J. Moore. *Hearing.* Handbook of Perception and Cognition, Second Edition, 1995.

[95] Chun-Ting Lin, Jyehong Chen, Po-Tsung Shih, Wen-Jr Jiang and Sien Chi. Ultra-High Data-Rate 60 GHz Radio-over-Fiber Systems Employing Optical Frequency Multiplication and OFDM Formats. *Journal of Lightwave Technology*, vol. 28, no. 16, pp. 2296–2306, August 2010.

[96] A. Narasimha, X.J. Meng, M.C. Wu and E. Yablonovitch. A "tandem" single sideband fiber-optic system using a dual-electrode Mach-Zehnder modulator. *Conference on Lasers and Electro-Optics (CLEO)*, San Francisco, CA, USA, May 2000.

[97] Toshiaki Kuri, Ken-ichi Kitayama and Yoshiro Takahashi. 60-GHz-Band Full-Duplex Radio-On-Fiber System Using Two-RF-Port Electroabsorption Transceiver. *IEEE Photonics Technology Letters*, vol. 12, no. 4, pp. 419–421, April 2000.

[98] Andreas Stöhr, Robert Heinzelmann and Dieter Jäger. Millimetre-wave Bandwidth Electro-Absorption Modulators and Transceivers. *International Topical Meeting on Microwave Photonics (MWP)*, Oxford, UK, September 2000.

[99] Gee-Kung Chang, Jianjun Yu and Zhensheng Jia. Architectures and Enabling Technologies for Super-Broadband Radio-over-Fiber Optical-Wireless Access Networks. *International Topical Meeting on Microwave Photonics*, Victoria, BC, Canada, October 2007.

[100] S. Fedderwitz, V. Rymanov, M. Weiss, A. Stöhr, D. Jäger, A.G. Steffan and A. Umbach. Ultra-Broadband and Low Phase Noise Photonic Millimeter-Wave Generation. *International Topical Meeting on Microwave Photonics & Asia-Pacific Microwave Photonics Conference (MWP/APMP)*, Gold Coast, Australia, September 2008.

[101] Ralf-Peter Braun, Gerd Grosskopf, Helmut Heidrich, Clemens von Helmolt, Ronald Kaiser, Kirsten Krüger, Udo Krüger, Detlef Rohde, F. Schmidt, Ralf Stenzel and Dirk Trommer. Optical Microwave Generation and Transmission Experiments in the 12- and 60-GHz Region for Wireless Communications. *IEEE Transactions on Microwave Theory and Techniques*, vol. 46, no. 4, pp. 320–330, April 1998.

[102] Wei Han, N.H. Zhu, Liang Xie, Min Ren, B.H. Zhang, Liang Li and H.G. Zhang. The optical injection locking technique and its applications for WDM-PON spare function. *Photonics and Optoelectronics Meetings (POEM): Fiber Optic Communication and Sensors*, Wuhan, China, November 2008.

[103] Atsushi Murakami, Kenta Kawashima and Kazuhiko Atsuki. Cavity Resonance Shift and Bandwidth Enhancement in Semiconductor Lasers With Strong Light Injection. *IEEE Journal of Quantum Electronics*, vol. 39, no. 10, pp. 1196–1197, October 2003.

[104] Hyuk-Kee Sung, Erwin K. Lau and Ming C. Wu. Optical Properties and Modulation Characteristics of Ultra-Strong Injection-Locked Distributed Feedback Lasers. *IEEE Journal of Selected Topics in Quantum Electronics*, vol. 13, no. 5, pp. 1215–1221, September 2007.

[105] D. Wake, C.R. Lima and P.A. Davies. Optical generation and transmission of 60GHz signals over 100km of optical fibre using a dual mode semiconductor laser. *25th European Microwave Conference*, Bologna, Italy, September 1995.

[106] Klaus Petermann. *Laser diode modulation and noise*.

[107] David Wake, Claudio R. Lima and Phillip A. Davies. Optical Generation of Millimeter-Wave Signals for Fiber-Radio Systems Using a Dual-Mode DFB Semiconductor Laser. *IEEE Transactions on Microwave Theory and Techniques*, vol. 43, no. 9, pp. 2270–2276, September 1995.

[108] F. Brendel, J. Poëtte, B. Cabon, T. Zwick, F. Lelarge and F. van Dijk. Analog Link Performance of Mode-Locked Laser Diodes in the 60 GHz Range. *International Topical Meeting on Microwave Photonics & Asia-Pacific Microwave Photonics Conference (MWP/APMP)*, Singapore, Republic of Singapore, October 2011.

[109] F. Lecoche, É. Tanguy, B. Charbonnier, H. Li, F. Van Dijk, A. Enard, F. Blache, M. Goix and F. Mallecot. Transmission Quality Measurement of two types of 60 GHz millimeter-wave generation and distribution systems. *Journal of Lightwave Technology*, vol. 27, no. 23, pp. 5469–5474, December 2009.

[110] B.L. Dang, R. Venkatesha Prasad and I. Niemegeers. On the MAC protocols for Radio over Fiber indoor networks. *1st International Conference on Communications and Electronics (ICCE)*, Hanoi, Vietnam, October 2006.

[111] H. Azgomi. Enabling Enterprise 10 Gigabit Ethernet Deployment with Long Reach Multimode Optics. *Cisco White Paper*, August 2007.

[112] Finisar's website. VCSELs and Detectors, consulted in July 2012. http://www.finisar.com/products/optical-components/VCSEL-and-Detectors.

[113] VI-Systems' official website. Vertically Integrated Systems, consulted in February 2012. http://v-i-systems.com.

[114] A. Rissons and J.C. Mollier. Le VCSEL, émetteur opto-électronique polyvalent. *Revue Scientifique et Technique de la Défense (RSTD)*, , no. 63, pp. 61–69, March 2004. Available on: .

[115] T. Wipiejewski, H.D. Wolf, L. Korte, W. Huber, G. Kristen, C. Hoyler, H. Hedrich, O. Kleinbub, T. Albrecht, J. Müller, A. Orth, Z. Spika, S. Lutgen, H. Pflaeging, J. Harrasser, K. Drögemüller, V. Plickert, D. Kuhl, J. Blank, D. Pietsch, H. Stange and H. Karstensen. VCSELs for datacom applications. *SPIE Photonics West, Vertical-Cavity Surface-Emitting Lasers III*, San Jose, CA, USA, January 1999.

[116] Newport's website. 15 and 25 GHz Photodetectors, consulted in July 2012. http://www.newport.com/15-and-25-GHz-Photodetectors/918055/1033/info.aspx.

[117] RayCan's website. 1550nm VCSEL, consulted in July 2012. http://www.raycan.com/product03.html.

[118] Datasheet Archive's website. PP-10G, consulted in July 2012. http://www.datasheetarchive.com/PP-10G-datasheet.html.

[119] U-L-M Photonics' website, consulted in July 2012. http://www.ulm-photonics.com.

[120] M.D. Rosales, J.L. Polleux and C. Algani. Design and Implementation of SiGe HPTs using an 80GHz SiGe Bipolar Process Technology. *8th IEEE International Conference on Group IV Photonics*, London, UK, September 2011.

[121] M.D. Rosales, J.L. Polleux and C. Algani. Improving Optical Detection in SiGe Heterojunction Phototransistors. *13th International Symposium on Microwave and Optical Technology (ISMOT)*, Prague, Czech Republic, June 2011.

[122] J. Guillory, Y. Ait Yahia, A. Pizzinat, B. Charbonnier, C. Algani, M.D. Rosales and J.L. Polleux. Comparison Between Two 60GHz Multipoint RoF Architectures for the Home Area Network. *17th European Conference on Networks and Optical Communications (NOC)*, Vilanova i la Geltru, Spain, June 2012.

[123] A. Valle, J. Sarma and K.A. Shore. Spatial Holeburning Effects on the Dynamics of Vertical Cavity-Emitting Laser Diodes. *Journal of Quantum Electronics*, vol. 31, no. 8, pp. 1423–1431, August 1995.

[124] A. Valle and L. Pesquera. Theoritical Calculation of Relative Intensity Noise of Multimode Vertical-Cavity Surface-Emitting Lasers. *Journal of Quantum Electronics*, vol. 40, no. 6, pp. 597–606, June 2004.

[125] Y. Le Guennec, A. Pizzinat, S. Meyer, B. Charbonnier, P. Lombard, M. Lourdiane, B. Cabon, C. Algani, A.L. Billabert, M. Terré, C. Rumelhard, J.L. Polleux, H. Jacquinot, S. Bories and C. Sillans. Low-Cost Transparent Radio-Over-Fiber System for In-Building Distribution of UWB Signals. *Journal of Lightwave Technology*, vol. 27, no. 14, pp. 2649–2657, July 2009.

[126] Ghaya Baili. *Contribution à la réduction du bruit d'intensité relatif des lasers à semiconducteurs pour des applications aux radars.* PhD thesis, University of Paris-Sud / U.F.R. Scientifique of Orsay, 2008.

[127] P.F. Moulton. Spectroscopic and laser characteristics of Ti-Al2O3. *Journal of the Optical Society of America B (JOSA B)*, vol. 3, no. 1, pp. 125–133, January 1986.

[128] J. Liu, H. Arslan and L.P. Dunleavy. Effect of Power Amplifier Impairments in Designing OFDM Based Wireless Communication System. *IEEE Topical Conference on Wireless Communication Technology*, Honolulu, HI, USA, October 2003.

[129] A.R.S. Bahai, M. Singh, A.J. Goldsmith and B.R. Saltzberg. A New Approach for Evaluating Clipping Distortion in Multicarrier Systems. *IEEE Journal on Selected Areas in Communications*, vol. 20, no. 5, pp. 1037–1046, June 2002.

[130] S.O. Rice. Distribution of the duration of fades in radio transmission. *Bell System Technology Journal*, vol. 37, no. 3, pp. 581–635, May 1958.

[131] J. Guillory, F. Richard, Ph. Guignard, A. Pizzinat, S. Meyer, B. Charbonnier, L. Guillo, E. Tanguy, H.W. Li and C. Algani. Towards a Multiservice & Multiformat Optical Home Area Network. *14ème ITG Conference on Electronic Media Technology*, Dortmund, Germany, March 2011.

[132] S. Moon, A.K. Jin and D.Y. Kim. 850nm single-mode transmission with a mode filter. *Conference on Lasers and Electro-Optics (CLEO)*, San Francisco, CA, USA, May 2004.

[133] D. Vez, S.G. Hunziker, R. Kohler, P. Royo, M. Moser and W. Bächtold. 850nm vertical-cavity laser pigtailed to standard singlemode fibre for radio over fiber transmission. *Electronics Letters*, vol. 40, no. 19, pp. 1210–1211, September 2004.

[134] Stephen H. Lampen. The Axia guide to choosing category cable. *Belden CDT*, 2005.

[135] R.A. Shafik, S. Rahman, and A.H.M. Razibul Islam. On the Extended Relationships Among EVM, BER and SNR as Performance Metrics. *International Conference on Electrical and Computer Engineering (ICECE)*, Dhaka, Bangladesh, December 2006.

[136] V.J. Urick, J.X. Qiu, and F. Bucholtz. Wide-Band QAM-Over-Fiber Using Phase Modulation and Interferometric Demodulation. *IEEE Photonics Technology Letters*, vol. 16, no. 10, pp. 2374–2376, October 2004.

[137] H. Zareian and V. TabaTaba Vakili. Impacts of both Tx and Rx IQ Imbalances on OFDM Systems - Analytical Approach. *National Conference on Communications (NCC)*, Mumbai, India, February 2008.

[138] Ellen Chu. Quantized QAM performance, consulted in July 2011. http://wiki.networkdictionary.com/index.php?title=16-QAM.

[139] Yadolah Dodge. *Statistique : dictionnaire encyclopédique.* Springer, 2004.

[140] Ramjee Prasad, Muhammad Imadur Rahman, Sekhar Suvra Das and Nicola Marchetti. *Single-And Multi-Carrier Mimo Transmission for Broadband Wireless Systems*. River Publishers Series in Communications, 2009.

[141] Marc Engels. *Wireless OFDM systems: how to make them work?* Kluwer Academic Publishers, 2002.

[142] Hisham A. Mahmoud and Hüseyin Arslan. Error Vector Magnitude to SNR Conversion for Nondata-Aided Receivers. *IEEE Transactions on Wireless Communications*, vol. 8, no. 5, pp. 2694–2704, May 2009.

[143] R. Chouitem. EVM based AMC for an OFDM system. *9th Conference on Wireless Telecommunications Symposium (WTS)*, Tampa, FL, USA, April 2010.

[144] T. Jiang and Y. Wu. An Overview: Peak-to-Average Power Ratio Reduction Techniques for OFDM Signals. *IEEE Transactions on Broadcasting*, vol. 54, no. 2, pp. 257–268, June 2008.

[145] L. Nadal, M. Svaluto Moreolo, J.M. Fabrega, G. Junyent. Low Complexity Bit Rate Variable Transponders Based on Optical OFDM with PAPR Reduction Capabilities. *17th European Conference on Networks and Optical Communications (NOC)*, Vilanova i la Geltru, Spain, June 2012.

[146] E. Tanguy, J. Guillory and A. Pizzinat. Rapport tests et performances du système RoF point-à-point (TRoF1). *ORIGIN deliverable, 6.1*, October 2010.

[147] WirelessHD. WirelessHD Compliance Test Specification (CTS). *Part 1: RF Performance. Version 1.0a*, February 2010.

[148] Su-Khiong Yong (SAIT). TG3c Channel Model Final Report Presentation. *IEEE 15-06-0483-02-003c*, November 2006.

[149] Hiroshi Harada (NICT) and Rick Roberts (Intel). The Matlab CM code. *IEEE 802.15-07/0559r3*, March 2007.

[150] Yoann Le Nevanen and Sylvain Meyer. Etude de faisabilité d'un système RoF dans le cadre du projet MTHD2. *Internal deliverable, Orange Labs*, June 2009.

[151] Amy Talley and John Sutherby. Murata develops second generation WirelessHD module, consulted in June 2012. http://mms.businesswire.com/bwapps/mediaserver/ViewMedia?mgid=257711&vid=1.

[152] A. Valdes-Garcia, S.T. Nicolson, Jie-Wei Lai, A. Natarajan, Chen Ping-Yu, S.K. Reynolds, Jing-Hong Conan Zhan, D.G. Kam, Duixian Liu and B. Floyd. A Fully Integrated 16-Element Phased-Array Transmitter in SiGe BiCMOS for 60-GHz Communications. *IEEE Journal of Solid-State Circuits*, vol. 45, no. 12, pp. 2757–2771, December 2010.

[153] IEEE 802.3af Standard. IEEE Standard for Information technology - Telecommunications and information exchange between systems - Local and metropolitan area networks - Specific requirements. Part 3: Carrier Sense Multiple Access with Collision Detection (CSMA/CD) Access Method and Physical Layer Specifications. *Amendment: Data Terminal Equipment (DTE) Power via Media Dependent Interface (MDI)*, June 2003.

[154] IEEE 802.3at Standard. IEEE Standard for Information technology - Telecommunications and information exchange between systems - Local and metropolitan area networks - Specific requirements. Part 3: Carrier Sense Multiple Access with Collision Detection (CSMA/CD) Access Method and Physical Layer Specifications. *Amendment 3: Data Terminal Equipment (DTE) Power via Media Dependent Interface (MDI) Enhancements*, October 2009.

[155] J. Guillory, S. Meyer, I. Siaud, A.M. Ulmer-Moll, B. Charbonnier, A. Pizzinat and C. Algani. RoF architectures for Multi-Gigabit Wireless Systems in the Home Area Network. *Wireless World Research Forum (WWRF)*, Penang, Malaisya., April 2010.

[156] J. Guillory, S. Meyer, I. Siaud, A.M. Ulmer-Moll, B. Charbonnier, A. Pizzinat and C. Algani. Radio-Over-Fiber Architectures. *IEEE Vehicular Technology Magazine (VTM)*, vol. 5, no. 3, pp. 30–38, September 2010.

[157] J. Guillory, D. Bernard, S. Roblot, P. Christin, A. Pizzinat, S. Meyer and B. Charbonnier. Analyse des formats radio et compatibilité PHY/MAC. *ORIGIN deliverable, 2.2*, January 2011.

[158] mbed official website. mbed NXP LPC1768, consulted in July 2012. http://www.mbed.org/nxp/lpc1768/.

[159] J. Guillory, Ph. Guignard, F. Richard, L. Guillo and A. Pizzinat. Multiservice Home Network based on Hybrid Electrical & Optical Multiplexing on a Low Cost Infrastructure. *OSA OPC Access Networks and In-house Communications (ANIC) conference*, Karlsruhe, Germany, June 2010.

[160] Ph. Guignard, H. Ramanitra and L. Guillo. Home Network based on CWDM Broadcast and Select technology. *33rd European Conference and Exposition on Optical Communications (ECOC)*, Berlin, Germany, September 2007.

[161] F. Richard, Ph. Guignard, J. Guillory, L. Guillo, A. Pizzinat and A.M.J. Koonen. CWDM Broadcast and Select Home Network based on Multimode Fibre and a Passive Star Architecture. *OSA OPC Access Networks and In-house Communications (ANIC) conference*, Karlsruhe, Germany, June 2010.

[162] F. Richard, Ph. Guignard, A. Pizzinat, L. Guillo, J. Guillory, B. Charbonnier, A.M.J. Koonen, E. Ortego Martinez, E. Tanguy and H.W. Li. Optical Home Network based on an NxN Multimode Fiber Architecture and CWDM Technology. *Optical Fiber Communication Conference and Exposition (OFC)*, Los Angeles, CA, USA, March 2011.

[163] Francis Richard. *Étude des architectures optiques pour le réseau local domestique, basées sur la fibre multimode (polymère et silice) et le multiplexage en longueur d'onde*. PhD thesis, Université de Nantes, Faculté des sciences et des techniques, 2012.

[164] Wikipedia, the free encyclopedia. Bande aéronautique VHF, consulted in June 2012. http://fr.wikipedia.org/wiki/Bande_aéronautique_VHF♯Sous-bande_UHF.

A selection of scientific publications

Some of my personal publications are reported subsequently:

- J. Guillory et al., "Radio-over-Fiber architectures, Future Multigigabit Wireless Systems in the Home Area Network", *IEEE Vehicular Technology Magazine* (September 2010) in page 242.

- J. Guillory et al., "A 60 GHz wireless Home Area Network with Radio over Fiber repeaters", *IEEE Journal Lightwave Technology* (August 2011) in page 251.

- J. Guillory et al., "Radio over Fiber architectures for 60GHz Wireless Systems in the Home Area Network", 14^{th} *International Symposium on Wireless Personal Multimedia Communications* (October 2011) in page 258 (*Invited Paper*).

- J. Guillory et al., "60GHz Intermediate Frequency over Fiber using a passive Multipoint-to-Multipoint architecture", 16^{th} *European Conference on Networks and Optical Communications* (July 2011) in page 266 (*IEEE best paper award*).

- J. Guillory et al., "Comparison Between Two 60GHz Multipoint RoF Architectures for the Home Area Network", 17^{th} *European Conference on Networks and Optical Communications* (June 2012) in page 270.

RADIO-OVER-FIBER ARCHITECTURES

Future Multigigabit Wireless Systems in the Home-Area Network

Joffray Guillory, Sylvain Meyer, Isabelle Siaud, Anne Marie Ulmer-Moll, Benoît Charbonnier, Anna Pizzinat, and Catherine Algani

Future multigigabit wireless systems (MGWS) dedicated to home-area networking are emerging or are under development. They achieve high data rate up to 5–6 Gb/s over short range. To expand the radio coverage, we propose radio-over-fiber (RoF) architectures, from the most basic (point-to-point) to the most innovative (multipoint-to-multipoint). These RoF infrastructures combine radio and optical links. The simple way to implement RoF technology is to manage the optical media, either using information from the physical (PHY) layer or using information from the media access control (MAC) layer of the radio system. This seems to be the most realistic solution even if it requires the establishment of cooperation between the radio MAC layer and the optical layer. This link can be made only if

Digital Object Identifier 10.1109/MVT.2010.937847

the RoF operation is taken into account at radio PHY MAC layer of future broadband wireless systems.

TABLE 1 *Radio standard properties in the 57–66 GHz band.*

Radio Standard	*ECMA-387*	*IEEE802.15.3c*	*IEEE802.11ad*
Released year	2008	2009	2012
Data rate (Mb/s)	20–25,400	20–5,670	385–6,757

Radio in Home-Area Network

The Home-Area Network

Today, we can note that the number of connected devices increases inside the home, and each of them require higher data rates up to multigigabit transmissions. This tendency will keep growing because new usage models arrive continuously. The ultimate goal for a telecommunication provider is to satisfy this demand. The solutions to this challenge shall be provided at the same time in the access network with fiber to the home technologies but also in the home-area network (HAN), in particular for in-house exchanges.

In the future, the instantaneous data rate in the HAN should reach 10 Gb/s. At these speeds, the wired technologies exist, but it will be difficult for the customers to come back to wired terminals. Indeed, today, we observe that the wireless connectivity is generally preferred for the final link to the device. Users find it easier to use and is more flexible.

Today, wireless fidelity (WiFi) 802.11g or 802.11n do increase the available wireless connection speed, but we are moving tomorrow to other standards that can offer even higher data rates. For this purpose, several standards of wireless personal-area network (WPAN) radio systems have emerged or are under development.

MGW Transmission: Statements

The main characteristics of the future radio standards are very high throughputs, wide bandwidths, and carrier frequencies around 5 GHz (cm-wave) or 60 GHz (mm-wave). Only mm-waves provide MGWS up to 5–6 Gb/s over one channel of 2.16 GHz. The associated standards dealing with these transmissions are ECMA 387 [1] and IEEE 802.15.3c [2]. More recently, the IEEE 802.11ad group has been created, dealing with 60-GHz components for the 802.11 family. The competition to impose these standards is rough and complex. The IEEE 802.11ad standard, supported by WiGig consortium [3], would lead the MGWS with WiFi certification, ensuring a good marketing name. Table 1 resumes these radio standards, and Figure 1 provides the spectrum mask in the mm-wave band.

The drawbacks of these standards are their short range due to low-power-spectrum density levels and the high channel attenuation. Consequently, the radio transmission is limited to a single room and to indoor open areas. As the home devices are not necessarily in the same room, how can we enlarge the coverage of the radio signal and extend the connectivity of our home gateway?

RoF Concept

Mixed architectures, combining fiber and radio technologies, are investigated to enlarge the multigigabit radio coverage and overcome 60-GHz multiroom transmissions. Only optic responds to a demand of high data rates: low attenuation, high RF bandwidth, high linearity, and immunity to electrical interferences. Inside the home, the optical fiber is a natural extension of the access networks that become all optical and is an ideal media to provide a long life-span communication infrastructure being able to adapt to new standards for years.

The RoF technology distributes the radio signal to several access points judiciously located in different rooms. The analog radio signal is just transposed onto an optical carrier without changing the modulation format. This ability to transmit radio signals in their native format provides the advantage of reduced cost, access point simplification, and transparency to radio layer protocols.

To be low cost, HAN have to be built with very simple basic blocks. The main function block in RoF systems is the electrooptic transducer (E/O and O/E conversion), at the interface between the wireless and wired medium. The simplest structure for this function is given in Figure 2. The radio signal directly modulates the intensity of a laser by driving its current, and a direct photo-detection is used for recovering the signal (intensity modulation with direct detection).

The main distortion in a RoF system is due to the laser nonlinearity. The power of radio signal must be optimized before the E/O conversion. It is also essential to adapt the

Channel Number	Low Freq. (GHz)	Center Freq. (GHz)	High Freq. (GHz)	Nyquist BW (MHz)	Roll-Off Factor
A1	57.240	58.320	59.400	1,728	0.25
A2	59.400	60.480	61.560	1,728	0.25
A3	61.560	62.640	63.720	1,728	0.25
A4	63.720	64.800	65.880	1,728	0.25

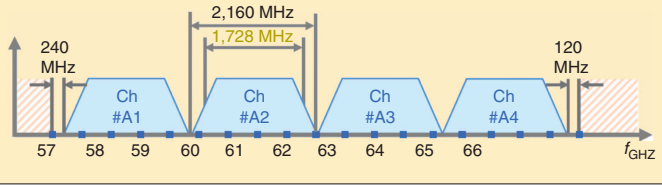

FIGURE 1 Channelization of the 57–66 GHz band.

RADIO WAVES WELL CONFINED IN A ROOM MINIMIZE THE ELECTROMAGNETIC FIELDS EXPOSURE AND KEEP DATA CLOSE TO THE USER.

emitted RF power to respect the maximum power level (regulations in unlicensed bands).

In the case of mm-waves, this solution is limited by the bandwidth of the optoelectronic components. So, the intermediate frequency over fiber (IFOF) option is preferred: mm-waves are first down-converted to a lower intermediate frequency before modulating the laser. The same local oscillator is used at the reception for the up-conversion.

The Optical RoF Architectures

Point-to-Point Architecture

Different options of point-to-point RoF links can be achieved, depending on the application (Figure 3). The first one with a single hop in the air is called remote antenna. The second one with two hops in the air is called optical tunnel. This latest architecture is helpful in a HAN where direct links between portable terminals are needed.

Point-to-Multipoint Architecture

The point-to-multipoint architecture is obtained by splitting the signal into different optical links. A $1 \times N$ optical splitter shares the optical power equally between all nodes. The drawback of this architecture is that the full home flows pass through the switch: the home gateway might become overloaded. Consequently, this architecture is preferred only for broadcast use cases, like television.

Active-Star Architecture

The active-star architecture (Figure 4) uses several remote antennas connected to a switch containing all the technological complexity and network intelligence. This architecture gives the best bandwidth $\times$ range/branch product, but with a significant number of branches; the cost of the switch can be important.

Multipoint-to-Multipoint Architecture

The multipoint-to-multipoint architecture (Figure 5) is based on an $N \times N$ optical splitter. Each laser at each remote antenna is connected to an input of the optical splitter, and each photodiode at each remote antenna is connected to an output of the splitter. When a remote antenna transmits data to the fiber, the signal is divided to all the outputs of the $N \times N$ optical splitter, and, thus, all the antennas receive the data. Thanks to this passive optical component, all the wireless devices are visible from one another through the optical fibers, whatever the distance between them, as if they were face to face in the same room. This optical infrastructure can be seen as a multiple input, multiple output repeater or as an optical bus.

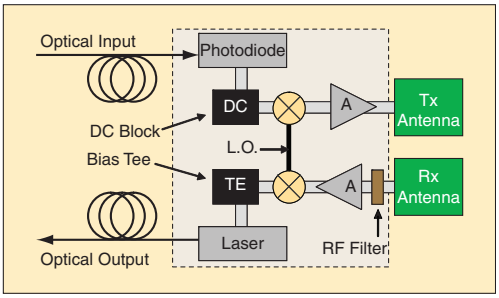

FIGURE 2 Radio-over-fiber transducers (IFOF).

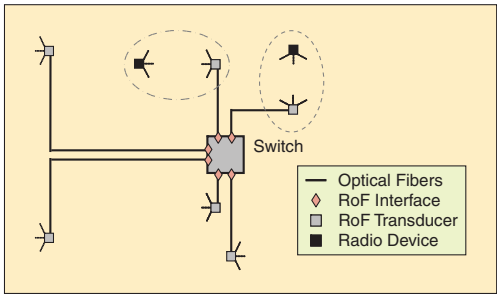

FIGURE 4 Active-star architecture.

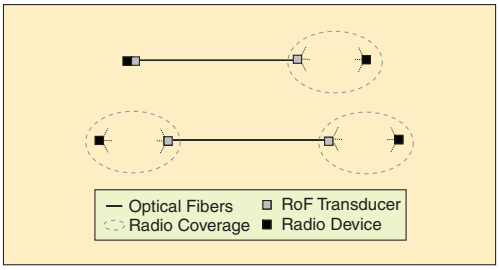

FIGURE 3 Point-to-point links, remote antenna, and optical tunnel.

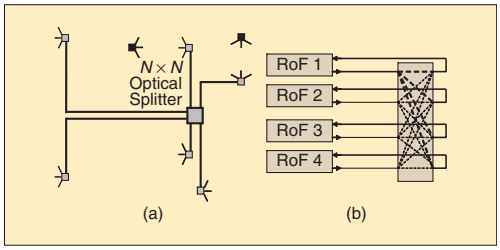

FIGURE 5 (a) The multipoint-to-multipoint architecture and (b) details about the mechanism of the optical splitter.

A key point of this transparent architecture is that the radio protocol alone is enough to control communications on the optical infrastructure. The radio-access methods, such as time-division multiple access (TDMA) or carrier sense multiple access (CSMA), are compatible. In CSMA, symbol collisions on the infrastructure are detected by the radio protocol implemented only in final devices.

Then, the data rate is shared between the different remote antennas because the optical links are not independent. However, in a HAN, the number of users is limited, so this architecture seems the best compromise between cost and efficiency.

Finally, this architecture distributes easily an oscillator. So, if a RoF transducer generates an oscillator frequency, all the other remote antennas can receive the same oscillator frequency. This architecture is well adapted to IFOF systems.

RoF Link-Budget Model

RoF link budget are designed and assessed at 60 GHz by considering a radio part derived from high-speed interfaces (HSI) orthogonal frequency-division multiplexing (OFDM) modes [7] of the IEEE802.15.3c standard [2]. The radio link-budget procedure is reminded and extended to RoF link-budget in introducing equivalent optical noise figure and optical loss components.

Radio Link Budget

Radio coverage evaluation of the transmission system is derived from the link-budget calculation in which the available power-to-noise ratio (SNR_a) (in dB) is compared with the required power-to-noise ratio SNR to achieve a given data rate D associated with a quality of service (QoS) (bit error ratio = 10^{-5}). The equality between the SNR_a and the SNR provides the maximum radio coverage of the system associated with the data rate D.

The available power-to-noise ratio SNR_a is the ratio of the available power to the thermal noise power Pb assorted with various contribution loss expressed as a function of noise temperature T of the system, the efficient bandwidth B_w, and loss contributions Lo. The available power depends on the path-loss attenuation of the propagation channel $PL(d,f_c)$, the radiated power equivalent isotropic radiated power (EIRP, in dB) and the received antenna gain G_r. The SNR_a is given by:

$$\begin{aligned}\mathrm{SNR_a}(d,f_c) = {} & G_r + \mathrm{EIRP} - \mathrm{PL}(d,f_c) \\ & - 10\cdot\mathrm{Log}(kT_0) - 10\cdot\mathrm{Log}\left(\frac{T}{T_0}\right) \\ & - 10\mathrm{Log}(B_w) - \mathrm{Lo}. \end{aligned} \quad (1)$$

The path-loss $PL(d,f_c)$ (in dB) is the sum of a reference path-loss PL_0, associated to the free space path-loss at a distance d_0 ($d_0 = 1$ m), and an additional exponential decay associated with realistic environment and a distance d between the transmitter and the receiver. The standard deviation σ is associated to shadowing effects:

$$\mathrm{PL}(d,f_c) = \mathrm{PL}_0(d_0,f_c) + 10\cdot n\cdot\mathrm{Log}\left(\frac{d}{d_0}\right) + \sigma. \quad (2)$$

The required power-to-noise ratio SNR to achieve a data rate D is derived from link-level simulations. The radio coverage is obtained by considering the equality between SNR_a and SNR as follows:

$$d = d_0\cdot 10^{((G_R+\mathrm{EIRP}-\mathrm{PL}_0(d_0,f_c)-\sigma-\mathrm{SNR}-\mathrm{Pb}-\mathrm{L0})/10n)}. \quad (3)$$

RoF Link Budget

Optical link leads to define an equivalent optical noise figure NF_{RoF} and an equivalent attenuation G_{RoF}. Optical losses L_{opt} associated with the fiber, connectors, and the optical splitter to simulate different architectures. The estimated gain of the RoF block (in dB) is:

$$\begin{aligned}G_{\mathrm{RoF}} = {} & 20\cdot\log(\eta_{\mathrm{Tx}}\eta_{\mathrm{Rx}}) - 2L_{\mathrm{opt}} - 10\cdot\log\left(\frac{Z_{\mathrm{in}}}{Z_{\mathrm{out}}}\right) \\ & + 20\cdot\log\left(\frac{Z_{\mathrm{TIA}}}{Z_{\mathrm{in}}}\right), \end{aligned} \quad (4)$$

where η_{Tx} is the slope efficiency of the laser (W/A), η_{Rx} is the photodiode responsivity (A/W), Z_{in} is the input impedance of the laser (Ω), Z_{out} is the output impedance of the photodiode (Ω), and Z_{TIA} is the impedance of the trans impedance amplifier (TIA) (Ω).

The main noise contributions of the RoF link are the relative intensity noise (RIN) of the laser, the shot noise of the photo-detection process, and the electrical noise of the TIA. These noise powers, P_{RIN}, P_{SHOT}, and P_{TIA}, are expressed in linear units (W). The total RoF noise figure (in dB) is then estimated by:

$$\mathrm{NF}_{\mathrm{RoF}} = 10\cdot\log\left(\frac{P_{\mathrm{RIN}}+P_{\mathrm{SHOT}}+P_{\mathrm{TIA}}}{kT_0\cdot G_{\mathrm{RoF}}\cdot\Delta F}\right). \quad (5)$$

The available power-to-noise ratio SNR_a is modified by G_{ROF} and by the noise of the additional components as follows:

$$\mathrm{SNR}_{\mathrm{a-RoF}} = \mathrm{EIRP} + \mathrm{G}_{\mathrm{RoF}} - \mathrm{PL}(d,f_c) + G_r - \mathrm{Lo} - P_n, \quad (6)$$

with P_n the noise contribution of the total link. We determine the noise Pn_j^{out} at the output of one block j (j=1..n)

THE ANALOG RADIO SIGNAL IS JUST TRANSPOSED ONTO AN OPTICAL CARRIER WITHOUT CHANGING THE MODULATION FORMAT.

THE POINT-TO-MULTIPOINT ARCHITECTURE IS OBTAINED BY SPLITTING THE SIGNAL INTO DIFFERENT OPTICAL LINKS.

from the noise Pn_{j-1}^{out} injected at its input. The noise figure N_j and gain G_j are the characteristics of the block, and ΔF is the bandwidth of the RF signal at the input of the block j.

$$Pn_j^{\text{out}} = 10 \cdot \log\left(10^{(P_{j-1}^{\text{out}}+G_j)/10} + kT_0(10^{\text{NF}_j/10} - 1) \cdot 10^{G_j/10} \cdot \Delta F_j\right). \quad (7)$$

RoF Coverage Results

A 60-GHz Link-Level Performances and Link Budget

The radio system refers to the modified IEEE802.15.3c HSI modes. HSI modes [2] enable to cover data rates up to 5,670 Mb/s (Table 1). These modes implement an OFDM modulation with 336 data subcarriers, 352 nonnull subcarriers, a fast Fourier transform length set to 512, and a cyclic prefix set to 25 ns.

TABLE 2 The 60-GHz multipath scenarios.

Multipath Scenario	LOS 72–60°	NLOS 72–60°	LOS 72–10°
Distance (m)	7.61	12.11	3.84
Delay spread σ_{DS}(ns)	2.73	12.75	2.17
RMS power σ_P (dB)	0.66	0.8	1.18

TABLE 3 Radio link-budget assessments [SNR (dB)].

MCS	Data Rate (Mb/s)	LOS 72–60°	NLOS 72–60°	LOS 72–10°
QPSK-1/2	1512	4.29	8.79	3.54
QPSK-3/4	2268.0	7.35	14.55	6.80
16-QAM-1/2	3024.0	9.30	13.30	8.80
16-QAM-3/4	4536.0	14.06	20.06	13.06

TABLE 4 A 60-GHz path loss attenuation of the channel.

Multipath Scenario	LOS 72–60°	NLOS 72–60°	LOS 72–10°
n	1.53	2.56	1.73
$PL_0(d_0)$ (dB)	71.2	79.79	4.30
σ (dB)	3.92	5.04	1.60

In the modified IEEE802.15.3c H.S.I. modes, low-density parity-checks are replaced with duobinary turbocodes [8] because of their good performance upon short forward error correction block sizes and data-rate scalability. An inner interleaver set to 41 B is considered, and four iterations are assessed in the decoding processing.

The link-level performances have been evaluated upon several multipath propagation scenarios considering a sectoral antenna at the transmitter (72°, $G_T = 8$ dB) and both sectoral antennas at the receiver side ({60°, $G_R = 13$ dB}, {10°, $G_R = 24$ dB}). The multipath scenarios are summarized in Table 2, and the required power-to-noise ratio (SNR) values are given in Table 3. A noise figure set to 8 dB and a connectivity loss set to 2.5 dB are considered.

WPAN Radio Coverage

The 60-GHz path-loss models resort from measurements detailed in [10]. Path-loss parameters are given in Table 4.

The data-rate radio coverage of the modified IEEE802.15.3c modes refers to multipath scenarios detailed in Table 4. Appropriate path-loss models are applied to the three propagation scenarios considered, assorted with antenna gains (Figure 6). Results prove that light of sight (LOS) is the most promising scenario to deploy 60-GHz radio transmissions. Using directive antennas may increase radio coverage. On the other hand, antenna misalignment may significantly damage the transmission as demonstrated in [11]. Results prove that 2 Gb/s on the air interface may be achieved with radio links ranging from 8 to 45 m depending on LOS/nonlight of sight (NLOS) criterion. Four gigabits per second on the air interface limits the radio coverage to 5–20 m. We recommend intermediate case with sectoral antennas to benefit from multipath diversity and reduce the impact of antenna misalignment.

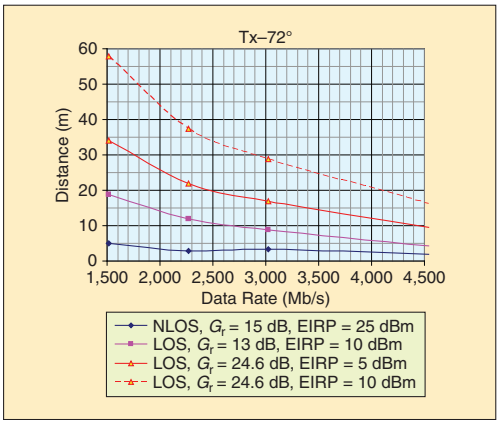

FIGURE 6 Modified IEEE802.3c HSI modes radio coverage.

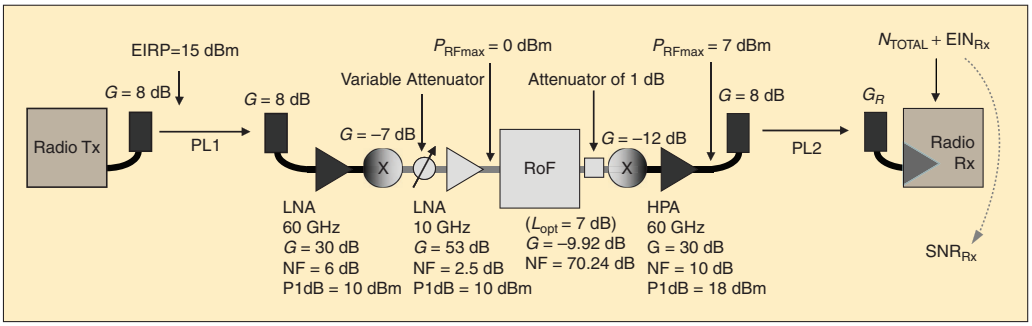

FIGURE 7 RoF setup based on an optical tunnel.

WPAN RoF Coverage

This section provides RoF coverage studies considering several radio transmission segments as illustrated in Figure 7.

This setup considered here is an optical tunnel. A radio power of 7 dBm is applied by the Tx device to a directional antenna with a gain of 8 dB (72°). The EIRP is 15 dBm. After a first hop in free space, the signal is boosted by a low-noise amplifier (LNA). The radio signal is multiplied with a local oscillator to transport the mm-wave over the fiber. To limit nonlinearities introduced by the laser, an automatic gain control (AGC), modeled by a variable attenuator follow up by a LNA, controls the input RF power. After the second hop in air, a radio Rx device with a built-in LNA receives the signal.

The optoelectronic components used are an Adopco VCSEL and a GaAs p-i-n photodiode at 850 nm, typical low-cost components used for 10 Gb/s digital communications.

We report our simulated results that show the feasibility of employing an optical multipoint-to-multipoint architecture. The used setup here is a point-to-point link with optical loss corresponding to a 4 × 4 splitter (6 plus 1 dB of various losses) to simulate a multipoint-to-multipoint architecture.

To characterize the RoF system, we study the maximum tolerated air distance in terms of SNR. In Figure 8, the *x*-axis represents the distance on the first hop in free space, and the *y*-axis represents the second hop. The different curve levels represent the SNR value at the reception. The results are computed using the analytical formulas reported earlier.

A SNR of 9.30 dB is required for correct reception of a 3,024–Mb/s IEEE 802.15.3c HSI-mode radio signal with an OFDM 16-QAM-1/2 MCS and with LOS Tx of 72°/Rx of 60°. Consequently, it is possible to achieve a 4-m first hop and a 4-m second hop (Figure 8).

RoF Issues

Multipath Issues

RoF systems make the achievable transmission distances between the wireless devices longer. Nonnegligible propagation delay through the optical fibers can create additional issues such as increased multipath interferences, especially for multipoint architectures. In general, only a rigorous engineering during the implementation of the RoF transducers in home can resolve this situation.

Echo Issues

The radio devices operate in half duplex. It can receive its own frames after a transmission when the echo delay becomes greater than the guard interval. The minimum interframe space (0.5 μs default) corresponds to 150 m of propagation on the air or 100 m over the fiber (IEEE802.15.3c HSI mode). The guard intervals are long enough to prevent any problem because the fiber length in the home does not exceed 100 m.

Coupling Issues

The RoF link is transparent, as it only transposes electrical signals in the optical domain and vice versa. This transparent nature can induce recoupling of the transmitted signal

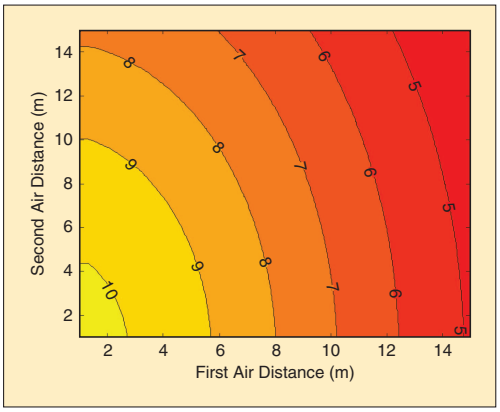

FIGURE 8 SNR at radio receiver versus distance on the two hops on the air (optical loss = 7dB – LOS – GR = 13dB / 60°).

THANKS TO THIS PASSIVE OPTICAL COMPONENT (N × N OPTICAL SPLITTER), ALL THE WIRELESS DEVICES ARE VISIBLE FROM ONE ANOTHER THROUGH THE OPTICAL FIBERS.

over the received signal. The radio wave power can become large and damage the electrooptic elements, as well as create a strong perturbation to the radio environment.

Optical Issues with Shared Architectures

The multipoint architectures use a shared optical media. Using multiple lasers simultaneously induces an excess of shot and RIN noise and potentially optical beating noise. To avoid this, the access to the media has to be controlled. A rule can ensure that only one laser is turned on at any time.

Solutions Using the Radio PHY Layer

One solution consists in running each RoF transducer in half duplex. Applying this rule and limiting the number of transducers in a room to one can solve RoF impairments.

To make each RoF transducer half duplex, the laser source is turned on only if it is driven by a useful signal. So, the transducer has to analyze the signal delivered by the receiving antenna. This analysis can be performed by a simple RF power detection placed after the AGC to be effective for any signal level. The direct detection of RF power seems an attractive solution for simplicity and cost reasons, but, in this case, the system becomes very sensitive to interference.

Solution Using the Radio MAC Layer

Principle

Another solution to improve the RoF system consists of using information from the radio MAC layer to manage the optical media (Figure 9). The optical network becomes a simple extension of the radio system, fully controlled by it, without proper intelligence. One of the devices (e.g., the home gateway) demodulates the radio signal, recovers useful data from the radio MAC layer, and sends instructions to the remote antennas, thanks to a simple monitoring signal. Thus, the radio system controls the optical functions of each RoF transducer.

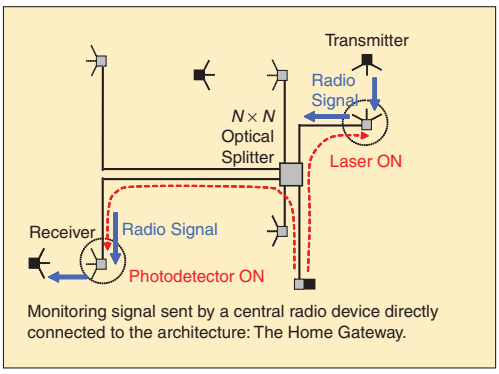

FIGURE 9 Solution using the radio MAC layer.

This option, requiring cooperation between the radio MAC layer and the monitoring signal, leads to a low-cost solution, a dedicated chip set is only necessary in the gateway [Piconet controller (PNC)], but the other transducers stay very simple without any intelligence.

Advantages

RoF with a monitoring signal based on the radio MAC layer optimizes the global spectral efficiency (b/s/Hz/m^2). Thanks to a full control of the optical components, power is radiated only in the spot where it is useful and when it is necessary. It is an advantage for health and hacking concerns. Radio waves well confined in a room minimize the electromagnetic fields exposure and keep data close to the user. Last, the management of the optical access improves the power consumption of the system by turning off some components when they are not used.

Study of the MAC Layer with IEEE 802.15.3c

First, to control the optical media, we must know the configuration of the network in real time, which means the knowledge of which radio device emits and which radio device receives. Second, we must know which remote antenna is paired to which wireless device.

The IEEE802.15.3c is an ad hoc architecture. One station assumes the role of the PNC to provide the basic timing for the network (Figure 10). Here, we propose to reuse the concept of the directional contention access period (CAP), considering that one direction corresponds to a RoF transducer (or a room). Originally, directional CAP enables the multisector transmission, thanks to devices with a large number of directional antennas.

The directional CAP divides the beacon period into different times associated with different remote antennas. In this period, only the PNC emits to transmit time references and information about the management of the Piconet. So, each photodiode is turned on one after the other.

Then, the directional CAP divides the CAP in different times, each of them corresponding to a different remote antenna. In this CSMA period, each laser is turned on one after the other, preventing any optical issues. The CAP is an association time. Because only one laser is turned on at a time, we can easily pair one radio device with one remote antenna.

The last period, the channel time access period, is a TDMA period. We know the wireless device that emits is because the reservation is based on source node. During a TDMA time slot, this information is contained inside the

frame sent by the source, so the PNC does not know, a priori, what radio device should receive data. Therefore, all the photodiodes must stay turned on. If we want to turn on only one photodiode at a time, the radio MAC layer has to undergo some changes. For example, the PNC can listen continuously to be aware of the destination of the packets and to turn on the laser of the right transducer for the acknowledgment by the receiver.

Final Architecture with a Monitoring Signal

The monitoring signal, emitted from the PNC, has to be present continuously to manage the RoF infrastructure. This signal cannot pass through a shared architecture because it must be intended to a specific transducer. So, we propose to distribute it through copper pairs that are included in the optical cables and that can be used to remote power supply the transducers. So, a simple electrical analog signal marked by the presence or absence of a low-RF carrier is sent to control the optical components. Finally, the PNC is located in the gateway near the optical splitter for a better implementation.

Conclusion

This article proposes a 60-GHz RoF infrastructure intended to expand the radio coverage of MGWS to multiroom transmissions. Radio coverage evaluation shows that 2 Gb/s on the air interface may be achieved with radio links ranging from 8 to 45 m depending on LOS/NLOS criterion and 4 Gb/s from 5 to 20 m coverage. Different RoF architectures can be chosen, but the multipoint-to-multipoint architecture based on totally transparent optical components seems to be a good compromise between cost-effectiveness and performance in a HAN. This architecture must be completed by a management of the optical access. In this aim, the future MGWS should take into account cooperation between the radio MAC layer and the optical layer, allowing an optimization of RoF architecture.

THE MULTIPOINT-TO-MULTIPOINT ARCHITECTURE BASED ON TOTALLY TRANSPARENT OPTICAL COMPONENTS SEEMS TO BE A GOOD COMPROMISE BETWEEN COST-EFFECTIVENESS AND PERFORMANCE IN A HAN.

Acknowledgments

This work was supported by the French government in the framework of the project Optical Radio Infrastructure for Gigabit Indoor Networks (ORIGIN).

Author Information

Joffray Guillory received his engineering degree in optical science with parallel expertise in electronics and computer science from École Nationale Supérieure des Sciences Appliquées et de Technologie (ENSSAT), France, in 2009. He joined Orange Labs, Lannion, France, where he has been engaged as Ph.D. student in the development of RoF communication systems.

Sylvain Meyer received his engineering degree from École Nationale Supérieure des Télécommunications (ENST), Paris, in 1977. His previous research activities have been in the field of subscriber systems using short-range radio in France and Japan. He is presently research engineer

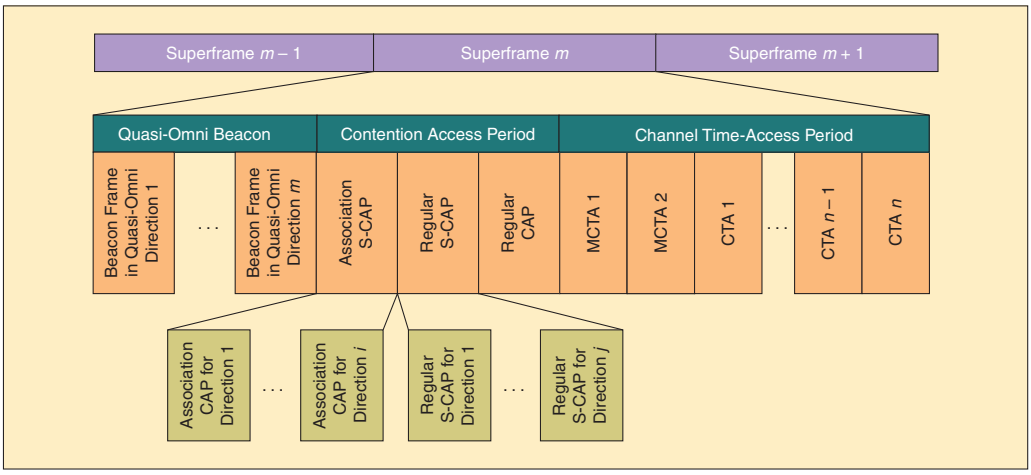

FIGURE 10 Piconet superframe structure.

ANOTHER SOLUTION TO IMPROVE THE RoF SYSTEM CONSISTS OF USING INFORMATION FROM THE RADIO MAC LAYER TO MANAGE THE OPTICAL MEDIA.

with France Télécom R&D (Orange Labs), Lannion, France. His research activities are to define a new architecture for high data-rate home networks hybridizing multiple connectivity technologies. He is a member of IEICE.

Isabelle Siaud received the master's degree in electronic from the Paris VI University in 1992. In 1993, she joined the France Telecom R&D to work on propagation modeling for mobile and short-range radio communications. In 1999, she joined the Broadband Wireless Access team of Rennes to contribute to innovative PHY layer system design. She investigates UWB and multicarrier techniques for MGWS promoted through European projects. She is cochair of the Wireless World Research Forum WG5 dealing with short-range radio communications.

Anne Marie Ulmer-Moll received the master's degree in telecommunication from St Jerome University Marseille, in 1978. She joined the Centre National d'Etudes des Télécommunications (CNET) of France Telecom (FT) to manage a team validating telecommunication exchanges. In 1985, she joined the French Guyana FT company to supervise a team in charge of QoS reliability for networks. Back CNET in 1990, she turned her activities on propagation modeling for satellite communications in the OLYMPUS project. In 1998, she integrated the Broadband Wireless Access team of Rennes to participate to the WLL field trials and contribute to PHY system design in European projects.

Benoît Charbonnier received his engineering and Ph.D. degrees in 40-Gb/s soliton transmission from Ecole Nationale Supérieure des Télécommunications de Paris, Paris, France, in 1994 and 1997, respectively. In 1997, he joined the Advanced Communications Group, Nortel Network, Harlow, United Kingdom, where he was engaged in 80-Gb/s long-haul transmission. In 2001, he joined Marconi Communications to develop an ultralong-haul 10-Gb/s-based transmission product. Since 2004, he has been a research engineer at France Télécom Research and Development, Lannion, France, where he is engaged in the study of the next-generation optical access and in-building networks.

Anna Pizzinat graduated with honors in electronic engineering in 1999 and obtained the Ph.D. degree from the University of Padova, Italy, in 2003. From 2003 to 2005, she was responsible for the Photonics Laboratory at University of Padova, working on polarization mode dispersion and high bit-rate systems. In 2006, she joined France Télécom—Orange Labs where she is engaged in research on the next-generation optical home and access networks with a focus on RoF systems. She is author of more than 60 papers on international journals and conferences.

Catherine Algani received her DEA degree in electronics and Ph.D. degree from the University of Paris 6, France, in 1987 and 1990, respectively. In 1991, she was a lecturer in the Electronics Engineering Department and the LISIF Laboratory at University of Paris 6. From 1991 to 2005, she worked on the design of microwave and millimeter-wave integrated circuits on different GaAs technologies. In 1997, she began to work in the area of microwave photonics (optically controlled microwave switches on GaAs and electrooptic organic modulator). In 2005, she joined ESYCOM at CNAM-Paris, where she is currently a full professor. Her research interests include the development of devices, circuits, and subsystems for ultrahigh-speed digital and analog communications for ROF and wireless applications. These researches include the modeling, design, and characterization of such structures.

References

[1] *High Rate 60 GHz PHY, MAC and HDMI PAL*, Standard ECMA-387, Dec. 2008.

[2] *Part 15.3: Wireless MAC and PHY Layer Specifications for High Rate Wireless Personal Area Networks (WPANs): Amendment 2: Millimeter-wave based Alternative Physical Layer Extension*, IEEE P802.15.3c/D13 July 2009.

[3] Available: http://wirelessgigabitalliance.org/

[4] L. Rakotondrainibe, I. Siaud, and Y. Kokar, "A low complexity wireless gigabit Ethernet IFoF 60 GHz H/W platform and issues," in *Proc. Wireless World Research Forum (WWRF#22)*, Paris, May 5–7, 2009.

[5] B. Charbonnier, H. Wessing, and M. Popov, "Home networking requirements," (invited paper), in *Proc. IPHOBAC Workshop*, Duisburg, May 18–20, 2009.

[6] A. Pizzinat, "Low cost transparent radio-over-fibre system for UWB based home network," in *Proc. European Conf. Optical Communication 2008*, Bruxelles, Sept. 21–25, 2008.

[7] I. Siaud and A. M. Ulmer-Moll, "Modified IEEE 802.15.3c H.S.I OFDM modes based on Turbo BIC system design," in *Proc. Wireless World Research Forum (WWRF#24)*, Penang, Apr. 12–14, 2010.

[8] C. Douillard and C. Berrou, "Turbo codes with rate m/m+1 constituent convolutional codes," *IEEE Trans. Commun.*, vol. 53, no. 10, Oct. 2005.

[9] I. Siaud and A. M. Ulmer-Moll, "Turbo-like processing for scalable interleaving pattern generation: Application to 60 GHz UWB OFDM systems," in *Proc. IEEE Int. Conf. UWB*, Singapore, Sept. 2007.

[10] I. Siaud, A. M. Ulmer-Moll, N. Malhouroux-Gaffet, and V. Guillet, "An introduction to 60 GHz communication systems: Regulation and services, channel propagation and advanced baseband algorithms," in *Short-Range Wireless Communications*. Hoboken, NJ: Wiley, Feb. 2009, ch. 18.

[11] I. Siaud, "Combined channel coding and receiver antenna pattern influence on radio COFDM performance: evaluation in a residential indoor multipath environment at 60 GHz," in *Proc. Int. OFDM Workshop*, Hamburg, Sept. 10–11, 2002.

[12] J. Guillory, S. Meyer, B. Charbonnier, T. Derham, and S. Roblot, "Radio over fiber for an optimal 60 GHz home area network," IEEE 11-10-0011-01-00ad Conf. Call. Jan. 7, 2010.

[13] J. Guillory, et al., "RoF architectures for multi-gigabit wireless systems in the home area network," in *Proc. Wireless World Research Forum (WWRF#24)*, Apr. 2010. VT

2482 JOURNAL OF LIGHTWAVE TECHNOLOGY, VOL. 29, NO. 16, AUGUST 15, 2011

A 60 GHz Wireless Home Area Network With Radio Over Fiber Repeaters

Joffray Guillory, Eric Tanguy, Anna Pizzinat, *Member, IEEE*, Benoît Charbonnier, Sylvain Meyer, Catherine Algani, and Hongwu Li

***Abstract*—Home area networks will have to deal with the future multigigabit wireless systems that are emerging or are under development. These millimeter-wave radio systems achieve data rates up to several Gb/s per channel, but over short distance. So, to expand the radio coverage, we propose to introduce a radio-over-fiber (RoF) infrastructure at home. This paper presents a complete study of a RoF system: the 60 GHz radio coverage is extended using a RoF link working at intermediate frequency with two hops in the air. An experimental setup of such an infrastructure has been realized and characterized. A low-cost solution, working at 850 nm, was chosen using multimode fiber and off-the-shelf millimeter-wave and photonic components. Finally, a real-time transmission between two commercial WirelessHD devices working at 3 Gb/s has been carried out.**

***Index Terms*—Home area network (HAN), IEEE 802.15.3c, IEEE 802.11ad, optical architecture, optical transducers, radio over fiber (RoF), WirelessHD.**

I. Introduction

THE EVOLUTION of the home area network (HAN) is determined by several trends [1]. A major one is the proliferation of connected devices in the home, used increasingly and simultaneously via wireless ultrahigh data rate connection. The current generation of WiFi systems (IEEE 802.11n) can achieve theoretically 600 Mb/s [2], but new radio standards allowing higher data rates have emerged or are under development. All these new standards address the unlicensed millimeter-wave band from 57 to 66 GHz as shown in Fig. 1. In this band, divided into four 2.16 GHz-bandwidth channels, it is possible to achieve bit rates up to 7 Gb/s per channel (see Table I). IEEE 802.15.3c [3] and WirelessHD [4] standards were finalized in 2009 and are devoted to wireless personal area network communication. More recently, the IEEE 802.11ad [5] group has been created by WiGig consortium [6]: it addresses networking with wireless local area network systems and targets WiFi Alliance certification. As a consequence, IEEE 802.11ad should lead the multigigabit wireless systems race. 60 GHz technologies are now mature: WirelessHD devices are already available in the market for wireless high-definition multimedia interface (HDMI) applications and IEEE 802.11ad products could be available by the end of 2011.

Channel Number	Low Freq. (GHz)	Center Freq. (GHz)	High Freq. (GHz)
A1	57.240	58.320	59.400
A2	59.400	60.480	61.560
A3	61.560	62.640	63.720
A4	63.720	64.800	65.880

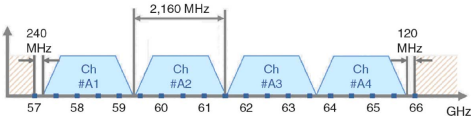

Fig. 1. Channelization of the 60 GHz band in Europe [7], [8].

However, the limitation of these systems is their short range due to the high-propagation attenuation and to the fact that signals in the 60 GHz band cannot cross the walls. Consequently, their coverage is limited to a single room and to a small indoor open area. The main challenge is to find solutions to ensure the coverage of the entire HAN, and to interconnect all the devices located in different rooms. In this paper, we propose to solve this problem by means of the radio-over-fiber (RoF) technology distributing 60 GHz radio signal to several access points spread around the home. Compared to other techniques, RoF is advantageous because of its capability of supporting multistandard systems due to its transparency to the radio protocol and to the modulation format. Moreover, an HAN based on an optical fiber infrastructure is future proof for the following aspects: higher data rate, delivery of a multiplicity of high-performance parallel services [9], high quality of service and minimization of the exposure to the electromagnetic field. Several studies have already been carried out on RoF for 60 GHz applications, principally on long-term-related topics [10], [11], such as optical frequency upconversion for millimeter-wave signals generation [12] and high-speed Mach–Zehnder Modulators [13], [14]. From the viewpoint of the HAN market, a RoF system can represent a competitive solution only if it is easy to deploy and the necessary transceivers are low cost and compact. In this paper, we address these issues on the basis of a system in which the 60 GHz radio signals are distributed over fiber at intermediate frequency (IFoF). In a previous paper [15], we

Manuscript received January 24, 2011; revised May 10, 2011; accepted June 09, 2011. Date of publication June 16, 2011; date of current version July 29, 2011. This work was supported by the French FUI8 ORIGIN (Optical-Radio Infrastructure for Gigabit/s Indoor Network) Project.

J. Guillory, A. Pizzinat, B. Charbonnier, and S. Meyer are with France Télécom R&D—Orange Labs, 22300 Lannion, France (e-mail: joffray.guillory@orangelabs-ftgroup.com; anna.pizzinat@orange-ftgroup.com; benoit.charbonnier@orange-ftgroup.com; sylvain.meyer@orange-ftgroup.com).

E. Tanguy and H. W. Li are with the Institut de Recherche en Electrotechnique et Electronique de Nantes Atlantique, University of Nantes, 44300 Nantes, France (e-mail: Eric.Tanguy@univ-nantes.fr; Hongwu.Li@univ-nantes.fr).

C. Algani is with ESYCOM laboratory, Conservatoire National des Arts et Métiers, 75003 Paris, France (e-mail: catherine.algani@cnam.fr).

Color versions of one or more of the figures in this paper are available online at http://ieeexplore.ieee.org.

Digital Object Identifier 10.1109/JLT.2011.2159776

TABLE I
RADIO STANDARD PROPERTIES WITH YEAR OF REALIZATION, DATA RATES, AND INDUSTRIAL PRODUCTS OUTLOOK

IEEE 802.15.3c	WirelessHD	IEEE 802.11ad
2009	2009	2012
20 to 5,670 Mbit/s	952 to 7,138 Mbit/s	385 to 6,757 Mbit/s
Future likely to be compromised	Based on IEEE 802.15.3c A/V mode	Should lead the market with Wi-Fi certification

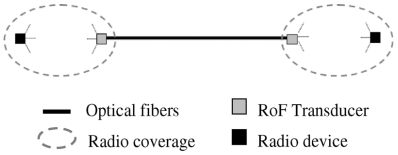

Fig. 2. Point-to-point RoF link: the optical tunnel.

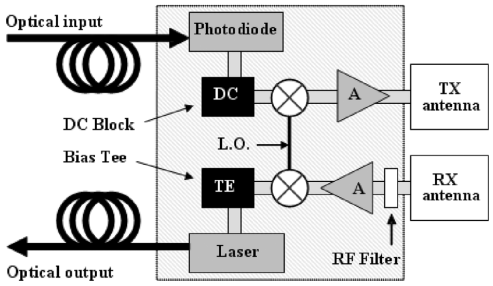

Fig. 3. RoF transducer in intermediate frequency configuration.

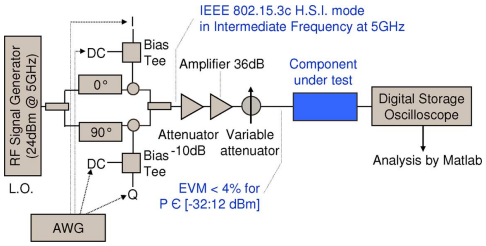

Fig. 4. Experimental test bench of radio OFDM signal generation at IF = 5 GHz.

have demonstrated that the direct optical distribution of millimeter-wave radio signals and IFoF distribution lead to comparable performances, but the cost of the system is drastically reduced in the second case. In this paper, we go further by presenting, for the first time to our knowledge, experimental results on the transmission of multigigabit orthogonal frequency division multiplexing (OFDM) signals at 60 GHz, by using a RoF tunnel. In other terms, after propagation over a first wireless link, the 60 GHz signal is downconverted at IF and used to modulate a laser diode for transmission over multimode fiber (MMF); after photodetection, the signal is upconverted to 60 GHz and retransmitted over a second wireless link.

This paper is organized as follows: after a short presentation of the optical tunnel (or repeater) and the IFoF transducers in Section II, we determine, in Section III, the best electrical and optical parameters in order to optimize the RoF link. Afterward, we characterize the proposed RoF infrastructure, building the architecture step by step: to the direct millimeter-wave radio link characterized first as the baseline, we add an electrical repeater, and finally we introduce the RoF repeater. As a final point, we show a real-time transmission between two commercial WirelessHD devices using a wireless link including a RoF tunnel.

II. RoF for the HAN

In previous papers, we have proposed and studied several RoF architectures [16], [17]. A very simple case is the optical tunnel shown in Fig. 2.

This optical link acts as a transparent radio repeater; indeed, the radio signal captured at the input is transmitted to the output of the tunnel. This scheme is advantageous because two wireless devices in two rooms separated by wall(s) can communicate as if they were visible to one another. At the same time, it is quite challenging for the RoF system due to the high and strongly variable losses and the distortions introduced by the two air links. Moreover, the demonstration of the feasibility of the optical tunnel is also the first step toward the implementation of multipoint-to-multipoint networks [17]. As a consequence, in the following, we focus on the optical tunnel architecture.

As anticipated in the previous section, to remain low cost, a RoF system for HAN applications has to be built with very simple and cheap bricks. The RoF transducers, key elements realizing electro-optic (E/O) and opto-electronic (O/E) conversions, are composed of two antennas, a laser diode, a photodiode, and RF amplifiers (see Fig. 3). Low cost vertical-cavity surface-emitting lasers (VCSELs) emitting at 850 nm and GaAs PIN photodiodes with built-in transimpedance amplifier (TIA), developed for 10 Gb/s digital communications over 50 μm MMF by Finisar, are chosen. Because of their bandwidth limited below 10 GHz, RoF transducers also need a local oscillator (LO) and associated mixers to transpose the millimeter-wave signal at IF before the laser direct modulation and to bring back the signal at 60 GHz after the photodetection for radio reemission. Finally, the antennas incorporated in the RoF transducers are horn antennas. Smart antennas performing beamforming within a room should improve the system; further investigations will be carried out on this topic.

III. Characterization of the Link With an IFoF

The experimental setup has been built step by step in order to determine the impact of each element in the link. First, we have characterized the propagation of a radio signal over fiber by means of the experimental setup shown in Fig. 4.

A 3.08 Gb/s pseudorandom OFDM baseband signal modulated with a quadrature phase-shift keying (QPSK) scheme is generated under MATLAB according to the high-speed interfaces (HSI) mode of the IEEE 802.15.3c standard. This baseband signal is fed into a 10 GSa/s arbitrary waveform generator

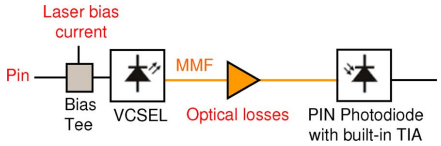

Fig. 5. RoF link to be placed as the "component under test" in Fig. 4.

(AWG). The generated in-phase (I) and quadrature (Q) components are transposed to IF by mixing with an RF oscillator split in two paths with a 90° phase shift. Finally, the two components are combined by an RF coupler to create the IF-OFDM input signal. A real-time digital storage oscilloscope, with 13 GHz bandwidth and 40 GSa/s speed, receives the transmitted signal through the system for analysis under MATLAB and calculation of the link error vector magnitude (EVM).

The direct link or back-to-back connection, i.e., the oscilloscope simply connected to the IF-OFDM signal generator, presents an EVM lower than 4% for an input power range of 44 dB, varying from -32 to $+12$ dBm, thanks to cascaded amplifiers and attenuators that control precisely the RF input power of the system. Note that the oscilloscope accepts a wide range of input power and automatically adjusts the signal level. This configuration and the corresponding EVM value are considered as a reference in order to make proper comparisons with the different tested configurations.

Before going to the complete optical tunnel setup, we characterize separately the RoF and wireless links in order to analyze the influence of each part of the complete architecture. The RoF link shown in Fig. 5 is composed of the optoelectronic components described in Section II and of a 1 m length MMF. A variable optical attenuator is introduced in the RoF link to analyze the effect of additional optical losses due to fiber attenuation, fiber bends, and optical splitters [17].

A. Analog Characterization of the RoF Link

The link has been characterized in terms of relative intensity noise (RIN) and nonlinearity. For RF up to 10 GHz and in the linear part of the VCSEL static characteristic (i.e., 6.5 mA bias current), the measured RIN is lower than -130 dBc/Hz, even at the frequency relaxation oscillation (4.5 GHz). At 3 GHz, with no optical loss and for the same laser bias current, an input 1 dB compression point (IP1 dB) of -15 dBm and an input third-order intercept point (IIP3) of -1.62 dBm were measured (this latter value is stable between 2 and 6 GHz). The IIP3 value increases linearly with the optical losses up to 10 dB, with a slope equal to 2 showing the limitation of the O/E receiver; beyond 10 dB, the IIP3 remains stable and close to 20 dBm.

B. Digital Characterization of the RoF Link

In order to identify the best parameters of the RoF link, we study its performance in terms of EVM by varying the RF input power, the laser bias current, and the optical losses. The experimental results are reported in Figs. 6 and 7.

Without optical loss, the minimum EVM equals 13.4%. This value is observed for a 4 mA laser bias current and a -17.1 dBm

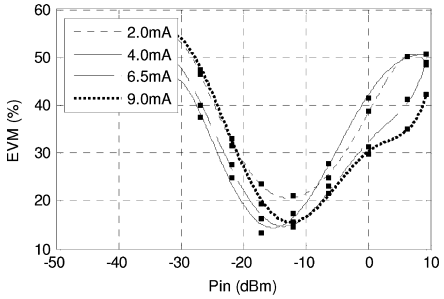

Fig. 6. Measured EVM versus RF input power for different laser bias currents. The optical loss is fixed to 0 dB.

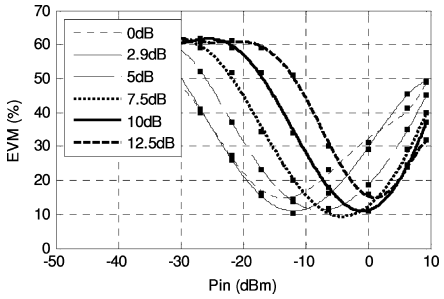

Fig. 7. Measured EVM versus RF input power for different optical losses. The laser bias current is fixed to 6.5 mA.

RF input power. This RF power corresponds to the IP1 dB parameter of the RoF link. For an RF power of -15 dBm, the results for the different laser bias currents are similar, except for 2 mA due to its closeness to the threshold current of the laser (1 mA), resulting in higher RIN, up to -120 dBc/Hz. Compared to the reference link, the minimum EVM has increased by 9.4%.

According to Fig. 7, the larger the optical losses, the higher the RF laser input power must be to attain the minimum EVM. For high RF input power, we observe the effects of the nonlinearity on the O/E receiving part; conversely, the nonlinearity of E/O emitting part does not affect the system because for all the optical losses the shape of the curves remains identical. These results are in agreement with the evolution of the IIP3 versus the RF input power. For lower RF power, the EVM rise is due to reduced SNRs, because the RIN and the reception noises are dominant. Finally, for a given value of optical losses, the EVM remains stable at its minimum over a range of 6 dB RF input power.

The curve in Fig. 8 shows the RF input power leading to the minimum EVM as a function of the optical losses. The measured results can be well fitted by a straight line of slope of 1.3 (dashed line), while a line of slope of 2 is expected as the electrical losses correspond to the double of the optical losses when they are expressed in logarithmic scale. The straight line fits quite well the central part of the experimental curve. However, at the beginning of the curve, the slope is lower because of

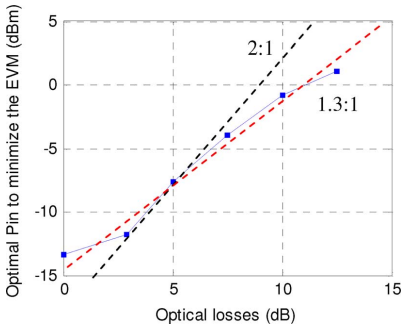

Fig. 8. Optimal RF input power leading to a minimal EVM value versus optical losses for a 6.5 mA laser bias current; continuous line corresponds to measurements and dashed lines to linear approximation and linear fitting of the measurements.

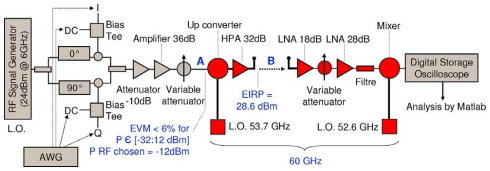

Fig. 9. 60 GHz radio-wireless link according to the IEEE 802.15.3c standard with free-space propagation.

predominant noises at low RF input level on one hand and the saturation of the TIA of the PIN photodiode at high RF input level on the other hand. In the final part of the curve, the laser nonlinearity impacts the slope.

IV. Characterization of Signal Transmission at an IFoF Tunnel

A. Implementation of a Single Millimeter-Wave Radio Link

The setup depicted in Fig. 9, used as the baseline, transmits IEEE 802.15.3c standard millimeter-waves in free space. The radio IF-OFDM signal is unchanged from Fig. 4; except that the center frequency is shifted from 5 to 6 GHz. The power of the IF-OFDM signal delivered is fixed at -12 dBm, the best experimental value achieved at the input of the first mixer (point A). This signal is up-converted to 59.7 GHz, in the frequency range corresponding to the second channel of the unlicensed millimeter-wave band (see Fig. 1).

At the radio emitter, an 8.6 dBm power is applied to a *V*-band horn antenna with 20 dB gain. The equivalent isotropically radiated power (EIRP) is 28.6 dBm, very close to the typical EIRP of commercial devices, i.e., 27 dBm (see Section V), and in agreement with the maximum EIRP allowed in Europe, i.e., 40 dBm mean [7], [8]. After a first hop in free space (point B), the signal is received by a second antenna and boosted by two low noise amplifiers (LNAs). The radio signal is then downconverted in order to be captured by the digital storage oscilloscope.

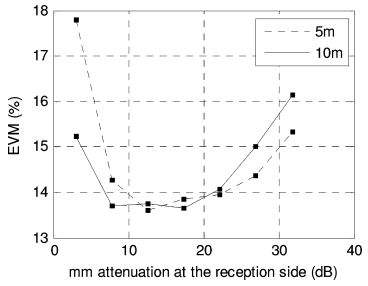

Fig. 10. EVM versus millimeter-wave attenuation at the receiver.

Fig. 10 represents the EVM at the radio receiver as a function of the millimeter-wave attenuation, introduced by a variable attenuator placed before the downconverted mixer, and for two fixed free-space distances, 5 and 10 m.

No significant variation can be observed between the two tested distances, just a reception attenuation shift equivalent to the loss difference between the two propagation distances. Indeed, the two considered distances correspond to free-space losses equal to 82 and 88 dB for 5 and 10 m, respectively (neglecting additional losses due to oxygen absorption). The EVM remains close to 14% over a 10 dB attenuation range. For shorter free-space distances, 1 m, for example, we have checked that the first LNA at the reception side does not saturate and that the millimeter-wave attenuator can adjust sufficiently the RF power.

Between 5 and 10 m free-space propagation distances, the optimal total millimeter-wave gain at the reception is 30 dB, plus 20 dB antenna gain, i.e., a total gain of 50 dB that does not compensate entirely the free-space propagation losses.

B. Implementation of an Electrical Repeater at 60 GHz.

The setup considered in Fig. 11 represents a repeater without RoF link. This setup allows us to check if the system tolerates the losses and distortions corresponding to two air links. The upper part in Fig. 11 is identical to the setup in Fig. 9.

After a first hop in free space, the signal is picked up by a horn antenna with 20 dB gain. A 28 dB LNA and a 32 dB high-power amplifier (HPA) boost the received signal. This radio signal is then downconverted to IF at 4.5 GHz and attenuated by 15 dB in order to simulate the RoF link behavior. Finally, the IF signal is upconverted to realize the second hop at 60 GHz. Finally, the received signal is analyzed on the oscilloscope.

The S21 parameter of the RoF link has been evaluated experimentally for a laser bias current of 6.5 mA. This latter is stable up to 6 GHz:

$$\mathrm{S21\,(dB)} = 2 \times \text{ optical losses} - 3\,\mathrm{dB}. \qquad (1)$$

To optimize the IF power applied to the upconverter, an attenuation of 15 dB is necessary for P3 corresponding approximately to a zero-optical loss RoF link. Indeed, as we have 0 dBm before P3 (see Fig. 11), an attenuation of 14 dB is needed to obtain the optimum IF power at the laser input (see Fig. 8). Moreover, 3 dB RF losses are added for the S21

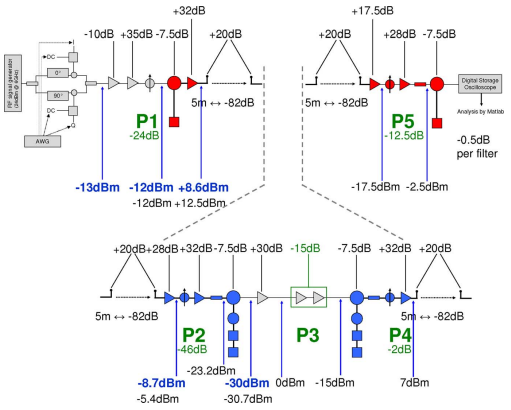

Fig. 11. Link budget for the radio tunnel at 60 GHz. P1 to P5, the different variable parameters, above the figure the RF gain, below in bold the measured power values, and below in regular the theoretical power values.

parameter (Formula 2). Finally, to simulate a RoF link without optical loss, 17 dB RF attenuation is required $(14\text{ dB} + 3\text{ dB})$.

Cascaded amplifiers and variable attenuators allow the optimization of the power applied not only to the input of each mixer (parameters P1, P2, P3, and P5), but also to the second 60 GHz air hop (parameter P4). The free-space distance, parameter P6, is fixed at 5 m for the two hops.

The EIRPs for these two air hops are, respectively, 28.6 and 27 dBm. For the configuration in Fig. 11, the measured EVM is 18.5%. The introduction of the electric repeater has increased the EVM by only 4.5%, thanks to the parameters optimization along the link.

C. Implementation of a RoF Tunnel at 60 GHz

The RF attenuator of the last configuration in Fig. 11 is replaced by the RoF link in Fig. 5 in this final step. A 300 m OM3 MMF and an optical attenuator are inserted; together they present 2.2 dB of intrinsic optical losses.

We fix the laser IF input power at -10 dBm, i.e., the optimal value to minimize the EVM for 4 dB optical losses according to Fig. 8. EVM are measured by varying the optical losses between 2 and 6 dB. This last value corresponds to the worst case for a point-to-point RoF link in an HAN. In this worst case, as the photodiode delivers an IF power of -22.7 dBm at the upconverter, the EIRP is then 19.3 dBm for the second hop and the received power is -62.7 dBm respecting the sensitivity of -65 dBm of the commercial HDMI transmitters from Gefen (cf., Section V).

Finally, we obtain the results of Table II. The measured EVM remains always below 25%. It corresponds to a theoretical bit error rate (BER) better than 10^{-5} [18], i.e., error-free transmission after coding implementation.

Fig. 13 represents the measured IF power spectrum at the receiver, for 3.2 dB total optical losses and 23.94% average EVM.

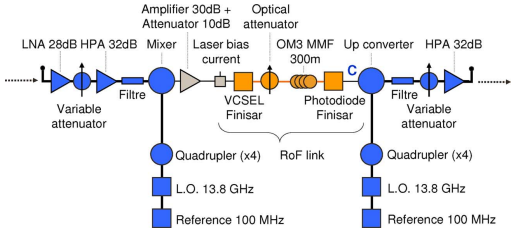

Fig. 12. RoF tunnel placed between the two hops in the air.

TABLE II
EVM (%) AS A FUNCTION OF THE TOTAL OPTICAL LOSSES FOR 300 mLENGTH OM3 MMF AND FOR $(5\text{ m} + 5\text{ m})$ AIR HOPS

Optical losses (dB)	EVM (%)
2.2	24.32
3.2	23.94
4.2	24.15
5.2	25.05

TABLE III
EVM AS A FUNCTION OF THE FREE-SPACE LENGTH

Distance (P6)	EVM (%)
5m + 5m	25.47
5m + 2m	22.52
2m + 5m	22.47

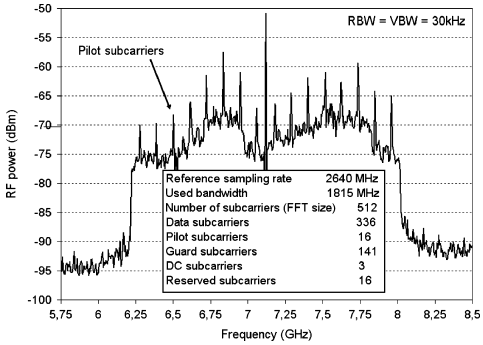

Fig. 13. Measured OFDM signal spectrum of IEEE 802.15.3c HSI mode at the receiver.

The two LOs of the optical tunnel working at the same frequency, 55.2 GHz; the center-received frequency is

$$6\text{ GHz} + 53.7\text{ GHz (1st LO)} - 52.6\text{ GHz (4th LO)} = 7.1\text{ GHz}. \quad (2)$$

Because of the large bandwidth of the standard channel, the received spectrum is slightly bumpy. A ripple of about 7 dB is introduced by the cumulated frequency responses of the RF circuits along the system. Nevertheless, the 16 pilot subcarriers

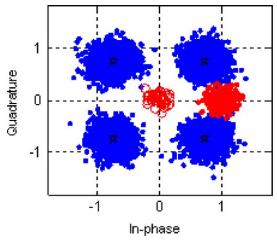

Fig. 14. QPSK constellation diagram in $(1,1)$, $(1,-1)$, $(-1,-1)$, and $(-1,1)$ with null subcarriers in $(0,0)$ and pilot subcarriers in $(1,0)$.

are clearly visible. The corresponding instantaneous EVM is 22.37% (see Fig. 14).

The signal has a bandwidth of 1.815 GHz with an average level of -72 dBm. As the bandwidth used on the spectrum analyzer is 30 kHz, the signal power is

$$\mathrm{P} = -72\,\mathrm{dBm} + 10\,\log_{10}(1.815\times 10^9/30\times 10^3) \sim -24\,\mathrm{dBm}. \quad (3)$$

This spectrum measurement was performed after the other measures, when the second amplifier and the variable attenuator of the reception stage have been removed. So, this value of -24 dBm is consistent with Fig. 11. The average noise level of the spectrum analyzer is -96 dBm, and the minimal carrier-to-noise ratio (CNR) is:

$$\mathrm{CNR\,min} = -75\,\mathrm{dBm} - (-90\,\mathrm{dBm}) = 15\,\mathrm{dB}. \quad (4)$$

A single RoF link with two different hop lengths has been also investigated. The configuration is the same as above, except that P parameters of Fig. 11 are optimized to simulate an amplifier with an automatic gain control after the first and the second hops in the air.

Measurements show identical results for 5 m+2 m and 2 m+5 m configurations. No free-space link configuration leads to larger damages on the system. In the worst wireless link case, the EVM is near the authorized BER limit.

V. IFoF Link Between Two Commercial WirelessHD Devices

Finally, a real-time transmission between two commercial Wireless-HD devices working at 3 Gb/s has been carried out. The main properties of these devices from Gefen are a transmitted power of 27 dBm and a receiver sensitivity of -65 dBm. An uncompressed 1080i video from Blu-ray player is displayed on an HD screen (cf., Fig. 15). The optical tunnel allows two wireless devices located in two rooms far away from each other to communicate as if they were in line of sight. The setup shown in Fig. 16 is similar to that in Fig. 12, except that two paths work in parallel: one for the downlink and other for the uplink.

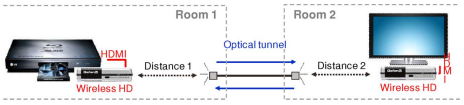

Fig. 15. Real-time bidirectional WirelessHD transmission through the RoF tunnel.

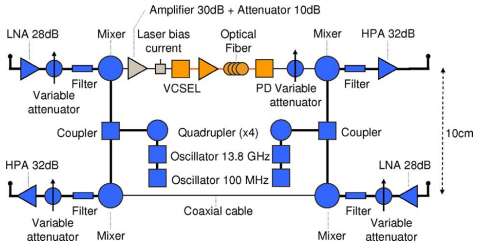

Fig. 16. Implemented bidirectional radio tunnel. Only the HRP WirelessHD signal (downlink) uses optical propagation.

TABLE IV
General Parameters of the HRP

Parameter	Value
Reference sampling rate	2.538 GSa/s
Used bandwidth	1.76GHz
Number of subcarriers (FFT size)	512
Data subcarriers	336
Pilots subcarriers	16
DC subcarriers	3
Null subcarriers	157

The downlink channel is a high data rate transmission called high-rate physical layer (HRP), whereas the uplink channel is at a low data rate for monitoring and it is called low-rate physical layer (LRP) [4]. LRP signal is also present over the downlink, but only temporarily. Both are OFDM signals, but with different physical characteristics. The HRP signal, based on the IEEE 802.15.3c A/V mode is also very close to the IEEE 802.15.3c HSI mode as it can be observed by comparing the general parameters of Table IV and Fig. 13. The HRP signal uses OFDM modulation with QPSK at 2.856 Gb/s PHY rate (1.904 Gb/s data rate) and uses the second channel of the millimeter-wave band as the radio signals of the previous parts. RoF is implemented only for the downlink, whereas the low data rate uplink uses a coaxial cable.

Even if radio systems operate in half-duplex, a RoF transparent tunnel transmits and receives simultaneously. A 10 cm distance between the adjacent Tx and Rx directional antennas is sufficient to avoid coupling issues. Otherwise, strong perturbations to the radio environment can happen.

The free-space lengths are fixed to 5 m plus 5 m. The bidirectional transmission was successful over both a 50 m length OM2 MMF and a 100 m length OM2 MMF, but the system has failed to operate with a 300 m length OM3 fiber probably due to restriction inside the radio medium access control layer [19].

Indeed, experimentally, we found a limit of 107 m length fiber. So, the propagation time cannot exceed $\sim$0.5 μs. Deeper investigations have shown that this delay corresponds to the total propagation time over the downlink and the uplink. Therefore, the system can operate with 50 m length fibers for both the downlink and the uplink.

The OM2 fiber length is fixed to 100 m. To verify the robustness of the link, an RF attenuator is added to the output of the photodiode. The RF attenuation can vary from 0 to 27 dB, beyond the connection stops.

A critical point for the WirelessHD transmission based on the IEEE 802.15.3c specification is the accuracy of LOs. According to the IEEE 802.15.3c standard, the transmitted center frequency tolerance shall be ± 25 μHz/Hz maximum, corresponding to ± 90.72 kHz at 60.48 GHz. We have measured the transmitted center frequency tolerance of the used commercial WirelessHD devices by changing the frequency of one LO of the optical tunnel, simulated by an RF signal generator. The transmission is interrupted when the 13.8 GHz oscillator is outside the window [13.8 GHz–38 kHz; 13.8 GHz+42 kHz]. This corresponds to an accuracy of ± 160 kHz with an LO at 55.2 GHz.

VI. Conclusion

The rise of the data rates in the HAN and the users demand for wireless solutions naturally lead to RoF technology. This paper has demonstrated that RoF systems can meet these needs. Indeed, real-time transmission between two commercial WirelessHD devices at 3 Gb/s has been achieved over 50 m, typical HAN size, and 100 m OM2 fiber lengths. To cover the whole house, more advanced RoF network architectures are under study, as the multipoint-to-multipoint infrastructure based on a passive optical splitter [20], [21]. For a massive adoption of the RoF technology, an advanced integration of the RoF transducers is also under consideration.

References

[1] B. Charbonnier, H. Wessing, and M. Popov, "Home networking requirements," presented at the presented at the IPHOBAC Workshop, Duisburg, Germany, May 2009, (invited paper).

[2] *Part 11: Wireless LAN Medium Access Control (MAC) and Physical Layer (PHY) Specifications. Amendment 5: Enhancements for Higher Throughput*, IEEE 802.11n, Oct. 2009.

[3] *Wireless Medium Access Control (MAC) and Physical Layer (PHY), Specifications for High Rate Wireless Personal Area Netwoks (WPANs)*, IEEE 802.15.3c, Oct. 2009, Version 1.0a.

[4] WirelessHD Specification Version 1.1 Overview May 2010 [Online]. Available: www.wirelesshd.org, WirelessHD

[5] IEEE 802.11ad, May 2010 [Online]. Available: www.ieee802.org/11

[6] WiGig [Online]. Available: http://wirelessgigabitalliance.org

[7] *Use of the 57–64 GHz Frequency Band for Point-to-Point Fixed Wireless Systems*, ECC Recommendation (09)01, 2009.

[8] *Use of the 64–66 GHz Frequency Band for Fixed Service*, ECC Revised Recommendation (05)02, 2009.

[9] J. Guillory, P. Guignard, F. Richard, L. Guillo, and A. Pizzinat, "Multiservice home network based on hybrid electrical & optical multiplexing on a low cost infrastructure," presented at the presented at the OSA OPC Access Netw. In-House Commun. Conf., Karlsruhe, Germany, Jun. 2010.

[10] A. Chowdury, H. C. Chien, Y. T. Hsueh, and G. K. Chang, "Advanced system technologies and field demonstration for in-building optical-wireless network with integrated broadband services," *J. Lightw. Technol.*, vol. 27, no. 12, pp. 1920–1927, Jun. 2009.

[11] A. Ng'oma, D. Fortusini, D. Parekh, W. Yang, M. Sauer, S. Benjamin, W. Hofman, M. C. Amann, and C. Chang-Hasnain, "Performance of a multi-Gb/s 60 GHz radio over fiber system empoying a directly modulated optically injection-locked VCSEL," *J. Lightw. Technol.*, vol. 28, no. 6, pp. 2436–2444, Aug. 2010.

[12] C. T. Lin, E. Z. Wong, W. J. Jiang, P. T. Shih, J. Chen, and S. Chi, "28 Gb/s 16-QAM OFDM radio-over-fiber system within 7 GHz license-free band at 60 GHz using all-optical up-conversion," presented at the presented at the Conf. Lasers and Electro-Opt., Baltimore, MD, May 2009, Paper CPDA8.

[13] A. Ng'oma, P. T. Shih, J. George, F. Annunziata, M. Sauer, C. T. Lin, W. J. Jiang, J. Chen, and S. Chi, "21 Gbps OFDM wireless signal transmission at 60 GHz using a simple IMDD radio-over-fiber system," presented at the presented at the IEEE OSA/Opt. Fiber Commun. Conf./ Collocated Natl. Fiber Opt. Eng. Conf., San Diego, CA, 2010, Paper OTuF4.

[14] C. T. Lin, J. Chen, P. T. Shih, W. J. Jiang, and S. Chi, "Ultra-high data-rate 60 GHz radio-over-fiber systems employing optical frequency multiplication and OFDM formats," *J. Lightw. Technol.*, vol. 28, no. 16, pp. 2296–2306, Aug. 2010.

[15] F. Lecoche, E. Tanguy, B. Charbonnier, H. W. Li, F. Van Dijk, A. Enard, F. Blache, M. Groix, and F. Mallécot, "Transmission quality measurement of two types of 60 GHz millimeter-wave generation and distribution system," *J. Lightw. Technol.*, vol. 27, no. 23, pp. 5469–5474, Dec. 2009.

[16] A. Pizzinat, I. Louriki, B. Charbonnier, F. Payoux, S. Meyer, M. Terré, C. Algani, A. L. Billabert, J. L. Polleux, C. Sillans, H. Jaquinot, S. Bories, Y. L. Guennec, and G. Frog, "Low cost transparent radio-over-fibre system for UWB based home network," presented at the presented at the Eur. Conf. Opt. Commun., Bruxelles, Belgium, 2008, Paper Tu.3.F.1.

[17] J. Guillory, S. Meyer, I. Siaud, A. M. Ulmer-Moll, B. Charbonnier, A. Pizzinat, and C. Algani, "Radio over fiber architectures, future Multi-Gigabit wireless systems in the home area network," *IEEE Veh. Technol. Mag.*, vol. 5, no. 3, pp. 1556–6072, Sep. 2010.

[18] R. A. Shafik, M. S. Rahman, and A. R. Islam, "On the extended relationships among EVM, BER and SNR as performance metrics," in *Proc. 4th Int. Conf. Electr. Comput. Eng.*, Dec. 2006, pp. 408–411.

[19] B. L. Dang and I. Niemegeers, "Analysis of IEEE 802.11 in radio over fiber home networks," in *Proc. IEEE Conf. Local Comput. Netw. 30th Anniversary*, 2005, pp. 744–747.

[20] J. Guillory, S. Meyer, B. Charbonnier, T. Derham, and S. Roblot, "Radio over fiber for an optimal 60 GHz home area network," in *IEEE 11-10-0011-01-00ad Conf. Call*, Jan. 2010 [Online]. Available: https://mentor.ieee.org/802.11/dcn/10/11-10-0011-01-00ad-radio-over-fiber-for-an-optimal-60-ghz-home-area-network.ppt

[21] J. Guillory, S. Meyer, I. Siaud, A. M. Ulmer-Moll, B. Charbonnier, A. Pizzinat, and C. Algani, "RoF architectures for multi-gigabit wireless systems in the home area network," in *Proc. 24 WWRF WG5*, Apr. 2010, pp. 1–9.

Authors' biographies not included at authors request due to space constraints.

Radio over Fiber architectures for 60 GHz Wireless Systems in the Home Area Network.

Joffray Guillory(1), Anna Pizzinat(1), Benoît Charbonnier(1), Catherine Algani(2)

(1)France Télécom - Orange Labs, Lannion, France.
(2)Conservatoire National des Arts et Métiers - ESYCOM, Paris, France.

October 6th, 2011.

WPMC'11 Brest FRANCE

Contents

The background of the Home Area Network

The evolution of the Home Area Network (HAN) is determined by several trends:

- Deployment of Fiber To The Home (FTTH) in the access network,
- Increasing number of connected devices
- Increasing data rates between the devices

} Need for Multi-Gigabit/s IP flows in the HAN

- Increasing and simultaneous use of the terminals in a Wireless way
- A great heterogeneity of signals has to be delivered:
  - Radio Frequency (RF) signals for terrestrial or satellite broadcasted TV.
  - Specific formats as High Definition Multimedia Interface (HDMI) signals.

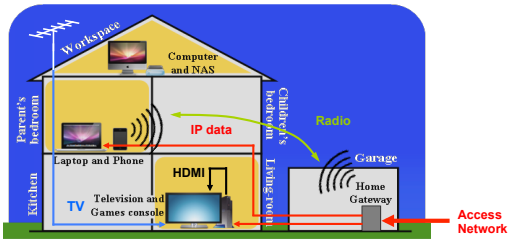

3

Towards an optical HAN

We choose the optical fiber for the home wire.

- It offers a very high bandwidth, a high linearity and a low attenuation, thus it can transfer high data rates over several hundred meters and transmit high RF frequencies.
- It will be a natural extension of access networks (Fiber To The Home).
- It is the ideal candidate to provide long life Home Area Networks.
- Perfect immunity to electrical interferences.

Consequently:

- All signals and all services can be transmitted on the same media simultaneously (frequency or wavelength multiplexing)
- Wireless signal can be transported natively

4

We focus on the new 60 GHz radio Standards

Today: Wi-Fi systems IEEE 802.11n can achieve up to 300 Mbit/s (2.4 and 5 GHz bands).

Tomorrow: New radio standards will achieve multi-Gigabit/s in the unlicensed mm-wave band (57 – 66 GHz).

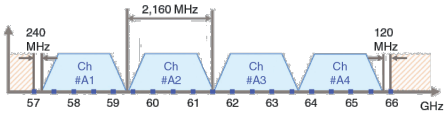

IEEE 802.15.3c	WirelessHD	IEEE 802.11ad
Released in 2009	Released in 2009	To be realised in 2012
20 to 5,670 Mbps	952 to 3,807 Mbps	385 to 6,757 Mbps
Existing products.		Certified Products "Wi-Fi" in 2012.

However, channel attenuation is very high in the 60 GHz band,
And the radio signals cannot cross the walls.
Thus, the coverage is limited to single rooms.

→ How to expand the coverage of the radio signal to the whole HAN?

Contents

The Radio over Fiber technology

The Radio over Fiber systems enlarge the coverage of the millimeter-wave. It consists in transporting the radio signal from wireless devices onto an optical carrier for distribution over optical fibre to different remote antennas, called RoF transducer.

Transporting the radio signals in their native format, provides the advantage of remote antenna simplification and transparency to radio layer protocols.

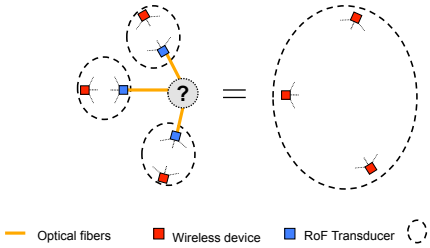

Optical fibers Wireless device RoF Transducer Radio coverage

7

The Radio over Fiber technology

A simple analogue repeater between two rooms

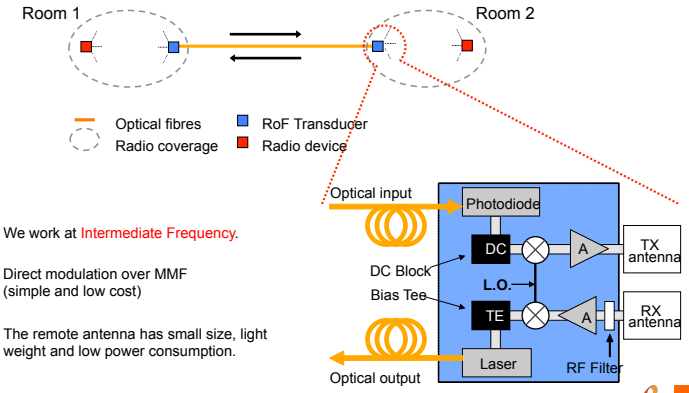

We work at Intermediate Frequency.

Direct modulation over MMF (simple and low cost)

The remote antenna has small size, light weight and low power consumption.

8

A passive and transparent RoF architecture: the Multipoint-to-Multipoint architecture

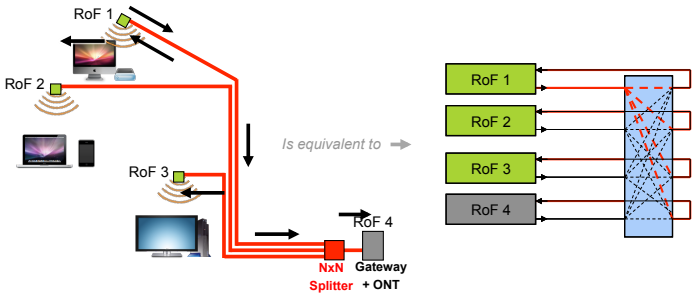

9

The experimental setup

A 3.08Gbit/s pseudo-random OFDM signal, with QPSK constellation, is generated according to the IEEE 802.15.3c, High Speed Interface mode.

The wireless device emitting at 59.7 GHz with a EIRP equals to 27dBm.

EVM (%) at the receiver.

Distance	Equivalent free space losses	Average EVM
1m	68dB	~14%
5m	82dB	~14%
10m	88dB	~14%
15m	91.5dB	~14%

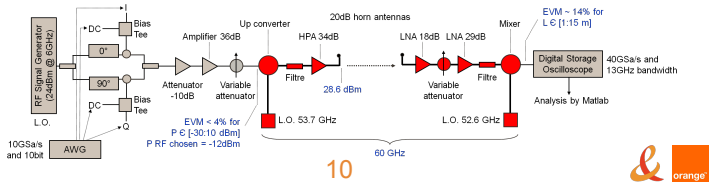

The experimental setup

Point-to-point RoF link with optical losses varying from 0 to 15dB to simulate the NxN optical splitter.

Radio over Fiber transmission in IF at 4.5 GHz.

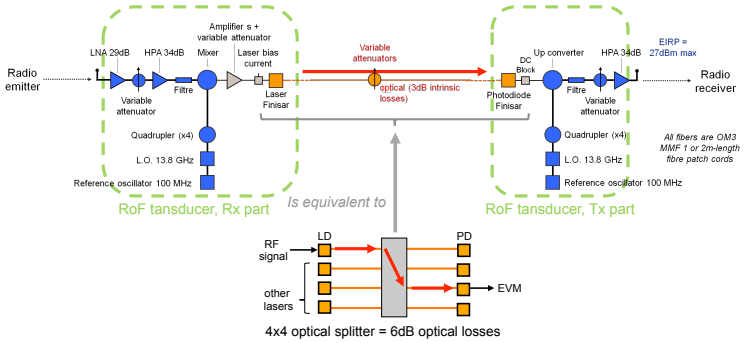

The results of the setup

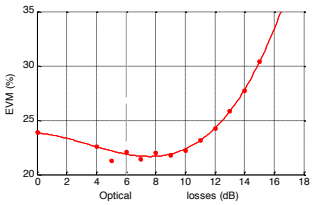

One 5m hop in the air
+ the multipoint-to-multipoint RoF architecture simulated by a variable optical attenuator
+ a second 5m hop in the air

EVM = 22.37% and CNR ~ 20dB

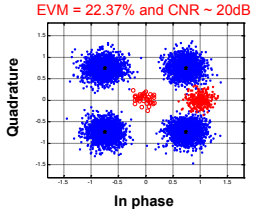

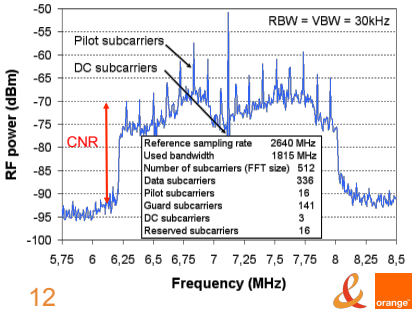

The experimental setup

In the multipoint-to-multipoint RoF architecture, all lasers are always turned on in order to be ready to transmit a radio signal if a wireless device emits.

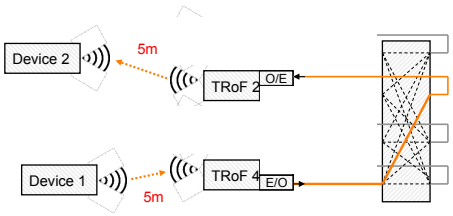

EVM = 22%

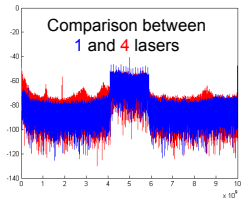

13

The experimental setup

In the multipoint-to-multipoint RoF architecture, all lasers are always turned on in order to be ready to transmit a radio signal if a wireless device emits.

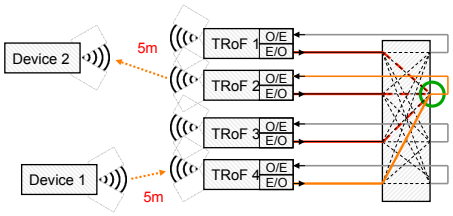

Copy of the ambient noise
+ Addition of the noise of each laser, means the Relative Intensity Noise (RIN)
+ Increase the received optical power and so the shot noise (noise inherent to the photodiode)
+ Optical beating

EVM = 22% ➡ 27%

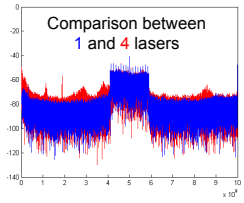

14

Intermediate Frequency over Fiber link between two WirelessHD devices

Finally, a real time transmissions between two commercial WirelessHD devices has been realized. (OFDM signal close to the IEEE 802.15.3c standard)

•The Downlink, from Blu-ray player to HD screen = High Rate Physical layer (HRP) for multi-gigabit/s video signal + Low Rate Physical layer (LRP) for monitoring.
•The uplink, from HD screen to Blu-ray player = Low Rate Physical layer (LRP) for monitoring.

Our HRP signal is QPSK-modulated at 2.856 Gbit/s PHY rates (1.904 Gbit/s data rates) on the second channel of the millimeter-wave band.

Transmitting power = 27dBm.
Receive sensitivity = -65dBm.

Systems run smoothly with multipoint-to-multipoint architecture

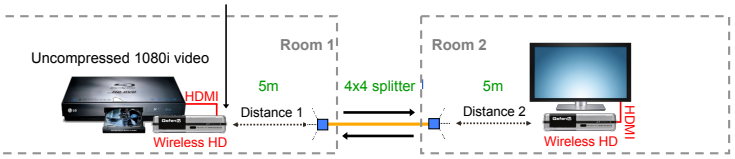

15

Contents

The management of the optical access

In the multipoint-to-multipoint RoF architecture, normally all lasers are always turned on in order to be ready to transmit a radio signal if a wireless device emits.

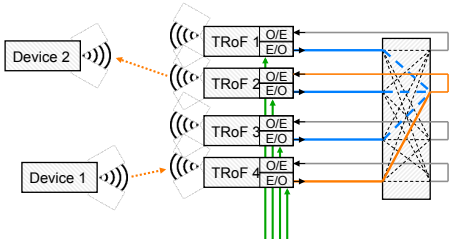

adding a monitoring signal to turn-off the blue emission and reduce the EVM by 5%.

To avoid the copy of the ambient noise and the add of optical noises.

Lasers emit only at the right time, and at the right place.

Same things for photodiode

The global spectral efficiency (bit/s/Hz/m²).

Essential argument for health and hacking concerns.

Essential mechanism for a green system.

17

The management of the optical access

- Standard PCP/AP with multiple antennas

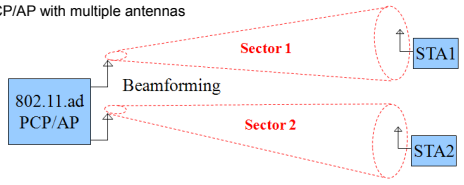

- Multi-room AP with remote antennas

Only one device recovers the information from the radio MAC layer and create all the monitoring signals

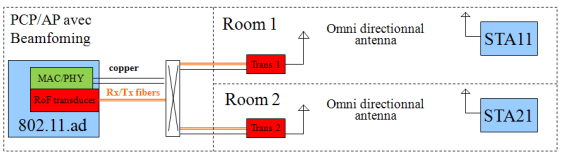

18

The management of the optical access

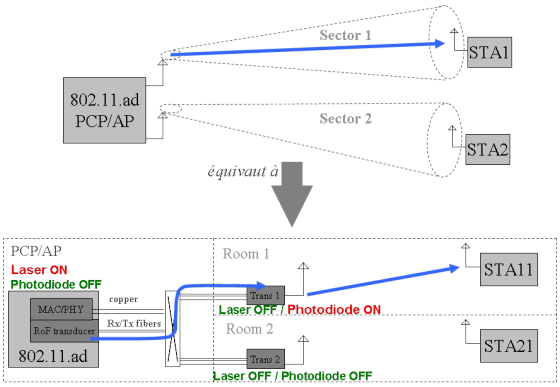

19

The management of the optical access

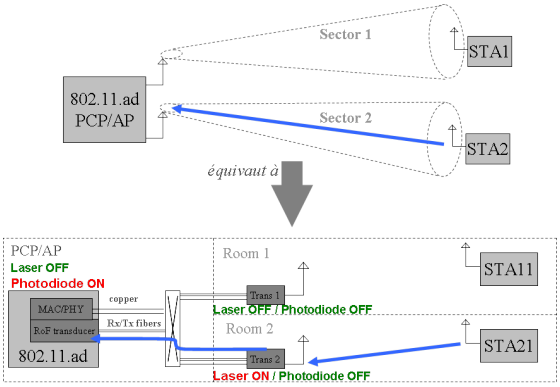

20

Conclusion

The rise of the data rates in the Home Area Network and the users demand for wireless solutions naturally lead to RoF technology.

We have demonstrated that RoF systems like the optical tunnel can meet these needs.

For a massive adoption of the RoF technology and to cover the whole house:

- advanced integration of the RoF transducers is under consideration.
- improvement of the RoF architectures are also under study: new components and towards a management of the optical access

WPMC'11 Brest FRANCE

21

Thanks for your attention

Joffray Guillory, joffray.guillory@orange-ftgroup.com

This work was carried out in the frame of the French FUI8 ORIGIN
(**O**ptical **R**adio **I**nfrastructure for **G**igabit **I**ndoor **N**etworks) project.

ORIGIN

images & réseaux

WPMC'11 Brest FRANCE

orange

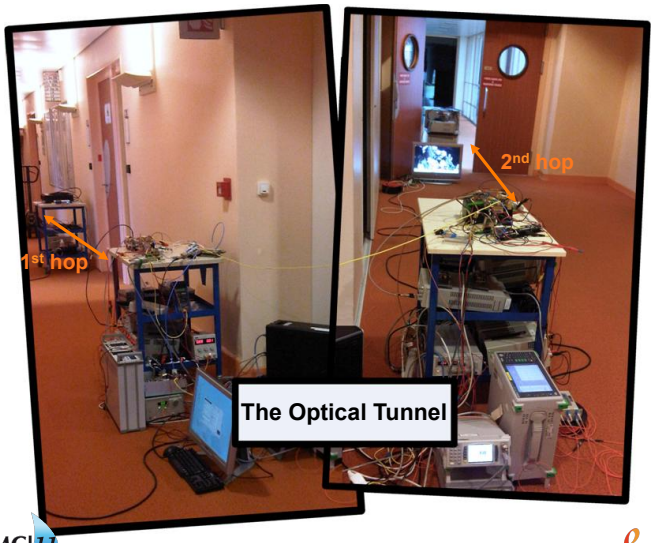

WPMC'11 Brest FRANCE

orange

NOC 2011 BAT - 6

60 GHz Intermediate Frequency over Fiber using a passive Multipoint-to-Multipoint architecture

J. Guillory*, A. Pizzinat*, B. Charbonnier*, and C. Algani**.

* France Télécom / Orange Labs, Lannion, France.
** CNAM / ESYCOM, Paris, France.
joffrayguillory@orange-ftgroup.com

***Abstract*— 60 GHz radio coverage is extended using a Radio over Fiber (RoF) multipoint-to-multipoint architecture. Two hops in the air are realized, transposition at Intermediate Frequency is performed for propagation over multimode fiber, and low-cost photonic components are used. This transparent RoF architecture has to allow a large optical budget for the NxN optical splitter sharing the media between the different Access Points. Finally, a real-time transmission between two commercial WirelessHD devices at 3 Gbit/s is achieved.**

I. INTRODUCTION

In order to meet all the needs of the customers, the future wireless solutions have to enable multi-gigabit speed. Indeed, users employ increasingly connected devices in a nomadic way, and current solutions like the last Wi-Fi update, IEEE 802.11n with 300 Mbit/s data rate, do not offer enough capacity for emerging new applications as display sharing or high data rate file transfers. Consequently, several wireless standards that deliver multi-gigabit data rate have been proposed and the first products arrive on the market. The IEEE 802.11ad standard [1], created by WiGig consortium [2], should lead the next generation of wireless systems thanks to Wi-Fi Alliance certification and compatibility with Wireless Local Area Network (WLAN) systems. It could be available by the end of 2011. Nevertheless, terminals equipped with WirelessHD standard interface [3] are already available for Wireless High Definition Multimedia Interface (HDMI) applications.

All these Home Area Network (HAN) standards use the 57-66 GHz unlicensed band. This 9 GHz bandwidth is composed of four 2.16 GHz channels, each with data rate up to 6 Gbit/s. But these high carrier frequencies induce high free space losses. Consequently the coverage of the millimeter-wave devices is significantly reduced and limited to a single room or a small open area.

II. RADIO OVER FIBER

A. Generality

The radio coverage can be extended using numerous Access Points (APs) judiciously located in home and interconnected by Radio over Fiber (RoF) links. First, large bandwidth, low attenuation and high linearity make the optical fiber a future proof solution for HAN. Additionally, RoF thanks to the transmission of radio signals in their native format is a good compromise between cost, performance and integration. The APs, called RoF Transducers (TRoF), are greatly simplified, containing only RF and optical components, no electronic intelligence (Figure 1). We have chosen to distribute millimeter-wave over multimode fiber (MMF) at Intermediate Frequency (IF) in order to realize Intensity Modulation with Direct Detection (IM-DD) at 850nm wavelength for low cost concern. A unique Local Oscillator (LO) down-converts and up-converts the radio signal. So, the radio signal modulates directly a 850nm Vertical-Cavity Surface-Emitting Laser (VCSEL), and a GaAs PIN photodiode with a built-in transimpedance amplifier (TIA) recovers it.

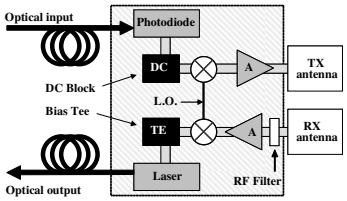

Figure 1. Intermediate Frequency over Fiber Transducer (TRoF).

B. Multipoint-to-multipoint RoF architecture

We propose an innovative multipoint-to-multipoint RoF architecture (Figure 2) offering a unique optical infrastructure for the whole HAN [4]. It's an evolution of the point-to-point architecture presented in [5], the key point is a NxN optical splitter.

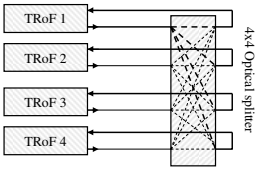

Figure 2. Multipoint-to-multipoint RoF architecture.

The optical fiber used for RoF transmission is connected to an optical input of the splitter and the fiber used for RoF reception is connected to an optical output of the splitter. This passive infrastructure acts as a logical bus, broadcasting the signal coming from any transmitter to all the receivers connected to the infrastructure. The data rate is shared between the different APs but the number of users being limited, this point is acceptable.

This multipoint-to-multipoint architecture has various advantages as the transparency to radio layer protocols, the possibility of direct communications between users in different locations of the HAN without intelligence, the support of multiservice and multiformat transmissions [6]

978-1-86135-373-3/11/$25.00 ©2011 IEEE

and the compatibility with an important number of nodes if the optical budget allows the NxN optical splitter.

This paper presents a study of the RoF multipoint-to-multipoint architecture. The influence of the optical splitter is first simulated by introducing optical losses in a point-to-point RoF link, and then a real optical splitter is inserted in order to characterize the signal transmission.

III. Characterization of a Multipoint-to-Multipoint RoF Architecture with Optical Losses.

As a baseline, we characterized the propagation of the radio signal over the experimental setup shown in Figure 3, first in a back-to-back connection, i.e. when the oscilloscope is simply connected to the IF-OFDM signal generator, then with the introduction of a RoF link.

A 3.08 Gbit/s pseudo-random Orthogonal Frequency Division Multiplexing (OFDM) baseband signal modulated with a Quadrature Phase Shift Keying (QPSK) scheme is built under Matlab according to the High Speed Interfaces (HSI) mode of the IEEE 802.15.3c standard. A 10 GSa/s Arbitrary Waveform Generator (AWG) generates two signals, the In-phase (I) and the Quadrature (Q) components, that are transposed to IF by a LO split in two paths with a 90° phase shift. Finally, a RF coupler creates the IF-OFDM signal by combining the two components of the radio signal.

A real-time digital storage oscilloscope, with 13 GHz bandwidth and 40 GSa/s speed, receives the transmitted signal for analysis under Matlab and calculation of the link Error Vector Magnitude (EVM).

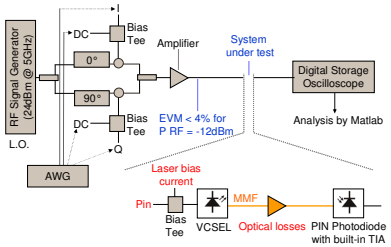

Figure 3. Back-to-back and RoF setup at IF (5 GHz).

The back-to-back connection of Figure 3 presents an EVM lower than 4%. The EVM measured after inserting the RoF link at IF is reported in Figure 4.

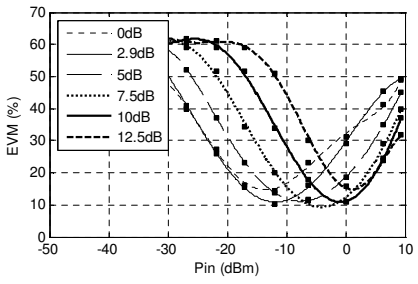

Figure 4. Measured EVM (%) as a function of the RF input power (dBm) for different values of optical losses. The laser bias current is fixed to 6.5mA and the IF-OFDM signal is fixed at 5 GHz.

The measured EVMs for different optical attenuations show that the larger the optical losses are, the higher the RF laser input power must be. For given optical losses, from 2.9 to 10dB, the best EVM is stable and close to 11%. Compared to the back-to-back connection, the EVM has increased by 7%. Without optical loss the best EVM is 15% because the PIN photodiode with a built-in TIA saturates and the Relative Intensity Noise (RIN) and the shot noise are significant at the reception. For 12.5dB optical losses the best EVM also equals to 15% due to laser saturation: we need important RF laser input power to compensate the optical losses. Deeper investigations are in progress. These results will be used until the end of this paper to optimize the transmission over the RoF multipoint-to-multipoint architecture depicted in Figure 6.

At the output of the OFDM generator, point A, a 53.7 GHz LO up-converts the 6 GHz IF radio signal to millimeter-wave for a first free space propagation at 59.7 GHz. The Equivalent Isotropically Radiated Power (EIRP) is 28.6dBm. Note that all antennas of the systems are horn antennas with 20dB gain. After that, the radio signal is caught by a RoF transducer, which distributes the millimeter-wave over MMF at 4.5 GHz after a frequency conversion with a 55.2 GHz LO. The RoF link is the same of Figure 3. The photodetected signal is up-converted in the second RoF transducer for a second free space propagation at 59.7 GHz. Here, the EIRP is a function of the optical losses as the RF power is adapted at the input of the laser according to Figure 4. The highest EIRP corresponds to a RoF link without optical loss, i.e. 26.5dBm. At the reception, the radio signal is down-converted again to capture it on the oscilloscope and to be analyzed under Matlab.

As a reference, the radio link, with one hop in the air going directly from point B to point C in Figure 6, without the RoF repeater, corresponds to an EVM of 14% for 5m and 10m-distances hops with an optimized millimeter-wave gain at the reception, as if we had an amplifier with an Automatic Gain Control (AGC).

Then, the RoF link based on the multipoint-to multipoint architecture, with two hops in the air, is added. The experimental results for the EVM as a function of optical losses are reported in Figure 5. They prove the feasibility of employing an optical transparent multipoint-to-multipoint architecture.

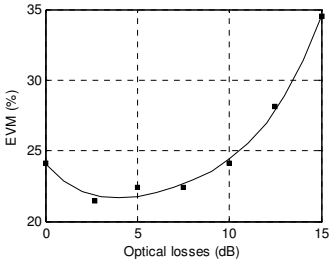

Figure 5. Measured EVM (%) as a function of the optical losses (dB). The laser bias current is fixed to 6.5mA, and the two hops to 5 meters.

The best EVM, 22%, is observed for 4dB optical losses. Beyond 11dB optical losses, the EVM is higher than 25%, corresponding to a BER of 10^{-5}, i.e. error-free after coding implementation [7].

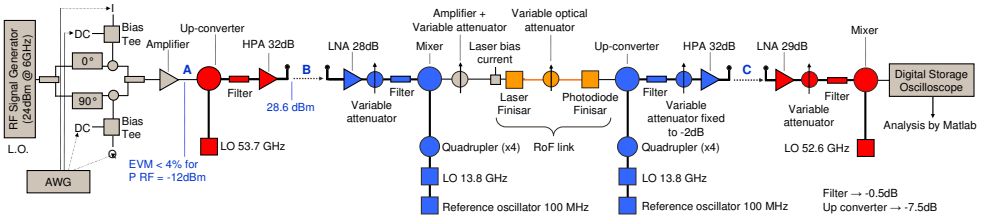

Figure 6. RoF setup based on the multipoint-to-multipoint architecture, with two hops in the air.

IV. Characterization of a multipoint-to-multipoint architecture with an optical splitter.

At this step, the IF-RoF link depicted in Figure 3 is realized again, but a 4x4 optical splitter replaces the optical attenuator (Figure 7).

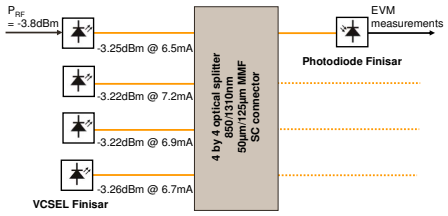

Figure 7. RoF setup with a 4x4 optical splitter.

The key element for a smooth functioning of the multipoint-to-multipoint architecture is the behaviour of the optical splitter. The tested splitter is a 4x4, designed for transmission at 850 and 1310nm over MMF, with a 50µm core diameter, and a 125µm cladding diameter. The optical splitter insertion losses of each port are reported in Table I.

TABLE I
INSERTION LOSSES (DB) OF THE 4X4 SPLITTER AT 850 NM.

IN / OUT	1	2	3	4
1	5.98	6.47	5;91	6.68
2	5.84	6.35	6.38	6;57
3	6.49	6.20	6;36	6.77
4	6.74	6.02	6.14	6.40

The optical splitter behaviour depends on the laser used. As the VCSEL presents a strong transverse multimode character, the splitter is well balanced with outputs optical losses varying from 5.84dB to 6.77dB. With a 6.33dB average value, the theory is confirmed.

Before performing EVM measurements, a Fast Fourier Transform (FFT) process is applied to the signal in order to observe the OFDM spectrum at the reception (Figures 8 and 9).

Only the main (first) laser is modulated by an input radio signal. Its bias current is fixed at 6.5mA. The bias current of the three other VCSELs is adapted to target an optical output power of -3.25dBm, like the main laser.

As can be known in optical multipoint-to-multipoint architecture, the simultaneous operation of multiple lasers induces an addition of each laser RIN and an excess of shot noises as the received optical power increases. But, we mostly observe optical heterodynings at the detection, in particular at the switching-on of the lasers (Figure 8).

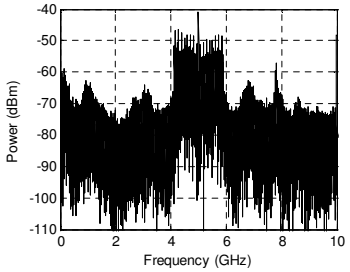

Figure 8. OFDM spectrum for 3 lasers turned-on (switching-on time).

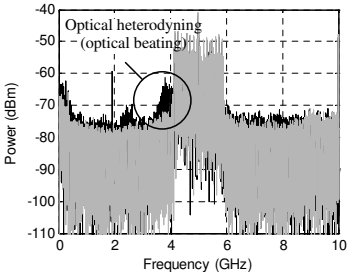

Figure 9. OFDM spectrum at the reception for one laser (grey) and for four lasers (black) turned-on.

At 850nm-wavelength, the two laser wavelengths must be separated from $\Delta\lambda$=0.012 nm to generate an electrical signal at a 5 GHz frequency. Indeed, from the formula $\nu = c/\lambda$, we obtain $\Delta\nu = c * \Delta\lambda / \lambda^2$, with λ the wavelength, ν the optical wave frequency and c the light velocity; so:

$$\Delta\lambda = \lambda^2 * \Delta\nu / c = ((850e\text{-}9)^2 * 5e9) / 3e8 = 0.012 \text{ nm} \quad (1)$$

Additionally, the generated microwave frequency is time-varying due to unstabilized lasers temperatures.

A. *EVM characterization of the only optical link*

For the EVM measurements, four scenarios were tested: they are presented in Table II. In the first case, only one laser is switched-on; the photodiode receives only the useful signal. In the second case, a second laser is turned-on adding RIN, enhancing shot noise, and generating optical heterodyning signals. The third and fourth cases correspond to the simultaneous operation of three and four lasers respectively.

TABLE II
EVM MEASUREMENTS FOR ROF LINK AT IF WITH OPTICAL SPLITTER.

Measurement number	1	2	3	4
1	13.82	15.11	15.69	14.89
2	16.52	14.50	16.60	13.83
⋮	⋮	⋮	⋮	⋮
19	34.11	13.73	34.22	18.46
20	12.51	16.20	18.12	15.95
Average EVM	13.58	14.17	16.68	16.45
number of unusual values	2	3	6	4

Table II shows the obtained EVM values at the output of the optical splitter over 20 measurements and for the four scenarios. The average EVM is calculated, ignoring the extreme or unusual values highlighted in grey. These errors can occur from a bad demodulation process under Matlab, but they seem particularly connected to lasers optical heterodynings that overlap the OFDM signal at the detection. Indeed, the number of erroneous values increases with the number of lasers operating simultaneously.

Equally, the average EVM value increases of 3% between the scenarios 1 and 4. Consequently, the previous results assuming only optical losses were too optimistic.

B. EVM characterization of the complete link

In a second time, the operation is repeated but for the RoF multipoint-to-multipoint architecture illustrated in Figure 6, considering two additional hops in the air. The results are reported in Table III.

TABLE III
MULTIPOINT-TO-MULTIPOINT ARCHITECTURE, WITH 5M+5M HOPS.

Measurement number	1	2	3	4
1	21.63	25.85	28.57	26.28
2	21.84	23.62	34.86	25.61
⋮	⋮	⋮	⋮	⋮
19	21.65	26.75	24.92	27.67
20	21.70	27.36	24.90	28.60
Average EVM	21.89	25.98	27.68	26.84
number of unusual values	2	3	6	5

The number of unusual values remains similar between Tables II and III, but now the two extreme scenarios have a 5% EVM difference. Otherwise, the first scenario, with only one laser turned-on, is in agreement with Figure 5 when the optical losses equal to 6dB: the EVM equals to 22%.

V. MULTIPOINT-TO-MULTIPOINT ROF ARCHITECTURE TESTED USING COMMERCIAL WIRELESSHD DEVICES.

A real-time transmission between two commercial wireless HDMI products from Gefen based on the wirelessHD standard has been tested over the multipoint-to-multipoint RoF architecture. A WirelessHD transmitter emits an uncompressed 1080i video signal from a Blu-ray player at 60.48 GHz, and a WirelessHD receiver displays the video signal on a HD screen. These wireless equipments are in two different rooms, and the RoF infrastructure connects them as described in Figure 6, with a 5 meters hop in each room and a 4x4 optical splitter.

To support bi-directional exchanges, a second link has been added in parallel. The signal is transposed to IF on both directions, but the RoF is implemented only on the downlink (from Blu-ray player to HD screen); the uplink radio signal uses a coaxial cable.

The radio signal transmitted over fiber operates at 2.856 Gbit/s PHY rates with QPSK modulation. The Wireless HD devices emit a RF power of 27dBm and have a receiver sensitivity of -65dBm.

No interruption during the transmission of the video signal is observed on the screen, even at the lasers switch-on. The radio signal resists to optical disturbances. Since the interferences created by the optical heterodynings have low bandwidth compared to 2.16 GHz bandwidth of the OFDM signal, an error correction code associated with advanced interleaving techniques provides adequate resistance to the signal. Cache memory of the radio signal at the receiver and requests for retransmission of lost frames could also explain the strength of the radio link.

Other tests were conducted, always with multipoint-to-multipoint architecture, but without optical splitter, just with optical losses as previously. From 0 to 17.5dB optical losses the system still works; for 20dB the system works intermittently, the image cuts regularly. The system meets its limits and beyond the connection cuts.

VI. CONCLUSION

We have characterized a multipoint-to-multipoint RoF architecture and shown the feasibility of this concept by transmitting in real-time an uncompressed HD video between two commercial WirelessHD devices working at 3 Gbit/s. We have also shown that optical losses are inadequate to simulate this kind of architecture as they give optimistic results. Indeed, we have important degradation mainly due to lasers optical heterodyning.

A solution to avoid this would consist in managing the optical media of the multipoint-to-multipoint architecture in order to have at a time only one laser turned-on. In this goal, we can use information from the radio MAC layer [4]. Another solution would consist in using point-to-point RoF links interconnected by a RF splitter.

ACKNOWLEDGMENT

This work is supported by the French government in the framework of the project ORIGIN (Optical Radio Infrastructure for Gigabit Indoor Networks).

REFERENCES

[1] IEEE 802.11ad, www.ieee802.org/11.
[2] WiGig, http://wirelessgigabitalliance.org
[3] WirelessHD, www.wirelesshd.org.
[4] J. Guillory and al., “Radio-over-Fiber architectures, Future Multi-Gigabit Wireless Systems in the Home Area Network”, IEEE Vehicular Technology Magazine, 1556-6072, September 2010.
[5] J. Guillory and al. “Radio over Fiber tunnel for 60 GHz wireless Home Network”, OFC/NFOEC, March 2011.
[6] F. Richard and al., “CWDM Broadcast and Select Home Network based on Multimode Fibre and a Passive Star Architecture”, OSA / ANIC conference, June 2010.
[7] R.A. Shafik, and al., “On the Extended Relationships Among EVM, BER and SNR as Performance Metrics”, 4th ICECE, December 2006.

Comparison between two 60GHz multipoint RoF architectures for the Home Area Network.

J. Guillory *, Y. Ait Yahia*, A. Pizzinat*, B. Charbonnier*, C. Algani**, M.D. Rosales***, J.L. Polleux***
* France Télécom - Orange Labs, Lannion, France.
** CNAM - ESYCOM laboratory, Paris, France. *** Université Paris-Est – ESYCOM – ESIEE Paris, France.
joffray.guillory@orange.com

***Abstract*—60GHz radio coverage is extended using low-cost multipoint-to-multipoint RoF architectures based on optical or electrical splitter. These infrastructures are compared in terms of EVM and real-time signals transmissions between commercial devices working at 3Gbit/s. Finally, improvements based on innovative SiGe photoreceptors are proposed.**

I. Introduction

Next generation Home Area Networks (HAN) will have to provide higher data rates associated to wireless connectivity. To fulfill this challenge, Multi-Gigabit Wireless Systems (MGWS) are emerging or are under development like IEEE 802.15.3c [1], WirelessHD [2] or IEEE 802.11ad [3], the future Wi-Fi standard. These radio standards exploit the unlicensed millimeter-wave band from 57 to 66 GHz to achieve data rates up to 7Gbit/s, but over distances limited to few meters and without being able to cross the walls. As explained in [4], Radio over Fiber (RoF) is a promising solution to distribute the millimeter-waves to the whole home by transposing the radio signal transparently onto an optical carrier which is transmitted over fiber to several access points.

We have demonstrated in [5], that two 60GHz wireless devices located in two separate rooms are able to communicate together, as if they were directly visible, thanks to an additional point-to-point RoF link working at Intermediate Frequency (IF) and acting as a repeater between two hops in the air. Unfortunately, this solution is limited to the communication between two rooms. To enable multi-room transmission and networking, we introduce multipoint-to-multipoint RoF architectures. Two solutions are proposed here and depicted in Figure 1: an optical and an electrical one.

The optical architecture is based on an NxN optical splitter whereas the electrical architecture is based on an NxN RF splitter. In the two cases, the lasers of the RoF transducers (TRoF in Figure 2) are connected to the inputs of the splitters while the photodiodes are connected to their outputs. In the electrical architecture, optoelectronic (O/E) and electro-optic (E/O) conversions at the input and at the output of the RF splitter are added. Thus, these two proposed architectures act as logical buses, broadcasting the signal coming from any transmitter to all the receivers connected to the infrastructure. The radio protocol alone is able to control communications on these architectures and to manage possible collisions, as the radio access methods are compatible with the bus topology.

Even if the optical solution seems advantageous due to a unique and passive component, it induces optical beating at the detection between the different active lasers, which creates interferences over the radio signal. This point, illustrated in Figure 2, has been discussed in details in [6]. In this paper, we propose an electrical version of the multipoint-to-multipoint architecture to avoid these interferences. Moreover, for the first time, we compare it to its optical counterpart in terms of performances. Finally, some analysis is performed on the optical components in order to identify how to improve the performances.

II. Experimental Setups and Results

A. Comparison between the two architectures.

To extend the coverage to the whole house, the multipoint-to-multipoint architectures depicted in Figure 1 have been tested only in one direction as the system has no asymmetry.

First, laboratory homemade radio emitter and receiver have been realized. According to the IEEE 802.15.3c standard, an OFDM pseudo-random signal with a Quadrature Phase-Shift Keying (QPSK) modulation and data rate of 3.08Gbit/s is generated on a 1.815GHz bandwidth [6] [7]. The signal is emitted in free-space in the second channel of the millimeter-wave band, at 59.7GHz center frequency, with an Equivalent Isotropically Radiated Power (EIRP) of 27dBm corresponding to the EIRP of commercial devices. At the receiver side, the radio signal is captured by a digital oscilloscope, and then, the Error Vector Magnitude (EVM) is calculated under Matlab. As a reference, with only one air-hop and for distances up to 15m, we obtain an EVM of 14% as a variable attenuator controls the reception gain.

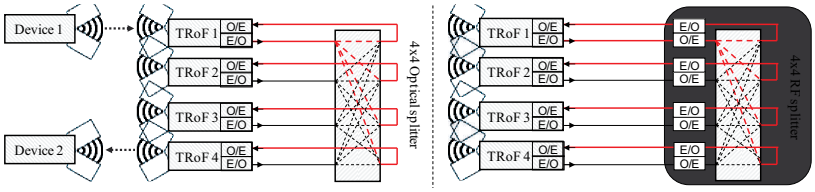

Figure 1: Optical (on the left) and electrical (on the right) multipoint-to-multipoint RoF architectures.

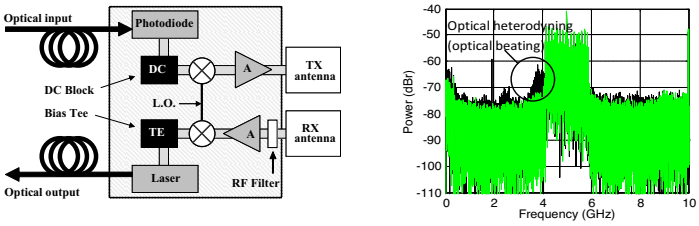

Figure 2: RoF transducer on the left and IEEE 802.15.3c IF OFDM spectrum at 5GHz on the right. The spectrum, from [6], has been measured at the photodiode output for a 4x4 optical architecture, without hop in the air, for 1 laser (green) and 4 lasers (black) turned-on simultaneously.

Then, the two multipoint-to-multipoint architectures represented in Figure 3 are tested. At the TRoF side, mm-waves are down-converted by a Local Oscillator (LO) to a lower IF before direct modulating a laser, then the photodetected signal is up-converted to 59.7GHz before the wireless emission. Concerning the central node, in the optical architecture, it is simply composed of a variable optical attenuator to simulate the NxN optical splitter. In the electrical architecture, it includes a photodiode for the O/E conversion, then a variable RF attenuator to simulate the two 1xN RF splitters (as no NxN RF splitter is commercially available) and at last a laser for the E/O conversion. As the IF equals to 4.5GHz, low cost optoelectronic components, with ~10GHz bandwidth, are used: a VCSEL at 850nm and a GaAs PIN photodiode with a built-in transimpedance amplifier (TIA) from Finisar. At the input of each laser, RF amplifiers cascaded by variable attenuators adjust the RF power to minimize the EVM, then variable optical attenuators are inserted in the optical links to simulate the linear attenuation, the bend losses and the optical splitters. These optical losses, necessary also to avoid saturation of the photodiode built-in TIA [7], are not introduced in the electrical architecture.

The tests have been conducted with two 5m-length hops in the air: the results are summarized in Figure 4.

With attenuators simulating the splitters, we obtain a bell-shaped curve for the optical architecture with minimum EVMs of about 22% for optical losses varying between 5 and 9 dB, and a straight line for the electrical architecture with constant EVMs around 28% as an Automatic Gain Control (AGC) amplifier is used after the RF attenuator to optimize the laser input power. In fact, in the two architectures, we limit the RF power at the input of the optical sources in order to not saturate the TIAs of the photoreceptors. In this compromise, the performances are degraded as the SNR at the RoF link output is low. In Figure 4, the two architectures responses intersect each other at 14dB optical or electrical losses, corresponding theoretically to a 16x16 optical splitter plus 2dB additional losses for fiber bends, or two 1x4 electrical splitters plus 1dB additional loss, respectively. For reference, an EVM of 32.5% corresponds to a Bit Error Rate (BER) of 10^{-3} in QPSK [8].

Tests have also been conducted using 4x4 splitters instead of attenuators. In the optical architecture, as the VCSELs offer a large number of transverse modes, the MMF splitter is well balanced, with 6.3dB (±0.5dB) insertion losses. The results are reported in Figure 4 in magenta: the previous EVM value is recovered as long as only one laser is turned-on, but when the setup is completed with the other 3 lasers, the resulting average EVM increases to 26.9% as optical beats occur. The simultaneous operation of multiple lasers induces the addition of each laser Relative Intensity Noise (RIN) and an excess of shot noise as the received optical power increases. In the electrical architecture, two 1xN RF splitters have been used, corresponding to 14.0dB (±1dB) measured electrical losses. With one RoF link activated the results are in agreement with previous results, but with all the RoF links activated the EVM value rises up to 37.6%. If only the photodiodes are turned-on, the EVM is equal to 30.4%: the impact of the thermal noises is low; RIN and shot noise are the main reasons for these deteriorated results.

B. Improvement using more linear components.

The electrical solution has the advantage to be laser beats independent, but it induces important EVM values. To improve the performances, less noisy and more linear components made for 10Gbit/s digital communications are tested: a FP laser at 1310nm and a PIN photodiode with a built-in TIA from Finisar.

In this part, the experimentations have been conducted only on the electrical architecture since the FP laser has a poor transverse mode character inducing a not well balanced splitter behavior with optical losses varying from 3 to 10 dB.

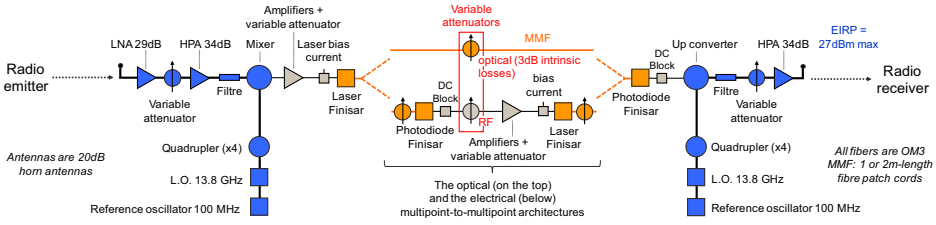

Figure 3: Experimental RoF multipoint-to-multipoint architectures, with the Rx part of the RoF transducer on the left, the two possible central nodes on the middle, optical and electrical, and the Tx part of the RoF transducer on the right.

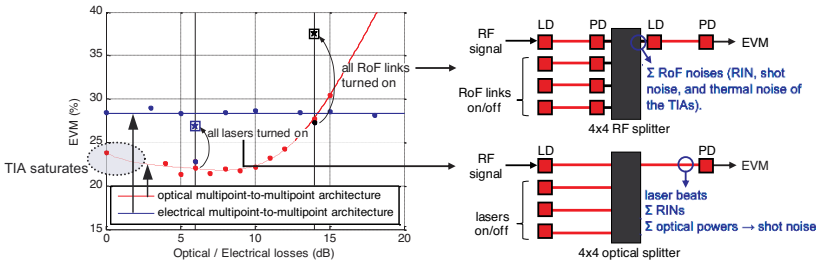

Figure 4: Comparison between optical and electrical architectures, with splitters simulated by attenuators (red and blue). The performances with real splitters have also been added to the plot (magenta and black) with only the main (first) laser modulated by a radio signal.

As previously, no optical loss is inserted in the RoF links of the multipoint electrical architecture.

EVM measurements, stable over a long time (tested for 12 hours), are provided in Table I for different optical configurations. The results are compared to the ones obtained for the Finisar VCSELs and the PIN photodiodes at 850nm: we observe a good improvement. If we observe the radio spectrum at the reception, we note that the EVM difference of 11% (37.57 vs. 26.46) corresponds to 7dB improvement on the SNR.

TABLE I
EVM OBSERVED IN THE ELECTRICAL ARCHITECTURES.

RoF1	RoF2	RoF3	RoF4	EVM (%) @850nm	EVM (%) @1310nm
ON	OFF	OFF	OFF	27.33	24.12
ON	ON	OFF	OFF	32.06	24.65
ON	OFF	ON	OFF	34.95	25.63
ON	OFF	OFF	ON	31.15	23.95
ON	ON	ON	OFF	36.56	26.35
ON	ON	ON	ON	37.57	26.46

To understand the reasons of such difference, analog characterizations have been performed on the components that constitute the first RoF link of Figure 3.

First, it has to be noted that the laser input powers have been optimized to minimize the EVM: they are fixed at -14dBm for the first link working at 850nm and biased at 6.5mA and at -1dBm for the link working at 1310nm and biased at 45mA.

Concerning the S21 measurements, a flat response from DC to 8.7GHz is experimentally obtained at 850nm with a gain of -1.9dB. On the contrary, a bumpy response is observed at 1310nm with a negative gain of -27dB at worst in the radio band, [3.5 - 5.5] GHz. As shown in Table II, large differences exist between the theoretical gains and their experimental values, probably due to bad connections between the evaluation boards (which are homemade circuits at 1310nm) and the optoelectronic components.

Like the S21 response, the RIN, presented in Figure 5, is also better at 850nm despite the presence of a peak at 4.5GHz due to the laser frequency relaxation oscillation. Finally, the highest RIN value observed in the radio band is -125.5dB/Hz at 850nm versus -122.5dB/Hz at 1310nm. The RIN depends on the bias current of the laser diode.

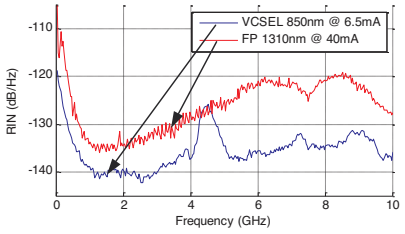

Figure 5: Measured RIN.

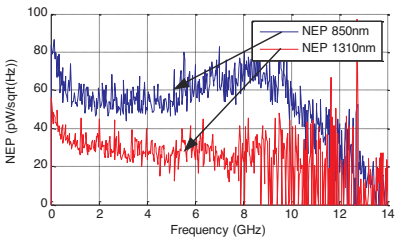

Figure 6: Measured NEP.

Concerning the shot noise, the optical power received by the photodiode working at 1310nm is twice the one received at 850nm according to the laser slope efficiencies. In fact the power received at 850nm is (6.5mA-0.9mA)×0.08mW/mA=0.45mW and at 1310nm it is (45mA-11mA)×0.018mW/mA=0.61mW. Therefore, the shot noise can have a significant impact.

TABLE II
ROF LINK CHARACTERISTICS

Parameter	Laser			Optical losses IL	Photodiode			Theoretical gain $G = 20\cdot\log(\eta_{OE}\times\eta_{EO}) - 2\times IL + 10\cdot\log(Z_{out}/Z_{in}) + 20\cdot\log(Z_{TIA}/Z_{out})$
	Slope efficiency η_{EO}	Threshold current Ith	Input impedance Zin		Slope efficiency η_{OE}	TIA impedance Z_{TIA}	Output impedance Zout	
λ=850nm	0.080W/A	0.9mA	60Ω	0dB	0.50A/W	2000Ω	50Ω	+1.34dB
λ=1310nm	0.018W/A	11mA	50Ω	0dB	0.85A/W	882.35Ω	50Ω	-15.70dB

Lastly, the NEP (Noise Equivalent Power), that measures the thermal noise at the output of the photodetector expressed as an equivalent optical power at the input of the photodiode, has been characterized. It is represented in Figure 6 as a function of frequency. Due to important spectrum analyzer noises for the high frequencies, the NEP measurements are significant only up to 11GHz at 850nm and up to 7GHz at 1310nm.

Now, the RoF link performance is analyzed. As a first point, even if at 1310nm the laser input power leading to the optimal EVM is higher, -1dBm versus -14dBm, this is compensated by a lowest laser gain response, -34.9dB versus -22.7dB. These gain value has been evaluated considering an ideal photodiode: η_{OE} = 1A/W and Z_{TIA} = Z_{out} = 50Ω. Thereby, the same dynamic optical power is emitted.

Besides, as the RIN and the shot noise values are lower at 850nm, only the thermal noise makes a difference. In fact at 1310nm, the thermal noise, expressed as a NEP, is 20pW/sqrt(Hz) lower for a similar dynamic optical power received by the photodiode. However, in point-to-point configurations, the thermal noise is generally not the limiting parameter. So, to understand why better results are obtained at 1310nm,the influence of non-linearities is investigated.

Concerning gain compression, the input 1dB compression point (P1dB) equals to -15dBm at 850nm and to +5dBm at 1310nm. The necessary power back-off experimentally measured for the radio signal is 8dB when the Peak to Average Power Ratio (PAPR) of this OFDM signal is 13dB. As a consequence, the required back-off is clearly not respected at 850nm with regard to the laser input power, even if the latter leads to the optimal EVM value [6]. At 1310nm, the power back-off seems sufficient since no EVM improvement has been observed increasing the optical losses, on the contrary of the RoF link at 850nm where the built-in TIA limits the performances.

Concerning the non-linearities, the input IP3, measured with two tones separated of 10MHz (a typical space between OFDM subcarriers), equals to -4.6dBm for a point-to-point RoF link at 850nm (tones centered at 3GHz) and to 12.5dBm at 1310nm (tones centered at 5GHz). The back-off equals 9.4dB at 850nm and 13.5dB at 1310nm, thus meaning a fundamental tone to intermodulation products ratio of 18.8dB and 27 dB, respectively.

The point-to-point RoF link composed of the FP at 1310nm and of the InGaAs PIN with a built-in TIA is clearly more linear than the RoF link at 850nm. As a consequence, better results are obtained at 1310nm.

III. Multipoint RoF Architectures Tested Using Commercial WirelessHD Devices

Lastly, the setups depicted in Figure 3, with variable attenuators then with the 4x4 splitters, have been tested at 850nm and at 1310nm successfully with commercial devices based on the WirelessHD standard. The setups have been completed with an uplink to be full duplex, a new link composed of the millimeter-wave blue sub-circuits of the Figure 3, the IF part being just a coaxial cable, like in [7]. The OFDM signal transmitted over the downlink is emitted from a Blu-Ray player with 27dBm EIRP on the millimeter-wave band until a HD screen requiring -65dBm input power (Figure 7). The signal uses QPSK subcarriers for a 2.856Gbit/s PHY rate (1.904 Gbit/s data rate) and conveys an uncompressed 1080i video perfectly. The two architectures run smoothly.

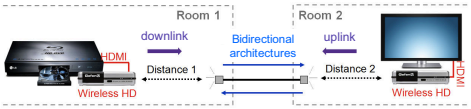

Figure 7: Real-time transmission between two commercial WirelessHD devices from Gefen.

IV. Perspectives

The previous results show that the choice of suitable highly linear components is essential for achieving good performances. In our experimentations, we have noted that the commercial photodiodes limit the performances as their built-in TIA saturates in point-to-point configurations, which makes necessary to add additional optical losses to improve somehow the results.

We investigate also another approach with SiGe Heterojunction bipolar Photo-Transistors (HPT) developed in a SiGe 80GHz technology [11] [12] that operate at 850nm. These are transistors modified to detect the light injected into the base (SiGe layer) and to amplify it by the transistor's current gain. Such Photo-transistors are expected to have a highly linear behavior and allow for a better integration of RF electronic technologies on a single chip.

In order to measure the HPT linearity and compare it to the PIN photodiodes at 850 and 1310nm, the setup shown in Figure 8 has been realized. The latter is equivalent to a RoF link with a highly linear laser that does not limit the measurement of the third order intermodulation products. The results we obtained are reported in Table III: the photodiodes have been characterized for two tones spaced of 10MHz and centered at 3GHz, while the HPT has been characterized at 1GHz with two tones spaced of 100KHz. It has to be noted that the HPT, not packaged yet, has been tested under probes. Input IP3 are measured to be greater than +25dBm, in the limit of the experimental setup, with therefore Output IP3 in excess of -27dBm at 1GHz.

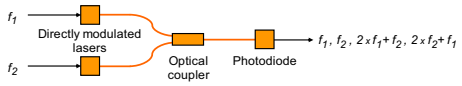

Figure 8: Third-order interception point test bed.

TABLE III
Grey rows: Output IP3 measured for different optical configurations.
Light rows: Extrapolated results using a high power Miteq [10] amplifier.

Tested photo-receiver	Lasers		Optical losses IL	RoF gain G	Output IP3
	Slope efficiency η_{EO}	Input impedance Zin			
PIN at 850nm	0.08W/A	60Ω	5.3dB	-12.5dB	-6dBm
PIN at 1310nm	0.018W/A	50Ω	4.3dB	-35.5dB	-7.3dBm
HPT at 850nm	0.62W/A	50Ω	4dB	-52dB	>-27dBm
HPT at 850nm + ext. amplifier	0.62W/A	50Ω	4dB	-52 + 44 = -8dB	+15dBm expected
HPT at 850nm + ext amplifier	0.08W/A	60Ω	5.3dB	an expected input IP3 of +17dBm	

The analysis of the first three lines in Table III (in grey) highlights that it is difficult to discriminate the different photo-receivers in terms of linearity since the RoF gains are not equivalent. However, we can easily find on the market high power amplifiers with, for example, a gain of 44dB, a bandwidth of 18GHz, and an output IP3 of 15.3dBm (at 3GHz), as the JS41-00102000-27-10P from Miteq [10] that we have characterized. Thus, a link composed of the HPT and followed by this amplifier will be highly attractive thanks to an output IP3 of approximately +15dBm (fourth line in Table III). In fact, the phototransistor output IP3 multiplied by the amplifier gain is 17dBm, which is higher than the amplifier output IP3. Therefore the phototransistor plus the amplifier IP3 is limited to the one of the amplifier at a level of 15dBm.

Finally, for a point-to-point RoF link composed of the Finisar VCSEL at 850nm and of the HPT we expect an input IP3 of 17dBm (fifth line in Table III), an improvement of more than 20dB compared to previous results at 850nm. In this case we will be limited by the VCSEL non linearities.

The next step will consist in packaging the HPT and in implementing it in a RoF infrastructure.

V. Conclusion

A comparison between optical and electrical multipoint-to-multipoint architectures has been realized in terms of EVM. The electrical solution has the advantage to be laser beats independent, but it induces more important EVM values. To go further, innovative highly linear and potentially low cost components, such as HPT, have to be introduced. Thus, the domestic RoF infrastructures will be significantly enhanced.

At the same time a solution using an optical multipoint-to-multipoint architecture continuously managed by the radio MAC layer is investigated [4] [9] in order to reduce the number of lasers turned-on simultaneously to one and further improve the performances.

Acknowledgment

This work was carried out in the frame of the French FUI8 ORIGIN project. The authors also acknowledge the contribution of the Engineering Research and Development for Technology - Department of Science and Technology (ERDT-DOST) of the Philippines.

References

[1] IEEE 802.15.3c, “Wireless MAC and PHY Layer, Specifications for High Rate WPANs”, October 2009.

[2] WirelessHD, http://www.wirelesshd.org/, August 2009.

[3] IEEE 802.11ad, http://www.ieee802.org/11/, May 2010.

[4] J. Guillory et al., “Radio-over-Fiber architectures, Future Multigigabit Wireless Systems in the Home Area Network”, IEEE Vehicular Technology Magazine, vol. 5, issue 3, pp. 30-38, 2010.

[5] J. Guillory et al., “Radio over Fiber tunnel for 60 GHz wireless home network”, OFC Conference, March 2011, Los Angeles, USA.

[6] J. Guillory et al., “60GHz Intermediate Frequency over Fibre using a passive Multipoint-to-Multipoint architecture”, NOC Conference, July 2011, Newcastle upon Tyne, UK.

[7] J. Guillory et al., “A 60 GHz Wireless Home Area Network With Radio Over Fiber Repeaters”, IEEE J. Lightwave Technology, vol. 29, issue 16, pp. 2482-2488, 2011.

[8] R.A. Shafik et al., “On the Extended Relationships Among EVM, BER and SNR as Performance Metrics”, ICECE, 2006, Dhâkâ, Bangladesh.

[9] J. Guillory et al., “Radio over Fiber for an optimal 60 GHz Home Area Network”, IEEE 11-10-0011-01-00ad Conf. Call, 7th January 2010.

[10] Miteq website, consulted on March 2011 and available on http://www.miteq.com/viewmodel.php?model=JS41-00102000-27-10P.

[11] M.D. Rosales, J.L. Polleux and C. Algani, “Design and Implementation of SiGe HPTs using an 80GHz SiGe Bipolar Process Technology”, in 8th IEEE International Conference on Group IV Photonics, 14-16 September 2011.

[12] M.D. Rosales, J.L. Polleux and C. Algani, “Improving Optical Detection in SiGe Heterojunction Phototransistors”, in 13th International Symposium on Microwave and Optical Technology, ISMOT, 20-23 June 2011.